

Trust, but verify

Collaborations between researchers and industry are essential to biomedical progress. But relations have to be completely open.

Among the lessons learned from the two-year-long investigation of financial disclosure in US biomedicine by Senator Charles Grassley (Republican, Iowa) (see page 330) is that an honour system is only as good as the clarity of its rules — and the effectiveness of the oversight.

Witness the *de facto* honour system that governs the financial activities of researchers receiving support from the US National Institutes of Health (NIH). Under conflict-of-interest rules in place since 1995, extramural grant applicants must report industry payments of more than US\$10,000 per year if those payments would “reasonably appear to be affected by the research” for which NIH funding is sought. The same disclosure rule applies to equity holdings of more than \$10,000, or more than 5% ownership in a company. The reports go to the researchers’ home institutions, which in turn must report the existence of a conflict to the NIH, and assure the agency that they have managed, reduced or eliminated it.

After much investigation, however, Grassley and his staff have alleged that some academic researchers have taken a relaxed approach to this reporting requirement, and that some institutions have been just as casual in monitoring their researchers. The ensuing bad publicity has threatened to undermine the public’s faith in the \$24-billion extramural research effort of the NIH.

But the efforts of Grassley’s team have had one positive effect: after years of ignoring warnings about sloppy conflict-of-interest enforcement — in a 2001 report by the Association of American Universities in Washington, DC, among others — research institutions are hastening to enforce the NIH rules aggressively. Some have even instituted more stringent rules of their own. Soon, they could have a new enforcement tool: the Physician Payments Sunshine Act of 2009, which Grassley has inserted into health-reform legislation now circulating on Capitol Hill. The act would require drug and device firms to post any payments to a physician in excess of \$100 annually on a public website.

Given the recent rash of publicity, some researchers fear that

the very appearance of their names on such a website would imply wrongdoing, as if they were inherently compromised by any collaboration with industry. That risk is real enough. Any website should thus make it very clear that industry–academic collaboration is a valuable, indeed an essential, driver of biomedical innovation; that the translation of basic research to the clinic depends on it; and that it is encouraged both by US law — specifically, the Bayh–Dole Act of 1980 — and by the NIH.

That said, the ubiquitous interconnections between industry and academia — and the very desirability of a permeable boundary between the two — are probably the most compelling argument for the Sunshine Act. The transparency it would provide is a long overdue corrective to a culture that has too often seemed to look the other way when it comes to potential conflicts of interest. Such transparency would both shore up public trust and prompt researchers to tougher self-scrutiny as they complete their disclosures.

It’s important to note that Grassley’s Sunshine Act does not apply to non-physician scientists; he drafted it with medication-prescribing doctors in mind. Yet PhD scientists, too, play a vital part in many industry collaborations. For the sake of fairness and consistency, the act should apply to them as well.

Whether or not the Sunshine Act becomes law, the NIH is moving on a parallel track to tighten its own reporting rules for extramural researchers. A lowering of its \$10,000 threshold for reporting is expected before the end of the year, for example. The agency should bear another principle in mind as it finalizes such changes: clarity in what is and is not reportable, with rules spelled out unambiguously. Increased clarity would protect NIH-funded researchers and the public they serve. ■

“An honour system is only as good as the clarity of its rules — and the effectiveness of the oversight”

Taking the NICE path

The United States can learn from the UK body that rates the effectiveness of medical procedures.

In the highly polarized debate over US health-care reform, opponents of increased government involvement in the system frequently caricature Britain’s National Health Service (NHS) as the disaster they want to avoid — an impenetrable snarl of red tape that keeps ailing pensioners on years-long waiting lists for even the most essential procedures. And at the heart of their nightmare is the UK National Institute for Health and Clinical Excellence (NICE), portrayed as a

bunch of callous government bureaucrats ruling life-saving medications as off-limits to dying patients.

Globally, however, NICE is widely regarded as a world leader in comparative-effectiveness studies: research that aims to show which of the available medical options is most effective at treating any given condition, and which is worth the money — what US reform opponents might call ‘health-care rationing’. Faced with an overwhelming yet incomplete medical literature, most medical professionals welcome NICE’s best-practice guidelines on everything from early testing for breast cancer to child nutrition.

NICE’s politically and emotionally fraught function can arouse intense feelings. In one example last year (see page 336), NICE had to make a Solomonic choice: should the NHS spend an extra £31,000

(US\$51,000) per patient for a treatment that would give a few more months of life to victims of a terminal renal-cell cancer? Or should it spend that money on other potentially life-saving interventions such as breast-cancer screenings, or insulin for diabetics? NICE, following its established cost-benefit guidelines, opted for the latter — and immediately found itself the target of intense organized lobbying to reconsider, which it eventually felt compelled to do, and the institute modified the guidelines for some patients with short life expectancy.

NICE should be extremely cautious about going too far down this road: changes made under pressure from one vocal patient group can make it that much harder to draw the line for the next — and to maintain the agency's commitment to evidence-based decision-making.

However, NICE's decision-making process remains an honest and increasingly open effort to take empirical evidence about clinical effectiveness, and combine it with the value that the British public — not faceless bureaucrats — put on their health and their lives. The available methods for assessing that value do leave something

to be desired. NICE asks people to rate various states of health on a numeric scale, for example — a standard technique in medical economics — even though it is hard to know whether such hypothetical assessments are meaningful to people who are facing death in reality. But there are efforts under way at NICE and by other health economists to improve on such methods. And the United States — where comparative-effectiveness research received a \$1.1 billion boost from the economic stimulus earlier this year — should contribute to this effort.

Meanwhile, even as Americans — and many British citizens — view the UK health-care system with bemusement, the British look across the Atlantic Ocean with equal puzzlement and sometimes horror. They see Americans dying with cancer and losing their homes because they cannot afford treatments that are not covered by a health insurance plan. Millions of people cannot afford to go to a doctor at all.

That is the nightmare that the American politicians must urgently resolve, and they would do well to stop being afraid of NICE and start taking cost-saving lessons from it. ■

SETI at 50

Despite the long odds against success, the search for extraterrestrial intelligence has come a long way.

The search for extraterrestrial intelligence (SETI), a research discipline that celebrates the 50th anniversary of its inaugural publication this week (see page 345), has always sat at the edge of mainstream astronomy. This is partly because, no matter how scientifically rigorous its practitioners try to be, SETI can't escape an association with UFO believers and other such crackpots. But it is also because SETI is arguably not a falsifiable experiment.

Regardless of how exhaustively the Galaxy is searched, the null result of radio silence doesn't rule out the existence of alien civilizations. It means only that those civilizations might not be using radio to communicate. Indeed, SETI is marked by a hope, bordering on faith, that not only are there civilizations broadcasting out there, but that they are somehow intent on beaming their signals at Earth. An alien SETI project relying on a similar faith in Earth would be sorely disappointed. It's true that a random mix of radar and television signals has been expanding outwards from Earth at the speed of light for the past 70 years. But there have been only a few short-lived attempts to target radio messages at other stars — with each attempt arousing concerns over alien reprisals. Understandably, many scientists who support SETI in spirit have instead pursued astronomical targets more likely to offer positive data — and tenure. Governments have also been averse to funding an effort so likely to turn up nothing.

Nonetheless, a small SETI effort is well worth supporting, especially given the enormous implications if it did succeed. And happily, a handful of wealthy technologists and other private donors have proved willing to provide that support. This summer, the Allen Telescope Array, funded mainly by Microsoft billionaire Paul Allen, has begun to sweep the skies with its 42 dishes in the California high

country (see page 324). The sophistication of this array, which it is hoped will grow even larger, shows just how far SETI has come. Whereas the first search in 1960 used a single radio channel, the Allen array can potentially monitor hundreds of millions of radio channels at once. With advances such as this, the speed of the searches — the rate at which star systems can be checked over multiple parts of the radio spectrum — has increased roughly as fast as the exponential growth in computer power described by a law named after yet another SETI supporter, Intel founder Gordon Moore. Moreover, the researchers at the Allen array are solving the immense computing challenges of operating large, multi-dish arrays, an expertise that will benefit the whole of radio astronomy when the time comes to build the huge arrays of the future.

Meanwhile, one of SETI's main missions — finding other worlds like our own — has become much more feasible than it was five decades ago. Very soon, probably within a few years, astronomers will find an Earth-sized planet orbiting another star. The next step will be to characterize it by studying spectroscopic signatures in the light from its atmosphere. Is there a fingerprint for life, in the form of oxygen or methane? How long is its day? What is its weather like? Does it have continents and oceans? For the 'Earths' orbiting nearby stars, answers to all of these questions should be within the reach of telescopes planned for the next decade.

Still, as momentous as it would be to find such indirect evidence for life elsewhere in the Universe, that would not be the same as finding other thinking creatures like ourselves. That will still require SETI in some form. Will we want to beam a message to these other Earths? That is a debate for another day. But we should at least train the Allen array on these worlds. Earth may decide it does not want to open its mouth, but it would be foolish to cover its ears. ■

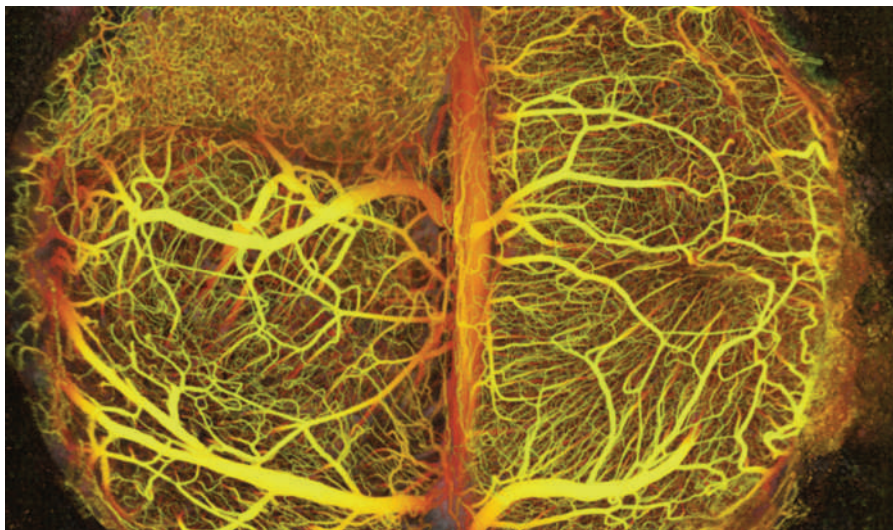
"A small SETI effort is well worth supporting, especially given the enormous implications if it did succeed."

RESEARCH HIGHLIGHTS

Now you see it

Nature Med. doi:10.1038/nm.1971 (2009)

A technique for imaging tissues in three dimensions can be used to visualize the tumour microenvironment in greater detail than previous methods. Brett Bouma, Rakesh Jain and their colleagues at Harvard Medical School and Massachusetts General Hospital in Boston imaged various tumour types using a system called optical frequency domain imaging. It involves scanning a laser beam with shifting wavelengths over a tissue sample, measuring the properties of the reflected light across depths, and processing the signals to reveal three-dimensional perspectives. The image shows the system of blood vessels in a mouse brain with a tumour at a depth of 2 millimetres.



TECHNOLOGY

Lightning-fast memory

Phys. Rev. Lett. **103**, 117201 (2009)

The speed at which information can be recorded on a magnetic disc is limited by the time it takes to 'flip' the magnetic bits on the surface. Like a spinning top, these bits have momentum, and it takes them time to reverse their magnetism from one orientation to another using traditional means.

Now Kadir Vahaplar of Radboud University Nijmegen in the Netherlands, and his colleagues have found a faster way to flip the bits. The team used a powerful pulse of laser light to temporarily destroy and reorient the bits. A second pulse allowed them to read back the data. The entire process took just 30 picoseconds — ten times faster than today's technology.

GENETICS

Yeast joins the club at last

Science doi:10.1126/science.1176945 (2009)

It seemed a stubborn exception. One of the most useful research tools, gene silencing by RNA interference (RNAi), can't be used in a laboratory workhorse organism, the yeast *Saccharomyces cerevisiae*. Indeed, it was thought that the ability to do RNAi had been lost from all budding yeast species at some point in evolution.

But David Bartel of the Massachusetts Institute of Technology in Cambridge and his colleagues took a closer look at some related yeast species. They found all the necessary

components of the RNAi pathway, including a previously unknown version of the Dicer protein, which is essential to the process.

By putting the components into *S. cerevisiae*, they were able to kick-start the pathway, potentially opening up new research directions for both the organism and the nature of gene silencing.

CHEMISTRY

Aluminium arches

Langmuir doi:10.1021/la902918m (2009)

How can the miniature arched structures pictured below be created? When droplets of dissolved or suspended matter dry on a surface, material often spreads to the edges of the droplet forming a 'coffee ring' stain. These rings can pile up into ridges that form cups or hollow domes.

Julian Evans and Lifeng Chen at University College London placed droplets containing an aluminium powder onto circular platforms about 1 millimetre apart. Powder ridges on

adjacent edges of the platforms grew slowly owing to high local humidity, and ridges on the far edges grew faster in the lower relative humidity. The drops eventually bumped into one another and connected, forming arches.

ACOUSTIC SCIENCE

A sonic one-way street

Phys. Rev. Lett. **103**, 104301 (2009)

Diodes act as one-way filters for electric current, protecting delicate devices from sudden reversals in flow. Sound waves can also travel easily in both directions along a given path, like electricity does, so acoustic devices could block wrong-way reflections. Alas, acoustic diodes do not yet exist.

Jian-chun Cheng of Nanjing University in China and his colleagues have now described a possible way to build one consisting of a sandwich of acoustic layers. Key to the structure would be a layer of nonlinear material that, by changing the frequency spectrum of incoming sound waves, could

act as a filter. The researchers suggest that acoustic diodes could be useful in improving ultrasound devices such as those used to break up kidney stones.

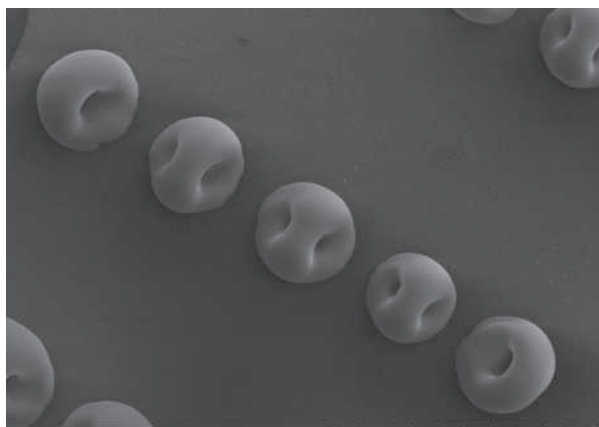
ATMOSPHERIC SCIENCE

Alien sprites

J. Geophys. Res. **114**, E09002 (2009)

Sprites — ghostly flashes of light that occur above some thunderstorms on Earth — may also illuminate other planets' atmospheres.

Calculations suggest that sprites could occur on both Venus and



AM. CHEM. SOC.

Jupiter, if thunderstorms on those planets build up the right amount of charge to trigger the flashes, say Yoav Yair of the Open University of Israel in Ra'anana and his colleagues. Neither Mars nor Saturn's moon Titan are likely to have sprites, though both have the right conditions for lightning.

Japan's Planet-C mission to Venus, due for launch next year, might be able to confirm the existence of the hypothetical sprites.

BIOLOGY

Turning tail

Biol. Lett. doi:10.1098/rsbl.2009.0577 (2009)

When threatened, geckos such as *Coleonyx brevis* (pictured) can jettison their tails in the hope that predators will be too distracted by the writhing appendage to notice the meal that is scurrying away.

Although many have observed the gecko's great escape, the behaviour of the newly autonomous decoys they leave behind is less well known.

Timothy Higham from Clemson

University in South Carolina and Anthony Russell at the University of Calgary in Alberta, Canada, used high-speed video cameras and implanted electrodes to study the tail of the leopard gecko (*Eublepharis macularius*) immediately after shedding. In addition to rhythmic swinging movements, which were probably controlled by motor circuits in the spinal cord, the tail also performed complex acrobatics such as flips and lunges.



D. HEUCUN/NHPA

MICROBIOLOGY

Sussing *Shewanella*

Proc. Natl Acad. Sci. USA doi:10.1073/pnas.0902000106 (2009)

For bacteria, which have notoriously twisted family trees, defining species boundaries requires close knowledge of both genetic and expressed characteristics.

A team led by Kostas Konstantinidis of the Georgia Institute of Technology in Atlanta and James Tiedje at Michigan State University in East Lansing investigated ten strains of bacteria from the genus *Shewanella*, a group with varied, often ecologically important, metabolic abilities. Genome and protein-expression data were

already available for the strains.

By comparing these data sets, the team was able to link genetic factors to ecological role in more detail than before. Also, despite identical culture conditions, protein expression varied more than genome sequence in some cases, so gene regulation could be important for describing species.

MATERIALS SCIENCE

Hard-headed theories

Phys. Rev. B **80**, 060103 (2009)

Physicists recently discovered that materials known as transition-metal diborides rival the hardness of diamonds in one direction but are relatively soft in another. Such materials

have the potential to revolutionize industrial processes — if scientists can work out what makes them so tough in certain orientations.

Theorists had thought that the strength came from strong vertical bonds within the crystal, similar to the ridges in a sheet of corrugated cardboard. But

Antonín Šimůnek of the Academy of Sciences of the Czech Republic in Prague thinks it might be just the opposite. He proposes a model in which strong horizontal bonds between surface atoms act as a tough shell that can resist denting by a sharp tip. The theory could lead to development of new super-hard materials.

NEUROBIOLOGY

Teamwork rewarded

Biol. Lett. doi:10.1098/rsbl.2009.0670 (2009)

Coordinated social activity, such as dancing or team sports, stimulates the brain to release high levels of mood-elevating endorphins that are believed to have a role in social bonding. But how can this be distinguished from the normal release of endorphins during exercise?

Emma Cohen of the University of Oxford, UK, and her colleagues looked at rowers training alone or with teammates on stationary rowing machines. Because measuring endorphins directly would require a spinal tap, the researchers instead used pain tolerance to gauge endorphin release after workouts. They found that rowers had greater increases in pain threshold after operating as a crew than when going solo.

JOURNAL CLUB

Rusty Feagin
Texas A&M University,
College Station, Texas

A coastal ecologist sees the hidden effects of hurricanes.

As part of my job, I often drive around looking at the impacts of hurricanes in coastal areas. The one thing that stands out from such trips is that the devastation always looks the same, regardless of where I am — the boats perched on the streets, the newly house-less stilts near the beach, the furniture on a lawn covered in mould.

I realized though, after reading a recent article by Hongcheng Zeng of Tulane University in New Orleans, Louisiana and his colleagues (H. Zeng *et al. Proc. Natl Acad. Sci. USA* **106**, 7888–7892; 2009), that I need to be concerned with the damage that I cannot see — the bleeding of carbon from the landscape, and the loss of future carbon stores.

Using field, satellite and modelled data, Zeng and his colleagues detail how damaging winds over the past 150 years have greatly reduced forest biomass through tree mortality, subsequent wood decay and carbon release. They estimate that between 1980 and 1990, 9–18% of the amount of carbon stored yearly by US forests was lost due to destruction caused by tropical cyclones. The carbon dioxide loss is cumulative because once a tree is lost, it cannot sequester CO₂ in the future. Thus, an extreme event such as Hurricane Katrina in 2005 or the Indian Ocean tsunami in 2004 could radically reduce carbon sequestration in the areas affected for several decades.

These findings force me to consider more than just the visible effects of hurricanes; I realize that tree loss is in effect altering the global carbon cycle. This paper also makes me wonder about the cumulative impact of cyclones on CO₂ in other ecosystems, such as grasslands that have been damaged by salt-water inundation, or even possible forest growth due to storm-induced rainfall inland.

Discuss this paper at <http://blogs.nature.com/nature/journalclub>

NEWS BRIEFING

● POLICY

Carbon tax: France may become the first major European economy to introduce a carbon tax, after President Nicolas Sarkozy announced on 10 September that he plans to implement a levy, from 2010, on activities emitting substantial amounts of carbon dioxide. Petrol, diesel, coal and natural gas would cost an extra €17 (US\$25) per tonne of carbon dioxide emitted. Sarkozy also suggested that a carbon tax could be put on imports. For more, see <http://tinyurl.com/lfv6th>

Climate strategy: The US Department of the Interior has launched a new strategy to tackle the impacts of global warming. On 14 September department secretary Ken Salazar announced he would head a climate-change response council, which will coordinate climate science and land management in the department. Eight regional science centres of the US Geological Survey are to expand into 'response centres', providing guidance on the impacts of climate change to department bureaux such as the Fish and Wildlife Service.

Emissions bill: The European Union (EU) might have to pay developing countries up to €15 billion (US\$22 billion) a year by 2020 to help them combat climate change, according to a proposal published by the European Commission on 10 September. The commission estimates that developing countries will need €100 billion annually by 2020, half of which would have to come from international public funds.

Pandemic flu: The US National Institute of Allergy and Infectious Diseases reported on 11 September that early data from its own trials of pandemic H1N1 flu vaccines, manufactured by French company Sanofi Pasteur and by CSL Biotherapies in



This image of the 'Butterfly nebula' (NGC 6302) was among a series of deep-space photos released by NASA from the upgraded Hubble Space Telescope last week — the first images to be published since the iconic orbiting observatory's servicing mission in May (see *Nature* 459, 21; 2009), which should allow it to keep producing images until 2014.

NASA; ESA; HUBBLE SM4 ERO TEAM

Pennsylvania (see *Nature* 460, 562; 2009), confirmed the encouraging results of company trials. All the data suggest that one dose is enough to provoke a robust immune response in healthy adults — not two doses as widely anticipated. The latest studies showed that an adjuvant (a booster chemical) is not required for this effect.

● BUSINESS

Stem-cell hype: The US Securities and Exchange Commission (SEC) has accused a stem-cell biotech company, and its former chief executive and former chief scientific officer, of inflating claims about an early-stage cell therapy. **CellCyte Genetics Corporation**, based in Bothell, Washington, told investors that an experimental compound that helps stem cells migrate to specific organs of the body had been approved for human trials to treat heart damage. In reality, the company had neither formulated the compound nor attempted experiments to repair tissue, the SEC claims. For more, see <http://tinyurl.com/ly75sp>

Vaccine venture: US pharmaceutical giant Merck and the UK's Wellcome Trust have launched a joint not-for-profit £90-million (US\$150-million) medical research centre in India to develop affordable vaccines for **neglected diseases**. This is the first time that a pharmaceutical company and a major medical research charity have entered into a bilateral partnership to create vaccines aimed at low-income countries. For more, see page 323.

Solar giant: A US company announced plans on 8 September to build what could be the world's largest solar-power plant in the **Inner Mongolia** region of China. Backed by a feed-in tariff that will guarantee long-term electricity sales, **First Solar**, based in Tempe, Arizona, plans to install thin-film panels that have a total generating capacity of 2,000 megawatts in Ordos City by 2019. First Solar also agreed to explore the possibility of building manufacturing sites in Ordos and expanding other operations in China.

**NUMBER
CRUNCH
\$11 billion**

The loss sustained by Harvard's invested endowment assets in the fiscal year ending 30 June, a 27.3% hit. The endowment fund now sits at \$26 billion.

● AWARDS

Lasker award: The US\$250,000 prize for basic medical research — which often presages a Nobel prize — has gone to British biologist **John Gurdon** at Cambridge University and **Shinya Yamanaka** at Kyoto University, Japan, for their independent work on the processes that instruct specialized adult cells to form stem cells. In 2006, Yamanaka created induced pluripotent stem cells from mouse skin cells (see *Nature* 458, 962–965; 2009). The achievement was the culmination of work begun by Gurdon in the late 1950s, when he first transplanted nuclei from a tadpole's intestinal cells into frog eggs, pioneering the technique of nuclear reprogramming to clone animals.

● RESEARCH

Researcher arrest: A senior scientist at RIKEN, Japan's premier research institute, was arrested last week for allegedly misappropriating research funds. Tatsuo Wada, who studies the behaviour of supramolecular assemblies of organic molecules, allegedly placed **fictitious orders** worth ¥11.7 million (US\$128,000) from RIKEN to Akiba Sangyo, a Tokyo-based company that distributes scientific equipment. The company's president, Etsuo Kato, was also arrested, and RIKEN has begun legal proceedings against Wada to recover the funds. For more, see page 327.

NEWS MAKER



London's Natural History Museum opened a £78-million (US\$130-million) Darwin Centre to the public on 15 September. Its Cocoon building houses a space for visitors to peer at scientists in the lab.

Brain drain: The immediate dismissal of 200 scientists from an Israeli government programme that provides jobs for high-level immigrant scientists was averted last week — but the future of the \$40-million-a-year programme remains in doubt. Protests by scientists and universities led to a cabinet decision to restore 2009 funding for the **KAMEA programme**,

which pays the base salaries of around 500 scientists who have emigrated to Israel, mainly from the former Soviet Union. Entrance to the programme has been frozen and further changes are under consideration. For more, see <http://tinyurl.com/news-2009-912>

Publication policy: Members of the National Academy of Sciences will from July 2010 no longer be able to communicate work by a non-member for publication in the *Proceedings of the National Academy of Sciences*, the journal announced last week. Instead, non-members must submit papers directly to the journal for peer review, although they may ask an academy member to edit their paper first.

● EVENTS

Agronomist dies: Norman Borlaug, who won the 1970 Nobel peace prize for his role in tackling world hunger, died on 12 September aged 95. Borlaug developed high-yield, disease-resistant wheat, kick-starting the “green revolution” in the 1960s, which dramatically increased food production in the developing world. He was a distinguished professor at Texas A&M University, in College Station. A full obituary will appear in a forthcoming issue.

Herschel glitch: One of three instruments on the Herschel Space Observatory, which was launched by the European Space Agency in May to study the young Universe, stopped

THE WEEK AHEAD

21-23 SEPTEMBER

Baltimore, Maryland, hosts the 2009 World Stem Cell Summit.

► www.worldstemcellsummit.com

22 SEPTEMBER

United Nations secretary-general Ban Ki-moon convenes a summit on climate change in New York.

► <http://tinyurl.com/mnjgw7>

23-25 SEPTEMBER

The research goals of a new international ocean drilling research programme will be set at the INVEST meeting in Bremen, Germany.

► www.marum.de/ioldp-invest.html

24-25 SEPTEMBER

Climate change looms large on the agenda of the G20 summit in Pittsburgh, Pennsylvania.

► www.pittsburghg20.org

working more than a month ago. The **Heterodyne Instrument for the Far Infrared (HIFI)**, performs high-resolution infrared spectroscopy and is intended to detect elements in gas clouds swirling in star-forming regions. HIFI's project leader, Peter Roelfsema, says he is confident it will be switched on again, but doesn't yet know what caused the instrument's shutdown. For more, see <http://tinyurl.com/r2l35t>

BUSINESS WATCH

Osiris Therapeutics of Columbia, Maryland, saw its share price plummet on 8 September (see chart) after announcing that its stem-cell therapy had failed late-stage clinical trials. Prochymal, which consists of cultured mesenchymal stem cells taken from bone marrow, was no better than a placebo at subduing graft-versus-host disease — a potentially fatal complication in bone-marrow transplants in which immune cells from the donated marrow attack the recipient.

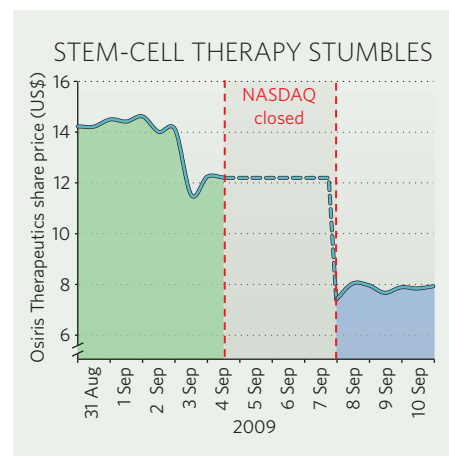
“I do think it's a blow to the stem-cell community,” says Edward Tenthoff, an analyst at Piper Jaffray in New York. The good news, he says, is that “it's a failed trial, not a safety concern”. Last month, biopharmaceutical firm

Geron, of Menlo Park, California, had to delay its trial of embryonic-stem-cell therapy for spinal-cord injury for a second time after animal data revealed microscopic cysts growing around the injury site.

Researchers think that mesenchymal stem cells could still be an effective way to treat some patients. “Even though it seems to the business world to be a setback, I think [researchers] can learn and go on,” says Pranela Rameshwar, a stem-cell scientist at New Jersey Medical School in Newark.

Shares in various other stem-cell companies were unaffected by the Osiris trial results.

For more, see <http://tinyurl.com/m8976j>



Vaccine venture boosts health hopes

Industry and academia join forces to develop cheap jabs against diseases that afflict the poorest.

US pharmaceutical giant Merck and Company and the UK Wellcome Trust will create a joint, not-for-profit £90-million (US\$150-million) research centre in India to develop affordable vaccines against diseases that afflict the poor — including neglected diseases for which inadequate or no vaccines exist. The move marks the first time that a major medical-research charity and a pharmaceutical company have directly partnered to create vaccines aimed at low-income countries.

“It’s a tremendous development,” says Adel Mahmoud, a former president of Merck Vaccines and now a professor at Princeton University in New Jersey. Unlike drugs for neglected diseases, he says, “vaccines for neglected diseases have not been given any significant attention over the years.”

The new research centre will be named after the late Maurice Hilleman, a Merck scientist who developed more than 40 vaccines, including against measles and hepatitis B. Its location in India has yet to be selected, but it is expected to open by the end of next year.

The centre will be headed by Altaf Lal, currently health attaché at the US embassy in New Delhi and the South Asia regional representative for the US health and human services department. Lal says it will bridge the translational research gap that exists between academic scientists and clinical programmes, to help take promising leads to the proof-of-concept stage.

Despite being a non-profit organization, the centre will be run as a business, and will be free beyond its £90-million seed funding to pursue partnerships with academics, companies, governments and philanthropic bodies. The centre’s portfolio will include high-risk research into diseases for which no vaccines are currently available, says Ted Bianco, director of technology transfer at the Wellcome Trust in London. It will also aim for more immediate pay-offs, such as improving existing vaccines that are too expensive or poorly adapted for distribution in hot, resource-poor countries, where maintaining a chain of refrigeration is complicated.

“The centre will bring the scientific and technical skills of an extremely advanced vaccine



Vaccines for neglected diseases are non-existent or unsuitable in poor countries.

company like Merck to bear,” says Marie-Paule Kieny, vaccine-research director at the World Health Organization (WHO) in Geneva, Switzerland, adding that the direct involvement of the Wellcome Trust confers considerable credibility on the venture’s goals.

Prospects for vaccines in low-income countries have recently improved. Public-private partnerships have been set up to develop vaccines against the big killers, such as HIV/AIDS and malaria, and the drug firm Novartis last year opened an in-house, non-profit research institute in northern Italy to develop vaccines for diarrhoeal diseases (see *Nature* 451, 1037; 2008). The Geneva-based global health partnership the GAVI Alliance, created in 2000, has also greatly increased and accelerated the introduction and distribution of large volumes of vaccines.

But the crucial missing component has been bringing academic development together with industrial expertise, says Bianco. “Merck are terrific partners to have,” he says. “When making vaccines, know-how is hugely significant, and vaccines are a struggle to get into developing countries without it.” As well as funding the centre, Merck will offer access to its own researchers, its technologies such as adjuvants and its expertise in clinical trials, says Mark Feinberg, the company’s vice-president of medical affairs and policy.

The joint venture has yet to decide which

diseases it will tackle, but will base the decisions on criteria such as scientific and technical feasibility, affordability and whether vaccine formulations will meet the field and other needs of the large procurement agencies such as the WHO, the United Nations Children’s Fund (UNICEF) and the GAVI Alliance. One candidate being explored for vaccine suitability is the Group A Streptococcus bacterium, which causes some 400,000 deaths annually in poor countries but has attracted little research funding.

To start whittling down the list of potential candidates, Wellcome and Merck organized a meeting of scientists and other stakeholders in January this year at a research centre in Kilifi, Kenya, part of the Kenya Medical Research Institute (KEMRI). The two partners have also created an advisory group of external scientists chaired by David Heymann, a former assistant director-general of the WHO and now chairman of the UK Health Protection Agency.

The Indian centre will also collaborate with local pharmaceutical companies that can cheaply produce any vaccines it develops. That’s novel, says Kieny, and may well pave the way for Western vaccine makers to allow generic versions of vaccines, such as those against human papillomavirus or pneumonia, which are available in rich countries but too expensive for poorer ones.

“Affordability will be key in the technical and other choices all along the product design and development path,” says Feinberg. “We really want to lower a lot of the barriers that exist for developing promising products.”

Declan Butler



“We really want to lower a lot of the barriers that exist for developing promising products.”

— Mark Feinberg



SETI INSTITUTE

The Allen Telescope Array, scanning for alien radio signals.

Ear to the Universe starts listening

A large array of radio telescopes has begun its first sustained search for extraterrestrial intelligence (SETI) and at rates faster than ever before. Even so, the project has scrambled to find money to stay open and reach its planned size. “We’ve had a chequered time here,” says Don Backer, director of the Allen Telescope Array (ATA) in Hat Creek, California. “We’re skating on thin ice.”

The ATA has 42 six-metre dishes swivelling in the high desert, far fewer than the 350 dishes planned. In May, the array began combing the centre of our Milky Way Galaxy for alien signals across a broad slice of the radio spectrum. The effort comes 50 years after the concept of SETI was invented (see Opinion, page 345).

Previous searches relied on weeks-long observing runs at facilities such as the Arecibo radio telescope in Puerto Rico. The last major search, Project Phoenix — run by the SETI Institute of Mountain View, California — ended in 2004 and required a decade to check 800 stars across a narrow frequency range. The ATA scans the sky much more quickly, allowing a million stars to be checked in just a few decades, says astronomer Seth Shostak of the SETI Institute, which operates the ATA jointly with the University of California at Berkeley. Shostak says sampling a million stars would offer a good chance of striking on one of the 10,000 intelligent civilizations that might be broadcasting

in the Milky Way, according to an estimate by Frank Drake, who in 1960 developed a formula to estimate this number.

Private donors, often technologists, began to support SETI in 1993, after the US Congress rescinded NASA funding for it. The family foundation of Microsoft co-founder Paul Allen provided US\$25 million, beginning in 2000, to start the ATA. But in 2006, that stream of money was cut off (see *Nature* 444, 9; 2006), as the SETI Institute and Berkeley struggled to find matching donations to complete the array, which to date has cost \$50 million.

Last year, the National Science Foundation (NSF) turned down a proposal to support operations at the array. SETI astronomer Jill Tarter says the NSF’s decision was “like a Catch-22”. The array was big enough at 42 dishes to begin work — and needed money for that — but was not yet big enough to achieve the sensitivity capable of transformational science. Backer hopes that once completed, the ATA, covering vast swaths of sky rapidly, will usher in an era of transient radio astronomy — the study of things, such as supernovae, that go bump in the night rather than shine constantly like stars. Science targets could include the star-fuelling hydrogen that surrounds galaxies, and the radio afterglow of the γ -ray bursts that follow supernovae.

Without the NSF money, the \$1.5-million-a-year operation cost is being paid by the US Air

Force, which uses the array to track satellites and orbital debris. “It’s keeping our doors open right now,” says Backer. The Allen Foundation has given an additional \$5 million since 2006.

Time at the array is split roughly equally: a third to the Air Force, a third to radio astronomy and third to SETI. Increasingly, however, SETI can piggyback on the radio astronomy work.

The ATA is also a testbed for technologies that will be important for the rest of radio astronomy. The array has a wide view of the sky, and within that picture, multiple stars can be analysed simultaneously. This technology, known as beam forming, as well as the immense computing challenge of making a picture from many individual dishes, will be needed in future projects, such as the Square Kilometre Array, which envisions thousands of dishes. “This is where radio astronomy has to go,” says Mark McKinnon, project manager for a \$94-million expansion of the 27-dish Very Large Array in New Mexico. The ATA, he says, “are the only people who are actively doing this”.

Backer has a proposal before the NSF to double the number of dishes to 84. The request would match \$6 million in NSF money with \$5 million committed by five donors, including the Allen Foundation and Taiwan’s Institute of Astronomy and Astrophysics. Backer says a decision is due before the end of the year. ■

Eric Hand

See Editorial, page 316.

“We’ve had a chequered time here — we’re skating on thin ice.”



PUBLICATION BIAS PERSISTS

Fewer than half of registered clinical trials publish their results.

www.nature.com/news

Ghosts still present in the medical machine

VANCOUVER

The medical literature continues to be haunted by ghostwriting — a practice that, in its most extreme form, involves pharmaceutical companies designing and paying for studies or reviews, then seeking a guest author to be credited while the company goes unacknowledged. The problem persists, said experts last week, despite recent drug-company policy changes and efforts by journals to cut down on the practice (see ‘Spectre of industry bias’).

A new survey attempting to quantify the phenomenon looked at more than 600 authors who had published papers in six major medical journals in 2008. Of them, 7.8% indicated there was a ‘ghost’ lurking behind the paper — someone who contributed significantly, perhaps as a writer or statistician, but who wasn’t credited as an author or elsewhere. In a similar 1996 survey, the percentage that identified ghosts was 11%. “It is still a problem,” says Josef Wislar, a research analyst for the *Journal of the American Medical Association (JAMA)* in Chicago, Illinois, who presented the work in Vancouver, Canada, at the 10–12 September Sixth International Congress on Peer Review and Biomedical Publication.

Recent media reports have described how pharmaceutical giant Merck sponsored work about its painkiller Vioxx (rofecoxib), and Wyeth did the same for its hormone-replacement therapy Prempro, without being fully acknowledged in some resulting papers. And GlaxoSmithKline ran a programme in which employees approached doctors to help them write up their experiences with the depression



A paper’s authors are not always apparent from the author list.

medicine Paxil (paroxetine). Three published case studies resulted, none acknowledging the assistant writer, says company spokesman Kevin Colgin.

These high-profile cases involve papers published largely in the late 1990s or early 2000s, and Merck, Wyeth and GlaxoSmithKline have all since changed their policies to strengthen rules on disclosure. Yet medical-journal editors say the issue continues.

“We receive several manuscripts a month that are suspicious,” says William Tierney, co-editor-in-chief of the *Journal of General*

Internal Medicine in Indianapolis, Indiana. These include, for example, favourable reviews for new drugs apparently penned by authors who had not previously published on that topic.

Whether such ghostwriting has an adverse effect is hard to pin down. The aim of sponsoring and writing papers is simply to “broaden knowledge about the latest science,” says Wyeth spokesman Doug Petkus. But Drummond Rennie, deputy editor at *JAMA*, says that ghostwritten papers tend to have more positive conclusions and can be used to market off-label uses of drugs.

Journal editors can fight the practice by having strict rules on disclosure and by publishing the specific contributions of each author, says Jenny White, a research analyst at the University of California, San Francisco. In work presented at the Vancouver meeting, White found that among journals targeted by a ghostwriting campaign by Parke-Davis — a subsidiary of Pfizer — for Neurontin (gabapentin), used to relieve neuropathic pain, the journals that published the work were less likely to have strong rules about authorship and disclosure than those that did not. Still, only 4 of 26 journals she studied explicitly mention ghostwriting in their policies today.

The World Association for Medical Editors recommends that journal editors “publish a notice that a manuscript has been ghost written, along with the names of the responsible companies and the submitting author”, alert the academic institution involved and provide the media with details if contacted about the case.

Many journal editors do this. “We name and shame constantly,” says Rennie. But, says Christine Laine, editor of the *Annals of Internal Medicine* in Philadelphia, Pennsylvania, the only way to stop the ghostwriting is if “respected names in academia” stop being “willing to put their names on papers they have not been fully involved in, or without proper acknowledgements”.

“I work regularly with scientists employed by drug companies, and to a person they are honest, ethical and interested in the truth,” says Tierney. “These ghostwriting misadventures are the product of the drug companies’ marketing offices, and they are maddening.”

Nicola Jones

Spectre of industry bias

In the fight against possible bias in industry-sponsored work, the *Journal of the American Medical Association (JAMA)* has gone further than most journals in attempting to root out ghost authors. Since 2005, it has insisted that industry-affiliated papers undergo independent statistical review.

To find out what effects this has had, Benjamin Djulbegovic, who studies

medical decision-making at the University of South Florida in Tampa, tracked publications in *JAMA*, as well as in the *Lancet* and the *New England Journal of Medicine*.

He found that commercially funded papers had dropped from 60% to 47% of studies published in *JAMA*, while increasing slightly at the other two journals. Catherine DeAngelis, editor of *JAMA*, says the journal’s overall

publication rate, impact factor and advertising sales have not gone down. One possible interpretation, both say, is that companies with something to hide are avoiding *JAMA*.

“They’re not going to send it to us if there’s going to be hanky-panky,” says DeAngelis.

Alternatively, says Djulbegovic, authors could be avoiding the cost of the extra analysis, or the change could be unrelated to the policy. **N.J.**

Q&A: Choon Fong Shih

On 23 September, King Abdullah of Saudi Arabia will open the new King Abdullah University of Science and Technology (KAUST), an endeavour to build an internationally competitive university from scratch. Officials say they have recruited some 70 professors, mainly in chemistry, physics, mathematics and engineering; fewer than 10% of them, however, are women. KAUST has furnished laboratories with cutting-edge equipment, including a 222-teraflop Shaheen supercomputer from IBM. But questions remain over whether KAUST can become a true player on the international stage and whether academic freedom can flourish there. *Nature* spoke to Choon Fong Shih, its first president.

Why did you take the job?

King Abdullah's vision captured my imagination. The king spoke of KAUST as rekindling the Islamic spirit of learning and scientific inquiry, of inspiring a new age of scientific achievement for the region.

In fact, the king spoke of KAUST as the new House of Wisdom. The Islamic House of Wisdom was a centre of learning; it drew the very best minds from the known world to discover knowledge, to share knowledge and to apply knowledge.

Why did the king decide to invest so much in KAUST?

He sees KAUST as a catalyst to bring about a new age of scientific achievement.

Western countries have invested in their universities for centuries. Today we see the fruits of that investment. The investment in higher education and in research is a recent investment for this part of the world, and I believe in time we will see the fruit and the benefit.

What are your key aims for the university?

I see KAUST as a new paradigm in academia, advancing the frontiers of science, harnessing science and technology to address some of the global challenges of our time. So that means discovery and the creation of results, and also applying those results to the problems that face humanity.

We want to stand with the leading research universities around the world. In a generation or so, we will stand among them.

How will you quantify success?

We hope in ten years that our publications per academic will be equal to those of the very best research universities. We are looking at the metrics, both qualitative and quantitative, to be comparable to the top research universities around the world.

But, more than that, we will encourage partnerships with major corporations.

How has the world financial downturn affected KAUST? Do you still have a \$10-billion endowment?

The endowment is in good hands; it is intact and we are doing well. Besides the endowment, we have other sources

from regions affected by the economic downturn.

Will home-grown talent eventually form the bulk of the faculty?

KAUST recruits by global standards. We will not be taking our own students as faculty members because they graduated from KAUST. They will be subject to the same standards we apply to candidates around the world.

I believe that our PhD graduates will be very competitive for faculty positions at KAUST and around the world.

How do you encourage women to come to KAUST? Aren't they put off coming to Saudi Arabia because of the stiff restrictions on life outside the university?

We have many women on campus. This is a research environment. Our people here — men and women — enjoy the same opportunities, the same resources, as they would find in America, in Europe and in Asia.

What research areas are you tackling? Will you eventually work in politically difficult fields, such as nuclear research?

We have a very active programme in renewable energy. We have a programme to turn sea water into clean, potable water. We are doing plant biology so we can grow plants in arid conditions and green the

desert land into arable land.

We are looking at some of the most pressing challenges of our time. There is no shortage of exciting problems. Our plate is full.

How long do you intend to stay at KAUST?

I spent 30 years in the East, I spent 30 years in North America, and with some luck I hope to spend 30 years at the confluence of East and West.

Interview by Daniel Cressey



KAUST

of revenue to support KAUST: we have sponsored research that brings in revenue from working with companies, we are sending proposals to government funding agencies and other funding agencies around the world, and we have benefactors who are contributing because KAUST has captured the imagination. We also have tuition income.

We see this as an opportunity. We work harder to recruit the best academics

RIKEN scientist arrested

A Japanese researcher, well known for his work on 'supramolecules', was arrested last week for allegedly misappropriating research funds. The scientist, Tatsuo Wada, is based at the Advanced Science Institute in Wako, part of Japan's network of research labs known as RIKEN.

The case is an embarrassment for RIKEN, which has an annual budget of ¥100 billion (US\$1 billion) and whose researchers are often looked at enviously for their generous funding. "We expect to get strong criticism for this," says Haruhiko Maekawa, director of RIKEN's general-affairs division. "We will have to show that our operations are sound." RIKEN president Ryoji Noyori says: "We will put in place thorough protective measures and redouble awareness of these matters throughout the institute so we can meet the public's expectations."

It is the first time in RIKEN's 92-year history that a researcher is alleged to have misappropriated research funds.

Wada is known for creating organic supramolecular systems — assemblies of organic molecules whose shape, size and orientation can be manipulated to convey information. He focuses on designing supramolecules that react to light in a way that would allow them to be used in sensors or solar cells. These 'soft optoelectronic' materials could replace semiconductors and other materials that are costly to process. He has also been working on supramolecules that could go into Japan's ubiquitous touch-and-go train passes.

An international review of Wada's work last year said he had "an original approach and the laboratory is to be highly commended for its accomplishments in this area". "He has made some very highly functional and original materials," says Hachiro Nakanishi, a materials scientist at Tohoku University in Sendai who was on the review committee.

But on 3 August, Wada called RIKEN's head of research affairs, Yoshiharu Doi, and apologized for "causing trouble for RIKEN through his transactions with the supplier". He gave no details, says Maekawa.

On 8 September, Tokyo's police department arrested Wada for allegedly transferring payments with RIKEN money of approximately ¥11 million on more than 20 fictitious orders. The orders were to

the account with Akiba Sangyo, a Tokyo-based company that distributes scientific equipment. The police also arrested Akiba Sangyo's president Etsuo Kato, on charges of breach of trust.

Both Wada and Kato are being detained. Neither could be reached for comment while in custody. A person who picked up the phone at Akiba Sangyo said that the company, which could not contact its president, was not prepared to make an official statement. A decision as to whether to proceed to trial is expected by 18 September.

As RIKEN waits for a full tally of the allegedly misappropriated money, it has started legal proceedings against Wada to recover the funds. It has also put together an eight-person committee, composed of a lawyer and accountant from outside the institute, two RIKEN scientists and four other RIKEN staff, to investigate. Maekawa says he expects to have a preliminary report within two months.

The timing is making RIKEN researchers nervous because the recently elected Democratic Party of Japan, which takes the reins this week, has already promised to pare down the "independent administrative institutions", of which RIKEN is one, in an attempt to cut down on corruption and waste. Three years ago, a misappropriation scandal at Waseda University in Tokyo put a funding programme there temporarily on ice (see *Nature* 442, 121; 2006).

Wada has been replaced as head of his group. Maekawa says it is unlikely that Wada will be able to retain his

position as a RIKEN scientist.

Nakanishi says that researchers in Japan suffer from overly strict rules about how grants are used and argues that they should be given more discretion as to how to use their funds. "The government talks on and on about internationalizing research, but if you try ... to invite a foreign researcher or take one out to eat, you can't use the funding," he says. "I've had to use my own money for such work-related expenses."

"But the numbers in this case go far beyond the kind of money I'm talking about," he adds.

Criminal proceedings against Wada and Kato could carry a jail term of 5 years or a ¥500,000 fine.

David Cyranoski

"He has made some very highly functional and original materials."

Wonder weed plans fail to flourish

The first of four weekly articles on biofuels looks at how investment in jatropha is slowing, as investors realize that basic research is needed.

THE BUSINESS OF BIOFUELS

The promise of green gold is fading from *Jatropha curcus*, a shrub that thrives in arid conditions and whose seeds yield a diesel-like oil. Many had seen it as a potential saviour for marginal lands, a plant that could lift developing countries out of poverty and into a sustainable oily future.

Just last year, some analysts were predicting that the area planted with jatropha worldwide — at the time, 721,000 hectares — would rise as high as 22 million hectares by 2014. The Jatropha Alliance, an advocacy group based in Berlin, was estimating that investments of up to US\$1 billion could be expected annually. More than 130 companies were in the race, dominated by D1 Oils of London, which in 2007 had landed a \$160-million deal with oil giant BP.

But this July, BP and D1 announced that their deal was off. And of 140 investments made in biofuels so far this year, says analyst Harry Boyle of London-based New Energy Finance, only four or five have been in jatropha projects. “Jatropha has gone very quiet,” he says.

What happened? It's difficult to untangle the impacts of the global financial downturn from disappointment with jatropha in particular, says Rob Bailis, an environmental scientist at Yale University. But “over the past three years, the investment got way ahead of the plant science,” he says.

Early investors are now realizing the plant's limitations. Jatropha can live in very dry conditions, but doesn't necessarily yield a lot of seeds. The plant takes three years or more to reach maturity, requiring care along the way. And jatropha seedlings are often not well-suited to the climate in which they are planted.

Even supporters acknowledge that the allure of jatropha is fading somewhat. “This year, a lot of projects did not continue,” admits Thilo Zelt, director of the Jatropha Alliance.

One blow came with the publication of a controversial paper in June, in which a team led by Arjen Hoekstra at the University of Twente in the Netherlands suggested that jatropha needs more water than other bioenergy crops, such as maize (corn), to produce the same amount of oil (W. Gerbens-Leenes *et al. Proc. Natl Acad. Sci. USA* **106**, 10219–10223; 2009). Jatropha

“Over the past three years, the investment got way ahead of the plant science.”



Billion-dollar investment plans for large-scale farming of the jatropha biofuel crop are on hold.

had nearly four times the water footprint of sugar-cane ethanol, for instance.

Critics point out what they see as flaws in that analysis, including the fact that it is difficult to compare jatropha, which is wild, with crops such as maize that were domesticated for optimal use thousands of years ago. In addition, the analysis looked at a small number of plantations, all of which had young trees, which could skew the conclusions, says Bart Muys, a forest ecologist at the University of Leuven in Belgium. But Hoekstra says that more thought needs to be given to variables such as where jatropha is planted and how it is harvested. “Jatropha was the hal-lelujah crop,” he says, but in reality “it is just another crop with its own characteristics”.

The split between D1 Oils and BP has hurt jatropha's reputation as a good business investment, says Boyle. In a statement, BP spokeswoman Sheila Williams said that “the decision to pull out of this is purely based on economics and a decision to focus on key strategic areas”, such as sugar-cane ethanol from Brazil, cellulosic ethanol from the United States and biobutanol. In the meantime, D1 Oils has shifted from planting jatropha to focusing on basic research

— including starting a breeding programme to develop seeds with high oil yields, says Henk Joos, the company's head of plant science.

Another company concentrating on basic science is SG Biofuels, based in Encinitas, California. It has collected samples from jatropha plants growing wild in different environments and is creating a library of genetic material from which it intends to develop enhanced seed strains to test, says chief executive Kirk Haney.

Eventually, jatropha might prove more useful on a local scale. For instance, Diligent Energy Systems, a company based in Eindhoven, the Netherlands, has set up small-scale operations in Tanzania, where it provides jatropha seeds for farmers to plant among other crops or on spare land that is unsuitable for food crops. The farmers are guaranteed a price for the oil seeds they produce, and so have an incentive to tend the crop and harvest it carefully, says company founder Ruud van Eck. Some 5,000 farmers are involved, he says, with a total of 3,500 hectares of jatropha planted between them. “The idea is to grow to 10,000 by the end of this year,” he says.

In other countries, jatropha has yet to capture local support. In the Lao People's Democratic Republic, farmers have been bombarded with seeds and promotional material from companies but received little to no support, says

K. SIA/AFP/GETTY IMAGES

**HAVE YOUR SAY**

Comment on any of our
News stories, online.

www.nature.com/news

Jakob Rietzler of the Lao Institute for Renewable Energy in Vientiane. As a result, he says, the jatropha they planted reached harvest at the same time as the rice crops. "Farmers neglect their jatropha seeds because they have to harvest their rice," he says.

In India, where much of the jatropha hype originated, success will come only if a conservative, realistic approach is adopted at the beginning, says Pushpito Ghosh, director of the Central Salt and Marine Chemicals Research Institute in Bhavnagar. Biodiesel from his institute's jatropha project (see *Nature* **449**, 652–655; 2007) has been used in test cars belonging to the project and in collaboration with General Motors. Ghosh's team has been working to improve the genetic stock of their jatropha, and is about to embark on a life-cycle analysis of how much biodiesel jatropha can generate from a 50-hectare plot.

Even so, "it would be premature to call [jatropha] a success in India," says Ghosh. "It is still in the take-off stage."

He sees the hype and subsequent disappointment surrounding jatropha as a weeding-out process, leaving behind smaller, more profes-



More oil per seed is the goal.

sional players. These include the Australia-based Jatofil, which in August announced a memorandum of understanding with the European biofuel producer PT Waterland. The deal is expected to give Jatofil between 1,000 and 2,000 hectares of established jatropha-bearing land in Java. And China, one of the world's leading biofuel manufacturers, is also taking an inter-

est in jatropha, with 105,000 hectares planted in the country by 2008 and a total of 700,000 predicted by 2015.

The next year is likely to see more basic research into the crop. Muys and his team, for instance, have analysed global land suitability and developed a high-resolution map to show where jatropha might grow best; Madagascar, Tanzania and Ethiopia are likely candidates. Meanwhile, Bailis is conducting jatropha life-cycle analyses to account for land-use change in India and Brazil. Zelt says that seeds optimized to produce more oil will be entering the market in the coming months, and the first real second-generation plants will be planted next year.

So although jatropha may not be a saviour plant, transforming vast quantities of desert land into biofuel-producing moneymakers, it is likely to find its niche as a local alternative in certain developing countries. "We need to find ways to use local business resources more efficiently," says Jeremy Woods from Imperial College London's Centre for Environmental Policy. "And jatropha can play a big part in that." ■

Katharine Sanderson

NEXT WEEK: BIOALGAE

T. SANTIKO BUDI/JIWA FOTO/ZUMA PRESS



THE SENATOR'S SLEUTH

Paul Thacker, a reporter-turned-Congressional-investigator, has disrupted the careers of several top researchers with lucrative industry ties. **Meredith Wadman** tracks his effect on US science.

In February 1991, a US Army specialist, one month past his 21st birthday, was busy driving huge supply trucks bearing tank ammunition through the Saudi Arabian desert as part of the US First Infantry Division in the Gulf War. At night, he would watch the vast desert sky, lit by the bombs of US warplanes pounding Saddam Hussein's Iraqi troops.

"You felt sorry for them," he recalls, "but better them than us."

At the same time, half a world away, a 41-year-old MD-PhD at Duke University in Durham, North Carolina, was preparing to move to Emory University in Atlanta, Georgia. There he would take over an academically obscure psychiatry department and turn it into a Mecca of psychiatric research — in the process making himself a magnet for megabucks from the pharmaceutical industry.

Both men were bright, driven, ambitious and not easily deterred from their goals. But in an unlikely collision, 17 years later, one would

dramatically change the life of the other.

The army specialist was Paul Thacker — now an investigator working for Senator Charles Grassley (Republican, Iowa). Thacker is the point person behind a far-reaching probe into the financial reports required from biomedical researchers who receive federal funds. The rising academic star was Charles Nemeroff, the chair of psychiatry at Emory until he was forced out of that position last December as a result of Grassley's investigation. Thacker had requisitioned documents from the pharmaceutical industry showing that Nemeroff had violated National Institutes of Health (NIH) rules by failing to declare to the university at least \$1.2 million in income from drugmakers.

Nemeroff is not the only academic target that Thacker has hounded in the past 18 months. He has identified seven other physician-researchers who broke NIH rules by not disclosing large payments from drug and device companies. In several cases, the researchers were involved in

human trials of the products made by some of the very companies with which they had financial relationships. The revelations and the ensuing negative publicity have had profound effects on US universities and biomedical scientists. So far, several dozen leading research institutions in the United States have tightened their financial oversight or are in the process of doing so. And the NIH is planning to strengthen the conflict-reporting requirements for universities and researchers who receive its funds. The outcry has also created support for a federal law proposed by Grassley, the Physician Payments Sunshine Act, which would require drug and device companies to register on a public website virtually all payments made to physicians.

By the unwritten rules of most congressional offices, employees such as Thacker work behind the scenes and rarely get mentioned by the press. But the path that Thacker took to becoming the ethics cop of US biomedicine shows how one Senate employee can affect an

M. TEMCHINE

entire field of research. Thacker has become worrisome enough to university officials that this March, administrators at Tufts University in Medford, Massachusetts, where Thacker was making preliminary inquiries about a researcher, refused to participate in a public ethics discussion unless Thacker was taken off the list of planned speakers.

The Grassley investigation "has changed the practice of medicine," says Steven Nissen, a cardiologist at the Cleveland Clinic in Ohio, which last December began requiring its physicians to publicly disclose industry payments of more than \$5,000 a year. "And Paul Thacker is the bulldog that's leading the charge."

That canine breed comes up frequently in descriptions of Thacker, a former investigative reporter. His tenaciousness, however, hasn't always been well received. Three years ago, Thacker was fired from *Environmental Science & Technology*, a publication of the American Chemical Society (ACS), based in Washington DC, which represents academic and industrial chemists. He had written a series of exposés that a senior ACS official claimed showed an anti-industry bias.

Many, both inside and outside the biomedical research community, have praised the Grassley team's investigation for helping to clean up the field. But others contend that Thacker's zeal, given the power of Senate backing, has crossed the line from vigilant to harmful; that, however egregious his findings about researchers such as Nemeroff may seem, he is using a damningly broad brush that tars an entire community, the great majority of whom are playing by the rules. What's more, institutions and the federal government, in the interest of fuelling drug discovery, encourage researchers to foster industry collaborations, an art that Nemeroff had perfected.

A case such as Nemeroff's "has been portrayed as this black and white thing and it's not. It's nuanced and it's subtle and it's difficult. And there are a lot of aspects to this whole issue where there are no right answers," says Joseph Cubells, a neurogeneticist at Emory and a colleague of Nemeroff.

From Iraq to Congress

Thacker is a compact man with short-cropped blond hair, intense blue eyes and an open, direct manner. He makes \$63,000 a year working in a small, windowless room deep in Grassley's warren of offices in the Hart Senate Office Building on Capitol Hill. He is assisted piecemeal by other employees, including interns, bringing to roughly two the number of full-time people that Grassley has devoted to the

NIH investigation.

Thacker grew up in California and Texas, the eldest child of a construction supervisor and a childcare worker. He joined the army after high school and served in Saudi Arabia and Iraq during the Gulf War. After obtaining a biology degree at the University of California, Davis, in 1997, he moved to Atlanta and went to work at Emory as a biomedical lab technician. He was thinking of going into science but dreaded the prospect of more classwork. Soon, he was writing pieces on faculty doings for *The Emory Report*. In 2000, he left for a journalism internship at *Audubon Magazine* and later joined the staff of *Environmental Science & Technology*, in an upscale office building two blocks from the White House.

Thacker became known there for both his charm and intensity. He was often seen pacing circuits of the office's square hallway, deep in thought, his hands jammed in his pockets. Alan Newman, Thacker's former editor, recalls Thacker's delight when he was closing in on a story. "He had this laugh — this sort of 'ah-hah' laugh [that said]: 'I got it. I'm seeing the pieces fall together.'"

In May 2006, Thacker published the article that would begin his undoing at the ACS. Called 'The Weinberg Proposal', it focused on a consulting firm based in Washington DC called the Weinberg Group, which offers corporate clients advice on how to 'shape the debate' about potentially toxic compounds. Acting on a tip, Thacker had dug up an unsolicited written sales pitch in which the Weinberg Group proposed using scientists and publications to help the materials firm DuPont dispel con-

cerns about a chemical — perfluorooctanoic acid — that DuPont was being sued over in a West Virginia class-action lawsuit alleging health effects. Dupont did not hire Weinberg for the proposed work but did engage the company in another capacity. Dupont says it settled the claims in 2005 for \$107 million.

Thacker's article would later prompt a congressional investigation by John Dingell (Democrat, Michigan) about Weinberg's involvement defending another controversial chemical. But it also hit a nerve with the ACS president, who communicated his unhappiness to Rudy Baum, the society's top news editor. In a meeting with Baum, Thacker was told that he was too immature for investigative reporting. Baum later



Thacker's probe has provided fodder for reporters.

described the Weinberg piece in the Society of Environmental Journalists' newsletter as a "hatchet job". He said he was "uniformly unimpressed with Paul's journalistic skills".

Others disagreed. The article generated media attention for the Weinberg group and it was part of a package that was honoured by the Society of Environmental Journalists. Baum told *Nature* that Thacker's article was factually correct.

Fired for insubordination

After the Weinberg piece ran, Thacker went on to pursue another investigative story — this time about White House interference in climate science, but he was not allowed to publish the piece. So he found a new job and gave his notice, then published the climate story on Salon.com. Two days before he was scheduled to leave the ACS, he was fired for insubordination.

Despite that setback, Thacker left with a set of new skills that soon helped him make the switch from journalism to congressional investigator, a position that tends to draw tenacious individuals who often view the world in stark ethical terms. Some journalists say that they look at Thacker with both respect and wariness. "When he started working for Grassley, my feeling was: 'My God, I hope I'm never on the other end of his gun,'" says a science journalist who did not want to be identified for commenting on a fellow reporter.

When Thacker arrived on Grassley's staff in April 2007, the senator was already well known for his investigations, including a probe of how drug-industry payments might be influencing advisers on government drug approvals. Thacker himself had spent little time thinking about the finances of biomedical researchers. But within weeks of his hiring, he was inspired

"The Grassley investigation has changed the practice of medicine."

— Steven Nissen

J. SCOTT APPLEWHITE/AP PHOTO

to pursue a new investigation on that topic. The impetus was an article in *The New York Times* describing payments from drug companies to psychiatrists in Minnesota, the only state that at the time required companies to make public their payments to physicians. *The New York Times* had found that the psychiatrists taking the most from companies were more likely to prescribe a controversial class of anti-psychotic drugs to children.

Melissa DelBello, a psychiatrist from the University of Cincinnati in Ohio, was quoted in the story, refusing to disclose how much she made from the drugmaker AstraZeneca. DelBello had published a company-funded study in 2002 that reported positive results for AstraZeneca's anti-psychotic drug Seroquel (quetiapine) in adolescents with bipolar disorder. Sales of the drug jumped 27% the year after publication. "Trust me, I don't make much," she told the newspaper. (DelBello later said she was misquoted, that she had been referring only to her fee for giving a single lecture.)

The "trust me" quote caught Thacker's eye. Still holding the newspaper, he walked into the office of Emilia DeSanto, Grassley's chief of investigations. "This reads like nonsense," Thacker told her. From working for the *Emory Report*, he added, he knew that researchers had to file financial-interest disclosure forms with their universities. Thacker drafted a letter to the general counsel of the University of Cincinnati, requesting copies of DelBello's disclosure forms. Days later, it went out with Grassley's signature.

Missing money

Three months later, Grassley made a nine-minute speech on the Senate floor launching his investigation by announcing that AstraZeneca had said it had paid DelBello more than \$180,000 in 2003 and 2004, the first two years after the Seroquel study was published. The money was for lectures, consulting fees, travel expenses and other services.

Within days, DelBello and the University of Cincinnati challenged Grassley in comments that appeared in the online publication *Inside Higher Ed*. University spokesman Richard Puff said that Grassley had falsely implied that she was disingenuous. "She has been completely open in disclosing her payments. She's made complete disclosures to the university and its [institutional review board]. Furthermore, she's made full disclosure to the Senate Finance Committee," he said.

Thacker read the article and wasn't happy. Several days later, on a "lark", he says, he attached a question to a letter going out the door to AstraZeneca from another Grassley staffer on another matter. He asked the company for records of



Senator Charles Grassley is keen to expose those who do not adhere to NIH rules.

how much it had paid DelBello in recent years.

Even as he was digging into the DelBello case, he was having trouble rationalizing Grassley's involvement in the issue. It had to be linked to the senator's work as an overseer of federal funds: he is the top Republican on the finance committee. Yet the arrangements between DelBello and AstraZeneca were in the private sector. Thacker eventually found the connection: NIH grant recipients are compelled, under federal rules in place since 1995, to disclose financial interests of more than \$10,000 in cash or 5% equity in a company to their universities. "That was the whole hook," Thacker recalls. "You tie in NIH money, that's when a senator can come forward and say: 'Hey look, you're taking taxpayer dollars.'"

After that, "it became a process", says Thacker, of identifying NIH-funded researchers who were probably earning top dollar from drug or device firms, often by following leads in the media or from whistleblowers. Thacker would solicit researchers' conflict-of-interest reports from their universities and simultaneously ask relevant companies to provide their own records of what they had paid those individuals. So far, Thacker and his colleagues have sent letters to more than 30 universities requesting the financial-disclosure forms filed by some 50 researchers. Among the first letters was one that went to Emory University on 25 October 2007, asking for the financial disclosure reports filed between January 2000 and January 2007 by Charles Nemeroff, a leader in the field of psychopharmacology.

Over the next few months, Thacker collected records methodically. He was in his element. "Good investigation to me is like doing science," he says. "You know something before

anybody else knows it."

By spring 2008, he had his ducks in a row. He was also getting ready to work the media as perhaps only a former reporter can, tipping journalists to findings published by Grassley in the obscure pages of the *Congressional Record*. That generated major stories in *The New York Times* and the *Wall Street Journal* along with *Nature* and *Science*, among other science publications. "He really knows how to work the phones and maintain contact with folks in a way I've never seen with anybody else," says Newman.

In April, Grassley took to the Senate floor to announce that AstraZeneca had paid DelBello \$238,000 between 2005 and 2007, during which she had reported receiving \$100,000 from all sources. "Obviously, the university is engaged in the practice of 'trust but did NOT verify,'" Grassley concluded. (When contacted last week by *Nature*, DelBello referred questions to the university, which said that she is closely following a conflict-management plan. The university also said it had strengthened its conflict-reporting policy for researchers.)

Relying on Thacker's harvest, Grassley was just getting warmed up. In June 2008, he reported that three psychiatrists at Harvard University had each under-reported hundreds of thousands of dollars in payments.

Storm at Stanford

The same month, he reported that Alan Schatzberg, the chair of psychiatry at Stanford University in Palo Alto, California, owned equity then worth \$6 million in the drug firm Corcept Therapeutics, in nearby Menlo Park. Schatzberg had co-founded the company to develop the drug mifepristone for treatment of psychotic depression. At the same time, he was principal investigator of an NIH-funded study, which included a component that tested the drug. Grassley's report triggered a media storm and Stanford removed Schatzberg as principal investigator, pending an investigation. The university said that although it believed that Schatzberg and Stanford had not broken any rules, "we can see how having Dr. Schatzberg as the principal investigator on this grant can create the appearance of a conflict of interest". (Schatzberg says that Stanford and the NIH had preapproved his service as the study's principal investigator and that "I did not run the [mifepristone] trial at all". Stanford reinstated him as principal investigator in late July this year after the NIH wrote to the university saying that no rules had been broken; by that time the mifepristone part of the study had concluded.)

Back in 2008, with his investigation making news, Grassley turned up the heat on then-NIH

director Elias Zerhouni to better police grant recipients. “NIH oversight of the extramural program is lax and leaves people with nothing more than questions,” said Grassley in a letter to Zerhouni that he inserted into the *Congressional Record* on 4 June.

Years of trouble

When Emory received Grassley’s letter about Nemeroff, the questions about his finances did not come as a surprise to research administrators there. Over the course of 16 years, Nemeroff had built the psychiatry department into one of the field’s leading centres. But at the same time, he had developed substantial financial ties to many companies and a history of failing to disclose them to the university.

Seen from one perspective, the connections to industry were just what universities and the federal government wanted. In fact, Nemeroff had won a \$3.95-million grant from the National Institute of Mental Health (NIMH) in 2003 that would test at least five new antidepressants developed by the British drug giant GlaxoSmithKline, whose advisory board Nemeroff chaired. In soliciting grant proposals, the NIMH had asked researchers to involve industry as a way to accelerate the development of new drugs.

But Nemeroff had made mistakes in managing these relationships, in the eyes of Emory administrators. By late 2003, officials there had grown concerned enough about his network of industry ties that the university’s conflict-of-interest committee launched an investigation. In a 14-page report issued in May 2004, it concluded that there were “serious lapses” in Nemeroff’s reporting of his relationships with 19 companies.

Two years later, Nemeroff’s name landed in the *Wall Street Journal*. He had favourably reviewed an implantable device as a treatment for depression, without disclosing that he had financial ties to the company

that made the device (C. B. Nemeroff *Neuropsychopharmacology* 31, 1345–1355; 2006). He was also editor of the journal *Neuropsychopharmacology*, where the review was published. A representative of that journal told the *Wall Street Journal* that Nemeroff had filled out author-disclosure forms but did not report his financial ties in the manuscript, as the journal required. Stories such as this one soon caught the attention of Thacker when he was looking for investigational targets.

Privately, Emory tried to rein in its star psychiatrist. “I can’t remember when I have gotten so many complaints about the action of one or



“I plan to use my experience to help others avoid problems with conflict of interest.”
— Charles Nemeroff

more of our faculty from inside and outside the institution,” one administrator wrote in an e-mail to Nemeroff in the wake of the *Neuropsychopharmacology* article controversy.

But the university was singing another tune publicly, especially after Nemeroff landed a \$9.3-million grant from the NIMH for a trial on depression. The three-armed trial aimed to compare the effectiveness of two drugs against cognitive behavioural therapy — ‘talk therapy’ — in people with major depression. Its investigators planned to use genetic scans and brain imaging to see whether there are factors that predispose some people to respond well to different treatments — creating a rational alternative to the ‘try-this-pill-and-see-if-it-works’ approach that is common practice in psychiatry today.

As is typical of large clinical trials — this one originally aimed to enrol 400 people — it took months to gear up. Participants weren’t

easy to find because they had to agree to an arduous 14-week course of investigations and treatment and they couldn’t participate if they had ever been treated for major depression. By August 2008, two years into their funding, the researchers had enrolled just a handful of patients. Still, there was a sense that enrolment momentum was growing.

The NIH, however, had become aware that Grassley’s investigation had found large discrepancies between what Nemeroff had disclosed to Emory and what he had actually earned. Zerhouni quietly approved a suspension of the study in mid-August, forcing the university to stop enrolling patients.

In mid-September, Emory learned in a letter from Grassley about the discrepancies. Of \$2 million he had collected from drug companies between 2000 and 2007, Nemeroff had failed to report at least \$1.2 million. Any hope of keeping those disclosure lapses private disappeared in October when the story broke in the media. At the same time, reporters learned that the NIH had suspended the study.

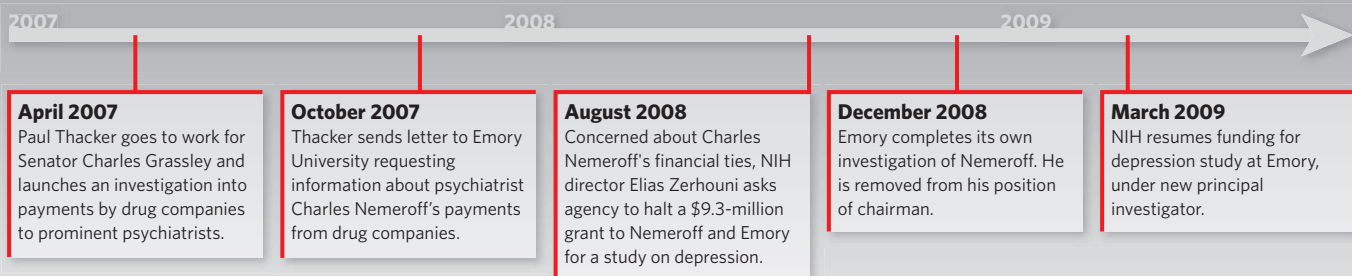
“Frankly, the integrity of the research was at stake,” Zerhouni says, explaining why the NIH had stopped supporting the study. “We said: This can’t continue [under this principal investigator].”

Grassley had wanted this outcome all along. “All NIH should have to do is pull back one grant or refuse to give a grant to a university that’s not [policing conflicts properly] and they all get in line,” Grassley told *Nature Medicine* last September (M. Wadman *Nature Med.* 14, 1006–1007; 2007).

Nemeroff’s study is the only one to have been suspended because of Grassley’s investigations. And ironically, although his financial connections with industry were the source of the problem, the Emory trial is not one that would necessarily be beloved by drugmakers. By including a cognitive-behavioural therapy group, in which patients take no drugs at all,

EMORY UNIV.

HOW DISCLOSURE ISSUES PLAGUED A RESEARCH PROJECT





"I wanted to do something that, when it hits, it reverberates for a while."

— Paul Thacker

it opens the distinct possibility of identifying patient subgroups for whom psychotherapy should be the first-line, or even the only, treatment. The trial's structure, says Cubells, "is a really important example of [Nemeroff's] intellectual honesty. There is a huge prejudice against non-medication treatment approaches in all of psychiatry, due in no small part to the fact that when well-executed psychosocial interventions are provided, no corporate interests profit. Charlie has bucked this trend actively."

What annoys Cubells, he says, is "the unproven insinuation of the Grassley witch hunt that [Nemeroff] is some kind of advocate for pharmaceutical companies because of his ties with the industry".

But others say that the investigation is on the mark and that anger at Grassley is misdirected. "People flouted the rules, didn't disclose, and did it for years on end, repeatedly," says Zerhouni. "That tells you the problem is not Grassley. The problem is our current system of managing conflicts," he says.

Prompted by Thacker's findings, Emory conducted its own investigation into Nemeroff. In December 2008, it announced that Nemeroff had received — and not declared — \$800,000 in payments from GlaxoSmithKline for giving more than 250 talks to psychiatrists between January 2000 and January 2006. Nemeroff told the university that, because the talks dealt with general educational topics, such as the treatment of depression, he didn't consider them promotional and thought they were off-the-books under Emory's rules for declaring outside income. The evidence that Emory examined supported Nemeroff's description of his talks, but the university concluded that he should have declared the income. He was removed from the position of chairman and the university forbade

him to apply for, or be involved with, any NIH grants for at least two years or to receive any outside compensation without prior review and approval by the dean's office. It also issued a statement that the investigation "found no evidence that Dr. Nemeroff's outside speaking activities affected clinical care for patients or persons enrolled in clinical trials, and no evidence that his activities biased scientific research in which he was engaged".

On 4 March this year, the depression study was restarted, this time with a different principal investigator.

Nemeroff, who has not talked with the press since last October when news broke about his disclosure lapses, told *Nature* last week that "I made mistakes in the area of conflict of interest for which I am sorry and remorseful. However the mistakes I made were honest mistakes." He explained that "my actions were, in my view at the time, in keeping with my understanding of the current Emory policies".

Nemeroff adds that he continues to see patients and teach and "I also plan to use my recent experience to help others avoid problems with conflict of interest from the lessons I have so painfully learned."

Open payments

He and others will have to keep up with a changing world. In the coming months, any health reform that becomes law may well include the Physician Payments Sunshine Act, which is part of legislation that is being developed in both the House and the Senate, with the House version lowering the threshold for reportable payments to \$5.

The prospect of a public website that documents every payment to physicians isn't

being received with enthusiasm by some researchers. "By dint of [Grassley] posting every relationship every physician has, it's guilt by association," says Jeffrey Garber, chief of endocrinology at Harvard Vanguard Medical Associates in Boston and an active member of the New York-based Association of Clinical Researchers and Educators, a group of physicians that sprang up in July to resist what it calls the overreach of the conflict-disclosure movement. A new sunshine law in Massachusetts, for example, requires companies to disclose online any payments to doctors of more than \$50.

Some researchers complain that the disclosures are an invasion of privacy; others argue that lowering the reporting threshold, as the NIH is expected to do, will take a toll. "The thing that I am concerned about is the regulatory burden. When it comes to practising scientists, we want them to have time to do experiments," says Paul Kincade, an immunobiologist at the Oklahoma Medical Research Foundation in Oklahoma City.

It remains unclear whether a national disclosure law would deter the industry-academic collaborations that are touted as the best way to fund cures into clinics, especially in this tight funding environment. In fact, many university administrators welcome the prospect. "It becomes a tool that complements our own public disclosures," says Steven Fluharty, vice-provost for research at the University of Pennsylvania in Philadelphia. On 1 July, the university's School of Medicine began posting on a public website all relationships between faculty members and any industry from which they receive any amount of money. Grassley's revelations, adds Fluharty, "have been an eye-opening experience for us all".

Thacker, in the meantime, has set his sights on some new targets: military doctors who fail to report financial disclosures as they are required to do; and spinal surgeons with lucrative ties to medical device-makers such as Medtronic in Minneapolis, Minnesota.

In an interview with *Nature* in June, Grassley said that he is pleased with his lead biomedical investigator and what he has been able to achieve in two short years. "Paul's good," said the senator, sitting across from Thacker. "If you're going to be successful in these investigations, you gotta have people like Paul."

Thacker, for his part, says he likes his job because "you can have an impact. I wanted to do something that, when it hits, it reverberates for a while."

Meredith Wadman is a reporter for *Nature* based in Washington DC.

See Editorial, page 315.



LIFE IN THE BALANCE

How do researchers and policy-makers decide on the value of health? **Daniel Cressey** looks at Britain's National Institute for Health and Clinical Excellence.

In May 2008, a research report concluded that it would be too expensive to keep some British people with kidney cancer alive.

The 290-page review and economic evaluation had been put together to assess the effectiveness of four new treatments — bevacizumab, sorafenib, sunitinib and temsirolimus — for renal-cell carcinoma. The research team concluded that there was some evidence that patients could benefit from these treatments, in some cases even doubling the time that they lived without their disease worsening from five to ten months. However, “the probability that any of these interventions would be considered cost effective” in Britain’s nationalized health system, it said, “is zero”¹. A few months later, an expert panel from Britain’s National Institute for Health and Clinical Excellence (NICE) confirmed that prediction, stating in an August decision based heavily on the report that the

four drugs “are not recommended as treatment options for advanced and/or metastatic renal cell carcinoma”.

The critics erupted. The drug manufacturers and patients were furious. “They are saying to me, as a cancer patient, that I don’t deserve the right to live, whether it’s for one month, two months, six months or even years,” a person with kidney cancer told the BBC. Britain’s leading cancer charity Cancer Research UK said that it was “very disappointed” with the decision, and that “NICE needs to consider how it can reconcile making recommendations so clearly at odds with current clinical opinion”. “We were not aware at the start that this was going to be controversial,” says Jo Thompson Coon, a researcher at the Peninsula Medical School in Exeter, UK, and the corresponding author of the research report.

This is the brutal reality of NICE, the body

that decides which medical treatments the nation can afford to buy. To some, NICE is a world-leading body — one at the forefront of ‘comparative effectiveness’ research, which compares one treatment with another, and exemplary for the tough decisions it makes on cost effectiveness. To others it is a loathed body ready to deny people life-giving treatment with little justification.

Which of these portraits is more accurate has implications for people far beyond the United Kingdom. NICE’s decisions and its decision-making methods have already been adopted by several other countries (see ‘NICE abroad’, overleaf). Some health economists say that the United States — where the debate over health-care reform has reached fever pitch — will have to incorporate techniques similar to those that NICE uses if the country is serious about reining in its more than \$2-trillion health-care

ILLUSTRATIONS BY DAVID PARKINS

bill. But to many others in the United States and elsewhere the idea of a NICE-like body is unfathomable. Former Republican vice-presidential candidate Sarah Palin summed up the feelings of many when she warned in a statement in August this year that health-care rationing would lead to a “death panel” for patients in which “bureaucrats can decide ... whether they are worthy of health care”.

In the United Kingdom, bureaucrats and health-care rationing are a way of life. What is sometimes lost in the midst of the debate is the research itself, which in the case of NICE involves synthesizing evidence and building models that attempt to assign hard values to the quality and cost of each additional month by which a treatment extends life. The researchers who do this work, however, are well aware that their results can have profound effects for the population. “You are obviously always very aware that this is a very important piece of work,” says Thompson Coon. “It is not going to sit on a dusty shelf for no one to read. On the other hand, you have to keep it evidence-based.”

Health arbiter

NICE was born in 1999 amid concerns that patients in Britain's National Health Service (NHS), which provides the vast majority of the nation's health care, were not being given the most effective treatments. Established by the Labour government, its purpose is to make sure that the NHS spends its budget — raised by taxation — wisely, using a transparent decision-making process that is based on the best evidence available.

For many conditions, there is scant evidence to show doctors and patients which of two or more medical alternatives — be it treatments, diagnostic techniques or prevention methods — is likely to be more successful. Comparative-effectiveness research aims to find out which one is best, either by pulling together existing research or by commissioning new studies.

On its own the research is relatively uncontroversial. Where NICE gets into hot water is when money is added to the mix. Even if a treatment is more effective clinically than a rival, NICE committee members can decide that the gain in health that it bestows is not worth the additional cost. NICE issues guidance on issues ranging from medical procedures to public health, and the ones that tend to be most controversial are its ‘technology appraisals’, which tell the NHS under what conditions treatments — particularly new ones — must be offered.

The decision over bevacizumab, sorafenib,

sunitinib and temsirolimus was one of the most divisive so far. In 2007, the Department of Health asked NICE to assess the drugs, made by Roche, Bayer, Pfizer and Wyeth, respectively. NICE turned, as it routinely does, to an external assessment group, in this case the group of seven health economists led by Thompson Coon.

The researchers considered the clinical effectiveness question first, namely, what is the effect of the four drugs compared to current standard treatment for renal-cell carcinoma, a particularly nasty type of kidney cancer that is diagnosed in around 6,000 people a year in Britain. One existing treatment option was to remove the tumour entirely by taking out the kidney. If the cancer had spread, or metastasized, then immunotherapy with interferon- α was commonly used. But even with treatment, only 10% of people whose cancer has metastasized survive for at least five years.

The team initially identified 888 potentially relevant studies through electronic searches of various databases. Many of these were excluded for being reviews, reanalyses of the same data or studies that did not meet the researchers’ experimental standards, such as being placebo controlled. This left them with 13 relevant papers from 8 clinical studies. For this study “there was actually quite a reasonable amount of evidence”, says Thompson Coon. “Because they’re new drugs there isn’t always that much data available. If you were doing a systematic review of a more established technology you’d probably expect to find more.”

“What about the people whose health care gets displaced because of the cost?”

— Karl Claxton

standard treatment for renal-cell carcinoma, a particularly nasty type of kidney cancer that is diagnosed in around 6,000 people a year in Britain. One existing treatment option was to remove the tumour entirely by taking out the kidney. If the cancer had spread, or metastasized, then immu-

In a number of patient groups and disease scenarios, the research team found that the new drugs were better than existing treatments. For example, one of the studies² they included showed that people with untreated metastatic renal-cell carcinoma who were given bevacizumab and interferon- α lived without their cancer progressing for just 10.2 months, compared with 5.4 months for those given a placebo and interferon- α .

But a drug that extends life is not much good if the individuals who take it spend that time in crippling pain. So the trick for the assessment team is to assign a somewhat abstract quality of life value — called a ‘utility value’ — to these additional months or years. Typically, perfect health scores a one. Dead is zero. Putting values in between is the complicated bit.

One way to measure quality of life is using a ‘time trade-off’ method. Individuals are asked: if you were going to be in a particular health state for ten years, how many years of life would you be prepared to forfeit to be in perfect health? To avoid constant pain, for example, someone might be prepared to give up eight years of life for two in perfect health: this state would be rated 0.2. To avoid a more minor condition a person might only be prepared to forfeit six months, rating 0.95 on the scale. “What’s very important is the measure of quality must be based on actual choices that people are willing to make,” says Karl Claxton, a health economist at the University of York, UK, who has served on various NICE appraisal committees.

Ideally, the quality of life of a person taking, say, cancer drugs, is measured from patients in a clinical trial. These can be translated



NICE's refusal to approve spending on new kidney cancer drugs caused outrage among patients.

J. SHORT/UPPA/PHOTOSHOT

NICE abroad

The National Institute for Health and Clinical Excellence (NICE) assesses treatments and procedures from a very British viewpoint. Its decisions are informed by NICE's Citizen's Council, which represent the views of the UK population, and the values it assigns to children, elderly people or those who are terminally ill reflect national attitudes and culture.

Yet NICE has influence across the world. Countries including Azerbaijan and Brazil have adapted the institute's guidance. Other countries, such as Australia, have their own NICE-like systems. In 2008, NICE started a non-profit consultancy arm — called NICE International — which does contract work in Canada, Bosnia and other countries looking to

use its guidance or to establish similar bodies. "The techniques we use are universal," says Michael Rawlins, chairman of the institute. "Whether a country wants to take them on and in what form is very much related to the culture of the health-care system."

Many health economists think that every country will eventually need some kind of NICE. But the decisions made by the institute are easier to implement in countries that have finite spending on health, such as through a national health service, and therefore a clear basis on which to accept or reject treatments as being affordable or too costly.

The United States has no such limit on health-care spending. The nation's Food and Drug Administration approves a

treatment for use if it is deemed to be both safe and effective for the licensed condition — cost is not a factor. The United States did set aside \$1.1 billion for comparative-effectiveness research in its economic stimulus package earlier this year. Policy-makers have not yet worked out whether or how to incorporate such research into decisions on cost. "Our job is the research," says Carolyn Clancy, director of the US Agency for Healthcare Research and Quality, the US body that researches health-care quality. "The policy-makers are going to have to struggle with 'how is this research applied'."

"We have had quite a lot of dialogue with the current American administration," Rawlins says. He is unsure how far the United States will go down the

clinical and cost-effectiveness road, but he agrees with a view that seems widespread among health economists. US citizens "don't get their money's worth and they can't afford it any longer. They can't go on as they are," he says.

Maynard argues that "the American health-care system rations on the basis of whether people have private insurance or not. Forty-six million people haven't got insurance." He adds that private health insurers ought to adopt assessments of clinical and cost effectiveness to make more rational decisions about what to pay for. "Private insurers are poor purchasers of health care because they don't use health-technology assessment to ration what they put in their benefit package," he says. **D.C.**

into standard utility values by, for example, attaching to them 'reference' measures of time trade-off from the general UK population."

For NICE assessments, research teams then combine the quantity of life that a treatment buys, with the quality of that time into the Quality Adjusted Life Year (QALY), a measure widely used by health economists. This is calculated by multiplying the utility value of a health state by the length of time spent in that state. One year spent in perfect health, for example, gives a QALY of one. Three years spent in a health state with a utility value of 0.5 equals 1.5 QALYs, equivalent to 1.5 years of perfect health.

Complex calculations

For most conditions, working out the QALY is more than a back-of-the-envelope calculation. Clinical trial results cover only the relatively short span of the trial, but researchers are trying to extrapolate from this a QALY for the rest of a patient's life, during which their health may change. For this they turn to mathematical models into which they put all the information on the effectiveness of the drugs from the literature search, the changes the treatments are likely to make to patients' quality of life, how the disease progresses and the timescales involved.

And the answer? The model developed by Thomson Coon's assessment team showed that treating renal-cell carcinoma with interferon- α gives 1.19 QALYs to the average patient. Adding one of the new drugs, bevacizumab, to interferon- α increased this

to 1.45 QALYs. Sunitinib was even better, producing 1.62 QALYs. If money were no object, then sunitinib would be the obvious choice.

But for the NHS, money is crucial — and when cost was added the outcome was much less clear-cut. A course of treatment with interferon- α alone cost £8,438 (US\$13,786) at the time of the assessment, whereas one with sunitinib was £39,623. This means the additional 0.44 QALYs — effectively just over five extra months of healthy life — costs an extra £31,185. NICE typically calculates the difference as the cost per QALY, which was £71,462 for sunitinib and £171,301 for interferon with bevacizumab.

How well the QALY system actually reflects patient preferences is still debated. Stephen Birch, a health economist at McMaster University in Ontario, Canada, says that it fails at this most fundamental of levels. A key problem, as Birch sees it, is the assumption built into calculation of QALYs that it is possible to separate time and health. "These two things are not separable," he says. A person who has been sick for a long time might rate their quality of life differently to someone who has only just become sick. "The QALY doesn't have that," Birch says.

Despite these criticisms and others, many health economists consider the QALY to be the best option available in comparative-effectiveness research. "The argument at a theoretical

level is whether the QALY is a good measure of utility or whether it's a crude measure of length and quality of life that doesn't bear close relationships to people's satisfaction," says Alan Maynard, a health economist at the University of York. "It's not strongly theoretically based. It's pragmatic best practice. That's where we're at."

Once calculated, the QALYs and their costs are returned by the assessment team to NICE, where a separate appraisal committee composed of researchers, medical practitioners and laypeople decide what to do with it. The committee produces a draft decision — called an appraisal consultation document — before accepting comments from interested parties and then releasing a final decision.

Generally anything coming in with a cost per QALY gained of under £30,000 is approved for use — and none of the four renal cancer drugs came even close. More than 80% of drugs are approved for use in some form, however (see table). The £30,000 threshold has been criticized for being somewhat arbitrary, but health economists say that it is broadly in line with other spending decisions taken in the NHS, such as those made by health authorities in the absence of NICE guidance. "You can argue that NICE is too generous," says Maynard. "It probably puts too many things on to the approved list for the NHS, but it's a system that is explicit."

"NICE probably puts too many things on to the approved list for the NHS, but it's a system that is explicit."

— Alan Maynard

An immediate solution for the cancer drugs would be to bring down the cost of the drug. But NICE is not allowed to engage in direct debates with drug companies about the cost of their products, although there are various schemes that allow manufacturers — who are keen to have their drug approved by NICE — to offer ‘discounts’ to the NHS. Pfizer, for example, offered a deal in which the first cycle of sunitinib would be free to the NHS. NICE’s chairman, Michael Rawlins, says it “gets up my nose a bit” when the agency is criticized for rationing when pharmaceutical companies escape criticism for their pricing.

In October, after two of the cancer-drug manufacturers submitted new clinical data or comments, NICE commissioned another review of the evidence, eventually concluding in its final appraisal that the cost of sunitinib “could be less than £50,000 per QALY gained”³.

Citizens advice

But in the end, redoing the calculations was not what made the difference. The outcry over NICE’s decision was such that at the start of January, NICE made a very significant move, effectively rewriting its procedures for drugs such as those for renal cancer. Based in part on the recommendations of its Citizens Council, NICE issued additional guidance for appraising treatments that “may be life-extending for patients with short life expectancy, and which are licensed for indications affecting small numbers of patients with incurable illnesses”.

For these drugs, says NICE, appraisal committees can consider “giving greater weight to QALYs achieved in the later stages of terminal diseases”. It was effectively telling its committees to be lenient about approving certain treatments that fall above its £30,000 threshold.

In its final appraisal a month later, the committee decided that sunitinib should be used in some circumstances despite its cost. The committee concluded that “in this case there was a significant step-change in treating a disease for which there is currently so little to offer patients”³. This August, it confirmed it was rejecting use of the other three drugs.



NICE’s chairman, Michael Rawlins, says the agency’s decisions reflect the desires of the British public.

“The difficulty with these drugs was they were in a disease area where there wasn’t much else,” says Peter Littlejohns, NICE’s clinical and public-health director. “Probably that was an issue that we weren’t sensitive enough to at that time. That was why there was a huge backlash.” Littlejohns says that the additional end-of-life guidance and the approval of sunitinib “represented NICE responding to scientific and public concern”. Rawlins agrees, saying that the guidance change reflects the beliefs and desires of the British public.

The new procedure does not sit well with everyone. “I’m very worried about the notion of weighting different people’s QALYs differently,” says Claxton. He worries that health gained by those on sunitinib will be health lost by others in the NHS when treatments they will need in future can no longer be afforded. “Of course the people who stand to benefit from a technology might have characteristics that we believe ought to give them a particular social weight,

but what about the people whose health care gets displaced because of the cost?” he asks.

As the renal-cancer story illustrates, whatever hard numbers the models spit out, the decisions about what to do with these figures — and hence the outcome of the appraisal process — are influenced by many other social, economic and political factors. Claxton is not the only one who thinks that two groups could well come up with different — and wholly legitimate — answers to the same cost-effectiveness question. Rawlins likens each decision made by an appraisal committee to being tried in court by a jury. “You might get off with one and not with the other,” he says. “We try to make sure they’re as consistent as possible but at the end of the day there are [scientific] judgements and then of course on top of that these social judgements too.”

“Ideologically this isn’t very pleasant,” sums up Maynard, “but as I tell my medical students, there are two certainties in life, one is death and the other one is scarcity of resources.”

Daniel Cressey is a reporter based in Nature’s London office.

FIVE MOST RECENT NICE TECHNOLOGY APPRAISALS

Drug	Condition	Cost per QALY range	Approved?
Cetuximab	Colorectal cancer	£26,700–33,300	Yes*
Alitretinoin	Eczema	£15,000–31,000	Yes
Bevacizumab, sorafenib and temsirolimus	Renal-cell carcinoma	Lowest estimate: £53,800	No
Tenofovir disoproxil	Chronic hepatitis B	Less than £20,000	Yes
Rituximab	Chronic lymphocytic leukaemia	Probably less than £30,000	Yes†

*In combination with 5-fluorouracil, folinic acid and oxaliplatin. †In combination with fludarabine and cyclophosphamide.

1. Thompson Coon, J. et al. *Bevacizumab, Sorafenib tosylate, Sunitinib and Temsirolimus for Renal Cell Carcinoma: A Systematic Review and Economic Evaluation* (Peninsula Technology Assessment Group, 2008).
2. Escudier, B. et al. *Lancet* **370**, 2103–2111 (2007).
3. National Institute for Health and Clinical Excellence *Final Appraisal Determination: Sunitinib for the First-line Treatment of Advanced and/or Metastatic Renal Cell Carcinoma* (NIH, 2009).

See Editorial, page 315.

CORRESPONDENCE

Non-lethal weapons and the civilian death toll in war time

SIR — The scientific community should think twice before it turns its back on non-lethal weapons, as Malcolm Dando suggests in his Opinion piece 'Biologists napping while work militarized' (*Nature* **460**, 950–951; 2009).

It is true that fentanyl killed scores of civilians when it was used to end the Moscow theatre siege in 2002. But that was partly down to Russia's desire to hide its use of caltivate agents, which meant that no life-saving antidote was to hand: the Russians had not disclosed the agent's identity even to their medical personnel.

Dando rightly points out that the US Army misused BZ and other chemical agents during the Vietnam War. But the US Army's use of BZ no more serves as a model for fighting with non-lethal weapons than Vietnam now serves as a model for conducting asymmetric wars — conflicts in which the two sides have very different strategies or levels of military power.

Modern asymmetric war poses a stiff challenge to military organizations searching for the means to defeat guerrilla and insurgency forces while sparing the surrounding civilian population. Many innocent civilians are still being killed as armies turn to drones, real-time surveillance and precision-guided missiles. Could chemical agents, electromagnetic devices and other non-lethal weapons reduce the death toll of modern armed conflicts? We don't yet know the answer.

The use of non-lethal weapons need not cause excessive casualties. Any weapon system carries the spectre of abuse. The purpose of humanitarian law in war is to prevent the abuses that Dando describes and to restrain the carnage of modern war. Sometimes it is successful and sometimes not. But it would be

strikingly ironic if disagreement in the scientific community left military organizations free to pursue their penchant for high-explosive weaponry without considering any of the available non-lethal alternatives.

Michael L. Gross Department of International Relations, School of Political Sciences, University of Haifa, Mount Carmel, 31905 Haifa, Israel
e-mail: mgross@poli.haifa.ac.il

Don't overlook the rigorously reviewed novel work in patents

SIR — Why are patent citations so conspicuously absent across academic journals, with most even omitting formatting instructions for these in their author guidelines? Patents present novel, rigorously reviewed unpublished work, as well as providing an unmatched resource for detail.

We randomly selected one month (December 2008) and reviewed all citations in the reviews, articles and letters/reports in *Nature* (1,773 citations) and *Science* (1,367). These citations included textbooks, arXiv.org preprints and abstracts — but no patents.

The lack of cited patents may come about partly because authors find academic papers more readable, or perhaps because the work reported and discussed in academic journals is not being commercialized. However, the scientific data within some patents may appear in abbreviated form in subsequent academic publications.

In 2008, the US Patent Office issued 185,246 patents. In the past, the patent literature has been difficult to search, but this is no longer the case. Matters have improved with the introduction of services such as Espacenet (<http://ec.espacenet.com>) from the European Patent Office, which is able to search more than

60 million patent publications worldwide, and Google Patents (www.google.com/patents), a free search engine indexing more than 7 million patents from the US Patent Office. Searches can also be undertaken at the US Patent and Trademark Office (www.uspto.gov) and the World Intellectual Property Organization (www.wipo.int).

These advances mean that there should now be a more comprehensive citation of the patent literature in scientific publications.

Donald F. Weaver Department of Medicine (Neurology), Chemistry Building, 6274 Coburg Road, Dalhousie University, Halifax, Nova Scotia B3H 4J3, Canada
e-mail: donald.weaver@dal.ca
Christopher Barden DeNovaMed Inc, c/o IWK Health Centre, 5850/5980 University Avenue, PO Box 9700, Halifax, Nova Scotia B3K 6R8, Canada

Keeping track of the Earth's carbon-cycle components

SIR — In a recent Editorial (*Nature* **460**, 436; 2009), you call for improved Earth-monitoring tools to verify whether climate policies are effective. I am pleased to report that the global carbon-monitoring activities of the Group on Earth Observations (GEO) are well on the way to meeting your recommended course of action and should make a useful contribution to climate discussions in Copenhagen at the end of the year.

More than 130 governments and leading international organizations are collaborating through the GEO to establish a Global Earth Observation System of Systems by the year 2015. They are interlinking their respective Earth-monitoring systems and developing common technical standards to pool information effectively and to promote the free dissemination of data.

This expanding coalition is

already transforming the ability of governments to manage their natural resources.

Our system for analysing the three components of the carbon cycle (atmosphere, land and ocean) aims to provide high-quality information on carbon dioxide and methane concentrations and on emission variations. Carbon tracking and carbon storage is being evaluated from atmospheric CO₂ observations, air-surface exchange flux networks, surface ocean CO₂ and related marine biochemistry observations, for example.

These coordinated data should help provide the monitoring, reporting and verification information that is likely to be required by future regulatory frameworks for the inclusion of forests in post-Kyoto climate agreements. They will build on the GEO's existing and planned efforts in forest monitoring. With collaboration from national governments, space agencies and relevant technical experts, a template should emerge for a reliable global carbon-monitoring system.

Close cooperation with the Committee on Earth Observation Satellites and with the GEO Carbon Community of Practice means that plans can be implemented for collecting space-based greenhouse-gas data, particularly those provided by Japan's GOSAT ('greenhouse gases observing satellite') mission and NASA's replacement Orbiting Carbon Observatory.

Understanding the ability of the carbon cycle to continue to act as a partial sink for fossil-fuel emissions is crucial to future carbon budgeting. The GEO's projects will enable participating governments to benefit from their investment in Earth observations and to provide essential environmental information to policy-makers.

José Achache Group on Earth Observations, 7bis, avenue de la Paix, 1211 Geneva, Switzerland
e-mail: jachache@geosec.org

"If they found extraterrestrials, they couldn't do much about it." Fred Kaplan, page 346

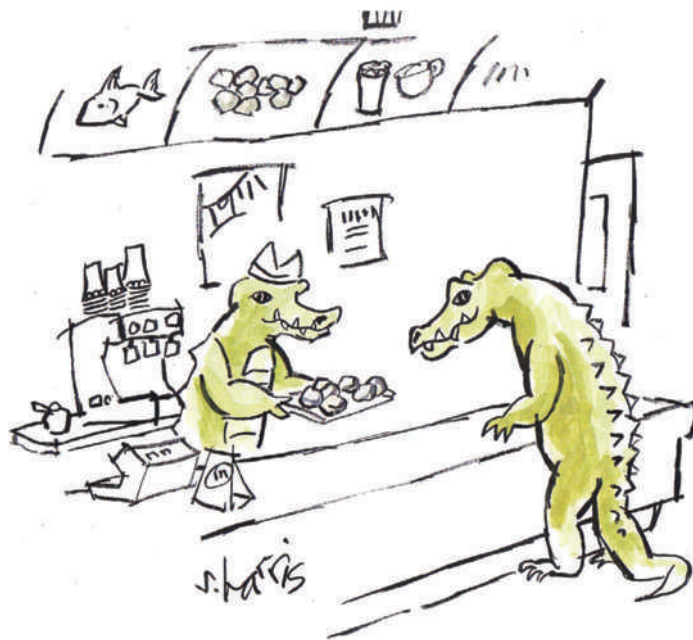
Were crocodiles responsible for the stones we call tools?

SIR — Could *Nature* have been unknowingly publishing papers for the past 80 years about crocodilian gastroliths (stomach stones) instead of stones concluded to be 2.5-million-year-old hominid tools? This possibility could cast doubt, for example, on the nature of the Oldowan specimens described by Michael Haslam and colleagues in their Review of primate archaeology (*Nature* **460**, 339–344; 2009).

Palaeontologists use a simple eyeball test to distinguish stone tools from gastroliths. If a specimen has wear marks on its outer surface but none on its inner surfaces, this indicates that the stone has been grinding away in some prehistoric stomach or other and is a gastrolith. But wear on both inner and outer surfaces indicates that it has been used for some sort of pounding or battering and can confidently be considered a tool. A quick look at the three Oldowan specimens reveals wear on only the extended surfaces, so they should be considered as gastroliths, not tools.

Identification of the Oldowan specimens as tools is based on the fact that the soft relict sands of Olduvai Gorge contain no natural stones of their own, so any stone found there must have been moved from distant river beds by some unknown animal transporter — concluded by high science to be *Homo habilis*. But crocodiles have the curious habit of swallowing rocks: these account for 1% of their body weight, so for a 1-tonne crocodile that's 10 kg of stones in its stomach at all times. Surprisingly, science has never even considered the crocodile as transporter.

Crocodiles and hippos have always lived happily together. Hippo herds would naturally trample riverside gravel stones into the shape of Oldowan cutting tools, quantities of which the



crocodile would then swallow and transport to other places.

The crocodile lives and dies at the water's edge. So far, all East African Oldowan specimens have come from the same waterside environments where crocodiles are known to have dwelt. Millions, perhaps trillions, of transported crocodile stomach stones must remain where the old crocodiles left them, deep in relict East African sediments, though none has ever been reported.

Patrick Dempsey 5091 Citation, Cypress, California 90630, USA
e-mail: greatbasinpat@msn.com

Ethical concerns over use of new cloning technique in humans

SIR — The announcement that induced pluripotent stem (iPS) cells have been used successfully to produce viable mice (X. Y. Zhao *et al. Nature* **461**, 86–90; 2009 and M. J. Boland *et al. Nature* **461**, 91–94; 2009) represents a great technical achievement. But enthusiasm should be tempered by ethical concerns over any extension of this technology to research in humans.

The mouse embryos

were created by 'tetraploid complementation', in which mouse iPS cells (produced from fibroblasts) are injected into a tetraploid blastocyst to allow them to express their developmental potential fully. As the authors point out, this technology provides a demonstration of true pluripotency/totipotency and usefully offers a stringent test of iPS-cell quality. Both groups also indirectly consider the wider application to human cells in suggesting that fully pluripotent iPS cells could eventually be important in cell-replacement therapy and therapeutic interventions.

It is important to remember that there would be severe ethical problems associated with using tetraploid complementation technology in humans, even without the intention of implanting the resulting artificially created embryos into a uterus (see, for example, H.-W. Denker *Reprod. Biomed. Online* **19**, suppl. 1, 34–37; 2009). The issues are similar to those that have arisen over embryonic stem cells and include aspects of patentability.

At present, human reproductive cloning is banned in all countries, and therapeutic cloning is

prohibited in several. But ethical standards may differ and/or change in the near future. The implications should be borne in mind by researchers everywhere in their impulse to follow up any application of tetraploid complementation technology with human iPS cells.

Hans-Werner Denker Institut für Anatomie, Universität Duisburg-Essen, Hufelandstrasse 55, 45122 Essen, Germany
e-mail: hans-werner.denker@uni-due.de

The need for a fresh symbol to designate copernicium

SIR — There could be a question mark hanging over the symbol proposed for the newly recognized element 112, copernicium (*Nature* **460**, 449; 2009).

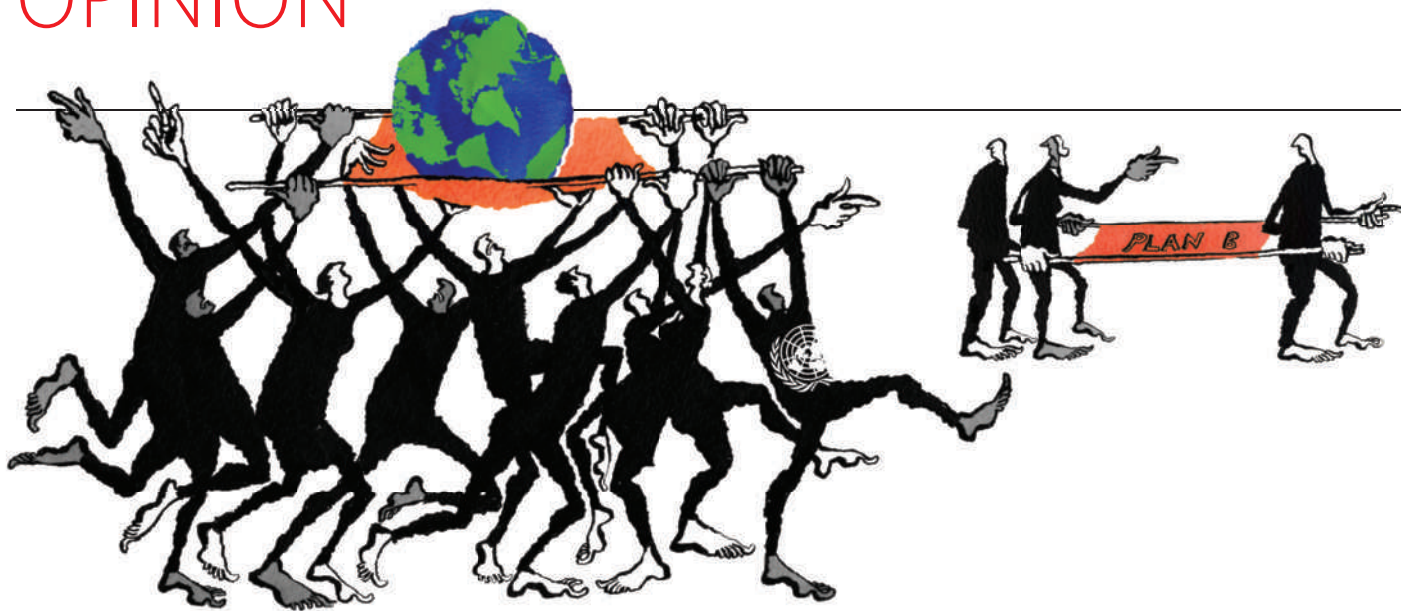
According to the current recommendations of the International Union of Pure and Applied Chemistry on naming new elements, a candidate name cannot be reused on another element (W. H. Koppenol *Pure Appl. Chem.* **74**, 787–791; 2002). For example, the names hahnium or joliotium can no longer be considered for any as-yet unnamed element, because both were once used to name element 105, which is now called dubnium.

If this rule is formally extended to symbols of elements, it will affect the proposed symbol (Cp) for copernicium. This symbol was used for element 71, cassiopeium, before that was formally named lutetium (F. A. Paneth *Nature* **159**, 8–10; 1947).

With C, Ce, Cm, Co, Cr and Cu already taken, Ci short for curie as a unit of radioactivity and Cp open to debate, a 'clean' option for copernicium could be the unprecedented Cc.

Juris Meija Institute for National Measurement Standards, National Research Council Canada, Government of Canada, 1200 Montreal Road M-12, B-16 Ottawa, Ontario K1A 0R6, Canada
e-mail: juris.meija@nrc-cnrc.gc.ca

OPINION



Plan B for Copenhagen

In 11 days the curtain will rise in Bangkok for the penultimate round of negotiations before the climate change conference in Copenhagen. **David Victor** warns of the dangers of a rushed, stapled-together deal.

'Plan A' for the United Nations climate-change conference in Copenhagen is an ambitious new global agreement to replace the ageing Kyoto treaty. But most signs point to disaster. Negotiators are grappling with issues more complex than practically any others in international diplomacy. Their progress has been so slow that the most recent round of climate talks, held last month in Bonn, Germany, ended with strident calls to work harder and faster.

In reality, no amount of hard work can meet the goal of producing a fully useful treaty in time for the conference in December. Working faster, in fact, would be counterproductive because slapdash fixes will make it harder to craft an effective, long-term strategy to slow global warming.

Rather than a mad sprint, success in Copenhagen hinges on crafting a more realistic 'plan B'. Some negotiators are privately pondering the question of what to do if Copenhagen fails. Those debates must now happen in public — starting in the upcoming meeting in Bangkok, Thailand — while there is still time to sift the issues that can be settled by December from those that require a new strategy and more realistic deadlines at least two years away.

Plan B would include an immediate standby agreement on the small number of issues on which governments already largely agree and in which failure would be harmful. At the same time, it would lay the foundations for a new approach that would rely less on the sprawling, all-inclusive United Nations process. Guided by lessons from economic diplomacy, more

progress will come from small groups of pivotal nations rather than global forums.

The looming disaster at Copenhagen is partly bad luck owing to the global economic meltdown. Concern about environmental issues has plummeted over the past two years even faster than the economy. Most governments are reluctant to spend huge resources on uncertain, distant goals when they face pressing local problems such as unemployment.

amendments and adjustments to the Montreal protocol on the ozone layer^{5,6}. Usually it works, because governments are able to control the activities that cause most environmental problems, and it is relatively easy for diplomats to make reliable promises on behalf of their governments. In such settings, international agreements on exacting targets and timetables are quickly reached and often effective.

Global warming is different because



SUMMARY

- No amount of hard work can produce a fully useful treaty for December
- Smaller, more flexible approaches can break the impasse
- Copenhagen, at best, is a starting point for the most influential nations to make ambitious commitments

But the main culprit is bad strategy. Simply too many issues are in play, and the aggressive timetable set in 2007 (ref. 1) to solve them was never realistic. Half that schedule was lost as negotiators dithered through 2008. Finally this spring, just four months ago, serious negotiations began when the secretariat that manages the talks cobbled together three negotiating texts to focus minds on areas of unfinished business²⁻⁴. Those documents had 1,142 pairs of brackets signalling lack of agreement. Over the summer months diplomats failed to settle any of the most divisive topics.

That swift two-year timetable followed the typical strategy for negotiating international environmental treaties, such as the successful

diplomats can't be so confident of what they can offer. Serious cuts in emissions require governments to adopt policy reforms that are costly and deeply intertwined with national and global economies. So much is at stake that negotiators can't be sure that domestic reactions will stay supportive, and what each government does hinges in part on what others are likely to implement. No country wants to be a sucker who bears the high cost of regulating emissions while their economic competitors run free⁷.

This style of policy-making is not without precedent, however. Although rare in environmental diplomacy, it is commonplace in negotiations over the interdependent issues that dominate international trade and other

aspects of global economic cooperation⁸.

The experience with the 1997 Kyoto treaty shows why global warming diplomacy should not be hurried. Working at a similar breakneck schedule to Copenhagen, the Kyoto diplomats made hasty promises that some countries, notably the United States, quickly abandoned as unrealistic. Others, such as Canada, balked in response. Still others, such as Russia, were allowed to make Kyoto promises so diluted that they required no real effort to honour⁹. Of the major economies, only the European nations and Japan actually made (and have so far honoured) promises that required much effort; but those countries are a relatively small and shrinking part of the warming problem.

Hurried deals are thus prone to create false expectations. On the critical issue of engaging the developing countries — which already emit about half of the world's warming gases and will probably account for nearly all future growth in emissions — the hasty Kyoto process crafted a Clean Development Mechanism (CDM) that has mushroomed into a political liability. The CDM was designed to encourage greater investment in low-emission technologies in developing countries. But it was obvious even during the sleepless negotiations at Kyoto that the CDM would only work if it included tough rules and strict oversight. With no time and little effort to craft a serious administrative system, the CDM has been a disaster. Many CDM credits do not represent real reductions in emissions^{10–12}, and the CDM excludes some of the best opportunities for emission reductions, such as nuclear power and carbon storage. And because the CDM was designed to reward countries that avoided binding limits on emissions, it has perversely made it harder to convince developing countries to make a bigger effort on their own¹⁰.

The diplomats preparing for Copenhagen, especially from the United States, are keen not to repeat the mistake of promising what they can't deliver. That's well-intentioned, but is not the most important lesson they should take from Kyoto. Such an approach prizes commitments that lack ambition. Indeed, compliance with binding international agreements is surprisingly high because diplomats are good at crafting agreements that are easy to honour even if they don't solve the underlying problem¹³.

I call this lesson the 'big stapler strategy' of international law. Facing impossible deadlines, diplomats promise only what they can surely deliver. In the tired waning hours at Copenhagen they will staple all those national promises

into a grand-sounding global effort. The big stapler is attractive to diplomats, who abhor visible failures, but it is terrible news for global warming. When each nation looks at the issue from a narrow national perspective, it offers conservative pledges that do not sum to what is needed to protect the planet.

The road ahead

Success in Copenhagen must start with the recognition that on just a few topics, a failure to agree would be immediately harmful. A 'standby' agreement is needed to extend the promises already made in Kyoto, such as existing emission targets and timetables. Most developed nations have already made such promises, so this modest outcome should be easy to deliver — along with an opt-in scheme through which countries can bind themselves to even stronger targets and other policies if they like. In addition to locking these targets in place, a clear commitment to the CDM is needed.

I am no fan of either targets or the CDM^{9,10}. But private companies have already poured billions of dollars into emissions controls on the back of these existing promises, and will watch Copenhagen for signs that future promises will be credible and worthy of investment. Developing countries, which are keen to turn the modest commitments made under the CDM into much larger funds for adaptation and technology programmes, are also watching. The most prized commodity in international diplomacy is credibility, which is why governments must not allow existing promises to expire even while they start on the harder, slower process of crafting new commitments.

In tandem with a standby agreement, Copenhagen should mark the start of climate talks that will elicit more credible and ambitious national policies. With a practical focus, that effort can bring success within two years. As

with many trade talks, negotiations should start with all the key players offering packages of efforts that they will implement unilaterally. In addition, they should outline extra promises that are contingent on the actions of others. The European Union provides a partial model for this kind of contingent offer. It has promised to boost its planned 20% cut in emissions to 30% if other industrialized countries make a similar reduction¹⁴. Yet outside that tantalizing offer, which itself is hard to assess because it is probably more than Europe can deliver, no other country has proposed a serious package of contingent actions.

More credible and ambitious contingent offers would not only help slow global warming but would also make national politics less nasty, because groups that bear the costs of regulation will see how their efforts will be multiplied globally. This kind of political engineering is just how trade diplomats build the necessary coalitions to pass new trade laws.

Smarter offers will also make it easier to avoid promises of the worst kind that are taking shape in US policy:

"Diplomats are good at crafting agreements that are easy to honour even if they don't solve the problem."

contingent commitments that slide only in the backward direction. The legislation¹⁵ now making its way through Congress threatens to abandon an already miserly proposal for US emissions controls if big developing countries fail to make comparable efforts. Contingent commitments of this variety are prone to unzip, and when that starts with big important countries it can spread quickly to infect the rest, as happened with the Kyoto treaty. The United States has caused similar harm to world trade talks with its unilateral anti-dumping rules, which are also a one-directional zipper. Climate plans taking shape in China and India may include similar negative offers.

As with trade talks, this approach is complicated to manage; with all 192 nations of the

UN Framework Convention on Climate Change sitting at the table it will fail. Luckily, just a dozen countries account for nearly all warming emissions. They should start the process, not just because they have the most influence but because their economies have the most at stake if warming regulation is handled badly. Of the several 'clubs' of big emitters formed in recent years, the best candidate to take this role is the 17-member Major Economies Forum on Energy and Climate (MEF). The MEF, like all other clubby attempts to address



Kyoto conference: hurried deals are prone to create false expectations.

T. YAMAMAKA/AFP/GETTY

warming, has lacked a clear mission and has been hobbled by diplomats who have scorned anything that might compete with the UN. It has also not treated developing countries with the respect they deserve. But after the likely disaster of Copenhagen, these smaller, more flexible approaches offer the only realistic expectations for making progress in 2010 and beyond.

Avoiding the zombie

The experience with international trade provides not only a model for how to make contingent offers but also what to expect. From the 1940s to 1960s, when major trade talks involved the relatively simple task of adjusting border tariffs between two dozen countries, negotiations were easy to plan and ended swiftly. But today's trade negotiations are a lot more like global warming — they are horrendously complex and cover so many issues that they are much harder to schedule and success is more elusive.

The global trade talks that began in the mid-1980s took eight years, engaged 123 countries and nearly collapsed. The current 'Doha' round of talks involves more than 150 countries with a sprawling agenda packed with issues that are nearly impossible to resolve. Doha has become a legal zombie that neither succeeds nor dies. The UN climate talks will suffer the same fate unless the parties learn from it: even as the global trade agenda has stalled, governments have made significant progress in smaller forums in which it is easier to craft complex agreements, and even through unilateral actions that spur better global efforts, such as India's recent unilateral decision to cut tariffs. Purists lambast these clubs and special deals because they are not universal, but they are the only practical way to manage such complex problems. Global talks still have a part to play, but they are no longer the engine of trade liberalization.

Signal and noise

An effective post-Copenhagen club will require its members to focus attention on the most genuine and credible contingent offers so that the talks do not stall. Sorting reliable policies from smoke and mirrors is never easy, but leading countries can nominate themselves for an intensive, open review of the promises they are making to aid transparency. Such systems are rare in formal diplomatic talks — even in trade, where strong enforcement mechanisms exist, but regular policy review remains weak — because diplomats tend to avoid intrusive processes. But many good models exist. For example, the International Energy Agency,



Major Economies Forum: less talk, more action?

which advises its 28 member governments on policy, has recently finished a review¹⁶ of China's options for cleaning coal — done with the full support of Beijing, even though China is not a member of the agency.

Seasoned observers of the climate process will recognize this idea as 'pledge and review', a concept that gained traction in the early 1990s but was then abandoned by climate diplomats, who were seduced by the notion of legally binding targets and timetables. A small club of key emitters that adopted pledge and review as an ongoing process could transform the credibility of climate actions and provide an effective alternative to over-ambitious global negotiations prone to yield legal zombies.

"Diplomats should recognize global warming for the problem of economic cooperation that it is."

For many observers, such a process would still seem slow, complicated, and not up to the task of halting global warming in its tracks. But it would reflect the reality of global diplomacy, which must rely on weak and often fragile legal mechanisms. Along the way, the world is doomed to experience some global warming, and countries must prepare for those changes. Some will also lament that progress hinges especially on offers from a few countries, notably the United States and China. But that is a reality of world politics.

Some hard-nosed unilateral decisions could also spur more effective international actions. For example, Europe and the United States have a pivotal opportunity to shape the carbon offset market. The EU's carbon market is the world's largest; the eventual US market will be even bigger. Both will rely heavily on international offsets yet are plagued by the poor quality and cumbersome bureaucracy of the CDM. These countries could fix that problem by setting their own tougher rules for offsets while also

promising full linkage to other markets that have comparably tough provisions. Overnight, such actions would force the CDM to adopt smarter rules lest its investors lose access to the markets that provide its revenue. Other disputes, such as over credits for forestry, would be easier to solve with similar unilateral decisions by these large markets and then a period of experimentation to see what works best.

Without a change of strategy, disaster at Copenhagen will be a disaster of choice, not of necessity. A well-managed disaster could be as constructive as the collapse of the 1986 Reykjavik summit between Ronald Reagan and Mikhail Gorbachev — which broke down in the final hours yet helped pave the way for later arms control. Rather than sprinting to Copenhagen, the world's diplomats should focus their attention on the few areas where failure would certainly be harmful. For the rest, they should junk the toolbox of environmental diplomacy and recognize global warming for the problem of economic cooperation that it is. Success hinges on more credible and ambitious commitments by a smaller number of countries. ■

David Victor is a professor in the School of International Relations and Pacific Studies at the University of California, San Diego, 9500 Gilman Drive, MC 0519, La Jolla, California 92093, USA. He is writing a book on climate diplomacy beyond Copenhagen for Cambridge University Press. e-mail: david.victor@ucsd.edu

1. *Report of the Conference of the Parties on its Thirteenth Session, Held in Bali from 3 to 15 December 2007 Addendum: Part Two, Decision 1/CP.13 (UNFCCC, 2008).*
2. *A Proposal for Amendments to the Kyoto Protocol Pursuant to its Article 3, Paragraph 9 (UNFCCC, 2009).*
3. *A Text on Other Issues Outlined in Document FCCC/KP/AWG/2008/8 (UNFCCC, 2009).*
4. *Negotiating Text (UNFCCC, 2009).*
5. Benedick, R. E. *Ozone Diplomacy: New Directions in Safeguarding the Planet* 2nd edn (Harvard Univ. Press, 1998).
6. Parson, E. A. *Protecting the Ozone Layer: Science and Strategy* (Oxford Univ. Press, 2003).
7. Barrett, S. *Environment and Statecraft: The Strategy of Environmental Treaty-Making* (Oxford Univ. Press, 2003).
8. Keohane, R. O. & Nye, J. S. *Power and Interdependence: World Politics in Transition* (Little, Brown, 1977).
9. Victor, D. G. *The Collapse of the Kyoto Protocol and the Struggle to Slow Global Warming* (Princeton Univ. Press, 2001).
10. Wara, M. W. & Victor, D. G. *A Realistic Policy on International Carbon Offsets* (Program on Energy and Sustainable Development, Stanford Univ., 2008).
11. Wara, M. *Nature* **445**, 595–596 (2007).
12. Schneider, L. *Is the CDM Fulfilling its Environmental and Sustainable Development Objectives? An Evaluation of the CDM and Options for Improvement* (Öko-Institut, 2007).
13. Downs, G. W., Locke, D. M. & Barsorum, P. N. *Int. Organ.* **50**, 379–406 (1996).
14. *20/20 by 2020: Europe's Climate Change Opportunity* (Commission of the European Communities, 2008).
15. H. R. 2454: *American Clean Energy and Security Act of 2009* (U.S. Government Printing Office, 2009).
16. *Cleaner Coal in China* (International Energy Agency, 2009).

Join the discussion at <http://tinyurl.com/oz4b8m>

OPINION

An alien concept

Fifty years ago this week, a *Nature* paper legitimized the idea that there could be civilizations elsewhere, able to communicate and wanting to contact us. **Fred Kaplan** reflects on its origins, impacts and legacy.

On 19 September 1959, *Nature* published an article called 'Searching for Interstellar Communication'. Speculation about life in space had been taboo in scientific circles since Percival Lowell wrecked his career in the late nineteenth century by claiming to have detected canals on Mars. Yet here was an article by two of the era's pre-eminent physicists, Giuseppe Cocconi and Philip Morrison reviving, and legitimizing, the idea that we might we not be alone in the Universe — and that we might soon discover our cohabitants.

1959 was the year when searching the skies took on the glow of practical enterprise. In January, the Soviets launched the space capsule Lunik 1, which accelerated to 25,000 miles per hour, the speed known as 'escape velocity', thus becoming the first man-made object to break free of Earth orbit. *Time* magazine hailed the feat as "a turning point in the multibillion-year history of the Solar System", for "one of the Sun's planets had at last evolved a living creature that could break the chains of its gravitational field".

It was a year for breaking all sorts of chains. The first non-stop jet passenger plane flew from New York to Los Angeles. Texas Instruments introduced the microchip. IBM came out with the first business computer. Meanwhile, the United States caught up with the Russians in the 'space race', as the Pioneer IV duplicated Lunik's feat (Pioneers I, II, and III failed to reach even halfway to the Moon before tumbling back to Earth). NASA's Project Mercury, the first US manned space programme, chose its seven astronauts, and newspaper stories started referring to space as the "new frontier", well over a year before John F. Kennedy invoked the phrase in his acceptance speech at the 1960 Democratic convention.

There was a widespread enchantment with the new, a longing to break out of the decade's drab confines. The *Nature* article appealed to this longing, lending credence to dreams of the ultimate breakout. It made an impact on the broader, popular culture to a degree that mathematical articles in scientific journals rarely achieve. And it had a direct impact on

the formal pursuit of this breakout as well.

The idea took form at the end of 1958, when, as part of International Geophysical Year (IGY), the National Academy of Sciences set up a Space Science Board to study "scientific-research opportunities opened up by the advent of modern rocket and satellite tools". Morrison, a professor of astronomy at Cornell University, was a member.

The group met twice, on 1 and 11 Decem-

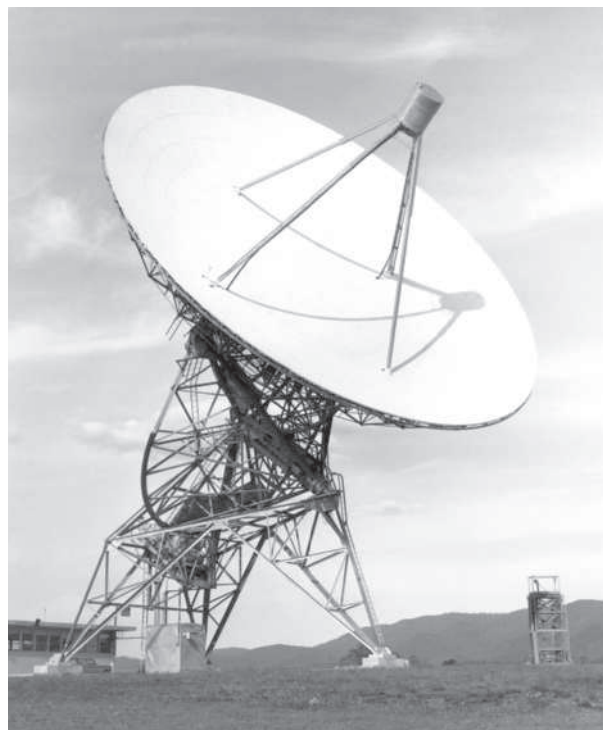
reports of sightings. Still, they were intrigued by the problem: If intelligent civilizations were out there, how would we make contact with them? How would they make contact with us? After some discussion, the two hit on the idea of radio signals. Celestial bodies emit lots of radio frequencies. The burgeoning field of radio astronomy was based on the discovery that much could be inferred about a star or a planet from the traits of these emissions.

From there, the men mused on another question. What frequency might an alien civilization use to transmit these signals? One of the most common elements in the Universe, they reasoned, was hydrogen. Hydrogen atoms emit electromagnetic waves at frequencies around 1,420 megahertz. If aliens were trying to communicate, they would have some familiarity with radio astronomy; they'd want to send a signal that someone out there might be trying to pick up; so that's the frequency they would probably use. More to the point, our own astronomers should dial in to that frequency when pointing their radio telescopes to the nearest stars.

This was the argument that the two spelled out in their article (G. Cocconi and P. Morrison *Nature* **184**, 844–845; 1959). They stopped short of claiming that intelligent aliens were definitely out there, beaming signals. But, they argued, it would be "unwarranted to deny... that near some star rather like the Sun, there are civilizations with scientific interests". These civilizations may have been eyeing our own Sun as a likely source of a similarly evolved species. It's

quite conceivable, therefore, that they "long ago established a channel of communication that would one day become known to us, and that they look forward patiently to the answering signal from the Sun which would make known to them that a new society has entered the community of intelligence". (This was the premise, nine years later, of Arthur C. Clarke and Stanley Kubrick's *2001: A Space Odyssey*.)

Cocconi and Morrison acknowledged that their argument seemed like the stuff of science fiction. But, they countered, "the presence of interstellar signals is entirely consistent with all we know", and "if signals are present, the means



"If signals are present, the means of detecting them is now at hand."

ber. The meetings' minutes indicate that much of the discussion focused on space probes: whether they should land on planets or take measurements from a distance, what kinds of measurements they should take, how to take them, and what signs might indicate the presence of life forms, past or present.

Radio days

When he got back to campus, Morrison discussed the issues with Cocconi, a colleague and close friend. Both men were sceptics about UFOs, which were the rage at the time; Morrison delighted in publicly debunking

SEARCHING FOR INTERSTELLAR COMMUNICATIONS

By GIUSEPPE COCCONI* and PHILIP MORRISON†
Cornell University, Ithaca, New York

NO theories yet exist which enable a reliable estimate of the probabilities of (1) planet formation; (2) origin of life; (3) evolution of societies possessing advanced scientific capabilities. In the absence of such theories, our environment suggests that stars of the main sequence with a lifetime of many billions of years can possess planets, that of a small set of such planets two (Earth and very probably Mars) support life, that life on one such planet includes a society recently capable of considerable scientific investigation. The lifetime of such societies is not known; but it seems unwarranted to deny that among such societies some might maintain themselves for times very long compared to the time of human history, perhaps for times comparable with geological time. It follows, then, that near some star rather like the Sun there are civilizations with scientific interests and with technical possibilities much greater than those now available to us.

* Now on leave at CERN, Geneva.

† Now on leave at the Imperial College of Science and Technology, London, S.W.7.

To the beings of such a society, our Sun must appear as a likely site for the evolution of a new society. It is highly probable that for a long time they will have been expecting the development of science near the Sun. We shall assume that long ago they established a channel of communication that would one day become known to us, and that they look forward patiently to the answering signals from the Sun which would make known to them that a new society has entered the community of intelligence. What sort of a channel would it be?

The Optimum Channel

Interstellar communication across the galactic plasma without dispersion in direction and flight-time is practical, so far as we know, only with electromagnetic waves.

Since the object of those who operate the source is to find a newly evolved society, we may presume that the channel used will be one that places a minimum burden of frequency and angular discrimi-

of detecting them is now at hand”.

They didn't know it at the time, but in the mountains of Green Bank, West Virginia, a man named Frank Drake was already looking. For half a year, Drake had been helping to set up the National Radio Astronomy Observatory (NRAO), the world's best, with an 26-metre telescope (pictured on previous page). A few years earlier, as a graduate student at Harvard University, Drake had reached the same conclusion as Cocconi and Morrison about the frequency of hydrogen atoms. He figured that if someone out there was beaming signals, this big, new radio telescope might pick them up. His superiors gave Drake permission to conduct an experiment, but only if he kept it quiet. The observatory was funded by tax dollars, and the whole project would be jeopardized if Congress got wind that the scientists at Green Bank were looking for little green men.

Tuning in to the Universe

When the Cocconi–Morrison article appeared, the observatory's director, Otto Struve, felt he could take the project out of the closet. The imprimatur of *Nature* made the subject open to serious discussion. Struve also wanted the world to know that his man had come up with the theory first. So he gave a public lecture at the Massachusetts Institute of Technology in Cambridge about Drake's project and its philosophical importance. At once the NRAO was the object of enormous curiosity. Electronics companies donated state-of-the-art equipment — amplifiers, tape recorders and the like — for the space hunt. Newspaper and magazine reporters came calling.

The enterprise was suddenly respectable, so much so that, in November 1960, the National Academy of Sciences sponsored a conference at the NRAO to discuss how to turn the experimental search into a systematic enquiry. The

assembled scientists and business leaders called themselves the Order of the Dolphin, in honour of John Lilly, one of the participants, who had recently led studies concluding that dolphins were an intelligent species. Also at the conference were Frank Drake, Otto Struve, Morrison, and a young astronomer named Carl Sagan, who later became the public face of the search for extra-terrestrial intelligence (SETI).

Most of those taking part in this quest realized its underlying irony: if they found extra-terrestrials, they couldn't do much about it. The nearest stars that seemed likely to have planets were 3 parsecs away. Even if the two civilizations found a common language for discourse (Drake hypothesized that binary code might be one avenue), it would take a century or more to conduct the most basic exchanges. As for visiting each other, the time and energy needed to travel such distances seemed preposterous.

To Drake, this didn't matter. He was (and still is) certain that advanced civilizations are out there. The 'Drake equation', which he introduced at the Order of the Dolphin conference, is a way to estimate the probability of their existence and summarize our ignorance of the relevant quantities. To his mind, the very discovery of other civilizations, the breakthrough in knowledge that it would represent, is reason enough to continue.

Morrison (who died in 2005) shared this curiosity, but he was also driven by a political passion. During the Second World War, he had worked on the Manhattan Project to build the atomic bomb. He personally calculated how much plutonium would be needed to trigger an implosion (about 6 kilograms). He installed the core of the test bomb at Alamogordo and witnessed the explosion's fireball. He assembled the bomb that was dropped on Nagasaki, piecing it together inside the plane as it hurtled toward

Japan. Morrison emerged from the destruction as one of several atomic scientists who feared a catastrophic arms race and who led a post-War campaign for nuclear disarmament.

In 1979, Morrison wrote an article for the magazine *Cosmic Search* called 'Twenty Years After', in which he reminisced about the *Nature* piece and what followed. He ended it with a passage from Arthur C. Clarke's science-fiction story, 'When the Aliens Come'. The most important result of contact, Clarke wrote, "might be the simple proof that other intelligent races ... had safely passed their nuclear crises," giving us hope that we too might pass our crises.

Signal failure?

To many in astrobiology today, this is IGY romanticism. The search for extraterrestrials focuses less on interstellar communications than on molecules and microbes, a hunt more mundane but more likely to bear fruit in our lifetime. Yet the quest inspired by Cocconi, Morrison and Drake presses on. Two years after the Order of the Dolphin conference, Ohio State University in Columbus commenced 'Big Ear', the first radio observatory dedicated full-time to SETI. In the wake of Apollo's Moon landing, NASA recruited Drake for an official SETI study. In 1980, Sagan set up the US Planetary Society, which four years later evolved into the SETI Institute, which thrives today, with Drake as one of its directors. In 1995, a radio telescope capable of monitoring 64 million channels started operation in Australia — radio waves remain a sweet spot in terms of cost and sensitivity. NASA has joined in with the Kepler space probe, which will stream back data on Earth-like planets later this year.

Sceptics cite the Fermi paradox, named for the physicist Enrico Fermi, who asked: if there are intelligent civilizations out there, why haven't we seen them? Indeed, in the 50 years since the search began, nothing has been heard. (There was one signal in the 1970s, picked up briefly by 'Big Ear', but its origin remains unclear.) But Jill Tarter, director of the institute's Center for SETI Research, argues that the absence of a signal hardly constitutes a paradox. Serious data-gathering, by far-seeing radio telescopes and digital processing, has been going on for barely a decade. She likens the nay-sayers to someone who dips an eight-ounce glass into the ocean, brings it up empty, and concludes that the oceans have no fish. ■

Fred Kaplan is a columnist for *Slate* based in New York and author of 1959: *The Year Everything Changed*.

e-mail: war_stories@hotmail.com

See also Editorial, page 316, News, page 324, and Futures, page 438.

"In the 50 years since the search began, nothing has been heard."

OPINION

Ocean fertilization: time to move on

Adding iron to the ocean is not an effective way to fight climate change, and we don't need further research to establish that, say **Aaron Strong, Sallie Chisholm, Charles Miller and John Cullen.**

In the face of seemingly accelerating climate change, some have proposed tackling the problem with geoengineering: intentionally altering the planet's physical or biological systems to counteract global warming. One such strategy — fertilizing the oceans with iron to stimulate phytoplankton blooms, absorb carbon dioxide from the atmosphere and export carbon to the deep sea — should be abandoned.

It is already commonly accepted that ocean iron fertilization should not be rushed into as a mitigation strategy. The Intergovernmental Panel on Climate Change regards it as supported by neither appropriate assessment of environmental side effects nor a clear institutional framework for implementation. Similarly, last year, two United Nations conventions passed resolutions restricting large-scale ocean iron fertilization activities, citing concerns about the environmental risks and lack of a scientific basis on which to justify such activities — concerns that have been recognized for some time. A Royal Society report released this month emphasized that the technique has a relatively small capacity to absorb carbon, and comes with “probably deleterious ecological consequences”.

Yet concerns about the profound consequences of global climate change have led to calls (see, for example, K. O. Buesseler *et al.* *Science* **319**, 162; 2008) for field studies of iron fertilization on larger and longer scales. Although we agree that the kinds of experiments being promoted have more to teach us about ocean processes, we argue that they will not resolve any remaining debate about the risks of iron fertilization for geoengineering. Engaging in experiments with the explicit purpose of assessing iron fertilization for geoengineering is both unnecessary and potentially counterproductive, because it diverts scientific resources and encourages what we see as inappropriate commercial interest in the scheme.

Global impact

The intended effect of ocean iron fertilization for geoengineering is to significantly disrupt marine ecosystems. The explicit goal is to stimulate blooms of relatively large phytoplankton that are usually not abundant, because carbon produced by such species is more likely to sink eventually to the deep ocean. This shift at the base of the food web would propagate



Modern commercial interests in ocean fertilization should not be confused with hypothesis-driven science such as the first IronEx experiment (shown).

throughout the ocean ecosystem in unpredictable ways. Moreover, nutrients such as nitrogen and phosphorus would sink along with the carbon, altering biogeochemical and ecological relationships throughout the system. Some models predict that ocean fertilization on a global scale would result in large regions of the ocean being starved of oxygen, dramatically affecting marine organisms from microbes to fish. Ecological disruption is the very mechanism by which iron fertilization would sequester carbon.

The specific effects of global-scale ocean fertilization are hard to predict, because the ocean's response is dependant on the scale at which such fertilization is done. Small-scale experiments are inherently inadequate to verify model predictions of the long-term side effects of global fertilization. Large-scale alteration of

the ocean would be needed to resolve fundamental uncertainties about environmental risks.

Ocean fertilization for climate mitigation would have to be widespread and cumulative over decades. Thus, properly field testing its geoengineering potential would entail fertilizing and sampling an enormous swath of ocean. Assessment would be needed for between decades and a century or so to demonstrate sequestration, and to document the downstream effects on ecosystem productivity — “nutrient robbing” as described in the Royal Society report — and oxygen depletion. Such a test would have to be implemented against the background of a dynamic ocean that would remain exposed to unprecedented climate change, making the impacts of iron fertilization difficult to extract from other ongoing

T. STANTON/J. STOCKEL/NAVAL POSTGRAD. SCHOOL

effects. In such a global experiment, there could be no 'control patch'.

Given that the efficacy and indirect effects of ocean fertilization for geoengineering cannot be tested directly without altering the ocean on unprecedented scales, we must resort to using global-ecosystem models to predict its promise and pitfalls. Many modelling analyses have shown that iron fertilization cannot reduce atmospheric CO₂ enough to significantly alter the course of climate change. A model published in 2008 (K. Zahariev *et al. Prog. Oceanogr.* 77, 56–82; 2008), which is as convincing as any available, found that even if the entire Southern Ocean were fertilized forever with iron sufficient to eliminate its limitation of phytoplankton production, less than 1 gigatonne of carbon a year of CO₂ of probable future emissions (currently about 8 gigatonnes a year) would be sequestered, and that amount for only a few years at best. This level of effort is simply not going to happen.

We think the idea of geoengineering by iron fertilization persists because of the blurry line between it and small-scale ocean fertilization experiments that address specific hypotheses.

The original goal of iron fertilization experiments was to answer fundamental questions about how iron and carbon are used and cycled in marine ecosystems. They began with a project called IronEx I in 1993. Since then, 11 experiments have been conducted in regions of the equatorial Pacific, subarctic Pacific, and Southern Ocean that have high levels of most nutrients but a relatively low phytoplankton biomass. The experiments confirmed the testable hypothesis that iron is the crucial limiting nutrient in these regions, and they provided insights into plankton community dynamics. They were conducted on a relatively small scale (less than 300 square kilometres) and over relatively short periods of time (less than 40 days), and had ephemeral effects on surface ocean ecosystems. These experiments fuelled the idea that iron fertilization, scaled up, might be used for geoengineering — even though they were not designed to investigate that possibility. This in turn prompted commercial interest in fertilizing the ocean to sell 'carbon credits'.

Setting rules

In response to concerns about the ecological impact of large-scale commercial iron fertilization, the UN Convention on Biological Diversity issued a decision in May 2008 requesting member states to restrict ocean iron fertilization activities, with the exception of small-scale studies. Several months later, the London

Convention on Marine Pollution issued a resolution stating that, given the present state of knowledge, ocean fertilization activities other than "legitimate scientific research" should not be allowed. These recommendations are a good start, but they are subject to interpretation. They do not resolve the blurred line between scientific hypothesis testing, and experiments focused on demonstrating geoengineering potential.

In January this year, for example, an experiment called LOHAFEX, which was designed to fertilize a small patch of the Southern Ocean with iron sulphate, was delayed for two weeks by the German government while it dealt with accusations from various environmental groups. The charge was that LOHAFEX was a dangerous 'geoengineering project' that violated the recent UN restrictions. It was allowed to proceed, after the scientists submitted environmental impact statements and the German government determined that it fell within UN

regulations. But the episode illustrates the persistent ambiguity that surrounds these types of experiments.

It is time to disentangle the science of small-scale ocean fertilization from geoengineering. In our view, small-scale projects addressing testable hypotheses should proceed unimpeded by unnecessary controversy or regulation, whereas larger projects aimed at exploring the geoengineering potential of ocean fertilization should not be allowed, as they cannot resolve crucial issues about this mitigation strategy. Differentiating between these two types of experiments requires regulatory clarity.

Working groups from the London convention met in February 2009 to develop an assessment framework for ocean fertilization that will define what constitutes "legitimate scientific research" under their rules. The framework drafted at that meeting requested rigorous environmental risk assessments and mandated that all legitimate research must be driven by predefined hypotheses. The scientific group of the London convention has also started the process of defining the parameters for assessing the environmental impact of small-scale iron fertilization. Although the details, scope and enforcement mechanisms of these provisions are yet to be developed, this type of structured framework could help to avoid the kind of controversy that surrounded LOHAFEX.

Such exacting regulation is particularly important given the continuing interest in commercial iron fertilization for the sale of carbon offset credits. CLIMOS, a company based in San Francisco, California, has plans to

conduct its first moderate-scale (40,000 square kilometres) 'demonstration experiment' in the Southern Ocean. Although it remains unclear where, when or if actual commercial iron fertilization might eventually take place, CLIMOS has attracted substantial initial investment on the prospect of selling carbon offsets from activities such as iron fertilization activities. CLIMOS has publicly agreed that all ocean iron fertilization activities should proceed only where there is an adequate scientific basis to justify them, and has promised to obtain any necessary permits. But there remains a lack of clarity over what might constitute an adequate scientific basis for such activities, given the scale-dependency of the ecosystem response to fertilization.

As for producing 'carbon credits' from experimental studies at any scale, the Kyoto Protocol's Clean Development Mechanism does not recognize ocean fertilization as a way to create carbon credits for regulated international trade. Thus, carbon credits generated from such activities, however they might be quantified, would presumably have to be sold on the voluntary carbon market. The London convention process cannot regulate the generation of carbon credits, but it could determine that experiments that are used to generate credits would not be considered 'legitimate scientific experiments'. The London convention has not yet addressed this issue. Given continued commercial interest in conducting moderate-scale demonstration experiments, which may or may not be considered 'legitimate scientific experiments', it seems essential to answer this question explicitly.

We already know enough about how ocean systems function to say that iron fertilization on large scales will be disruptive to ocean ecosystems and is unlikely to be effective for climate mitigation. Continuing to justify small-scale iron fertilization experiments in the context of global-scale geoengineering distorts the focus of oceanographic science, and encourages for-profit companies to continue pursuit of this strategy. It is time to move on. ■

Aaron Strong was a research associate at the Massachusetts Institute of Technology in Cambridge, Massachusetts, and is enrolled in the Fletcher School of Law and Diplomacy at Tufts University in Medford, Massachusetts.

Sallie Chisholm is in the Department of Civil and Environmental Engineering at the Massachusetts Institute of Technology, **Charles Miller** is in the College of Oceanic and Atmospheric Sciences, Oregon State University, Corvallis, Oregon, and **John Cullen** is in the Department of Oceanography at Dalhousie University, Halifax, Nova Scotia, Canada.
e-mail: chisholm@mit.edu

"It is time to disentangle the science of small-scale ocean fertilization from geoengineering."

BOOKS & ARTS

On the origin of technology

An overdue theory of how machines and tools evolve downplays human creativity, argues **Jon Agar**.

Technological change, implies economist and complexity theorist W. Brian Arthur, is a lot like climbing a mountain. You could never do it in a single bound. You break the journey into parts by walking the foothills, aiming for a base camp and ascending a sheer face with ropes and pitons before reaching the summit. Each stage needs further consideration. Do you place your foot on that rock or go through the mud? Each movement harnesses some natural phenomenon. Walking uses the friction between land and sole. Climbing exploits the solidity of rock and steel, the tensile strength of polypropylene yarn and the physical laws of pulleys. Combining many solutions, you achieve your purpose of standing at the top to enjoy the view.

To invent a jet engine, say, you might start with the idea of an explosive mix of fuel and oxygen that exploits the physics of action and reaction as an alternative to propellers that fail at high altitudes. But that goal must be achieved in stages using existing technologies — compressors, fuel systems, containers, turbines — each of which is the outcome of its own development process, down to the smallest rivet.

Arthur's theory, outlined in his engaging and provocative new book *The Nature of Technology*, builds on three principles. First, all technologies are made up of pre-existing components, so technological change involves assembling new combinations of old and refined technologies — Arthur calls this process 'combinatorial evolution'. Second, each component is itself a technology, meaning that technologies have a hierarchical and recursive nature. Finally, he writes, "all technologies harness or exploit some effect or phenomenon" and fulfil a human purpose. Arthur distinguishes between individual technologies (for example, a sink); between bodies of related technologies that he calls domains (such as all plumbing systems); and the "collective of technology", meaning everything, including the kitchen sink. Because each level is a nested assemblage, Arthur treats them similarly in his theory.

His model of invention as combination and change as accumulation is not new; he nods to the 1920s pioneers of this idea, William Fielding Ogburn and S. Colum Gilfillan. The notion that technology evolves is older still, going back at least to Charles Darwin's contemporaries, such as the author Samuel Butler and



Every rivet of a jet engine is the outcome of a development process.

N. KLEINMAN/GETTY

the archaeologist Augustus Pitt Rivers. Arthur correctly records that historians of science have been some of the best guides to the logic of technology. Thomas P. Hughes, for example, offers a model of technological change similar to Arthur's to explain the growth of systems in his book *Networks of Power* (Johns Hopkins University Press; 1983). But Hughes gives more room for human organizations and individuals, considering an invention to be useless without the social system that supports it.

Arthur's theory captures many well-known features of technological change. These include 'lock-in', in which an early choice between tech-

nologies becomes difficult to undo because it is more profitable to refine existing components than develop new ones; and 'clustering', in which certain geographical regions become hot spots of innova-

tion by hosting those with crucial know-how. The theory also answers interesting questions, explaining that technology is modular because nested assemblages are easier to improve; and that it is related to but different from science because it manipulates new effects generated by the skills base of research. As technology increasingly harnesses natural phenomena that are far from everyday experience, so it relies on science even more. Thus, technology can feel unnatural, yet "in its deepest essence it is natural".

Arthur's argument will gain notoriety because of the analogy between biological and technological evolution. He is right to distinguish his combinatorial evolution from Darwinian evolution. Imagining combinatorial

evolution in living organisms, he notes, would be like putting together "an organ that had proved particularly useful in lemurs, say, and another organ from iguanas, and another one from macaque monkeys... in combination with others to create a new creature". Combination in nature can happen, such as in the ancient incorporation of bacteria to form mitochondria in the eukaryotic cell, but not routinely. Yet Arthur cannot resist a few one-liners that will bait critics, such as "Conceptually at least, biology is becoming technology. And physically, technology is becoming biology."

In its favour, Arthur's theory does not appeal to mysterious entities such as creativity. Ernest Lawrence's 1929 invention of the first cyclotron is as mundane as fixing a bicycle when viewed as the assembly of pre-existing technologies. But, by focusing on logic, *The Nature of Technology* downplays human achievement. Arthur does conclude that the collective of technology builds itself "with the agency of human inventors", although merely as a "coral reef builds itself from itself from the activities of small organisms".

This is the US west-coast entrepreneur's philosophy of technology as fluid combinations, forever reconfigurable in the interests of profit. Arthur wants us to think that technology has always been this way, and that it is natural. Portraying something new and man-made as permanent and natural is one of the oldest and most effective strategies to depoliticize a subject.

Jon Agar is a senior lecturer in science and technology studies at University College London, Gower Street, London WC1E 6BT, UK. e-mail: ucrhjea@ucl.ac.uk

**The Nature of Technology:
What It Is and How It Evolves**
by W. Brian Arthur
Free Press/Allen Lane: 2009.
256 pp. \$27.00/£22.00

Sound for the masses

Perfecting Sound Forever: An Aural History of Recorded Music

by Greg Milner

Faber & Faber/Granta Books: 2009.
416 pp/464 pp. \$35/£20

The first person to make a reproducible recording of sound was not Thomas Edison. As Greg Milner explains in *Perfecting Sound Forever*, it was a French printer, Edouard-Léon Scott de Martinville, who etched sound waves on to a thin film of soot in 1857, some two decades before Edison. It took another 150 years for Scott de Martinville's recording of the human voice to be heard. In March 2008, scientists at the Lawrence Berkeley National Laboratory in Berkeley, California, devised a way of reproducing the sounds he had captured in soot, and the recording — ten seconds of the popular folk song 'Au Clair de la Lune' — was 'played' for the first time.

So Edison's phonograph was the first practical machine for recording the human voice. Milner's book charts the history of recorded music from the late nineteenth century to today, examining how the role of recording has evolved, from merely capturing sound to creating it. Pioneers such as Edison could exert little influence on the recording process other than positioning performers in front of an acoustic horn, offering advice on voice projection or warming the wax on the phonograph's recording cylinder. And once the performance was under way, they could only stand back; a few minutes' worth of sound waves were etched on to the surface of a wax cylinder to create a permanent record (see page 351).

The advent of electrical recording in the 1920s gave recording engineers more scope for shaping sounds by positioning microphones to emphasize certain instruments at certain times. But recording remained passive, the electrical impulses being fed straight from the microphone to a gramophone disc-cutting machine.

Magnetic tape brought with it the possibility of editing, blowing away the notion of a recording being a reproduction of a real-time event. When the Bing Crosby *Philco Radio Time* show aired in October 1947, the audience thought it was hearing a live performance. It wasn't. The show had been recorded in August and the aired version stitched together from different takes, to remove mistakes and improve the

flow. The man wielding the editing scissors was Jack Mullin, who had spent the Second World War monitoring communications for the Allies and marvelling at the clarity of the music he had listened to on German radio. At the end of the war, Mullin visited Radio Frankfurt at Bad Neuheim and discovered the source of that quality — Magnetophon tape recorders, superior to any recording device in the United States. He shipped two of them home and used them for those first edited radio shows.

Multi-track recording, developed in the 1950s and 1960s, meant that instruments and vocals could be captured separately and mixed together. Effects such as echo and reverberation could be added. The Beatles and their producer George Martin were among the first to see the



Les Paul's experiments with layered sound led to multi-track recording.

creative possibilities of multi-track and used it in the *Sgt. Pepper's Lonely Hearts Club Band* sessions in 1966–67. It is difficult to imagine The Beatles standing on a stage performing any of the *Sgt. Pepper's* songs live. The album is a performance that was created by recording technology, not one captured by it.

The latest major development documented by Milner is digital recording: turning analog sound signals into binary code that can be stored and manipulated on computers. In the early 1980s, the first commercial digital instruments appeared — samplers, synthesizers and drum machines. By the late 1990s these had morphed into digital audio workstations: digital boxes of tricks that sample and synthesize sounds, process them and combine them to form tracks. A singer who is out of tune or a drummer who is out of time can be digitally corrected. Milner suggests that digital recording is a core skill needed by today's musicians.

Central to the book is whether or not recordings are better as a result of this technological progress. Milner devotes a weighty section to how the move from analog to digital has affected the quality of recorded music. With a wider dynamic range, the compact disc should offer listeners a more sonically interesting ride than a vinyl LP. But Milner doesn't think it does. The extra dynamic range, he says, has been used to wage a 'loudness war'. Engineers compress signals so that the faintest sounds are boosted up to the level of the loudest. The result is a recording where everything is loud, all of the time.

Milner suggests that this loudness war reflects changes in the way we listen to music. In the pre-digital era, the emphasis was on quality. Record engineers and audiophiles were obsessed with 'presence', trying to recreate the concert-hall experience in our homes. But as

we listen to more music from small, cheap speakers in our cars, on our laptops and from MP3 players, the emphasis is now on loudness and convenience. Indeed, the MP3 format is designed to strip music down so that we can cram more songs on to our iPods.

Although these developments are documented elsewhere, *Perfecting Sound Forever* brings them together in a lively and accessible way. Milner focuses on the fascinating characters behind the technology. There is Edison, whose hearing became so bad that he had to 'listen' to music by biting on the wooden frame of his phonograph. The conductor Leopold Stokowski, best known for his score for the

Disney animated film *Fantasia*, comes across like a 1920s version of the Nigel Tufnel character in the 1984 film *This Is Spinal Tap*, urging the engineers to turn up the volume of the new-fangled electrical recording equipment to the maximum.

There are John and Alan Lomax, the father and son team who toured the United States in the 1930s in a desperate race to record 'authentic' music before it disappeared as performers started to emulate the styles they heard on their gramophones and radios. And there is Les Paul, the guitarist whose experiments with layering sound onto single-track tape paved the way for multi-track recording. King Tubby also stands out: he was the Jamaican recording engineer who pioneered the idea that you could take pre-existing sounds and turn them into new music in the studio.

One outcome of the developments that Milner describes is the shift in the balance of

MICHAEL OCHS ARCHIVES/GETTY

power between the recording industry and musicians. Digital audio workstations allow musicians to produce professional-quality recordings at home, with the result that many recording studios have closed down. Musicians can disseminate tracks though the Internet,

bypassing the distribution channels controlled by the big recording companies. Karl Marx would have approved — control of the means of production has passed from the elite to the man in the street. It is a shame that *Perfecting Sound Forever* doesn't dwell on the political

significance of the developments it charts — a subject for a future book, perhaps. ■

Peter Border is deputy director of the Parliamentary Office of Science and Technology, 7 Millbank, Westminster, London SW1P 3JA, UK. e-mail: peter.border@googlemail.com

Q&A: The inventor with an ear for the past

Engineer **Duncan Miller** has spent decades reviving the lost art of acoustic recording to wax cylinders, a technique pioneered by Thomas Edison. *Nature* finds out how his Vulcan Cylinder Record Company, based in Sheffield, UK, has combined sleuthing and modern chemistry to craft a new repertoire for the hand-cranked phonograph.

D. BOCKING

Why did you become interested in old recording techniques?

As a teenager I played with gramophones. I found out that many 78 rpm discs were recorded and played back without electricity. It surprised me that something as complex and delicate as sound should be captured by purely mechanical means. I've studied radio and microphones, and built amplifiers and transistors, but I was drawn to acoustic recording. In 1981, I started making new phonograph cylinders, just as Thomas Edison had done about a century earlier.

When was the wax cylinder invented?

In 1877, Edison patented a device that would inscribe a groove of variable depth using a diaphragm set in vibration by sound. He called it the phonograph. First he tried tin foil as a recording material but it got damaged quickly, turning into a Christmas decoration when played a couple of times. While Edison was inventing the light bulb, the people working for his competitor, Alexander Graham Bell, realized that wax supported on a cardboard tube was more durable. Seeing what they'd done, Edison perfected a phonograph that used a solid wax cylinder. His innovation was to use metallic stearates, which are harder and less crystalline than Bell's wax.

Is it easy to make such cylinders today?

The process by which Edison made a copper mould from a wax master is documented in outline, but I've had to invent the details on my own. Some of it was quite secret; I've examined court cases and figured out what works. He actually stopped using wax in 1912 and moved to celluloid plastic. I have adapted modern plastics to suit the product. The raw materials have also changed — the stearic acid used to make the cylinders more durable is now vacuum distilled, not



Waxing lyrical: Duncan Miller's cylinders can capture more overtones than gramophone discs.

pressed as it was in the 1900s, for example — so minor adjustments have to be made to the compound formulae to get the best results.

How was Edison's 'talking machine' received?

Edison's device was never intended to record and sell music. It was supposed to be a dictation machine; when you finished, you shaved the cylinder and dictated again. But the demand for music was so strong that the Edison company had to crank out recordings. The machines weren't designed to make duplicates, so a band would have had to play all day, simultaneously into 20 phonographs making 20 records at a time. But soon the cylinder had competition from the disc. It was partly a matter of branding. The cylinder was associated with cheap and vulgar music, such as that played by travelling showmen at fairs and circuses.

Is wax recording different for musicians?

The instruments have to be placed at the proper distance from the recording horn to get the right balance. I recently had a nine-piece jazz band in my dining room, which was fine until the sousaphone hit the chandelier. Unlike with a microphone, I can't do anything on the cylinder to make you sound better; if you lose energy the finished record sounds distant. Singers must learn to produce more sound pressure and can feel the way the horn responds to their voice.

Is there a difference in fidelity between discs and cylinders?

A new phonograph cylinder sounds better than most discs. The stylus can vibrate quicker without dissipating energy, so there is nearly another octave of overtones in the higher registers that you need for speech, strings and brass. A cylinder's groove speed is constant, so the recording fidelity is the same at both ends. With a disc, the fidelity at the inside is lower because it's going slower. So a new cylinder will have less noise than a new disc. But when we get our hands on them these days, cylinders have often been badly treated and eaten by mould because the waxes contain soaps and fatty acids. By contrast, the 78 rpm discs, which are often made of slate powder and shellac resin, don't deteriorate so badly.

Is there a market for wax cylinders today?

The Edison company alone made 2 million machines capable of playing cylinders, and thousands of them are still in operation. A fraternity of people has these machines and wants recordings for them. Our goal is to produce a cylinder record that plays well — one that would have stood up to the market in its day. The great thing at the moment is that we have little competition. ■

Interview by **Jascha Hoffman**, a writer based in New York.

e-mail: jascha@jaschahoffman.com

power between the recording industry and musicians. Digital audio workstations allow musicians to produce professional-quality recordings at home, with the result that many recording studios have closed down. Musicians can disseminate tracks though the Internet,

bypassing the distribution channels controlled by the big recording companies. Karl Marx would have approved — control of the means of production has passed from the elite to the man in the street. It is a shame that *Perfecting Sound Forever* doesn't dwell on the political

significance of the developments it charts — a subject for a future book, perhaps. ■

Peter Border is deputy director of the Parliamentary Office of Science and Technology, 7 Millbank, Westminster, London SW1P 3JA, UK. e-mail: peter.border@googlemail.com

Q&A: The inventor with an ear for the past

Engineer **Duncan Miller** has spent decades reviving the lost art of acoustic recording to wax cylinders, a technique pioneered by Thomas Edison. *Nature* finds out how his Vulcan Cylinder Record Company, based in Sheffield, UK, has combined sleuthing and modern chemistry to craft a new repertoire for the hand-cranked phonograph.

D. BOCKING

Why did you become interested in old recording techniques?

As a teenager I played with gramophones. I found out that many 78 rpm discs were recorded and played back without electricity. It surprised me that something as complex and delicate as sound should be captured by purely mechanical means. I've studied radio and microphones, and built amplifiers and transistors, but I was drawn to acoustic recording. In 1981, I started making new phonograph cylinders, just as Thomas Edison had done about a century earlier.

When was the wax cylinder invented?

In 1877, Edison patented a device that would inscribe a groove of variable depth using a diaphragm set in vibration by sound. He called it the phonograph. First he tried tin foil as a recording material but it got damaged quickly, turning into a Christmas decoration when played a couple of times. While Edison was inventing the light bulb, the people working for his competitor, Alexander Graham Bell, realized that wax supported on a cardboard tube was more durable. Seeing what they'd done, Edison perfected a phonograph that used a solid wax cylinder. His innovation was to use metallic stearates, which are harder and less crystalline than Bell's wax.

Is it easy to make such cylinders today?

The process by which Edison made a copper mould from a wax master is documented in outline, but I've had to invent the details on my own. Some of it was quite secret; I've examined court cases and figured out what works. He actually stopped using wax in 1912 and moved to celluloid plastic. I have adapted modern plastics to suit the product. The raw materials have also changed — the stearic acid used to make the cylinders more durable is now vacuum distilled, not



Waxing lyrical: Duncan Miller's cylinders can capture more overtones than gramophone discs.

pressed as it was in the 1900s, for example — so minor adjustments have to be made to the compound formulae to get the best results.

How was Edison's 'talking machine' received?

Edison's device was never intended to record and sell music. It was supposed to be a dictation machine; when you finished, you shaved the cylinder and dictated again. But the demand for music was so strong that the Edison company had to crank out recordings. The machines weren't designed to make duplicates, so a band would have had to play all day, simultaneously into 20 phonographs making 20 records at a time. But soon the cylinder had competition from the disc. It was partly a matter of branding. The cylinder was associated with cheap and vulgar music, such as that played by travelling showmen at fairs and circuses.

Is wax recording different for musicians?

The instruments have to be placed at the proper distance from the recording horn to get the right balance. I recently had a nine-piece jazz band in my dining room, which was fine until the sousaphone hit the chandelier. Unlike with a microphone, I can't do anything on the cylinder to make you sound better; if you lose energy the finished record sounds distant. Singers must learn to produce more sound pressure and can feel the way the horn responds to their voice.

Is there a difference in fidelity between discs and cylinders?

A new phonograph cylinder sounds better than most discs. The stylus can vibrate quicker without dissipating energy, so there is nearly another octave of overtones in the higher registers that you need for speech, strings and brass. A cylinder's groove speed is constant, so the recording fidelity is the same at both ends. With a disc, the fidelity at the inside is lower because it's going slower. So a new cylinder will have less noise than a new disc. But when we get our hands on them these days, cylinders have often been badly treated and eaten by mould because the waxes contain soaps and fatty acids. By contrast, the 78 rpm discs, which are often made of slate powder and shellac resin, don't deteriorate so badly.

Is there a market for wax cylinders today?

The Edison company alone made 2 million machines capable of playing cylinders, and thousands of them are still in operation. A fraternity of people has these machines and wants recordings for them. Our goal is to produce a cylinder record that plays well — one that would have stood up to the market in its day. The great thing at the moment is that we have little competition. ■

Interview by **Jascha Hoffman**, a writer based in New York.

e-mail: jascha@jaschahoffman.com

NEWS & VIEWS

M. BILDSTRÖM/SKOGENBILD



Boreal forest in Norrland, Sweden.

ATMOSPHERIC CHEMISTRY

Thwarting the seeds of clouds

Paul J. Ziemann

Atmospheric oxidation of hydrocarbons emitted from plants leads to the formation of aerosol particles that affect cloud properties. Contrary to what was thought, this process might add to global warming.

The ephemeral cloud of tiny drops that you see above the spout of your teapot forms in the same way as clouds in the sky — by the condensation of water vapour onto microscopic ‘seed’ particles, known as nuclei. In your kitchen, the nuclei are nanometre-sized clusters of tens of water molecules. But in the atmosphere, where much larger particles of dust, soot, salt and organic compounds are present, water molecules do not wait for water nuclei to form (nucleate). Instead, they condense onto a subset of particles called cloud condensation nuclei (CCN), which are typically about 60 to 100 nanometres in size and contain some water-soluble material.

The number of CCN in the atmosphere affects the properties of clouds, which in turn affect climate. In particular, clouds formed at higher CCN concentrations have more and smaller drops than those formed at lower concentrations, and so reflect more sunlight and are longer-lived — effects that, at the global scale, enhance the planetary cooling that counteracts some of the warming caused by greenhouse gases¹. On page 381 of this issue, Kiendler-Scharr *et al.*² explore the interplay between terpenes (organic compounds) emitted from boreal forests, atmospheric oxidants and CCN. They conclude that this

interplay could lead to higher global temperatures through a climate feedback mechanism that is currently predicted to slow the rate of warming.

In the air above boreal forests, away from urban centres, the particles that act as CCN are composed primarily of oxidized organic compounds of low volatility. These compounds form when volatile monoterpene compounds emitted from coniferous trees — $C_{10}H_{16}$ hydrocarbons such as pinenes, which are responsible for the smell of pine forests — react with hydroxyl radicals (OH) or ozone (O_3) (ref. 3). These reactions can affect CCN concentrations by providing a source of condensable material from which new particles grow to the size required for them to act as CCN⁴. They might also increase the number of nanometre-sized particles formed through nucleation, similar to what happens above the teapot, except that organic molecules rather than water molecules are involved.

Emissions of monoterpenes are known to increase with temperature. It has been proposed⁵ that, as global temperatures rise, this could lead to higher CCN concentrations that will increase cloud reflectivity and cooling, thereby providing negative feedback to the warming caused by greenhouse gases. In a

series of plant-chamber experiments, Kiendler-Scharr *et al.*² add a new twist to this scenario. They show that, when emissions of isoprene — the C_5H_8 hydrocarbon that dominates global emissions from vegetation — from deciduous trees are added to air containing a mixture of monoterpenes and ozone in light, the number and mass of organic aerosol particles formed by oxidation reactions are reduced.

This inhibitory effect of isoprene on particle nucleation and growth provides an explanation for seasonal variations in particle-formation events observed in European boreal forests: here, the ratio of isoprene to monoterpene emissions is low in the spring and autumn but high in the summer⁶, whereas particle formation follows the opposite trend⁴. Future temperature-induced changes in the species composition of boreal forests are predicted to increase the ratio of isoprene to monoterpene emissions⁷. An important implication of Kiendler-Scharr and colleagues’ results is that such changes could reverse the direction of the proposed climate feedback, thereby leading to increased warming instead of cooling.

The details of the mechanism by which isoprene inhibits the nucleation and growth of organic particles are not known, but the chemical complexity implied by these results²

is typical of atmospheric chemistry. Years of field, laboratory and modelling studies indicate that, in the atmosphere, particle nucleation and growth might involve both gas and condensed-phase reactions, together with a myriad of compounds such as sulphuric acid, water, ammonia, organic compounds and several oxidants⁴.

Kiendler-Scharr *et al.*² nevertheless provide a plausible explanation for the effect of isoprene on the reactions occurring in their plant chamber. They measured lower concentrations of OH radicals when they added isoprene to the chamber, indicating that isoprene reacts with OH radicals that would otherwise react with monoterpenes. Because the isoprene reaction products are unlikely to contribute much to nucleation or condensation processes (unlike the products of reactions between monoterpenes and OH radicals), the authors propose that the scavenging of OH radicals by isoprene reduces the occurrence of these processes. The authors also observed a strong exponential dependence of the nucleation rate on the concentration of OH radicals and on the isoprene-to-monoterpene ratio; this suggests that the nucleation process is complicated, involving several reaction products or reactions with OH radicals.

Intriguingly, Kiendler-Scharr and colleagues' results² seem to conflict with recent field measurements⁸ and the results of laboratory experiments⁹, which suggested that isoprene causes relatively minor suppression of OH-radical concentrations because of efficient OH-radical recycling. There could be a few reasons for the discrepancy, but one possibility is that reactions involving hydroperoxy radicals (HO₂) — key participants in the recycling mechanism — are suppressed in plant-chamber experiments because of the higher relative concentration of organoperoxy radicals, which take part in competing reactions.

Some of the remarkable sensitivity of particle nucleation and growth to terpene composition² could be due to interactions between the reaction products of monoterpenes and isoprene. It will therefore be necessary to see what happens when other atmospheric components, such as anthropogenic hydrocarbons and nitrogen oxides, are added to the mix, as these compounds will alter which reaction products form. Furthermore, if Kiendler-Scharr and colleagues' results are to be extrapolated to the atmosphere, further work is needed to unravel what happens at both the molecular and global scales. Consideration must be given not only to chemical-reaction and nucleation mechanisms, but also to issues such as the potential suppression of terpene emissions by elevated carbon dioxide concentrations¹⁰, and the quantitative relationship between new particle formation and CCN concentrations¹¹. The outcome could have major implications for predictions of global climate change. ■

Paul J. Ziemann is at the Air Pollution Research

Center and the Department of Environmental Sciences, University of California, Riverside, California 92521, USA.

e-mail: pziemann@ucr.edu

1. Andreae, M. O. & Rosenfeld, D. *Earth Sci. Rev.* **89**, 13–41 (2008).
2. Kiendler-Scharr, A. *et al. Nature* **461**, 381–384 (2009).
3. Tunved, P. *et al. Science* **312**, 261–263 (2006).

4. Kulmala, M. *et al. J. Aerosol Sci.* **35**, 143–176 (2004).
5. Kulmala, M. *et al. Atmos. Chem. Phys.* **4**, 557–562 (2004).
6. Hakola, H. *et al. Atmos. Environ.* **37**, 1623–1634 (2003).
7. Kellomäki, S., Rouvinen, I., Peltola, H., Strandman, H. & Steinbrecher, R. *Glob. Change Biol.* **7**, 531–544 (2001).
8. Lelieveld, J. *et al. Nature* **452**, 737–740 (2008).
9. Paulot, F. *et al. Science* **325**, 730–733 (2009).
10. Arneth, A. *et al. Geophys. Res. Lett.* **34**, L18813 (2007).
11. Pierce, J. R. & Adams, P. J. *Atmos. Chem. Phys.* **9**, 1339–1356 (2009).

DEVELOPMENTAL BIOLOGY

Asexual healing

Eric A. Shoubridge

The development of healthy monkeys from embryos in which the egg contains nuclear DNA from one donor and mitochondrial DNA from another suggests a method to prevent inheritance of certain human diseases.

Preventing the transmission of harmful genetic mutations from parent to baby is a double challenge for reproductive biologists as there are two genomes in our cells that can carry mutations — one in the nucleus and one in the mitochondria. The mitochondrial genome is tiny, encoding only a handful of proteins, all essential for cellular energy production. However, despite its small size, disorders associated with mutations in mitochondrial DNA are among the most common genetically inherited metabolic diseases, and there are currently no effective treatments¹. On page 367 of this issue, Tachibana *et al.*² report the development of a technique that could prevent transmission of defective mitochondrial DNA from mother to baby.

About 1:5,000 people have, or are likely to develop, a mitochondrial disease³, and as many as 1:200 newborns carry one of the common mitochondrial DNA mutations⁴. All mitochondria in the developing embryo come from the egg, or oocyte, and none from the sperm. So transmission of mutated mitochondrial DNA from mother to offspring could theoretically be prevented by correcting the defect in the egg. This is exactly what Tachibana *et al.* have done.

Working with rhesus macaque monkeys (*Macaca mulatta*), the authors² reconstructed mature oocytes containing the nuclear genome from one oocyte and the mitochondrial genome from another. To do this they removed the nuclear genetic material from one oocyte, leaving behind all of the mitochondrial DNA, then transferred it to another oocyte whose nucleus had been removed (a cytoplast), but which contained a full complement of mitochondrial DNA (Fig. 1).

Although this sounds simple, it is, in fact, a technical tour de force. Mature oocytes are arrested in the second meiotic division, a stage of the cell cycle in which the nuclear genetic material is present as a spindle–chromosomal complex, consisting of condensed chromosomes

attached to the thread-like spindle fibres that distribute chromosomes to daughter cells as meiosis progresses. The nuclear membrane has broken down by the second meiotic division and so the spindle–chromosomal complex is hard to visualize except with toxic dyes. It is also incredibly difficult to remove this complex intact. To get around these problems, Tachibana *et al.*² used polarized microscopy — a technique that they had developed⁵ to create spindle-free oocytes for reprogramming nuclei from non-gametes (somatic cells). Using this technique, the authors could remove the spindle–chromosomal complex from the donor oocyte with essentially 100% efficiency, taking with it only a small amount of cytoplasm (and so avoiding transferring mitochondria) and a cell membrane (a structure called a karyoplast). This manoeuvre was crucial to the success of the experiments.

Next, Tachibana and colleagues had to find a way to fuse the karyoplast with the cytoplast containing the mitochondrial DNA. They first tried fusion using an electric current, but this induced the oocyte to resume meiosis prematurely. The authors therefore resorted to using an extract from a virus that is known to promote cellular fusion.

The reconstructed oocytes could be fertilized and went on to develop normally as pre-implantation embryos *in vitro*. Embryonic stem cells derived from these embryos had a normal set of chromosomes and could mature into different cell types in culture, indicating that they developed normally. The real test, however, was to implant the embryos into female macaques to see whether they could produce normal offspring. Of the nine female macaques that were implanted, three became pregnant, one with twins. So far, three apparently healthy baby macaques have been born. Tests to determine the genetic make-up of these animals showed that the nuclear genome was inherited exclusively from the karyoplast donor, and that the mitochondrial DNA

is typical of atmospheric chemistry. Years of field, laboratory and modelling studies indicate that, in the atmosphere, particle nucleation and growth might involve both gas and condensed-phase reactions, together with a myriad of compounds such as sulphuric acid, water, ammonia, organic compounds and several oxidants⁴.

Kiendler-Scharr *et al.*² nevertheless provide a plausible explanation for the effect of isoprene on the reactions occurring in their plant chamber. They measured lower concentrations of OH radicals when they added isoprene to the chamber, indicating that isoprene reacts with OH radicals that would otherwise react with monoterpenes. Because the isoprene reaction products are unlikely to contribute much to nucleation or condensation processes (unlike the products of reactions between monoterpenes and OH radicals), the authors propose that the scavenging of OH radicals by isoprene reduces the occurrence of these processes. The authors also observed a strong exponential dependence of the nucleation rate on the concentration of OH radicals and on the isoprene-to-monoterpene ratio; this suggests that the nucleation process is complicated, involving several reaction products or reactions with OH radicals.

Intriguingly, Kiendler-Scharr and colleagues' results² seem to conflict with recent field measurements⁸ and the results of laboratory experiments⁹, which suggested that isoprene causes relatively minor suppression of OH-radical concentrations because of efficient OH-radical recycling. There could be a few reasons for the discrepancy, but one possibility is that reactions involving hydroperoxy radicals (HO₂) — key participants in the recycling mechanism — are suppressed in plant-chamber experiments because of the higher relative concentration of organoperoxy radicals, which take part in competing reactions.

Some of the remarkable sensitivity of particle nucleation and growth to terpene composition² could be due to interactions between the reaction products of monoterpenes and isoprene. It will therefore be necessary to see what happens when other atmospheric components, such as anthropogenic hydrocarbons and nitrogen oxides, are added to the mix, as these compounds will alter which reaction products form. Furthermore, if Kiendler-Scharr and colleagues' results are to be extrapolated to the atmosphere, further work is needed to unravel what happens at both the molecular and global scales. Consideration must be given not only to chemical-reaction and nucleation mechanisms, but also to issues such as the potential suppression of terpene emissions by elevated carbon dioxide concentrations¹⁰, and the quantitative relationship between new particle formation and CCN concentrations¹¹. The outcome could have major implications for predictions of global climate change. ■

Paul J. Ziemann is at the Air Pollution Research

Center and the Department of Environmental Sciences, University of California, Riverside, California 92521, USA.

e-mail: pziemann@ucr.edu

1. Andreae, M. O. & Rosenfeld, D. *Earth Sci. Rev.* **89**, 13–41 (2008).
2. Kiendler-Scharr, A. *et al.* *Nature* **461**, 381–384 (2009).
3. Tunved, P. *et al.* *Science* **312**, 261–263 (2006).

4. Kulmala, M. *et al.* *J. Aerosol Sci.* **35**, 143–176 (2004).
5. Kulmala, M. *et al.* *Atmos. Chem. Phys.* **4**, 557–562 (2004).
6. Hakola, H. *et al.* *Atmos. Environ.* **37**, 1623–1634 (2003).
7. Kellomäki, S., Rouvinen, I., Peltola, H., Strandman, H. & Steinbrecher, R. *Glob. Change Biol.* **7**, 531–544 (2001).
8. Lelieveld, J. *et al.* *Nature* **452**, 737–740 (2008).
9. Paulot, F. *et al.* *Science* **325**, 730–733 (2009).
10. Arneth, A. *et al.* *Geophys. Res. Lett.* **34**, L18813 (2007).
11. Pierce, J. R. & Adams, P. J. *Atmos. Chem. Phys.* **9**, 1339–1356 (2009).

DEVELOPMENTAL BIOLOGY

Asexual healing

Eric A. Shoubridge

The development of healthy monkeys from embryos in which the egg contains nuclear DNA from one donor and mitochondrial DNA from another suggests a method to prevent inheritance of certain human diseases.

Preventing the transmission of harmful genetic mutations from parent to baby is a double challenge for reproductive biologists as there are two genomes in our cells that can carry mutations — one in the nucleus and one in the mitochondria. The mitochondrial genome is tiny, encoding only a handful of proteins, all essential for cellular energy production. However, despite its small size, disorders associated with mutations in mitochondrial DNA are among the most common genetically inherited metabolic diseases, and there are currently no effective treatments¹. On page 367 of this issue, Tachibana *et al.*² report the development of a technique that could prevent transmission of defective mitochondrial DNA from mother to baby.

About 1:5,000 people have, or are likely to develop, a mitochondrial disease³, and as many as 1:200 newborns carry one of the common mitochondrial DNA mutations⁴. All mitochondria in the developing embryo come from the egg, or oocyte, and none from the sperm. So transmission of mutated mitochondrial DNA from mother to offspring could theoretically be prevented by correcting the defect in the egg. This is exactly what Tachibana *et al.* have done.

Working with rhesus macaque monkeys (*Macaca mulatta*), the authors² reconstructed mature oocytes containing the nuclear genome from one oocyte and the mitochondrial genome from another. To do this they removed the nuclear genetic material from one oocyte, leaving behind all of the mitochondrial DNA, then transferred it to another oocyte whose nucleus had been removed (a cytoplast), but which contained a full complement of mitochondrial DNA (Fig. 1).

Although this sounds simple, it is, in fact, a technical tour de force. Mature oocytes are arrested in the second meiotic division, a stage of the cell cycle in which the nuclear genetic material is present as a spindle–chromosomal complex, consisting of condensed chromosomes

attached to the thread-like spindle fibres that distribute chromosomes to daughter cells as meiosis progresses. The nuclear membrane has broken down by the second meiotic division and so the spindle–chromosomal complex is hard to visualize except with toxic dyes. It is also incredibly difficult to remove this complex intact. To get around these problems, Tachibana *et al.*² used polarized microscopy — a technique that they had developed⁵ to create spindle-free oocytes for reprogramming nuclei from non-gametes (somatic cells). Using this technique, the authors could remove the spindle–chromosomal complex from the donor oocyte with essentially 100% efficiency, taking with it only a small amount of cytoplasm (and so avoiding transferring mitochondria) and a cell membrane (a structure called a karyoplast). This manoeuvre was crucial to the success of the experiments.

Next, Tachibana and colleagues had to find a way to fuse the karyoplast with the cytoplast containing the mitochondrial DNA. They first tried fusion using an electric current, but this induced the oocyte to resume meiosis prematurely. The authors therefore resorted to using an extract from a virus that is known to promote cellular fusion.

The reconstructed oocytes could be fertilized and went on to develop normally as pre-implantation embryos *in vitro*. Embryonic stem cells derived from these embryos had a normal set of chromosomes and could mature into different cell types in culture, indicating that they developed normally. The real test, however, was to implant the embryos into female macaques to see whether they could produce normal offspring. Of the nine female macaques that were implanted, three became pregnant, one with twins. So far, three apparently healthy baby macaques have been born. Tests to determine the genetic make-up of these animals showed that the nuclear genome was inherited exclusively from the karyoplast donor, and that the mitochondrial DNA

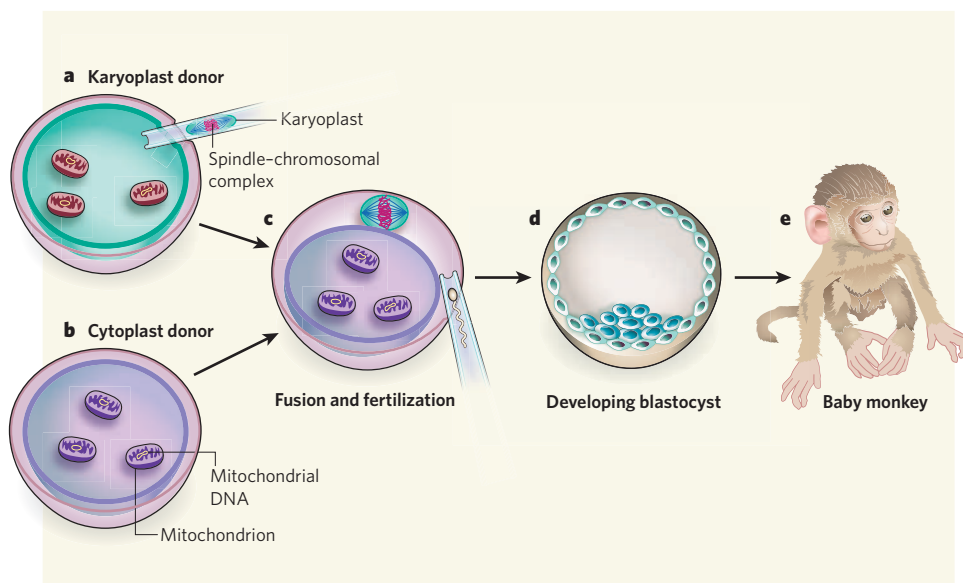


Figure 1 | Swapping mitochondrial DNA in mammalian oocytes. Working with rhesus macaque monkeys, Tachibana *et al.*² removed the nuclear material plus a cellular membrane (a karyoplast) from a mature oocyte, leaving behind its mitochondria (a). They transferred the karyoplast to an oocyte whose nucleus had been removed (a cytoplasm; b). The nuclear material in the karyoplast consists of condensed chromosomes attached to thread-like spindle fibres (the spindle–chromosomal complex). The authors fused the karyoplast with the cytoplasm and then fertilized the reconstructed oocyte (c). The developing blastocyst (d) was implanted in a surrogate mother, which gave birth to a healthy baby (e). This technique has the potential to prevent transmission of human mutated mitochondrial DNA from mother to baby.

was derived from the cytoplasm donor.

It is encouraging that the technique used by Tachibana and colleagues² seems to have worked so efficiently in a primate model, but there are many hurdles, some practical, some ethical, that need to be overcome before this method could be transferred to the clinic. The practical issues relate to the safety of the viral agent used to fuse the spindle–chromosomal complex with the enucleated oocyte, as well as the efficiency with which spindle–chromosomal complexes can be safely removed and transferred from human oocytes. Also, it's not known whether the presence of foreign mitochondrial DNA in cells will have any biological consequences for the offspring, and this will have to be carefully investigated.

As discussed in a recent Editorial in *Nature*⁶, the ethical debates that surround human reproductive research will probably be revived by this work. The procedure used by Tachibana and colleagues² requires the use of donor eggs with normal mitochondrial DNA, and certainly the research necessary to test the efficiency and safety of the procedure will require the destruction of embryos. However, unlike therapeutic cloning procedures, in which somatic-cell nuclei are transferred to enucleated eggs with the goal of isolating embryonic stem cells, here, the donor egg is not destroyed, but rather allows the birth of a healthy child.

But the mixing of nuclear and mitochondrial genomes brings other ethical issues to the fore, not least the production of offspring with genetic contributions from three parents — a

combination forbidden by most jurisdictions. Thus, the laws regulating human germline DNA manipulation would have to be rewritten. It is worthwhile pointing out that if donor eggs could be obtained from a maternal relative who has not inherited the mutation, the reconstructed embryo would be genetically identical to one conceived naturally because of the exclusive transmission of mitochondrial DNA through the female germline.

Currently, the only way to prevent transmission of mutated mitochondrial DNA is pre-implantation genetic diagnosis, in which cells of the early embryo are tested for the presence of mitochondrial-DNA mutations, and only genetically normal embryos are implanted⁷. There is, however, no guarantee that embryos without the mutation will be identified, and it is also not always clear whether embryos with low proportions of mutated mitochondrial DNA will be free of disease. The technique reported in the present paper, if proven safe and effective, could provide a universal solution to the problem.

Eric A. Shoubridge is at the Montreal Neurological Institute, McGill University, Montreal, Quebec H3A 2B4, Canada.
e-mail: eric@ericpc.mni.mcgill.ca

1. Taylor, R. W. & Turnbull, D. M. *Nature Rev. Genet.* **6**, 389–402 (2005).
2. Tachibana, M. *et al.* *Nature* **461**, 367–372 (2009).
3. Schaefer, A. M. *et al.* *Ann. Neurol.* **63**, 35–39 (2008).
4. Elliott, H. R., Samuels, D. C., Eden, J. A., Relton, C. L. & Chinnery, P. F. *Am. J. Hum. Genet.* **83**, 254–260 (2008).
5. Byrne, J. A. *et al.* *Nature* **450**, 497–502 (2007).
6. *Nature* **460**, 1057 (2009).
7. Steffann, J. *et al.* *J. Med. Genet.* **43**, 244–247 (2006).



50 YEARS AGO

More science means more information, in the form of books, journals and conferences. No scientist needs to be reminded of this. It was estimated recently that to keep up with all the current work a physiologist would have to read nearly four hundred papers a day; Sir George Thomson has even gone so far as to suggest that it is the impossibility of absorbing the necessary information that will ultimately halt scientific progress.

From *Nature* 19 September 1959.

100 YEARS AGO

The position and prospects of polar exploration have been given great attention in the daily Press during the last few days. No precise information as to Dr. Cook's journey to the North Pole has yet been published, but the general narrative of Commander Peary's expedition leaves little room for doubt that Commander Peary reached the neighbourhood of the pole, and probably the pole itself, though an element of uncertainty must exist until his observations for latitude are examined critically ... Announcement has also just been made that a British Antarctic expedition will start next August under Captain R. F. Scott, who commanded the National Antarctic Expedition of 1900–4, with the object of reaching the South Pole. As all the world knows, Mr Shackleton's record of this year has given Great Britain the premier position in Antarctic exploration, and an earnest desire is felt by British explorers to place to the credit of this country the feat of first reaching the South Pole ... The full narrative of Commander Peary's expedition to the North Pole appeared in the *Times* of September 11 and 13 ... The expedition left Etah, Greenland, on August 18, 1908, in the *Roosevelt*, having on board 22 Eskimo men, 17 women, 236 dogs, and about 40 walrus.

From *Nature* 16 September 1909.

50 & 100 YEARS AGO

FLUID DYNAMICS

To merge or not to merge ...

Frieder Mugele

... that is the dilemma addressed in a study of oppositely charged liquid drops controlled by an electric field. Contrary to conventional wisdom, beyond a critical charge, the drops fail to merge.

Just as we may be guided by a sense of 'more is more' in our daily lives, so physicists often use this principle as a good first guess to explain physical phenomena. For example, in a situation as simple as two objects with electrically opposite charges, the expectation is that the more strongly charged the objects are, the more they should attract each other. In the case of liquid drops, we would expect them to bump into each other and coalesce into one larger drop, and that, the higher their charge, the quicker this would happen. It seems that the simpler a situation is, the more stunned we are if nature 'refuses' to follow our expectations. Such a refusal is exactly what Ristenpart *et al.*¹ find in experiments described on page 377 of this issue. Counter-intuitively, the authors show that two oppositely charged drops bounce off each other and do not coalesce if their charge exceeds a threshold value.

Ristenpart and colleagues' experiment¹ is simple. A millimetre-sized water drop immersed in a beaker filled with oil becomes positively charged when brought into contact with a metal wire at high voltage. A second, much bigger drop, covering the bottom of the beaker, is kept at ground voltage and becomes negatively charged. The resulting electric field pulls the small drop towards the big one. For low to moderate electric-field strengths, or equivalently for low drop charges, the small drop is attracted towards the large one, deforms, touches and coalesces with it. For high field strengths, and beyond a critical

value, the droplet is still attracted towards the larger drop and deforms on approaching it, but instead of coalescing, it bounces off and moves away towards the wire.

The authors¹ show that this phenomenon is independent of the fluids involved in the process: the non-coalescence behaviour occurs for clean water drops in silicone oil, brine drops in crude oil, vinegar drops in olive oil, and water drops in air. Under suitable conditions, the small drop can even shuttle back and forth several times between the wire and the big drop. This effect is similar to the to-and-fro motion that small scraps of paper or Styrofoam experience when placed between the two electrodes of a high-voltage generator, and is usually demonstrated in first-year undergraduate laboratory experiments on electrostatics.

To understand the non-coalescence of oppositely charged drops, Ristenpart *et al.* used high-speed video microscopy to record drop motion right at the moment of coalescence/non-coalescence. By doing so, they found that all drops, irrespective of their charge, established contact by forming a microscopic capillary bridge. But whereas for low-charge drops the bridge remained stable and sucked the small drop into the big one, for high-charge drops it broke up in less than a millisecond.

One of the beauties of Ristenpart and colleagues' work¹ is that it provides a simple and convincing explanation for the observed phenomenon. As long as the drops are apart, electrostatic forces pull their surfaces towards each other, producing conically shaped protrusions

known as Taylor cones² at the drops' leading edges. But as soon as the capillary bridge is formed, the two drops are immediately electrically short-circuited and hence all electrostatic forces vanish abruptly. From that moment on, the surface tension of the drops in combination with the geometry of the Taylor cones determines the fate of the capillary bridge. For low-charge drops, the cones are blunt and hydrodynamically stable. They grow and suck the small drop into the big one. For high-charge drops, the cones are sharper and unstable. As a result, they break and the drops bounce off each other. The coalescence/non-coalescence phenomenon is thus a consequence of the geometry of the Taylor cones initially formed under the influence of the electric field and the subsequent sudden vanishing of the electrostatic forces (Fig. 1).

Interestingly, Ristenpart *et al.* find that the threshold charge for non-coalescence increases for very low salt concentrations in water — that is, for poorly conducting water. Such conductivity dependence has also been observed in other electrohydrodynamic phenomena, including the emission of jets and drops from Taylor cones³ and the periodic detachment and reattachment of sessile liquid drops from a wire through the application of a voltage⁴. The latter experiment⁴ explains the conductivity dependence in terms of the increasing electrical resistivity during the break-up of the capillary bridge, and might well help to explain Ristenpart and co-workers' observations at low salt concentrations.

What will be the impact of Ristenpart and colleagues' work¹? Their observation of the counter-intuitive, non-coalescing behaviour of charged liquid drops doesn't have an immediate link to a specific scientific problem or technological application. However, given the general validity of the phenomenon for any liquid–liquid or liquid–gas system, their study will provide insights into our understanding of a variety of well-known physical problems that involve drops in electric fields. For example, it should further our understanding of electrocoalescence-based de-emulsification processes that are widely used to separate residual water from crude oil. Moreover, it should help to explain the long-standing problem of cloud electrification in thunderstorms, which was addressed by Lord Rayleigh⁵ and Geoffrey Taylor² in their seminal contributions to the field of electrohydrodynamics.

Frieder Mugele is at the MESA+ Institute for Nanotechnology and the Faculty of Science and Technology, University of Twente, 7500 AE Enschede, the Netherlands.
e-mail: f.mugele@utwente.nl

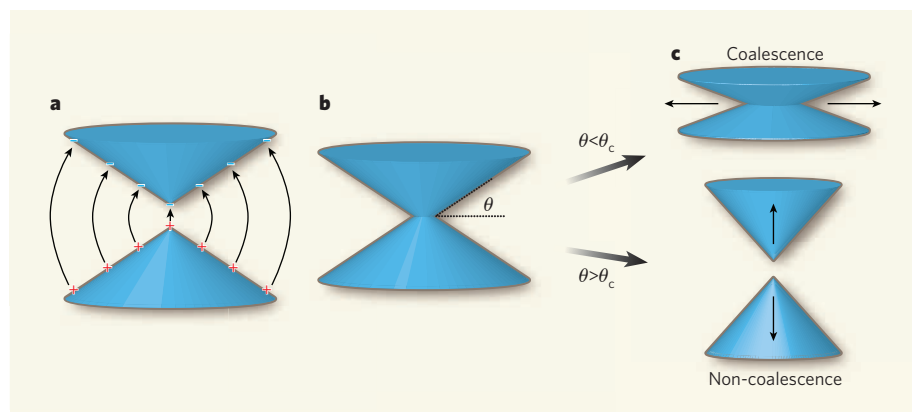


Figure 1 | Geometry of liquid-drop motion. **a**, The leading edges of two approaching liquid drops of opposite charge elongate and acquire a conical shape just before contact; the black lines represent the electric field created by the charged drops. **b**, On contact, the intersecting cones are characterized by a cone angle, θ , that depends on the strength of the electric field just before contact. **c**, Ristenpart and colleagues¹ show that the fate of the drops is determined by the cone angle at contact: below a critical cone angle, θ_c , the drops coalesce; above θ_c , the drops fail to coalesce.

1. Ristenpart, W. D., Bird, J. C., Belmonte, A., Dollar, F. & Stone, H. A. *Nature* **461**, 377–380 (2009).
2. Taylor, G. *Proc. R. Soc. Lond. A* **280**, 383–397 (1964).
3. Collins, R. T., Jones, J. J., Harris, M. T. & Basaran, O. A. *Nature Phys.* **4**, 149–154 (2008).
4. Baret, J.-C. & Mugele, F. *Phys. Rev. Lett.* **96**, 016106 (2006).
5. Lord Rayleigh *Proc. R. Soc. Lond.* **28**, 405–409 (1879).

GENOMICS

Hepatitis C virus gets personal

Shawn P. Iadonato and Michael G. Katze

Many people infected with the hepatitis C virus are not cured despite gruelling therapy. A human genetic variant that predicts successful treatment has been identified. So is personalized therapy now a possibility?

A staggering 170 million people are persistently infected with the hepatitis C virus (HCV), including 1–1.7% of people in the United States and roughly the same proportion in the European Union¹. HCV infection causes a slowly progressive liver disease that can lead to cirrhosis over several decades. People can be infected by one of several genetic types of HCV, each of which varies in its sensitivity to therapy. Genotype 1 HCV is the most difficult to treat, with clearance occurring in only about 50% of infected people during therapy. On page 399 of this issue, Ge *et al.*², as part of David Goldstein's group, report the identification of a variant, or polymorphism, in the human genome that is significantly associated with virus clearance during treatment. Two independent studies, one by Suppiah *et al.*³ and the other by Tanaka *et al.*⁴, report similar findings in *Nature Genetics*.

The only approved treatment for HCV infection is weekly injection of polyethylene glycol-conjugated interferon- α plus daily oral ribavirin. Interferon is thought to work by stimulating the body's natural defences against virus infection; the mechanism of action of ribavirin is not completely understood. The 48-week treatment course is often poorly tolerated, so new approaches are needed that enhance the effectiveness and shorten the duration of therapy, while targeting the longest antiviral courses to the most appropriate patients.

Ge and colleagues² tackled this problem by applying a relatively new methodology in genetics, the genome-wide association study (GWAS). These types of study test the association of a characteristic of interest, usually a disease, with typically hundreds of thousands of single nucleotide polymorphisms (SNPs) — variations in one of the three billion nucleotide base pairs that make up the human genome. If, for instance, the variant SNP is found to be significantly more common in people with a disease than in a disease-free control group, the variant is considered to be associated with that disease. The power of GWAS to detect such associations derives from the large number of variants that are screened and the many people included in these studies.

Ge *et al.*² analysed 1,137 patients with HCV infection who were enrolled in a clinical trial to test the relative effectiveness of two commercial interferon preparations⁵. They identified several SNPs near the *IL28B* gene on chromosome 19 that were significantly more common in the

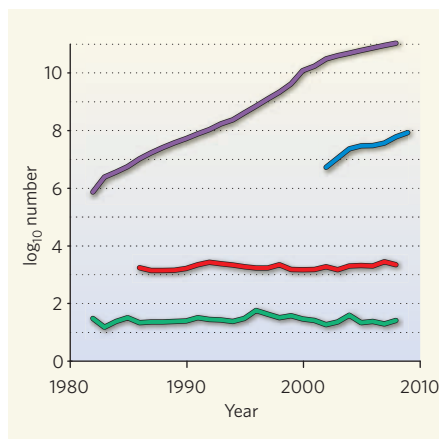


Figure 1 | The gap between genetic information and medical innovation. Although the amount of genetic and genomic information available to researchers is expanding rapidly, advances in medical innovation have not followed suit. The graph shows the size of the GenBank database (a collection of all publicly available DNA sequences) between 1982 and 2008 (purple); the number of submissions of human single nucleotide polymorphisms (SNPs) to the SNP database (dbSNP) of the National Center for Biotechnology Information (NCBI) between 2002 and 2009 (blue); the number of Investigational New Drug (IND) applications received by the Center for Drug Evaluation and Research/US Food and Drug Administration (CDER/FDA) during 1986–2008 (red); and the number of new molecular entities (drugs not previously marketed in the United States in any form) approved by the CDER/FDA between 1982 and 2008 (green). Data are compiled from the NCBI and FDA websites.

patients that responded to interferon therapy than in non-responders. Across a multi-ethnic population, approximately 80% of patients who carry two copies of the advantageous variant cleared the virus during interferon therapy and remained virus-free for a period of 24 weeks post-treatment. Patients who meet these initial criteria for response rarely experience a resurgence of virus and are widely considered to be cured.

Ge and colleagues' results² are independently confirmed by two GWAS published online in *Nature Genetics*^{3,4}. Suppiah *et al.*³ and Tanaka *et al.*⁴ characterize an overlapping group of SNPs in the same region of chromosome 19 in responders from different populations — Suppiah *et al.* studying HCV-infected patients of European origin, and Tanaka *et al.*

studying a group of Japanese patients.

Although all of the identified variants in the three studies lie in or near the *IL28B* gene, none of them has an obvious effect on the function of this gene, which encodes interferon- λ 3, a growth factor with similarities to the interferon- α preparations used as treatment. The interferon- λ proteins have lower antiviral activity than interferon- α in laboratory experiments⁶, but despite this, interferon- λ 3 may contribute to virus clearance either spontaneously or during drug treatment. A study by Thomas and colleagues published online in *Nature*⁷ reports that the same variant described by Ge *et al.*² is also associated with spontaneous clearance of HCV, that is, in the absence of drug treatment. And a related interferon- λ protein encoded by the *IL29* gene was shown to reduce the amount of HCV virus in the body when given to genotype-1-infected patients⁸.

An important finding from Ge and colleagues' work² is the population distribution of the advantageous SNP, which is significantly more frequent in the Caucasian and Asian populations than in African Americans. About 30–50% of Sub-Saharan Africans carry this variant, compared with about 90% of Chinese and Japanese people⁹. Clinicians have long struggled to explain the relatively poorer outcomes among HCV-infected African Americans in trials of interferon and ribavirin therapy. Using a standard definition of treatment response, African Americans clear the virus roughly half as frequently as Caucasians¹⁰, and some of this difference now seems to be explained by population differences in the incidence of the advantageous *IL28B* genotype.

The question remains, however, as to how readily these and other observations from GWAS can be translated into meaningful changes in patient care. The field of human genetics has described many associations between specific mutations and medically important outcomes, but rarely have these observations resulted in new therapies to treat disease or in major shifts in existing treatments. This failure is exemplified by the lack of clinical benefit that followed the cloning in 1989 of the gene responsible for cystic fibrosis¹¹ — the first example of the use of molecular genetics to discover the cause of an otherwise poorly understood condition. Although some progress has been made in treating patients with cystic fibrosis, in the ensuing 20 years neither of the two newly approved drugs for this condition were developed using knowledge of the gene mutations that cause it. Apart from a few well-characterized beneficial mutations (for example, those resulting in resistance to HIV infection¹²), genetics has been an inefficient tool for drug discovery.

So, although these findings^{2–4} raise the tantalizing prospect of a more personalized approach to treating HCV by tailoring treatment to patients who are most likely to benefit, the reality is more sobering. Diagnostic testing to identify likely responders to interferon may

be a future possibility, but clinical decision-making will be clouded by the fact that the effect of the advantageous variant is not absolute — not all carriers of the variant clear the virus, nor do all patients lacking the variant fail to benefit from treatment. Furthermore, there is currently no alternative to interferon therapy for the HCV-infected population.

Although the amount of genetic information available to researchers across various disciplines has expanded, advances in data collection have historically failed to translate into equivalent advances in medical innovation (Fig. 1). And although GWAS can probe the subtler effects of a larger number of gene variants, little attention has been paid to the

black box that stands between most genetic discoveries and the promise of personalized treatments. A challenge for the future will be to apply genetic tools in a way that accelerates drug and diagnostics development, including better integration of genetic studies into the drug-development process, a reduced emphasis on modest genetic contributions to a disease, and a focus on the role of genetic variation in maintaining health as a blueprint for designing new drugs.

Shawn P. Iadonato is at Kineta, Inc., 307 Westlake Avenue North, Seattle, Washington 98109, USA. Michael G. Katze is in the Department of Microbiology and the National Primate Center, University of Washington,

Seattle, Washington 98195-8070, USA.

e-mails: siadonato@kinetabio.com;
honey@u.washington.edu

1. www.who.int/mediacentre/factsheets/fs164/en
2. Ge, D. *et al. Nature* **461**, 399–401 (2009).
3. Supiah, V. *et al. Nature Genet.* doi:10.1038/ng.447 (2009).
4. Tanaka, Y. *et al. Nature Genet.* doi:10.1038/ng.449 (2009).
5. McHutchison, J. G. *et al. N. Engl. J. Med.* **361**, 580–593 (2009).
6. Sheppard, P. *et al. Nature Immunol.* **4**, 63–68 (2003).
7. Thomas, D. L. *et al. Nature* doi:10.1038/nature08463 (2009).
8. Shiffman, M. L. *et al. Proc. 44th Annu. Meet. Eur. Assoc. Study Liver (EASL)*, Copenhagen, abstr. 520 (2009).
9. The International HapMap Consortium *Nature* **437**, 1299–1320 (2005).
10. Conjeevaram, H. S. *et al. Gastroenterology* **131**, 470–477 (2006).
11. Riordan, J. R. *et al. Science* **245**, 1066–1073 (1989).
12. Fatkenheuer, G. *et al. Nature Med.* **11**, 1170–1172 (2005).

BIOLOGICAL CHEMISTRY

Beyond radical thinking

Léon Sanche

Radiation-induced DNA damage has been attributed to hydroxyl radicals, which form when water absorbs high-energy photons or charged particles. But another product of water's radiolysis might be the real culprit.

When high-energy radiation — X-rays, γ -rays and fast-moving charged particles such as ions, electrons and protons — interacts with DNA inside living cells, it can cause damage to the genome that leads to cell death¹. For this reason, such radiation is used in radiotherapy to destroy cancer cells. Unfortunately, radiation damage can itself initiate the development of cancer cells¹. To improve radiotherapy, it is therefore desirable to control more precisely the cell damage caused by radiation, while minimizing potentially harmful mutagenic effects. This requires greater understanding of the molecular processes involved.

Radiation particles produce ions, radicals and free electrons as they travel through matter. The electrons in turn generate large quantities of a second generation of radicals, ions and free electrons. Both the primary and the secondary products cause the biological effects associated with radiation damage². In the vicinity of cellular DNA, these species arise from DNA itself, from water and from other nearby biomolecules. It was already known that free electrons that have kinetic energy can damage DNA. But in the *Journal of the American Chemical Society*, Wang *et al.*³ report a remarkable discovery: free electrons that have lost all of their kinetic energy also react with the building blocks of DNA. This challenges conventional ideas about the molecular source of

genomic damage in irradiated cells.

When electrons are generated by the radiolysis of water, they become hydrated: that is, they form a complex with several water molecules (Fig. 1). Hydrated electrons do not cause much DNA damage, and so it has long been assumed that hydroxyl radicals — the other major product of water's radiolysis — are the guilty party. But before hydration occurs,

electrons enter a prehydrated state⁴ that lasts for less than a picosecond (1 picosecond is 10^{-12} seconds). Could prehydrated electrons be a source of DNA damage?

The fleeting existence of prehydrated electrons means that their reactions are difficult to observe in real time. Wang *et al.*³ therefore used femtosecond-resolved laser spectroscopy (1 femtosecond is 10^{-15} seconds) to study the reaction of prehydrated electrons with deoxyribonucleotides, the building blocks of DNA. Each deoxyribonucleotide consists of one of the four DNA bases (thymine, T; cytosine, C; guanine, G; and adenine, A) attached to a phosphate unit, and is denoted as dXMP, where X can be T, C, G or A. The authors performed their experiments in water, which provides a good model for cells (which contain 70–80% water by mass).

Free electrons generated from water by ionizing radiation have a lot of kinetic energy; such electrons can damage DNA before they enter the prehydrated state. Wang *et al.* therefore ionized the water molecules in an aqueous solution of dXMP by the successive absorption of two ultra-violet photons from a laser. This method generates exclusively electrons that have essentially no kinetic energy, and which therefore immediately enter the prehydrated state. The authors observed that, before hydration occurred, some of the prehydrated electrons reacted with dXMP molecules in the solution to form dXMP^{•-} anions. These transient negative ions can either decompose (dissociate) or relax to their ground-state configuration by releasing energy to the solvent.

To monitor the fate of the anions, Wang *et al.* fired a second laser pulse picoseconds after the initial ionizing pulse, and measured its absorption by the anions in solution. The absorption is related to the amount of dXMP^{•-} ions initially

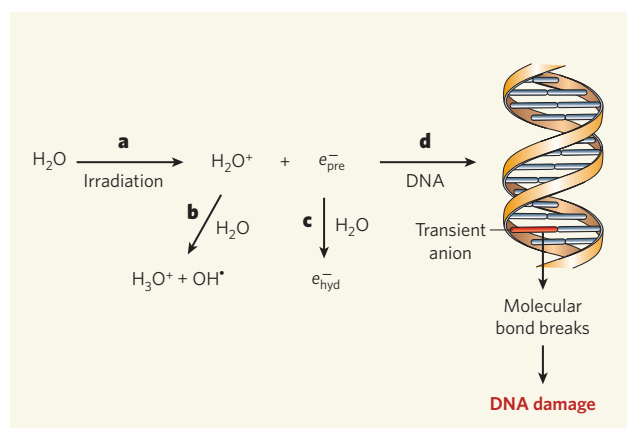


Figure 1 | Radiation damage in DNA. **a**, When water molecules absorb high-energy radiation, they form H₂O⁺ ions and free electrons. After losing their kinetic energy, the electrons enter a short-lived, prehydrated state (e⁻_{pre}). **b**, The H₂O⁺ ions react with more water molecules to form protonated water (H₃O⁺) and hydroxyl radicals (OH[•]). These radicals have long been thought to cause the DNA damage observed in irradiated cells. **c**, Prehydrated electrons form complexes with water molecules and turn into hydrated electrons (e⁻_{hyd}). **d**, Wang *et al.*³ show that prehydrated electrons also react with the bases of certain nucleotides (dGMP and dTMP) in aqueous solution. This suggests that prehydrated electrons can react with the bases of DNA duplexes, forming transient anions. In some cases, these anions could decompose, breaking molecular bonds in the DNA and so damaging it.

be a future possibility, but clinical decision-making will be clouded by the fact that the effect of the advantageous variant is not absolute — not all carriers of the variant clear the virus, nor do all patients lacking the variant fail to benefit from treatment. Furthermore, there is currently no alternative to interferon therapy for the HCV-infected population.

Although the amount of genetic information available to researchers across various disciplines has expanded, advances in data collection have historically failed to translate into equivalent advances in medical innovation (Fig. 1). And although GWAS can probe the subtler effects of a larger number of gene variants, little attention has been paid to the

black box that stands between most genetic discoveries and the promise of personalized treatments. A challenge for the future will be to apply genetic tools in a way that accelerates drug and diagnostics development, including better integration of genetic studies into the drug-development process, a reduced emphasis on modest genetic contributions to a disease, and a focus on the role of genetic variation in maintaining health as a blueprint for designing new drugs.

Shawn P. Iadonato is at Kineta, Inc., 307 Westlake Avenue North, Seattle, Washington 98109, USA. Michael G. Katze is in the Department of Microbiology and the National Primate Center, University of Washington,

Seattle, Washington 98195-8070, USA.

e-mails: siadonato@kinetabio.com; honey@u.washington.edu

1. www.who.int/mediacentre/factsheets/fs164/en
2. Ge, D. *et al. Nature* **461**, 399–401 (2009).
3. Suppiah, V. *et al. Nature Genet.* doi:10.1038/ng.447 (2009).
4. Tanaka, Y. *et al. Nature Genet.* doi:10.1038/ng.449 (2009).
5. McHutchison, J. G. *et al. N. Engl. J. Med.* **361**, 580–593 (2009).
6. Sheppard, P. *et al. Nature Immunol.* **4**, 63–68 (2003).
7. Thomas, D. L. *et al. Nature* doi:10.1038/nature08463 (2009).
8. Shiffman, M. L. *et al. Proc. 44th Annu. Meet. Eur. Assoc. Study Liver (EASL)*, Copenhagen, abstr. 520 (2009).
9. The International HapMap Consortium *Nature* **437**, 1299–1320 (2005).
10. Conjeevaram, H. S. *et al. Gastroenterology* **131**, 470–477 (2006).
11. Riordan, J. R. *et al. Science* **245**, 1066–1073 (1989).
12. Fatkenheuer, G. *et al. Nature Med.* **11**, 1170–1172 (2005).

BIOLOGICAL CHEMISTRY

Beyond radical thinking

Léon Sanche

Radiation-induced DNA damage has been attributed to hydroxyl radicals, which form when water absorbs high-energy photons or charged particles. But another product of water's radiolysis might be the real culprit.

When high-energy radiation — X-rays, γ -rays and fast-moving charged particles such as ions, electrons and protons — interacts with DNA inside living cells, it can cause damage to the genome that leads to cell death¹. For this reason, such radiation is used in radiotherapy to destroy cancer cells. Unfortunately, radiation damage can itself initiate the development of cancer cells¹. To improve radiotherapy, it is therefore desirable to control more precisely the cell damage caused by radiation, while minimizing potentially harmful mutagenic effects. This requires greater understanding of the molecular processes involved.

Radiation particles produce ions, radicals and free electrons as they travel through matter. The electrons in turn generate large quantities of a second generation of radicals, ions and free electrons. Both the primary and the secondary products cause the biological effects associated with radiation damage². In the vicinity of cellular DNA, these species arise from DNA itself, from water and from other nearby biomolecules. It was already known that free electrons that have kinetic energy can damage DNA. But in the *Journal of the American Chemical Society*, Wang *et al.*³ report a remarkable discovery: free electrons that have lost all of their kinetic energy also react with the building blocks of DNA. This challenges conventional ideas about the molecular source of

genomic damage in irradiated cells.

When electrons are generated by the radiolysis of water, they become hydrated: that is, they form a complex with several water molecules (Fig. 1). Hydrated electrons do not cause much DNA damage, and so it has long been assumed that hydroxyl radicals — the other major product of water's radiolysis — are the guilty party. But before hydration occurs,

electrons enter a prehydrated state⁴ that lasts for less than a picosecond (1 picosecond is 10^{-12} seconds). Could prehydrated electrons be a source of DNA damage?

The fleeting existence of prehydrated electrons means that their reactions are difficult to observe in real time. Wang *et al.*³ therefore used femtosecond-resolved laser spectroscopy (1 femtosecond is 10^{-15} seconds) to study the reaction of prehydrated electrons with deoxyribonucleotides, the building blocks of DNA. Each deoxyribonucleotide consists of one of the four DNA bases (thymine, T; cytosine, C; guanine, G; and adenine, A) attached to a phosphate unit, and is denoted as dXMP, where X can be T, C, G or A. The authors performed their experiments in water, which provides a good model for cells (which contain 70–80% water by mass).

Free electrons generated from water by ionizing radiation have a lot of kinetic energy; such electrons can damage DNA before they enter the prehydrated state. Wang *et al.* therefore ionized the water molecules in an aqueous solution of dXMP by the successive absorption of two ultra-violet photons from a laser. This method generates exclusively electrons that have essentially no kinetic energy, and which therefore immediately enter the prehydrated state. The authors observed that, before hydration occurred, some of the prehydrated electrons reacted with dXMP molecules in the solution to form dXMP^{•−} anions. These transient negative ions can either decompose (dissociate) or relax to their ground-state configuration by releasing energy to the solvent.

To monitor the fate of the anions, Wang *et al.* fired a second laser pulse picoseconds after the initial ionizing pulse, and measured its absorption by the anions in solution. The absorption is related to the amount of dXMP^{•−} ions initially

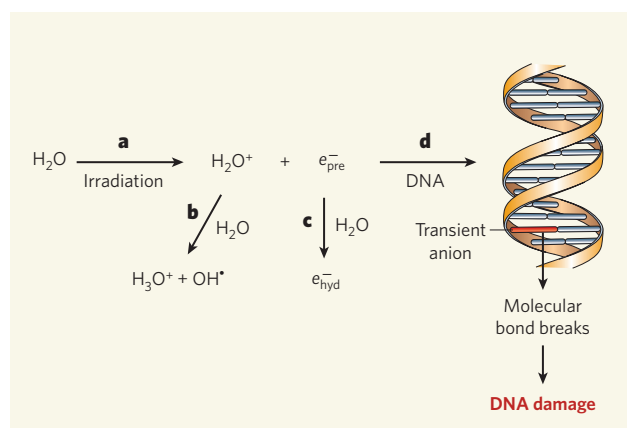


Figure 1 | Radiation damage in DNA. **a**, When water molecules absorb high-energy radiation, they form H₂O⁺ ions and free electrons. After losing their kinetic energy, the electrons enter a short-lived, prehydrated state (e[−]_{pre}). **b**, The H₂O⁺ ions react with more water molecules to form protonated water (H₃O⁺) and hydroxyl radicals (OH[•]). These radicals have long been thought to cause the DNA damage observed in irradiated cells. **c**, Prehydrated electrons form complexes with water molecules and turn into hydrated electrons (e[−]_{hyd}). **d**, Wang *et al.*³ show that prehydrated electrons also react with the bases of certain nucleotides (dGMP and dTMP) in aqueous solution. This suggests that prehydrated electrons can react with the bases of DNA duplexes, forming transient anions. In some cases, these anions could decompose, breaking molecular bonds in the DNA and so damaging it.

produced, and to the kinetics of their disappearance. The authors' results indicated several things. First, the formation of dXMP⁻ anions is complete within the lifetime of prehydrated electrons. Second, dGMP and dAMP are more efficient at capturing prehydrated electrons than dTMP and dCMP. Finally, transient dAMP⁻ and dCMP⁻ are stable anions, whereas 60% of dGMP⁻ ions and 35% of dTMP⁻ ions dissociate.

By comparing transient photon absorption in solutions of DNA bases with that of solutions of nucleotides, Wang *et al.* concluded that the prehydrated electrons attach specifically to the DNA base within dXMP molecules. Thus, the transfer of prehydrated electrons to G and T bases can break apart two of the basic components of DNA. Because most of the radiation damage caused to cellular DNA occurs through the generation of reactive species within the surrounding water, the authors' proposed mechanism of dissociative electron transfer might be responsible for a large portion of such damage (Fig. 1).

The formation of transient anions by attachment of near-zero-energy electrons to the bases of DNA is known² from both experiments and theory to break single strands in duplexes under dry conditions. In water, such anions may exist in lower energy states, which means that prehydrated electrons should produce single-strand breaks more easily. Indeed, Wang *et al.*³ found that significant quantities of single- and double-strand breaks of irradiated aqueous DNA are induced by prehydrated electrons.

In cancer treatment, low-energy secondary electrons are believed to be at least partially responsible for the enhancement of tumour regression observed when radiation is administered at the same time as a chemotherapeutic agent. For the anticancer agent cisplatin, this superadditive effect has been attributed to the formation of transient anions at cisplatin's binding site in the DNA of cancer cells⁵. It has previously been shown⁶ that the lowest energy state of transient anions of cisplatin lies very close to the energy of prehydrated electrons. Taken together with the current paper³, this suggests that dissociative transfer of prehydrated electrons may have an important role in chemoradiation therapy.

Wang and colleagues' discovery³ contests the long-held notion that ionizing radiation damages the genome mostly through the action of hydroxyl radicals. Their newly proposed molecular mechanism of DNA damage could have far-reaching consequences for our understanding of the reactions of weakly bound electrons in biological systems (of which there are many), and may also help in the development of new strategies for radioprotection and cancer radiotherapy.

Léon Sanche is at the Center for Radiobiology and Radiotherapy Research, Faculté de Médecine, Université de Sherbrooke, Sherbrooke, Québec J1H 5N4, Canada.
e-mail: leon.sanche@usherbrooke.ca

1. von Sonntag, C. *The Chemical Basis for Radiation Biology* (Taylor & Francis, 1987).
2. Sanche, L. in *Radiation Induced Molecular Phenomena in Nucleic Acids* (eds Shukla, M. K. & Leszczynski, J.) 531–575 (Springer, 2008).
3. Wang, C.-R., Nguyen, J. & Lu, Q.-B. *J. Am. Chem. Soc.* **131**, 11320–11322 (2009).

4. Migus, A., Gauduel, Y., Martin, K. L. & Antonetti, A. *Phys. Rev. Lett.* **58**, 1559 (1987).
5. Zheng, Y. *et al.* *Phys. Rev. Lett.* **100**, 198101 (2008).
6. Lu, Q.-B., Kalantari, S. & Wang, C.-R. *Mol. Pharm.* **4**, 624–628 (2007).

EPIGENETICS

Ready for the marks

Robert Feil

Genomic imprinting, in which genes are expressed from either the maternal or paternal genome, involves the addition of methyl marks to DNA. Paradoxically, demethylation of histone proteins is an essential first step.

For its development in the womb, a baby needs the genetic information inherited from both mother and father. This is because some of our genes are expressed from only one of the two inherited parental genomes. This remarkable phenomenon — genomic imprinting — is controlled by marks placed on the genome in germ cells (oocytes and sperm), in particular by the methylation of DNA. In this issue (page 415), Ciccone and colleagues¹ explore how other methyl marks — not on the genome itself, but on the histone proteins around which the DNA fibre is wrapped — contribute to genomic imprinting. The authors find that methyl marks on histones need to be removed for the genome to 'get ready' for the establishment of imprints.

The genome is packaged in the cell nucleus by becoming associated with multiple proteins to form a complex structure called chromatin.

Segments of the DNA fibre are wrapped around histone proteins, forming disc-shaped nucleosomes that are arranged in arrays, like beads on a string. The tails of histone proteins protrude from the nucleosomes and can be chemically modified in different ways, for example by adding methyl groups to lysine amino-acid residues. Histone modifications can be recognized by proteins, and binding of a particular type of protein partly determines whether the associated genes are expressed or not. The DNA fibre itself is also modified by methylation to regulate the expression of genes².

Genomic imprinting is an essential biological process that has evolved in both mammals and plants to regulate levels of gene expression³. About a hundred genes are imprinted in mammals, many of which have important roles in development or are associated with disease. Whether imprinted genes are

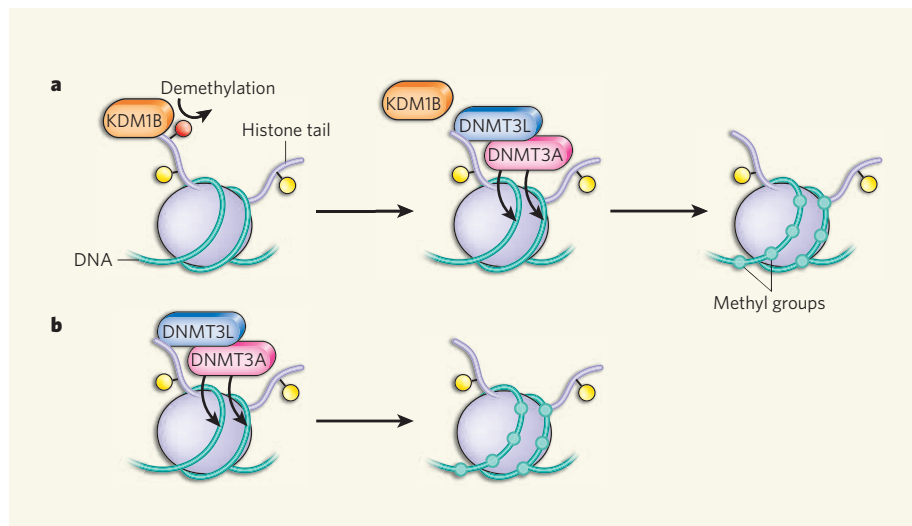


Figure 1 | Imprinting involves histone demethylation and DNA methylation. In the nucleus, the genomic DNA is wrapped around histone proteins (purple) to form nucleosomes. The histone tails protrude from the nucleosomes and can be altered by different chemical modifications. **a**, Methylation of lysine (red) on histone H3 (H3K4) prevents binding of DNMT3L–DNMT3A methyltransferase complexes. In this model, KDM1B, a demethylase described by Ciccone and colleagues¹, removes K4 methylation from the H3 tails. DNMT3L–DNMT3A is then recruited, possibly through KDM1B and other specific histone modifications (yellow), and DNMT3A puts methyl groups onto the DNA. **b**, At some regions, imprint establishment is independent of KDM1B. Here, recruitment of DNMT3L–DNMT3A could involve other as-yet-unknown mechanisms, but would still require the absence of H3K4 methylation.

produced, and to the kinetics of their disappearance. The authors' results indicated several things. First, the formation of dXMP⁻ anions is complete within the lifetime of prehydrated electrons. Second, dGMP and dAMP are more efficient at capturing prehydrated electrons than dTMP and dCMP. Finally, transient dAMP⁻ and dCMP⁻ are stable anions, whereas 60% of dGMP⁻ ions and 35% of dTMP⁻ ions dissociate.

By comparing transient photon absorption in solutions of DNA bases with that of solutions of nucleotides, Wang *et al.* concluded that the prehydrated electrons attach specifically to the DNA base within dXMP molecules. Thus, the transfer of prehydrated electrons to G and T bases can break apart two of the basic components of DNA. Because most of the radiation damage caused to cellular DNA occurs through the generation of reactive species within the surrounding water, the authors' proposed mechanism of dissociative electron transfer might be responsible for a large portion of such damage (Fig. 1).

The formation of transient anions by attachment of near-zero-energy electrons to the bases of DNA is known² from both experiments and theory to break single strands in duplexes under dry conditions. In water, such anions may exist in lower energy states, which means that prehydrated electrons should produce single-strand breaks more easily. Indeed, Wang *et al.*³ found that significant quantities of single- and double-strand breaks of irradiated aqueous DNA are induced by prehydrated electrons.

In cancer treatment, low-energy secondary electrons are believed to be at least partially responsible for the enhancement of tumour regression observed when radiation is administered at the same time as a chemotherapeutic agent. For the anticancer agent cisplatin, this superadditive effect has been attributed to the formation of transient anions at cisplatin's binding site in the DNA of cancer cells⁵. It has previously been shown⁶ that the lowest energy state of transient anions of cisplatin lies very close to the energy of prehydrated electrons. Taken together with the current paper³, this suggests that dissociative transfer of prehydrated electrons may have an important role in chemoradiation therapy.

Wang and colleagues' discovery³ contests the long-held notion that ionizing radiation damages the genome mostly through the action of hydroxyl radicals. Their newly proposed molecular mechanism of DNA damage could have far-reaching consequences for our understanding of the reactions of weakly bound electrons in biological systems (of which there are many), and may also help in the development of new strategies for radioprotection and cancer radiotherapy.

Léon Sanche is at the Center for Radiobiology and Radiotherapy Research, Faculté de Médecine, Université de Sherbrooke, Sherbrooke, Québec J1H 5N4, Canada.
e-mail: leon.sanche@usherbrooke.ca

1. von Sonntag, C. *The Chemical Basis for Radiation Biology* (Taylor & Francis, 1987).
2. Sanche, L. in *Radiation Induced Molecular Phenomena in Nucleic Acids* (eds Shukla, M. K. & Leszczynski, J.) 531–575 (Springer, 2008).
3. Wang, C.-R., Nguyen, J. & Lu, Q.-B. *J. Am. Chem. Soc.* **131**, 11320–11322 (2009).

4. Migus, A., Gauduel, Y., Martin, K. L. & Antonetti, A. *Phys. Rev. Lett.* **58**, 1559 (1987).
5. Zheng, Y. *et al.* *Phys. Rev. Lett.* **100**, 198101 (2008).
6. Lu, Q.-B., Kalantari, S. & Wang, C.-R. *Mol. Pharm.* **4**, 624–628 (2007).

EPIGENETICS

Ready for the marks

Robert Feil

Genomic imprinting, in which genes are expressed from either the maternal or paternal genome, involves the addition of methyl marks to DNA. Paradoxically, demethylation of histone proteins is an essential first step.

For its development in the womb, a baby needs the genetic information inherited from both mother and father. This is because some of our genes are expressed from only one of the two inherited parental genomes. This remarkable phenomenon — genomic imprinting — is controlled by marks placed on the genome in germ cells (oocytes and sperm), in particular by the methylation of DNA. In this issue (page 415), Ciccone and colleagues¹ explore how other methyl marks — not on the genome itself, but on the histone proteins around which the DNA fibre is wrapped — contribute to genomic imprinting. The authors find that methyl marks on histones need to be removed for the genome to 'get ready' for the establishment of imprints.

The genome is packaged in the cell nucleus by becoming associated with multiple proteins to form a complex structure called chromatin.

Segments of the DNA fibre are wrapped around histone proteins, forming disc-shaped nucleosomes that are arranged in arrays, like beads on a string. The tails of histone proteins protrude from the nucleosomes and can be chemically modified in different ways, for example by adding methyl groups to lysine amino-acid residues. Histone modifications can be recognized by proteins, and binding of a particular type of protein partly determines whether the associated genes are expressed or not. The DNA fibre itself is also modified by methylation to regulate the expression of genes².

Genomic imprinting is an essential biological process that has evolved in both mammals and plants to regulate levels of gene expression³. About a hundred genes are imprinted in mammals, many of which have important roles in development or are associated with disease. Whether imprinted genes are

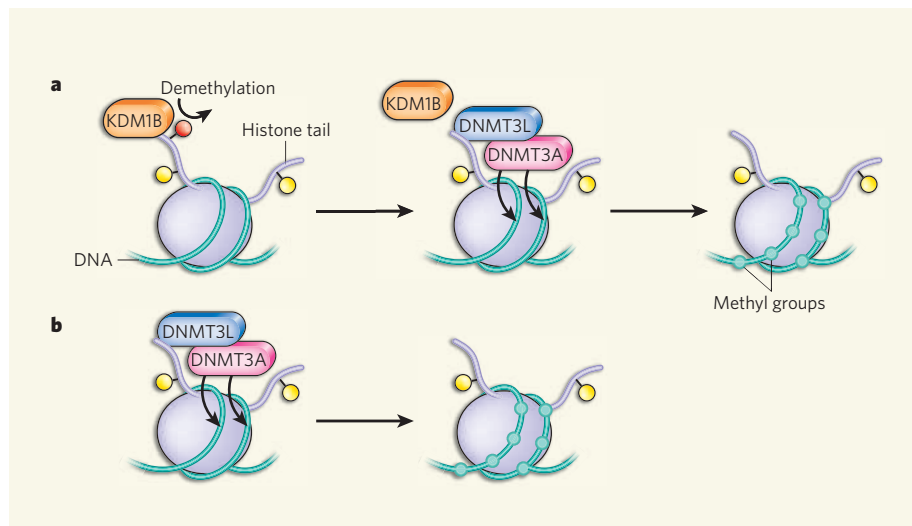


Figure 1 | Imprinting involves histone demethylation and DNA methylation. In the nucleus, the genomic DNA is wrapped around histone proteins (purple) to form nucleosomes. The histone tails protrude from the nucleosomes and can be altered by different chemical modifications. **a**, Methylation of lysine 4 (red) on histone H3 (H3K4) prevents binding of DNMT3L–DNMT3A methyltransferase complexes. In this model, KDM1B, a demethylase described by Ciccone and colleagues¹, removes K4 methylation from the H3 tails. DNMT3L–DNMT3A is then recruited, possibly through KDM1B and other specific histone modifications (yellow), and DNMT3A puts methyl groups onto the DNA. **b**, At some regions, imprint establishment is independent of KDM1B. Here, recruitment of DNMT3L–DNMT3A could involve other as-yet-unknown mechanisms, but would still require the absence of H3K4 methylation.

MICROBIOLOGY

Showering with bacteria

Singing in the shower may never feel the same again, if one dwells on the results of a study by Norman Pace and colleagues (L. M. Feazel *et al.* *Proc. Natl Acad. Sci. USA* doi:10.1073/pnas.0908446106; 2009). While you trill to an aria from your favourite operetta, an audience of "microbes of potential public health concern" may well have prime seats in your shower head.

Shower heads are known to harbour microorganisms, mainly because they provide a warm, moist environment prone to the formation of biofilms — aggregates of microbes that adhere to surfaces. Previous studies have sought to identify the organisms that reside in shower heads by culturing them. But as most bacteria can't easily be grown

in the laboratory, shower-head biofilm assemblages have remained largely uncharacterized.

In their study, Pace and colleagues use molecular techniques to analyse the microbes found in 45 shower heads obtained from nine cities in the United States. The authors sequenced bacterial genes isolated from each shower-head biofilm and identified the resident microbes by comparing their results with the genes of known bacteria. Such non-culture — or metagenomic — techniques have revolutionized our ability to characterize the microbial communities that live among us.

Pace and co-workers found that the shower heads contained many types of bacteria commonly found in water and soil. The striking result, however, was the abundance of

non-tuberculous mycobacteria, in particular *Mycobacterium avium* — the amounts in the biofilm were 100-fold higher than those found in the associated water supply. About 20% of shower-head swabs harboured *M. avium* DNA sequences, and this figure rose to a staggering 78% when the authors used molecular techniques that specifically detect this organism.

Why are non-tuberculous mycobacteria so common in shower-head environments? These organisms are known to be chlorine-resistant, and they may actually be enriched by the treatments used to disinfect municipal water supplies. In fact, when the researchers attempted to clean one shower head harbouring a *Mycobacterium gordonae* species with bleach, they managed only to increase its relative abundance.

Non-tuberculous mycobacteria are opportunistic pathogens



R. FARIS/CORBIS

that can cause severe disease in immunocompromised people, and they can also infect healthy people. The rates of infection with these mycobacteria are increasing in resource-rich countries. Pace and colleagues' work lends support to the possibility that our predilection to soap in the shower, rather than soak in the bath, may be a contributory factor.

Shannon Amoils

expressed from the maternal or the paternal chromosome is controlled by methylation of stretches of regulatory DNA, the imprinting control regions³. Most methylation imprinting marks are inherited from the mother and are put onto the genome in oocytes by the DNA-methyltransferase enzyme DNMT3A⁴.

It has been a challenge to unravel how, in germ cells, DNMT3A restricts its DNA-methylation activity to imprinting control regions⁴. A breakthrough was the discovery that DNMT3L, a similar but enzymatically inactive protein, forms complexes with DNMT3A. Like DNMT3A, DNMT3L is essential for imprinting⁵. It recognizes and binds to the tail of histone H3 and can thereby recruit DNMT3A to chromatin and to its target DNA sequences. However, when H3 is methylated on its amino-acid residue lysine 4 (designated H3K4), DNMT3L cannot bind, suggesting that methylated H3K4 might prevent DNA methylation⁶.

It has long been known that there are enzymes that methylate lysine residues; some of these enzymes control DNA methylation in fungi and plants². More recently, proteins with the opposite action have been discovered. These lysine demethylases include KDM1 (lysine demethylase-1, also called LSD1 or AOF2), an enzyme that specifically demethylates H3K4. KDM1 is expressed in many tissues and is essential for mammalian development, but it is probably not involved in imprinting⁷. Ciccone and colleagues¹ now describe KDM1B (AOF1), an H3K4 demethylase that, in adult mice, is almost exclusively expressed in oocytes. Significantly, if this demethylase is disrupted, there is an overall increase in H3K4 methylation in oocytes, which subsequently

fail to acquire DNA-methylation marks at imprinting control regions. These exciting findings raise the possibility that H3K4 methylation needs to be removed (by KDM1B) to allow DNA methylation (Fig. 1). Not surprisingly, embryos that are derived from KDM1B-deficient oocytes show aberrant expression of imprinted genes and so die halfway through gestation¹.

An intriguing theory is that KDM1B may have evolved in mammals specifically to control imprinting in female germ cells. However, KDM1B deficiency does not affect all of the maternal imprints¹, indicating that, at some imprinting control regions, other mechanisms guide the acquisition of DNA methylation by DNMT3A. Another unresolved problem is how KDM1B and the DNMT3L–DNMT3A complex are recruited to their targets. Does the DNA-methylation machinery recognize all nucleosomes that lack H3K4 methylation, or are there additional requirements for its recruitment?

One hypothesis is that specific histone modifications need to be present to instruct the DNA-methylation machinery (Fig. 1). Besides modifications on other amino acids of histone H3 (ref. 2), one candidate for such an instructive histone code could be methylation at amino-acid arginine 3 on histone H4 (H4R3). A recent study⁸ of developing blood cells suggests that H4R3 methylation is recognized by DNMT3A and facilitates DNA methylation. Furthermore, although KDM1B does not control the establishment of the few imprints that originate from sperm, changes in H3K4 methylation could nevertheless guide their acquisition⁹. It also seems plausible that

similar mechanisms could aid the acquisition of new DNA methylation, unrelated to genomic imprinting, in the developing embryo.

Even with Ciccone and colleagues' inspiring work¹, we are still far from understanding the intricacies of genomic imprinting. Those who thought this was going to be a simple story will be disappointed. Besides DNA methylation, histone methylation is clearly part of the imprinting business. Specific DNA-binding proteins may be involved in imprint establishment as well, possibly by inducing local histone modifications that could facilitate DNA methylation^{2,10}. To make matters even more complicated, gene expression also seems to play a part: in oocytes, transcription is detected across several maternal imprinting control regions and was shown, in one case¹¹, to be essential for imprint acquisition. Despite the complexity of imprinting, however, future research promises to unravel the closely interdependent mechanisms that regulate this intriguing process.

Robert Feil is at the Institute of Molecular Genetics, CNRS, and University of Montpellier, 1919 route de Mende, 34293 Montpellier, France. e-mail: robert.feil@igmm.cnrs.fr

1. Ciccone, D. N. *et al.* *Nature* **461**, 415–418 (2009).
2. Cedar, H. & Bergman, Y. *Nature Rev. Genet.* **10**, 295–304 (2009).
3. Feil, R. & Berger, F. *Trends Genet.* **23**, 192–199 (2007).
4. Kaneda, M. *et al.* *Nature* **429**, 900–903 (2004).
5. Bourc'his, D., Xu, G. L., Lin, C. S., Bollman, B. & Bestor, T. H. *Science* **294**, 2536–2539 (2001).
6. Ooi, S. *et al.* *Nature* **448**, 714–717 (2007).
7. Wang, J. *et al.* *Nature Genet.* **41**, 125–129 (2009).
8. Zhao, Q. *et al.* *Nature Struct. Mol. Biol.* **16**, 304–311 (2009).
9. Delaval, K. *et al.* *EMBO J.* **26**, 720–729 (2007).
10. Li, X. *et al.* *Dev. Cell* **15**, 547–557 (2008).
11. Chotalia, M. *et al.* *Genes Dev.* **23**, 105–117 (2009).

MICROBIOLOGY

Showering with bacteria

Singing in the shower may never feel the same again, if one dwells on the results of a study by Norman Pace and colleagues (L. M. Feazel *et al.* *Proc. Natl Acad. Sci. USA* doi:10.1073/pnas.0908446106; 2009). While you trill to an aria from your favourite operetta, an audience of "microbes of potential public health concern" may well have prime seats in your shower head.

Shower heads are known to harbour microorganisms, mainly because they provide a warm, moist environment prone to the formation of biofilms — aggregates of microbes that adhere to surfaces. Previous studies have sought to identify the organisms that reside in shower heads by culturing them. But as most bacteria can't easily be grown

in the laboratory, shower-head biofilm assemblages have remained largely uncharacterized.

In their study, Pace and colleagues use molecular techniques to analyse the microbes found in 45 shower heads obtained from nine cities in the United States. The authors sequenced bacterial genes isolated from each shower-head biofilm and identified the resident microbes by comparing their results with the genes of known bacteria. Such non-culture — or metagenomic — techniques have revolutionized our ability to characterize the microbial communities that live among us.

Pace and co-workers found that the shower heads contained many types of bacteria commonly found in water and soil. The striking result, however, was the abundance of

non-tuberculous mycobacteria, in particular *Mycobacterium avium* — the amounts in the biofilm were 100-fold higher than those found in the associated water supply. About 20% of shower-head swabs harboured *M. avium* DNA sequences, and this figure rose to a staggering 78% when the authors used molecular techniques that specifically detect this organism.

Why are non-tuberculous mycobacteria so common in shower-head environments? These organisms are known to be chlorine-resistant, and they may actually be enriched by the treatments used to disinfect municipal water supplies. In fact, when the researchers attempted to clean one shower head harbouring a *Mycobacterium gordonae* species with bleach, they managed only to increase its relative abundance.

Non-tuberculous mycobacteria are opportunistic pathogens



R. FARIS/CORBIS

that can cause severe disease in immunocompromised people, and they can also infect healthy people. The rates of infection with these mycobacteria are increasing in resource-rich countries. Pace and colleagues' work lends support to the possibility that our predilection to soap in the shower, rather than soak in the bath, may be a contributory factor.

Shannon Amoils

expressed from the maternal or the paternal chromosome is controlled by methylation of stretches of regulatory DNA, the imprinting control regions³. Most methylation imprinting marks are inherited from the mother and are put onto the genome in oocytes by the DNA-methyltransferase enzyme DNMT3A⁴.

It has been a challenge to unravel how, in germ cells, DNMT3A restricts its DNA-methylation activity to imprinting control regions⁴. A breakthrough was the discovery that DNMT3L, a similar but enzymatically inactive protein, forms complexes with DNMT3A. Like DNMT3A, DNMT3L is essential for imprinting⁵. It recognizes and binds to the tail of histone H3 and can thereby recruit DNMT3A to chromatin and to its target DNA sequences. However, when H3 is methylated on its amino-acid residue lysine 4 (designated H3K4), DNMT3L cannot bind, suggesting that methylated H3K4 might prevent DNA methylation⁶.

It has long been known that there are enzymes that methylate lysine residues; some of these enzymes control DNA methylation in fungi and plants². More recently, proteins with the opposite action have been discovered. These lysine demethylases include KDM1 (lysine demethylase-1, also called LSD1 or AOF2), an enzyme that specifically demethylates H3K4. KDM1 is expressed in many tissues and is essential for mammalian development, but it is probably not involved in imprinting⁷. Ciccone and colleagues¹ now describe KDM1B (AOF1), an H3K4 demethylase that, in adult mice, is almost exclusively expressed in oocytes. Significantly, if this demethylase is disrupted, there is an overall increase in H3K4 methylation in oocytes, which subsequently

fail to acquire DNA-methylation marks at imprinting control regions. These exciting findings raise the possibility that H3K4 methylation needs to be removed (by KDM1B) to allow DNA methylation (Fig. 1). Not surprisingly, embryos that are derived from KDM1B-deficient oocytes show aberrant expression of imprinted genes and so die halfway through gestation¹.

An intriguing theory is that KDM1B may have evolved in mammals specifically to control imprinting in female germ cells. However, KDM1B deficiency does not affect all of the maternal imprints¹, indicating that, at some imprinting control regions, other mechanisms guide the acquisition of DNA methylation by DNMT3A. Another unresolved problem is how KDM1B and the DNMT3L–DNMT3A complex are recruited to their targets. Does the DNA-methylation machinery recognize all nucleosomes that lack H3K4 methylation, or are there additional requirements for its recruitment?

One hypothesis is that specific histone modifications need to be present to instruct the DNA-methylation machinery (Fig. 1). Besides modifications on other amino acids of histone H3 (ref. 2), one candidate for such an instructive histone code could be methylation at amino-acid arginine 3 on histone H4 (H4R3). A recent study⁸ of developing blood cells suggests that H4R3 methylation is recognized by DNMT3A and facilitates DNA methylation. Furthermore, although KDM1B does not control the establishment of the few imprints that originate from sperm, changes in H3K4 methylation could nevertheless guide their acquisition⁹. It also seems plausible that

similar mechanisms could aid the acquisition of new DNA methylation, unrelated to genomic imprinting, in the developing embryo.

Even with Ciccone and colleagues' inspiring work¹, we are still far from understanding the intricacies of genomic imprinting. Those who thought this was going to be a simple story will be disappointed. Besides DNA methylation, histone methylation is clearly part of the imprinting business. Specific DNA-binding proteins may be involved in imprint establishment as well, possibly by inducing local histone modifications that could facilitate DNA methylation^{2,10}. To make matters even more complicated, gene expression also seems to play a part: in oocytes, transcription is detected across several maternal imprinting control regions and was shown, in one case¹¹, to be essential for imprint acquisition. Despite the complexity of imprinting, however, future research promises to unravel the closely interdependent mechanisms that regulate this intriguing process. ■

Robert Feil is at the Institute of Molecular Genetics, CNRS, and University of Montpellier, 1919 route de Mende, 34293 Montpellier, France. e-mail: robert.feil@igmm.cnrs.fr

1. Ciccone, D. N. *et al.* *Nature* **461**, 415–418 (2009).
2. Cedar, H. & Bergman, Y. *Nature Rev. Genet.* **10**, 295–304 (2009).
3. Feil, R. & Berger, F. *Trends Genet.* **23**, 192–199 (2007).
4. Kaneda, M. *et al.* *Nature* **429**, 900–903 (2004).
5. Bourc'his, D., Xu, G. L., Lin, C. S., Bollman, B. & Bestor, T. H. *Science* **294**, 2536–2539 (2001).
6. Ooi, S. *et al.* *Nature* **448**, 714–717 (2007).
7. Wang, J. *et al.* *Nature Genet.* **41**, 125–129 (2009).
8. Zhao, Q. *et al.* *Nature Struct. Mol. Biol.* **16**, 304–311 (2009).
9. Delaval, K. *et al.* *EMBO J.* **26**, 720–729 (2007).
10. Li, X. *et al.* *Dev. Cell* **15**, 547–557 (2008).
11. Chotalia, M. *et al.* *Genes Dev.* **23**, 105–117 (2009).

The structural basis of tail-anchored membrane protein recognition by Get3

Agnieszka Mateja¹, Anna Szlachcic^{1,3}, Maureen E. Downing¹, Malgorzata Dobosz^{1,4}, Malaiyalam Mariappan², Ramanujan S. Hegde² & Robert J. Keenan¹

Targeting of newly synthesized membrane proteins to the endoplasmic reticulum is an essential cellular process. Most membrane proteins are recognized and targeted co-translationally by the signal recognition particle. However, nearly 5% of membrane proteins are 'tail-anchored' by a single carboxy-terminal transmembrane domain that cannot access the co-translational pathway. Instead, tail-anchored proteins are targeted post-translationally by a conserved ATPase termed Get3. The mechanistic basis for tail-anchored protein recognition or targeting by Get3 is not known. Here we present crystal structures of yeast Get3 in 'open' (nucleotide-free) and 'closed' (ADP·AlF₄⁻-bound) dimer states. In the closed state, the dimer interface of Get3 contains an enormous hydrophobic groove implicated by mutational analyses in tail-anchored protein binding. In the open state, Get3 undergoes a striking rearrangement that disrupts the groove and shields its hydrophobic surfaces. These data provide a molecular mechanism for nucleotide-regulated binding and release of tail-anchored proteins during their membrane targeting by Get3.

Eukaryotic cells have evolved sophisticated machinery to ensure high fidelity targeting and insertion of membrane proteins into intracellular organelles. For targeting to the endoplasmic reticulum (ER), the best understood mechanism is a co-translational pathway mediated by the cytosolic signal recognition particle (SRP), the ER-associated SRP receptor, and the Sec61 protein translocation channel^{1–3}. This pathway is conserved from bacteria to humans and is essential for biosynthesis of a wide range of membrane proteins. However, many ER-targeted proteins cannot access the SRP-dependent co-translational pathway.

A particularly important example is the tail-anchored (TA) protein, defined by a single C-terminal transmembrane domain (TMD)^{4,5} and a cytosolic facing amino-terminal domain. TA proteins mediate numerous essential biochemical activities in nearly every cellular membrane. Well-known examples include SNARE proteins involved in vesicle trafficking, components of the mitochondrial and ER protein translocation apparatus, members of the Bcl2 family of apoptotic proteins, and several viral envelope and non-structural proteins^{4,6,7}. The targeting information for TA proteins resides solely within the TMD. Because the TMD is still within the ribosomal tunnel when the termination codon is reached, co-translational targeting is precluded⁸. Thus, TA proteins are obligatorily recognized and targeted post-translationally by an SRP-independent pathway.

A central component of the TA protein pathway to the ER is a highly conserved cytosolic ATPase termed Asn1 or TRC40 (refs 9, 10). Although originally annotated Asn1 owing to ~27% sequence identity to ArsA, the catalytic subunit of the *Escherichia coli* arsenite resistance operon^{11–13}, eukaryotic TRC40s have evolved different functions. Both mammalian TRC40 and its yeast homologue Get3 recognize and selectively bind the TMD of TA proteins in the cytosol. This complex then targets to the ER by membrane-bound receptors (termed Get1 and Get2 in yeast¹⁴), where the TA protein is released for insertion. This spatially restricted unidirectional targeting is regulated by ATP binding and hydrolysis, but the mechanistic basis of this process is not

understood. To address this, we determined the crystal structures of yeast Get3 in the nucleotide-free and ADP·AlF₄⁻-bound states. Our structural and functional analysis suggests how Get3 binds selectively to TMD substrates, and how ATP hydrolysis regulates TA protein binding and release during targeting to the ER.

Overall structure of the Get3 homodimer

We determined the X-ray crystal structures of ADP·AlF₄⁻-bound *Saccharomyces cerevisiae* Get3 and nucleotide-free *Schizosaccharomyces pombe* Get3 (~58% identical to *S. cerevisiae* Get3) at 2.0 and 3.0 Å resolution, respectively (Supplementary Table 1 and Supplementary Figs 1 and 2). Both structures show a symmetric homodimer (Fig. 1a, b). Each monomer comprises a core ATPase subdomain and an α -helical subdomain (Supplementary Fig. 3a). The Get3 ATPase subdomain shows structural similarity to other members of the SIM1B (after signal recognition particle, MinD and BioD) class of NTP-binding proteins¹⁵, including its closest sequence homologue of known structure, ArsA¹⁶, and the more distantly related nitrogenase iron protein (NifH)¹⁷, Soj¹⁸, MinD¹⁹ and the SRP GTPases^{20,21}.

The nucleotide-free structure of *S. pombe* Get3 shows the two subunits splayed apart (Fig. 1a) with ~900 Å² of surface area buried in the interface (Fig. 1c). A 3.8 Å resolution structure of nucleotide-free *S. cerevisiae* Get3 shows the same open dimer architecture (Supplementary Table 1 and Supplementary Fig. 2), suggesting that the open form reflects a conserved conformation of nucleotide-free Get3. In contrast, the ADP·AlF₄⁻-bound form of *S. cerevisiae* Get3 (Fig. 1b) shows a large conformational change approximated by a ~37° rotation of one subunit towards the other. This movement 'closes' the quaternary structure into a more compact form that buries ~2,400 Å² of surface area in an extensive dimer interface that spans both subdomains (Fig. 1d).

The open-to-closed transition in Get3 occurs about a hinge point centred on a zinc ion bound at the homodimer interface. This zinc is

¹Department of Biochemistry & Molecular Biology, The University of Chicago, Gordon Center for Integrative Science, Room W238, 929 East 57th Street, Chicago, Illinois 60637, USA.

²Cell Biology and Metabolism Program, Eunice Kennedy Shriver National Institute of Child Health and Human Development, National Institutes of Health, Room 101, Building 18T, 18 Library Drive, Bethesda, Maryland 20892, USA. ³Department of Protein Engineering, Faculty of Biotechnology, University of Wrocław, Tamka 2, 50-137 Wrocław, Poland. ⁴Faculty of Chemistry, Jagiellonian University, Ingardena 3, 30-060 Krakow, Poland.

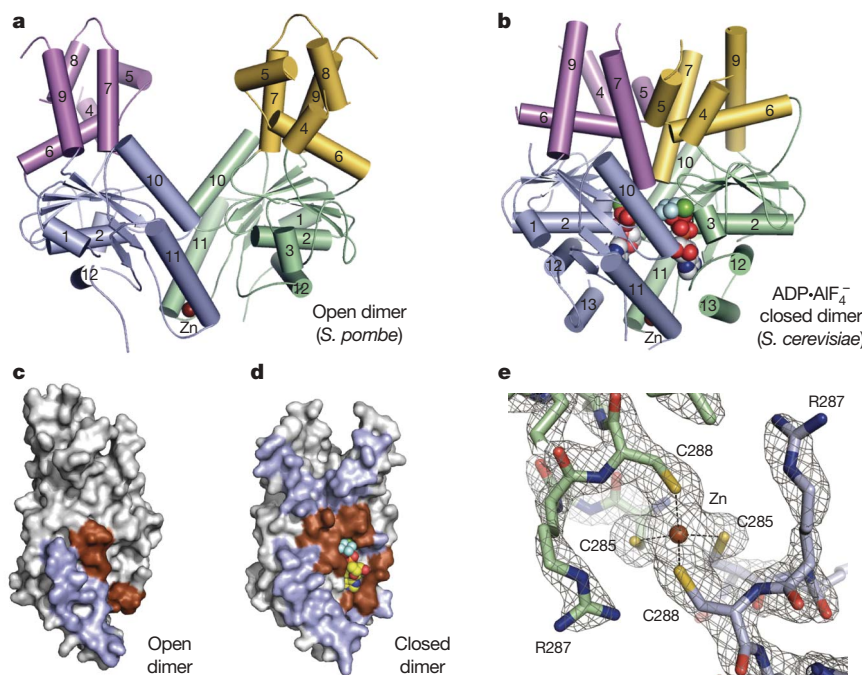


Figure 1 | Get3 is a dynamic, metal-stabilized homodimer. **a, b,** Crystal structures of Get3 in open (**a**) and closed (**b**) dimer states. Each monomer comprises a core ATPase subdomain (blue, green) and an α -helical subdomain (magenta, yellow). A tightly bound zinc atom (brown sphere) lies at the dimer interface. **c, d,** Residues in the homodimer interface (blue, brown) are mapped to the surface of a Get3 monomer from the open (**c**) and closed (**d**) dimer structures. Monomers are rotated $\sim 90^\circ$ about the dimer

coordinated by the side chains of two cysteine residues from each monomer (Fig. 1e), which are conserved in eukaryotic Get3 homologues ('CXXC motif'; Supplementary Fig. 3b). Although no exogenous zinc was added during the experiment, the tetrahedral geometry, the identity of the coordinating ligands, and the X-ray fluorescence spectrum of bacterially purified Get3 assign this ion as zinc. Variants in which these cysteines are mutated do not coordinate zinc, fail to dimerize in solution, and are unable to complement the growth defect of Δ get3 yeast²². Thus, Get3 is an obligate dimer containing a structural metal ion that stabilizes functionally distinct conformations.

The composite hydrophobic groove

The α -helical subdomain of Get3 overlaps with the allosteric metalloid binding site of ArsA, but shows important differences in sequence, structure and function. Eukaryotic TRC40s lack conserved residues used by ArsA to bind As/Sb(III). Instead, this region is enriched in methionine (Supplementary Fig. 3b, red), which is observed at 2–3 times greater frequency than typically found in vertebrate proteins. Furthermore, the eukaryotic TRC40 homologues contain a unique ~ 20 -residue insertion in the α -helical subdomain that we term the 'TRC40-insert' (Supplementary Fig. 3b, yellow).

In the Get3 open dimer, the α -helical subdomains are separated by more than 20 Å, creating a large cleft between the two subunits (Figs 1a and 2a). The surface of the cleft is charged rather than hydrophobic, making it unsuitable for TMD binding. In contrast, in the closed dimer state, the α -helical subdomains are in direct contact and define a continuous, solvent-exposed, hydrophobic groove that spans both monomers (Figs 1b and 2b).

Each α -helical subdomain contributes six amphipathic helices to the composite groove. The bottom of the groove is formed by two 'crossing' helices ($\alpha 6$), whereas eight further helices ($\alpha 4$, $\alpha 5$, $\alpha 7$ and $\alpha 9$), that are roughly orthogonal to the crossing helices, form the sides of an extended groove (Fig. 2c). Electron density in this region is generally weaker than in the rest of the protein, and this is reflected

pseudo-two-fold axis, relative to **a** and **b**. Interfacial regions involving the conserved ATPase motifs are coloured brown. **e,** Details of the Get3 dimerization motif in the closed dimer structure, highlighting the tetrahedral coordination of zinc by the conserved CXXC sequence motif. Electron density is from a σ_A -weighted $2F_o - F_c$ map calculated at 2.0 Å resolution and contoured at 2σ .

in higher B-factors; indeed, the regions connecting helices $\alpha 4$ – $\alpha 5$ and $\alpha 7$ – $\alpha 9$ (including helix $\alpha 8$ of the TRC40-insert) are disordered in electron density maps of the closed dimer (Supplementary Fig. 1b).

The Get3 composite groove exposes more than 3,000 Å² of hydrophobic surface area to solvent. In contrast, the signal sequence binding groove in the M-domain of *Thermus aquaticus* Ffh (the homolog of eukaryotic SRP54) exposes only $\sim 1,500$ Å² of hydrophobic surface area²³. The non-polar character of the Get3 groove is conserved across eukaryotic TRC40s, but the sequence identity of residues lining the groove is not (Supplementary Fig. 3b). Polar and charged residues are almost completely excluded from the groove, whereas the ends, which are open to solvent, are delineated by two conserved, positively charged surface patches (Lys 147, Lys 150 and Lys 215). The hydrophobic region of the groove is approximately 30 Å long, 15 Å wide, and 15 Å deep (Fig. 2b), which is sufficient to accommodate an α -helical TMD of ~ 20 residues, and could therefore form the TA substrate-binding site.

To test this, 24 Get3 variants with single aspartate substitutions for hydrophobic residues on the surface of the groove were analysed for substrate interaction *in vitro* and functional complementation of a Δ get3 yeast strain *in vivo*. All but one of these expressed at wild-type levels in *E. coli*, were soluble after purification, and possessed detectable levels of ATPase activity (Supplementary Table 2). A native pull-down assay showed that wild-type Get3 bound to *in-vitro*-synthesized SEC61 β (a model TA protein) in a TMD-dependent manner (Supplementary Fig. 4). Among the variant Get3 proteins, reduced TA substrate binding was seen for mutations clustered along helices $\alpha 7$ and $\alpha 8$ (Fig. 3a, c, green and magenta). Notably, these regions include the C-terminal end of Switch II (helix $\alpha 7$), and the N-terminal end of the TRC40-insert (helix $\alpha 8$). In qualitative agreement with the substrate pull-down assay, the strongest *in vivo* defects clustered along helices $\alpha 7$ and $\alpha 8$ (Supplementary Fig. 5).

As expected, a set of double aspartate mutants, as well as the dimerization-deficient Cys285Ser/Cys288Ser double mutant,

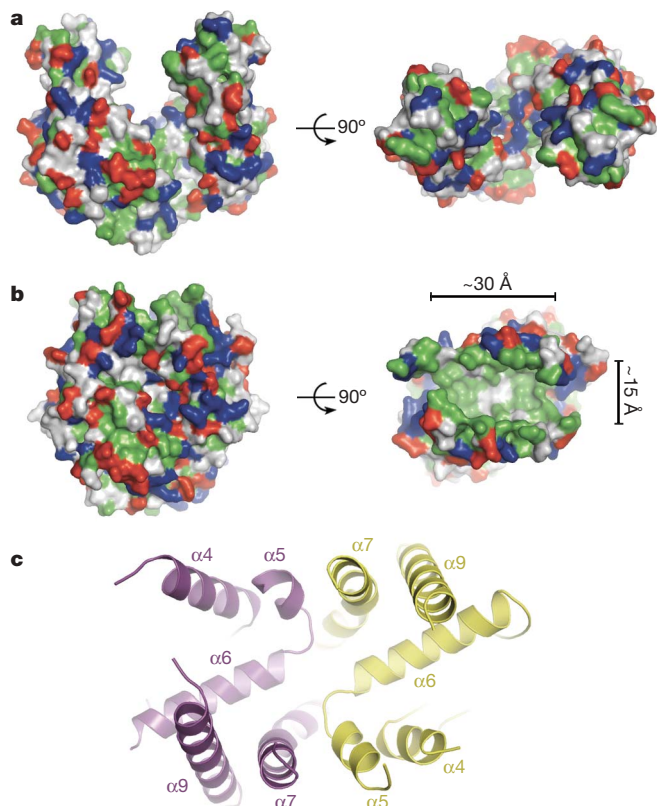


Figure 2 | A composite hydrophobic groove at the closed dimer interface.

a, Surface representation of the Get3 open dimer with hydrophobic residues coloured green; positively and negatively charged residues are coloured blue and red, respectively. **b**, As in **a**, but for the Get3 closed dimer. The approximate dimensions of the large hydrophobic groove (right panel) are indicated. **c**, Architecture of the composite hydrophobic groove formed by the association of α -helical subdomains (magenta and yellow, coloured as in Fig. 1 and oriented as in **b**, right panel) at the homodimer interface.

showed stronger growth defects that correlated well with *in vitro* TA substrate binding activity (Fig. 3a, d). Notably, two single mutations (Met200Asp and Met205Asp) that showed relatively modest *in vitro* and *in vivo* defects had a much stronger effect when combined. The double mutants expressed to high levels in *E. coli*, were soluble, and showed ATPase activities that are within ~2–3-fold of wild-type Get3 (Fig. 3b and Supplementary Table 2), suggesting that the observed defects were not due to improper folding or impaired catalysis. Considered together with the crystallographic analysis, these functional data suggest that newly synthesized TA substrates bind to the composite hydrophobic groove of Get3 during targeting to the ER.

The nucleotide sensor

In the ADP·AlF₄[−]-bound Get3 crystal structure, two nucleotides are buried in a head-to-head conformation at the homodimer interface (Fig. 1b). Nearly 30% of the surface area buried in this interface involves the conserved ATPase sequence motifs (Fig. 1d). Although each nucleotide is principally associated with one monomer, key contacts are also made to the second monomer, explaining why dimerization-deficient mutants of Get3, including Cys285Ser/Cys288Ser (Fig. 3a, b, d), are functionally inactive²².

The active sites of both Get3 monomers are locked in virtually identical conformations mimicking the transition state (Fig. 4a). This contrasts with ArsA, in which the nucleotide-binding sites seem to be structurally and functionally non-equivalent²⁴. In Get3, the square-planar AlF₄[−] and α - and β -phosphates of ADP interact with the P-loop through backbone amide nitrogens of residues 28–33 and the side chains of Thr 32 and Thr 33. Mg²⁺ is octahedrally coordinated

by three water molecules, a β -phosphate oxygen, one of the fluoride ligands of AlF₄[−], and by the side chain of Thr 32. Furthermore, the Switch II residues Asp 166 and Thr 167 each make second shell interactions with Mg²⁺. A well-ordered water molecule, coordinated by the side chain of Asp 57 (in Switch I) and only 3.6 Å from Pro 169 (in Switch II), is positioned for in-line nucleophilic attack on the γ -phosphate of ATP. This interaction is essential because an Asp57Asn mutant is defective for ATP hydrolysis and unable to rescue the hygromycin B-sensitive phenotype of *Δget3* yeast (Fig. 3b, d). In addition, the conserved P-loop residue Lys 26 reaches across the dimer interface to contact the α - and β -phosphates and AlF₄[−] in the opposing active site. This intersubunit interaction is essential for catalysis in related systems, including NifH²⁵ and Soj¹⁸. In Get3, Lys 26 probably functions analogously to stabilize the transition state by neutralization of the negative charge at the γ -phosphate.

The observation that ATP hydrolysis is required for efficient release of the TA substrate at the ER membrane¹⁰ suggests that the ATPase and α -helical subdomains of Get3 are functionally linked. Consistent with this, we found that a subset of aspartate point mutations within the α -helical subdomain reduced the rate of ATP hydrolysis *in vitro* (Fig. 3b, c, blue and magenta). These mutations are adjacent to the conserved Switch II region (Fig. 3c, yellow), which undergoes nucleotide-mediated conformational changes in related systems, including NifH^{25,26}. In the Get3 crystal, the transition from an open to a closed state is accompanied by a coil-to-helix transition in the N-terminal end of helix α 7, part of Switch II (Fig. 4b). In the helical conformation, the side chain of the Switch II residue His 172 (which binds to metalloid substrates in ArsA) stacks against the His 172 side chain from the opposing subunit. Each His 172 makes an additional cross-monomer interaction with Glu 138 (part of helix α 6), and Arg 175 (located in helix α 7, immediately C-terminal to Switch II) forms an inter-monomer salt bridge to Asp 137 (part of helix α 6). Remarkably, these residues are conserved from yeast to human.

The network of Switch-II-mediated cross-monomer interactions between the ATPase and α -helical subdomains in the closed dimer provides a direct link between nucleotide switching and formation of the composite TA binding site. Consistent with this, the nucleotide-free crystal structure shows Switch II/ α 7 in a coiled conformation, and the network of inter-subunit interactions observed in the closed dimer is completely disrupted (Fig. 4b, grey). In this open state, the α -helical subdomains are separated by more than 20 Å (Fig. 1a), and the composite hydrophobic groove is disrupted. Helices within the isolated α -helical subdomains are rearranged (Fig. 4c, grey); most notably, helix α 8, which is disordered in the closed dimer structure, packs against the α -helical subdomain, where it shields the hydrophobic surface from solvent. Taken together, and by analogy to other SIMIBI proteins^{25,27,28}, the Get3 crystal structures suggest that Switch II functions to relay structural changes induced by ATP binding and hydrolysis to the homodimer interface and the TA substrate binding site.

Implications for TA protein binding

We propose that the composite hydrophobic groove observed in the closed configuration of the Get3 homodimer forms the TMD binding site. This assignment is consistent with our biochemical, genetic and structural analysis. The dimensions of the groove are well suited for binding to an α -helical TMD of ~20 residues (Fig. 5a). The conserved TRC40-insert, which is disordered in the closed dimer structure (presumably reflecting the absence of a bound TA substrate), is a dynamic feature of the TA binding site. It may serve as a 'lid' to shield the exposed face of a bound TMD from solvent during targeting, and to protect the hydrophobic surface of the isolated α -helical subdomain in the absence of substrate.

The extensive hydrophobic surface area (>3,000 Å²) within the groove suggests that Get3 binds to a wide range of ER-directed targeting signals with high affinity. Consistent with this, many of the single aspartate Get3 mutants remain capable of interacting with TA

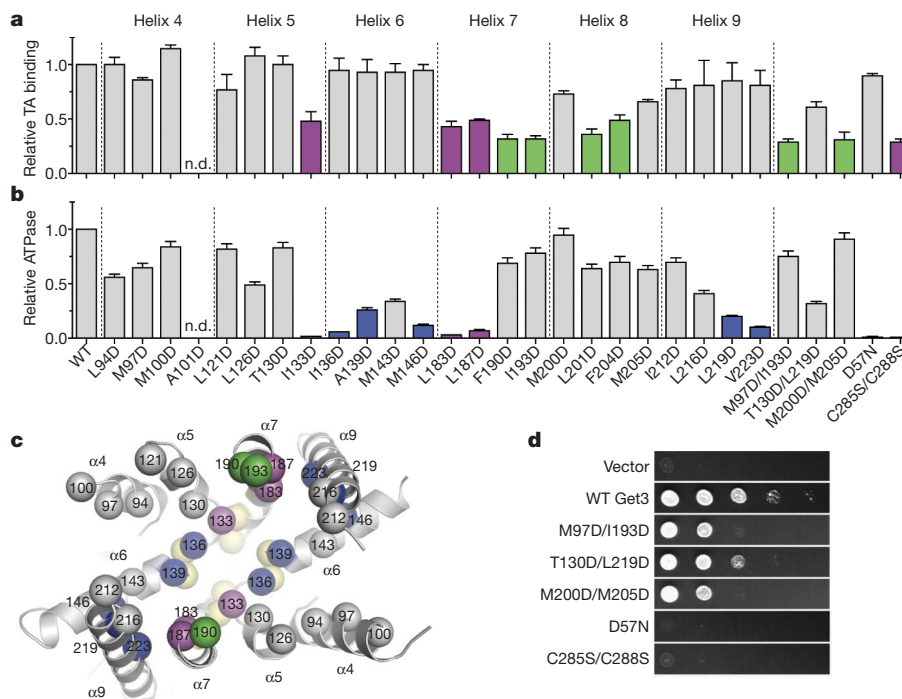


Figure 3 | Functional analysis of the hydrophobic groove. **a**, The effect of site-specific Get3 mutations on binding to full-length human SEC61 β was measured by native immunoprecipitation. Each value is the average of between three and six independent measurements, performed on different days, relative to wild type. Error bars denote s.e.m. Variants showing less than $\sim 50\%$ of wild-type binding are highlighted (green, magenta). **b**, ATPase activity was determined in triplicate, and values are V_{\max} relative to wild type. Error bars denote s.e.m. Variants showing less than $\sim 25\%$ of wild-type

ATPase activity are highlighted (blue, magenta). **c**, Mutations showing the strongest defects in TA substrate binding (green), ATP hydrolysis (blue), or both (magenta) are mapped onto the composite hydrophobic groove (oriented as in Fig. 2c). ATPase mutants localize to the base of the groove, adjacent to the Get3 nucleotide sensor (yellow; see Fig. 4b). Helix $\alpha 8$ is disordered in the Get3 closed dimer structure and is therefore not visible here. **d**, *In vivo* analysis of Get3 mutants. WT, wild type.

substrates despite the presence of charge within the hydrophobic groove (Fig. 3a and Supplementary Fig. 5). Phylogenetic analysis of eukaryotic TRC40 sequences indicates that methionine is unusually abundant within the groove. Similar to previous proposals for signal sequence binding by the methionine-rich M-domain of SRP54 and Ffh^{23,29}, the intrinsic side- and main-chain dynamics of the groove probably contribute to the ability of Get3 to accommodate diverse TA protein targeting signals.

The structures also suggest how Get3 distinguishes between closely related ER and mitochondrial outer membrane (MOM)-directed targeting signals. ER-targeted TA proteins typically possess longer and more hydrophobic TMDs than TA proteins destined for the MOM³⁰. Thus, the composite groove in Get3 may function as a molecular ruler, preferentially binding to ER-directed TA proteins of sufficient

length (~ 30 Å) and hydrophobicity. Similarly, MOM-directed targeting signals generally contain positive charge immediately C-terminal to the TMD^{31,32}. Thus, further discrimination may occur at the positively charged ends of the Get3 hydrophobic groove (Fig. 2b), where charge repulsion biases Get3 against binding to MOM targeting signals. Together, these structural features may allow selective binding to ER-directed targeting signals.

A model for TA protein targeting

Our structural and functional data allow us to propose a physically plausible model by which ATP binding and hydrolysis regulate TA substrate binding and release during targeting to the ER (Fig. 5b). Targeting is initiated in the cytosol when ATP binding drives Get3 towards the closed dimer state, facilitating recognition of newly

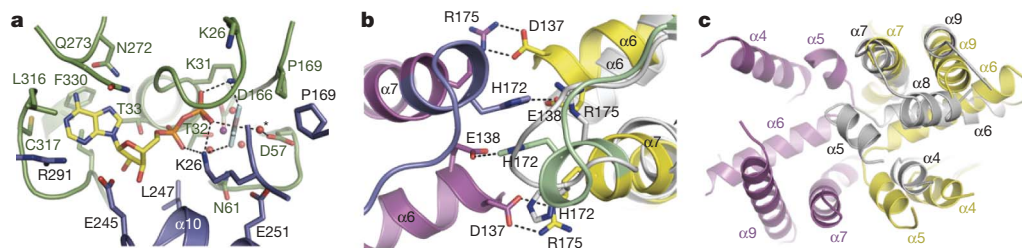


Figure 4 | The Get3 nucleotide sensor. **a**, Key interactions within the composite ATP-binding site of one subunit (green) of the closed dimer. The essential catalytic residue Asp 57 coordinates the putative nucleophilic water molecule (red sphere, asterisk), adjacent to AlF_4^- . The nucleotide makes further interactions with residues in the second subunit (blue), including the P-loop residue Lys 26. **b**, A coil-to-helix transition in the Switch II region (green and blue) is observed in the presence of $\text{ADP} \cdot \text{AlF}_4^-$ relative to the nucleotide free state (grey subunit). Viewed $\sim 180^\circ$ from the orientation in

c, looking along the dimer pseudo-two-fold axis, and coloured as in Fig. 1. Conserved, cross-monomer interactions between Switch II/ $\alpha 7$ and the α -helical subdomain are disrupted in the open dimer (the second subunit of the nucleotide-free dimer is not visible here). **c**, The α -helical subdomains move apart in the open dimer (grey), and helices within each of the resulting 'half-sites' rearrange; helix $\alpha 8$, disordered in the closed dimer, inserts into the hydrophobic half-site to shield it from solvent.

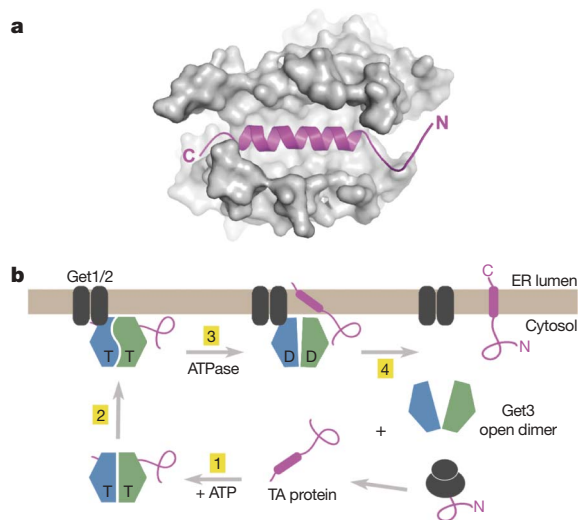


Figure 5 | Model for TA protein targeting. **a**, The 20-residue α -helical TMD of the *Methanococcus jannaschii* TA protein Sec61 β (PDB accession 1RHZ)³⁸ can be modelled into the Get3 hydrophobic groove with good physicochemical complementarity. **b**, The Get3 open dimer binds ATP and newly synthesized TA proteins destined for the ER (step 1). The Get3-substrate complex is targeted to the ER by an interaction with the membrane bound receptor, Get1/2 (step 2). After ATP hydrolysis, conformational changes in the nucleotide sensor destabilize the composite groove, driving TA substrate release (step 3). Membrane insertion may be spontaneous, or facilitated by a dedicated integrase (not shown). Disruption of the closed dimer following ATP hydrolysis and TA substrate insertion drives release from the membrane and restores Get3 to its open dimer configuration (step 4).

synthesized TA membrane proteins in a TMD-dependent manner^{9,10,14}. To minimize unproductive ATP hydrolysis, active site residues in the closed dimer interface (for example, Lys 26) are held in non-catalytic conformations until the pre-targeting complex is delivered to the Get1/2 receptor at the ER membrane¹⁴. Because ATP hydrolysis is required for insertion¹⁰, association with the receptor, the lipid bilayer and/or a putative integrase drives the 'loose' pre-targeting complex into a catalytically competent conformation. After ATP hydrolysis and dissociation of ADP and/or inorganic phosphate, the Switch II region collapses, thereby disrupting the network of conserved cross-monomer interactions that stabilize the composite groove (Fig. 4b). Initially, these conformational changes may be propagated through helix $\alpha 7$ to 'pop' open the TRC40-insert lid, as observed in the closed dimer, facilitating TA substrate release. An intriguing possibility is that the conserved TRC40-insert transiently partitions into the outer leaflet of the ER lipid bilayer to drive TA substrate insertion into the membrane. Subsequently, Get3 reverts towards the open dimer state, lowering its affinity for the Get1/2 receptor, and returning it to the cytosol to initiate a new round of targeting.

METHODS SUMMARY

Wild-type and selenomethionyl proteins were expressed in *E. coli* and purified using Ni-NTA and size-exclusion chromatography. Crystals were grown in hanging drop, vapour diffusion format. Diffraction data were collected from cryo-protected crystals at beamline 21-IDG of the Advanced Photon Source (Argonne National Laboratories). The structure of *S. cerevisiae* Get3 complexed with ADP·AlF₄⁻ was determined by single-wavelength anomalous dispersion (SAD) from selenomethionine-containing protein using PHENIX³³. The structures of nucleotide-free *S. cerevisiae* and *S. pombe* Get3 were solved by molecular replacement in PHASER³⁴. A monomer of the *S. cerevisiae* Get3-ADP·AlF₄⁻ complex (with nucleotide and the α -helical subdomain removed) was used as the search model. Refinement and model building were carried out with PHENIX³³ and COOT³⁵.

A series of *GET3* genes containing site-specific mutations were generated by Quik-Change mutagenesis. The identity of each mutant was confirmed by DNA sequencing. Proteins were expressed in *E. coli* and purified by Ni-NTA

chromatography. TA substrate binding was monitored using a native pull-down assay in which full-length ³⁵S-labelled human SEC61 β was translated in a TRC40-depleted reticulocyte lysate translation extract with or without recombinant wild-type or mutant Get3 protein. After translation, Get3 was immunoprecipitated under native conditions, analysed by SDS-PAGE, and quantified by phosphorimaging. The ATPase activity of Ni-NTA-purified protein was determined using an NADH-coupled microplate photometric assay^{36,37}.

Wild-type and mutant *GET3* genes were subcloned into a low copy number URA plasmid under the control of a medium-strength, constitutive ACT1 promoter, and transformed into a *Δget3* strain (Open Biosystems); serial dilutions of each transformant were spotted (along with wild type and vector only controls) onto synthetic defined medium (–uracil) supplemented with 100 μ g ml⁻¹ hygromycin B. Plates were photographed after 2 days at 37 °C.

Full Methods and any associated references are available in the online version of the paper at www.nature.com/nature.

Received 29 June; accepted 27 July 2009.

Published online 12 August; corrected 17 September 2009 (see full-text HTML version for details).

1. Egea, P. F., Stroud, R. M. & Walter, P. Targeting proteins to membranes: structure of the signal recognition particle. *Curr. Opin. Struct. Biol.* **15**, 213–220 (2005).
2. Keenan, R. J., Freymann, D. M., Stroud, R. M. & Walter, P. The signal recognition particle. *Annu. Rev. Biochem.* **70**, 755–775 (2001).
3. Rapoport, T. A. Protein translocation across the eukaryotic endoplasmic reticulum and bacterial plasma membranes. *Nature* **450**, 663–669 (2007).
4. Beilharz, T., Egan, B., Silver, P. A., Hofmann, K. & Lithgow, T. Bipartite signals mediate subcellular targeting of tail-anchored membrane proteins in *Saccharomyces cerevisiae*. *J. Biol. Chem.* **278**, 8219–8223 (2003).
5. Kalbfleisch, T., Cambon, A. & Wattenberg, B. W. A bioinformatics approach to identifying tail-anchored proteins in the human genome. *Traffic* **8**, 1687–1694 (2007).
6. Borgese, N., Brambilla, S. & Colombo, S. How tails guide tail-anchored proteins to their destinations. *Curr. Opin. Cell Biol.* **19**, 368–375 (2007).
7. Wattenberg, B. & Lithgow, T. Targeting of C-terminal (tail)-anchored proteins: understanding how cytoplasmic activities are anchored to intracellular membranes. *Traffic* **2**, 66–71 (2001).
8. Kutay, U., Ahnert-Hilger, G., Hartmann, E., Wiedenmann, B. & Rapoport, T. A. Transport route for synaptobrevin via a novel pathway of insertion into the endoplasmic reticulum membrane. *EMBO J.* **14**, 217–223 (1995).
9. Favalaro, V., Spasic, M., Schwappach, B. & Dobberstein, B. Distinct targeting pathways for the membrane insertion of tail-anchored (TA) proteins. *J. Cell Sci.* **121**, 1832–1840 (2008).
10. Stefanovic, S. & Hegde, R. S. Identification of a targeting factor for posttranslational membrane protein insertion into the ER. *Cell* **128**, 1147–1159 (2007).
11. Kurdi-Haidar, B. *et al.* Isolation of the ATP-binding human homolog of the arsA component of the bacterial arsenite transporter. *Genomics* **36**, 486–491 (1996).
12. Kurdi-Haidar, B., Heath, D., Aebi, S. & Howell, S. B. Biochemical characterization of the human arsenite-stimulated ATPase (hASNA-I). *J. Biol. Chem.* **273**, 22173–22176 (1998).
13. Rosen, B. P., Bhattacharjee, H., Zhou, T. & Walmsley, A. R. Mechanism of the ArsA ATPase. *Biochim. Biophys. Acta* **1461**, 207–215 (1999).
14. Schuldiner, M. *et al.* The GET complex mediates insertion of tail-anchored proteins into the ER membrane. *Cell* **134**, 634–645 (2008).
15. Leipe, D. D., Wolf, Y. I., Koonin, E. V. & Aravind, L. Classification and evolution of P-loop GTPases and related ATPases. *J. Mol. Biol.* **317**, 41–72 (2002).
16. Zhou, T., Radaev, S., Rosen, B. P. & Gatti, D. L. Structure of the ArsA ATPase: the catalytic subunit of a heavy metal resistance pump. *EMBO J.* **19**, 4838–4845 (2000).
17. Georgiadis, M. M. *et al.* Crystallographic structure of the nitrogenase iron protein from *Azotobacter vinelandii*. *Science* **257**, 1653–1659 (1992).
18. Leonard, T. A., Butler, P. J. & Lowe, J. Bacterial chromosome segregation: structure and DNA binding of the Soj dimer—a conserved biological switch. *EMBO J.* **24**, 270–282 (2005).
19. Hayashi, I., Oyama, T. & Morikawa, K. Structural and functional studies of MinD ATPase: implications for the molecular recognition of the bacterial cell division apparatus. *EMBO J.* **20**, 1819–1828 (2001).
20. Freymann, D. M., Keenan, R. J., Stroud, R. M. & Walter, P. Structure of the conserved GTPase domain of the signal recognition particle. *Nature* **385**, 361–364 (1997).
21. Montoya, G., Svensson, C., Lührink, J. & Sinning, I. Crystal structure of the NG domain from the signal-recognition particle receptor FtsY. *Nature* **385**, 365–368 (1997).
22. Metz, J., Wachter, A., Schmidt, B., Bujnicki, J. M. & Schwappach, B. The yeast Arr4p ATPase binds the chloride transporter Gef1p when copper is available in the cytosol. *J. Biol. Chem.* **281**, 410–417 (2006).
23. Keenan, R. J., Freymann, D. M., Walter, P. & Stroud, R. M. Crystal structure of the signal sequence binding subunit of the signal recognition particle. *Cell* **94**, 181–191 (1998).
24. Jiang, Y. *et al.* Nonequivalence of the nucleotide binding domains of the ArsA ATPase. *J. Biol. Chem.* **280**, 9921–9926 (2005).

25. Schindelin, H., Kisker, C., Schlessman, J. L., Howard, J. B. & Rees, D. C. Structure of ADP·AlF₄[−]-stabilized nitrogenase complex and its implications for signal transduction. *Nature* **387**, 370–376 (1997).
26. Sprang, S. R. G protein mechanisms: insights from structural analysis. *Annu. Rev. Biochem.* **66**, 639–678 (1997).
27. Gasper, R., Meyer, S., Gotthardt, K., Sirajuddin, M. & Wittinghofer, A. It takes two to tango: regulation of G proteins by dimerization. *Nature Rev. Mol. Cell Biol.* **10**, 423–429 (2009).
28. Zhou, T., Radaev, S., Rosen, B. P. & Gatti, D. L. Conformational changes in four regions of the *Escherichia coli* ArsA ATPase link ATP hydrolysis to ion translocation. *J. Biol. Chem.* **276**, 30414–30422 (2001).
29. Bernstein, H. D. *et al.* Model for signal sequence recognition from amino-acid sequence of 54K subunit of signal recognition particle. *Nature* **340**, 482–486 (1989).
30. Horie, C., Suzuki, H., Sakaguchi, M. & Mihara, K. Characterization of signal that directs C-tail-anchored proteins to mammalian mitochondrial outer membrane. *Mol. Biol. Cell* **13**, 1615–1625 (2002).
31. Kaufmann, T. *et al.* Characterization of the signal that directs Bcl-x_L, but not Bcl-2, to the mitochondrial outer membrane. *J. Cell Biol.* **160**, 53–64 (2003).
32. Kuroda, R. *et al.* Charged amino acids at the carboxyl-terminal portions determine the intracellular locations of two isoforms of cytochrome b5. *J. Biol. Chem.* **273**, 31097–31102 (1998).
33. Adams, P. D. *et al.* PHENIX: building new software for automated crystallographic structure determination. *Acta Crystallogr. D* **58**, 1948–1954 (2002).
34. McCoy, A. J., Grosse-Kunstleve, R. W., Adams, P. D. & Winn, M. D. Phaser crystallographic software. *J. Appl. Crystallogr.* **40**, 658–674 (2007).
35. Emsley, P. & Cowtan, K. Coot: model-building tools for molecular graphics. *Acta Crystallogr. D* **60**, 2126–2132 (2004).
36. Kiianitsa, K., Solinger, J. A. & Heyer, W. D. NADH-coupled microplate photometric assay for kinetic studies of ATP-hydrolyzing enzymes with low and high specific activities. *Anal. Biochem.* **321**, 266–271 (2003).
37. Vogel, G. & Steinhart, R. ATPase of *Escherichia coli*: purification, dissociation, and reconstitution of the active complex from the isolated subunits. *Biochemistry* **15**, 208–216 (1976).

Supplementary Information is linked to the online version of the paper at www.nature.com/nature.

Acknowledgements Data were collected at beamlines 21-IDG and 23-IDD at the Advanced Photon Source (APS), Argonne National Laboratory, and we thank the beamline staff for support. Use of the APS was supported by the US Department of Energy, Office of Science, Office of Basic Energy Sciences, under contract no. DE-AC02-06CH11357. We thank B. Glick and R. Strack for reagents and advice, X. Li for assay characterization, and A. Shiao and T. Steck for comments on the manuscript. This work was supported by a grant from the Edward Mallinckrodt, Jr. Foundation (to R.J.K.) and by the Intramural Research Program of the National Institutes of Health (to R.S.H.).

Author Contributions A.M., A.S. and M.E.D. carried out cloning, protein purification and crystallization. A.M. performed the mutagenesis. M.M. and R.S.H. performed the TA substrate-binding assay. M.D. carried out the ATPase assay. M.E.D. performed the yeast genetic complementation assay. A.M., A.S. and R.J.K. carried out data collection. A.M. and R.J.K. carried out structure determination and model building. R.J.K. supervised the work and wrote the manuscript. All authors discussed the results and commented on the manuscript.

Author Information Atomic coordinates and structure factors for the *S. pombe* Get3 and Mg²⁺·ADP·AlF₄[−]-bound *S. cerevisiae* Get3 crystal structures are deposited in the Protein Data Bank under accession codes 2WOO and 2WOJ. Reprints and permissions information is available at www.nature.com/reprints. Correspondence and requests for materials should be addressed to R.J.K. (bkeenana@uchicago.edu).

METHODS

Protein cloning, expression and purification. The genes encoding full-length *S. cerevisiae* and *S. pombe* Get3 were amplified by PCR using genomic DNA, and subcloned into a pET28 derivative (Novagen) modified to incorporate a tobacco etch virus (TEV) protease cleavage site between an N-terminal 6×His tag and the polylinker. Proteins were expressed in *E. coli* Rosetta2(DE3)/pLysS (Novagen) at 37 °C for 3 h by induction with 0.1 mM IPTG after the cells reached an A_{600} of ~0.6. Cells were disrupted in lysis buffer (50 mM Tris, pH 7.5, 500 mM NaCl, 5 mM β -mercaptoethanol, 10 mM imidazole, 10% glycerol and 1 mM PMSF) using a high-pressure microfluidizer (Avestin). After clearing by centrifugation, the supernatant was batch-purified by nickel-affinity chromatography (Ni-NTA His Bind Resin, Novagen) and dialysed into 10 mM Tris, pH 7.5, 100 mM NaCl, 2 mM dithiothreitol (DTT), 40% glycerol. This was followed optionally by cleavage with 6×His-tagged TEV protease and removal of residual uncleaved Get3 and the 6×His-tagged TEV protease by subtractive Ni-NTA purification. For crystallization, protein was further purified by gel filtration (Superdex 200 10/300 GL, GE Healthcare). Fractions were pooled, concentrated to ~10 mg ml⁻¹ in 10 mM Tris, pH 7.5, 100 mM NaCl and 2 mM DTT, and stored at -80 °C. Selenomethionyl *S. cerevisiae* Get3 protein was prepared by feedback inhibition³⁹ in BL21(DE3) cells (Novagen) using the Overnight Express Autoinduction System 2 (Novagen). Incorporation of selenomethionine was confirmed by matrix-assisted laser desorption/ionization (MALDI) mass spectrometry. Selenomethionyl Get3 was purified in the same way as the native protein.

Crystallization. Crystals of 6×His-tagged *S. cerevisiae* Get3 complexed with ADP·AlF₄⁻ were grown at room temperature using hanging drop vapour diffusion by mixing equal volumes of a protein solution containing 2 mM ADP, 2 mM MgCl₂, 2 mM AlCl₃ and 8 mM NaF with a reservoir solution containing 33% PEG 3350, 0.1 M Tris, pH 8.4, 0.2 M ammonium acetate and 75 mM Na/K tartrate. Selenomethionine-containing crystals were grown under similar conditions by mixing equal volumes of protein solution with 31% PEG 3350, 0.1 M Tris, pH 8.4, 0.2 M ammonium acetate and 50 mM glycine. Crystals were cryo-protected in 30% PEG3350, 0.1 M Tris, pH 8.4, 0.2 M ammonium acetate, 75 mM Na/K tartrate, 2 mM ADP, 2 mM MgCl₂, 2 mM AlCl₃, 8 mM NaF and 20% ethylene glycol (native) or 31% PEG3350, 0.1 M Tris, pH 8.4, 0.2 M ammonium acetate, 50 mM glycine, 2 mM ADP, 2 mM MgCl₂, 2 mM AlCl₃, 8 mM NaF and 20% glycerol (selenomet) and flash frozen in liquid nitrogen.

Crystals of *S. pombe* Get3 (cleaved) were grown at room temperature using hanging drop vapour diffusion by mixing equal volumes of protein solution with a reservoir solution containing 25% PEG 3350, 0.1 M MES, pH 6.5 and 0.4 M MgCl₂. Crystals were collected directly and flash-frozen in liquid nitrogen.

Crystals of 6×His-tagged *S. cerevisiae* Get3 (apo) were grown at room temperature using hanging drop vapour diffusion by mixing equal volumes of protein solution with a reservoir solution containing 1.5 M ammonium sulphate, 0.1 M MES, pH 6.5, 0.1 M NaCl, 5 mM proline and 0.2 mM C₁₂E₈. Crystals were cryoprotected in 2 M ammonium sulphate, 0.1 M MES, pH 6.5, 0.1 M NaCl, 5 mM proline and 25% glycerol, and flash-frozen in liquid nitrogen.

Structure determination and refinement. Native and selenium SAD data were collected at 100K at APS beamline 21-IDG ($\lambda = 0.97856$), and processed using HKL2000 (HKL Research). Data collection statistics are listed in Supplementary Table 1.

The structure of *S. cerevisiae* Get3 in complex with ADP·AlF₄⁻ was determined by SAD. The positions of 38 out of 52 selenium sites in the asymmetric unit were located using PHENIX³³. After phasing and density modification the resulting electron density maps were of high quality, allowing us to manually place four copies of Get3 (using the core ATPase region of ArsA as a starting model) and revealing clear density for nucleotide in the active site. A native data set to 2.0 Å was used for model rebuilding and refinement with COOT³⁵ and PHENIX. The final model contains two Get3 homodimers, four Mg²⁺·ADP·AlF₄⁻ complexes, two zinc atoms and 507 water molecules, and was refined to an *R*-factor (*R*_{free}) of 17.6% (21.3%). No electron density was observed for residues 1–4, 101–120, 191–211, 279–284, 353 and 354 in chain A; 1–3, 106–125, 154–158, 194–209, 280–284 and 351–354 in chain B; 1–4, 100–125, 153–158, 189–212, 278–284 and 352–354 in chain C; and 1–4, 105–117, 152–159, 192–211, 282–284, 353 and 354 in chain D.

The structure of nucleotide-free *S. pombe* Get3 was determined to 3.0 Å by molecular replacement with PHASER³⁴ using a monomer of *S. cerevisiae* Get3 (with the α -helical subdomain removed) as the search model (58% sequence identity to *S. pombe*). Although these crystals diffract relatively poorly, sixfold NCS averaging yielded interpretable electron density maps. Model building and refinement (with NCS restraints) were carried out with COOT and PHENIX. The final model contains three Get3 homodimers and three zinc atoms and was refined with tight NCS restraints to an *R*_{free} of 23.7% (28.8%). Side-chain density is generally weakest in the α -helical subdomains, and no interpretable electron density was observed for residues 1–6, 101–108, 191–195 and 323–329 in each chain.

The structure of nucleotide-free *S. cerevisiae* Get3 was determined by molecular replacement using PHASER. Identical solutions were found using either a monomer of *S. cerevisiae* Get3 or the *S. pombe* nucleotide-free open dimer as the search model (with the α -helical subdomain removed). Initial electron density maps calculated after fourfold NCS averaging clearly defined the orientation of the core ATPase domains of each monomer, and difference maps were used to confirm the presence of zinc at the dimer interface (Supplementary Fig. 2b). Helical features, including portions of α_6 , α_7 and α_9 , are also observed in the α -helical subdomains. Although the *S. cerevisiae* apo structure shows the same open dimer architecture observed in the *S. pombe* apo structure (Supplementary Fig. 2c), because these crystals diffract weakly (to 3.8 Å) and anisotropically, no attempt was made to refine the model.

Refinement statistics are listed in Supplementary Table 1. All structure figures in the manuscript were generated using Pymol⁴⁰ and COOT.

Preparation of site-directed mutants. Site-directed *S. cerevisiae* Get3 mutants were generated using the QuikChange mutagenesis kit (Stratagene), and verified by DNA sequencing. Protein expression was carried out in *E. coli* as described earlier, except cells were grown at 25 °C and induced overnight. All mutants expressed to high levels. With the exception of Ala101Asp (which was insoluble), wild-type and mutant proteins were purified under non-denaturing conditions (as above) in a single step by nickel-affinity chromatography and dialysed into 10 mM Tris, pH 7.5, 100 mM NaCl, 2 mM DTT and 40% glycerol. Protein concentrations were determined using the Bradford protein assay (Bio-Rad) standardized by calculated A₂₈₀ extinction coefficients.

Get3 pull-down assay for TA substrate interaction. Full-length ³⁵S-labelled human SEC61 β was synthesized in phenyl-depleted rabbit reticulocyte lysate translation extract (see later) with or without Get3 (or mutant Get3) protein at 50 μ g ml⁻¹. After translation for 15 min at 32 °C, the reactions were placed immediately on ice. To each reaction, 2.5 μ l of anti-Get3 serum was added, incubated for 30 min on ice, and diluted to 1 ml with ice-cold pull-down buffer (50 mM HEPES, pH 7.4, 150 mM potassium acetate, and 2 mM magnesium acetate). Ten microlitres of Protein-A agarose (BioRad) was added, incubated with end-over-end mixing for 90 min at 4 °C, and washed 3 × 1 ml with pull-down buffer. Immunoprecipitated products were analysed by SDS-PAGE and quantified by phosphorimaging.

Each experiment included a reaction without Get3 to assess the extent of background pull-down. This value was subtracted from all samples. Wild-type Get3 was arbitrarily set at 100% pull-down. Each value is the average of between three and six independent measurements performed on different days. The error bars denote s.e.m. Coomassie staining verified that the polyclonal anti-Get3 antibody pulled down equal amounts of all Get3 mutants, indicating that the site-specific mutations did not affect antibody binding.

Preparation of phenyl-depleted translation extract. Rabbit reticulocyte lysate supplemented with all components needed for translation was passed by gravity over a column of highly substituted phenyl-sepharose (GE/Amersham). The column volume was one-third of the lysate volume (typically 200 and 600 μ l, respectively). The leading and trailing edges of the flow-through were not collected. Only the peak flow-through fractions (~400 μ l) containing undiluted lysate were collected and frozen in aliquots in liquid nitrogen and stored at -80 °C. Prepared in this manner, the lysate was more than 98% depleted of TRC40, but retained full translation capacity. By Coomassie staining, 95% or more of the proteins were not affected by the depletion.

ATPase assay. ATPase activity was determined at 30 °C using a microplate photometric assay in which ATP hydrolysis is coupled to NADH oxidation^{36,37}. The assay buffer contained 50 mM Tris, pH 7.5, 20 mM NaCl, 5 mM MgCl₂, 1 mM DTT, 5% glycerol, 0.02% *n*-dodecyl- β -D-maltopyranoside, 4.5 mM phosphoenolpyruvate, 8.0 U lactate dehydrogenase (Sigma), 6.3 U pyruvate kinase (Sigma), 0.3 mM NADH and 2 μ M Get3 (wild-type or mutant), and reactions were carried out in a final reaction volume of 200 μ l. The reactions were initiated by adding ATP and the decrease in NADH concentration was followed spectrophotometrically at 340 nm. Linear steady state rates between 100 and 400 s were used to calculate *V*_{max} and apparent *K*_{m,ATP} values using a pathlength-corrected molar extinction coefficient for NADH. Kinetic parameters were determined by fitting the data to the Michaelis-Menten equation by nonlinear regression. All measurements were carried out in triplicate.

Yeast growth assay. Wild-type and mutant *GET3* genes were subcloned into a low copy number URA plasmid under the control of a medium-strength, constitutive ACT1 promoter, and transformed into a *Δget3* strain (Open Biosystems). Serial dilutions of each transformant were spotted (along with wild type and vector only controls) onto synthetic defined medium (-uracil) supplemented with 100 μ g ml⁻¹ hygromycin B. Plates were photographed after 2 days at 37 °C.

38. Van den Berg, B. *et al.* X-ray structure of a protein-conducting channel. *Nature* **427**, 36–44 (2004).

39. Van Duyn, G. D., Standaert, R. F., Karplus, P. A., Schreiber, S. L. & Clardy, J. Atomic structures of the human immunophilin FKBP-12 complexes with FK506 and rapamycin. *J. Mol. Biol.* **229**, 105–124 (1993).

40. Delano, W. L. *The PyMOL Molecular Graphics System* (<http://www.pymol.org>) (2002).

Mitochondrial gene replacement in primate offspring and embryonic stem cells

Masahito Tachibana¹, Michelle Sparman¹, Hathaitip Sritanandomchai¹, Hong Ma¹, Lisa Clepper¹, Joy Woodward¹, Ying Li¹, Cathy Ramsey¹, Olena Kolotushkina¹ & Shoukhrat Mitalipov^{1,2,3}

Mitochondria are found in all eukaryotic cells and contain their own genome (mitochondrial DNA or mtDNA). Unlike the nuclear genome, which is derived from both the egg and sperm at fertilization, the mtDNA in the embryo is derived almost exclusively from the egg; that is, it is of maternal origin. Mutations in mtDNA contribute to a diverse range of currently incurable human diseases and disorders. To establish preclinical models for new therapeutic approaches, we demonstrate here that the mitochondrial genome can be efficiently replaced in mature non-human primate oocytes (*Macaca mulatta*) by spindle–chromosomal complex transfer from one egg to an enucleated, mitochondrial-replete egg. The reconstructed oocytes with the mitochondrial replacement were capable of supporting normal fertilization, embryo development and produced healthy offspring. Genetic analysis confirmed that nuclear DNA in the three infants born so far originated from the spindle donors whereas mtDNA came from the cytoplasm donors. No contribution of spindle donor mtDNA was detected in offspring. Spindle replacement is shown here as an efficient protocol replacing the full complement of mitochondria in newly generated embryonic stem cell lines. This approach may offer a reproductive option to prevent mtDNA disease transmission in affected families.

Mitochondria have important roles in cellular processes, for example, production of cellular energy in the form of ATP and programmed cell death (apoptosis). Each mitochondrion contains between two and ten copies of mtDNA, and because cells have numerous mitochondria, a cell may harbour several thousand mtDNA copies. Mutations in mtDNA occur at a tenfold or higher rate than in nuclear DNA, possibly due to a high concentration of free oxygen radicals, lack of histones and limited mtDNA repair mechanisms. Diseases caused by mtDNA mutations were first described in 1988^{1–3}. Since then, over 150 mutations (including 100 deletions and approximately 50 point mutations) have been identified that are associated with serious human disorders, including myopathies, neurodegenerative diseases, diabetes, cancer and infertility⁴. Interest in mtDNA mutations has grown owing to the increasing number of associated diseases and because they can affect patients throughout life. In addition, mtDNA mutations are increasingly implicated in a range of prevalent public health conditions, including Alzheimer's, Parkinson's and Huntington's diseases^{5–9}.

Typically, a cell contains only one type of mtDNA (homoplasmy). If an individual cell contains two or more types of mtDNA—that is, as a mixture of normal and mutant mtDNA—the phenomenon is known as heteroplasmy. Heteroplasmy allows lethal mutations to persist and most importantly to pass to the next generation. MtDNA is maternally inherited through the egg's cytoplasm, whereas sperm mitochondria constitute a minor fraction of the zygote's cohort and are rapidly eliminated after fertilization¹⁰. It is estimated that 1 in 3,500–6,000 people has either mtDNA disease or is at risk for development of mtDNA-based disorders^{11–13}. At present, there are no cures for mitochondrial disorders and available treatments only alleviate symptoms

and slow disease progression. Pre-implantation genetic diagnosis has previously been applied, in a few cases, to identify and transfer embryos devoid of pathogenic mtDNA mutations and resulted in the birth of a healthy baby¹⁴. However, genetic counselling in most patients at risk of maternally inherited mtDNA mutations is challenging due to limitations in assessing the extent of mtDNA heteroplasmy and accurately predicting risks¹⁵. Therefore, there is a significant need to consider new therapeutic approaches that could prevent transmission of mtDNA mutations from mother to child.

Spindle–chromosomal complex transfer

The complete replacement of mutant mtDNA in patients' eggs with healthy mtDNA would be the most reliable method to avoid recurrence of mtDNA diseases, but neither the feasibility nor safety of such a substitution has been evaluated. We hypothesized that mtDNA can be efficiently replaced by a novel approach, that is, spindle–chromosomal complex transfer (ST) in mature eggs (metaphase II, or MII, oocytes) without perturbing subsequent fertilization and developmental competence. To this end, the nuclear genetic material from a patient's egg containing mtDNA mutations could be removed, and transplanted into an enucleated egg containing normal mtDNA donated by a healthy female. A child born after fertilization with the partner's sperm would be free of risk from maternal mtDNA mutations as well as being the biological child of the patients (Supplementary Fig. 1).

Initially, we investigated the distribution of active mitochondria in rhesus macaque oocytes by labelling with MitoTracker red and monitoring with confocal laser scanning microscopy. In mature MII-stage oocytes, mitochondria were distributed relatively uniformly throughout the cytoplasm but spindles and metaphase chromosomes were

¹Oregon National Primate Research Center, ²Oregon Stem Cell Center and ³Departments of Obstetrics and Gynecology and Molecular and Medical Genetics, Oregon Health and Science University, 505 N.W. 185th Avenue, Beaverton, Oregon 97006, USA.

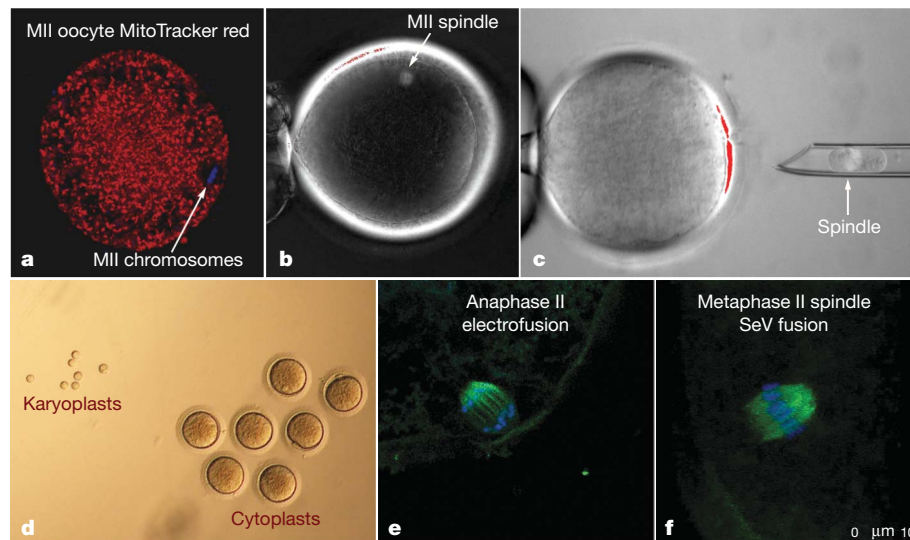


Figure 1 | Spindle–chromosomal complex transfer and meiotic analysis of reconstructed monkey oocytes. **a**, Confocal microscopy of a rhesus macaque MII oocyte labelled with DAPI (blue) to depict chromosomes and MitoTracker red to label active mitochondria. **b**, MII spindle visualization with Oosight Imaging System. **c**, Karyoplast isolation. **d**, Isolated karyoplasts

devoid of mitochondria (Fig. 1a). These results suggested that the isolation and transfer of MII spindle–chromosomal complexes can be accomplished without significant mtDNA carryover from the nuclear donor oocyte. Until now, two major technical obstacles have hampered the feasibility and success of this approach: (1) difficulties in visualization and isolation of intact MII chromosomes; and (2) the susceptibility of meiotic spindles and chromosomes to damage secondary to premature oocyte activation during manipulations. The visualization of DNA in mature oocytes is difficult because the nucleus is no longer evident after re-initiation of meiosis and breakdown of nuclear membrane. However, enucleating MII oocytes became routine after development of techniques for DNA staining with fluorophores (such as Hoechst 33342) and subsequent visualization under ultraviolet light, notably during cloning of embryos by somatic cell nuclear transfer (SCNT). However, unlike in cloning where the extracted chromosomes are discarded, the viability and integrity of the oocyte spindle-associated DNA during ST must be maintained.

We recently accomplished successful SCNT in primates with adult skin cells as nuclear donors and went on to isolate functional embryonic stem (ES) cells^{16,17}. The key to this success was implementation of several technical modifications to avoid damage to the cytoplasm during spindle removal. This involved non-invasive visualization of the metaphase spindle during enucleation with polarized microscopy to avoid deleterious effects of Hoechst staining and ultraviolet exposure (Fig. 1b). We reasoned that the modified enucleation technique should be applicable to the isolation of intact MII spindle–chromosomal complexes and their subsequent transfer to spindle-free, donor cytoplasts. Indeed, we were able to isolate intact spindle–chromosomal complexes surrounded by a small amount of cytoplasm and cell membrane (karyoplast) with 100% efficiency (Fig. 1c and Supplementary Movie). We measured diameters of both karyoplasts and enucleated oocytes (cytoplasts) and calculated that the average volume of a karyoplast was 11.3 ± 1.2 pl (mean \pm s.e.m.; $n = 7$) whereas the average volume of a cytoplast was 752.1 ± 18.3 pl (Fig. 1d). Thus, a karyoplast contained approximately 1.5% of the volume of a cytoplast, suggesting that a negligible amount of mitochondria/mtDNA surrounding the spindle would be carried over during ST.

Next, we investigated the re-introduction of spindle–chromosomal complexes into enucleated oocytes derived from unrelated females. Karyoplasts were placed into the perivitelline space of cytoplasts, on

and cytoplasts. Original magnifications: **a–c**, $\times 300$; **d**, $\times 40$. **e**, Confocal microscopy of progression to the anaphase II stage induced by electrofusion. **f**, Intact metaphase II spindle after SeV fusion. Spindles are labelled with DAPI (blue) to depict chromosomes and with α/β -tubulin (green) to show microtubules.

the side opposite the first polar body, and fusion with the cytoplasm was accomplished by electroporation. Approximately 1 h after fusion, reconstructed oocytes were fixed and analysed by immunocytochemistry for spindle–chromosomal complex integrity. A spindle was present in all analysed oocytes, but the majority of oocytes unexpectedly resumed the meiotic division and progressed to the anaphase of meiosis II or completed meiosis and formed a second polar body (Fig. 1e).

We hypothesized that fusion by electroporation may have triggered premature activation and subsequent resumption of meiosis. To test this assumption, we used an alternative karyoplast fusion technique using an extract from Sendai virus (SeV). Isolated karyoplasts were briefly exposed to SeV extract and then placed into the perivitelline space of cytoplasts (Supplementary Movie) where fusion was observed within 20–30 min. Analysis of reconstructed oocytes demonstrated that spindle–chromosomal complexes were maintained in the MII stage and had morphology similar to intact controls (Fig. 1f). Resumption of meiosis and separation of the second polar body was observed in the SeV group only after fertilization. Thus, these results indicate that electrofusion pulse induces premature activation and resumption of meiosis during spindle introduction. In contrast, this artefact was prevented by using SeV-assisted fusion.

Developmental potential of reconstructed oocytes

We next determined the developmental competence of ST-generated oocytes produced by electrofusion or SeV, following fertilization by intracytoplasmic sperm injection (ICSI) and *in vitro* embryo culture. Karyoplast–cytoplast fusion rates were comparable between the two ST approaches. However, pronuclear formation in the electrofusion group was not observed; instead, sperm-injected oocytes cleaved prematurely by the morning after ICSI and arrested between the 8-cell and morula stages. In contrast, fertilization, cleavage and blastocyst rates in the SeV group were similar to those of intact control oocytes (Table 1). These results are consistent with the conclusion that spindle transfer in MII oocytes using SeV does not compromise subsequent fertilization and *in vitro* embryonic developmental competence. In order to assess the quality of the blastocysts produced, we carried out cell counts by labelling with DAPI (all cells) and NANOG (the inner cell mass, ICM) (Supplementary Fig. 2). Five expanded or hatched blastocysts for each ST and corresponding control group were analysed. The mean number of total cells and ICM cells in ST

Table 1 | *In vitro* development of embryos after ST into enucleated oocytes and ICSI

Treatment	n	Fusion (%)	Fertilization (%)	8-cell (%)*	Morula (%)*	Blastocyst (%)*
ST (SeV)	87	78 (90)	74 (95)	69 (93)	58 (78) [†]	45 (61) [†]
ST (elect.)	15	11 (73)	11 (100)	8 (73)	2 (18) [‡]	1 (9) [‡]
Control	72	NA	68 (94)	57 (84)	51 (75) [†]	41 (60) [†]

SeV and elect. indicate fusion with Sendai virus extract or electrofusion, respectively. Different footnote symbols (dagger and double dagger) indicate significant difference ($P < 0.05$). Data were analysed using χ^2 test. ICSI, intracytoplasmic sperm injection; NA, not applicable (no fusion step).

* The percentage of 8-cell-, morula- and blastocyst-stage embryos was calculated based on the number of fertilized embryos.

blastocysts were 152 ± 34 and 21 ± 10 , respectively, and similar to controls (127 ± 79 and 23 ± 10 , respectively; $P > 0.05$).

To define further the developmental potential, we isolated ES cell lines from ST blastocysts. Two stable ES cell lines were established from eight ST embryos (designated as STES-1 and STES-2) with derivation efficiency (25%) similar to controls (Supplementary Table 1). Both cell lines exhibited typical primate pluripotency markers and were able to differentiate into neuronal cell types and spontaneously contracting cardiomyocytes (Supplementary Fig. 3). To determine if the ST procedure induced lasting chromosomal abnormalities, we conducted a cytogenetic analysis of STES cell lines by G-banding. The analysis revealed that these cell lines contained normal rhesus macaque karyotypes (one male 42 XY and one female 42 XX) with no detectable chromosomal anomalies (Supplementary Fig. 4). Finally, we tested the *in vivo* developmental potential of ST embryos by transfer into the reproductive tract of recipient females. We transferred 15 ST embryos into oviducts of 9 recipients: 6 females received either 1 or 2 blastocysts each whereas three recipients received 2 cleavage stage (4–8-cell) embryos each (Table 2). Three females became pregnant—one carrying twins and two with singletons—all derived from the transfer of ST embryos at the blastocyst stage (Table 2). Remarkably, the pregnancy (33%) and implantation rates (27%) with ST embryos were even higher than those previously reported for non-manipulated, ICSI-produced embryos (Supplementary Table 2)¹⁸. On 24 April 2009 the first pregnant monkey delivered a set of healthy twins by caesarean section (called Mito and Tracker; Fig. 2). To our knowledge, these infants represent the first animals to be born after MII spindle–chromosomal complex transfer. The second pregnant monkey gave birth to a healthy infant on 8 May 2009 whereas the third is ongoing at time of publication. All three ST infants are healthy and their birth weights and gestational lengths were within normal ranges for rhesus macaques (Supplementary Table 3)¹⁸. Overall, these results demonstrate that MII spindle–chromosomal complexes can be efficiently isolated and transplanted into enucleated oocytes. Reconstructed oocytes produced with this technology were suitable for fertilization and developed to blastocysts at rates similar to controls. Moreover, the isolation of normal ES cells and the birth of healthy offspring support further evaluation of this approach for mitigating the consequences of mtDNA defects.



Figure 2 | Mito and Tracker, the first primates to be produced by spindle–chromosomal complex transfer (ST) into enucleated oocytes followed by fertilization and embryo transfer. Twin pregnancy was established by transfer of two ST-derived blastocysts into a recipient. Both infants are healthy and their growth and development is within a normal range for rhesus macaques. The photo was taken at 6 days of age.

Analysis of nuclear and mtDNA in ST offspring

Finally, we investigated the degree of heteroplasmy extant in infants and cell lines as a result of mtDNA carryover during spindle transfer. We isolated DNA samples from ST infants and STES cell lines to analyse genomic DNA by microsatellite parentage analysis and mtDNA by direct sequencing of the mitochondrial D-loop hypervariable region 1 (rhDHV1) as previously described¹⁶. We also collected and analysed DNA from four differentiated cultures derived from the outgrowth of plated ST blastocysts (designated as ST1, ST2, ST3 and ST4). Detailed analysis of nuclear DNA using 41 microsatellite markers confirmed that all three infants and all cell lines inherited their nuclear genome from the spindle donor animals (Fig. 3a and Supplementary Table 4). Spindle and cytoplasm donor animals contained multiple single nucleotide polymorphisms (SNPs) within the rhDHV1 region (nucleotide positions 15974–16516 of the *Macaca mulatta* NCBI reference sequence NC_005943) that were informative and permitted to distinguish the mtDNA origin of infants and cell lines (Fig. 3a). Initially, we performed direct sequencing of rhDHV1 and the results confirmed that in all samples the mtDNA originated from the cytoplasm donors (Fig. 3b). No contribution of spindle donor mtDNA was detected in any ST offspring using this approach. As indicated above, a small amount of cytoplasm is usually carried over with the spindle during the ST procedure. Therefore, we conducted three independent quantitative mtDNA assays. The first involved cloning of mtDNA PCR products containing rhDHV1 region and the direct sequencing of multiple individual clones. We randomly selected and sequenced 20–25 clones for each sample and the results indicated that mtDNA in all analysed clones was from cytoplasm donors (Supplementary Table 5). Thus, if

Table 2 | Embryo transfers and pregnancies with ST embryos

Spindle donor	Cytoplasm donor	Embryo stage (age)*	Number of embryos transferred	Recipient stage†	Pregnancy
Female 1	Female 2	ExB (d7)	2	Day 4	Twin
Female 2	Female 1	ExB (d8)	2	Day 2	No
Female 4	Female 3	4-cell (d2)	2	Day 2	No
Female 3	Female 4	EB (d7)	1	Day 4	Single
Female 13	Female 14	8-cell (d3)	2	Day 2	No
Female 14	Female 13	8-cell (d3)	2	Day 2	No
Female 13	Female 14	ExB (d8)	2	Day 4	No
Female 15	Female 16	ExB (d8)	1	Day 4	No
Female 8	Female 7	ExB (d7)	1	Day 4	Single

EB, early blastocyst; ExB, expanded blastocyst.

* Day of ICSI is calculated as day 0 (d0).

† The next day after oestrogen surge is considered as ovulation day or day 0. Embryo transfers were scheduled to synchronize the stage of early embryo development with uterine development leading to the implantation interval.

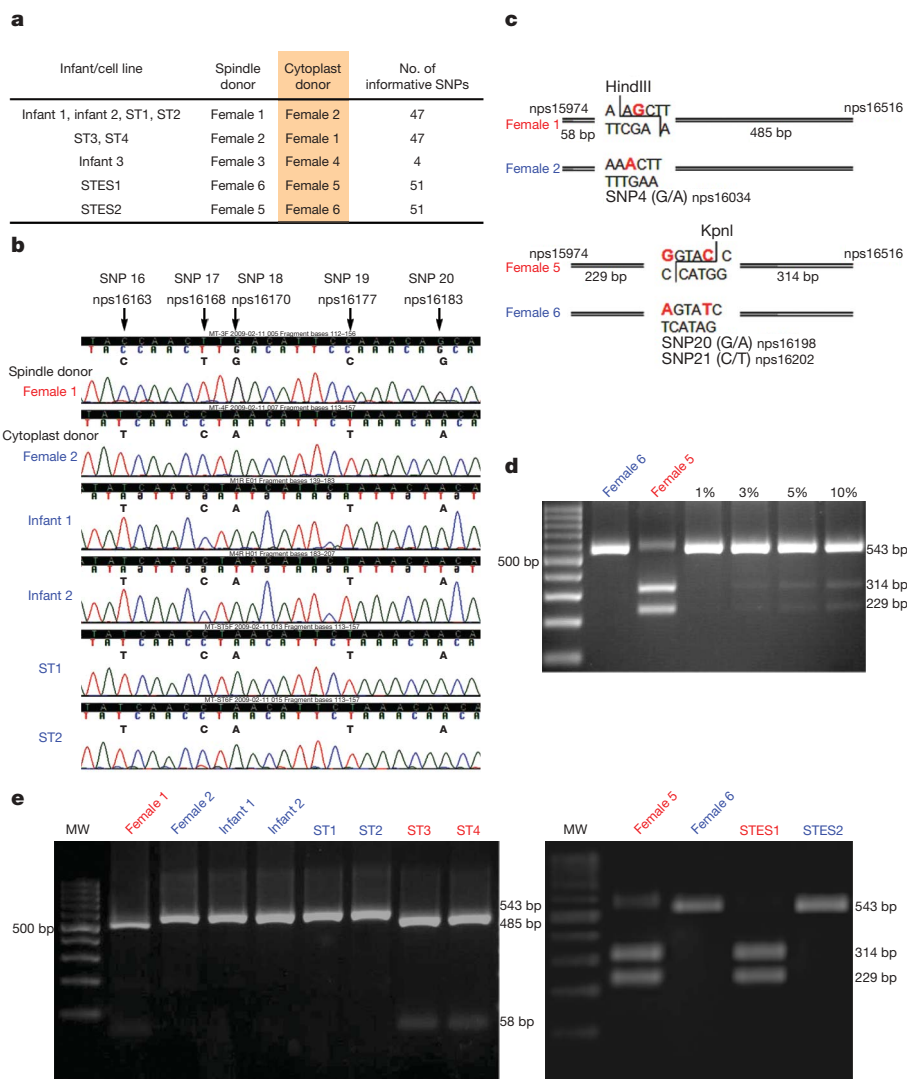


Figure 3 | MtDNA analysis in ST offspring. **a**, Origin of ST offspring and informative mtDNA SNPs. **b**, MtDNA chromatogram demonstrating SNPs. Infants 1 and 2 and ST1 and ST2 cell lines were produced by transfer of spindles from female 1 to cytoplasts from female 2. **c**, Restriction enzyme recognition sites within SNP area. Female 1 mtDNA can be digested by HindIII whereas G to A nucleotide change precludes restriction of female 2

mtDNA. KpnI digests mtDNA from female 5 but not from female 6. **d**, MtDNA from females 5 and 6 were mixed at various proportions and were detectable at the level of 3%. **e**, RFLP analysis of ST offspring demonstrating undetectable contributions of spindle donor mtDNA. MW, molecular mass marker.

heteroplasmy existed, any contribution of spindle mtDNA in ST infants and cell lines is below detectable levels.

The second approach used mtDNA restriction fragment length polymorphism (RFLP)¹⁹. SNPs in the mitochondrial genome can result in the loss of a restriction site; thus digestion of PCR fragments with endonucleases can be used to reveal the presence of a population of mtDNA originating from the spindle donors. We identified unique restriction enzyme recognition sites within SNP areas for all ST samples except for the third infant. Specifically, mtDNA of female 1 (a spindle donor for infants 1 and 2 plus ST1 and ST2 cell lines) possessed a unique HindIII digestion site that includes the G/A SNP site (Fig. 3c). In contrast, female 2 (a cytoplasm donor) carried mtDNA with an A allele at this SNP precluding recognition and digestion by HindIII (Fig. 3c). To confirm the sensitivity of this approach, we performed RFLP analysis of serial mixtures (1 to 100%) of mtDNA from females 5 and 6. The results indicate that RFLP can detect as little as 3% of heteroplasmy (Fig. 3d). MtDNA heteroplasmy was undetectable in any experimental sample by RFLP (Fig. 3e).

Finally, we used a quantitative real-time PCR analysis based on existing SNP differences between spindle and cytoplasm donor animals.

Two different fluorescent probes were designed for identification of mtDNA from females 5 and 6 based on SNPs and specificity was validated (Supplementary Fig. 5a). To build a standard curve and establish sensitivity, we conducted real-time PCR analysis of mtDNA mixtures from the two females at various ratios. The technique detected heteroplasmy at the minimal level of 3% (Supplementary Fig. 5b). Next, we analysed STES1 and STES2 cell lines derived from these females and results confirmed that contribution of the spindle donor mtDNA is undetectable (Supplementary Fig. 5b). Similarly, we performed a real-time PCR analysis of mtDNA from infants 1 and 2 as well as ST1–ST4 cultures; the results indicated that all ST offspring are nearly homoplasmic.

These results provide strong support for the notion that mtDNA can be efficiently replaced in mature primate oocytes by ST, resulting in offspring with undetectable or negligible amounts of spindle-derived mtDNA.

Karyoplast fusion using SeV extract was instrumental in our study but clinical applications of the viral extract may be problematical. Therefore, we analysed SeV extract, ST infants and STES cells for the presence of the SeV genetic material. We used reverse transcription (RT)–PCR assay using commonly used primers for the F protein-coding sequence²⁰. We

did not detect the presence of viral genome in analysed samples (Supplementary Fig. 6), indicating that the extract is inactivated and purified from the genomic RNA.

Discussion

Assisted reproductive technologies that could eliminate the transmission of mitochondrial diseases in affected families include cytoplasmic, germinal vesicle and pronuclear transfer^{15,21,22}. Cytoplasmic transfer—the augmentation of patient eggs with a small amount of donor cytoplasm—was designed to improve viability and developmental competence of compromised, ‘ooplasmic deficient’ oocytes. The introduction of large amounts of donor cytoplasm by electrofusion was unsuccessful²³; however, the co-injection of a small volume (1–5%) of donor cytoplasm with sperm as an extension of ICSI has been successful with acceptable IVF outcomes^{23–26}. Although heteroplasmy was detected in small amounts in six of thirteen embryos studied and in two of four fetal cord blood samples²⁷, this procedure is not suitable for women carrying mtDNA mutations because it would require transferring significantly larger, practically impossible, cytoplasmic volumes (30–50% of the final volume) to ensure adequate dilution of mutant mtDNA. A relatively high number of chromosomal abnormalities and birth defects in infants resulting from the initial application of this technique²⁸ led to it being banned in the United States by the Food and Drug Administration because of safety concerns.

Another possibility is transferring nuclear DNA from a mother with mtDNA disease to a cytoplasm (or spindle-free oocyte) containing normal mtDNA as obtained from a healthy egg donor. Experiments in mice suggested that it is technically feasible to transfer DNA between immature oocytes where nuclear DNA is enclosed in a clearly visible germinal vesicle²⁹. However, if this approach were applied to human oocytes, efficacy would be limited by the poor developmental competence of oocytes produced after the *in vitro* maturation of germinal-vesicle-intact oocytes. Moreover, germinal vesicle oocytes have polarized cyto-architecture with mitochondria concentrated in the perinuclear space³⁰ and germinal vesicle transplantation would inevitably result in the introduction of significant amounts of patient mtDNA into the donor cytoplasm. Pronuclear transfer is essentially the same procedure, except that the nuclear material, both the male and female pronucleus, is removed after fertilization. This technique in the mouse has resulted in the birth of live offspring; however, reconstructed embryos contained karyoplast mtDNA (on average 19%) and progeny were all heteroplasmic^{31–33}.

Thus, these nuclear transfer approaches are associated with the transmission of a significant amount of mtDNA from the nuclear donor (patient), resulting in heteroplasmy and rendering them inappropriate for patients with mtDNA-associated disease.

Chromosome transfer in mature oocytes was thought to be unattainable because of the unique biological characteristics of MII-arrested oocytes until we introduced several procedural innovations that overcame these biological barriers¹². Here we also provide evidence that the ST approach is efficient, safe and does not generate any detectable heteroplasmy. This could be due to the fact that spindle–chromosomal complexes were isolated into karyoplasts containing very small amounts of cytoplasm. Moreover, in primates, karyoplasts are mostly occupied by a spindle–chromosomal apparatus that is free of mitochondria. Another advantage is that ST does not require the *in vitro* oocyte maturation and can be performed with minimum procedural upgrades in a standard clinical IVF setting.

Assuming that our protocols are applicable to human oocytes, ST with cryopreserved oocytes would undoubtedly benefit future clinical applications. Current technology requires that the oocyte donor and recipient undergo synchronous ovarian stimulation protocols; however, the increasing availability of oocyte cryopreservation protocols will abrogate this requirement.

As we show here, the ST strategy will probably contribute the least amount of spindle-associated mtDNA compared to the other

approaches discussed above. The sensitivity of our assays did not allow detection of mtDNA heteroplasmy levels below the 3% threshold. However, owing to random genetic drift and segregation of mtDNA, some tissues and organs of ST offspring may contain a higher degree of heteroplasmy. Another concern is the possibility of recurrence of mtDNA diseases in the next generation, in children of heteroplasmic females produced by ST, owing to the phenomenon known as ‘genetic bottleneck’^{34,35}. Future clinical applications of mtDNA replacement therapy will largely depend on the safety and efficiency of this technology. Thus, appropriate long-term preclinical studies addressing these important concerns in a clinically relevant non-human primate model are warranted before this technology can be applied to humans.

MtDNA mutations contribute to a diverse range of human diseases, encompassing both tissue-specific and multiple system disorders, with the onset of disease appearing throughout life. We demonstrate here that the transmission of mtDNA mutations from mother to child can be abrogated by the efficient transfer of mother’s spindle-associated chromosomes into donor cytoplasts. In the rhesus macaque, spindle-associated chromosomal transfer did not show adverse effects on fertilization or on subsequent embryo/fetal development to term. Hence, we propose that this procedure may represent a new, reliable therapeutic approach to prevent the transmission of mtDNA mutations in affected families.

Note added in proof: The third pregnant monkey gave birth to a healthy infant on 6 July 2009 while this paper was under review.

METHODS SUMMARY

Mature MII oocytes were recovered from females undergoing controlled ovarian stimulations. Oocytes were transferred to a manipulation chamber containing medium with 5 µg ml^{−1} cytochalasin B and MII spindle–chromosomal complexes were aspirated and isolated using Oosight imaging system (<http://www.cri-inc.com>) as described before¹⁶. Isolated karyoplasts were briefly exposed to SeV extract (<http://www.cosmobio.co.jp>) and placed into perivitelline space on the side opposite to the 1st polar body (Supplementary Movie). During manipulations, the oocyte’s zona pellucida was penetrated by laser-assisted zona drilling (<http://www.hamiltonthorne.com>). After fusion, reconstructed oocytes were fertilized by ICSI and cultured as described previously¹⁶. Detailed methods are described in Supplementary Information.

Received 29 June; accepted 10 August 2009.

Published online 26 August 2009.

- Wallace, D. C. *et al.* Mitochondrial DNA mutation associated with Leber’s hereditary optic neuropathy. *Science* **242**, 1427–1430 (1988).
- Holt, I. J., Harding, A. E. & Morgan-Hughes, J. A. Deletions of muscle mitochondrial DNA in patients with mitochondrial myopathies. *Nature* **331**, 717–719 (1988).
- Zeviani, M. *et al.* Deletions of mitochondrial DNA in Kearns-Sayre syndrome. *Neurology* **38**, 1339–1346 (1988).
- Solano, A., Playan, A., Lopez-Perez, M. J. & Montoya, J. Genetic diseases of the mitochondrial DNA in humans [in Spanish]. *Salud Publica Mex.* **43**, 151–161 (2001).
- Keating, D. J. Mitochondrial dysfunction, oxidative stress, regulation of exocytosis and their relevance to neurodegenerative diseases. *J. Neurochem.* **104**, 298–305 (2008).
- Lin, M. T. & Beal, M. F. Mitochondrial dysfunction and oxidative stress in neurodegenerative diseases. *Nature* **443**, 787–795 (2006).
- Reeve, A. K., Krishnan, K. J. & Turnbull, D. Mitochondrial DNA mutations in disease, aging, and neurodegeneration. *Ann. NY Acad. Sci.* **1147**, 21–29 (2008).
- Trushina, E. & McMurray, C. T. Oxidative stress and mitochondrial dysfunction in neurodegenerative diseases. *Neuroscience* **145**, 1233–1248 (2007).
- Brandon, M., Baldi, P. & Wallace, D. C. Mitochondrial mutations in cancer. *Oncogene* **25**, 4647–4662 (2006).
- Sutovsky, P. *et al.* Ubiquitin tag for sperm mitochondria. *Nature* **402**, 371–372 (1999).
- Majamaa, K. *et al.* Epidemiology of A3243G, the mutation for mitochondrial encephalomyopathy, lactic acidosis, and stroke-like episodes: prevalence of the mutation in an adult population. *Am. J. Hum. Genet.* **63**, 447–454 (1998).
- Taylor, R. W. & Turnbull, D. M. Mitochondrial DNA mutations in human disease. *Nature Rev. Genet.* **6**, 389–402 (2005).
- Schaefer, A. M. *et al.* Prevalence of mitochondrial DNA disease in adults. *Ann. Neurol.* **63**, 35–39 (2008).
- Steffann, J. *et al.* Analysis of mtDNA variant segregation during early human embryonic development: a tool for successful NARP preimplantation diagnosis. *J. Med. Genet.* **43**, 244–247 (2006).

15. Thorburn, D. R. & Dahl, H. H. Mitochondrial disorders: genetics, counseling, prenatal diagnosis and reproductive options. *Am. J. Med. Genet.* **106**, 102–114 (2001).
16. Byrne, J. A. *et al.* Producing primate embryonic stem cells by somatic cell nuclear transfer. *Nature* **450**, 497–502 (2007).
17. Mitalipov, S. M. *et al.* Reprogramming following somatic cell nuclear transfer in primates is dependent upon nuclear remodeling. *Hum. Reprod.* **22**, 2232–2242 (2007).
18. Wolf, D. P. *et al.* Use of assisted reproductive technologies in the propagation of rhesus macaque offspring. *Biol. Reprod.* **71**, 486–493 (2004).
19. Moraes, C. T., Atencio, D. P., Oca-Cossio, J. & Diaz, F. Techniques and pitfalls in the detection of pathogenic mitochondrial DNA mutations. *J. Mol. Diagn.* **5**, 197–208 (2003).
20. Tsuboniwa, N. *et al.* Safety evaluation of hemagglutinating virus of Japan—artificial viral envelope liposomes in nonhuman primates. *Hum. Gene Ther.* **12**, 469–487 (2001).
21. Poulton, J., Kennedy, S., Oakeshott, P. & Wells, D. Preventing transmission of maternally inherited mitochondrial DNA diseases. *BMJ* **338**, b94 (2009).
22. Roberts, R. M. Prevention of human mitochondrial (mtDNA) disease by nucleus transplantation into an enucleated donor oocyte. *Am. J. Med. Genet.* **87**, 265–266 (1999).
23. Cohen, J. *et al.* Ooplasmic transfer in mature human oocytes. *Mol. Hum. Reprod.* **4**, 269–280 (1998).
24. Lanzendorf, S. E. *et al.* Pregnancy following transfer of ooplasm from cryopreserved-thawed donor oocytes into recipient oocytes. *Fertil. Steril.* **71**, 575–577 (1999).
25. Cohen, J., Scott, R., Schimmel, T., Levron, J. & Willadsen, S. Birth of infant after transfer of anucleate donor oocyte cytoplasm into recipient eggs. *Lancet* **350**, 186–187 (1997).
26. Barritt, J. A., Brenner, C. A., Malter, H. E. & Cohen, J. Mitochondria in human offspring derived from ooplasmic transplantation. *Hum. Reprod.* **16**, 513–516 (2001).
27. Brenner, C. A., Barritt, J. A., Willadsen, S. & Cohen, J. Mitochondrial DNA heteroplasmy after human ooplasmic transplantation. *Fertil. Steril.* **74**, 573–578 (2000).
28. Brown, D. T. *et al.* Transmission of mitochondrial DNA disorders: possibilities for the future. *Lancet* **368**, 87–89 (2006).
29. Takeuchi, T., Neri, Q. V., Katagiri, Y., Rosenwaks, Z. & Palermo, G. D. Effect of treating induced mitochondrial damage on embryonic development and epigenesis. *Biol. Reprod.* **72**, 584–592 (2005).
30. Wilding, M. *et al.* Mitochondrial aggregation patterns and activity in human oocytes and preimplantation embryos. *Hum. Reprod.* **16**, 909–917 (2001).
31. Meirelles, F. V. & Smith, L. C. Mitochondrial genotype segregation in a mouse heteroplasmic lineage produced by embryonic karyoplast transplantation. *Genetics* **145**, 445–451 (1997).
32. Meirelles, F. V. & Smith, L. C. Mitochondrial genotype segregation during preimplantation development in mouse heteroplasmic embryos. *Genetics* **148**, 877–883 (1998).
33. Sato, A. *et al.* Gene therapy for progeny of mito-mice carrying pathogenic mtDNA by nuclear transplantation. *Proc. Natl Acad. Sci. USA* **102**, 16765–16770 (2005).
34. Cree, L. M. *et al.* A reduction of mitochondrial DNA molecules during embryogenesis explains the rapid segregation of genotypes. *Nature Genet.* **40**, 249–254 (2008).
35. Wai, T., Teoli, D. & Shoubridge, E. A. The mitochondrial DNA genetic bottleneck results from replication of a subpopulation of genomes. *Nature Genet.* **40**, 1484–1488 (2008).

Supplementary Information is linked to the online version of the paper at www.nature.com/nature.

Acknowledgements The authors acknowledge the Division of Animal Resources, Surgical Team, Endocrine Technology Core, Imaging & Morphology Core and Molecular & Cellular Biology Core at the Oregon National Primate Research Center for providing expertise and services that contributed to this project. We are grateful to W. Sanger and M. Nelson for karyotyping services, C. Penedo for microsatellite analysis and S. Wong for providing Sendai virus. We thank J. Hennebold, R. Stouffer and D. Wolf for consulting, helpful discussions and critical reading of the manuscript. This study was supported by start-up funds from Oregon National Primate Research Center, Oregon Stem Cell Center and grants from the National Institutes of Health.

Author Contributions S.M. and M.T. conceived the study, designed experiments and conducted ST micromanipulations. M.S. performed ICSI, mitochondrial staining and analysis in oocytes. H.S., J.W. and Y.L. conducted ES cell derivation, characterization and differentiation. M.T., H.M., L.C., H.S. and Y.L. performed DNA/RNA isolations and mtDNA analyses. C.R. and O.K. conducted ovarian stimulations, oocyte recovery, ICSI and embryo transfers. S.M. and M.T. analysed the data and wrote the paper.

Author Information Reprints and permissions information is available at www.nature.com/reprints. Correspondence and requests for materials should be addressed to S.M. (mitalipo@ohsu.edu).

Misaligned spin and orbital axes cause the anomalous precession of DI Herculis

Simon Albrecht^{1,2}, Sabine Reffert³, Ignas A. G. Snellen¹ & Joshua N. Winn²

The orbits of binary stars precess as a result of general relativistic effects, forces arising from the asphericity of the stars, and forces from any additional stars or planets in the system. For most binaries, the theoretical and observed precession rates are in agreement¹. One system, however—DI Herculis—has resisted explanation for 30 years^{2–4}. The observed precession rate is a factor of four slower than the theoretical rate, a disagreement that once was interpreted as evidence for a failure of general relativity⁵. Among the contemporary explanations are the existence of a circumbinary planet⁶ and a large tilt of the stellar spin axes with respect to the orbit^{7,8}. Here we report that both stars of DI Herculis rotate with their spin axes nearly perpendicular to the orbital axis (contrary to the usual assumption for close binary stars). The rotationally induced stellar oblateness causes precession in the direction opposite to that of relativistic precession, thereby reconciling the theoretical and observed rates.

We observed DI Herculis (HD 175227, apparent *V* magnitude outside eclipse = 8.45, spectral type B4+5V, orbital period $P = 10.55$ days, orbital eccentricity $e = 0.49$)⁹ with Sophie¹⁰, a high-resolution échelle spectrograph on the 1.93-m telescope of the Observatoire de Haute-Provence. Figure 1 shows four representative spectra obtained during the primary eclipse and four from the secondary eclipse. Supplementary Figs 1–3 show all the spectra.

By analysing the distortions of the spectral lines that occur during eclipses (the “Rossiter–McLaughlin effect”^{11–13}), the relative orientation of the spin and orbital axes as projected on the sky can be derived. Our model of the spectra and of the Rossiter–McLaughlin effect is based on the method of ref. 14, as summarized here. Because of the light from the foreground star, we could not treat the Rossiter–McLaughlin effect as a simple wavelength shift, as is commonly done for eclipses of stars by planets^{15,16}. Instead, we modelled the line profiles of both stars, taking into account stellar rotation, surface

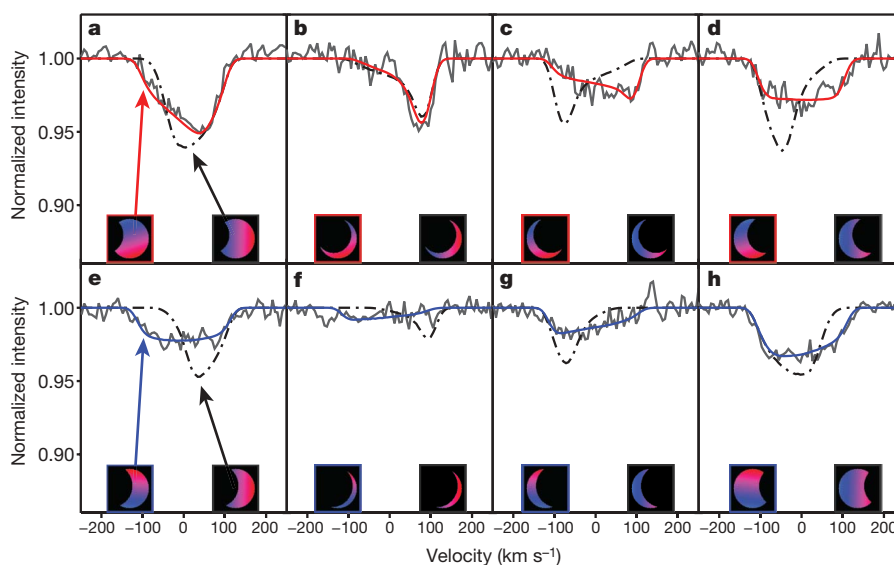


Figure 1 | Distortion of stellar absorption lines during eclipses. We observed DI Herculis during eclipses on 20/21 May, 13/14 July and 30 June/1 July 2008. We obtained 22 spectra during primary eclipses, 15 spectra during the secondary eclipse and 15 spectra outside eclipses. During an eclipse the lines of the background star are distorted because they are missing some of the components that produce rotational broadening. This phenomenon, the Rossiter–McLaughlin effect, was foreseen as early as 1893 (ref. 11) and observed definitively in 1924 (refs 12, 13). We began with the reduced two-dimensional spectra delivered by the Sophie instrument software. Bad pixels were identified and removed, and the continuum level in each order was normalized. The uncertainty in the wavelength scale is equivalent to a few metres per second, and is negligible for our purposes. The spectra have a resolution of 40,000 and the median signal-to-noise ratio is 80 in the vicinity

of 4,500 Å. Each panel shows the Mg II line (4,481 Å) of the eclipsed star. For clarity, a model of the lines of the foreground star was subtracted, and the data were binned by four pixels. The upper panels (a–d) show data from the primary eclipse, and the lower panels (e–h) show data from the secondary eclipse. (Supplementary Figs 1–3 show all the spectra.) The grey solid lines are the data, and the red and blue lines are the best-fitting model, with $\beta_p = 72^\circ$ and $\beta_s = -84^\circ$. The dashed-dotted lines show the model assuming co-aligned stellar and orbital axes, which gives a poor fit to the data. Each panel has two inset illustrations. The left inset illustrates the line-of-sight component of the rotational velocity of the eclipsed star in the best-fitting model, with blue and red indicating approaching and receding velocities, respectively. The right panels show the same for the co-aligned model.

¹Leiden Observatory, Leiden University, Postbus 9513, 2300 RA Leiden, The Netherlands. ²Department of Physics, and Kavli Institute for Astrophysics and Space Research, Massachusetts Institute of Technology, Cambridge, Massachusetts 02139, USA. ³Zentrum für Astronomie Heidelberg, Landessternwarte, Königstuhl 12, 69117 Heidelberg, Germany.

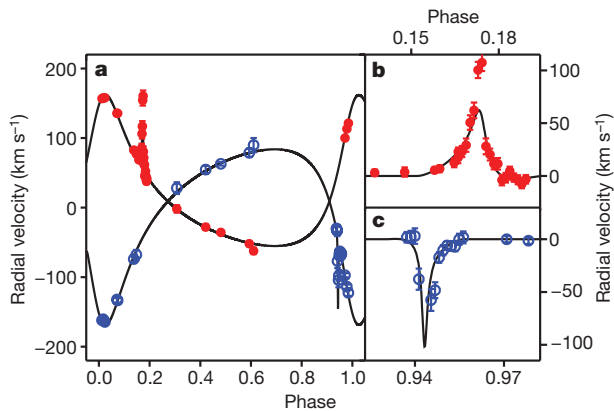


Figure 2 | Apparent radial velocities of DI Herculis. **a**, The apparent radial velocity of the primary (red filled circles) and secondary (blue open circles) as a function of orbital phase. The solid line is the calculated radial velocity based on our model, including Keplerian motion and the Rossiter–McLaughlin effect. Outside the eclipses, the line positions were determined by fitting Gaussian functions. During eclipses, the apparent radial velocity was defined as the intensity-weighted mean wavelength of the line. **b**, **c**, Close-ups of the Rossiter–McLaughlin anomaly during the primary eclipse (upper) and secondary eclipse (lower). The anomaly is a redshift throughout the primary eclipse, and a blueshift throughout the secondary eclipse, indicating large spin-orbit misalignments. Had the spins and orbit been aligned, the anomaly would have been a redshift during the first half of the eclipse, and a blueshift during the second half. The error bars shown are $1-\sigma$ errors based only on the signal-to-noise ratio of the spectra. For radial velocities obtained during eclipses, the true errors are larger owing to imperfect subtraction of the foreground light, which is why there are apparently large deviations between the data and the model at mid-eclipse (indeed, one radial velocity at the secondary mid-eclipse lies outside the plotted range). We emphasize that the eclipse radial velocities are shown here for illustration only, as a concise visual summary of the complex distortions of the eclipse spectra: they were not used in our quantitative calculations.

velocity fields, orbital motion, and partial blockage during eclipses. By adjusting the parameters of the model to fit the observed spectra, we derived estimates of the orbital and stellar parameters, including the angles β_p and β_s (subscripts ‘p’ and ‘s’ refer to primary and secondary) between the sky projections of the primary and secondary spin axes and the orbital axis. The angles are defined such that $\beta = 0^\circ$ when the axes are parallel, and $\beta = \pm 90^\circ$ when they are perpendicular.

We focused on the Mg II line at $4,481 \text{ \AA}$ because it is the strongest line that is broadened mainly by stellar rotation. However, it is located in the red wing of the stronger pressure-broadened He I line at $4,471 \text{ \AA}$. Therefore, we fitted a Lorentzian model to the encroaching wing of the He I line and subtracted it before modelling the Mg II line. (Similar results were obtained when both lines were modelled simultaneously.)

In the model, the simulated absorption lines were shifted in wavelength according to the Keplerian radial velocity, and were broadened by anisotropic macroturbulence (using the parameterization of Gray¹⁷) and rotation (parameterized by $v_p \sin i_p$ and $v_s \sin i_s$). For each star, and for each phase of the eclipse, we modelled a limb-darkened, uniformly rotating stellar disk with several thousand pixels. Each pixel was further divided into 17 sub-pixels to represent the distribution of turbulent velocities. The light from the sub-pixels was Doppler-shifted according to a Gaussian distribution for the tangential and radial turbulent velocity fields ($\xi_{R,T}$), assuming the tangential and radial fields to have equal amplitudes and equal surface fractions. (Although we included macroturbulence for completeness, the results for β_p and β_s do not depend on the details, and similar results were obtained even when macroturbulence was ignored.)

It was also necessary to include parameters for the equivalent widths of the Mg II lines (Table 1). Finally, we adopted values of

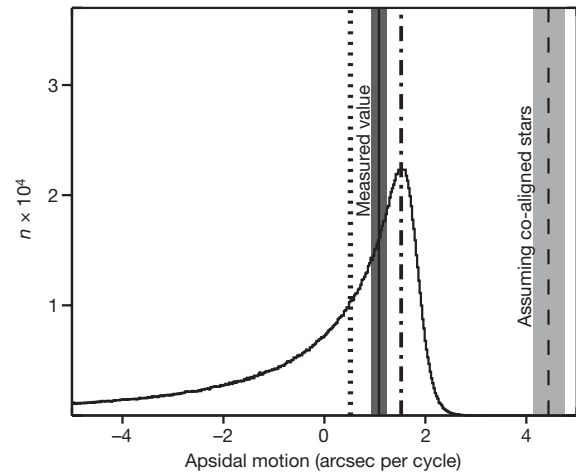


Figure 3 | Apsidal motion of DI Herculis, calculated and observed. The plot shows the observed apsidal motion²¹ of 1.08 ± 0.16 arcsec per cycle (solid line and dark grey area), the apsidal motion expected assuming aligned axes³ of 4.44 ± 0.31 arcsec per cycle (dashed line and light grey area on the right side of the plot), and the histogram of the expected apsidal motion based on our results (solid black line). For the expected apsidal motion, we performed a Monte Carlo calculation in which stellar inclinations are drawn from a uniform distribution in $\cos i$ after restricting the stellar rotation speed to be slower than 600 km s^{-1} . The median of the distribution (0.52 arcsec per cycle) is indicated by the dotted line and the mode by the dashed-dotted line (1.52 arcsec per cycle). The long tail to negative values corresponds to rapid rotation in a nearly pole-on configuration.

the stellar radii from the literature (Table 1), and assumed the limb-darkening law to be linear with a coefficient of $u = 0.4$ at $4,500 \text{ \AA}$ for both stars¹⁷. The emergent spectra from the uneclipsed pixels of both stars were summed to create the model spectrum.

We used Levenberg–Marquardt least-squares minimization¹⁸ to derive the best fitting parameters, and the bootstrap method¹⁹ to derive the statistical $1-\sigma$ parameter uncertainties (Tables 1 and 2). This uncertainty analysis did not take into account some possible systematic errors. We investigated the possible error due to gravity brightening by assuming the emergent intensity to be proportional to the local acceleration due to gravity²⁰, finding the resultant changes in β_p and β_s to be smaller than 1° and therefore negligible. Likewise, we did not allow for the possible effects of differential rotation, nor did we allow for any changes in the limb-darkening law within the lines as compared to the continuum. We found no evidence for those effects, though it remains possible that they are present and that our macro-turbulence model is compensating for them. In addition, because the lines are relatively broad, errors in the normalization of the continuum could influence the results. To account for these effects in our error analysis, we refitted our model to a collection of spectra normalized using different functional forms, and choosing different wavelength domains over which those functions are fitted. We also re-fitted using limb-darkening coefficients ranging from 0 to 1, and characteristic macroturbulent velocities in the range $5\text{--}50 \text{ km s}^{-1}$. From the scatter in the results for the fitted parameters, we derived our final $1-\sigma$ uncertainties in the $v \sin i$ and β parameters, with the largest effects arising from changes in normalization.

Figure 1 shows the observed spectra after subtracting the model spectrum of the foreground star, for clarity. This figure also shows the best-fitting model, and the model assuming co-aligned spins and orbit, which fits the data poorly. Our main result is that the stellar rotation axes are strongly tilted with respect to each other, and with respect to the projected orbital axis: $\beta_p = 72 \pm 4^\circ$ and $\beta_s = -84 \pm 8^\circ$. Although we reiterate that our quantitative results were obtained by fitting the line profiles of both stars directly, in Fig. 2 we show the apparent radial velocity of each star, a form of presentation that may make the result of a large misalignment more obvious.

Table 1 | Orbital and physical parameters of DI Herculis

	Literature values	Reference	This study
Orbital period, P	10.550164 ± 0.000001 days	3	
Minimum light of primary eclipse, T_{\min}	2442233.3481 ± 0.0007 HJD	3	
Argument of periastron, ω	$330.2 \pm 0.6^\circ$	9	
Orbital eccentricity, e	0.489 ± 0.003	9	
Orbital inclination, i_o	$89.3 \pm 0.03^\circ$	9	
Primary velocity semi-amplitude, K_p	$110.7 \pm 0.5 \text{ km s}^{-1}$	9	$109 \pm 1 \text{ km s}^{-1}$
Secondary velocity semi-amplitude, K_s	$126.6 \pm 1.2 \text{ km s}^{-1}$	9	$127 \pm 1 \text{ km s}^{-1}$
Primary additive velocity offset, γ_p	$9.1 \pm 0.3 \text{ km s}^{-1}$	9	$7 \pm 1 \text{ km s}^{-1}$
Secondary additive velocity offset, γ_s	$= \gamma_p$	9	$11 \pm 1 \text{ km s}^{-1}$
Primary stellar radius, R_p	$2.68 \pm 0.05 R_{\text{sun}}$	9	
Secondary stellar radius, R_s	$2.48 \pm 0.05 R_{\text{sun}}$	9	
Primary stellar mass, M_p	$5.15 \pm 0.10 M_{\text{sun}}$	9	$5.1^{+0.2}_{-0.1} M_{\text{sun}}$
Secondary stellar mass, M_s	$4.52 \pm 0.06 M_{\text{sun}}$	9	$4.4^{+0.2}_{-0.1} M_{\text{sun}}$
Average equivalent width of Mg II in DI Herculis	0.27 \AA	9	0.24 \AA
Primary macroturbulence velocity, $\xi_{R,T}$			$12 \pm 2 \text{ km s}^{-1}$
Secondary macroturbulence velocity, $\xi_{R,T}$			$10 \pm 1 \text{ km s}^{-1}$
Primary projected spin-orbit angle, β_p			$72 \pm 4^\circ$
Secondary projected spin-orbit angle, β_s			$-84 \pm 8^\circ$

HJD, heliocentric Julian day. The ref. 9 value for ω (329.9°), based on observations made in 1968–1978, was precessed forward to 2008. We used two independent velocity offsets to account for effective centroid shifts that depend on spectral type, owing to temperature-dependent blended features. We allowed K_1 , K_2 , γ_1 and γ_2 to be free parameters. We fixed the values of P , e , i_o and T_{\min} at values from the literature. If, instead, all the parameters are allowed to be free, we find results that are consistent with the literature values, but with reduced precision. We also find that the results for β_p and β_s agree with those obtained from the externally constrained model.

The factor-of-four discrepancy between the theoretical and observed rates of apsidal precession was based on the premise that the stellar spin axes are perpendicular to the orbital plane. Now that this premise has been proved false, the theoretical precession rate must be recalculated. For this calculation it is necessary to know the true angles between the spin and orbital axes, and the actual rotation velocities of the stars, even though only their sky projections are measured. The unmeasured angles are the inclinations i_p and i_s of the stellar spin axes with respect to the line of sight. We performed a Monte Carlo calculation of the theoretical precession rate^{7,8}, in which the cosine of each inclination was drawn from a uniform distribution. We excluded inclinations giving rotation speeds faster than 600 km s^{-1} , the approximate breakup speeds. To calculate the precession due to the rotationally induced oblateness, we adopted apsidal motion constants of $k_{21} = 0.0087$ and $k_{22} = 0.0081$ (ref. 4). The oblateness causes retrograde apsidal motion (-2.23 arcsec per cycle), whereas tidal deformations and general relativity cause prograde apsidal motion ($+1.35$ and $+2.40$ arcsec per cycle, respectively). The net theoretical precession rate is $1.52^{+0.06}_{-0.04}$ arcsec per cycle, where the value quoted is the mode of the Monte Carlo distribution, and the quoted error interval encloses 68.3% of the results. This agrees with the observed precession rate of 1.08 ± 0.16 arcsec per cycle (ref. 21) (Fig. 3). We therefore consider the mystery of the anomalous apsidal precession of DI Herculis to be solved.

The solution to the mystery of DI Herculis raises the questions of how the stars became so strongly tilted with respect to their orbit. It seems unlikely that they formed in such a state, although it is not clear at what point in their relatively short lifetime (~ 5 Myr; ref. 4) the misalignment occurred. One possible mechanism is the Kozai effect, whereby a third body in the system excites oscillations of the binary's eccentricity and orbital orientation²². Whatever the route to the present configuration of DI Herculis, it would be interesting to know whether it is unique or whether spin-orbit misalignment is more common among close binaries than has been expected. A survey to measure the relative orientations of spin axes in selected eclipsing

binaries, or systems that can be resolved with interferometry^{23,24}, may help to answer these questions.

Received 12 June; accepted 14 August 2009.

- Claret, A. & Giménez, Á. The apsidal motion test of the internal stellar structure—comparison between theory and observations. *Astron. Astrophys.* **277**, 487–502 (1993).
- Martynov, D. I. & Khaliullin, K. F. On the relativistic motion of the periastron in the eclipsing binary system DI Herculis. *Astrophys. Space Sci.* **71**, 147–170 (1980).
- Guinan, E. F. & Maloney, F. P. The apsidal motion of the eccentric eclipsing binary DI Herculis—an apparent discrepancy with general relativity. *Astron. J.* **90**, 1519–1528 (1985).
- Claret, A. Some notes on the relativistic apsidal motion of DI Herculis. *Astron. Astrophys.* **330**, 533–540 (1998).
- Moffat, J. W. The orbital motion of DI Herculis as a test of a theory of gravitation. *Astrophys. J.* **287**, L77–L79 (1984).
- Hsuan, K. & Mardling, R. A. A Three body solution for the DI Her system. *Astrophys. Space Sci.* **304**, 243–246 (2006).
- Shakura, N. I. On the apsidal motion in binary stars. *Sov. Astron. L.* 224–226 (1985).
- Company, R., Portilla, M. & Giménez, Á. On the apsidal motion of DI Herculis. *Astrophys. J.* **335**, 962–964 (1988).
- Popper, D. M. Rediscussion of eclipsing binaries. XIII—DI Herculis, a B-type system with an eccentric orbit. *Astrophys. J.* **254**, 203–213 (1982).
- Perruchot, S. *et al.* The SOPHIE spectrograph: design and technical key-points for high throughput and high stability. *SPIE Conf. Ser.* **7014**, doi:10.1117/12.787379 (2008).
- Holt, J. R. Spectroscopic determination of stellar rotation. *Astron. Astrophys.* **12**, 646 (1893).
- Rossiter, R. A. On the detection of an effect of rotation during eclipse in the velocity of the brighter component of beta Lyrae, and on the constancy of velocity of this system. *Astrophys. J.* **60**, 15–21 (1924).
- McLaughlin, D. B. Some results of a spectrographic study of the Algol system. *Astrophys. J.* **60**, 22–31 (1924).
- Albrecht, S., Reffert, S., Snellen, I., Quirrenbach, A. & Mitchell, D. S. The spin axes orbital alignment of both stars within the eclipsing binary system V1143 Cyg using the Rossiter-McLaughlin effect. *Astron. Astrophys.* **474**, 565–573 (2007).
- Queloz, D. *et al.* Detection of a spectroscopic transit by the planet orbiting the star HD209458. *Astron. Astrophys.* **359**, L13–L17 (2000).
- Winn, J. N. *et al.* Measurement of spin-orbit alignment in an extrasolar planetary system. *Astrophys. J.* **631**, 1215–1226 (2005).
- Gray, D. F. *The Observation and Analysis of Stellar Photospheres* 3rd edn (Cambridge Univ. Press, 2005).

Table 2 | $v \sin i$ measurements

Year (and reference) of	1948 (ref. 26)	1974 (ref. 25)	1985 (ref. 25)	1988 (ref. 25)	2008 (this study)
Primary $v_p \sin i_p$ (km s^{-1})	76	34 ± 6	50 ± 30	61 ± 4	108 ± 4
Secondary $v_s \sin i_s$ (km s^{-1})	76	50 ± 7	50 ± 30	75 ± 4	116 ± 4

We note that the apparent time variations in $v_p \sin i_p$ and $v_s \sin i_s$ were previously reported²⁵, and taken as possible evidence for spin precession (which would imply a substantial misalignment), although those authors could not draw a firm conclusion from the available data. In principle, one might derive the three-dimensional orientation of the stellar spin axes by modelling the time variations in $v_p \sin i_p$ and $v_s \sin i_s$. At present, however, it is not possible to improve on the calculation of the theoretical precession rate using this technique, because the analysis hinges on the measurement from 1948 for which the uncertainty is unknown.

18. Markwardt, C. B. Non-linear least squares fitting in IDL with MPFIT. Preprint at (<http://arXiv.org/abs/0902.2850>) 2009.
19. Press, W. H., Teukolsky, S. A., Vetterling, W. T. & Flannery, B. P. *Numerical Recipes in C. The Art of Scientific Computing* 2nd edn, 689–699 (Cambridge Univ. Press, 1992).
20. Von Zeipel, H. The radiative equilibrium of a slightly oblate rotating star. *Mon. Not. R. Astron. Soc.* **84**, 684–701 (1924).
21. Guinan, E. F., Marshall, J. J. & Maloney, F. P. A new apsidal motion determination for DI Herculis. *Inform. Bull. Variable Stars* **4101**, 1–44 (1994).
22. Fabrycky, D. & Tremaine, S. Shrinking binary and planetary orbits by Kozai cycles with tidal friction. *Astrophys. J.* **669**, 1298–1315 (2007).
23. Chelli, A. & Petrov, R. G. Model fitting and error analysis for differential interferometry. II. Application to rotating stars and binary systems. *Astron. Astrophys.* **109** (Suppl.), 401–415 (1995).
24. Le Bouquin, J. B. The spin-orbit alignment of the Fomalhaut planetary system probed by optical long baseline interferometry. *Astron. Astrophys.* **498**, L41–L44 (2009).
25. Reisenberger, M. P. & Guinan, E. F. A possible rescue of general relativity in DI Herculis. *Astron. J.* **97**, 216–221 (1989).
26. Van Dien, E. Axial rotation of the brighter stars in the Pleiades cluster. *J. R. Astron. Soc. Can.* **42**, 249–261 (1948).

Supplementary Information is linked to the online version of the paper at www.nature.com/nature.

Acknowledgements We are grateful to Á. Giménez, E. Guinan and T. Mazeh for bringing DI Herculis to our attention. We thank J. Lub, R. Tubbs, C. Hopman, Y. Levin and D. Fabrycky for discussions about double stars and their properties. We also thank H. Reckman for essential help during one observing run. We are grateful to the Sophie team for building the spectrograph and reduction pipeline. This research has made use of the SIMBAD database, operated at CDS, Strasbourg, France, and the Vienna Atomic Line database (VALD) located at <http://ams.astro.univie.ac.at/vald/>. S.A. acknowledges support during part of this project by a Rubicon fellowship from the Netherlands Organisation for Scientific Research (NWO). J.N.W. acknowledges support from a NASA Origins grant (NNX09AD36G). S.A. and S.R. acknowledge funding from the Optical Infrared Coordination network (OPTICON).

Author Contributions S.A. participated in the development of the concept of this research and the analysis code, participated in the observations, the analysis and interpretation of the data and writing the manuscript. S.R. participated in the development of the concept of this research and the analysis code and the observations. I.A.G.S. participated in the analysis and interpretation of the data and in writing the manuscript. J.N.W. participated in the analysis and interpretation of the data and in writing the manuscript.

Author Information Reprints and permissions information is available at www.nature.com/reprints. Correspondence and requests for materials should be addressed to S.A. (albrecht@space.mit.edu).

Non-coalescence of oppositely charged drops

W. D. Ristenpart^{1,2}, J. C. Bird³, A. Belmonte⁴, F. Dollar³ & H. A. Stone^{3†}

Electric fields induce motion in many fluid systems, including polymer melts¹, surfactant micelles² and colloidal suspensions³. Likewise, electric fields can be used to move liquid drops⁴. Electrically induced droplet motion manifests itself in processes as diverse as storm cloud formation⁵, commercial ink-jet printing⁶, petroleum and vegetable oil dehydration⁷, electrospray ionization for use in mass spectrometry⁸, electrowetting⁹ and lab-on-a-chip manipulations¹⁰. An important issue in practical applications is the tendency for adjacent drops to coalesce, and oppositely charged drops have long been assumed to experience an attractive force that favours their coalescence^{11–13}. Here we report the existence of a critical field strength above which oppositely charged drops do not coalesce. We observe that appropriately positioned and oppositely charged drops migrate towards one another in an applied electric field; but whereas the drops coalesce as expected at low field strengths, they are repelled from one another after contact at higher field strengths. Qualitatively, the drops appear to ‘bounce’ off one another. We directly image the transient formation of a meniscus bridge between the bouncing drops, and propose that this temporary bridge is unstable with respect to capillary pressure when it forms in an electric field exceeding a critical strength. The observation of oppositely charged drops bouncing rather than coalescing in strong electric fields should affect our understanding of any process involving charged liquid drops, including de-emulsification, electrospray ionization and atmospheric conduction.

The non-coalescence behaviour is readily demonstrated experimentally (Fig. 1, left), using a container with the bottom half filled with water and the top half with an immiscible and poorly conducting oil. Metal wires are inserted into each liquid (at top and bottom) to serve as electrodes. A high-voltage power supply provides a potential difference of the order of 1 kV over approximately 1 cm. Although the applied potential is large, the total current density is low because of the insulating oil. After application of the field, a water drop is pipetted manually into the oil near the top electrode. Dielectrophoretic forces¹⁴ cause the drop to move towards and contact the top electrode, thereby providing the drop a net charge. The drop then moves down towards the oppositely charged oil/water meniscus. Drop motion is recorded with high-speed video.

The behaviour of a 2- μ l water drop (0.2 mM KCl) in silicone oil is captured in the series of images shown in Fig. 1, right. For low field strengths (Fig. 1, top), the drop slowly approaches the oil/water meniscus and coalesces immediately on contact (Supplementary Movie 1). This behaviour is consistent with prior work on electrocoalescence^{13,15}, where it was found that application of a field simply increases the rate of coalescence; this increase was attributed to charge polarization induced by the applied field. For our experimental configuration shown in Fig. 1, the bottom edge of the small droplet becomes positively charged, whereas the oil/water meniscus beneath it becomes negatively charged. The opposite charges attract, forcing the drop into contact and hastening the overall rate of coalescence.

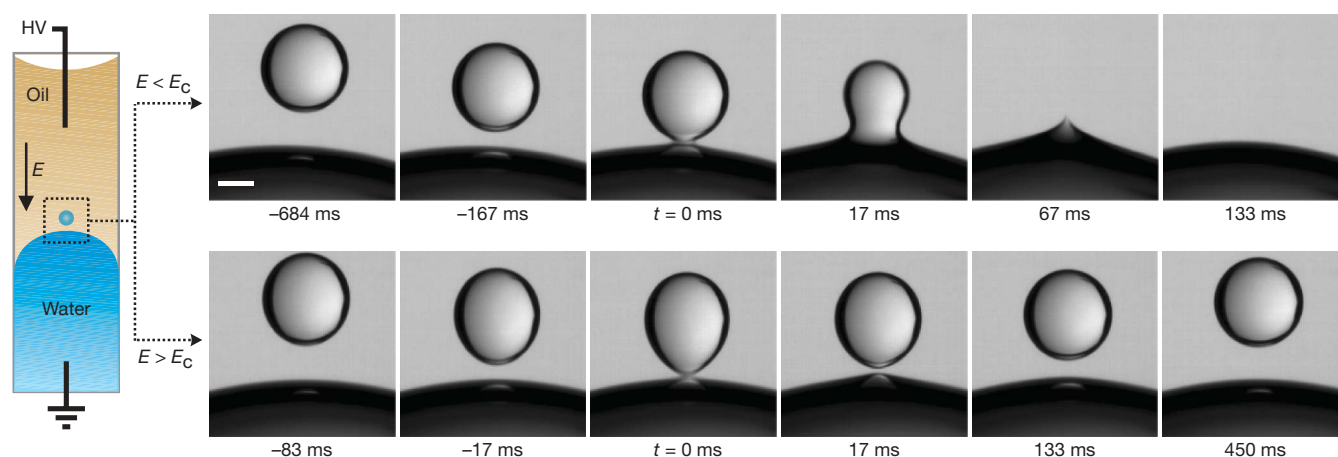


Figure 1 | Electrically driven bouncing of water in oil. Left, diagram of the experimental apparatus ('water' indicates 0.2 M KCl). A high-voltage (HV) power supply provides the electric field. Right, droplet coalescence (top) and bouncing (bottom); time (t in ms) is relative to the video frame labelled $t = 0$. Top, $E = 160 \text{ V mm}^{-1}$, d.c. The drop slowly approached the oil/water

interface, and then coalesced on contact. Bottom, $E = 300 \text{ V mm}^{-1}$, d.c. The drop quickly approached the oil/water meniscus, briefly made apparent contact, then moved away in the opposite direction. Scale bar, 0.5 mm. Oil is 1,000 centistokes (1,000 cSt) polydimethylsiloxane.

¹Department of Chemical Engineering and Materials Science, ²Department of Food Science and Technology, University of California at Davis, 1 Shields Drive, Davis, California 95616, USA. ³School of Engineering and Applied Sciences, Harvard University, Cambridge, Massachusetts 02138, USA. ⁴W. G. Pritchard Laboratories, Department of Mathematics, Pennsylvania State University, University Park, Pennsylvania 16802, USA. [†]Present address: Department of Mechanical and Aerospace Engineering, Princeton University, Princeton, New Jersey 08544, USA.

Above a critical field strength E_c , however, drops fail to coalesce (Fig. 1, bottom). Before contact, the leading edge of the drop noticeably elongates. This elongation results from the electrical stress acting on the charged liquid/liquid interface; the resulting conical shape is often referred to as a Taylor cone^{16,17}. In this configuration, the cone is positively charged and therefore attracted towards the negatively polarized oil/water meniscus. After apparent contact with the meniscus, however, the cone recoils and the drop reverses direction, moving upwards against gravity (Supplementary Movie 2). After bouncing, the drop typically moves back to the top electrode. On contact with the metal, the drop again reverses direction and migrates back to the oil/water meniscus, whereupon it bounces again, repeating the cycle. In this fashion, individual drops are observed to bounce back and forth indefinitely (Supplementary Movie 3). We emphasize that the applied potential difference remains constant throughout the experiment, and that coalescence does not occur until the applied field is sufficiently reduced. Although water drops are known to bounce off metallic electrodes^{18,19,20}, to our knowledge the only previous observation of bouncing off a water/oil meniscus was by Allan and Mason²¹, who reported that water drops in silicone oil ‘repelled’ one another after the drops moved within a critical separation distance. They speculated that an electrical discharge had occurred, but did not otherwise explain the bouncing behaviour.

Why do the droplets bounce? The familiar bouncing of a ball occurs because of a combination of inertia and elasticity, but scaling arguments based on the observed droplet velocities indicate that here inertia does not have a dominant role (Supplementary Information). Instead, the bouncing demonstrated in Fig. 1 appears to be driven entirely by charge transfer dynamics. Recalling that the applied field remains constant, the only way for the drop to travel upwards against gravity is if the electrostatic force is oriented in that direction. The reversal of direction following each bounce indicates that the net charge in the drop switches sign, which means charge must be transmitted during the bounce. A striking consequence of this charge transfer is demonstrated in Fig. 2, in which multiple water drops were inserted into the oil phase. The drops rapidly arranged into a chain extending from the oil/water meniscus, whereupon individual droplets within the chain oscillated back and forth between their neighbours in a coordinated fashion. The leading edges of neighbouring drops extended towards each other in a ‘double-cone’ geometry, briefly made contact, then recoiled. The bouncing events propagated up and down the chain, suggesting that charge is conducted through the chain in this manner (Supplementary Movie 4). The behaviour qualitatively resembles the motion in ‘Newton’s cradle’ (a series of vertically aligned pendula, set into motion by contact with one another), except here linear momentum is apparently conveyed via charge transfer and is not necessarily conserved. For example, drops

were frequently observed with a larger absolute velocity after contact, yielding an apparent coefficient of restitution larger than unity. Because the motion is electrically driven, the increased velocity indicates that an increased net charge was acquired during the bounce.

As the charge consists of dissociated ionic species (for example, K^+ and Cl^-) in the water phase, the ions must transfer from one drop to another during each bounce. There are several possible mechanisms for charge transfer, including conduction through the oil, dielectric breakdown or electrospray⁸ of smaller drops, but our direct high-speed observations show that, at least in silicone oil, a short-lived aqueous bridge forms between the drops. By zooming-in on a bounce (with a $\times 10$ microscope objective) and capturing images at 25,000 frames s^{-1} , an image of such a bridge was captured (Fig. 3a, Supplementary Movie 5). The bridge was short lived—the frames immediately before and after show a gap of oil between the drops, indicating that the bridge existed for less than 80 μs . Charge transfer presumably occurs by ionic conduction through the water phase during the short lifespan of the bridge.

A temporary meniscus bridge is thus the conduit of charge between bouncing drops, but it is not obvious why it pinches off. Coalescence would reduce the system’s energy by minimizing the total surface area and corresponding surface energy. The usual explanations for drop stability invoke prevention of direct contact by the presence of surfactants, polymers or colloids at the oil/water interface^{22,23}, but these do not apply because the drops clearly make physical contact (as shown in Fig. 3a).

To explore possible driving forces for pinch-off, we systematically measured the critical field strength E_c above which bouncing occurs. The threshold field strength depended sensitively on the magnitude of charge on the droplet, Q , which itself depends on the details of charge transfer between the droplet and the previous interface it contacted (for example, the metal electrode). We determined Q using Stokes’ drag for a sphere and the measured drop velocity (Supplementary Information). By taking into account both Q and E , we found that the threshold between bouncing and coalescence for water in silicone oil is well defined in terms of a critical electric force $F_E^{crit} = QE_c$, the magnitude of which depends on the dissolved salt concentration. Whenever drop charge and applied field are such that $QE_c > F_E^{crit}$, the drops invariably bounced (the upper region of Fig. 3c).

The data in Fig. 3c rule out thermal Marangoni flows or Maxwell stresses as the driving force for pinch off (see Supplementary Information for details), and suggest instead that capillary forces render the meniscus bridge intrinsically unstable above a critical cone angle. The experimental observations show that drops assume a ‘double-cone’ geometry in the vicinity of the meniscus bridge (Fig. 3b). The Young–Laplace equation approximates the capillary pressure inside the bridge as

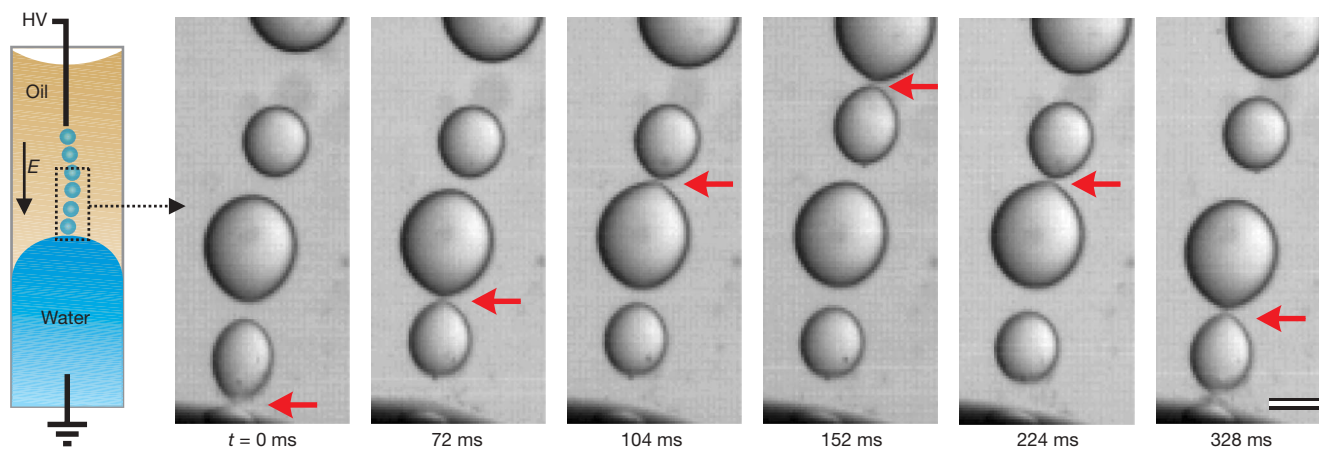


Figure 2 | Bouncing within a chain of water droplets in oil. Left, diagram of the apparatus, showing area magnified at right (‘oil’ and ‘water’ as Fig. 1). Right, bouncing of droplets. Arrows indicate the location of charge exchange during each bounce. $E = 300 \text{ V mm}^{-1}$, d.c. Scale bar, 0.5 mm.

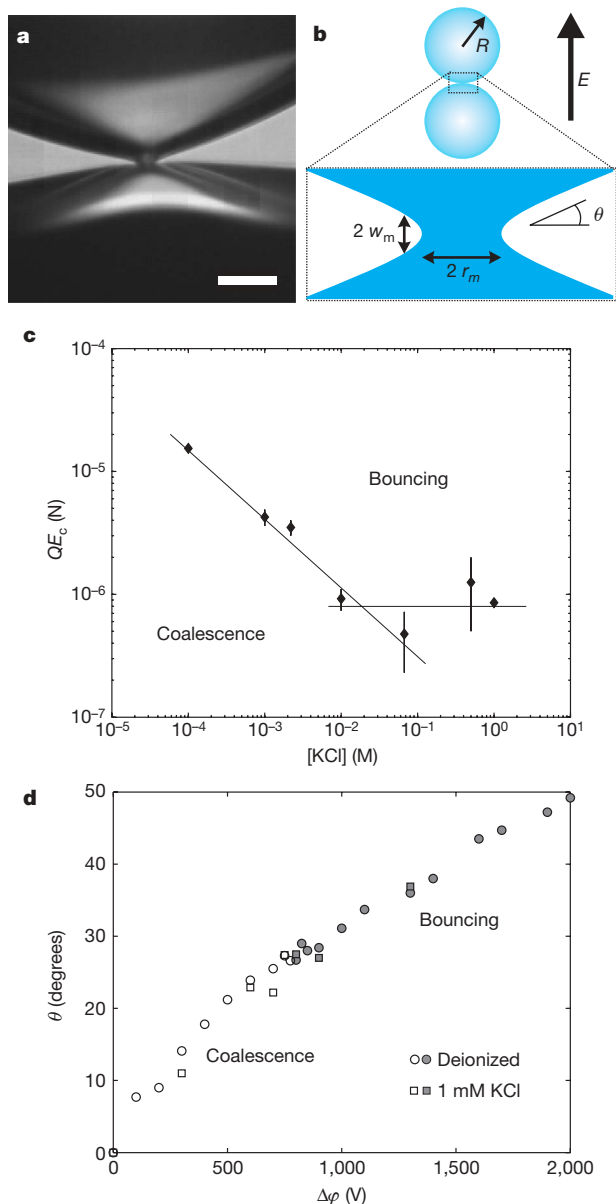


Figure 3 | Meniscus bridge, critical field strength and critical cone angle. **a**, High-magnification, high speed image of the temporary meniscus bridge between two bouncing water drops (1 M KCl) in silicone oil (1,000 cSt). Dark regions are water, the brighter areas within the water are reflections. $E = 200 \text{ V mm}^{-1}$; scale bar, 0.1 mm. **b**, Definition sketch of the meniscus bridge. **c**, The critical electric force as a function of salt concentration for 2- μL water droplets in 1,000 cSt silicone oil. Lines are to guide the eye. Error bars indicate the range of observed transitions between bouncing and coalescence. **d**, The cone angle at the time of contact between water drops in air as a function of applied potential ($\Delta\phi$). Open symbols denote coalescence; filled symbols denote bouncing. Circles, deionized water ($4 \mu\text{S cm}^{-1}$); squares, 1 mM KCl ($163 \mu\text{S cm}^{-1}$).

$$p_{\text{bridge}} = p_0 + \gamma \left(\frac{1}{r_m} - \frac{1}{w_m} \right) \quad (1)$$

where p_0 is the ambient pressure, γ is the oil/water interfacial tension, and the two curvatures are defined by the radius and width of the meniscus bridge, r_m and w_m , respectively (Fig. 3b). This approximate expression neglects dynamic effects, but helps estimate the flow direction in the meniscus bridge. For the double-cone angle θ formed by the intersection of two Taylor cones, the meniscus width scales as $w_m \approx r_m \tan \theta$, and since the capillary pressure in the bulk of the drops (each assumed to have radius R) is $p_{\text{drop}} = p_0 + 2\gamma/R$, the pressure

difference between the bulk of the drop and the meniscus bridge is $\Delta p \equiv p_{\text{drop}} - p_{\text{bridge}} = \frac{2\gamma}{R} - \frac{\gamma}{r_m} (1 - \cot \theta)$. The meniscus bridge is small, so the inequality $r_m \ll R$ holds and to good approximation the pressure difference is:

$$\Delta p \approx \frac{\gamma}{r_m} (\cot \theta - 1) \quad (2)$$

The sign of the pressure difference and corresponding flow direction thus depend only on θ . For sufficiently steep cones ($\theta > 45^\circ$), the pressure is higher in the meniscus bridge (that is, $\Delta p < 0$), so fluid moves from the meniscus back into the drop, driving pinch-off. The cone angle between approaching drops increases with field strength, as evidenced by the observations here and in previous numerical studies^{24,25} (which did not consider the behaviour after contact). Likewise, drops with larger net charge form cones more readily when a field is applied¹⁶, which is consistent with the observed dependence of

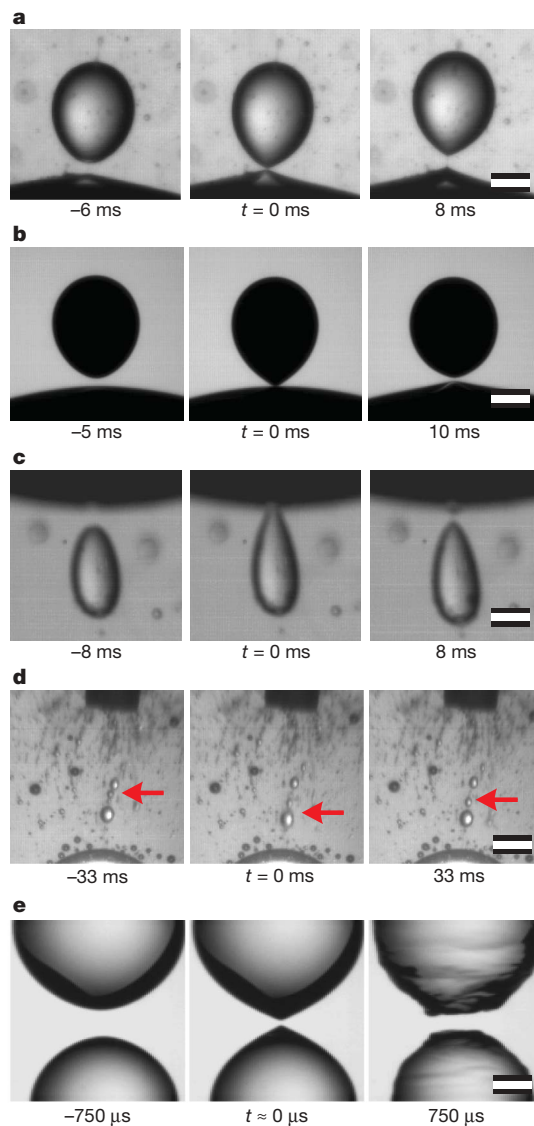


Figure 4 | Non-coalescence behaviour in different liquid systems. **a**, Vinegar (5% acetic acid) in olive oil. $E = 600 \text{ V mm}^{-1}$. **b**, Deionized water with polystyrene particles (0.82- μm diameter, 2.2%) in 1,000 cSt silicone oil. $E = 300 \text{ V mm}^{-1}$. **c**, Ethanol (95%, at top in dark regions) in mineral oil. $E = 400 \text{ V mm}^{-1}$. **d**, Multiple droplets of 1 M KCl in light Louisiana Gulf sweet crude oil. $E = 300 \text{ V mm}^{-1}$. Dark rectangle near top is the electrode; curved dark region near bottom is the water/oil meniscus. **e**, Deionized water drops in air. $E = 500 \text{ V mm}^{-1}$. The drops are attached directly to electrified nozzles. Scale bars: **a–d**, 0.5 mm; **e**, 0.3 mm.

the bouncing threshold on the drop charge for a given applied field strength.

The preceding model says nothing about the conductivity of the droplet, whereas Fig. 3c shows that it can have an important role, especially for lower salt concentrations. We therefore measured the cone angle at the time of contact between two water droplets in air as a function of the applied potential (Fig. 3d). To isolate the cone dynamics from the drop motion, the water drops were attached directly to electrified nozzles and slowly brought together; this procedure also ensured that the cones contacted at a known location, simplifying the high-speed photography (67,000 frames s^{-1}). Two significant results were obtained. First, the drops invariably coalesced for $\theta \lesssim 30^\circ$, but recoiled for larger angles. Second, the critical angle was the same for drops with no added salt (deionized water) and for drops with 1 mM KCl, concentrations that correspond to the regime of high sensitivity to salt concentration shown in Fig. 3c. The data indicate that conductivity plays a significant part in determining how large an electric force must be applied to a moving charged drop to achieve a certain cone angle; but whether coalescence occurs or not depends only on the cone angle following contact.

Inspection of Fig. 3d suggests that the critical cone angle is closer to 30° than 45° , and a more detailed analysis of the nonlinear free-boundary problem for the capillary pressure (J.C.B., W.D.R., A.B. and H.A.S., manuscript in review) predicts in fact a critical cone angle of approximately 31° . But the key point here is that above a critical field strength pinch-off is inherently favoured, with other material parameters having only an indirect role in governing the coalescence behaviour. Specifically, interfacial tension, conductivity and electric field define the cone angle before contact; but after contact, only the geometry of the meniscus bridge matters. A significant implication of this model is that non-coalescence will occur for any liquid/liquid or gas/liquid system, provided that the electric field induces a sufficiently steep meniscus bridge. Indeed, our experiments show that the bouncing behaviour is quite general, occurring in a variety of systems including olive oil, crude oil and air (Fig. 4). That non-coalescence occurs in such diverse systems is consistent with the independence of this phenomenon on system material properties as predicted by the capillary pinch-off model.

The universal nature of the non-coalescence behaviour can explain observations in very different fields. For example, a study²⁶ of atmospheric charge conduction reported that the coalescence efficiency of oppositely charged water drops in air plateaus above a critical charge density. A similar plateau has been observed in the context of oil dehydration^{27,28}, while experiments²⁹ on drop pairs in microfluidic devices revealed that adjacent water drops repelled one another above a frequency-dependent critical field strength. Although the applied waveform differed in these studies, the stresses giving rise to Taylor cones (and hence the double-cone geometry) scale as the square of the applied field¹⁷. Electric fields that are steady, oscillatory or pulsed will thus all fail to induce coalescence above some critical field strength. Reviewing de-emulsification experiments using pulsed fields³⁰, Eow *et al.* noted⁷ that "...chains of water droplets are usually created during periods of high voltage, followed by rapid coalescence during periods of reduced or no voltage". The capillary pinch-off mechanism presented here helps to explain the above observations.

Received 6 January; accepted 9 July 2009.

- Schaffer, E., Thurn-Albrecht, T., Russell, T. P. & Steiner, U. Electrically induced structure formation and pattern transfer. *Nature* **403**, 874–877 (2000).
- Trau, M. *et al.* Microscopic patterning of orientated mesoscopic silica through guided growth. *Nature* **390**, 674–676 (1997).
- Leunissen, M. E. *et al.* Ionic colloidal crystals of oppositely charged particles. *Nature* **437**, 235–240 (2005).

- Baygents, J. C. & Saville, D. A. Electrophoresis of drops and bubbles. *J. Chem. Soc. Farad. Trans.* **87**, 1883–1898 (1991).
- Ochs, H. T. & Czys, R. R. Charge effects on the coalescence of water drops in free-fall. *Nature* **327**, 606–608 (1987).
- Calvert, P. Inkjet printing for materials and devices. *Chem. Mater.* **13**, 3299–3305 (2001).
- Eow, J. S., Ghadiri, M., Sharif, A. O. & Williams, T. J. Electrostatic enhancement of coalescence of water droplets in oil: a review of the current understanding. *Chem. Eng. J.* **84**, 173–192 (2001).
- Fenn, J. B., Mann, M., Meng, C. K., Wong, S. F. & Whitehouse, C. M. Electrospray ionization for mass-spectrometry of large biomolecules. *Science* **246**, 64–71 (1989).
- Baret, J. C. & Mugele, F. Electrical discharge in capillary breakup: controlling the charge of a droplet. *Phys. Rev. Lett.* **96**, 016106 (2006).
- Link, D. R. *et al.* Electric control of droplets in microfluidic devices. *Angew. Chem. Int. Edn* **45**, 2556–2560 (2006).
- Rayleigh, Lord The influence of electricity on colliding water drops. *Proc. R. Soc. Lond.* **28**, 405–409 (1879).
- Sartor, D. A. Laboratory investigation of collision efficiencies, coalescence and electrical charging of simulated cloud droplets. *J. Meteorol.* **11**, 91–103 (1954).
- Allan, R. S. & Mason, S. G. Effects of electric fields on coalescence in liquid + liquid systems. *Trans. Farad. Soc.* **57**, 2027–2040 (1961).
- Pohl, H. A. *Dielectrophoresis* (Cambridge Univ. Press, 1978).
- Jayaratne, O. W. & Mason, B. J. Coalescence + bouncing of water drops at air/water interface. *Proc. R. Soc. Lond. A* **280**, 545–565 (1964).
- Taylor, G. Disintegration of water drops in electric field. *Proc. R. Soc. Lond. A* **280**, 383–397 (1964).
- de la Mora, J. F. The fluid dynamics of Taylor cones. *Annu. Rev. Fluid Mech.* **39**, 217–243 (2007).
- Mochizuki, T., Mori, Y. H. & Kaji, N. Bouncing motions of liquid-drops between tilted parallel-plate electrodes. *Am. Inst. Chem. Eng. J.* **36**, 1039–1045 (1990).
- Hase, M., Watanabe, S. N. & Yoshikawa, K. Rhythmic motion of a droplet under a dc electric field. *Phys. Rev. E* **74**, 046301 (2006).
- Jung, Y. M., Oh, H. C. & Kang, I. S. Electrical charging of a conducting water droplet in a dielectric fluid on the electrode surface. *J. Colloid Interface Sci.* **322**, 617–623 (2008).
- Allan, R. S. & Mason, S. G. Particle motions in sheared suspensions 14: coalescence of liquid drops in electric and shear fields. *J. Colloid Sci.* **17**, 383–408 (1962).
- Bibette, J., Morse, D. C., Witten, T. A. & Weitz, D. A. Stability criteria for emulsions. *Phys. Rev. Lett.* **69**, 2439–2442 (1992).
- Binks, B. P. & Lumsdon, S. O. Pickering emulsions stabilized by monodisperse latex particles: effects of particle size. *Langmuir* **17**, 4540–4547 (2001).
- Brazier-Smith, P. R. Stability and shape of isolated and pairs of water drops in an electric field. *Phys. Fluids* **14**, 1–6 (1971).
- Brazier-Smith, P. R., Jennings, S. G. & Latham, J. Investigation of behavior of drops and drop-pairs subjected to strong electrical forces. *Proc. R. Soc. Lond. A* **325**, 363–376 (1971).
- Brazier-Smith, P. R., Latham, J. & Jennings, S. G. Interaction of falling water drops - coalescence. *Proc. R. Soc. Lond. A* **326**, 393–408 (1972).
- Sadek, S. E. & Hendrick, C. D. Electrical coalescence of water droplets in low-conductivity oils. *Ind. Eng. Chem. Fund.* **13**, 139–142 (1974).
- Urdahl, O., Williams, T. J., Bailey, A. G. & Thew, M. T. Electrostatic destabilization of water-in-oil emulsions under conditions of turbulent flow. *Chem. Eng. Res. Des.* **74**, 158–165 (1996).
- Chabert, M., Dorfman, K. D. & Viovy, J. L. Droplet fusion by alternating current (AC) field electrocoalescence in microchannels. *Electrophoresis* **26**, 3706–3715 (2005).
- Taylor, S. E. Theory and practice of electrically-enhanced phase separation of water-in-oil emulsions. *Chem. Eng. Res. Des.* **74**, 526–540 (1996).

Supplementary Information is linked to the online version of the paper at www.nature.com/nature.

Acknowledgements We thank M. Poitzsch and M. Sullivan at the Schlumberger-Doll Research Center for supplying samples of crude oil, C. Holtze, T. Schneider and D. A. Weitz for feedback and the Harvard Nanoscale Science and Engineering Center for support. A.B. acknowledges support from Harvard University's MRSEC.

Author Contributions W.D.R., J.C.B., A.B. and H.A.S. designed the research; W.D.R., J.C.B., A.B. and F.D. performed research; W.D.R., J.C.B., A.B. and H.A.S. analysed data; W.D.R. wrote, and all authors commented on, the manuscript.

Author Information Reprints and permissions information is available at www.nature.com/reprints. Correspondence and requests for materials should be addressed to W.D.R. (wdristenpart@ucdavis.edu).

New particle formation in forests inhibited by isoprene emissions

Astrid Kiendler-Scharr¹, Jürgen Wildt², Miikka Dal Maso^{1,3}, Thorsten Hohaus¹, Einhard Kleist², Thomas F. Mentel¹, Ralf Tillmann¹, Ricarda Uerlings², Uli Schurr² & Andreas Wahner¹

It has been suggested that volatile organic compounds (VOCs) are involved in organic aerosol formation, which in turn affects radiative forcing and climate¹. The most abundant VOCs emitted by terrestrial vegetation are isoprene and its derivatives, such as monoterpenes and sesquiterpenes². New particle formation in boreal regions is related to monoterpene emissions³ and causes an estimated negative radiative forcing⁴ of about -0.2 to -0.9 W m^{-2} . The annual variation in aerosol growth rates during particle nucleation events correlates with the seasonality of monoterpene emissions of the local vegetation, with a maximum during summer⁵. The frequency of nucleation events peaks, however, in spring and autumn⁵. Here we present evidence from simulation experiments conducted in a plant chamber that isoprene can significantly inhibit new particle formation. The process leading to the observed decrease in particle number concentration is linked to the high reactivity of isoprene with the hydroxyl radical (OH). The suppression is stronger with higher concentrations of isoprene, but with little dependence on the specific VOC mixture emitted by trees. A parameterization of the observed suppression factor as a function of isoprene concentration suggests that the number of new particles produced depends on the OH concentration and VOCs involved in the production of new particles undergo three to four steps of oxidation by OH. Our measurements simulate conditions that are typical for forested regions and may explain the observed seasonality in the frequency of aerosol nucleation events, with a lower number of nucleation events during summer compared to autumn and spring⁵. Biogenic emissions of isoprene are controlled by temperature and light², and if the relative isoprene abundance of biogenic VOC emissions increases in response to climate change or land use change, the new particle formation potential may decrease, thus damping the aerosol negative radiative forcing effect.

Land vegetation contributes 90% of the global VOC emissions². The main compound classes emitted by terrestrial vegetation are isoprene and its derivatives, such as monoterpenes and sesquiterpenes. Isoprene comprises one-third of the annual global VOC emission from all natural and anthropogenic sources. Annual global isoprene emissions are estimated to be in the range 440–660 teragrams of carbon (Tg C)⁶. While the detailed biological functionality of isoprene and monoterpene emissions is not fully understood⁷, the dependence of emissions on light intensity and temperature has been investigated in detail^{2,7}.

In addition to their importance for gas phase chemistry, the involvement of biogenic VOCs in tropospheric aerosol formation, first suggested in ref. 8, underlines the importance of taking into account biogenic VOCs in particle formation. Globally, the amount of secondary organic aerosols (SOA) produced from biogenic sources is still unclear. A source strength of $61\text{--}79 \text{ Tg yr}^{-1}$ at present

day conditions has been estimated⁹. Bottom-up approaches, based on SOA yields for single compounds derived in laboratory experiments, estimate a global SOA production of $12\text{--}70 \text{ Tg yr}^{-1}$ (ref. 10). Recent estimates suggest that SOA production may be even higher, of the order of $223\text{--}615 \text{ Tg yr}^{-1}$ (ref. 11).

In regions with low primary aerosol concentrations, biogenic SOA production proceeds via nucleation of gas phase species. Investigations of the mechanism underlying the frequently observed nucleation events in the European boreal forest demonstrate a straightforward relation between monoterpene emissions and gas-to-particle formation³. This is important, because nucleation can provide substantial numbers of aerosols.

Number density and size distribution of aerosols are key quantities that determine direct and indirect climate effects of aerosols. Current radiative forcing by new particle formation in boreal regions has been estimated⁴ as -0.2 to -0.9 W m^{-2} . Extrapolating current monoterpene emission rates into the year 2100 has led to a prediction¹² of a 40% increase of cloud condensation nuclei over boreal forests caused by a temperature increase of 5.8°C .

With their potential impact on climate, aerosol particles generated from biogenic emissions constitute a possible link in a feedback loop between climate, atmosphere and biosphere¹. Biogenic emissions of isoprene, for instance, are controlled by temperature and light². It is therefore expected that future biogenic isoprene emissions will change as temperature and land cover change¹³. For example, the impact of European afforestation may be significant, with a 126% increase in isoprene and a 13% increase in monoterpenes^{14,15} on the European scale.

Here we present laboratory evidence that isoprene can significantly inhibit new particle formation. Experiments were conducted in a plant chamber over a period of 21 days for a small mixed stand consisting of birch (*Betula pendula* L.), beech (*Fagus sylvatica* L.) and spruce (*Picea abies* L.), and over a period of 10 days for pines (*Pinus sylvestris* L.). These species emit only low amounts of isoprene, allowing the study of the influence of isoprene on particle formation by adding it to the natural emissions. The isoprene concentration was varied between 2 and 30 parts per billion (p.p.b.), which is within the range of atmospheric observations^{16,17}. In order to minimize effects of changes in the amount and composition of the plant VOC emissions, experiments with and without isoprene addition were conducted alternately on a daily basis.

Figure 1 presents the observed number concentration and volume concentration for particle formation from the VOCs emitted from the plants, and from the plant-emitted VOCs with the addition of isoprene. The presence of isoprene in plant-emitted VOCs decreases both the number and volume concentration compared to the case of particle formation from the VOC mixture from the plants alone. As indicated in Fig. 1, isoprene was switched off 3 hours after new

¹Institut ICG-2, Troposphäre, ²Institut ICG-3, Phytosphäre, Forschungszentrum Jülich, Jülich 52425, Germany. ³Department of Physics, University of Helsinki, 00014 Helsinki, Finland.

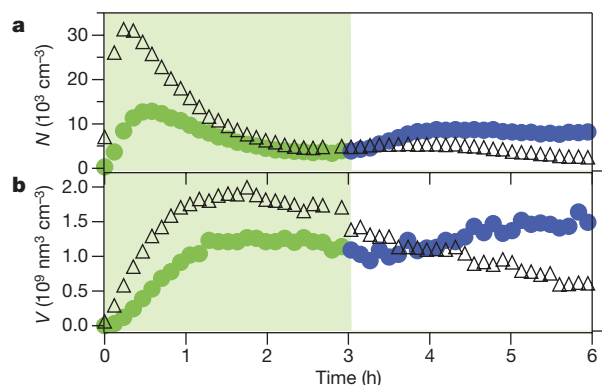


Figure 1 | Time series of particle properties for two experiments. **a**, Particle number concentration; **b**, particle volume concentration. The influence of isoprene on particle number concentration is clearly seen when comparing plant emissions plus isoprene (green filled circles) with plant emissions only (open triangles). The addition of isoprene reduces both particle number and volume concentration. Stopping the isoprene addition after 3 h (blue filled circles) results in an increase of both aerosol number and volume concentration.

particle formation had started. Total number and volume concentrations are increasing after the removal of isoprene. This clearly indicates that the presence of isoprene suppresses the formation of new particles with diameters larger than 5 nm.

The observation of a reduction of the total particle number and volume concentration indicates that isoprene affects the particle formation at an early stage. Our measurements (see Supplementary Information for details) show a significant reduction of OH concentrations in the presence of isoprene. Figure 2 shows the dependence of the nucleation rate on the OH concentration. The nearly linear power-law dependence of the nucleation rate on the OH concentration is indicative of the nucleation mechanism, where OH oxidation is the rate-limiting step determining the production rate of the nucleating vapours. Henceforth we regard the formation rate of particles with threshold diameters of 5 nm as the nucleation rate.

Thus the concentrations of nucleating vapours depend on the OH concentration. The identity of the nucleating vapour is unknown in our experiments. The nucleation rate is clearly dependent on the precursor VOC concentration¹⁸, showing that the VOC oxidation products are controlling the particle formation process.

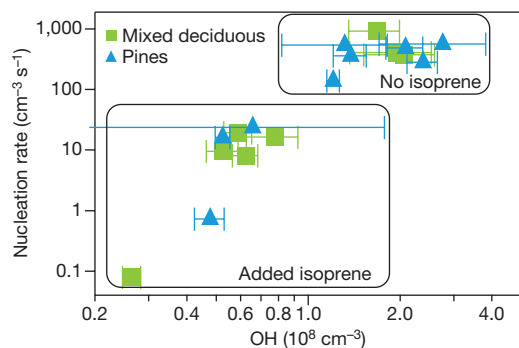


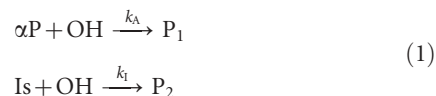
Figure 2 | Experimentally observed particle number as function of OH concentration. The OH concentration, [OH], was calculated from the decrease of camphene and 1,8-cineole in the chamber. Data for [OH] are the mean obtained from the calculations using both VOCs, and the error limits show minimum and maximum [OH] as calculated from either camphene or 1,8 cineole. The emissions were generated from a mixed deciduous stand (one birch, two beech, and one spruce; squares), and from two pines (triangles). Lower OH concentrations result in decreased particle number concentrations.

According to the nucleation theorem, the slope of the logarithm of nucleation rate versus the logarithm of concentration of the nucleating vapour determines the number of molecules in the critical cluster¹⁹. By analogy, we can read from the slope in Fig. 2 that the number of OH oxidation steps leading to observable particles is 3 to 4. This can involve parallel or consecutive OH oxidations or a combination of both.

This power-law exponent of 3–4 is approximately a factor 2 above the exponents observed in atmospheric nucleation. For atmospheric conditions, data are only available for the relation of new particle formation rates and the OH-dependent sulphuric acid concentration (see, for example, ref. 20). Under such conditions, the dependence shows an exponent of 1–2 (see, for example, refs 20, 21). In laboratory experiments (see, for example, ref. 22), this dependence has exponents of the order of 4–10. In the very recent literature, evidence is mounting that VOC oxidation products may play a key role in atmospheric nucleation events²³. So far no systematic information on the dependence of nucleation rates on VOC oxidation products is available, impeding the direct comparison of our results with ambient observations.

According to our measurements, isoprene OH oxidation products do not contribute to the nucleation process. Therefore, the main factor controlling the nucleation rate should be the concentration of OH radicals reacting with non-isoprene VOCs to form particles.

In order to allow a straightforward modelling approach to the observations, a set of experiments was conducted replacing the plant emissions by α -pinene only. If we consider the reactions:



we obtain simple expressions for the steady state concentrations of α -pinene ([αP]), isoprene ([Is]) and OH (Supplementary Information). Here P_1 denotes the first-generation oxidation product of α -pinene, and P_2 is the first-generation oxidation product of isoprene. We used the Master Chemical Mechanism (version 3.1; ref. 24) applied to the oxidation of α -pinene and isoprene to model a range of isoprene (Q_{Is}) versus α -pinene ($Q_{\alpha\text{P}}$) source rates. The resulting normalized source term of product P_1 (Q_{P_1}) is given by a fitted function of the form

$$\frac{Q_{\text{P}_1}}{Q_{\text{P}_1,0}} = \frac{1}{1 + \beta \frac{Q_{\text{Is}}}{Q_{\alpha\text{P}}}} \quad (2)$$

Here $Q_{\text{P}_1,0}$ is the source rate of P_1 in the absence of isoprene, and β ($=1.5 \pm 0.1$) is a fitting parameter derived from log-least squares fitting of the experimental data (see Supplementary Information).

Assuming that the nucleating vapour concentration C is proportional to Q_{P_1} and the rate of particle production (J) is proportional to C^n (see, for example, ref. 21), we obtain the following expression for the inhibition of particle production:

$$\frac{J}{J_0} = \left(\frac{1}{1 + \beta \frac{Q_{\text{Is}}}{Q_{\alpha\text{P}}}} \right)^n \quad (3)$$

where J_0 is the particle production rate in the absence of isoprene.

Figure 3 presents data of the observed suppression of particle formation as a function of the concentration ratio of isoprene to all other VOCs for the α -pinene and plant experiments. With increasing isoprene to monoterpene ratio, the number of particles decreases. Both data sets can be represented with equation (3), with n equal to 6.8 ± 0.5 for the α -pinene experiments and 3.7 ± 0.4 for the tree

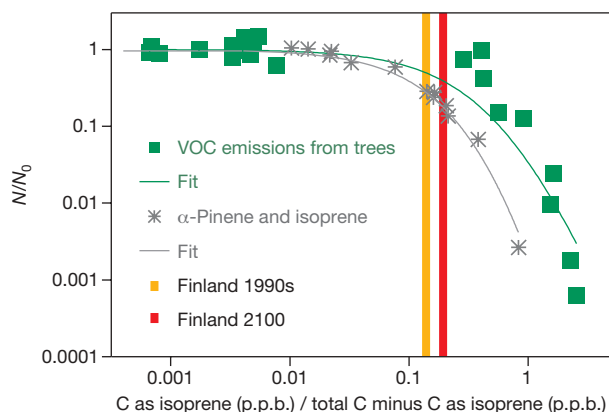


Figure 3 | Inhibition of particle number concentration as a function of the carbon based ratio of isoprene to other VOC concentrations. Data are shown for all plant emissions studied (filled squares) and α -pinene (asterisks). The fit functionality is derived from MCM modelling of the first generation of OH oxidation products of non-isoprene emissions: $N/N_0 = [1/(1 + 1.5R)]^n$, where $n = 3.7 \pm 0.4$ (green line) and $n = 6.8 \pm 0.5$ (grey line). Vertical bars indicate modelled concentration ratios of isoprene and monoterpenes for Finland²⁸ in the 1990s (orange) and in 2100 (red).

emissions. Note that our experiments were performed in the absence of seed aerosols. The experimental results are comparable to atmospheric conditions with negligible condensational sink only, and the expression for inhibition will only be applicable for such conditions. In comparison with the α -pinene experiments, we find that for tree-emitted VOCs a larger relative isoprene concentration is needed for the same suppression. This is consistent with the finding that the mixture of the VOCs emitted from trees forms more efficiently nucleating vapours than α -pinene¹⁸. The observed exponent of 3.7 ± 0.4 for the tree emissions is the same as the exponent of 3–4 derived from the dependence of the nucleation rate on OH (Fig. 2).

Comparing different ecosystems, the maximum ratio R of emitted isoprene carbon to monoterpene carbon is observed for temperate broadleaf summer green trees ($R = 56$; ref. 15), and the minimum R is reported for Finland country means ($R = 0.16$; ref. 25) and the south boreal forest ($R = 0.15$; ref. 26). The ratios used in our study range from 0 to 2.5 (see Fig. 3), and are thus representative for boreal and temperate forests.

The boreal forests are strong monoterpene emitters but have a maximum of R during summer²⁷. The observed inhibition of new particle formation by the presence of isoprene in a biogenic VOC mixture may thus explain observations from the boreal forest in which the number of nucleation events is lower during the summer period than in spring and autumn⁵.

Our research points to an efficient suppression of new particle formation by isoprene. This efficient suppression could be verified when an oak tree (*Quercus robur*) was added to the mixed stand. *Quercus robur* is a high isoprene emitter, resulting in an R of 19.5 in this experiment. No significant particle formation event was detectable under these conditions. The observed reduction in nucleation rate is highly correlated with the reduction of OH concentrations. The reaction with OH is the rate limiting step in the formation of new particles from plant-emitted VOCs.

We therefore conclude that through its effect on OH concentration isoprene plays an important role in atmospheric new particle formation. It is expected that future isoprene emissions from land vegetation will change as climate and land cover change. Our results show that besides the magnitude of VOC input into the atmosphere, the specific pattern of the emitted VOC affects SOA formation. It is to be expected that this effect will be most pronounced for regions already susceptible to nucleation, that is, regions with low pre-existing aerosol concentration. Certainly this includes the boreal forests. Owing to the local to regional dimensions of nucleation events,

isoprene emissions from, for example, monocultures adjacent to areas with large terpene emissions, are expected to regionally suppress new particle formation.

Future particle formation potential may thus critically depend on the relative increase of isoprene and other VOCs in response to climate change. In particular, an increase of the isoprene/monoterpene emission ratio R can lead to a suppression of nucleation events. If rising temperatures cause an increase in R , which in turn causes a decrease in particle formation rates, the observed suppression of particle formation by isoprene constitutes a positive feedback in the climate–biosphere–atmosphere interactions. Current estimates predict an increase of R from 0.14 in the 1990s to 0.19 in 2100²⁸ for boreal forests in Finland. From our results, we conclude that this implies a decrease of nucleation mode particles by 20% compared to present day values. If isoprene emissions were completely stopped in Finland, nucleation mode particles would be doubled. Following the approach used in ref. 4, a 20% decrease in nucleation mode particles translates into a 12% change in radiative forcing, decreasing the aerosol cooling effect. By changing R , land vegetation thus influences new particle formation and subsequent radiative forcing.

METHODS SUMMARY

Experiments were conducted in the Jülich plant aerosol chamber (JPAC), which has been described in detail elsewhere^{18,29}. In brief, the set-up consists of two borosilicate glass chambers. The chambers are housed in individual climate chambers. Each chamber can be temperature controlled individually between 10 and 50 °C with a stability of ± 0.5 °C. The chambers are operated as continuously stirred tank reactors, with residence times of 20 min in the plant chamber and 65 min in the reaction chamber. Purified air with an added CO₂ concentration of 350 p.p.m. and humidified with Milli-Q water was passed through the plant chamber. The air stream leaving the plant chamber carried the VOCs emitted by the plants in representative mixing ratios. This air was fed into the reaction chamber. Ozone concentration and relative humidity in the reaction chamber were controlled by two additional air streams and held at 80 p.p.b. and 60%, respectively (reaction chamber temperature, 15 °C). For photochemical generation of OH radicals, the reaction chamber was equipped with an internal ultraviolet source (Philips, TUV 40 W, $\lambda_{\text{max}} = 254$ nm). Plants used for these experiments were birch, beech, spruce and pines. Isoprene (Aldrich, 99% purity) was added at different concentrations to the plant chamber air through a varied flow from a diffusion source. For the reference experiments, α -pinene (Fluka, 99% purity) and isoprene were added to the reaction chamber to give concentrations ranging from 7 to 12 p.p.b. and 0 to 20 p.p.b., respectively. Aerosol number concentrations were measured with a condensation particle counter (CPC) (TSI Model 3022A). The maximum number concentration measurable was $1 \times 10^7 \text{ cm}^{-3}$. The size distribution of the particles was measured with a scanning mobility particle sizer (SMPS) system (TSI Model 3934), consisting of a TSI Model 3071 electrostatic classifier and a TSI Model 3025 CPC. The SMPS was operated to measure particles between 15 and 750 nm.

Received 11 December 2008; accepted 13 July 2009.

- Kulmala, M. et al. A new feedback mechanism linking forests, aerosols, and climate. *Atmos. Chem. Phys.* **4**, 557–562 (2004).
- Guenther, A. et al. A global model of natural volatile organic compound emissions. *J. Geophys. Res.* **100**, 8873–8892 (1995).
- Tunved, P. et al. High natural aerosol loading over boreal forests. *Science* **312**, 261–263 (2006).
- Kerminen, V. M., Lihavainen, H., Komppula, M., Viisanen, Y. & Kulmala, M. Direct observational evidence linking atmospheric aerosol formation and cloud droplet activation. *Geophys. Res. Lett.* **32**, L14803, doi:10.1029/2005GL023130 (2005).
- Kulmala, M. et al. Formation and growth rates of ultrafine atmospheric particles: a review of observations. *J. Aerosol Sci.* **35**, 143–176 (2004).
- Guenther, A. et al. Estimates of global terrestrial isoprene emissions using MEGAN (Model of Emissions of Gases and Aerosols from Nature). *Atmos. Chem. Phys.* **6**, 3181–3210 (2006).
- Sharkey, T. Isoprene emission from plants: why and how. *Ann. Bot. (Lond.)* **101**, 5–18 (2008).
- Went, F. W. Blue hazes in the atmosphere. *Nature* **187**, 641–643 (1960).
- Tsigaridis, K. & Kanakidou, M. Global modelling of secondary organic aerosol in the troposphere: a sensitivity analysis. *Atmos. Chem. Phys.* **3**, 1849–1869 (2003).
- Kanakidou, M. et al. Organic aerosol and global climate modelling: a review. *Atmos. Chem. Phys.* **5**, 1053–1123 (2005).
- Goldstein, A. H. & Galbally, I. E. Known and unexplored organic constituents in the Earth's atmosphere. *Environ. Sci. Technol.* **41**, 1515–1521 (2007).

12. Tunved, P. *et al.* The natural aerosol over Northern Europe and its relation to anthropogenic emissions—implications of important climate feedbacks. *Tellus B* **60**, 473–484 (2008).
13. Wiedinmyer, C., Tie, X. X., Guenther, A., Neilson, R. & Granier, C. Future changes in biogenic isoprene emissions: how might they affect regional and global atmospheric chemistry? *Earth Interact.* **10**, 1–16 (2006).
14. Lathiere, J., Hauglustaine, D. A., De Noblet-Ducoudre, N., Krinner, G. & Folberth, G. A. Past and future changes in biogenic volatile organic compound emissions simulated with a global dynamic vegetation model. *Geophys. Res. Lett.* **32**, L20818, doi:10.1029/2005GL024164 (2005).
15. Lathiere, J. *et al.* Impact of climate variability and land use changes on global biogenic volatile organic compound emissions. *Atmos. Chem. Phys.* **6**, 2129–2146 (2006).
16. Greenberg, J. P. *et al.* Tethered balloon measurements of biogenic VOCs in the atmospheric boundary layer. *Atmos. Environ.* **33**, 855–867 (1999).
17. Kesselmeier, J. *et al.* Concentrations and species composition of atmospheric volatile organic compounds (VOCs) as observed during the wet and dry season in Rondonia (Amazonia). *J. Geophys. Res.* **107**, doi:10.1029/2000JD000267 (2002).
18. Mentel, T. F. *et al.* Photochemical production of aerosols from real plant emissions. *Atmos. Chem. Phys.* **9**, 3041–3094 (2009).
19. Kashcheyev, D. On the relation between nucleation work, nucleus size, and nucleation rate. *J. Chem. Phys.* **76**, 5098–5102 (1982).
20. Weber, R. J. *et al.* Measured atmospheric new particle formation rates: implications for nucleation mechanisms. *Chem. Eng. Commun.* **151**, 53–64 (1996).
21. Riipinen, I. *et al.* Connections between atmospheric sulphuric acid and new particle formation during QUEST III–IV campaigns in Heidelberg and Hyytiälä. *Atmos. Chem. Phys.* **7**, 1899–1914 (2007).
22. Berndt, T., Boge, O., Stratmann, F., Heintzenberg, J. & Kulmala, M. Rapid formation of sulfuric acid particles at near-atmospheric conditions. *Science* **307**, 698–700 (2005).
23. Laaksonen, A. *et al.* The role of VOC oxidation products in continental new particle formation. *Atmos. Chem. Phys.* **8**, 2657–2665 (2008).
24. Bloss, C. *et al.* Development of a detailed chemical mechanism (MCMv3.1) for the atmospheric oxidation of aromatic hydrocarbons. *Atmos. Chem. Phys.* **5**, 641–664 (2005).
25. Lindfors, V. & Laurila, T. Biogenic volatile organic compound (VOC) emissions from forests in Finland. *Boreal Environ. Res.* **5**, 95–113 (2000).
26. Lindfors, V., Laurila, T., Hakola, H., Steinbrecher, R. & Rinne, J. Modeling speciated terpene emissions from the European boreal forest. *Atmos. Environ.* **34**, 4983–4996 (2000).
27. Hakola, H. *et al.* Seasonal variation of VOC concentrations above a boreal coniferous forest. *Atmos. Environ.* **37**, 1623–1634 (2003).
28. Kellomaki, S. Impact of global warming on the tree species composition of boreal forests in Finland and effects on emissions of isoprenoids. *Glob. Change Biol.* **7**, 531–544 (2001).
29. Heiden, A. C., Kobel, K., Langebartels, C., Schuh-Thomas, G. & Wildt, J. Emissions of oxygenated volatile organic compounds from plants Part I: Emissions from lipooxygenase activity. *J. Atmos. Chem.* **45**, 143–172 (2003).

Supplementary Information is linked to the online version of the paper at www.nature.com/nature.

Acknowledgements We gratefully acknowledge support by the European Commission (IP-EUCAARI, contract number 036833-2).

Author Contributions A.K.-S., T.F.M. and J.W. developed the basic JPAC set-up and designed the study. All measurements were conducted by E.K., T.H., R.T. and R.U. Interpretation of the data was performed by A.K.-S., M.D.M. and J.W. A.K.-S. wrote the manuscript. A.K.-S., J.W., T.F.M., M.D.M. and A.W. discussed and commented on the manuscript. A.W. and U.S. provided the working environment and financial support.

Author Information Reprints and permissions information is available at www.nature.com/reprints. Correspondence and requests for materials should be addressed to A.K.-S. (a.kiendler-scharr@fz-juelich.de).

Holocene thinning of the Greenland ice sheet

B. M. Vinther¹, S. L. Buchardt¹, H. B. Clausen¹, D. Dahl-Jensen¹, S. J. Johnsen¹, D. A. Fisher², R. M. Koerner^{2,†}, D. Raynaud³, V. Lipenkov⁴, K. K. Andersen¹, T. Blunier¹, S. O. Rasmussen¹, J. P. Steffensen¹ & A. M. Svensson¹

On entering an era of global warming, the stability of the Greenland ice sheet (GIS) is an important concern¹, especially in the light of new evidence of rapidly changing flow and melt conditions at the GIS margins². Studying the response of the GIS to past climatic change may help to advance our understanding of GIS dynamics. The previous interpretation of evidence from stable isotopes ($\delta^{18}\text{O}$) in water from GIS ice cores was that Holocene climate variability on the GIS differed spatially³ and that a consistent Holocene climate optimum—the unusually warm period from about 9,000 to 6,000 years ago found in many northern-latitude palaeoclimate records⁴—did not exist. Here we extract both the Greenland Holocene temperature history and the evolution of GIS surface elevation at four GIS locations. We achieve this by comparing $\delta^{18}\text{O}$ from GIS ice cores^{3,5} with $\delta^{18}\text{O}$ from ice cores from small marginal icecaps. Contrary to the earlier interpretation of $\delta^{18}\text{O}$ evidence from ice cores^{3,6}, our new temperature history reveals a pronounced Holocene climatic optimum in Greenland coinciding with maximum thinning near the GIS margins. Our $\delta^{18}\text{O}$ -based results are corroborated by the air content of ice cores, a proxy for surface elevation⁷. State-of-the-art ice sheet models are generally found to be underestimating the extent and changes in GIS elevation and area; our findings may help to improve the ability of models to reproduce the GIS response to Holocene climate.

Ice cores from six locations^{3,8} have now been synchronized to the Greenland Ice Core Chronology 2005 (GICC05) throughout the

Holocene epoch (Fig. 1a). The GICC05 annual layer counting was performed simultaneously on the DYE-3, GRIP and NGRIP ice cores for the entire Holocene^{9,10}. For the Agassiz¹¹, Renland¹¹ and Camp Century ice cores the timescale was transferred by using volcanic markers identifiable in electrical conductivity measurements¹² (Supplementary Information). The six synchronized Holocene $\delta^{18}\text{O}$ records show large differences in millennial scale trends (Fig. 1b). All $\delta^{18}\text{O}$ records were obtained in the same laboratory (the Copenhagen Isotope Laboratory), ensuring maximum confidence in the homogeneity of the data sets. The differences are therefore real features that need to be understood and explained before firm conclusions about the evolution of Greenland climate during the Holocene can be supported by the data.

Changes in regional temperatures, moisture source regions, moisture transport and precipitation seasonality affect the $\delta^{18}\text{O}$ of precipitation⁶. However, all these parameters are expected to produce regional patterns of change, implying that trends in nearby $\delta^{18}\text{O}$ records should always be similar, except where the records are heavily influenced by a combination of ice flow and post-deposition phenomena, such as wind-scouring. Ice cores from Agassiz and Renland are retrieved from icecap domes and are therefore not influenced by ice flow. The Camp Century site is only slightly affected by a steady ice flow, yet the trends in the neighbouring Agassiz and Camp Century cores are dissimilar; in fact, the $\delta^{18}\text{O}$ signal at Agassiz is much more similar to the signal recorded at Renland on the other side of the GIS.

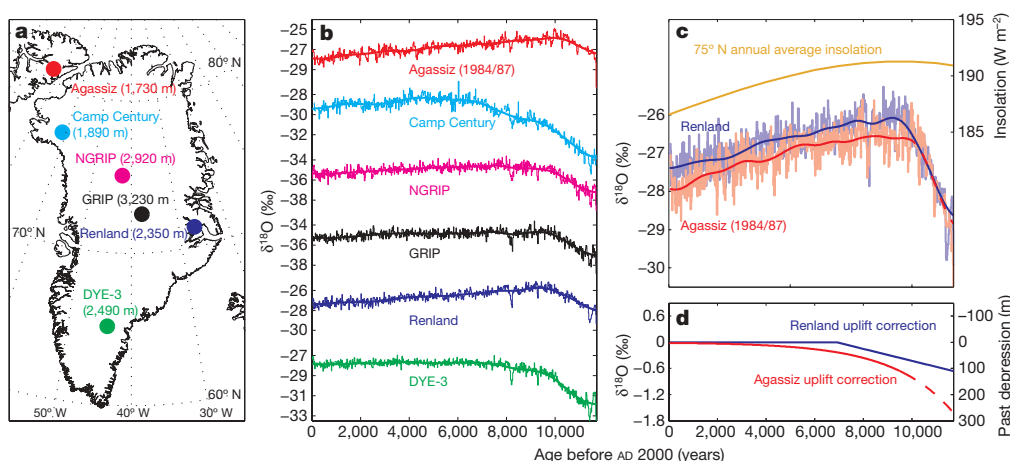


Figure 1 | Holocene $\delta^{18}\text{O}$ records. **a**, Drill site locations for the ice cores that have been cross-dated to the GICC05 timescale. Site elevations are given in parenthesis. **b**, 20-year averages and millennial scale trends of $\delta^{18}\text{O}$ during the Holocene as observed in ice core records from six locations in Greenland and Canada. All $\delta^{18}\text{O}$ values are expressed with respect to Vienna standard

mean ocean water (V-SMOW). **c**, Uplift-corrected Renland and Agassiz Holocene $\delta^{18}\text{O}$ values: 20-year averages and millennial scale trends in the Agassiz and Renland Holocene $\delta^{18}\text{O}$ records. Annual average insolation at 75°N is shown in orange. **d**, Agassiz and Renland post-glacial bedrock uplift histories and corresponding $\delta^{18}\text{O}$ correction values.

¹Centre for Ice and Climate, Niels Bohr Institute, University of Copenhagen, Juliane Maries Vej 30, DK-2100 Copenhagen Oe, Denmark. ²Glaciology Section, Terrain Sciences Division, Geological Survey of Canada, 601 Booth Street, Ottawa, Ontario, Canada K1A 0E8. ³Laboratoire de Glaciologie et Géophysique de l'Environnement, CNRS/UJF, BP 96, 38402 Saint-Martin-d'Hères, France. ⁴Arctic and Antarctic Research Institute, 38 Bering Street, St Petersburg 199397, Russia.

†Deceased.

Given the dissimilarity of some neighbouring $\delta^{18}\text{O}$ records, a more likely cause of the differences in $\delta^{18}\text{O}$ trends is past changes in the elevation of the GIS. Elevation change influences trends in the $\delta^{18}\text{O}$ records (Supplementary Information), and the differences in the long-term $\delta^{18}\text{O}$ trends seem to be related to changing GIS elevation: the pairs of records from the centre of the ice sheet (GRIP and NGRIP), those closer to the margin of the ice sheet (DYE-3 and Camp Century) and those from the small icecaps close to the GIS (Agassiz and Renland) are all similar.

For the GIS ice core records, the hypothesis that elevation change affected $\delta^{18}\text{O}$ in the past is difficult to evaluate, because little is known of the elevation history of the GIS. Ice sheet modelling is of little help because modelled elevation histories for GIS are highly dependent on poorly known boundary conditions, such as the past positions of the GIS margin¹³. However, for the small Agassiz and Renland icecaps it is possible to reconstruct past elevation histories with some confidence. Neither of these icecaps is believed to have experienced significant change in ice sheet thickness during most of the Holocene as a result of topographical constraints and the limited thickness of the icecaps^{8,14} (Supplementary Information). Both the Renland and the Agassiz bedrocks have experienced a significant post-glacial uplift. For Renland the uplift resulted from the retreat of the GIS, whereas the Agassiz uplift was caused by the disintegration of the Innuitian ice sheet that covered most of the Queen Elizabeth Islands during the last glaciation¹⁵. For both locations robust estimates of bedrock elevation have been obtained through studies of past changes in sea level in nearby fjords^{15,16}. The elevation history of the Renland bedrock is based on such studies throughout the Holocene, whereas that of the Agassiz bedrock is based on data sets back to 9.5 kyr before AD 2000. For the period from 9.5 kyr ago back to 11.7 kyr ago Agassiz bedrock elevation can be estimated by extrapolation, using the observed exponential half-life for the bedrock elevation change in the period 0–9.5 kyr before AD 2000 (ref. 17). If we assume that Agassiz and Renland $\delta^{18}\text{O}$ records have not been significantly influenced by changes in ice thickness during the Holocene, it is possible to correct the $\delta^{18}\text{O}$ records for past elevation changes, simply by using their respective bedrock elevation histories and the observed Greenland $\delta^{18}\text{O}$ –height relationship (Fig. 1c, d, and Supplementary Information).

The similarity between the uplift-corrected Agassiz and Renland $\delta^{18}\text{O}$ records is astounding given that the two icecaps are separated by about 1,500 km and by the entire GIS. The similarity suggests that

Greenland climate during the Holocene was homogeneous, with the same millennial-scale $\delta^{18}\text{O}$ evolution both east and northwest of the ice sheet. The homogeneous climatic history for the Greenlandic region is probably related to the regional change in solar insolation¹⁸, at least for the past 10 kyr.

Given the similarity of the Agassiz and Renland elevation-corrected $\delta^{18}\text{O}$ records, we assume that their common millennial-scale $\delta^{18}\text{O}$ trends would have been present in the ice cores from the GIS if the GIS had not changed surface elevation. The elevation histories for the four drill sites on the GIS (Fig. 2a) can then be estimated from the changes in difference between $\delta^{18}\text{O}$ records from the GIS sites and uplift-corrected $\delta^{18}\text{O}$ records from the two adjacent icecaps. The changes in elevation seen in Fig. 2a are corrected for upstream effects due to ice flow at the drill sites^{19,20} (Supplementary Information), thus showing changes in GIS elevation at the locations of the four drill sites. The derivation of the uncertainty bands for the changes in GIS elevation shown in Fig. 2a is discussed in the Supplementary Information.

From Fig. 2a it is seen that the initial response of the GIS to Holocene climatic conditions was a slight increase in elevation at all locations right after the onset of the Holocene (most probably in response to increased precipitation and bedrock uplift). Next the GIS responded to the effects of increased melt at the margins and ice break-off because of rising sea level. The melt and ice break-off induced rapid thinning at the Camp Century and DYE-3 sites, which are located relatively close to the margin. Then the thinning process propagated slowly towards the centre of the GIS, reaching GRIP at the present summit about 4,000 years after the onset of the Holocene.

The total gas content of air bubbles trapped in the ice is the only other known parameter in ice cores that is significantly and directly influenced by elevation change. A comparison between the elevation histories for GRIP and Camp Century and their total gas content records^{7,21} (Fig. 2b) shows an excellent qualitative agreement between past elevation change and change in total gas content. A detailed quantitative study of the differences between Camp Century and GRIP elevation and total gas content histories also yields strong support for the isotope-based elevation histories (Supplementary Information).

Figure 2c shows a reconstruction of the evolution of Greenland temperatures during the Holocene. This temperature reconstruction is based on Agassiz and Renland average $\delta^{18}\text{O}$ values, corrected for uplift and changes in $\delta^{18}\text{O}$ content of the ocean²². The conversion

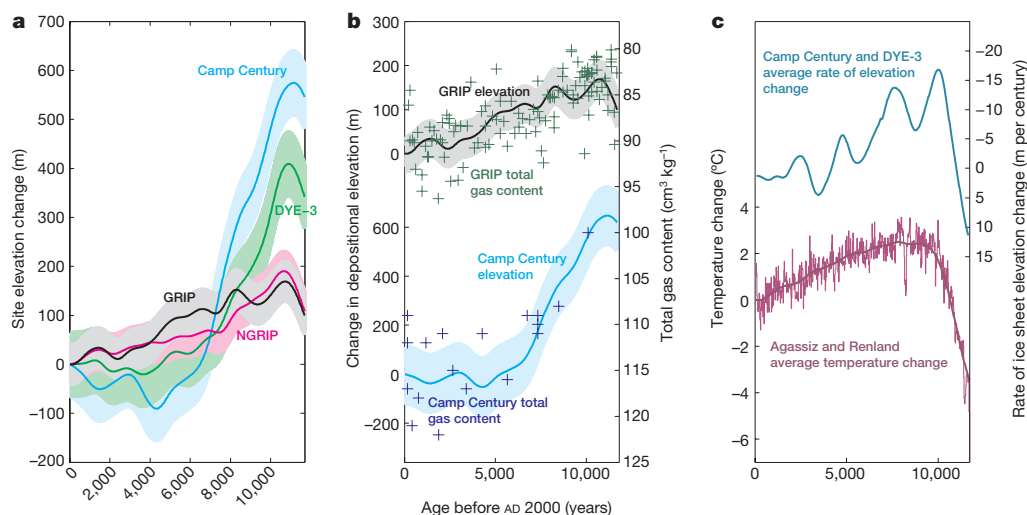


Figure 2 | Holocene elevation change histories for Greenland ice sheet locations. **a**, Changes in elevation at the drill sites, after correction for ice-flow-related upstream effects. The shaded bands show the 1 σ uncertainties on the elevation histories. **b**, Depositional elevation histories at the GRIP and Camp Century drill sites compared with total gas measurements

performed on the two ice cores. **c**, Average rate of elevation change of ice sheets at the DYE-3 and Camp Century drill sites compared with temperature change in Greenland derived from Agassiz and Renland $\delta^{18}\text{O}$ records.

from $\delta^{18}\text{O}$ to temperature has been obtained through a calibration with borehole temperatures from the Camp Century, DYE-3, GRIP and NGRIP drill sites²³. The borehole temperature profiles are fully consistent with the Agassiz and Renland average $\delta^{18}\text{O}$ record, supporting our assertion that the climate in and around Greenland was homogeneous during the Holocene (Supplementary Information).

The average rate of elevation change at the Camp Century and DYE-3 drill sites is also shown in Fig. 2c. It can be inferred that elevations at these two sites near the margin of the GIS respond rapidly to Greenland temperature change. The most significant periods of decrease in elevation coincided with the climatic optimum 7–10 kyr before AD 2000. This suggests that the GIS responds significantly to a temperature increase of a few degrees Celsius, even though part of the GIS response in the early Holocene was also associated with ice break-off resulting from rising sea level. The colder climate prevailing during the past two millennia induced a slight increase in elevation of the GIS at these sites.

The 600-m decrease in surface elevation observed at Camp Century in the period from 11 to 6 kyr before AD 2000 can be taken as strong support for the finding that the Hall basin, the Kennedy channel and the Kane basin were completely covered by sheet ice during the earliest Holocene, thereby connecting Greenland to the Innuitian ice sheet on Ellesmere Island^{15,24}. The breakdown of this interconnection and the retreat of the GIS from the continental shelf edge in Melville Bay then led to a significant decrease in surface elevation at Camp Century. At DYE-3, GIS elevation was reduced by about 400 m as the width of the southern GIS probably decreased by one-third during the transition from glacial to Holocene climatic conditions²⁵.

The novel concept of using the combined evidence from Greenland and Canadian ice cores to extract both a Holocene temperature history (Fig. 2c) and Holocene elevation histories (Fig. 2a) for the GIS is essential for the validation of efforts to model the evolution of the GIS. By comparing the results of two conceptual

modelling efforts^{13,26} with the new GRIP Holocene elevation curve it is possible to give a semi-empirical estimate of the position of the GIS margin during the last glaciation, because only a marginal position at the continental shelf edge is consistent with the observed GRIP elevation history (Fig. 3a). A comparison of the GRIP elevation change with more recent state-of-the-art three-dimensional thermomechanical models of ice sheets^{27–30} strongly suggests that none of these models captures the evolution in GRIP elevation during the Holocene (Fig. 3b). The results of the conceptual modelling shown in Fig. 3a indicate that the three-dimensional models fail to advance the GIS sufficiently far onto the continental shelf during the last glaciation, possibly because of an insufficient understanding of interactions between ice sheets and oceans. The poor performance of the three-dimensional models might also be a consequence of similarly simplified climatic forcing series being applied in all model runs, for example an underestimation of the amplitude of the Holocene climatic optimum in Greenland.

The clear Greenland Holocene climatic optimum now unmasked in $\delta^{18}\text{O}$ records from GIS ice cores brings these records into line with borehole temperature data. This rehabilitates $\delta^{18}\text{O}$ as a reliable temperature proxy, paving the way for temperature reconstructions based on high-resolution $\delta^{18}\text{O}$ records from ice cores. The GIS temperature and elevation histories presented here also suggest that the GIS responds more vigorously to climatic change than indicated by the three-dimensional models used for GIS projections. It is therefore entirely possible that a future temperature increase of a few degrees Celsius in Greenland will result in GIS mass loss and contribution to sea level change larger than previously projected.

Received 5 January; accepted 24 July 2009.

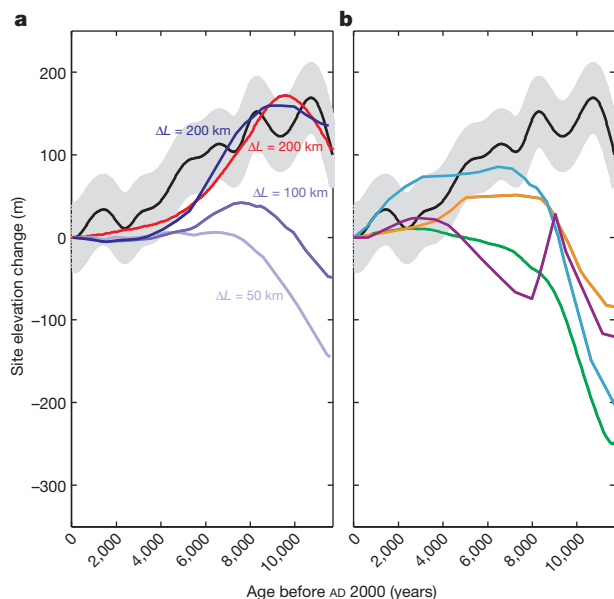


Figure 3 | Empirical and modelled Holocene elevation change histories for the summit of the Greenland ice sheet. **a**, Elevation change at the GRIP drill site (black line) compared with four different estimates from two different simple models of ice sheets (red line, ref. 26; blue lines, ref. 13). The shaded band shows the 1σ uncertainty in the elevation history. The modelled estimates are based on three different assumed maximum advances (ΔL) of the margin of the Greenland ice sheet during the Last Glacial Maximum. **b**, Change in elevation at the GRIP drill site (black line) compared with elevation estimates from four different complex three-dimensional thermomechanical models of ice sheets (orange, ref. 27; magenta, ref. 28; green, ref. 29; turquoise, ref. 30). The shaded band shows the 1σ uncertainty in the elevation history.

- Alley, R. B. *et al.* Ice-sheet and sea-level changes. *Science* **310**, 456–460 (2005).
- Rignot, E. & Kanagaratnam, P. Changes in the velocity structure of the Greenland Ice Sheet. *Science* **311**, 986–990 (2006).
- Johnsen, S. J. & Vinther, B. M. in *Encyclopedia of Quaternary Science* (ed. Elias, S.) Vol. 2 1250–1258 (Elsevier, 2007).
- Kaufman, D. S. *et al.* Holocene thermal maximum in the western Arctic (0–180°W). *Quat. Sci. Rev.* **23**, 529–560 (2004).
- Fisher, D. A. *et al.* Inter-comparison of ice core $\delta^{18}\text{O}$ and precipitation records from sites in Canada and Greenland over the last 3500 years and over the last few centuries in detail using EOF techniques. *NATO ASI Ser.* **141**, 297–328 (1996).
- Masson-Delmotte, V. *et al.* Holocene climatic changes in Greenland: different deuterium excess signals at Greenland Ice Core Project (GRIP) and NorthGRIP. *J. Geophys. Res.* **110**, D14102 (2005).
- Raynaud, D. & Lorius, C. Climatic implications of total gas content in ice at Camp Century. *Nature* **243**, 283–284 (1973).
- Koerner, R. M. & Fisher, D. A. A record of Holocene summer climate from a Canadian high-Arctic ice core. *Nature* **343**, 630–632 (1990).
- Rasmussen, S. O. *et al.* A new Greenland ice core chronology for the last glacial termination. *J. Geophys. Res.* **111**, D06102 doi:10.1029/2005JD006079 (2006).
- Vinther, B. M. *et al.* A synchronized dating of three Greenland ice cores throughout the Holocene. *J. Geophys. Res.* **111**, D13102, doi:10.1029/2005JD006921 (2006).
- Vinther, B. M. *et al.* Synchronizing ice cores from the Renland and Agassiz ice caps to the Greenland Ice Core Chronology. *J. Geophys. Res.* **113**, D08115, doi:10.1029/2007JD009143 (2008).
- Hammer, C. U. *et al.* Greenland ice sheet evidence of post-glacial volcanism and its climatic impact. *Nature* **288**, 230–235 (1980).
- Cuffey, K. M. & Clow, G. D. Temperature, accumulation, and ice sheet elevation in central Greenland through the last deglacial transition. *J. Geophys. Res.* **102**, 26383–26396 (1997).
- Johnsen, S. J. *et al.* A deep ice core from east Greenland. *Meddr Grøn.* **29**, 3–29 (1992).
- Blake, W. Jr. Studies of glacial history in Arctic Canada. I. Pumice, radiocarbon dates and differential post-glacial uplift in the eastern Queen Elizabeth Islands. *Can. J. Earth Sci.* **7**, 634–664 (1970).
- Funder, S. Holocene stratigraphy and vegetation history in the Scoresby Sund area, East Greenland. *Grøn. Geol. Unders. Bull.* **129** (1978).
- Dyke, A. S. & Peltier, W. R. Forms, response times and variability of relative sea-level curves, glaciated North America. *Geomorphology* **32**, 315–333 (2000).
- Laskar, J. *et al.* A long term numerical solution for the insolation quantities of Earth. *Astron. Astrophys.* **428**, 261–285 (2004).
- Buchardt, S. L. & Dahl-Jensen, D. Estimating the basal melt rate at NorthGRIP using a Monte Carlo technique. *Ann. Glaciol.* **45**, 137–142 (2007).
- Reeh, N. *et al.* Dating the Dye-3 ice core by flow model calculations. *Am. Geophys. Un. Geophys. Monogr.* **33**, 57–65 (1985).

21. Raynaud, D. *et al.* Air content along the Greenland Ice Core Project core: a record of surface climatic parameters and elevation in central Greenland. *J. Geophys. Res.* **102**, 26607–26613 (1997).
 22. Waelbroeck, C. *et al.* Sea-level and deep water temperature changes derived from benthic foraminifera isotopic records. *Quat. Sci. Rev.* **21**, 295–305 (2002).
 23. Dahl-Jensen, D. *et al.* Past temperatures directly from the Greenland ice sheet. *Science* **282**, 268–271 (1998).
 24. Blake, W. & Jr.. Glaciated landscapes along Smith Sound, Ellesmere Island, Canada and Greenland. *Ann. Glaciol.* **28**, 40–46 (1999).
 25. Long, A. J. *et al.* Late Weichselian relative sea-level changes and ice sheet history in southeast Greenland. *Earth Planet. Sci. Lett.* **272**, 8–18 (2008).
 26. Johnsen, S. J. *et al.* Greenland palaeotemperatures derived from GRIP bore hole temperature and ice core isotope profiles. *Tellus B* **47**, 624–629 (1995).
 27. Huybrechts, P. Sea-level changes at the LGM from ice-dynamic reconstructions of the Greenland and Antarctic ice sheets during the glacial cycles. *Quat. Sci. Rev.* **21**, 203–231 (2002).
 28. Tarasov, L. & Peltier, W. R. Greenland glacial history, borehole constraints and Eemian extent. *J. Geophys. Res.* **108** (B3), 2124–2143 (2003).
 29. Greve, R. Relation of measured basal temperatures and the spatial distribution of the geothermal heat flux for the Greenland ice sheet. *Ann. Glaciol.* **42**, 424–432 (2005).
 30. Lhomme, N. *et al.* Tracer transport in the Greenland Ice Sheet: constraints on ice cores and glacial history. *Quat. Sci. Rev.* **24**, 173–194 (2005).
- Supplementary Information** is linked to the online version of the paper at www.nature.com/nature.
- Acknowledgements** We thank laboratory technician A. Boas, who meticulously performed most of the stable-isotope measurements presented in this paper during her 38 years at the Copenhagen stable isotope laboratory; W. Blake Jr for providing his insight, suggestions and corrections during the drafting of this paper; R. Greve for providing elevation data from his GIS modelling effort. B.M.V. thanks the Carlsberg Foundation for funding, and the Climatic Research Unit at University of East Anglia for hosting his research during all of 2007. V.L. and D.R. thank the Groupement de Recherche Européen (GDRE) Vostok (Institut national des sciences de l'Univers (INSU)/Centre national de la recherche scientifique (CNRS) for funding and Russian Foundation for Basic Research (RFBR)–CNRS grant 05-05-66801 for support.
- Author Information** Reprints and permissions information is available at www.nature.com/reprints. Correspondence and requests for materials should be addressed to B.M.V. (bo@gfy.ku.dk).

Genotypic sex determination enabled adaptive radiations of extinct marine reptiles

Chris L. Organ¹, Daniel E. Janes¹, Andrew Meade² & Mark Pagel²

Adaptive radiations often follow the evolution of key traits, such as the origin of the amniotic egg and the subsequent radiation of terrestrial vertebrates. The mechanism by which a species determines the sex of its offspring has been linked to critical ecological and life-history traits^{1–3} but not to major adaptive radiations, in part because sex-determining mechanisms do not fossilize. Here we establish a previously unknown coevolutionary relationship in 94 amniote species between sex-determining mechanism and whether a species bears live young or lays eggs. We use that relationship to predict the sex-determining mechanism in three independent lineages of extinct Mesozoic marine reptiles (mosasaurs, sauropterygians and ichthyosaurs), each of which is known from fossils to have evolved live birth^{4–7}. Our results indicate that each lineage evolved genotypic sex determination before acquiring live birth. This enabled their pelagic radiations, where the relatively stable temperatures of the open ocean constrain temperature-dependent sex determination in amniote species. Freed from the need to move and nest on land^{4,5,8}, extreme physical adaptations to a pelagic lifestyle evolved in each group, such as the fluked tails, dorsal fins and wing-shaped limbs of ichthyosaurs. With the inclusion of ichthyosaurs, mosasaurs and sauropterygians, genotypic sex determination is present in all known fully pelagic amniote groups (sea snakes, sirenians and cetaceans), suggesting that this mode of sex determination and the subsequent evolution of live birth are key traits required for marine adaptive radiations in amniote lineages.

Sea snakes, which comprise more than 60 species, are the only living obligate seagoing reptiles and they rely on sex chromosomes (a genotypic mechanism) to determine the sex of their liveborn offspring (although some semi-aquatic elapid snakes such as *Laticauda* lay eggs on land). Roughly 20% of non-avian reptile species give birth to live offspring (viviparity); the trait is thought to have evolved at least 100 times in lizards and snakes⁹ alone and may be an adaptation critical for survival, as it is among species living in cold climates¹⁰. Other living marine reptiles include sea turtles and saltwater crocodiles, totalling fewer than ten species, all of which lay eggs on land, relying on environmental temperature to determine the sex of their offspring. Temperature-dependent sex determination (TSD) may be adaptive in environments that confer differential fitness on males and females³, whereas genotypic sex determination (GSD) permits balanced offspring sex ratios and buffers a species' sex determination from environmental fluctuations. Researchers have reported at least six independent origins of GSD in turtles and at least three losses of the trait in lizards^{11,12}.

Life-history theory suggests that various reproductive, physiological and behavioural traits may have coevolved because they result in differential reproductive success in populations¹³. Notwithstanding the individual importance of sex determination and reproductive mode to life history and reproductive success^{3,10,14}, their coevolutionary

relationship has remained unclear. We produced a data set that scored 94 extant amniote species for their reproductive mode and sex-determining mechanism (Fig. 1), and used it to test for an evolutionary correlation in these two traits¹⁵. The method we used employed a reversible-jump Markov-chain Monte Carlo algorithm to find a Bayesian posterior probability distribution of models of correlated change, and simultaneously estimated the rates at which the traits changed between their possible states (Fig. 2a). We find that sex-determining mechanism and reproductive mode coevolved throughout the history of amniotes (Bayes factor test of correlated evolution ~ 6). Viviparity depends on the prior evolution of GSD (that is, $q_{12} > q_{43}$, Bayes factor ~ 3 ; Fig. 2a), whereas oviparity occurs in combination with either sex-determining mechanism (that is, $q_{21} = q_{34}$).

Sex-determining mechanisms are important adaptations for survival in many species^{1–3}, but their evolutionary history and connection to major adaptive radiations within amniotes has remained unclear because the trait does not fossilize. However, the sex chromosomes of cetaceans and sirenians (XX in females and XY in males) and sea snakes (ZZ in males and ZW in females) suggest that GSD may be a trait required for pelagic radiations in amniotes. Three separate lineages of extinct reptiles (mosasaurs, sauropterygians and ichthyosaurs) also underwent pelagic radiations during the Mesozoic era, and recent discoveries^{4–7} show that they independently evolved viviparity, with parturition occurring underwater^{4–7,16}. All three groups of extinct marine reptiles breathed air, but they evolved other various adaptations to life in the open ocean, such as fin-shaped limbs, scale reduction (with the exception of mosasaurs), streamlined bodies and changes in bone histology¹⁵. Ichthyosaurs, and possibly mosasaurs, even evolved tail-first birth, an adaptation that helps air-breathing cetacean and sirenian neonates to avoid drowning during birth¹⁷. These traits were critical for their evolutionary transition to, and pelagic radiation within, the open ocean^{4,5}.

To test the prediction that GSD had a function in promoting adaptive radiations in amniotes (and that it would therefore be found in extinct marine reptiles), we developed a Bayesian approach that made use of the correlation between GSD and reproductive mode to predict the unknown sex-determining mechanism of extinct species whose position in the phylogeny of amniotes can be identified. The method used the posterior distribution of evolutionary models derived from the analysis of the living species to produce posterior predictive distributions for the unknown character states in the extinct species. Posterior predictions are summed over the distribution of evolutionary models to account for uncertainty about the overall model.

As a test of the approach we first predicted trait values for seven species whose sex-determining mechanism and reproductive mode were both known. The approach correctly predicted GSD in a viviparous snake, *Vipera aspis* (posterior probability of GSD 99.6%), and *Propalaeotherium*, an extinct horse for which pregnant specimens are

¹Museum of Comparative Zoology, Harvard University, 26 Oxford Street, Cambridge, Massachusetts 02138, USA. ²School of Biological Sciences, University of Reading, Reading RG6 6AJ, UK.

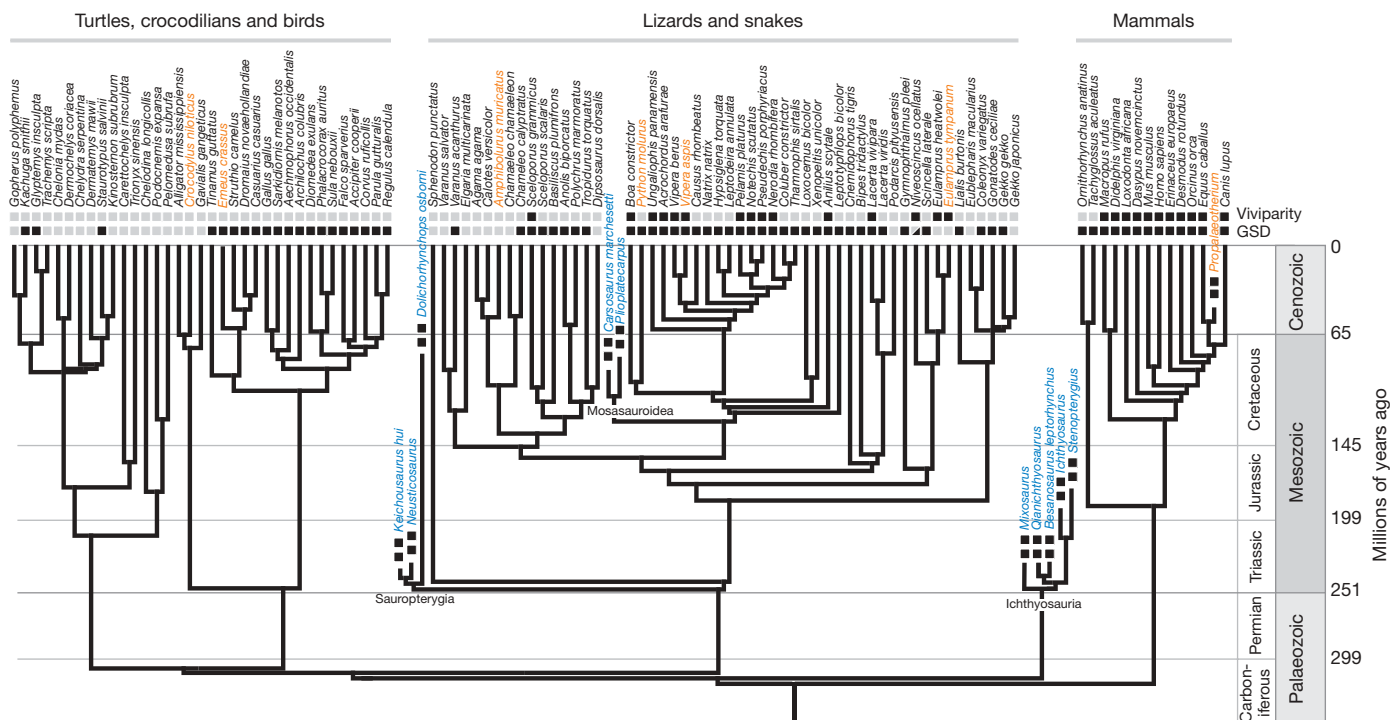


Figure 1 | Distribution of viviparity and GSD within amniotes. Grey squares indicate the absence and black squares the presence of viviparity (top row) and GSD (bottom row). Species names in orange belong to the test group; species names in blue are the extinct marine reptiles. Whereas viviparity is

known (posterior probability of GSD 99.7%). The southern water skink *Eulamprus tympanum*, unusually among amniotes, has TSD and viviparity (Fig. 1). Our method nevertheless correctly avoids predicting GSD in this species (Table 1), despite its phylogenetic position surrounded by species that have GSD (although the sister species of *E. tympanum*, *Eulamprus heatwolei*, also has TSD and is viviparous).

Because viviparity is closely linked to GSD, we can accurately predict GSD in viviparous species, but our predictions in oviparous species are less accurate. However, predictions for *Emeus crassus* (an extinct moa) and *Python molurus*, both of which have GSD and are oviparous, are stronger because of their phylogenetic position, but less so than for the viviparous species (Table 1).

In deriving our posterior distribution of evolutionary models we allowed all possible transitions among the character states to be equally likely a priori. However, theory and empirical data suggest that rates of change into species with TSD and viviparity (q_{24} and q_{43} in Fig. 2) are low because of the improbability of losing and then re-evolving complex structures (Dollo's rule)¹⁸. This is probably because viviparous species with TSD bear the burden of maintaining bimodal body temperatures to produce both sons and daughters¹⁴, although at least two examples of such species are known^{2,14}. Given this information, we constrained the transition rates into TSD/viviparity (transitions q_{24} and q_{34} in Fig. 2b) and the rates from viviparity to oviparity (transition rates q_{21} and q_{43}) to be initially 1% of the other rates. Predictions derived from the posterior distribution of models generated with the constrained priors are more accurate in all counts for the test species (Table 1). The constrained-prior approach correctly predicted GSD for the two oviparous species *Emeus crassus* and *Python molurus*, whereas the unconstrained approach failed to distinguish between the sex-determining mechanisms (*Emeus crassus*, posterior probability of GSD 97.6%; *Python molurus*, posterior probability of GSD 96.1%).

The test group analysis shows that our correlated prediction method yields accurate predictions, and that its performance is improved when prior information is taken into account. With this

fixed within therian mammals and oviparity is fixed within archosauromorphs (crocodilians, turtles and birds), lepidosauromorphs (tuatara, lizards and snakes) show a mixture of these traits. GSD is most variable within non-avian and non-serpent reptiles.

In mind, we turned to predicting the sex-determining mechanism in extinct marine reptiles. We placed mosasaurs, sauropterygians and ichthyosaurs on the amniote phylogeny used in the test group analysis. Fossil evidence (Fig. 3) shows each of these groups to have given live birth^{4–7}. We used this partial information along with the unconstrained and constrained posterior distribution of models of correlated evolution to infer the unknown character states (sex determination) for species in the three extinct lineages.

The unconstrained models strongly favour GSD in the mosasaurs (Table 1; posterior probabilities of GSD ~97%). The sauropterygians and the porpoise-like ichthyosaurs are also predicted to have had GSD (posterior probabilities of GSD ~82%), although the support is weaker than for the mosasaurs. Use of the posterior distribution of models derived from the constrained priors strengthens the prediction of GSD in the mosasaurs (posterior probabilities of GSD ~99%). This approach also favours GSD in sauropterygians (posterior probabilities of GSD 90–99%), with the strongest prediction of GSD in the derived plesiosaur *Dolichorhynchops osburni*. Like the plesiosaur *D. osburni*, under the constrained approach the predictions strongly favour GSD in ichthyosaurs (posterior probabilities of GSD 98–99%).

Our analysis suggests that GSD and viviparity conferred important advantages on amniote species with coastal marine and pelagic lifestyles. For example, freed by viviparity¹⁹ from returning ashore to lay eggs, sea snakes (Hydrophiinae) are the only extant reptiles that are completely marine, unable to survive on land. Saltwater crocodiles, marine iguanas and sea turtles, although marine, lay eggs on land. Reptiles cannot successfully lay eggs under water because gas exchange across the eggshell is much slower in water than in air (some turtles in the family Chelidae lay eggs under water, but the eggs undergo diapause until the dry season)^{8,20}.

Viviparous species include those with egg retention, in which hatching occurs *in utero* (so-called ovoviviparity), and those with placentae formed from the yolk-sac or chorioallantois²¹. Because intermediate stages of egg retention would probably provide no immediate advantage to marine reptiles (marine species would still

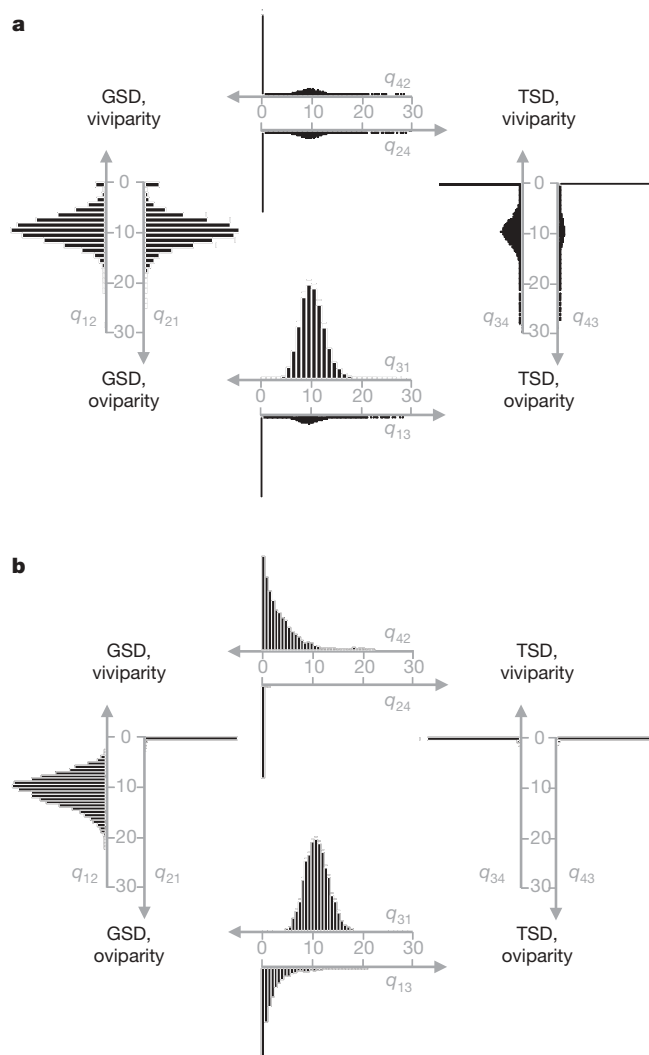


Figure 2 | Posterior distributions of evolutionary transition rates between sex-determining mechanism and reproductive mode in extant amniote species. The q_{ij} transition rates denote changes in one trait that are dependent on the state of the other binary trait. **a**, Bar charts on the arrows indicate the posterior distribution of the transition rates integrated across models using reversible-jump MCMC. **b**, As in **a** except that the transition rates into TSD/viviparity (transitions q_{24} and q_{34}) and the rates from viviparity to oviparity (transition rates q_{21} and q_{43}) were set initially to 1% of the other rates.

Table 1 | Summary of posterior predictive results

Predictions	Posterior probability of GSD	
	Unconstrained	Constrained
Test group		
<i>Crocodylus niloticus</i>	0.584	0.576
<i>Emeus crassus</i>	0.898	0.976
<i>Amphibolurus muricatus</i>	0.578	0.565
<i>Python molurus</i>	0.889	0.961
<i>Vipera aspis</i>	0.996	1
<i>Eulamprus tympanum</i>	0.508	0.507
<i>Propalaeotherium</i>	0.997	1
Marine reptiles		
Sauropterygians		
<i>Keichousaurus hui</i>	0.836	0.907
<i>Neusticosaurus</i>	0.828	0.923
<i>Dolichorhynchops osborni</i>	0.824	0.988
Mosasaurs		
<i>Carsosaurus marchesetti</i>	0.971	0.998
<i>Plioplatecarpus</i>	0.970	0.998
Ichthyosaurs		
<i>Besanosaurus leptorhynchus</i>	0.818	0.976
<i>Ichthyosaurus</i>	0.822	0.985
<i>Mixosaurus</i>	0.845	0.977
<i>Qianichthyosaurus</i>	0.823	0.978
<i>Stenopterygius</i>	0.822	0.987

need to return to land to lay eggs), it has been suggested that viviparity evolved in the terrestrial or amphibious ancestors of the three groups of marine reptiles⁹. For example, GSD followed by viviparity in primitive mosasaurs (*Carsosaurus*) and sauropterygians (*Keichousaurus* and *Neusticosaurus*) may have freed these amphibious species from the necessity of laying eggs on land, and subsequently permitted the diversification of more derived marine forms that were obligate sea-goers^{4,5}. Similar semi-aquatic ancestral forms of ichthyosaurs are unknown but must have existed, and we speculate that they would have had GSD as well.

Freed ultimately by GSD from ovipositing on land, mosasaurs, sauropterygians and ichthyosaurs invaded the Mesozoic seas at different times between 251 and 100 Myr ago. Part of their affect on the marine ecosystem was the evolution of enormous key predatory species^{4,22}, such as the ichthyosaur *Shonisaurus*, which grew to more than 20 m in length²³. As top predators, marine reptile species would have affected prey species' population dynamics, and their pelagic marine radiations brought these invading amniote species into direct competition with one another (mosasaurs eating plesiosaurs, for example) as well as with pre-existing marine predators such as sharks¹⁵.

Our results also suggest, more generally, that with rare exceptions (such as *Eulamprus*), newly discovered amniote species will have GSD if they are also viviparous. It is also likely, given our findings,



Figure 3 | A specimen of *Stenopterygius quadriscissus*, an extinct ichthyosaur from the Early to Middle Jurassic Period. This specimen shows live birth in an extinct marine reptile, demonstrating tail-first birth similar to cetaceans and sirenia. Copyright © The Natural History Museum, London.

that GSD was present within early lineages of diapsid reptiles, pushing back the first occurrence of this trait to more than 300 Myr ago. Furthermore, by connecting sex determination with amniote marine radiations, these results help to explain genome-level evolutionary constraints involved with major macroevolutionary shifts in completely extinct lineages—in this instance, from small land-dwelling reptilian ancestors to enormous sea-going marine predators. With the inclusion of ichthyosaurs, mosasaurs and sauropterygians, GSD is present in all known fully marine amniote groups (for example cetaceans, sirenians and sea snakes), matching the prediction that this mode of sex determination and viviparity are key traits involved with fully marine radiations in amniote lineages.

METHODS SUMMARY

Sex determination data were obtained from published studies (see Supplementary Information for more information) and coded as binary variables. We accounted for plasticity in the character states²⁴ of some species by using ambiguous character coding (species could be coded as 0 and 1). We used three data sets for our analyses, the first including 94 extant species (the 'extant' group), a second including an additional seven species (the 'extant + test' group) used to test the prediction method, and a third group including ten extinct marine reptiles (the 'extant + test + prediction' group).

We used Mesquite v2.5 (ref. 25) to construct phylogenetic trees compiled from published studies. We integrated our analyses over two trees during the Markov-chain Monte Carlo analysis (MCMC; see below), one with turtles as basal archosaurs (shown in Fig. 3) and the other with turtles as basal reptiles (not shown). Mosasaurs were also analysed as close relatives to varanid lizards (not shown) to explore the impact of an alternative phylogenetic hypothesis²⁶, but both phylogenetic positions yielded similar predictions.

We used the discrete method²⁷ implemented in a reversible-jump MCMC algorithm²⁸ to investigate correlated evolution between the two traits. The test for correlated evolution is made against a model in which the two traits are forced to evolve independently, and the fit of the two models to the observed data is compared using Bayes factors. The posterior set of models can be used to produce a posterior predictive distribution of unknown character states for taxa that can be positioned on the tree. Holding the set of posterior models constant, the posterior predictive distribution is obtained by running a Markov chain that proposes values for the unknown states, assessing their likelihoods given the models and the known state of the other variable. For full details of methods see Supplementary Information.

Received 29 April; accepted 28 July 2009.

1. Janzen, F. J. & Phillips, P. C. Exploring the evolution of environmental sex determination, especially in reptiles. *J. Evol. Biol.* **19**, 1775–1784 (2006).
2. Robert, K. A. & Thompson, M. B. Viviparous lizard selects sex of embryos. *Nature* **412**, 698–699 (2001).
3. Warner, D. A. & Shine, R. The adaptive significance of temperature-dependent sex determination in a reptile. *Nature* **451**, 566–568 (2008).
4. Caldwell, M. W. & Lee, M. S. Y. Live birth in Cretaceous marine lizards (mosasauroids). *Proc. R. Soc. B* **268**, 2397–2401 (2001).
5. Cheng, Y.-n., Wu, X.-c. & Ji, Q. Triassic marine reptiles gave birth to live young. *Nature* **432**, 383–386 (2004).
6. Dal Sasso, C. & Pinna, G. *Besanosaurus leptorhynchus* n. gen. n. sp., a new shastasaurid ichthyosaur from the Middle Triassic of Besano. *Paleontol. Lombarda* **4**, 1–24 (1996).
7. Maxwell, E. E. & Caldwell, M. W. First record of live birth in Cretaceous ichthyosaurs: closing an 80 million year gap. *Proc. R. Soc. B* **270**, S104–S107 (2003).
8. Andrews, R. M. & Mathies, T. Natural history of reptilian development: constraints on the evolution of viviparity. *Bioscience* **50**, 227–238 (2000).
9. Shine, R. in *Biology of the Reptilia* Vol. 15 (eds Gans, C. & Billett, F.) 605–694 (Wiley, 1985).

10. Hodges, W. L. Evolution of viviparity in horned lizards (Phrynosoma): testing the cold climate hypothesis. *J. Evol. Biol.* **17**, 1230–1237 (2004).
11. Janzen, F. J. & Krenz, J. G. in *Temperature-Dependent Sex Determination in Vertebrates* (eds Valenzuela, N. & Lance, V. A.) 121–130 (Smithsonian Books, 2004).
12. Organ, C. L. & Janes, D. E. Evolution of sex chromosomes in Sauropsida. *Integr. Comp. Biol.* **48**, 512–519 (2008).
13. Clobert, J., Garland, T. & Barbault, R. The evolution of demographic tactics in lizards: a test of some hypotheses concerning life history evolution. *J. Evol. Biol.* **11**, 329–364 (1998).
14. Wapstra, E. et al. Maternal basking behaviour determines offspring sex in a viviparous reptile. *Proc. R. Soc. B* **271**, S230–S232 (2004).
15. Everhart, M. J. *Oceans of Kansas: a Natural History of the Western Interior Sea* (Indiana Univ. Press, 2005).
16. Bell, G. L. J., Sheldon, M. A., Lamb, J. P. & Martin, J. E. The first direct evidence of live birth in Mosasauridae (Squamata): exceptional preservation in Cretaceous Pierre Shale of South Dakota. *J. Vertebr. Paleontol.* **16** (suppl. 3), 21A (1996).
17. Harrison, R. J. in *The Biology of Marine Mammals* (ed. Andersen, H.) 253–348 (Academic, 1969).
18. Lee, M. S. Y. & Shine, R. Reptilian viviparity and Dollo's Law. *Evolution Int. J. Org. Evolution* **52**, 1441–1450 (1998).
19. Blackburn, D. G. Evolutionary origins of viviparity in the reptilia. II. Serpentes, Amphisbaenia, and Ichthyosauria. *Amphib.-reptil.* **6**, 259–291 (1985).
20. Kennett, R., Christian, K. & Bedford, G. Underwater nesting by the Australian freshwater turtle *Chelodina rugosa*: effect of prolonged immersion and eggshell thickness on incubation period, egg survivorship, and hatchling size. *Can. J. Zool.* **76**, 1019–1023 (1998).
21. Blackburn, D. G., Vitt, J. L. & Beuchat, C. A. Eutherian-like reproductive specializations in a viviparous reptile. *Proc. Natl Acad. Sci. USA* **81**, 4860–4863 (1984).
22. Motani, R. Evolution of fish-shaped reptiles (Reptilia: Ichthyopterygia) in their physical environments and constraints. *Annu. Rev. Earth Planet. Sci.* **33**, 395–420 (2005).
23. Nicholls, E. L. & Manabe, M. Giant ichthyosaurs of the Triassic—a new species of *Shonisaurus* from the Pardonet Formation (Norian: Late Triassic) of British Columbia. *J. Vertebr. Paleontol.* **24**, 838–849 (2004).
24. Quinn, A. E. et al. Temperature sex reversal implies sex gene dosage in a reptile. *Science* **316**, 411 (2007).
25. Maddison, W. P. & Maddison, D. R. Mesquite: a modular system for evolutionary analysis. Version 2.5. <<http://mesquiteproject.org>> (2008).
26. Lee, M. S. Y. The phylogeny of varanoid lizards and the affinities of snakes. *Phil. Trans. R. Soc. B* **352**, 53–91 (1997).
27. Pagel, M. Detecting correlated evolution on phylogenies: a general method for the comparative analysis of discrete characters. *Proc. R. Soc. B* **255**, 37–45 (1994).
28. Pagel, M. & Meade, A. Bayesian analysis of correlated evolution of discrete characters by reversible-jump Markov chain Monte Carlo. *Am. Nat.* **167**, 808–825 (2006).

Supplementary Information is linked to the online version of the paper at www.nature.com/nature.

Acknowledgements We thank M. Everhart, R. Shine, M. Laurin, T. Quental, L. Cooper, S. Faul, M. Patten, N. Hobbs and C. Venditti for comments that improved the clarity of this paper. D.E.J. and C.L.O. thank S. V. Edwards for postdoctoral support. We thank the Department of Organismic and Evolutionary Biology and the Museum of Comparative Zoology at Harvard University for providing support that enabled this research, and the Centre for Advanced Computing and Emerging Technologies (ACET) at the University of Reading for making the ThamesBlue supercomputer available for our use. This research was supported in part by a travel grant from the Museum of Comparative Zoology at Harvard University, National Institutes of Health Postdoctoral Fellowships (1 F32 GM075490-01 to C.L.O., and 5 F32 GM072494 to D.E.J.), and Natural Environment Research Council grant NE/C51992X/1 to M.P.

Author Contributions All authors contributed to the design of the project. A.M. wrote the computer code. C.L.O., A.M. and M.P. performed the analyses.

Author Information Reprints and permissions information is available at www.nature.com/reprints. Correspondence and requests for materials should be addressed to C.L.O. (corgan@oeb.harvard.edu) or M.P. (m.pagel@reading.ac.uk).

Genome sequence and analysis of the Irish potato famine pathogen *Phytophthora infestans*

Brian J. Haas^{1*}, Sophien Kamoun^{2,3*}, Michael C. Zody^{1,4}, Rays H. Y. Jiang^{1,5}, Robert E. Handsaker¹, Liliana M. Cano², Manfred Grabherr¹, Chinnappa D. Kodira^{1†}, Sylvain Raffaele², Trudy Torto-Alalibo^{3†}, Tolga O. Bozkurt², Audrey M. V. Ah-Fong⁶, Lucia Alvarado¹, Vicky L. Anderson⁷, Miles R. Armstrong⁸, Anna Avrova⁸, Laura Baxter⁹, Jim Beynon⁹, Petra C. Boevink⁸, Stephanie R. Bollmann¹⁰, Jorunn I. B. Bos³, Vincent Bulone¹¹, Guohong Cai¹², Cahid Cakir³, James C. Carrington¹³, Megan Chawner¹⁴, Lucio Conti¹⁵, Stefano Costanzo¹⁶, Richard Ewan¹⁵, Noah Fahlgren¹³, Michael A. Fischbach¹⁷, Johanna Fugelstad¹¹, Eleanor M. Gilroy⁸, Sante Gnerre¹, Pamela J. Green¹⁸, Laura J. Grenville-Briggs⁷, John Griffith¹⁴, Niklaus J. Grünwald¹⁰, Karolyn Horn¹⁴, Neil R. Horner⁷, Chia-Hui Hu¹⁹, Edgar Huitema³, Dong-Hoon Jeong¹⁸, Alexandra M. E. Jones², Jonathan D. G. Jones², Richard W. Jones²⁰, Elinor K. Karlsson¹, Sridhara G. Kunjeti²¹, Kurt Lamour²², Zhenyu Liu³, LiJun Ma¹, Daniel MacLean², Marcus C. Chibucos²³, Hayes McDonald²⁴, Jessica McWalters¹⁴, Harold J. G. Meijer⁵, William Morgan²⁵, Paul F. Morris²⁶, Carol A. Munro²⁷, Keith O'Neill^{1†}, Manuel Ospina-Giraldo¹⁴, Andrés Pinzón²⁸, Leighton Pritchard⁸, Bernard Ramsahoye²⁹, Qinghu Ren³⁰, Silvia Restrepo²⁸, Sourav Roy⁶, Ari Sadanandom¹⁵, Alon Savidor³¹, Sebastian Schornack², David C. Schwartz³², Ulrike D. Schumann⁷, Ben Schwessinger², Lauren Seyer¹⁴, Ted Sharpe¹, Cristina Silvar², Jing Song³, David J. Studholme², Sean Sykes¹, Marco Thines^{2,33}, Peter J. I. van de Vondervoort⁵, Vipaporn Phuntumart²⁶, Stephan Wawra⁷, Rob Weide⁵, Joe Win², Carolyn Young³, Shiguo Zhou³², William Fry¹², Blake C. Meyers¹⁸, Pieter van West⁷, Jean Ristaino¹⁹, Francine Govers⁵, Paul R. J. Birch³⁴, Stephen C. Whisson⁸, Howard S. Judelson⁶ & Chad Nusbaum¹

Phytophthora infestans is the most destructive pathogen of potato and a model organism for the oomycetes, a distinct lineage of fungus-like eukaryotes that are related to organisms such as brown algae and diatoms. As the agent of the Irish potato famine in the mid-nineteenth century, *P. infestans* has had a tremendous effect on human history, resulting in famine and population displacement¹. To this day, it affects world agriculture by causing the most destructive disease of potato, the fourth largest food crop and a critical alternative to the major cereal crops for feeding the world's population¹. Current annual worldwide potato crop losses due to late blight are conservatively estimated at \$6.7 billion². Management of this devastating pathogen is challenged by its remarkable speed of adaptation to control strategies such as genetically resistant cultivars^{3,4}. Here we report the sequence of the *P. infestans* genome,

which at ~240 megabases (Mb) is by far the largest and most complex genome sequenced so far in the chromalveolates. Its expansion results from a proliferation of repetitive DNA accounting for ~74% of the genome. Comparison with two other *Phytophthora* genomes showed rapid turnover and extensive expansion of specific families of secreted disease effector proteins, including many genes that are induced during infection or are predicted to have activities that alter host physiology. These fast-evolving effector genes are localized to highly dynamic and expanded regions of the *P. infestans* genome. This probably plays a crucial part in the rapid adaptability of the pathogen to host plants and underpins its evolutionary potential.

The size of the *P. infestans* genome is estimated by optical map and other methods at 240 Mb (Supplementary Information). It is several-fold larger than those of the related *Phytophthora* species *P. sojae*

¹Broad Institute of MIT and Harvard, Cambridge, Massachusetts 02141, USA. ²The Sainsbury Laboratory, Norwich NR4 7UH, UK. ³Department of Plant Pathology, The Ohio State University, Ohio Agricultural Research and Development Center, Wooster, Ohio 44691, USA. ⁴Department of Medical Biochemistry and Microbiology, Uppsala University, Box 597, Uppsala SE-751 24, Sweden. ⁵Laboratory of Phytopathology, Wageningen University, 1-6708 PB, Wageningen, The Netherlands. ⁶Department of Plant Pathology and Microbiology, University of California, Riverside, California 92521, USA. ⁷University of Aberdeen, Aberdeen Oomycete Laboratory, College of Life Sciences and Medicine, Institute of Medical Sciences, Foresterhill, Aberdeen AB25 2ZD, UK. ⁸Plant Pathology Programme, Scottish Crop Research Institute, Invergowrie, Dundee DD2 5DA, UK. ⁹University of Warwick, Wellesbourne, Warwick CV35 9EF, UK. ¹⁰Horticultural Crops Research Laboratory, USDA Agricultural Research Service, Corvallis, Oregon 97330, USA. ¹¹Royal Institute of Technology (KTH), School of Biotechnology, Alfabeta University Centre, Stockholm SE-10691, Sweden. ¹²Department of Plant Pathology and Plant-Microbe Biology, Cornell University, Ithaca, New York 14853, USA. ¹³Center for Genome Research and Biocomputing and Department of Botany and Plant Pathology, Oregon State University, Corvallis, Oregon 97331, USA. ¹⁴Biology Department, Lafayette College, Easton, Pennsylvania 18042, USA. ¹⁵Plant Molecular Sciences Faculty of Biomedical and Life Sciences, Bower Building, University of Glasgow, Glasgow G12 8QQ, UK. ¹⁶USDA-ARS, Dale Bumpers National Rice Research Center, Stuttgart, Arkansas 72160, USA. ¹⁷Department of Molecular Biology, Massachusetts General Hospital, Boston, Massachusetts 02114, USA. ¹⁸Delaware Biotechnology Institute, University of Delaware, Newark, Delaware 19711, USA. ¹⁹Department of Plant Pathology, North Carolina State University, Raleigh, North Carolina 27695, USA. ²⁰USDA-ARS, Beltsville, Maryland 20705, USA. ²¹Department of Plant and Soil Sciences, University of Delaware, Newark, Delaware 19716, USA. ²²Department of Entomology and Plant Pathology, University of Tennessee, Knoxville, Tennessee 37996, USA. ²³Institute for Genome Sciences, University of Maryland School of Medicine, Baltimore, Maryland 21201, USA. ²⁴Department of Biochemistry, Vanderbilt University School of Medicine, Nashville, Tennessee 37232, USA. ²⁵The College of Wooster, Department of Biology, Wooster, Ohio 44691, USA. ²⁶Department of Biological Sciences, Bowling Green State University, Bowling Green, Ohio 43403, USA. ²⁷University of Aberdeen, School of Medical Sciences, College of Life Sciences and Medicine, Institute of Medical Sciences, Foresterhill, Aberdeen AB25 2ZD, UK. ²⁸Mycology and Phytopathology Laboratory, Los Andes University, Bogotá, Colombia. ²⁹Institute of Genetics and Molecular Medicine, University of Edinburgh, Cancer Research Centre, Western General Hospital, Edinburgh EH4 2XU, UK. ³⁰J. Craig Venter Institute, Rockville, Maryland 20850, USA. ³¹Department of Plant Sciences, Tel Aviv University, Tel Aviv 69978, Israel. ³²Department of Chemistry, Laboratory of Genetics, Laboratory for Molecular and Computational Genomics, University of Wisconsin Biotechnology Center, University of Wisconsin-Madison, Madison Wisconsin 53706, USA. ³³University of Hohenheim, Institute of Botany 210, D-70593 Stuttgart, Germany. ³⁴Division of Plant Science, College of Life Sciences, University of Dundee (at SCRI), Invergowrie, Dundee DD2 5DA, UK. [†]Present addresses: 454 Life Sciences, Branford, Connecticut 06405, USA (C.D.K.); Virginia Bioinformatics Institute, Virginia Polytechnic and State University, Blacksburg, Virginia 24061, USA (T.T.-A.); Biomedical Diagnostics Institute, Dublin City University, Dublin 9, Ireland (K.O.).

*These authors contributed equally to this work.

(95 Mb) and *P. ramorum* (65 Mb), which cause soybean root rot and sudden oak death, respectively^{5,6}. We sequenced the genome of *P. infestans* strain T30-4 using a whole-genome shotgun approach, and generated a ninefold coverage assembly spanning 229 Mb (Table 1 and Supplementary Information). The unassembled fraction of the genome consists of high copy repeat sequences (Supplementary Information). The assembled genome sequence provides near complete coverage of genes, with 98.2% of *P. infestans* T30-4 complementary DNAs aligning (Supplementary Information). We identified 17,797 protein-coding genes by *ab initio* gene prediction, protein and expressed sequence tag (EST) homology, and direct genome-to-genome comparative gene modelling with *P. sojae* and *P. ramorum* (Supplementary Information). Changes in gene content, number or length do not explain the marked difference in genome size (Table 1 and Supplementary Table 1). No evidence of whole-genome duplication or large-scale dispersed segmental duplication was detected. However, specific disease effector gene families are expanded in *P. infestans* (see later).

P. infestans, *P. sojae* and *P. ramorum* represent three major phylogenetic clades of *Phytophthora*⁶. Among the three genomes, we identified a core set of 8,492 orthologue clusters (including 9,583 *P. infestans* orthologues and close paralogues), of which 7,113 genes show 1:1:1 orthology relationships (Table 1, Supplementary Fig. 1 and Supplementary Table 2). The core proteome is enriched in genes involved in cellular processes including DNA replication, transcription and protein translation, whereas genes with functions involved in cellular defence mechanisms are underrepresented (Supplementary Fig. 2). Differences in gene family expansion, in particular dynamic repertoires of effector genes (see later), are probably responsible for different traits among *Phytophthora* species, such as altered host specificity.

Comparison of the three *Phytophthora* genomes reveals an unusual genome organization, comprised of blocks of conserved gene order in which gene density is relatively high and repeat content is relatively low, separated by regions in which gene order is not conserved, gene density is low and repeat content is high (Table 1 and Fig. 1). The conserved blocks represent ~90% of core orthologous groups in all three genomes, including ~70% (12,440) of all *P. infestans* protein-coding genes and ~78% of genes in both *P. sojae* (13,225) and *P. ramorum* (11,246). Within conserved blocks, genes are typically tightly spaced in all three genomes (Table 1 and Fig. 1), with median intergenic distances of 633 base pairs (bp) for *P. ramorum*, 804 bp for

P. sojae, and 603 bp for *P. infestans*. In regions between conserved blocks, intergenic distances are greater and increase with increasing genome size (median 1.5 kb for *P. ramorum*, 2.2 kb for *P. sojae*, and 3.7 kb for *P. infestans*). The differences in spacing between genes among the three genomes, within and outside regions of conserved gene order, are evident in Fig. 2a–f. The expansion of regions between conserved blocks results from increased density of repetitive elements (Supplementary Fig. 3), and overall differences in genome size among the three species are largely explained by proliferation of repeats in regions in which gene order is not conserved. This difference between conserved blocks and non-conserved regions is particularly apparent in the greatly expanded *P. infestans* genome (Fig. 2d, f). Further, it is evident that rapidly evolving secreted effector genes (see later) lie predominantly in the gene-sparse regions (Fig. 2g, h). This dual pattern of intergenic spacing and repeat content has been suggested for large, unsequenced genomes in the *Poaceae* such as maize^{7–9}, but it is not seen in the genomes of other sequenced eukaryotes (Supplementary Fig. 4).

Recent proliferation of Gypsy elements in *P. infestans* underlies the genome expansion. Approximately one-third of the genome assembly corresponds to families of Gypsy elements (Supplementary Fig. 5). The two families with the highest relative expansion in *P. infestans* are Gypsy Pi-1 and a new Gypsy long terminal repeat (LTR) element we named 'Albatross', which together account for at least 29% of the genome (Supplementary Table 3). Albatross elements cover ~32 Mb and are enriched (>2-fold) in the regions in which gene order is not conserved (Supplementary Table 4 and Supplementary Fig. 6), contributing appreciably to relative expansion of gene-sparse regions (Supplementary Fig. 3). Gypsy Pi-1 elements cover ~22 Mb and, in contrast to Albatross elements, are relatively evenly distributed across the genome.

Overall, the *P. infestans* genome contains a strikingly rich and diverse population of transposons (Supplementary Table 3). We identified 273 full-length elements belonging to two large classes of autonomous rolling-circle type helitron DNA transposons (7.3-kb and 6.4-kb elements), in much larger numbers than described in any other genome (Supplementary Tables 3 and 5). Most helitron open reading frames (ORFs) are degenerate pseudogenes, but 13 are intact and presumed functional. Some apparently non-autonomous helitrons have intact termini so their transposition may be driven by gene products from the functional classes. In contrast, the *P. sojae* and *P. ramorum* genomes contain no intact helitron elements. The *P. infestans* genome carries

Table 1 | Genome assembly and annotation statistics

	<i>P. infestans</i>	<i>P. sojae</i>	<i>P. ramorum</i>
Genome			
Estimated genome size	240 Mb	95 Mb*	65 Mb*
Coverage (fold)	7.6	7.9*	5.6*
Number of scaffolds	4,921	1,810*	2,576*
N50 scaffold length	1,570 kb	463 kb*	308 kb*
Total scaffold length	228.5 Mb	86.0 Mb*	66.7 Mb*
Number of contigs	18,288	5,577*	7,588*
N50 contig length	44.5 kb	105.7 kb*	47.5 kb*
Total contig length	190 Mb	78 Mb*	54.4 Mb*
G+C content	51.0%	54.4%	53.9%
Repeat† (%)	74%	39%	28%
Collinear blocks‡	85 Mb	52 Mb	37 Mb
Repeat† (%) in collinear blocks‡	57%	28%	13%
Repeat† (%) outside collinear blocks‡	86%	60%	56%
Intergenic region spacing in collinear blocks‡ (25–75 percentiles)	224–3,070 bp	307–2,319 bp	270–1,551 bp
Intergenic region spacing outside collinear blocks‡ (25–75 percentiles)	664–19,144 bp	753–5,896 bp	566–4,351 bp
Genes			
Number of genes§	17,797	16,988	14,451
<i>Phytophthora</i> orthologues	11,893	12,427	12,136
<i>Phytophthora</i> core orthologues	9,583	9,550	9,664

* Statistics derived from supplementary materials accompanying ref. 5.

† Measured by RepeatMasker with *de novo* RepeatScout libraries (see Supplementary Information).

‡ Union of collinear blocks derived from pairwise genome comparisons (see Supplementary Information).

§ *P. sojae* and *P. ramorum* annotations were obtained from JGI (see Supplementary Information). Newly discovered mobile elements were removed, and specific gene families of interest were reannotated (see Supplementary Information).

|| Core orthologous groups contain at least one orthologous gene from each of the three *Phytophthora* species.

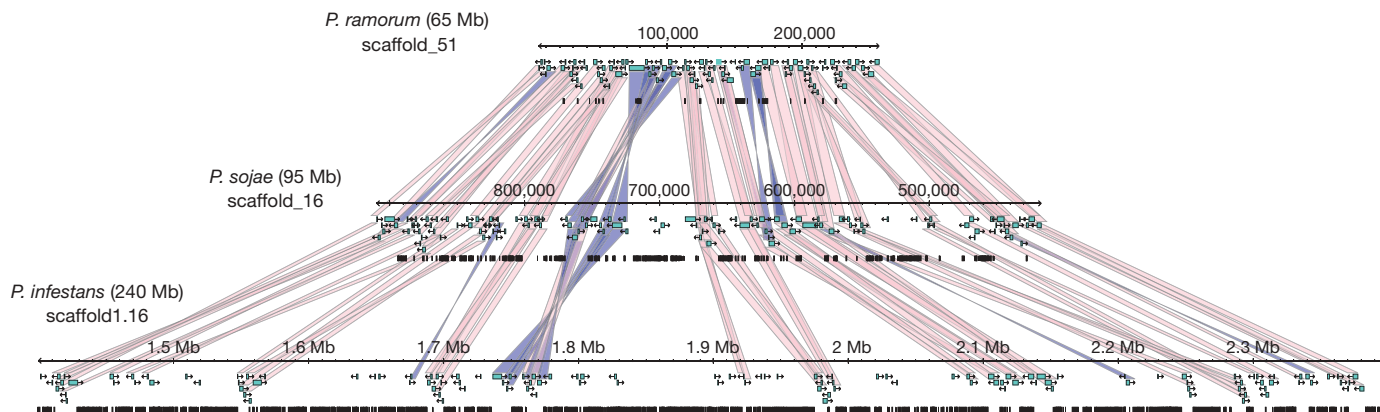


Figure 1 | Repeat-driven genome expansion in *Phytophthora infestans*. Conserved gene order across three homologous *Phytophthora* scaffolds. Genome expansion is evident in regions of conserved gene order, a

increased numbers of mobile elements across diverse families as compared to *P. sojae* and *P. ramorum*, with ~5 times as many LTR retrotransposons and ~10 times as many helitrons (Supplementary Fig. 7).

Consistent with a model of repeat-driven expansion of the *P. infestans* genome, the vast majority of repeat elements in the genome are highly similar to their consensus sequences, indicating a high rate of recent transposon activity (Supplementary Fig. 8). In addition, we have observed and experimentally confirmed examples of recently active elements (Supplementary Figs 9–11).

Phytophthora species, like many pathogens, secrete effector proteins that alter host physiology and facilitate colonization. The genome of *P. infestans* revealed large complex families of effector genes encoding secreted proteins that are implicated in pathogenesis¹⁰. These fall into two broad categories: apoplastic effectors that accumulate in the plant intercellular space (apoplast) and cytoplasmic effectors that are translocated directly into the plant cell by a specialized infection structure called the haustorium¹¹. Apoplastic effectors include secreted hydrolytic enzymes such as proteases, lipases and glycosylases that probably degrade plant tissue; enzyme inhibitors to protect against host defence enzymes; and necrotizing toxins such as the Nep1-like proteins (NLPs) and PcF-like small cysteine-rich proteins (SCRs) (Supplementary Table 6).

As in the other *Phytophthora* species⁵, candidate effector genes are numerous and typically expanded compared to non-pathogenic relatives (Supplementary Table 6). Most notable among these are the RXLR and Crinkler (CRN) cytoplasmic effectors, described later.

The archetypal oomycete cytoplasmic effectors are the secreted and host-translocated RXLR proteins¹². All oomycete avirulence genes (encoding products recognized by plant hosts and resulting in host immunity) discovered so far encode RXLR effectors, modular secreted proteins containing the amino-terminal motif Arg-X-Leu-Arg (in which X represents any amino acid) that defines a domain required for delivery inside plant cells¹¹, followed by diverse, rapidly evolving carboxy-terminal effector domains^{13,14}. Several of these C termini have been shown to exhibit virulence activities as host cell death suppressors^{15,16}. We exploited the known motifs and other conserved sequence features to predict 563 RXLR genes in the *P. infestans* genome (Supplementary Tables 6, 7 and Supplementary Information). RXLR genes are notably expanded in *P. infestans*, with ~60% more predicted than in *P. sojae* and *P. ramorum* (Supplementary Tables 6 and 7). We observed that 70 of these are rapidly diversifying (Supplementary Table 8). Approximately half of *P. infestans* RXLRs are lineage-specific, largely accounting for the expanded repertoire (Supplementary Figs 12 and 13). In contrast to the core proteome, RXLR genes show evidence of high rates of turnover with only 16 of the 563 genes with 1:1 orthology relationships (Supplementary Table 2) and many (88) putative RXLR

consequence of repeat expansion in intergenic regions. Genes are shown as turquoise boxes, repeats as black boxes. Collinear orthologous gene pairs are connected by pink (direct) or blue (inverted) bands.

pseudogenes (Supplementary Table 9). This high turnover in *Phytophthora* is probably driven by arms-race co-evolution with host plants^{5,13,14,17}.

RXLR effectors show extensive sequence diversity. Markov clustering (TribeMCL¹⁸) yields one large family (*P. infestans*: 85, *P. ramorum*: 75, *P. sojae*: 53) and 150 smaller families (Supplementary Fig. 14). The largest family shares a repetitive C-terminal domain structure (Supplementary Figs 15 and 16). Most families have distinct sequence homologies (Supplementary Fig. 14) and patterns of shared domains (Supplementary Fig. 17) with greater diversity than expected if all RXLR effectors were monophyletic.

In contrast to the core proteome, RXLR effector genes typically occupy a genomic environment that is gene sparse and repeat-rich (Fig. 2g and Supplementary Figs 18 and 19). The mobile elements contributing to the dynamic nature of these repetitive regions may enable recombination events resulting in the higher rates of gene gain and gene loss observed for these effectors.

CRN cytoplasmic effectors were originally identified from *P. infestans* transcripts encoding putative secreted peptides that elicit necrosis *in planta*, a characteristic of plant innate immunity¹⁹. Since their discovery, little had been learned about the CRN effector family. Analysis of the *P. infestans* genome sequence revealed an enormous family of 196 CRN genes of unexpected complexity and diversity (Supplementary Table 10), that is heavily expanded in *P. infestans* relative to *P. sojae* (100 CRNs) and *P. ramorum* (19 CRNs) (Supplementary Table 6). Like RXLRs, CRNs are modular proteins. CRNs are defined by a highly conserved N-terminal ~50-amino-acid LFLAK domain (Supplementary Fig. 20) and an adjacent diversified DWL domain (Fig. 3a, b). Most (60%) possess a predicted signal peptide. Those lacking predicted signal peptides are typically found in CRN families containing members with secretion signals (Supplementary Table 10). CRN C-terminal regions exhibit a wide variety of domain structures, with 36 conserved domains and a further eight unique C termini identified among the 315 *Phytophthora* CRN proteins (Supplementary Table 11). We observed evidence of recombination between different clades as a mechanism driving CRN diversity (Supplementary Figs 21–23).

We explored the ability of diverse CRNs to perturb host cellular processes. In assays for necrosis *in planta* (Supplementary Information), deletion mutants of the previously described CRN2 secreted protein¹⁹ defined a C-terminal 234 amino-acid region (positions 173–407, domain DXZ) that is sufficient to induce cell death when expressed inside plant cells (Supplementary Fig. 24). Assays with representative *P. infestans* CRN genes identified four other distinct C termini that also trigger cell death inside plant cells (Fig. 3c). These include the newly defined DC domain (*P. infestans*: 18 genes and 49 pseudogenes (ψ)) and the D2 (14 and 43 ψ) and DBF (2 and 1 ψ) domains, which have similarity to protein kinases (Supplementary Table 11). These results indicate that the CRN protein domains

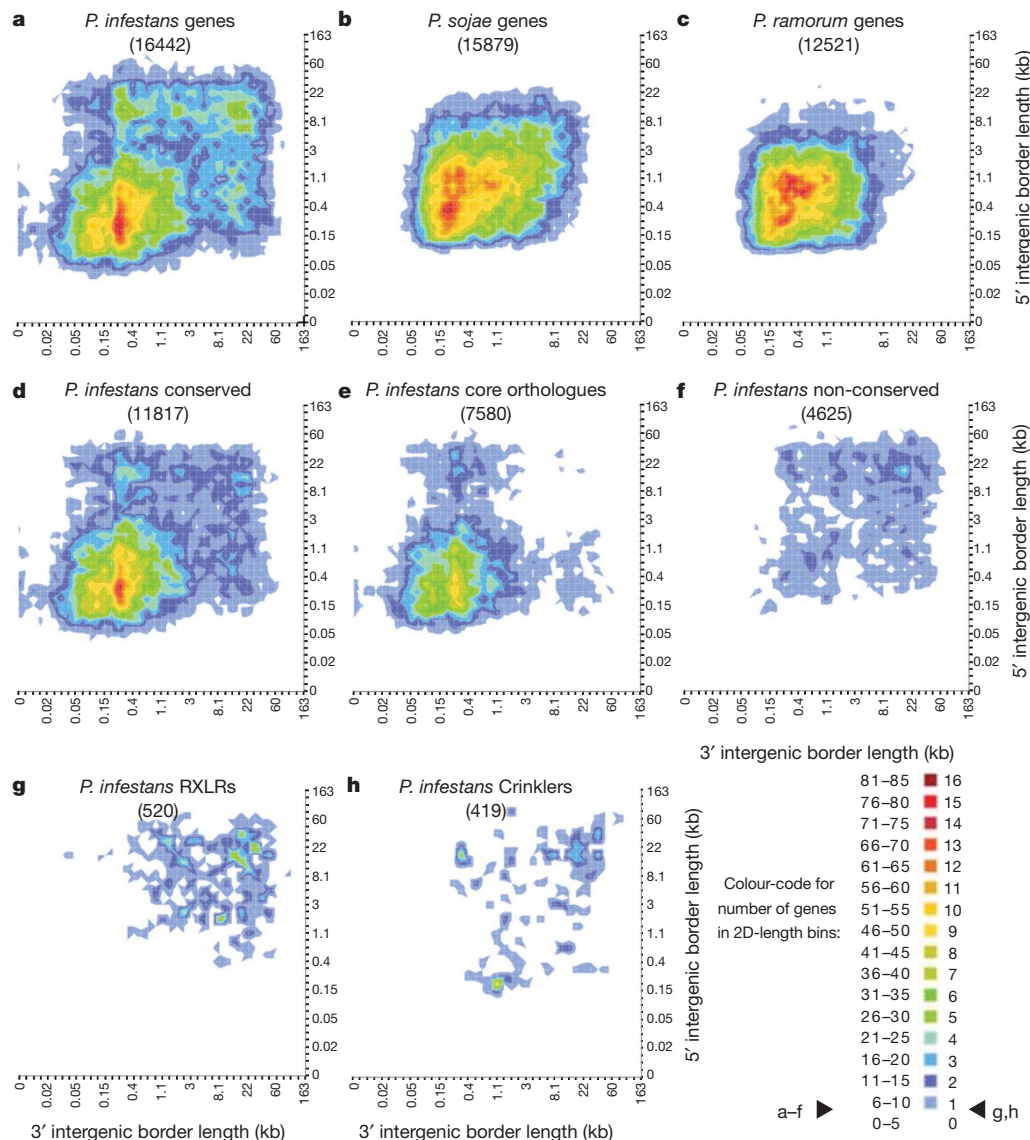


Figure 2 | The *P. infestans* genome shows an unusual distribution of intergenic region lengths. The flanking distance between neighbouring genes provides a measurement of local gene density. *P. infestans* genes were sorted into two dimensional bins on the basis of the lengths of flanking intergenic distances to neighbouring genes at their 5' and 3' ends. **a–h**, The number of genes in each bin is shown as a colour-coded heat map on orthogonal projection. *P. infestans* whole-genome analysis (**a**) shows most genes with intergenic regions between 20-bp and 3-kb long, as well as sets of genes flanked by one or two intergenic region(s) between 5 kb and 36 kb.

expressed *in planta* are retained (lacking signal peptides and hence not secreted) by the plant cell and stimulate cell death by an intracellular mechanism, supporting the view that CRNs, like RXLRs, are cytoplasmic effectors. We propose that the conserved CRN N-terminal LFLAK domain may function similarly to the RXLR motif for delivery of CRN effectors into plant cells, and experiments to test this hypothesis are under way.

A further 255 CRN genes are fragmented or otherwise disrupted and presumably non-functional (Supplementary Table 10). CRN genes and pseudogenes are aggregated in large clusters at several genomic loci, typically clustered by domain type (Supplementary Fig. 25). One extraordinary example is scaffold 1.48 (~1.2 Mb), containing 21 CRN genes and 31 CRN pseudogenes of the DXZ and D2 necrosis inducing domain-types (Fig. 3d). Many of the pseudogenes show only a few base changes, indicating recent conversion to pseudogenes. This high degree of expansion and pseudogene formation

Comparison with other *Phytophthora* genomes (**b, c**) indicates that this separation is observed in *P. infestans* but not the other two sequenced genomes. Genes in collinear blocks (**d**) and the core orthologue clusters (**e**) have primarily shorter intergenic distances, whereas genes outside of collinear blocks (**f**) reside mostly in gene sparse regions. Genes belonging to the RXLR (**g**) and Crinkler (CRN) (genes and pseudogenes) (**h**) effector families have flanking intergenic distances among the longest. Genes found at the ends of scaffolds and hence lacking neighbouring genes were necessarily excluded.

suggests that, like RXLR effector genes, CRN genes have undergone relatively rapid birth and death evolution.

Both CRN and RXLR genes typically occur in repeat-rich, gene-sparse regions of the genome, where conserved gene order with *P. sojae* and *P. ramorum* is either absent or disrupted (Fig. 2g, h and Supplementary Fig. 19). Expansion of large RXLR and CRN effector gene families seems to have been driven by non-allelic homologous recombination and tandem gene duplication. Although the genome is heavily populated by mobile elements, no direct evidence of transposition of effector genes was observed. Instead, the repeat-rich regions of effector clusters probably facilitate non-allelic-homologous-recombination-based expansion. In one intriguing case, nearly identical tandem arrays of CRNs are present on scaffold 1.6 in a perfect head-to-tail arrangement that is similar to that observed for some helitrons (Supplementary Fig. 26). This region of the genome is heavily enriched for helitron elements, implicating helitron-based rolling

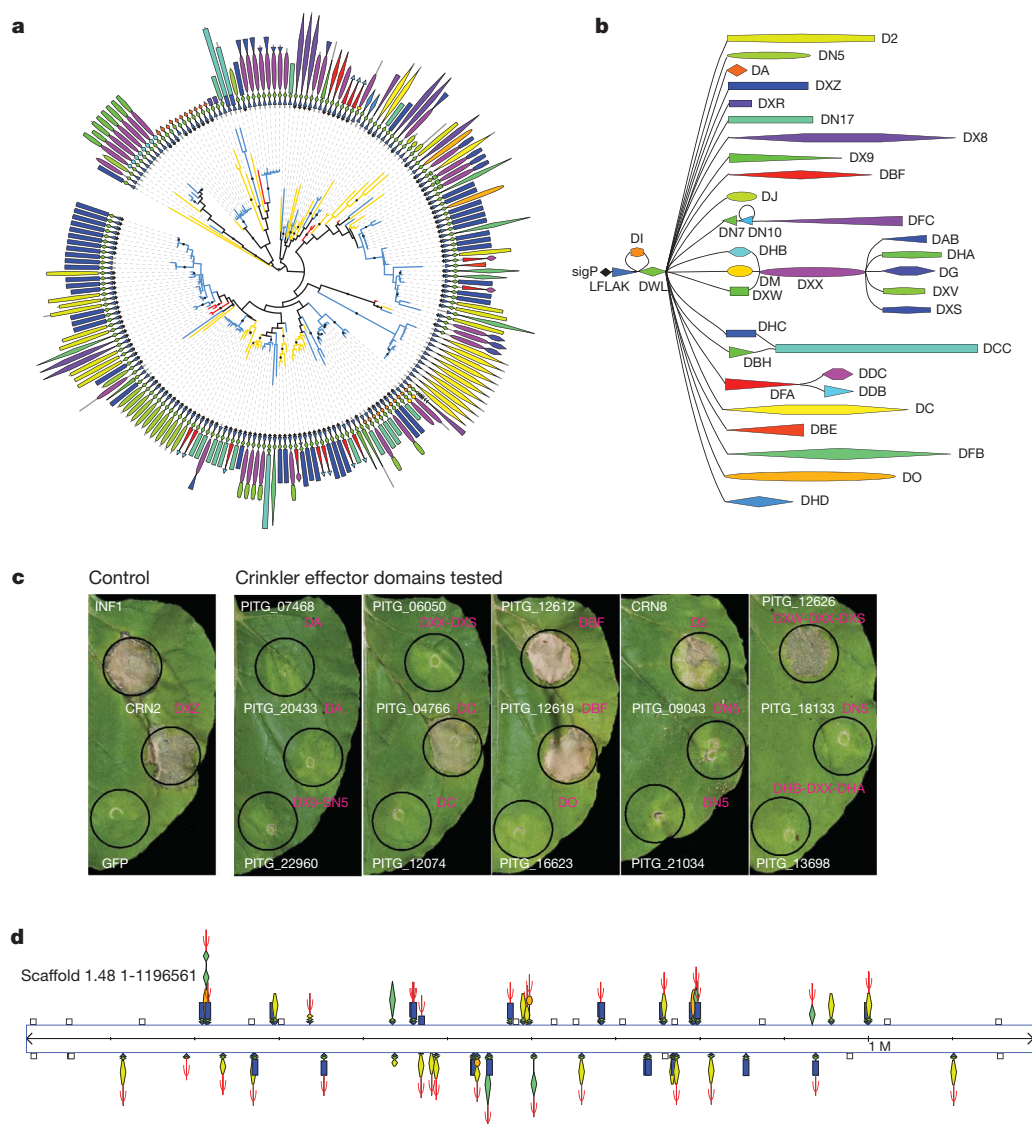


Figure 3 | Diverse Crinkler (CRN) families exhibit necrosis phenotypes in planta. **a**, CRN family phylogeny on the basis of the conserved N-terminal sequence, computed using PhyML with default parameters and 100 bootstrap replicates. CRN C-terminal domain structures are shown along the circumference. Branches are coloured according to organism: *P. infestans* in blue, *P. sojae* in yellow, and *P. ramorum* in red. Internal nodes with $\geq 80\%$ bootstrap support are marked with a black dot. **b**, Graphical representation of the CRN family domain architecture, exhibiting a conserved N-terminal region followed by diverse C-terminal domains. **c**, Phenotypes observed on *Nicotiana benthamiana* leaves upon *in planta* overexpression of CRN effectors. C-terminal effector domains of CRNs were

tested for cell death phenotypes on *N. benthamiana* leaves by *Agrobacterium tumefaciens*-mediated transient expression of CRNs, *inf1* (positive control), *crn2* (positive control), and green fluorescent protein (GFP) (negative control). The domains DC, DBF, D2 and DXW-DXX-DXS, like the DXZ domain of *crn2*, were found to induce necrosis. Cell death phenotypes were visible at 4 days post infiltration. Photos were taken 7 days after infiltration. **d**, CRNs with necrosis domains D2 and DXZ along with pseudogene copies are found co-clustered across *P. infestans* scaffold 1.48 (~1.2 Mb). Genes and domain structures are illustrated according to the top and bottom strands of the genomic scaffold. Pseudogenes are indicated by Ψ ; non-CRN genes are shown as unfilled boxes.

circle replication as a possible mechanism for establishing this CRN cluster.

To explore transcriptional responses to plant infection, we constructed a NimbleGen microarray based on the genome annotation. *P. infestans* gene expression during potato infection was monitored using samples from infected potato at 2–5 days post-inoculation (d.p.i.). In all, 494 genes were induced at least twofold during infection relative to mycelial growth. Days 2–4 of infection correlate with formation of infectious structures called haustoria. Mycelial necrotrophic growth on dead plant material occurs later at 5 d.p.i., and shows a similar expression profile to mycelial growth in plant extract media (Supplementary Fig. 27a and Supplementary Table 12). Seventy-nine RXLR genes exhibited this pattern of expression, including previously studied avirulence genes *Avr3a* (ref. 20), *Avr4* (ref. 21), and *Avr-blb1* (also known as *ipiO*) (ref. 22) (Supplementary Fig. 27b). Apoplastic

effector genes, including protease inhibitors, cysteine-rich secreted proteins, and NPP1-family members, were among the most highly upregulated genes during infection of potato. Few CRNs were induced during infection; however most CRNs were very highly expressed, with ~50% of CRNs within the top 10% of gene expression intensities (Supplementary Fig. 28). Several genes encoding metabolic enzymes were upregulated *in planta* (Supplementary Table 12), suggesting considerable metabolic adaptation of the pathogen to the host environment²³. A related pattern of downregulation mirrors the induction of effectors, involving ~115 genes (Supplementary Table 12). Among those repressed were elicitor-like genes and pseudogenes, suggesting that reduced expression during infection or mutation to pseudogene could contribute to evading activation of host innate immunity²⁴.

P. infestans remains a critical threat to world food security, and the genome sequence is a key tool to understanding its pathogenic success.

The sequence of the *P. infestans* genome showed an extremely high repeat content (~74%) and unusual discontinuous distribution of gene density that correlate intriguingly with its biology. Gene-dense regions with conserved gene order across *Phytophthora* species are interrupted by repeat-rich expanded regions that are sparsely populated with genes, many of which are fast-evolving pathogenicity effectors such as the RXLR and CRN families. The localization of the effectors to dynamic regions of the genome probably both enables the rapid evolutionary changes and accounts for the considerable expansion in CRN and RXLR effector genes observed in *P. infestans*. This expansion provides a species-specific repertoire of effector genes, the dynamic nature of which probably provides an advantage in the arms race with host species. We postulate that these dynamic regions promote the evolutionary plasticity of effector genes, generating the enhanced genetic variation required to drive the rapid evasion of plant resistance that is a hallmark of the potato late blight pathogen.

METHODS SUMMARY

Genomic sequence and gene annotations. The updated *P. infestans* genome sequence and annotation can be accessed through GenBank accession number AATU01000000, and are available through the Broad Institute website at http://www.broad.mit.edu/annotation/genome/phytophthora_infestans. All genome sequence reads have been deposited in the NCBI trace repository (<http://www.ncbi.nlm.nih.gov/Traces/home/>). Paired reads of *P. infestans* cDNAs are available in dbEST with accessions in the range GR284383–GR301386. The NimbleGen microarray data are available in GEO under accession number GSE14480. Full methods description and associated references are provided as Supplementary Information.

Received 23 April; accepted 31 July 2009.

Published online 9 September 2009.

1. Reader, J. *Potato: A History of the Propitious Esculent* (Yale Univ. Press, 2009).
2. Haverkort, A. J. *et al.* Societal costs of late blight in potato and prospects of durable resistance through cisgenic modification. *Potato Res.* **51**, 47–57 (2008).
3. Fry, W. *Phytophthora infestans*: the plant (and R gene) destroyer. *Mol. Plant Pathol.* **9**, 385–402 (2008).
4. McDonald, B. A. & Linde, C. Pathogen population genetics, evolutionary potential, and durable resistance. *Annu. Rev. Phytopathol.* **40**, 349–379 (2002).
5. Tyler, B. M. *et al.* *Phytophthora* genome sequences uncover evolutionary origins and mechanisms of pathogenesis. *Science* **313**, 1261–1266 (2006).
6. Blair, J. E., Coffey, M. D., Park, S. Y., Geiser, D. M. & Kang, S. A multi-locus phylogeny for *Phytophthora* utilizing markers derived from complete genome sequences. *Fungal Genet. Biol.* **45**, 266–277 (2008).
7. Haberer, G. *et al.* Structure and architecture of the maize genome. *Plant Physiol.* **139**, 1612–1624 (2005).
8. Ma, J. & Bennetzen, J. L. Rapid recent growth and divergence of rice nuclear genomes. *Proc. Natl Acad. Sci. USA* **101**, 12404–12410 (2004).
9. Yuan, Y., SanMiguel, P. J. & Bennetzen, J. L. Methylation-spanning linker libraries link gene-rich regions and identify epigenetic boundaries in *Zea mays*. *Genome Res.* **12**, 1345–1349 (2002).
10. Kamoun, S. A catalogue of the effector secretome of plant pathogenic oomycetes. *Annu. Rev. Phytopathol.* **44**, 41–60 (2006).
11. Whisson, S. C. *et al.* A translocation signal for delivery of oomycete effector proteins into host plant cells. *Nature* **450**, 115–118 (2007).
12. Morgan, W. & Kamoun, S. RXLR effectors of plant pathogenic oomycetes. *Curr. Opin. Microbiol.* **10**, 332–338 (2007).
13. Jiang, R. H., Tripathy, S., Govers, F. & Tyler, B. M. RXLR effector reservoir in two *Phytophthora* species is dominated by a single rapidly evolving superfamily with more than 700 members. *Proc. Natl Acad. Sci. USA* **105**, 4874–4879 (2008).
14. Win, J. *et al.* Adaptive evolution has targeted the C-terminal domain of the RXLR effectors of plant pathogenic oomycetes. *Plant Cell* **19**, 2349–2369 (2007).
15. Bos, J. I. *et al.* The C-terminal half of *Phytophthora infestans* RXLR effector AVR3a is sufficient to trigger R3a-mediated hypersensitivity and suppress INFL1-induced cell death in *Nicotiana benthamiana*. *Plant J.* **48**, 165–176 (2006).
16. Dou, D. *et al.* Conserved C-terminal motifs required for avirulence and suppression of cell death by *Phytophthora sojae* effector Avr1b. *Plant Cell* **20**, 1118–1133 (2008).
17. Qutob, D. *et al.* Copy number variation and transcriptional polymorphisms of *Phytophthora sojae* RXLR effector genes *Avr1a* and *Avr3a*. *PLoS One* **4**, e5066 (2009).
18. Enright, A. J., Kunin, V. & Ouzounis, C. A. Protein families and TRIBES in genome sequence space. *Nucleic Acids Res.* **31**, 4632–4638 (2003).
19. Torto, T. A. *et al.* EST mining and functional expression assays identify extracellular effector proteins from the plant pathogen *Phytophthora*. *Genome Res.* **13**, 1675–1685 (2003).
20. Armstrong, M. R. *et al.* An ancestral oomycete locus contains late blight avirulence gene *Avr3a*, encoding a protein that is recognized in the host cytoplasm. *Proc. Natl Acad. Sci. USA* **102**, 7766–7771 (2005).
21. van Poppel, P. M. *et al.* The *Phytophthora infestans* avirulence gene *Avr4* encodes an RXLR-dEER effector. *Mol. Plant Microbe Interact.* **21**, 1460–1470 (2008).
22. Vleeshouwers, V. G. *et al.* Effector genomics accelerates discovery and functional profiling of potato disease resistance and *Phytophthora infestans* avirulence genes. *PLoS One* **3**, e2875 (2008).
23. Grenville-Briggs, L. J. *et al.* Elevated amino acid biosynthesis in *Phytophthora infestans* during appressorium formation and potato infection. *Fungal Genet. Biol.* **42**, 244–256 (2005).
24. Kamoun, S. *et al.* A gene encoding a protein elicitor of *Phytophthora infestans* is down-regulated during infection of potato. *Mol. Plant Microbe Interact.* **10**, 13–20 (1997).

Supplementary Information is linked to the online version of the paper at www.nature.com/nature.

Acknowledgements We thank L. Gaffney for help with figures and tables, E. Blanco and R. Guigo for training the GeneID gene prediction software, J. Crabtree for providing a Sybil (<http://sybil.sf.net>) software component used to render genome comparison illustrations, the Broad Institute Genome Sequencing Platform for sequence data generation, and C. Cuomo and D. Neafsey for comments on the manuscript. The project was supported by the National Research Initiative of the USDA Cooperative State Research, Education and Extension Service, grant numbers 2004-35600-15024 and 2006-35600-16623, and the National Science Foundation grants EF-0333274 and EF-0523670, and the Gatsby Charitable Foundation.

Author Contributions B.J.H., S.K., M.C.Z. and C.N. coordinated genome annotation, data analyses and manuscript preparation. B.J.H. and S.K. made equivalent contributions and should be considered joint first authors (listed by alphabetical order). R.H.Y.J., R.E.H., L.M.C., M.G., C.D.K., S.R., T.T.-A., T.O.B. and K.O. made major contributions to genome sequencing, assembly, analyses and production of complementary data and resources. All other authors are members of the genome sequencing consortium and contributed annotation, analyses or data throughout the project.

Author Information Reprints and permissions information is available at www.nature.com/reprints. This paper is distributed under the terms of the Creative Commons Attribution-Non-Commercial-Share Alike licence, and is freely available to all readers at www.nature.com/nature. Correspondence and requests for materials should be addressed to S.K. (sophien.kamoun@tsl.ac.uk) or C.N. (chad@broad.mit.edu).

Genetic variation in *IL28B* predicts hepatitis C treatment-induced viral clearance

Dongliang Ge¹, Jacques Fellay¹, Alexander J. Thompson², Jason S. Simon³, Kevin V. Shianna¹, Thomas J. Urban¹, Erin L. Heinzen¹, Ping Qiu³, Arthur H. Bertelsen³, Andrew J. Muir², Mark Sulkowski⁴, John G. McHutchison² & David B. Goldstein¹

Chronic infection with hepatitis C virus (HCV) affects 170 million people worldwide and is the leading cause of cirrhosis in North America¹. Although the recommended treatment for chronic infection involves a 48-week course of peginterferon- α -2b (PegIFN- α -2b) or - α -2a (PegIFN- α -2a) combined with ribavirin (RBV), it is well known that many patients will not be cured by treatment, and that patients of European ancestry have a significantly higher probability of being cured than patients of African ancestry. In addition to limited efficacy, treatment is often poorly tolerated because of side effects that prevent some patients from completing therapy. For these reasons, identification of the determinants of response to treatment is a high priority. Here we report that a genetic polymorphism near the *IL28B* gene, encoding interferon- λ -3 (IFN- λ -3), is associated with an approximately twofold change in response to treatment, both among patients of European ancestry ($P = 1.06 \times 10^{-25}$) and African-Americans ($P = 2.06 \times 10^{-3}$). Because the genotype leading to better response is in substantially greater frequency in European than African populations, this genetic polymorphism also explains approximately half of the difference in response rates between African-Americans and patients of European ancestry.

To identify human genetic contributions to anti-HCV treatment response, we have performed a genome-wide association study of more than 1,600 individuals who were part of the IDEAL study², and we included a further 67 patients from another prospective treatment study³. Briefly, the IDEAL study compared the effectiveness of three treatment regimens involving PegIFN- α -2b or PegIFN- α -2a combined with RBV. It demonstrated similar efficacy of the two IFN preparations and a significantly lower efficacy in self-reported African-Americans compared with Americans of European ancestry (European-Americans). All patients included were treatment-naïve Americans who were chronically infected with genotype 1 HCV. Patients received 48 weeks of treatment and 24 weeks of follow-up. A total of 1,671 individuals were genotyped using the Illumina Human610-quad BeadChip, and we then searched for determinants of treatment response as a primary endpoint. We defined successful treatment response and non-response according to standard definitions⁴, concentrating on sustained virological response (SVR), which is the absence of detectable virus at the end of follow-up evaluation (Supplementary Information I). We included 1,137 patients who satisfied stringent compliance criteria (Supplementary Information I) in the analyses of treatment response, and 1,475 patients in a separate analysis of baseline viral load.

We found that a polymorphism on chromosome 19, rs12979860, is strongly associated with SVR in all patient groups (Fig. 1), with the

European-American population sample showing overwhelming genome-wide significance ($P = 1.06 \times 10^{-25}$). Combining the P values across the population groups, the variant shows association at 1.37×10^{-28} . The polymorphism resides 3 kilobases (kb) upstream of the *IL28B* gene (Fig. 2), encoding IFN- λ -3.

In patients of European ancestry, the CC genotype is associated with a twofold (95% confidence interval 1.8–2.3) greater rate of SVR than the TT genotype (Fig. 1), with similar ratios in both the African-American (threefold, 95% confidence interval 1.9–4.7) and the Hispanic (twofold, 95% confidence interval 1.4–3.2) population groups. The magnitude of this association is compared in Table 1 with other host or viral factors known to influence SVR in patients infected with genotype 1 HCV, including baseline viral load, fibrosis and ethnicity^{4,5}. Not only does the *IL28B* polymorphism strongly influence response within each of the major population groups, it also appears to explain much of the difference in response between different population groups (European-Americans compared with African-Americans). We estimate that approximately half of the difference in SVR between populations can be accounted for by the difference in frequency of the C allele between African-Americans and individuals of European ancestry (Supplementary Information XI). Interestingly, it has also been well documented that East Asians have

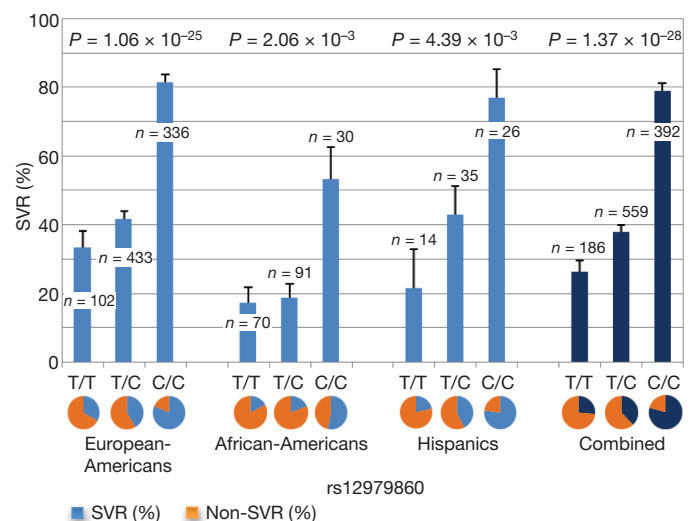


Figure 1 | Percentage of SVR by genotypes of rs12979860. Data are percentages + s.e.m.

¹Institute for Genome Sciences & Policy, Center for Human Genome Variation, Duke University, Durham, North Carolina 27708, USA. ²Duke Clinical Research Institute and Division of Gastroenterology, School of Medicine, Duke University, Durham, North Carolina 27705, USA. ³Schering-Plough Research Institute, Kenilworth, New Jersey 07033, USA. ⁴Johns Hopkins University School of Medicine, Baltimore, Maryland 21205, USA.

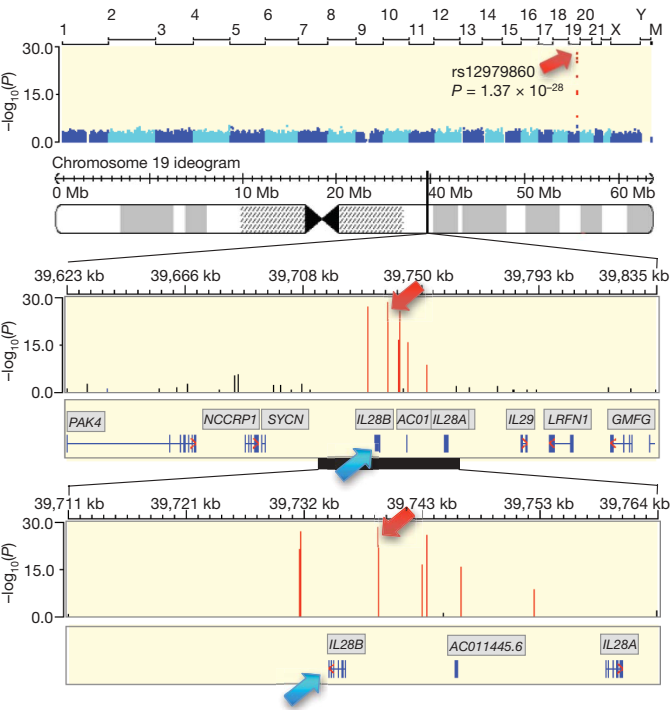


Figure 2 | Genomic overview of the region of 19q13.13 surrounding the genome-wide significant determinant of response to treatment and including the *IL28B* gene. The top panel shows a genome-wide view of the *P* values [$-\log_{10}(P)$]. Panels below show all genotyped SNPs in the region of significance and the structures of the surrounding genes. The SNPs that show genome-wide significant association with SVR are marked in red. The polymorphism rs12979860 (red arrow) is 3 kb upstream to the gene encoding IFN- λ -3 (*IL28B*, blue arrow). Other SNPs in the same region showing genome-wide significant *P* values largely reflect the same signal (Supplementary Information IX). The results were annotated using the WGAViewer software¹⁹.

higher SVR rates than patients of European ancestry^{6,7}. By looking at a random multi-ethnic population sample with unknown hepatitis C status (Supplementary Information II), we observed a substantially higher frequency of the C allele in East Asians (Fig. 3). Collectively, the SVR rates across different population groups displayed a striking concordance with C-allele frequency (Fig. 3). Finally, it is also noteworthy that African-Americans with the CC genotype have a significantly higher rate of response (53.3%) than individuals of European ancestry who have the TT genotype (33.3%, $P < 0.05$), which emphasizes the greater importance of individual genotype compared with ethnicity in predicting treatment response⁸.

We next tested whether this variant influences baseline (pre-treatment) viral load and found a significant association in all groups (Supplementary Information XIII). Interestingly, the C allele, associated with better treatment response, is also associated with higher baseline viral load (CC 6.35, $n = 485$; TC 6.33, $n = 744$; TT 6.16, $n = 246$; $P = 1.21 \times 10^{-10}$; viral loads given as \log_{10} international

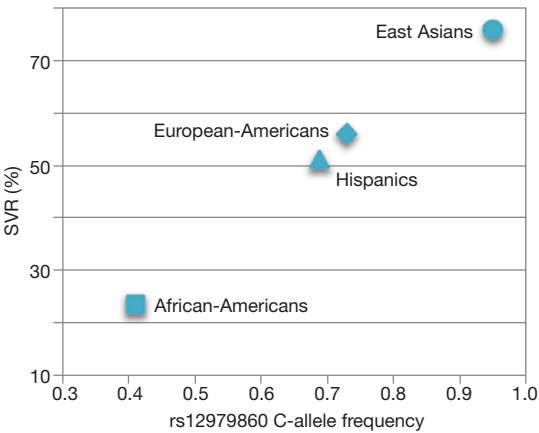


Figure 3 | Rate of SVR and rs12979860 C-allele frequency in diverse ethnic groups. The SVR rate in East Asians is adopted from Liu *et al.*⁷. Sample sizes for C-allele frequency: $n = 61$ (African-Americans); $n = 271$ (European-Americans); $n = 16$ (Hispanics); $n = 107$ (East Asians); sample sizes for SVR rate: $n = 191$ (African-Americans); $n = 871$ (European-Americans); $n = 75$ (Hispanics); $n = 154$ (East Asians).

units (IU) ml^{-1}). Although this finding is counter-intuitive in that lower baseline viral loads predict a better response to treatment, it could relate to recent speculation about the role of IFN-stimulated genes in modulating response to PegIFN⁹, and it seems plausible that the *IL28B* polymorphism has a role in the regulation of intra-hepatic IFN-stimulated gene expression with consequences both for viral load and treatment response (Supplementary Information XIII). We also note that the polymorphism has no association with whether individuals are classified as having baseline viral loads above or below a commonly used threshold that predicts respectively worse or better treatment response (Supplementary Information XIII), indicating that the association of the polymorphism with clearance and viral load may be independent. In addition, we note that the C-allele frequency was significantly reduced in the chronically infected cohort compared with ethnically matched controls (0.63 versus 0.73, controlled for population structure, $P < 2.5 \times 10^{-6}$, Supplementary Information II and XVI), which suggests an association between the C allele and a higher rate of natural clearance of hepatitis C. We note, however, that determination of the precise effect of the C allele on clearance will require comparison between matched cohorts known to have and have not naturally cleared this viral infection.

We sequenced the *IL28B* gene in 96 individuals, and found two variants highly associated with rs12979860 ($r^2 > 0.85$ for all comparisons in all populations): a G > C transition 37 base pairs (bp) upstream of the translation initiation codon (rs28416813), and a non-synonymous coding single nucleotide polymorphism (SNP) (rs8103142) encoding the amino-acid substitution Lys70Arg. These new variants were then genotyped in the full cohort. Owing to the high degree of correlation among the three SNPs, tests for independence among these variants, using all available patients, were not able

Table 1 | Comparison between the genetic and conventional clinical factors associating with SVR

	Odds ratio (95% confidence interval)		
	European-Americans	African-Americans	Hispanics
<i>IL28B</i> rs12979860 genotype CC (versus CT and TT)*	7.3 (5.1–10.4)	6.1 (2.3–15.9)	5.6 (1.4–22.1)
Baseline viral load (<600,000 IU ml^{-1} versus $\geq 600,000$ IU ml^{-1})†	4.2 (2.6–6.6)	5.1 (1.9–13.9)	2.4 (0.7–8.8)
Baseline fibrosis (METAVIR F0–2 versus F3–4)‡	3.0 (1.8–5.1)	1.1 (0.3–5.2)	4.1 (0.7–25.5)
Ethnicity (European-Americans/African-Americans)	3.1 (2.1–4.7)		

Odds ratios and 95% confidence intervals are generated from the logistic regression model.

* Corresponding relative risks for rs12979860: 2.0 (95% confidence interval 1.8–2.3) in European-Americans; 3.0 (95% confidence interval 1.9–4.7) in African-Americans; 2.1 (95% confidence interval 1.4–3.2) in Hispanics.

† In clinical practice it is customary to divide patients into high and low viral-load groups, reflecting a well-described threshold effect. The IDEAL trial used a threshold of 600,000 (ref. 2).

‡ Fibrosis was scored by METAVIR stage on a baseline centrally evaluated liver biopsy²¹⁸.

to resolve which, if any, of these sites is uniquely responsible for the association with SVR. Additional HCV-infected cohorts may help to determine whether one of these SNPs, or any other SNP in the region, is causal for the association, as the pattern of association suggests the possibility of more than one functional variant in the region (Supplementary Information IX). Ultimately, identification and elucidation of the functional SNPs will depend on in-depth functional studies.

Given the significant effect of the *IL28B* polymorphism on treatment response, and its likely clinical relevance, it was considered important to compare the magnitude of different predictors of response for the patients studied here. We developed a logistic regression model that related clinical predictors to response rates (Supplementary Information XI). We noted that the regression model showed that the CC genotype is associated with a more substantial difference in rate of response than other known baseline predictors included in the model.

It seems likely therefore that advance knowledge of host genotype of patients infected with HCV could in the future become an important component of the clinical decision to initiate treatment with PegIFN and RBV. Many important clinical questions remain. The current data are specific to patients with genotype 1 infection. It will therefore be necessary to evaluate the role of host *IL28B* genotype and treatment response in other less common HCV genotypes. Novel small molecules, including HCV protease inhibitors, are currently being developed and may soon be used in combination with PegIFN and RBV for the treatment of genotype 1 HCV¹⁰; the role of the *IL28B* genotype in these novel treatment regimens should therefore be investigated.

In conclusion, we have identified a polymorphism 3 kb upstream of *IL28B* that is significantly associated with response to PegIFN and RBV for patients with chronic genotype 1 HCV infection. The polymorphism explains much of the difference in response between European-American and African-American patients. Given that the polymorphism appears to associate with natural clearance as well as treatment response, it seems likely that the gene product is involved in the innate control of HCV. Indeed, IFN- λ s have demonstrated antiviral activity against genotype 1 HCV *in vitro*¹¹ and *in vivo*¹². The IFN- λ proteins, encoded by the *IL28A/B* and *IL29* genes, were first described in 2003 (refs 13, 14). These IFNs signal through a unique receptor but appear to share a common downstream signalling system with the type 1 IFNs, including IFN- α . These findings, and further study of the functional mechanism underlying the *IL28B*-response association, may help identify patients for whom therapy is likely to be successful, and highlight the IFN- λ signalling axis as a potential target for novel antiviral drug development.

METHODS SUMMARY

Our primary association tests involved single-marker genotype trend tests performed in three independent groups (European-Americans, $n = 871$; African-Americans, $n = 191$; Hispanics, $n = 75$; Supplementary Information I), using logistic regression models for treatment response and linear regression for baseline viral load (Supplementary Information VI). Association tests were implemented in the PLINK software¹⁵, correcting for several clinical covariates, including baseline (pre-treatment) HCV viral load and severity of fibrosis. Then the association signals (P values) were combined using Stouffer's weighted Z -method¹⁶, correctly taking into account sample sizes, effect sizes and effect directions in each population. This combined P value was then reported as the main result, along with the P values in each ethnic group. A series of quality-control steps resulted in 565,759 polymorphisms for the association tests. We applied methods to assess copy number variants and tested the relation between copy number variants and SVR. To control for the possibility of spurious

associations resulting from population stratification, we used a modified EIGENSTRAT¹⁷ method and corrected for population ancestry within each group. We assessed significance with a Bonferroni correction ($P_{\text{cutoff}} = 4.4 \times 10^{-8}$; see Supplementary Information VIII for details).

Received 27 May; accepted 17 July 2009.

Published online 16 August; corrected 17 September 2009 (see full-text HTML version for details).

1. World Health Organization. *Hepatitis C* (<http://www.who.int/mediacentre/factsheets/fs164/en/>) (2009).
2. McHutchison, J. G. *et al.* Peginterferon alfa-2b or alfa-2a with ribavirin for treatment of hepatitis C infection. *N. Engl. J. Med.* **361**, 580–593 (2009).
3. Muir, A. J., Bornstein, J. D. & Killenberg, P. G. Peginterferon alfa-2b and ribavirin for the treatment of chronic hepatitis C in blacks and non-Hispanic whites. *N. Engl. J. Med.* **350**, 2265–2271 (2004).
4. Ghany, M. G., Strader, D. B., Thomas, D. L. & Seeff, L. B. Diagnosis, management, and treatment of hepatitis C: an update. *Hepatology* **49**, 1335–1374 (2009).
5. Shiffman, M. L. *et al.* Peginterferon alfa-2a and ribavirin in patients with chronic hepatitis C who have failed prior treatment. *Gastroenterology* **126**, 1015–1023; discussion 947 (2004).
6. Yan, K. K. *et al.* Treatment responses in Asians and Caucasians with chronic hepatitis C infection. *World J. Gastroenterol.* **14**, 3416–3420 (2008).
7. Liu, C. H. *et al.* Pegylated interferon- α -2a plus ribavirin for treatment-naïve Asian patients with hepatitis C virus genotype 1 infection: a multicenter, randomized controlled trial. *Clin. Infect. Dis.* **47**, 1260–1269 (2008).
8. Wilson, J. F. *et al.* Population genetic structure of variable drug response. *Nature Genet.* **29**, 265–269 (2001).
9. Sarasin-Filipowicz, M. *et al.* Interferon signaling and treatment outcome in chronic hepatitis C. *Proc. Natl Acad. Sci. USA* **105**, 7034–7039 (2008).
10. McHutchison, J. G. *et al.* Telaprevir with peginterferon and ribavirin for chronic HCV genotype 1 infection. *N. Engl. J. Med.* **360**, 1827–1838 (2009).
11. Robek, M. D., Boyd, B. S. & Chisari, F. V. Lambda interferon inhibits hepatitis B and C virus replication. *J. Virol.* **79**, 3851–3854 (2005).
12. Shiffman, M. L. *et al.* PEG-IFN- λ : antiviral activity and safety profile in a 4-week phase 1b study in relapsed genotype 1 hepatitis C infection. *J. Hepatol.* **50** (suppl. 1), abstr. A643 s237 (2009).
13. Kotenko, S. V. *et al.* IFN- λ s mediate antiviral protection through a distinct class II cytokine receptor complex. *Nature Immunol.* **4**, 69–77 (2003).
14. Sheppard, P. *et al.* IL-28, IL-29 and their class II cytokine receptor IL-28R. *Nature Immunol.* **4**, 63–68 (2003).
15. Purcell, S. *et al.* PLINK: a toolset for whole-genome association and population-based linkage analysis. *Am. J. Hum. Genet.* **81**, 559–575 (2007).
16. Whitlock, M. C. Combining probability from independent tests: the weighted Z -method is superior to Fisher's approach. *J. Evol. Biol.* **18**, 1368–1373 (2005).
17. Price, A. L. *et al.* Principal components analysis corrects for stratification in genome-wide association studies. *Nature Genet.* **38**, 904–909 (2006).
18. The French METAVIR Cooperative Study Group. Intraobserver and interobserver variations in liver biopsy interpretation in patients with chronic hepatitis C. *Hepatology* **20**, 15–20 (1994).
19. Ge, D. *et al.* WGAViewer: software for genomic annotation of whole genome association studies. *Genome Res.* **18**, 640–643 (2008).

Supplementary Information is linked to the online version of the paper at www.nature.com/nature.

Acknowledgements We are indebted to the IDEAL principal investigators, the study coordinators, nurses and patients involved in the study. We also recognize E. Gustafson, P. Savino, D. Devlin, S. Novello, M. Geffner, J. Albrecht and A. C. Need for their contributions to the study. This study was funded by Schering-Plough Research Institute, Kenilworth, New Jersey. A.J.T. received funding support from the National Health and Medical Research Council of Australia and the Gastroenterological Society of Australia.

Author Contributions D.G., J.F., A.J.T. and J.S.S. contributed equally to this work. D.G., J.F. and A.J.T. performed the statistical and bioinformatical analyses. J.F. and A.J.T. defined the clinical phenotypes. K.V.S. performed the genotyping. D.B.G. and D.G. drafted the manuscript. J.S.S., J.G.M. and D.B.G. designed the study. All authors collected and analysed data and contributed to preparing the manuscript.

Author Information Reprints and permissions information is available at www.nature.com/reprints. The authors declare competing financial interests: details accompany the full-text HTML version of the paper at www.nature.com/nature. Correspondence and requests for materials should be addressed to D.B.G. (d.goldstein@duke.edu).

LETTERS

Modelling pathogenesis and treatment of familial dysautonomia using patient-specific iPSCs

Gabsang Lee¹, Eirini P. Papapetrou², Hyesoo Kim¹, Stuart M. Chambers¹, Mark J. Tomishima^{1,2,3}, Christopher A. Fasano¹, Yosif M. Ganat^{1,6}, Jayanthi Menon⁴, Fumiko Shimizu⁴, Agnes Viale⁵, Viviane Tabar^{2,4}, Michel Sadelain² & Lorenz Studer^{1,2,4}

The isolation of human induced pluripotent stem cells (iPSCs)^{1–3} offers a new strategy for modelling human disease. Recent studies have reported the derivation and differentiation of disease-specific human iPSCs^{4–7}. However, a key challenge in the field is the demonstration of disease-related phenotypes and the ability to model pathogenesis and treatment of disease in iPSCs. Familial dysautonomia (FD) is a rare but fatal peripheral neuropathy, caused by a point mutation in the *IKBKAP*⁸ gene involved in transcriptional elongation⁹. The disease is characterized by the depletion of autonomic and sensory neurons. The specificity to the peripheral nervous system and the mechanism of neuron loss in FD are poorly understood owing to the lack of an appropriate model system. Here we report the derivation of patient-specific FD-iPSCs and the directed differentiation into cells of all three germ layers including peripheral neurons. Gene expression analysis in purified FD-iPSC-derived lineages demonstrates tissue-specific mis-splicing of *IKBKAP* *in vitro*. Patient-specific neural crest precursors express particularly low levels of normal *IKBKAP* transcript, suggesting a mechanism for disease specificity. FD pathogenesis is further characterized by transcriptome analysis and cell-based assays revealing marked defects in neurogenic differentiation and migration behaviour. Furthermore, we use FD-iPSCs for validating the potency of candidate drugs in reversing aberrant splicing and ameliorating neuronal differentiation and migration. Our study illustrates the promise of iPSC technology for gaining new insights into human disease pathogenesis and treatment.

Familial dysautonomia (FD), also known as hereditary sensory and autonomic neuropathy III (HSAN-III) or Riley–Day syndrome, is a fatal autosomal recessive disease characterized by the degeneration of sensory and autonomic neurons^{8,10}. The pathogenesis of the disease and its specificity to the peripheral nervous system are poorly understood. Most FD patients carry a point mutation in the I- κ -B kinase complex-associated protein (*IKBKAP*) gene resulting in a tissue-specific splicing defect with various levels of exon 20 skipping and reduced levels of normal IKAP protein^{8,11}. Reduced IKAP protein levels are associated with a defect in cell motility⁹. However, it is unclear whether decreased cell motility is functionally related to the specific peripheral neuron pathology observed in FD. On the basis of the splicing defect, *in vitro* drug screens have been performed in patient lymphoblast cell lines to identify compounds that improve normal *IKBKAP* splicing and increase IKAP protein levels¹². However, lack of access to tissues affected by FD, such as neural crest precursors and peripheral neurons, has hampered functional validation of candidate drugs and a systematic analysis of disease pathogenesis. Here we demonstrate the potential of human iPSC

technology to model FD pathogenesis and treatment (Supplementary Fig. 1).

We obtained fibroblasts from a 10-year-old female FD patient and established two independent clones of FD-iPSCs (FD-4, FD-22) after transduction with lentiviral vectors encoding for OCT4 (also known as POU5F1), SOX2, KLF4 and c-MYC (Fig. 1a–c). Further iPSCs clones were derived from two other FD patients (16-year-old male and 12-year-old female FD patients) and from non-affected control fibroblasts using the same procedure. The vector system used for iPSC generation allowed convenient monitoring of transgene expression by individual fluorescence tags by P2A technology¹³. All FD and control iPSCs used in this study showed silencing of the four transgenes, exhibited characteristic human embryonic stem cell (ESC) morphology, expressed pluripotency markers including Nanog, SSEA3, SSEA4, TRA-1-81 and had a normal karyotype (Fig. 1b–f and Supplementary Figs 2 and 3). Pluripotent properties of FD-iPSCs were also assessed by monitoring the methylation status of the *NANOG* promoter (Fig. 1g), by global transcriptome analysis in comparison to FD-fibroblasts, human ESCs (line H9) and control-iPSC lines (Fig. 1h and Supplementary Fig. 3), and by teratoma formation on intramuscular injection of undifferentiated FD-iPSCs into non-obese diabetic/severe combined immunodeficient (NOD-SCID) mice (Fig. 1i). Genetic identity was confirmed by DNA fingerprinting analysis for microsatellite markers (Supplementary Table 1). The genetic defect was confirmed as a homozygous 2507+6T > C mutation in the *IKBKAP* gene (Fig. 1j) known to induce tissue-specific skipping of exon 20. Gene expression analysis for *IKBKAP* revealed that FD-fibroblasts and FD-iPSCs express both the wild-type and the mutant *IKBKAP* transcript, although the ratio of normal to mutant transcript was higher in FD-iPSCs than in FD-fibroblasts (Fig. 1k).

The pluripotent nature of iPSCs offers the opportunity for probing the tissue specificity of the *IKBKAP* splicing defect *in vitro*. FD- and control-iPSCs (two clones each) were differentiated into five major tissues comprising all three embryonic germ layers. No reactivation of transgenes was observed in differentiated progeny (Supplementary Fig. 2). After directed differentiation towards central nervous system (CNS)¹⁴, peripheral nervous system¹⁵, haematopoietic¹⁶, endothelial¹⁷, and endodermal¹⁸ precursors, iPSC derivatives were further enriched by prospective isolation using lineage-specific surface markers (Fig. 2a–f). Early neural differentiation was characterized by the formation of neural rosette structures in both FD- and control-iPSCs (Supplementary Fig. 4). No major differences were observed in the efficiency of differentiation towards any of the five lineages comparing FD- versus control-iPSCs (data not shown). However, marked differences were observed for the ratio of normal:mutant transcript

¹Developmental Biology Program, ²Center for Cell Engineering, ³SKI Stem Cell Research Facility, ⁴Department of Neurosurgery, ⁵Genomics Core Facility, Sloan-Kettering Institute, 1275 York Ave, ⁶Weill Cornell Graduate School, New York, New York 10065, USA.

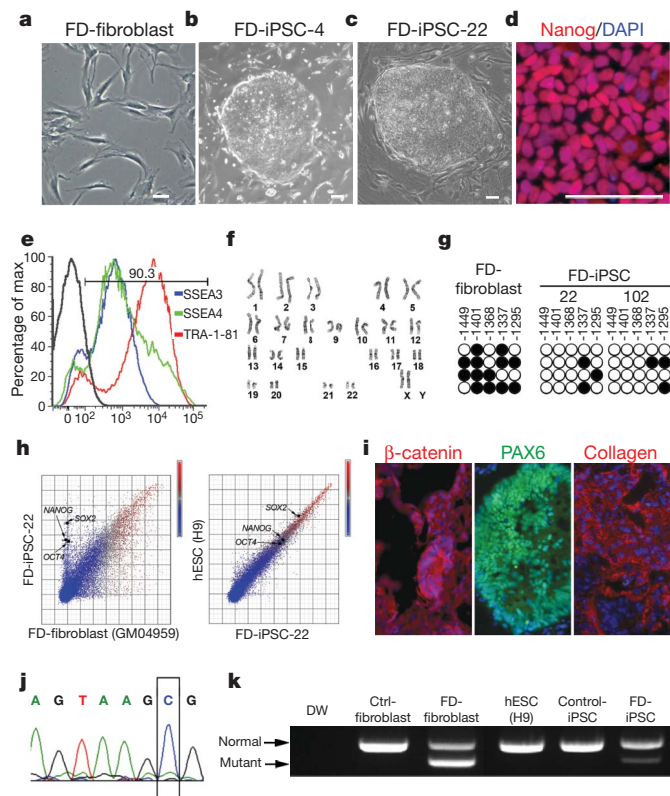


Figure 1 | Establishment of FD-iPSCs from patient fibroblasts. **a–c**, FD patient fibroblasts (**a**) were converted into FD-iPSCs (**b, c**) after lentiviral transduction with OCT4, SOX2, KLF4 and c-MYC. **d**, Nanog protein expression in FD-iPSC cell line. **e**, Flow-cytometry analysis of FD-iPSCs for pluripotent surface markers. **f**, Karyotype analysis of FD-iPSCs. **g**, Bisulphite sequencing analysis of the *NANOG* promoter in FD-fibroblast and FD-iPSC clones. **h**, Global gene expression patterns were compared among FD-fibroblast, FD-iPSCs and human ESCs. **i**, Teratoma from FD-iPSCs showed three germ-layer differentiation as illustrated by the presence of endodermal epithelia expressing β -catenin, $PAX6^+$ neuroectodermal precursors and mesodermal collagen $^+$ cells. **j**, Sequencing result showed the 2507+6T > C mutation of *IKBKAP* in FD-iPSCs. **k**, Analysis of *IKBKAP* RT-PCR products in messenger RNA derived from normal and FD-specific fibroblasts and pluripotent stem cells. Ctrl, control; DW, distilled water (negative control). Scale bars, 50 μ m.

among the five FD-iPSCs-derived tissues (Fig. 2a–f, insets). The mutant transcript predominated particularly in $CXCR4^+$ purified endodermal precursors ($SOX17^+$) and, to a lesser extent, in neural crest precursors (Fig. 2g). The disease symptoms in FD are thought to be caused by loss of sufficient levels of normal *IKBKAP* transcript. Therefore, we next performed quantitative PCR with reverse transcription (qRT-PCR) analysis to determine the absolute levels of normal spliced *IKBKAP* transcript in each of the five FD- or control-iPSC-derived cell populations (Fig. 2h). These data showed particularly low levels of normal *IKBKAP* transcript in FD-iPSC-derived neural crest precursors *in vitro*, compatible with the tissue-specific human pathology observed in FD patients. High levels of mutant *IKBKAP* expression in endodermal precursors are of interest in view of the debilitating gastrointestinal problems observed in FD—although such symptoms are thought to be a consequence of a primary defect in the peripheral nervous system.

Directed differentiation of patient-specific iPSCs towards neural crest lineages, the primary tissue affected in FD, enables modelling functional aspects of pathogenesis *in vitro*. Neuropathological studies have demonstrated a marked depletion of autonomic and sensory neurons in FD patients. However, the cause for peripheral neuron loss in FD remains unclear, and there are at present no mouse models that faithfully replicate the disease. Mouse modelling in other neural crest disorders has identified several potential disease mechanisms, such as impaired neural precursor cell migration in Hirschsprung's disease¹⁹ or degeneration of established neural crest tissues in Treacher Collins syndrome²⁰. We explored the involvement of candidate disease mechanisms in FD by performing comparative transcriptome analysis of fluorescence-activated cell sorting (FACS)-purified FD-iPSC versus control-iPSC-derived neural crest precursors (Fig. 3a and Supplementary Table 2; raw data of microarray data available at the Gene Expression Omnibus (<http://www.ncbi.nlm.nih.gov/geo/>) under accession number GSE17043). Among 48,000 probe sets, 35 transcripts were significantly increased and 54 transcripts decreased in FD-iPSC versus control iPSC- or ESC-derived neural crest precursors (fold-change ≥ 2 -fold; corrected *P* value of 0.05). Differential expression of key transcripts from the microarray study was confirmed by qPCR analysis for neural crest precursors of both FD-iPSC clones (Supplementary Fig. 5). Notably, among the 20 most decreased transcripts in FD neural crest precursors were many genes involved in peripheral neurogenesis and neuronal differentiation. Examples include *SLC17A6* (also known as *VGLUT2*) expressed in sensory

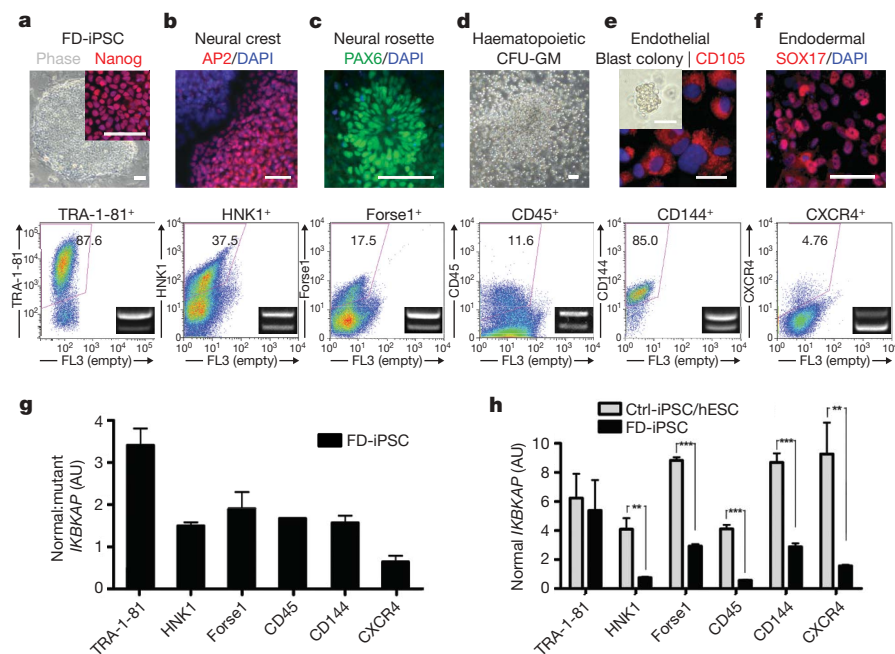


Figure 2 | FD-iPSC-derived cell lineages model the tissue specificity of FD *IKBKAP* splicing defect. **a**, Undifferentiated iPSCs were defined by Nanog expression and quantitative analysis of TRA-1-81. **b–f**, FD-iPSCs were directed towards specific lineages and purified by flow-cytometric sorting for appropriate surface markers. The cell types analysed included $AP2^+$ neural crest precursors purified on the basis of $HNK1^+$ expression (**b**), FACS-purified $Forse1^+$ neural rosette cells ($PAX6^+$) (**c**), haematopoietic cells that were collected from colony forming unit (CFU) culture and sorted with CD45 marker (**d**), FACS-isolated $CD144^+$ (VE-cadherin) endothelial cells ($CD105^+$) from blast-colony culture (**e**), and FACS-isolated $CXCR4^+$ endodermal precursors ($SOX17^+$) from activin-A-induced differentiation culture (**f**). The bottom inset panels show *IKBKAP* RT-PCR products of FACS-purified lineages. **g, h**, The ratio of normal:mutant splicing (**g**) and the expression of normal *IKBKAP* transcript (**h**) are shown. $n = 3–6$; $**P < 0.01$; $***P < 0.001$. All values are mean and s.d. Scale bars, 50 μ m. AU, arbitrary units.

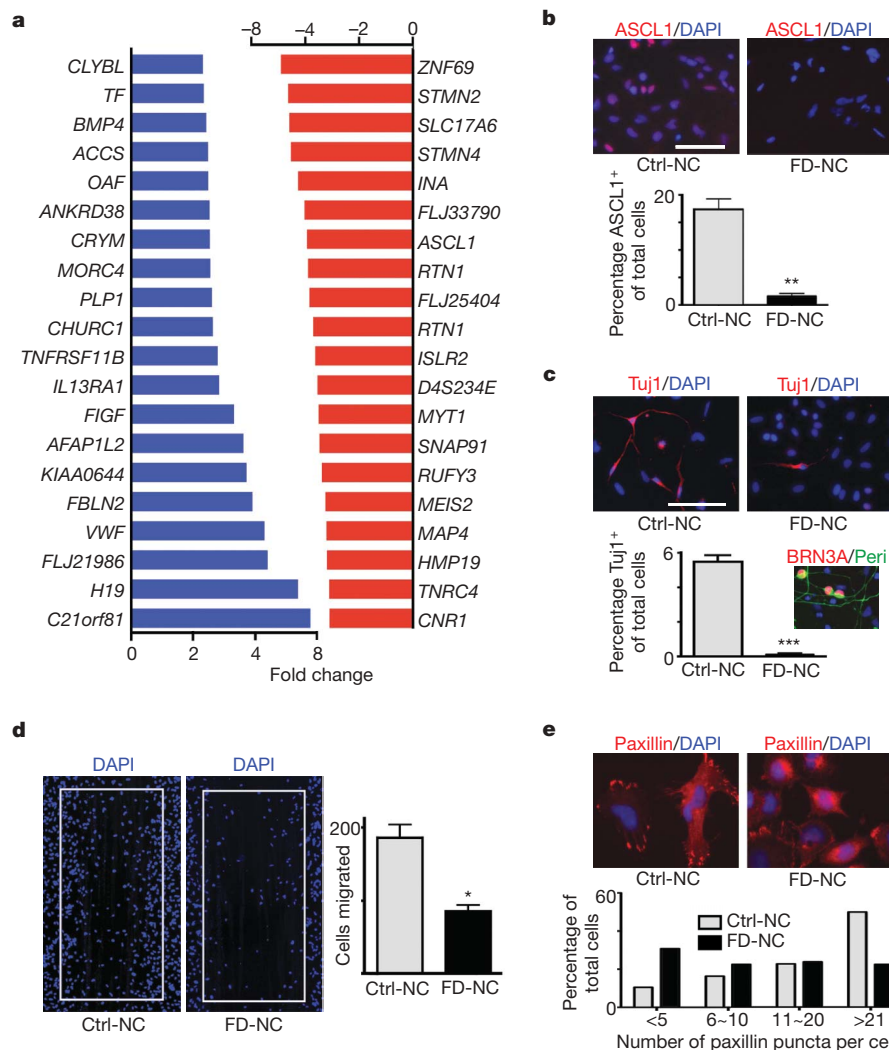


Figure 3 | Molecular and functional characterization of FD-iPSC-derived neural crest precursor cells. **a**, List of the unselected top increased (blue) and top decreased (red) genes comparing FD-iPSC- versus (C14 and H9)-derived neural crest (NC) cells, as assessed by microarray analysis.

ANKRD38 is also known as *KANK4*; *FLJ33790* is also known as *KLHL35*; *FLJ25404* is also known as *C16orf92*; *FLJ21986* is also known as *C7orf58*; *KIAA0644* EntrezGene ID 9865; *D4S234E* EntrezGene ID 27065, *HMP19* EntrezGene ID 51617. **b**, **c**, Representative images and quantifications of ASCL1 (**b**) and Tuj1 (**c**) expression in spontaneously differentiated neural

crest cells derived from FD-iPSCs and C14-iPSCs. $n = 4$; ** $P < 0.01$; *** $P < 0.001$. The inset in **c** shows a representative image of putative sensory neuron progeny (BRN3A⁺ and peripherin⁺ (Peri)) from FD-iPSC-derived neural crest cells. **d**, **e**, Representative images of wound-healing assay (fixed at 48 h after scratching) (**d**) and paxillin staining (fixed at 1.5 h after plating) (**e**) of FD-iPSC- and C14-iPSC-derived neural crest cells. $n = 4$; * $P < 0.05$. Quantification of paxillin staining was performed by counting the number of paxillin puncta marking focal adhesion complex. All values are mean and s.d. Scale bars, 50 μ m.

neurons, the neuronal intermediate filaments *MAP4* and *INA*, and *STMN2* (also known as *SCG10*; a known marker of autonomic neurons²¹). Of particular interest were the significant differences in *ASCL1* (previously known as *Mash1* in mice) expression between FD- and control-iPSC given the essential role of *ASCL1* for the development of autonomic neurons during mouse development²¹. Differential expression of *ASCL1* was further confirmed at the protein level by quantifying the percentages of ASCL1-immunoreactive cells (Fig. 3b). The marked differences in neurogenesis were also reflected by a reduction in the percentage of spontaneously differentiating Tuj1⁺ neurons in FD-iPSC-derived neural crest precursor cultures (Fig. 3c). Peripheral neurogenesis was not completely blocked, as FD-iPSC-derived BRN3A⁺ (also known as POU4F1⁺) and peripherin⁺ neurons were observed on further *in vitro* differentiation (Fig. 3c, inset). These data indicate a defect in the propensity of FD-iPSC-derived neural crest precursors to undergo neuronal differentiation. Previous studies in *IKBKAP*-depleted or patient-specific fibroblasts indicated that reduced levels of normal *IKBKAP* are associated with defects in cell migration^{9,22}. Using a wound healing ('scratch') assay we observed a

significant decrease in the migration of FD-iPSC- versus control-iPSC-derived neural crest precursors (Fig. 3d). FD-iPSC-derived neural crest precursors also showed a reduction in the number of paxillin⁺ focal adhesions critical for cell spreading and migration (Fig. 3e).

Our study shows defects in *IKBKAP* splicing, neurogenesis, and migration of FD-iPSC-derived neural crest precursors. Results were validated in several independent FD-iPSC clones (see Supplementary Fig. 6) and compared to both non-affected control-iPSC and control human ESC cultures. These data demonstrate that FD-iPSC-derived neural crest precursors represent a powerful model system to probe disease pathogenesis, although larger sets of FD-iPSC lines may be useful to further validate disease phenotype.

Another key promise of human iPSC research is the use of patient-specific cells in drug discovery. Our study has demonstrated three easily quantifiable parameters of the disease state: a defect in *IKBKAP* splicing, decreased rate of neurogenesis, and reduced migration in FD-iPSC-derived neural crest precursors. We next tested whether exposure to candidate drugs can affect any of these three parameters. The plant hormone kinetin was previously shown to reduce levels of

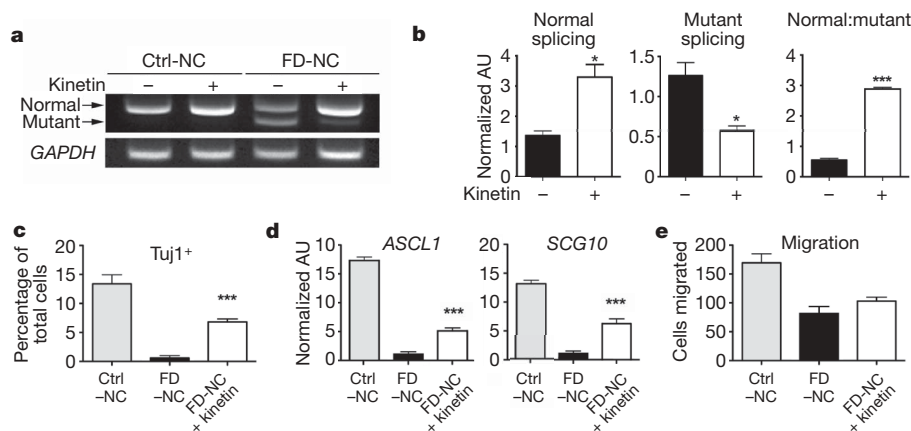


Figure 4 | Validating kinetin as a candidate compound for treating FD-iPSC-derived neural crest cells. **a**, Gel image of RT-PCR products for *IKBKAP* splicing rescued by kinetin treatment in control and FD-iPSC-derived neural crest (NC) cells. **b**, Quantification of band intensity of FD-iPSC-derived neural crest cells normalized by *GAPDH* and the ratio of normal and mutant spliced *IKBKAP* transcripts. $n = 5$; * $P < 0.05$;

*** $P < 0.001$. **c**, **d**, *Tuj1* (**c**) and *ASCL1* and *SCG10* (**d**) expression in neuronal differentiation with kinetin-treated neural crest cells derived from FD-iPSC. $n = 4$; *** $P < 0.001$. **e**, Results of kinetin treatment on cell motility (wound-healing assay) in FD-iPSC derived neural crest cells. $n = 4-6$. All values are mean and s.d.

the mutant *IKBKAP* splice form in FD-derived lymphoblast cell lines¹². Epigallocatechin gallate (ECGC) and tocotrienol have also been reported to effect splicing and the absolute levels of *IKBKAP*^{23,24}. Exposure of FD-iPSC-derived neural crest precursors to kinetin resulted in a marked reduction of the mutant *IKBKAP* splice form (Fig. 4a). In contrast, no significant improvements in *IKBKAP* splicing were observed after ECGC or tocotrienol exposure (Supplementary Fig. 7). The kinetin-mediated decrease in mutant *IKBKAP* was associated with an increase in normal *IKBKAP* levels and the ratio of normal:mutant transcript (Fig. 4b). No significant increase in normal *IKBKAP* transcript levels was observed after kinetin treatment of neural crest precursors derived from control iPSCs (Supplementary Fig. 8). Although short-term (1 or 5 day) kinetin treatment of FD-iPSC-derived neural crest precursors had considerable effects on *IKBKAP* splicing, it did not result in a significant increase in the expression of neurogenic markers or improve migration behaviour (Supplementary Figs 9 and 10). We next tested the effect of continuous (28 day) kinetin treatment of FD-iPSCs starting at the pluripotent stage 1 day before differentiation (Supplementary Fig. 11). Notably, continuous kinetin treatment induced a significant increase in the percentage of differentiating neurons and in the expression of key peripheral neuron markers such as *ASCL1* and *SCG10* at the neural crest precursor stage (Fig. 4c, d). No significant increase was observed in FD-iPSC neural crest precursor cell migration (Fig. 4e), suggesting incomplete restoration of disease phenotype. These data demonstrate the feasibility of exploring disease mechanism and action of candidate drugs in FD-iPSCs. Although future studies will be required to define the developmental windows of kinetin action in greater detail, our data indicate that early stage long-term treatment may be particularly beneficial in FD patients.

Since the initial reports on human iPSC isolation¹⁻³, several patient-specific iPSC lines have been developed⁴⁻⁷. Modelling human disease in iPSCs has remained challenging owing to difficulties in directing iPSC fate and identifying disease-related behaviours. Previous reports have demonstrated the derivation of patient-specific motoneurons as an initial step in modelling amyotrophic lateral sclerosis (ALS) and spinal muscular atrophy (SMA) and dopamine neurons for modelling Parkinson's disease^{4,5,7}. Although the study using SMA-iPSCs reported a potentially disease-related loss of cholinergic neurons⁵, the other studies did not observe⁷ or did not report⁴ any disease-related phenotypes. Interestingly, both SMA and FD are early onset disorders, suggesting that iPSC technology may be particularly suited to model developmental disorders. Here we extend the approach to modelling disease in the neural crest

lineage and provide clear evidence of disease-related behaviours in FD-iPSCs. Although FD is a rare genetic disorder with an incidence of 1/3,600 live births among the Ashkenazi Jewish population (~600 registered patients worldwide²⁵), it provides a platform to demonstrate the potential of iPSC technology for exploring disease mechanism in a human genetic disorder. Studying aberrant tissue-specific *IKBKAP* splicing in iPSCs will be particularly attractive given the pluripotent nature and unlimited number of cells available for mechanistic studies and for high-throughput drug discovery. Our data on defects in neurogenic propensity and migration of FD-iPSC-derived neural crest precursors provide new insights into disease pathogenesis and suggest alternative functional assays for the identification and validation of candidate drugs. Furthermore, kinetin treatment illustrates the potential of iPSC technology for modelling therapeutic action in human neural disease *in vitro* using patient-specific cells.

METHODS SUMMARY

iPSC generation and differentiation. FD and control fibroblasts were obtained from Coriell and reprogrammed towards iPSCs using a lentiviral four factor protocol (OCT4, SOX2, KLF4 and c-MYC) described recently¹³. Undifferentiated human ESCs and iPSC lines were maintained on mitotically inactivated mouse embryonic fibroblasts (MEFs) in serum-replacement medium in the presence of 4 ng ml⁻¹ FGF2 (ref. 15). For neural induction, human ESCs were plated on a confluent layer of irradiated stromal cells (MS-5) as described previously^{15,26}. After 3–4 weeks of differentiation, ESC progeny was triturated into single cells after Accutase dissociation (Innovative cell technologies) and labelled with antibodies for flow cytometry. Protocols for directed differentiation into all the other individual lineages are described in the Methods.

Karyotype analysis and teratoma formation. Standard G-banding analysis was performed by the Memorial Sloan-Kettering Cancer Center molecular cytogenetics core laboratory as described previously²⁷. For teratoma formation FD-iPSCs were injected into the hindlimb muscle of NOD-SCID *Il2rg*-null mice (Jackson Laboratory) and analysed histologically 4–6 weeks after injection. Animal studies were approved by MSKCC Institutional Animal Care and Use Committee.

Molecular analyses. Total RNA was extracted using the RNeasy kit and DNase I treatment (Qiagen), and reverse transcribed (Superscript, Invitrogen). Primer sequences, cycle numbers, and annealing temperatures (Supplementary Table 3) for *IKBKAP* correspond to those used previously¹², the quantification of PCR bands was performed using ImageJ software (NIH) and the ratio of normal:mutant transcript was determined. qRT-PCR analysis was performed as described previously²⁸. Gene expression microarray analysis was carried out by the Sloan-Kettering Institute genomics core laboratory using the human Illumina-12 and Illumina-6 platforms. Bisulphite sequencing analysis of the *NANOG* promoter was performed according to ref. 3.

Immunocytochemistry. Cells were fixed in 4% paraformaldehyde, permeabilized with Triton-X-100-containing buffer and stained with primary antibodies

(list of antibodies provided in the Methods section). Appropriate fluorescent-labelled secondary antibodies (Molecular Probes) and 4,6-diamidino-2-phenylindole (DAPI) counterstaining was used for visualization.

Full Methods and any associated references are available in the online version of the paper at www.nature.com/nature.

Received 30 March; accepted 28 July 2009.

Published online 19 August 2009.

1. Yu, J. *et al.* Induced pluripotent stem cell lines derived from human somatic cells. *Science* **318**, 1917–1920 (2007).
2. Takahashi, K. *et al.* Induction of pluripotent stem cells from adult human fibroblasts by defined factors. *Cell* **131**, 861–872 (2007).
3. Park, I. H. *et al.* Reprogramming of human somatic cells to pluripotency with defined factors. *Nature* **451**, 141–146 (2008).
4. Dimos, J. T. *et al.* Induced pluripotent stem cells generated from patients with ALS can be differentiated into motor neurons. *Science* **313**, 1218–1221 (2008).
5. Ebert, A. D. *et al.* Induced pluripotent stem cells from a spinal muscular atrophy patient. *Nature* **457**, 277–280 (2009).
6. Park, I. H. *et al.* Disease-specific induced pluripotent stem cells. *Cell* **134**, 877–886 (2008).
7. Soldner, F. *et al.* Parkinson's disease patient-derived induced pluripotent stem cells free of viral reprogramming factors. *Cell* **136**, 964–977 (2009).
8. Slaugenaupt, S. A. *et al.* Tissue-specific expression of a splicing mutation in the *IKBKAP* gene causes familial dysautonomia. *Am. J. Hum. Genet.* **68**, 598–605 (2001).
9. Close, P. *et al.* Transcription impairment and cell migration defects in elongator-depleted cells: implication for familial dysautonomia. *Mol. Cell* **22**, 521–531 (2006).
10. Axelrod, F. B., Goldberg, J. D., Ye, X. Y. & Maayan, C. Survival in familial dysautonomia: impact of early intervention. *J. Pediatr.* **141**, 518–523 (2002).
11. Anderson, S. L. *et al.* Familial dysautonomia is caused by mutations of the *IKAP* gene. *Am. J. Hum. Genet.* **68**, 753–758 (2001).
12. Slaugenaupt, S. A. *et al.* Rescue of a human mRNA splicing defect by the plant cytokinin kinetin. *Hum. Mol. Genet.* **13**, 429–436 (2004).
13. Papapetrou, E. P. *et al.* Stoichiometric and temporal requirements of Oct4, Sox2, Klf4 and cMyc expression for efficient human iPSC induction and differentiation. *Proc. Natl Acad. Sci. USA* **106**, 12759–12764 (2009).
14. Elkabetz, Y. *et al.* Human ES cell-derived neural rosettes reveal a functionally distinct early neural stem cell stage. *Genes Dev.* **22**, 152–165 (2008).
15. Lee, G. *et al.* Isolation and directed differentiation of neural crest stem cells derived from human embryonic stem cells. *Nature Biotechnol.* **25**, 1468–1475 (2007).
16. Lee, G. S., Kim, B. S., Sheih, J. H. & Moore, M. Forced expression of HoxB4 enhances hematopoietic differentiation by human embryonic stem cells. *Mol. Cells* **25**, 487–493 (2008).
17. Lu, S. J. *et al.* Generation of functional hemangioblasts from human embryonic stem cells. *Nature Methods* **4**, 501–509 (2007).
18. D'Amour, K. A. *et al.* Efficient differentiation of human embryonic stem cells to definitive endoderm. *Nature Biotechnol.* **23**, 1534–1541 (2005).
19. Iwashita, T., Kruger, G. M., Pardal, R., Kiel, M. J. & Morrison, S. J. Hirschsprung disease is linked to defects in neural crest stem cell function. *Science* **301**, 972–976 (2003).
20. Jones, N. C. *et al.* Prevention of the neurocristopathy Treacher Collins syndrome through inhibition of p53 function. *Nature Med.* **14**, 125–133 (2008).
21. Sommer, L., Shah, N., Rao, M. & Anderson, D. J. The cellular function of MASH1 in autonomic neurogenesis. *Neuron* **15**, 1245–1258 (1995).
22. Johansen, L. D. *et al.* IKAP localizes to membrane ruffles with filamin A and regulates actin cytoskeleton organization and cell migration. *J. Cell Sci.* **121**, 854–864 (2008).
23. Anderson, S. L., Qiu, J. & Rubin, B. Y. EGCG corrects aberrant splicing of IKAP mRNA in cells from patients with familial dysautonomia. *Biochem. Biophys. Res. Commun.* **310**, 627–633 (2003).
24. Anderson, S. L., Qiu, J. & Rubin, B. Y. Tocotrienols induce IKBKAP expression: a possible therapy for familial dysautonomia. *Biochem. Biophys. Res. Commun.* **306**, 303–309 (2003).
25. Axelrod, F. B. Familial dysautonomia: a review of the current pharmacological treatments. *Expert Opin. Pharmacother.* **6**, 561–567 (2005).
26. Perrier, A. L. *et al.* From the Cover: derivation of midbrain dopamine neurons from human embryonic stem cells. *Proc. Natl Acad. Sci. USA* **101**, 12543–12548 (2004).
27. Placantonakis, D. G. *et al.* BAC transgenesis in human ES cells as a novel tool to define the human neural lineage. *Stem Cells* **27**, 521–532 (2009).
28. Chambers, S. M. *et al.* Highly efficient neural conversion of human ES and iPS cells by dual inhibition of SMAD signaling. *Nature Biotechnol.* **27**, 275–280 (2009).

Supplementary Information is linked to the online version of the paper at www.nature.com/nature.

Acknowledgements We thank J. Hendrikx, M. Leversha and C. Zhao for technical help. The work was supported by grants from the Starr Foundation and NYSTEM, by the New York Stem Cell Foundation (NYCSF, Druckenmiller fellowships to G.L. and C.A.F.) and by the Starr Scholar fellowship to S.M.C.

Author Contributions G.L.: conception and study design, maintenance and directed differentiation of iPSCs, cellular/molecular assays for disease modelling, data assembly, analysis and interpretation, and writing of manuscript; E.P.P., H.K. and C.A.F.: iPSC clone derivation and maintenance; S.M.C., M.J.T. and A.V.: data collection, analysis and interpretation; Y.M.G., J.M. and F.S.: *in vivo* experiments and histological analyses; V.T. and M.S.: study design, data analysis and interpretation; L.S.: conception and study design, data analysis and interpretation, and writing of manuscript.

Author Information Reprints and permissions information is available at www.nature.com/reprints. Correspondence and requests for materials should be addressed to L.S. (studerl@mskcc.org).

METHODS

Human iPSC generation. Lentiviral vectors encoding human OCT4, SOX2, KLF4 and c-MYC under the transcriptional control of human phosphoglycerate kinase (*PGK*) promoter were constructed¹³. Overlapping PCR was used to generate bi-cistronic expression cassettes encoding *vexGFP*, *mCitrine*, *mCherry* and *mCerulean* linked by a P2A peptide preceded by a Gly-Ser-Gly linker to the complementary DNAs of human *OCT4*, *SOX2*, *KLF4* and *c-MYC*, respectively, which were cloned in a lentiviral vector under the transcriptional control of human *PGK* promoter. Vector supernatants were produced as previously described¹³. Lentiviral vector supernatants were produced by triple co-transfection of the plasmid DNA encoding the vector, pCMVΔR8.91 and pUCMD.G into 293T cells, filtered through a 0.22-μm pore-size cellulose acetate filter (Whatman) and concentrated by ultracentrifugation. Human FD and normal fibroblasts (GM04959, GM04589, GM04899, GM02341, GM02342 and GM023036) purchased from Coriell, and human fetal lung fibroblasts (MRC-5) purchased from ATCC (CCL-171), were seeded at 1.5×10^5 cells per well of a 6-well plate in EMEM supplemented with 10% FBS. The next day the fibroblasts were transduced with supernatants of the four lentiviral vectors in the presence of $4 \mu\text{g ml}^{-1}$ polybrene for ~16 h. Five days after transduction, fibroblasts were collected by trypsinization and plated at 2×10^4 cells per 60-mm dish on a feeder layer of mitomycin-C-treated MEFs (GlobalStem, Inc.). The next day, the medium was switched to human ESC medium supplemented with 6 ng ml^{-1} FGF2 and was replaced every day thereafter. Twenty days after transduction, colonies with human ESC morphology were mechanically dissociated and transferred into 24-well plates on MEFs. Cells were thereafter passaged with dispase and expanded to establish iPSC lines.

Cell culture and differentiation. Undifferentiated human ESCs and iPSC lines were cultured on mitotically inactivated MEFs in a serum-replacement containing culture medium supplemented with 4 ng ml^{-1} FGF2 as used routinely for human ESC cultures^{15,26}. For neural induction, human ESCs were plated at $5\text{--}20 \times 10^3$ cells on a confluent layer of irradiated (50 Gy) stromal cells (MS-5) in 60-mm cell culture plates in KSR medium²⁶. After 16 days in serum-replacement medium, cultures were switched to N2 medium. Medium was changed every 2–3 days, and growth factors were added at the following concentrations as described previously: 200 ng ml^{-1} SHH, 100 ng ml^{-1} FGF8, 20 ng ml^{-1} brain-derived neurotrophic factor (BDNF) (all R&D Systems), and 0.2 mM ascorbic acid (Sigma-Aldrich). Rosette structures were collected mechanically at day 14–20 of differentiation (termed passage 0; P0) and gently replated on $15 \mu\text{g ml}^{-1}$ polyornithine/ $1 \mu\text{g ml}^{-1}$ laminin (PO/Lam)-coated culture dishes in N2 medium (termed passage 1; P1). P1 cultures were supplemented with FGF2, ascorbic acid and BDNF or any alternative growth factor conditions as listed in the main text. After 6–7 days of P1 culture, cells were tritured into single cells after exposure to Accutase (Innovative cell technologies, Inc., 10 min at incubator) and labelled with antibodies for flow cytometry. FACS sorting (HNK1 (ref. 15), Sigma; or Forse1 (ref. 14), DSHB) was performed on a MoFlo (Dako). Sorted cells were plated on culture dishes precoated with PO/Lam and 10 ng ml^{-1} fibronectin (PO/Lam/Fib). Human ESC-NCSCs (neural crest stem cells) were maintained in N2 medium supplemented with 20 ng ml^{-1} FGF2 and 20 ng ml^{-1} EGF changed every 2–3 days and passaged every 7–8 days, as previously described. For differentiation of ESC-NCSCs towards peripheral neurons, FGF2/EGF-expanded ESC-NCSCs were subjected to mitogen withdrawal in medium supplemented with BDNF, GDNF, NGF and dibutyryl-cAMP. Formation of human embryoid bodies for haematopoietic¹⁶ and endothelial^{17,29} differentiation was performed as previously described. Intact human ESC or iPSC colonies were collected and plated in low-attachment dishes (Corning) with DMEM, 20% Hyclone serum, 1% non-essential amino acids, 1 mM L-glutamine (Glut), 0.1 mM β-mercaptoethanol (MTG), 50 ng ml^{-1} BMP4, 50 ng ml^{-1} VEGF. Every other day, medium was changed with serum-free medium (Sigma) supplemented with Glut, non-essential amino acids, MTG, and the following cytokines: 5 ng ml^{-1} BMP4, 10 ng ml^{-1} bFGF, 20 ng ml^{-1} VEGF, 20 ng ml^{-1} SCF, 20 ng ml^{-1} Flt3L (also known as FLT3LG), and 20 ng ml^{-1} TPO. Cells are dissociated with trypsin for 10 min in incubator. Subsequently, cells are passed through a 22G needle 3–4 times and through a 40-μm strainer. Embryoid-body-derived cells were plated into semi-solid culture (StemCell Technologies) for further differentiation. For haematopoietic cell, 0.05–0.1 million cells per 35-mm dish were plated at day 10 of embryoid body culture; for endothelial differentiation, 0.1–0.2 million cells per 35-mm dish were plated at day 5 of embryoid body culture. Endothelial cells were obtained after seeding of the blast-like colony (at day 5–6 of methylcellulose culture) onto a matrigel-coated plate in EBM2 medium (Lonza). After 3–4 passages, human ESC and iPSC-derived endothelial cells were sorted for CD144 (VE-cadherin) antibody (BD Biosciences). Haematopoietic cells (at day 14 of methylcellulose culture) were collected and sorted for CD45 antibody (BD Biosciences). For endodermal

cell differentiation, semi-confluent human ESC or iPSC maintained feeder-free on matrigel were cultured in RPMI containing Glutamax, penicillin/streptomycin and 0.5% defined FBS (Hyclone) and recombinant human activin A (100 ng ml^{-1} , Peprotech) for 1 week. Cells were then dissociated using 0.05% trypsin/EDTA (Invitrogen), resuspended in PBS with 2% serum and sorted for CXCR4 antibody¹⁸. For cardiac differentiation, fully grown FD-iPSC colonies were detached by dispase and plated into ultra-low attachment dishes in knock-out DMEM supplemented with glutamax, penicillin/streptomycin and 20% defined FBS (Hyclone) in the presence of recombinant human BMP4 (25 ng ml^{-1} , R&D). Resulting embryoid body cultures were maintained for 4 days, collected by quick spinning and plated onto gelatin-coated dishes under the same medium conditions for a further 2 weeks. Tissues with beating foci were observed at 2 weeks of differentiation on gelatin and isolated manually for further characterization. For immunocytochemical analysis, beating foci were trypsinized for 10 min, tritured and replated onto fibronectin-coated plates for a 24-h period. Spontaneous beating of putative cardiac tissues was monitored on an Olympus IX81 microscope under Normarski optics using a Hamamatsu ORCA CCD camera. Cells were maintained in enclosed chamber with temperature and CO₂ control (Weather Station, Precision Control) and time-lapse images were assembled using a commercial software package (Slidebook). For evaluation of chemical treatment, $100 \mu\text{M}$ kinetin¹² (Sigma), $12.5 \mu\text{g ml}^{-1}$ D-tocotrienol²⁴ (Caymanchem) and $50 \mu\text{g ml}^{-1}$ EGCG²³ (Calbiochem) were used for 24 h for the initial test. Kinetin treatment was tested in different treatment schedules including continuous treatment from 1 day before differentiation to analysis at the neural crest stage, and treatments for either 24 h or 5 days upon isolation of iPSC-derived neural crest progeny. Migration/motility assay was performed using published protocols³⁰. In brief, cells were treated with mitomycin C (2 ng ml^{-1} for neural crest cells) for 2 h and dissociated with Accutase. A total of 100,000 cells were plated in each well of a PO/Lam/Fib-coated 24-well plate. At 24 h of plating, each well was scratched using a 100 μl pipette tip, washed and image was taken (0 h) as reference point for subsequent quantification. At 48 h after scratching, cells were fixed by 4% paraformaldehyde and stained with DAPI for quantification of DAPI⁺ nuclei (48 h) in the identical fields marked at day 0.

Assay for teratoma formation. For teratoma formation, 2×10^6 cells were resuspended in human ESC medium and injected intramuscularly into immunocompromised NOD/SCID *Il2rg*^{−/−} mice. Xenografted masses were retrieved 4–6 weeks after injection and cryosectioned samples were stained with haematoxylin and eosin for histological analysis and subjected to immunofluorescence for marker characteristic of tissues derived from the three main germ layers.

Immunocytochemistry and flow cytometry. Cells were fixed in 4% paraformaldehyde, permeabilized with buffer containing Triton X-100 and stained with primary antibodies (Nanog (R&D), BRN3A (Peripherin), CD105 (Millipore), p75 (Advanced targeting system), Paxillin, CD45, CD144, CXCR4, ASCL1 and β-catenin from BD Biosciences; AP2 (3B5), PAX6, HNK1, Forse1, MF20 from DSHB; Tuj1 (Covance), α-actinin (Sigma), and collagen (Chondrex)). Appropriate Alexa Fluor 488-, 568- or 647-labelled secondary antibodies (Molecular Probes) and/or DAPI counterstaining was used for visualization. Cells were stained for paxillin at 1.5 h after plating²². For quantification of paxillin staining, paxillin⁺ puncta as defined by >1 μm diameter were quantified per individual cell. For FACS analysis, cells were dissociated with Accutase, stained with Alexa Fluor 647-conjugated anti-human SSEA3, SSEA4, TRA-1-81 and phycoerythrin (PE)-Cy5-conjugated anti-HLA-ABC antibodies (BD Biosciences) and analysed in a LSRII cytometer (BD Biosciences). Analysis was performed with the FlowJo software (version 8.8.4; TreeStar).

Molecular analysis. Total RNA was extracted using the RNeasy kit and DNase I treatment (Qiagen) to avoid genomic contamination. Samples were collected and frozen for further RNA extraction. Total RNA was reverse transcribed (Superscript, Invitrogen) and approximately the equivalent of 50 ng of RNA was used for each RT-PCR reaction. The quantification of intensity of PCR bands was performed using ImageJ software (NIH). Primer sequences, cycle numbers, and annealing temperatures (Supplementary Table 3) correspond to those used by others previously^{8,12}. Quantitative RT-PCR was performed using the Mastercycler RealPlex2 (Eppendorf) platform following the manufacturer's instruction. All results were normalized to HPRT or S18 control. For microarray analysis, total RNA was isolated from two independent sample each of undifferentiated H9, C14-iPSC, FD-iPSC-22, FD-iPSC-102 cells, and fibroblast samples (4589 and 4959); and from HNK1⁺ neural crest precursors derived from H9, C14-iPSC and FD-iPSC-22 were processed by the MSKCC Genomic core facility and hybridized on Illumina Human Ref-6v2 or Human HT-12 arrays. Normalization and model-based expression measurements were performed with the Illumina analysis package (LUMI) available through the open-source Bioconductor project (<http://www.bioconductor.org>) within the statistical programming language R (<http://cran.r-project.org/>). A pair-wise comparison of

neural crest cell from (H9 and C14-iPSC) versus FD-iPSC was performed using the Linear Models for Microarray Data package (LIMMA) available through Bioconductor. Genes found to have an adjusted *P*-value < 0.05 and a fold change greater than two were considered significant. Some of the descriptive microarray data analyses and presentation was performed using a commercially available software package (Partek Genomics Suite (version 8.4.17)). Genomic DNA (gDNA) is isolated using Qiagen kit from patient fibroblast lines and iPSC clones. For validation of sequencing, conventional PCR was used (the conditions are in Supplementary Table 3). Microsatellite analysis of gDNA was performed at the Rockefeller genomic core facility. For bisulphite genomic sequencing, gDNA samples from FD-fibroblast and FD-iPSC were extracted. Bisulphite treatment of gDNA was carried out using a CpGenome DNA Modification Kit (Chemicon) according to the manufacturer's protocol. Converted gDNA was amplified by PCR using *NANOG* primer sets⁶. PCR products were gel-purified and cloned into bacteria using TOPO TA cloning (Invitrogen). Bisulphite conversion efficiency of non-CpG cytosines ranged from 80% to 99% for individual clones for each sample.

Statistical analysis. The data were processed using Prism 4.0c software. Values are reported as means and s.d. Comparisons among values for all groups were

performed by one-way analysis of variance (ANOVA). Bartlett's test for equal variances and Newman-Keuls Multiple Comparison Test were used to determine the level of significance.

29. Kennedy, M., D'Souza, S. L., Lynch-Kattman, M., Schwantz, S. & Keller, G. Development of the hemangioblast defines the onset of hematopoiesis in human ES cell differentiation cultures. *Blood* **109**, 2679–2687 (2007).
30. Rodriguez, L. G., Wu, X. & Guan, J. L. Wound-healing assay. *Methods Mol. Biol.* **294**, 23–29 (2005).

Optogenetic dissection of a behavioural module in the vertebrate spinal cord

Claire Wyart^{1*}, Filippo Del Bene^{2*}, Erica Warp¹, Ethan K. Scott^{2†}, Dirk Trauner³, Herwig Baier² & Ehud Y. Isacoff^{1,4}

Locomotion relies on neural networks called central pattern generators (CPGs) that generate periodic motor commands for rhythmic movements¹. In vertebrates, the excitatory synaptic drive for inducing the spinal CPG can originate from either supraspinal glutamatergic inputs or from within the spinal cord^{2,3}. Here we identify a spinal input to the CPG that drives spontaneous locomotion using a combination of intersectional gene expression and optogenetics⁴ in zebrafish larvae. The photo-stimulation of one specific cell type was sufficient to induce a symmetrical tail beating sequence that mimics spontaneous slow forward swimming. This neuron is the Kolmer–Agduhr cell⁵, which extends cilia into the central cerebrospinal-fluid-containing canal of the spinal cord and has an ipsilateral ascending axon that terminates in a series of consecutive segments⁶. Genetically silencing Kolmer–Agduhr cells reduced the frequency of spontaneous free swimming, indicating that activity of Kolmer–Agduhr cells provides necessary tone for spontaneous forward swimming. Kolmer–Agduhr cells have been known for over 75 years, but their function has been mysterious. Our results reveal that during early development in zebrafish these cells provide a positive drive to the spinal CPG for spontaneous locomotion.

We searched for novel spinal neurons that trigger the CPG in the zebrafish larva by using ‘intersectional optogenetics’, a combination of transgene expression in specific cell types⁷ and genetic tools for manipulating neuronal activity with light⁴. The light-gated channel LiGluR^{8,9} was selectively expressed in distinct subsets of spinal cord neurons by crossing transgenic animals carrying *UAS:LiGluR*¹⁰ with a series of fish lines¹¹ that express GAL4, the transcription factor that activates the UAS promoter, in distinct cellular patterns. We looked for common behavioural outcomes induced by light stimulation in lines with partly overlapping expression patterns that could be attributed to the activity of a common cell type (Supplementary Fig. 1).

Five-day-old zebrafish larvae exhibit spontaneous forward slow swims¹². These occur in brief bursts, with each burst consisting of a series of symmetrical, dampening left–right oscillations (Fig. 1a). We chose several *Gal4* transgenic lines to drive expression of LiGluR in different subsets of spinal neurons, and asked whether optical activation of these neurons elicits a forward swim-like behaviour. We first tested the *Gal4^{s1020t}* line, which labels a heterogeneous population of ventral spinal neurons. When crossed to *UAS:LiGluR* and labelled with the chemical photoswitch MAG1 (refs 8–10), 94% of the double-transgenic animals ($n = 37$) exhibited robust tail oscillations upon stimulation of the caudal spinal cord with a short light pulse (see Methods) (Fig. 1b and Supplementary Movie 2). The frequency and initial deflection angle of these oscillations closely resembled the spontaneous slow swim that we observed in unrestrained animals

(Fig. 1c–f). The optical stimulation had no effect on non-transgenic larvae ($n = 12$) or on LiGluR-expressing larvae not incubated with MAG1 ($n = 12$).

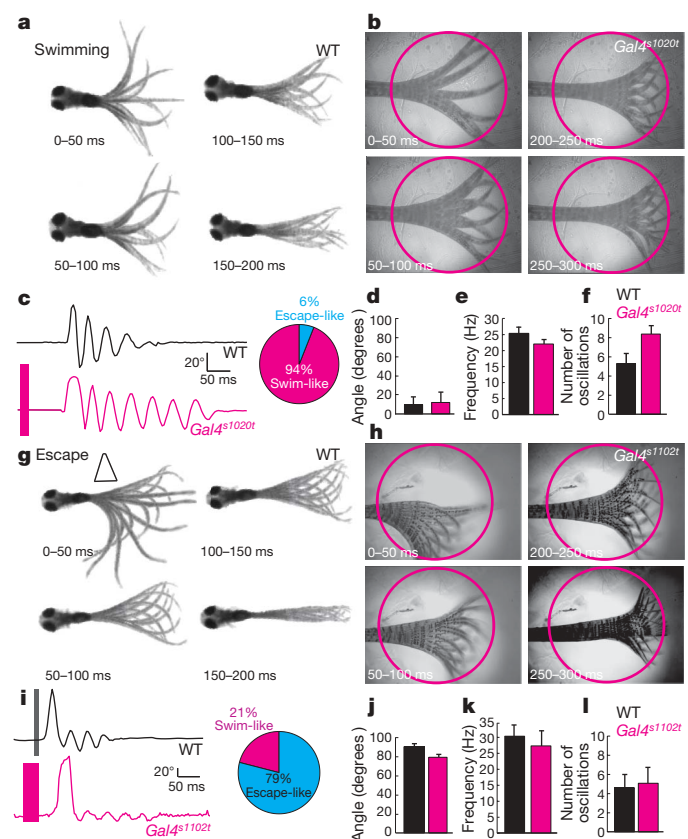


Figure 1 | Optical stimulation of specific spinal neurons leads to distinct locomotor behaviours. **a**, Spontaneous swim (superimposed frames). **b**, Optical stimulation (circle) of *Gal4^{s1020t}/UAS:LiGluR* evokes a ‘spontaneous swim’-like behaviour. **c**, Comparison of deflection angle traces corresponding to **a** (top, black) and **b** (bottom, magenta, bar for stimulation) (inset: 94% of responses were a swim ($n = 18$)). No difference in angle ($P = 0.51$) (**d**) or frequency ($P = 0.09$) (**e**), but more oscillations ($P < 0.01$) (**f**) in light-induced swims. Values are given + s.e.m. ($n = 9$). **g**, Escape elicited by a water jet (triangle) consists of sharp C-turn away from stimulus followed by a forward swim. **h**, Light-induced escape induced by stimulation of Rohon-Beard cells in *Gal4^{s1102t}/UAS:LiGluR* larvae. **i**, Tail deflection traces corresponding to **g** (top) and **h** (bottom) (inset: 79% of responses were an escape ($n = 11$)). **j–l**, No difference in (**j**) deflection angle ($P = 0.13$), (**k**) frequency ($P = 0.42$) and (**l**) number of oscillations ($P = 0.41$). Values are given + s.e.m. ($n = 7$).

¹Helen Wills Neuroscience Institute and Department of Molecular and Cell Biology, University of California in Berkeley, Berkeley, California 94720, USA. ²Department of Physiology, Program in Neuroscience, University of California in San Francisco, San Francisco, California 94158-2324, USA. ³Department of Chemistry, Ludwig Maximilians-Universität, Munich, Germany. ⁴Physical Bioscience Division and Material Science Division, Lawrence Berkeley National Laboratory, Berkeley, California 94720, USA. [†]Present address: School of Biomedical Sciences, University of Queensland, Queensland 4072, Australia.

*These authors contributed equally to this work.

The swim-like response induced by light in *Gal4^{s1020t}/UAS:LiGluR* larvae differed from the well-described touch–escape response¹³, in which larvae respond to touch on one side of the tail by an initial sharp bend of the tail (‘C-bend’) to the opposite side that propels the fish away from the touch (Fig. 1g and Supplementary Movie 3). A C-bend to either the left or right side was elicited by bilateral illumination of the tail in *UAS:LiGluR/Gal4^{s1102t}* line¹⁰ larvae expressing the LiGluR in Rohon–Beard touch sensing neurons of the tail. A C-bend was evoked in 79% of trials (seven larvae tested five times each) (Fig. 1h, i and Supplementary Movie 4), resembling the natural escape of free-swimming fish (see initial one-sided tail bend, the frequency and the number of the ensuing tail beats in Fig. 1i–l). The left/right symmetry of the beating oscillations and small deflection angle seen in the *Gal4^{s1020t}* line distinguish it from this Rohon–Beard-cell-induced asymmetric escape response of the *Gal4^{s1102t}* line (compare Fig. 1c, d with Fig. 1i, j).

Gal4^{s1020t} drives expression in several cell types in the ventral spinal cord (Fig. 2a). Inverse PCR cloning indicates that the transposon is integrated near the *Olig2* gene¹¹. Indeed, the expression pattern of *Gal4^{s1020t}* is indistinguishable from that seen in an *Olig2:GFP* transgenic line¹⁴ (Supplementary Fig. 2). Using the *BGUG* expression system to determine which cell types express GAL4 in the *Gal4^{s1020t}* line (Supplementary Methods), we found that 79% of the 250 cells imaged in 73 fish were motor neurons (26.4% primary motor neurons: Fig. 2b, top panel; 52.4% secondary motor neurons: Fig. 2b, bottom panel). The remaining cells (20.4%) were neurons with a central ascending axon and lacking dendrites (Fig. 2c, d, f). A few cells (two out of 250 cells (0.8%)) resembling oligodendrocytes were also green fluorescent protein (GFP)-positive (data not shown).

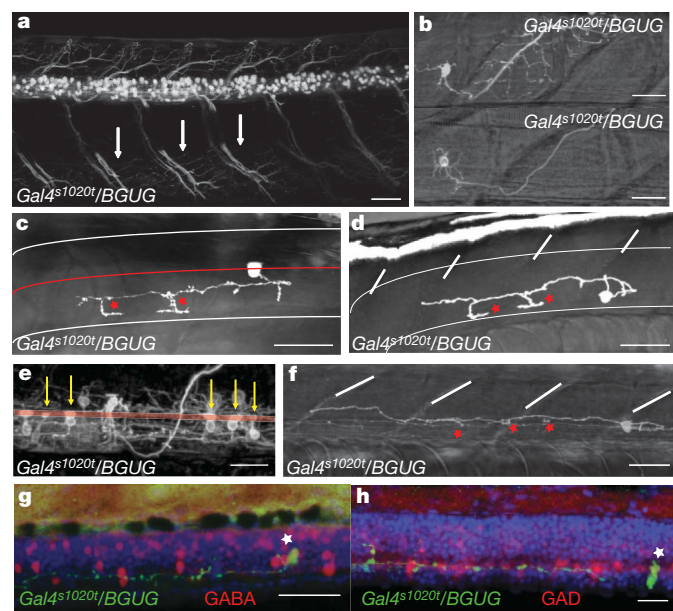


Figure 2 | The *Gal4^{s1020t}* line drives expression in motor neurons and Kolmer–Agduhr neurons. **a**, Expression in ventral cells including motor neurons projecting out of cord (arrows) (lateral view). **b–e**, Random labelling in *Gal4^{s1020t}/BGUG* identifies solely two cell types: **b**, motor neurons (primary motor neurons, top; secondary motor neurons, bottom) and **c–f**, Kolmer–Agduhr neurons (dorsal (**c**) and lateral (**d–f**) views of neuron with a central ipsilateral ascending axon; segment boundaries: white lines). Note contact feet (red stars in **c** and **d**) and ‘toothbrush’ morphology of cilia (yellow arrows in **e**) characteristic of Kolmer–Agduhr cells. In **c**, larva is tilted to show enlarged contacts on axon (midline, red line and segment, white lines). **e**, Dense *BGUG* pattern with multiple Kolmer–Agduhr cells shows the alignment of the brush of cilia (arrows) with central canal. **f**, The ascending axon runs near the ventral edge of the spinal cord before aiming dorsally. **g, h**, Kolmer–Agduhr cells at 5 days post-fertilization in *Gal4^{s1020t}/BGUG* (green) are GABAergic neurons (anti-GAD (**g**) and anti-GABA (**h**) immunostaining in red). Scale bars, 25 μ m.

408

The neurons with a central axon appeared to represent a single cell type. They are located near the central canal and have an ascending axon that projects ipsilaterally, making terminals in a series of two to six consecutive segments (Fig. 2c, d, f). Instead of dendrites these cells have a brush of cilia emanating from the somata, which appear to contact the cerebrospinal fluid (CSF), as shown by the alignment of the cilia with the central canal (Fig. 2e). Antibody staining showed that these neurons are GABA (γ -aminobutyric acid)- and GAD65/67-positive (Fig. 2g, h and Supplementary Fig. 3) as well as somatostatin-positive (Supplementary Fig. 4). Combined, these features are consistent with these neurons being Kolmer–Agduhr cells^{5,15}.

To find out whether the Kolmer–Agduhr neurons are responsible for triggering the swim-like behaviour in the *Gal4^{s1020t}/UAS:LiGluR* fish, we screened more *Gal4* lines and found one line, *Gal4^{s1003t}*, in which expression in the spinal cord is restricted to Kolmer–Agduhr cells. These cells shared morphology, cell body position and marker expression with the sensory neuron labelled in *Gal4^{s1020t}* (Fig. 3a–d and Supplementary Fig. 5). As in *Gal4^{s1020t}/UAS:LiGluR*, the light-induced response in *Gal4^{s1003t}/UAS:LiGluR* consisted of an alternating symmetrical tail beat at the slow swim frequency (Fig. 3e–i and Supplementary Movie 5), confirming that Kolmer–Agduhr cells are indeed able to trigger the CPG. The properties of the light-induced swim in the *Gal4^{s1003t}/UAS:LiGluR* larvae were indistinguishable from those of *Gal4^{s1020t}/UAS:LiGluR* (Fig. 3), which suggests that at the intensities applied, motor neurons are not activated in *Gal4^{s1020t}/UAS:LiGluR*. Indeed, calcium imaging in tetrodotoxin (to block action potentials and confine activity to the optically stimulated cells) revealed that the light pulses used in the behavioural

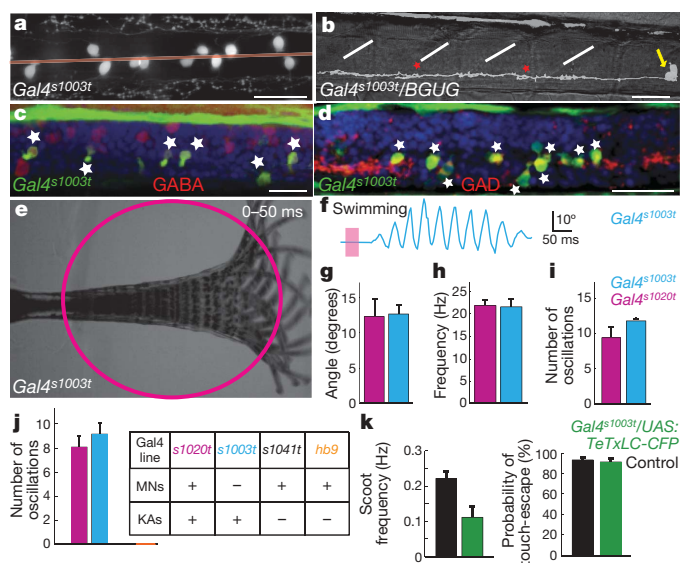


Figure 3 | Optical stimulation of Kolmer–Agduhr cells of *Gal4^{s1003t}* line induces a forward swim. **a**, Expression in spinal cord is confined to cells close to the midline (dorsal view). **b**, Lateral view in *BGUG* shows ventral neurons with central axons forming contact feet (red stars) and toothbrush morphology (arrow). White lines are segment boundaries. **c, d**, These cells (green) are GABAergic (anti-GAD and anti-GABA staining in red). **e, f**, Optical stimulation induces a swim-like response. **e**, Superimposed images. **f**, Deflection angle trace. **g–i**, No difference in deflection angle (**g**), frequency (**h**) and number of oscillations (**i**) between *Gal4^{s1003t}* (blue) and *Gal4^{s1020t}* (magenta) (respectively $P = 0.85$, $P = 0.98$, $P = 0.36$); values are given \pm s.e.m. ($n = 9$). **j**, Side-to-side comparison of number of oscillations evoked by a 100-ms pulse of light shows that only lines expressing in Kolmer–Agduhr cells show a swim-like response whereas line with motor neurons (MNs) and no Kolmer–Agduhr cells (KAs) (*Gal4^{s1041t}*, black; *Hb9:Gal4*, orange) do not ($n = 6$ for each line). **k**, Reduction of the spontaneous swimming frequency in *Gal4^{s1003t}/UAS:TeTxLC-CFP* ($P < 0.0075$) but no change in the probability of touch-response ($P = 0.45$). Values are given \pm s.e.m. ($n = 10$ and 12, respectively).

experiments were strong enough to activate the narrow region surrounding the central canal where Kolmer–Agduhr cells are located, but not elsewhere in the ventral spinal cord where most motor neurons are situated (Supplementary Fig. 6).

To eliminate the possibility that motor neuron activation in *Gal4^{s1020t}/UAS:LiGluR* fish elicits swimming movements, we tested two additional *Gal4* lines with motor neuron expression but no expression in Kolmer–Agduhr cells: *Gal4^{s1041t}* and *Hb9:Gal4* (ref. 16) (Supplementary Fig. 7). Light pulses that reliably triggered swim-like behaviour in animals expressing LiGluR in the *Gal4^{s1020t}* and *Gal4^{s1003t}* lines produced no effect in either of these motor neuron lines (six LiGluR larvae tested for each line; Fig. 3j). However, increasing the intensity or duration of illumination by at least tenfold evoked contraction on the illuminated side of the tail, which was distinct from the forward swim-like behaviour (Supplementary Fig. 8). The requirement for stronger illumination to evoke the contraction is consistent with the larger size and lower input resistance of motor neurons¹⁷. Altogether, these observations show that the forward swim can be attributed specifically to the activation of the Kolmer–Agduhr cells.

Kolmer–Agduhr cells are GABAergic. To test the role of GABAergic transmission in the light-induced response of *Gal4^{s1020t}/UAS:LiGluR*, we injected the GABA-A antagonist bicuculline into the spinal cord. This treatment greatly reduced the number of oscillations evoked by light in *Gal4^{s1020t}/UAS:LiGluR* fish ($P < 10^{-6}$, $t(7) = 11.2950$; Supplementary Fig. 9), abolishing the light-induced response entirely in four out of eight larvae. These experiments indicate that the optical stimulation of Kolmer–Agduhr cells is sufficient to initiate a swim-like behaviour by a GABA-dependent process.

Having shown that activation of Kolmer–Agduhr cells is sufficient for inducing a swim-like behaviour, we next asked whether they are also necessary for spontaneous swimming by blocking synaptic transmission from Kolmer–Agduhr cells by a targeted expression of the tetanus toxin light chain (TeTxLC) fused to cyan fluorescent protein (CFP) (*UAS:TeTxLC-CFP* (ref. 18) crossed with *Gal4^{s1020t}* and *Gal4^{s1003t}*). Three- to five-day-old larvae expressing TeTxLC-CFP were easily identified by their CFP fluorescence (Methods). We compared the swimming behaviour of CFP-positive larvae with that of siblings that did not have CFP fluorescence (that is, did not express TeTxLC). *Gal4^{s1020t}/UAS:TeTxLC-CFP* larvae expressing the TeTxLC were paralysed at five days, as expected for expression of GAL4 in motor neurons. On the other hand, *Gal4^{s1003t}/UAS:TeTxLC-CFP* larvae, which lack motor neuron expression, were not paralysed, enabling behavioural assays. *Gal4^{s1003t}/UAS:TeTxLC-CFP* exhibited spontaneous burst-swimming, but the frequency of the swims was greatly reduced ($P < 0.0075$; $t(9) = -3.4278$) (Fig. 3k). These results indicate that Kolmer–Agduhr cells provide a positive drive to spontaneous swimming. It should be noted that only half of the Kolmer–Agduhr cells express the UAS transgene in the *Gal4^{s1003t}* line (Supplementary Fig. 3), which suggests that block of synaptic transmission in all of the Kolmer–Agduhr cells could have an even more profound effect on spontaneous swimming. Strikingly, we found that *Gal4^{s1003t}/UAS:TeTxLC-CFP* still respond to touch by a touch–escape ($P = 0.45$; $t(11) = 0.7863$) (Fig. 3k), indicating that Kolmer–Agduhr cells do not play a significant role in initiating touch–escape.

We further examined the Kolmer–Agduhr-induced swim and the Rohon–Beard-induced escape behaviours by performing local photo-activation. Because mechanical activation on one side of the larva elicits, as part of the escape response, a C-turn on the opposite side (Fig. 1g), we predicted that one-sided optical activation of Rohon–Beard cells would have the same effect. We tested this by confining the illumination to a small portion of the spinal cord with a digital light processing array (Fig. 4a). One-sided optical stimulation of Rohon–Beard cells in the *Gal4^{s1102t}* line triggered a reliable large-angle contralateral bend ($n = 9$ out of 9; Fig. 4c), resembling the C-bend induced by one-sided mechanical stimulation (Fig. 1i). In contrast, one-sided optical stimulation of *Gal4^{s1020t}* elicited a symmetrical forward

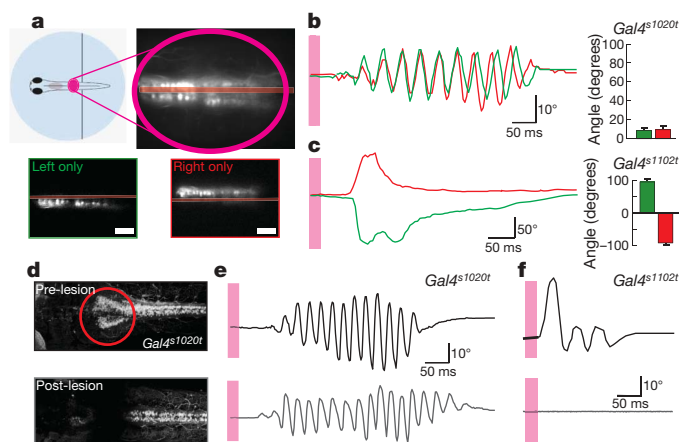


Figure 4 | Dissection of the light-evoked responses in *Gal4^{s1020t}* and *Gal4^{s1102t}* by unilateral stimulation and lesion studies. a–c, Patterned illumination for stimulation. a, Semi-restrained *Gal4^{s1020t}* larva aimed bilaterally (cartoon and fluorescence image of Kaede expression in three segments, top) and on left or right side (bottom panels; scale bar, 25 μm). b, c, Deflection angle traces and mean values induced by left (green) and right (red) stimulation. Values are given + s.e.m. b, Left and right activations induce similar symmetric oscillations of the tail in *Gal4^{s1020t}* line ($n = 5$). c, Left and right activations induce large and opposite-directed C-bends in *Gal4^{s1102t}* ($n = 9$). d–f, Effect induced by section of the cerebrospinal connections. d, Pattern in *Gal4^{s1020t}* pre- (top) and post- (bottom) lesion. e, f, No reduction of the light-induced swim behaviour in *Gal4^{s1020t}* (e, $n = 7$) but abolition of the light-induced escape behaviour in *Gal4^{s1102t}* (f, $n = 4$) (pre- and post-lesion, top and bottom).

swim-like behaviour (Fig. 4b), closely resembling the response to bilateral optical stimulation (Fig. 1c).

To test the involvement of supraspinal inputs in the Kolmer–Agduhr-elicited swim-like behaviour, we performed hindbrain lesions that ablated the connections between the brain and the spinal cord (Fig. 4d). Tactile stimuli sensed by Rohon–Beard cells are known to be transmitted to the hindbrain¹³ where the command for escape is relayed back to the tail, and ablation of the hindbrain was shown earlier to suppress the fast contralateral C-bend that begins the escape¹³. Consistent with this, the C-bend component of the response to optical activation of Rohon–Beard cells in the *Gal4^{s1102t}/UAS:LiGluR* line was abolished by the hindbrain lesion ($n = 4$ out of 4; Fig. 4f). In contrast, the light-evoked swim-like behaviour in *Gal4^{s1020t}* remained intact after the lesion ($n = 7$; Fig. 4e), which demonstrates that intra-spinal activation of *Gal4^{s1020t}*-positive neurons is sufficient to drive the swim-like behaviour.

Previous work in vertebrates has implicated specific classes of spinal interneuron in regulating locomotion speed^{19,20} or movement strength, and their activity was associated with specific states of the spinal networks recorded during fictive locomotion^{16,21}. These studies were based on either loss of function¹⁹ or on correlation of the activity of neurons with specific phases of ventral root activity during fictive locomotion^{16,20}. We show that it is possible to employ a light-gated channel to show sufficiency of genetically targeted neurons in behaviour. Genetically encoded blockers of activity can then be used to also show the necessity of neuronal function in behaviour (Supplementary Fig. 1).

Previous studies in the lamprey showed that the GABAergic system is a strong modulator of fictive swimming²², but there are many types of spinal GABAergic neuron and the neuronal basis for the observed modulation was not known. We demonstrate here that a single GABAergic cell, the Kolmer–Agduhr neuron, is a major modulator of locomotion in the awake behaving animal. Although Kolmer–Agduhr neurons were first described decades ago⁵, their role in spinal circuits remained enigmatic. We show that Kolmer–Agduhr cells are necessary for the normal frequency of spontaneous swimming and are sufficient to drive the CPG in early development, when GABAergic transmission is excitatory²³.

The Kolmer–Agduhr neurons of zebrafish resemble the CSF-contacting cells of lamprey and other vertebrates, including mammals^{24,25}, in that they express GABA and the transcription factor *olig2* (ref. 26) (Supplementary Fig. 2), are located next to the central canal and project a brush of stereocilia into the CSF, and have axons that run longitudinally²⁵. It remains to be determined whether potential homologues of Kolmer–Agduhr cells may affect locomotor patterns in mammals.

Although we have determined that Kolmer–Agduhr cells provide a positive drive to the CPG in larval fish, in adult fish and in postnatal mammals, GABAergic transmission is inhibitory and blocking GABA receptor in the adult lamprey enhances swim frequency²². This suggests that Kolmer–Agduhr activity may suppress swimming in adult zebrafish. The ‘liquor-contacting’ cilia of the Kolmer–Agduhr neurons in the central canal^{5,15,22} could allow them to sense mechanical deformation of the spine or chemical signals in the central canal, such as low pH, as proposed recently for mammalian CSF-contacting neurons²⁷. The natural drive to Kolmer–Agduhr cells and their function later in life remain to be defined.

METHODS SUMMARY

To determine which cell types express in a GAL4 line and to quantify their abundance, we used the *BGUG* transgene (short for *Brn3c:Gal4; UAS: mGFP*), which labels a small, random subset of the GAL4-expressing cells owing to variegated expression of the gene encoding a membrane-targeted GFP^{11,28}. The transgenic line *UAS:LiGluR*, as well as all Gal4 lines from the enhancer trap screen, were published previously^{10,11}. To make the *Hb9:Gal4* transgenic construct, 3 kilobases of genomic sequence upstream of the *hb9* coding sequence^{18,29} was amplified by PCR and inserted upstream of the *GAL4* coding sequence³⁰. Synthesis of MAG-1 was performed as described^{8–10}. Five-day-old larvae were bathed in 200 μ M MAG-1, 4% dimethylsulphoxide (DMSO) for 45 min at 28.5 °C in the dark. The fast photoswitching light source was coupled to an upright Zeiss epifluorescence microscope. Patterned illumination was accomplished using a digital micromirror device. Motion of the tail was monitored at 250 frames per second by using a high-speed camera. Lesions were performed on anaesthetized larvae bathed in Evans solution with a fine tungsten needle. Embryos at appropriate stages were fixed in 4% PFA in PBS and processed for immunohistochemistry according to published protocols²⁸. Injection of the calcium dye was performed 30–60 min after MAG-1 labelling. Fluorometric Ca^{2+} measurements were performed using a confocal Olympus laser-scanning microscope equipped with an ultraviolet SIM Scanner. Tracking of the tail position and calcium imaging analysis were performed using a custom-made script written in Matlab 2007 (Mathworks).

Full Methods and any associated references are available in the online version of the paper at www.nature.com/nature.

Received 6 March; accepted 27 July 2009.

- Grillner, S. Biological pattern generation: the cellular and computational logic of networks in motion. *Neuron* **52**, 751–766 (2006).
- Fenaux, F. *et al.* Effects of an NMDA-receptor antagonist, MK-801, on central locomotor programming in the rabbit. *Exp. Brain Res.* **86**, 393–401 (1991).
- Kiehn, O. *et al.* Excitatory components of the mammalian locomotor CPG. *Brain Res. Rev.* **57**, 56–63 (2008).
- Luo, L., Callaway, E. M. & Svoboda, K. Genetic dissection of neural circuits. *Neuron* **57**, 634–660 (2008).
- Agduhr, E. in *Cytology and Cellular Pathology of the Nervous System* (ed. Penfield, W.) Vol. 2 535–573 (Hoeber, 1932).
- Higashijima, S., Mandel, G. & Fetcho, J. R. Distribution of prospective glutamatergic, glycinergic, and GABAergic neurons in embryonic and larval zebrafish. *J. Comp. Neurol.* **480**, 1–19 (2004).
- Douglas, J. R. *et al.* The effects of intrathecal administration of excitatory amino acid agonists and antagonists on the initiation of locomotion in the adult cat. *J. Neurosci.* **13**, 990–1000 (1993).
- Volgraf, M. *et al.* Allosteric control of an ionotropic glutamate receptor with an optical switch. *Nature Chem. Biol.* **2**, 47–52 (2006).
- Gorostiza, P. *et al.* Mechanisms of photoswitch conjugation and light activation of an ionotropic glutamate receptor. *Proc. Natl Acad. Sci. USA* **104**, 10865–10870 (2007).
- Szobota, S. *et al.* Remote control of neuronal activity with a light-gated glutamate receptor. *Neuron* **54**, 535–545 (2007).
- Scott, E. K. *et al.* Targeting neural circuitry in zebrafish using GAL4 enhancer trapping. *Nat. Methods* **4**, 323–326 (2007).

- Budick, S. A. & O'Malley, D. M. Locomotor repertoire of the larval zebrafish: swimming, turning and prey capture. *J. Exp. Biol.* **203**, 2565–2579 (2000).
- Liu, K. S. & Fetcho, J. R. Laser ablations reveal functional relationships of segmental hindbrain neurons in zebrafish. *Neuron* **23**, 325–335 (1999).
- Shin, J., Park, H. C., Topczewska, J. M., Mawdsley, D. J. & Appel, B. Neural cell fate analysis in zebrafish using *olig2* BAC transgenics. *Methods Cell Sci.* **25**, 7–14 (2003).
- Dale, N. *et al.* The morphology and distribution of ‘Kolmer–Agduhr cells’, a class of cerebrospinal-fluid-contacting neurons revealed in the frog embryo spinal cord by GABA immunocytochemistry. *Proc. R. Soc. Lond. B* **232**, 193–203 (1987).
- Liao, J. C. & Fetcho, J. R. Shared versus specialized glycinergic spinal interneurons in axial motor circuits of larval zebrafish. *J. Neurosci.* **28**, 12982–12992 (2008).
- Drapeau, P. *et al.* In vivo recording from identifiable neurons of the locomotor network in the developing zebrafish. *J. Neurosci. Methods* **88**, 1–13 (1999).
- Asakawa, K. *et al.* Genetic dissection of neural circuits by Tol2 transposon-mediated *Gal4* gene and enhancer trapping in zebrafish. *Proc. Natl Acad. Sci. USA* **105**, 1255–1260 (2008).
- Gosgnach, S. *et al.* V1 spinal neurons regulate the speed of vertebrate locomotor outputs. *Nature* **440**, 215–219 (2006).
- McLean, D. L. *et al.* Continuous shifts in the active set of spinal interneurons during changes in locomotor speed. *Nature Neurosci.* **11**, 1419–1429 (2008).
- Ritter, D. A., Bhatt, D. H. & Fetcho, J. R. In vivo imaging of zebrafish reveals differences in the spinal networks for escape and swimming movements. *J. Neurosci.* **21**, 8956–8965 (2001).
- Alford, S., Sigvardt, K. A. & Williams, T. L. GABAergic control of rhythmic activity in the presence of strychnine in the lamprey spinal cord. *Brain Res.* **506**, 303–306 (1990).
- Brustein, E. & Drapeau, P. Serotonergic modulation of chloride homeostasis during maturation of the locomotor network in zebrafish. *J. Neurosci.* **25**, 10607–10616 (2005).
- Vigh, B. & Vigh-Teichmann, I. Actual problems of the cerebrospinal fluid-contacting neurons. *Microsc. Res. Tech.* **41**, 57–83 (1998).
- Stoeckel, M. E. *et al.* Cerebrospinal fluid-contacting neurons in the rat spinal cord, a gamma-aminobutyric acidergic system expressing the P2X2 subunit of purinergic receptors, PSA-NCAM, and GAP-43 immunoreactivities: light and electron microscopic study. *J. Comp. Neurol.* **457**, 159–174 (2003).
- Furusho, M. *et al.* Involvement of the *Olig2* transcription factor in cholinergic neuron development of the basal forebrain. *Dev. Biol.* **293**, 348–357 (2006).
- Huang, A. L. *et al.* The cells and logic for mammalian sour taste detection. *Nature* **442**, 934–938 (2006).
- Xiao, T. & Baier, H. Lamina-specific axonal projections in the zebrafish tectum require the type IV collagen Dnagen. *Nature Neurosci.* **10**, 1529–1537 (2007).
- Flanagan-Steet, H., Fox, M. A., Meyer, D. & Sanes, J. Neuromuscular synapses can form in vivo by incorporation of initially aneural postsynaptic specializations. *Development* **132**, 4471–4481 (2005).
- Koster, R. W. & Fraser, S. E. Tracing transgene expression in living zebrafish embryos. *Dev. Biol.* **233**, 329–346 (2001).

Supplementary Information is linked to the online version of the paper at www.nature.com/nature.

Acknowledgements We thank M. Volgraf for MAG-1 synthesis, K. Kawakami for the *UAS:TeTxLC-CFP* line, B. Appel for the *Olig2-DsRed* line, W. Staub for animal care, D. Li for help with screening *BGUG* larvae, B. Vigh, C. Girit, E. Brustein, P. Drapeau and S. Hugel for discussions, P. G. de Gennes and Noam Sobel for support and O. Wyart for aesthetic input. We are grateful to K. Best, P. Tavormina, H. Aaron, R. Ayer, B. Nowak and M. Ulbrich for advice on the design of the photostimulation setup. Support for the work was from the Marie Curie Outgoing International Fellowship (with the CNRS – UMR5020 ‘Neurosciences Sensorielles, Comportement Cognition’ laboratory, Lyon, France) (C.W.), the Human Frontier Science Program Long-term Postdoctoral Fellowship (F.D.B.), the National Institutes of Health Nanomedicine Development Center for the Optical Control of Biological Function (SPN2EY018241) (E.Y.I., D.T. and H.B.), the Human Frontiers Science Program (RGP23-2005) (E.Y.I. and D.T.), the Lawrence Berkeley National Laboratory Directed Research and Development Program (E.Y.I. and D.T.), R01 NS053358 (H.B.) and a Sandler Opportunity Award (H.B.).

Author Contributions C.W., F.D.B. H.B. and E.Y.I. made critical primary contributions to this study. C.W. built the photostimulation setup, performed behavioural experiments, lesions, pharmacology, calcium imaging, imaging of the immunolabelled larvae, anatomical analysis based on *BGUG* imaging and wrote the Matlab scripts for analysing behaviour and imaging. F.D.B. generated the transgenic lines *UAS:LiGluR*¹⁰ and *Hb9:Gal4*, as well as performing the immunocytochemistry experiments. E.W. participated in the anatomical analysis of *BGUG*. E.K.S. and H.B. generated the enhancer trap *Gal4* screen, which made the ‘intersectional optogenetic’ approach possible¹¹. E.Y.I. and D.T. developed chemical optogenetics with *LiGluR*⁸. C.W. and E.Y.I. wrote the manuscript with feedback from H.B. and F.D.B. H.B. and E.Y.I. supervised C.W. and F.D.B. and contributed to the planning of all aspects of this project.

Author Information Reprints and permissions information is available at www.nature.com/reprints. Correspondence and requests for materials should be addressed to E.Y.I. (ehud@berkeley.edu) or H.B. (herwig.baier@ucsf.edu).

METHODS

Generation of transgenic lines. Zebrafish were maintained at 28 °C in the Tubingen Line genetic background. To make the *Hb9:Gal4* transgenic construct, 3 kilobases of genomic sequence upstream of the *hb9* coding sequence^{18,29} was amplified by PCR and inserted upstream of the *GAL4* coding sequence³⁰. This expression cassette was inserted between the Tol2 recognition sequences in the pTKXIGΔin vector³¹. Wild-type TL embryos were injected at the one-cell stage with a solution of 25 ng μl⁻¹ *Hb9:GAL4* DNA, 50 ng μl⁻¹ transposase mRNA (prepared using the Ambion mMESSAGE mMACHINE T7 kit) and 0.04% Phenol Red. F1 embryos were pooled and screened for the transgene by crossing them with *UAS:Kaede* carriers. F0 founder animals were then mated to wild-type TL fish to create stable lines.

The following transgenic lines were used (designations according to official zebrafish nomenclature; previously published synonyms or abbreviated name are in parentheses): Tg(*UAS:LiGluR6(L439C)*)s1995 (*UAS:LiGluR*); Tg(*UAS:Elb:Kaede*)s1999/+ (*UAS:Kaede*); Et(-1.5hsp70l:*Gal4-VP16*)s1003t (*Gal4^{s1003t}*); Et(-0.6hsp70l:*Gal4-VP16*)s1020t (*Gal4^{s1020t}*); Et(*fos:Gal4-VP16*)s1041t (*Gal4^{s1041t}*); Et(*Elb:GAL4-VP16*)s1102t (*Gal4^{s1102t}*); Tg(*pou4f3:GAL4,UAS:gap43-GFP*)s314t (*BGUG*); Tg(*5xUAS:TeTxLC-CFP*)zf85 (*UAS:TeTxLC-CFP*). Because the *GAL4* lines carry the *UAS:Kaede* construct, embryos positive for Kaede produced in a cross with *UAS:LiGluR* carriers were selected for behaviour experiments (50% were also *UAS:LiGluR* expressers). Dark embryos were used for calcium-imaging experiments. Genotyping of larvae for the *LiGluR* transgene was performed after behavioural experiments using the following primers: forward primer GGCTTGA GGATGGGAATATG and reverse primer GGGTTGCAAGGGTGTGGGTT ATACC.

To determine which cell types expressed *GAL4* in the *Gal4s1020t* line and to quantify their abundance, we used the *BGUG* transgene (an abbreviation of *Brn3c:Gal4; UAS: mGFP*), which labels a small, random subset of the *GAL4*-expressing cells owing to variegated expression of the gene encoding a membrane-targeted GFP^{11,28}.

MAG-1 labelling and mounting of zebrafish larvae. Synthesis of MAG-1 was performed as previously described^{8–10}. MAG-1 was first diluted to 5 mM in DMSO and pre-activated by ultraviolet light (365 nm) for 1 min. The medium E3 was then added to reach the final concentration of 200 μM MAG-1, 4% DMSO. Five days after fertilization, larvae were bathed in the labelling solution for 45 min at 28.5 °C in the dark. The larvae were then washed three times with fresh E3 medium. After recovery period of 1 h, all spontaneously swimming larvae were embedded in 2% agar and free-tailed. The agar was removed up to the fins for the behaviour experiments where illumination of the tail was global under a ×5 air objective (numerical aperture = 0.25), whereas the agar was removed only up to the anus for experiments where single (group of) cells were illuminated under the ×40 water immersion objective (numerical aperture = 0.8).

Photostimulation. The light source used for fast photoswitching was a DG-4 (Sutter Instruments) coupled to an upright Zeiss AxioImager epifluorescence microscope. Patterned illumination was accomplished using a digital micromirror device (Mosaic System, Photonic Instruments) coupled to the epifluorescence path of the microscope. For global illumination experiments, we illuminated the caudal portion of the tail bilaterally using a ×5 air objective (the light power was 0.24 mW mm⁻² at 390 nm and 0.71 mW mm⁻² at 500 nm; as a comparison the low power illumination previously used¹⁰ was 0.04 mW mm⁻² at 365 nm for 15 min), whereas local illumination of single segments or groups of cells was achieved using a ×40 water immersion objective (light power 24.6 mW mm⁻² at 390 nm and 37.7 mW mm⁻² at 500 nm).

The *Gal4* transgenic lines carry the *UAS:Kaede* constructs. Therefore, in all behavioural experiments reported here with *Gal4* lines, we selected the larvae expressing Kaede. Half of the larvae tested were positive for *UAS:LiGluR*, meaning that the tests were always run blindly and genotyping was performed afterwards. The light-induced responses of *Gal4^{s1020t}/UAS:LiGluR*, *Gal4^{s1102t}/UAS:LiGluR* and *Gal4^{s1003t}/UAS:LiGluR* labelled with MAG-1 were abolished by bath application of tricaine (0.02%; *n* = 8, 8 and 7, respectively).

We used patterned illumination to ask whether optical stimulation of CSF-contacting neurons in three consecutive segments on either the left or the right side of the animal would also evoke asymmetrical tail motions (experiments were

done in the *Gal4^{s1020t}* line because it reliably targets all Kolmer–Agduhr neurons, whereas *Gal4^{s1003t}* drives expression in only half of them).

Monitoring of behavioural responses. Five-day-old larvae exhibit spontaneous forward swims, also referred to as slow swims¹². These occur in brief bursts, with each burst consisting of a series of symmetrical, dampening left–right oscillations, which can be analysed quantitatively in ‘head-centred’ movies, where the image of the fish in each frame is repositioned to register the head in one spot so that the movements of the tail can be visualized (Fig. 1a and Supplementary Movie 1). Swimming movements can also be observed in semi-restrained larvae with their heads fixed in agar and tails free to move (Methods), thus allowing targeted optical stimulation of the central nervous system to be combined with behavioural analysis and providing an easy comparison with the head-centred free swim. We chose several *Gal4* transgenic lines that allowed us to drive expression of *LiGluR* in different subsets of spinal neurons, and we asked whether optical activation of these neurons elicits a forward swim-like behaviour.

Motion of the tail was monitored at 250 frames per second using a high-speed camera (Fastec Inline, Itronix Imaging Technologies). The camera was coupled to the side port of the AxioImager microscope in global illumination experiments using the ×5 objective, or coupled to a ×4 objective under the stage when local photoswitching was performed using a higher magnification (×40) objective. The tracking of the tail position was performed using a custom-made script written in Matlab 2007 (Mathworks). Lesions were performed on larvae anaesthetized by a cold exposure and bathing in Evans solution using a fine tungsten needle at the boundary of the hindbrain and spinal cord. Animals were tested after a period of 60 min recovery. The quantification of spontaneous swimming in *Gal4^{s1003t}/UAS:TeTxLC-CFP* and dark siblings was performed by isolating six 5-day-old larvae at a time and counting swimming events in a 10-min recording. Thirty larvae were observed for each group. All experiments were conducted at room temperature.

Immunocytochemistry. Embryos at appropriate stages were fixed in 4% PFA in PBS and processed for immunohistochemistry according to published protocols²⁸. The following primary antibodies and concentrations were used for whole-mount immunohistochemistry: antibody to GFP (rabbit anti-GFP; Molecular Probes A11122, or chick anti-GFP; GeneTex GTX13970) 1:500; antibody to GABA (rabbit anti-GABA; Sigma A2052) 1:2,000; antibody to GAD65/67 (rabbit anti GAD65+GAD67; Abcam ab11070-50) 1:500; antibody to Somatostatin (ImmunoStar 20067) 1:200. GABA immunostaining required fixation in 0.1% glutaraldehyde/4%PFA in PBS. Secondary antibodies conjugated to Alexa-488 or Alexa-555 (Invitrogen) were selected accordingly and used at 1:500 dilutions. Nuclei were counterstained with DAPI (Invitrogen).

Dye preparation and loading. Injection of the calcium dye was performed 30–60 min after MAG-1 labelling. Oregon Green Bapta 1-AM was freshly diluted in DMSO with 20% pluronic acid (Invitrogen) to yield to a 10 mM stock solution and further diluted in Evans solution with 0.01% Fast-Green (Sigma-Aldrich) to a final concentration of 1 mM. A fine borosilicate pipette of 1 mm outer diameter and 0.5 mm internal diameter (FHC; 5 MΩ resistance when filled with Evans solution) was used to inject the dye in the spinal cord using a Picospritzer (General Valve; 50 ms, 20 pounds per square inch, one to three puffs). Calcium recordings were performed between 1 and 5 h after the dye loading.

Calcium imaging. Fluorometric Ca²⁺ measurements were performed at room temperature using a confocal Olympus Fluoview laser scanning microscope equipped with a ×40 (numerical aperture = 0.8) water immersion objective. The 488-nm argon laser (20 mW) was used at 1–3% power for exciting the dye, and a 405-nm laser (50 mW) used at 1–30% power for photoswitching. Frames were acquired at 4–10 Hz. Local photoactivation of cells was performed by one scan at the same acquisition speed repeated every 10 s unless otherwise stated. Values of ΔF/F₀ were computed using a custom-made script in Matlab 2007.

Pharmacology. Tricaine (0.02%) was dissolved in E3 and added to the bath. Bicuculline dissolved in fish Ringer's solution was injected at 40 μM, and TTX at 10 μM.

31. Masahira, N. *et al.* Olig2-positive progenitors in the embryonic spinal cord give rise not only to motoneurons and oligodendrocytes, but also to a subset of astrocytes and ependymal cells. *Dev. Biol.* 293, 358–369 (2006).

Response and resistance to MEK inhibition in leukaemias initiated by hyperactive Ras

Jennifer O. Lauchle¹, Doris Kim¹, Doan T. Le¹, Keiko Akagi⁵, Michael Crone¹, Kimberly Krisman¹, Kegan Warner¹, Jeannette M. Bonifas¹, Qing Li², Kristen M. Coakley³, Ernesto Diaz-Flores¹, Matthew Gorman¹, Sally Przybranowski⁶, Mary Tran¹, Scott C. Kogan⁴, Jeroen P. Roose³, Neal G. Copeland⁷, Nancy A. Jenkins⁷, Luis Parada⁸, Linda Wolff⁹, Judith Sebolt-Leopold⁶ & Kevin Shannon¹

The cascade comprising Raf, mitogen-activated protein kinase kinase (MEK) and extracellular signal-regulated kinase (ERK) is a therapeutic target in human cancers with deregulated Ras signalling, which includes tumours that have inactivated the *Nf1* tumour suppressor^{1,2}. *Nf1* encodes neurofibromin, a GTPase-activating protein that terminates Ras signalling by stimulating hydrolysis of Ras-GTP. We compared the effects of inhibitors of MEK in a myeloproliferative disorder (MPD) initiated by inactivating *Nf1* in mouse bone marrow and in acute myeloid leukaemias (AMLs) in which cooperating mutations were induced by retroviral insertional mutagenesis. Here we show that MEK inhibitors are ineffective in MPD, but induce objective regression of many *Nf1*-deficient AMLs. Drug resistance developed because of outgrowth of AML clones that were present before treatment. We cloned clone-specific retroviral integrations to identify candidate resistance genes including *Rasgrp1*, *Rasgrp4* and *Mapk14*, which encodes p38 α . Functional analysis implicated increased RasGRP1 levels and reduced p38 kinase activity in resistance to MEK inhibitors. This approach represents a robust strategy for identifying genes and pathways that modulate how primary cancer cells respond to targeted therapeutics and for probing mechanisms of *de novo* and acquired resistance.

Aberrant Ras signalling contributes to the pathogenesis of myeloid malignancies and can result from acquired RAS mutations or from alternative genetic mechanisms that include *FLT3* internal tandem duplications, the *BCR-ABL* fusion, *PTPN11* mutations and *NF1* inactivation (reviewed in ref. 3). Children with neurofibromatosis type 1 (NF1) have a 200- to 500-fold excess incidence of juvenile myelomonocytic leukaemia, an aggressive MPD characterized by leukocytosis, splenomegaly and tissue infiltration (reviewed in ref. 4). The bone marrows of affected patients frequently show loss of the normal parental *NF1* allele and elevated ERK activity⁵⁻⁷. Bi-allelic inactivation of murine *Nf1* causes an MPD in *Mx1-Cre, Nf1^{flox/flox}* mice that closely models juvenile myelomonocytic leukaemia⁸.

We injected the MOL4070LTR retrovirus⁹ into *Mx1-Cre, Nf1^{flox/flox}* pups to identify genes and pathways that might cooperate with *Nf1* inactivation to induce progression of MPD to AML³. These mice developed acute leukaemia sooner and at a higher rate than control *Mx1-Cre*-negative littermates that retain normal *Nf1* function (Fig. 1a). *Nf1*-deficient AMLs are highly aggressive (Fig. 1b, c), show variable expression of myeloid surface markers, are transplantable into sublethally irradiated recipients and form cytokine-dependent blast colonies in methylcellulose cultures.

The MEK inhibitor CI-1040 (ref. 10) reduced the growth of myeloid progenitor colonies from the bone marrows of *Mx1-Cre, Nf1^{flox/flox}* mice with MPD and wild-type controls to a similar extent (Fig. 1d). By contrast, blast colony growth from many *Nf1*-deficient AMLs was exquisitely sensitive, with abrogation of colony growth at 10- to 100-fold lower drug concentrations (Fig. 1d). These *in vitro* data suggested that cooperating mutations render *Nf1*-mutant AMLs more dependent on Raf/ERK/MEK signalling. To pursue this question, we first determined the maximally tolerated dose of CI-1040 to be 100 mg kg⁻¹ twice daily in wild-type mice, collected bone marrow at defined time points after a single drug dose, and showed that CI-1040 treatment transiently reduced the ability of granulocyte-macrophage

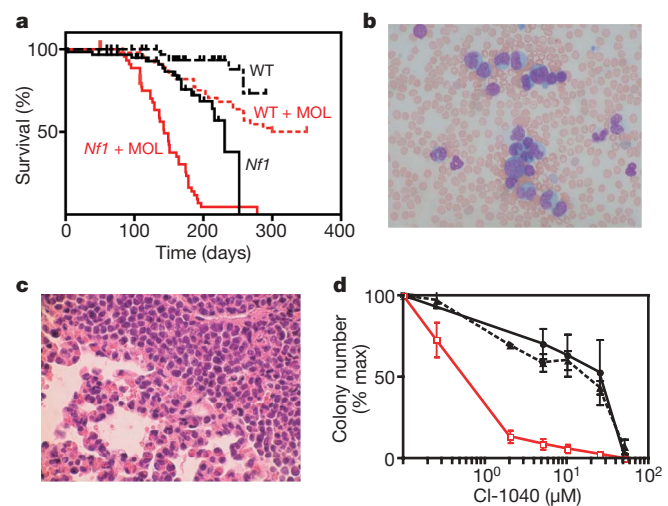


Figure 1 | Retroviral mutagenesis induces AML in *Mx1-Cre, Nf1^{flox/flox}* mice and alters response to MEK inhibition. **a**, *Mx1-Cre, Nf1^{flox/flox}* mice that were infected with MOL4070LTR (*Nf1* + MOL; $n = 47$) had markedly reduced survival compared with control littermates that received this virus (wild type + MOL; $n = 49$; $P < 0.0001$). Survival curves for *Mx1-Cre, Nf1^{flox/flox}* (*Nf1*) and wild-type mice that were not injected with MOL4070LTR are also shown. **b**, **c**, Myeloblasts in the peripheral blood (**b**) and infiltrating into lung tissues (**c**) of *Mx1-Cre, Nf1^{flox/flox}* mice with AML. **d**, Myeloid colony growth from the bone marrows of wild-type mice (filled circles, $n = 12$) *Mx1-Cre, Nf1^{flox/flox}* mice with MPD (filled triangles, $n = 6$), and *Mx1-Cre, Nf1^{flox/flox}* mice with AML (open squares, $n = 8$) over a range of CI-1040 concentrations (log scale). Colony growth was assayed in the presence of a saturating concentration of GM-CSF. Error bars, s.e.m.

¹Department of Pediatrics, ²Department of Medicine, ³Department of Anatomy, ⁴Department of Laboratory Medicine, University of California, San Francisco, California 94143, USA. ⁵Mouse Cancer Genetics Program, National Cancer Institute, Frederick, Maryland 21702, USA. ⁶Pfizer Global Research and Development, Ann Arbor, Michigan 48105, USA. ⁷Institute of Molecular and Cell Biology, Singapore 138673, Singapore. ⁸University of Texas Southwestern, Dallas, Texas 75235, USA. ⁹Laboratory of Cellular Oncology, National Cancer Institute, National Institutes of Health, Bethesda, Maryland 20892, USA.

colony-stimulating factor (GM-CSF) to increase phosphorylated ERK levels (Supplementary Fig. 1a). We then treated control or *Mx1-Cre, Nf1^{flox/flox}* mice with MPD for 28 days ($n = 5$ per group). Consistent with the *in vitro* data, CI-1040 had no beneficial therapeutic index in mice with MPD (Supplementary Fig. 1b, c and data not shown). Biochemical analysis of bone marrow obtained 2–8 h after the 56th and final dose of CI-1040 revealed reduced ERK phosphorylation that was similar to the responses of wild-type mice that received a single drug dose (Supplementary Fig. 1a, d).

To investigate the unexpected *in vitro* sensitivity of *Nf1* mutant AMLs to CI-1040, we transplanted four independent leukaemias into 23 recipients. Mice with AML blasts in the peripheral blood were assigned to treatment with either vehicle ($n = 11$) or CI-1040 ($n = 12$) at the same dose and schedule that was ineffective in the MPD. CI-1040 treatment induced rapid and extensive reductions in blood leukocyte counts (Fig. 2a), with clearance of blasts and reappearance of normal neutrophils (data not shown). Survival increased greater than threefold (Fig. 2b). However, recipients of *Mx1-Cre, Nf1^{flox/flox}* AMLs invariably died with recurrent leukaemia despite ongoing treatment (Fig. 2b). These relapsed AMLs had similar morphological and immunophenotypic features as the parental leukaemias, but demonstrated *in vitro* resistance to MEK inhibitors and were refractory to treatment in secondary recipients (Fig. 2c and data not shown). Sensitive AMLs showed a greater reduction in 5'-bromodeoxyuridine incorporation after CI-1040 exposure than either wild-type or resistant leukaemia cells (Supplementary Fig. 2). We also exposed pairs of sensitive and resistant AMLs to CI-1040 *in vitro* to ask if resistance is associated with reactivation of MEK. Importantly, ERK phosphorylation in response to GM-CSF was inhibited at the same concentration of CI-1040 (Fig. 2d, e).

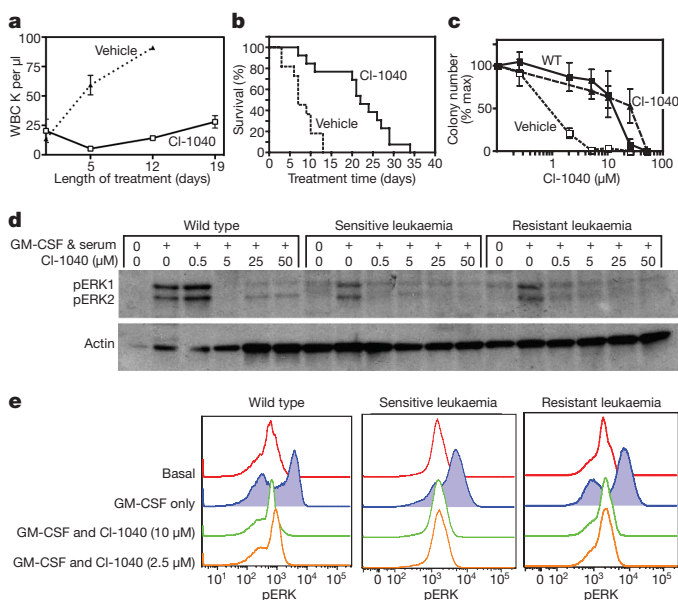


Figure 2 | Response and resistance to CI-1040 in *Mx1-Cre, Nf1^{flox/flox}* mice with AML. **a**, Leukocyte counts were markedly decreased in mice treated with CI-1040 ($n = 13$) compared with the vehicle ($n = 12$). Error bars, s.e.m. **b**, Survival was prolonged by approximately threefold in mice that received CI-1040 (odds ratio 3.1; confidence interval (CI) 2.7–3.6; $P < 0.0001$). **c**, Myeloid colony growth from the bone marrows of mice with recurrent leukaemia are less sensitive to CI-1040 inhibition than the parental AMLs. Colony growth in methylcellulose is compared for wild-type bone marrow (filled squares, $n = 2$), for primary AML cells harvested from vehicle-treated mice (open squares, $n = 4$) and for AML cells obtained after relapse in recipients that were treated with CI-1040 (filled triangles, $n = 3$). Error bars, s.e.m. **d**, **e**, CI-1040 abrogates the ability of GM-CSF to stimulate ERK phosphorylation in both sensitive and resistant AMLs as assessed by western blotting (**d**) or phospho-flow cytometry (**e**).

PD0325901 is a MEK inhibitor with more favourable pharmacological characteristics than CI-1040 (ref. 11). We defined a maximally tolerated dose of $12.5 \text{ mg kg}^{-1} \text{ d}^{-1}$ for PD0325901, and found that doses greater than $5 \text{ mg kg}^{-1} \text{ d}^{-1}$ reduced ERK activation in response to GM-CSF for 24 h (Supplementary Fig. 3a). To ask if prolonging the duration of MEK inhibition affects drug response and resistance *in vivo*, we administered PD0325901 to mice that were transplanted with two AMLs from the CI-1040 trial (AMLs 6554 and 6537). Recipients that received PD0325901 demonstrated the same pattern of response, relapse and overall survival (Supplementary Fig. 3b). We also tested two other *Nf1*-deficient AMLs for response to PD0325901. AML 7723 was less sensitive to MEK inhibition in methylcellulose cultures, and administering PD0325901 to recipient mice neither prolonged survival nor changed the half-maximal inhibitory concentration (IC_{50}) for blast colony formation (Supplementary Fig. 4). AML 7710 showed an *in vitro* response to PD0325901 that was similar to sensitive leukaemias; however, *in vivo* treatment did not prolong survival or select for clones with altered drug responsiveness (Supplementary Fig. 4). Together, these studies define a heterogeneous response of *Nf1*-deficient AMLs to MEK inhibition.

Digesting DNA from AML 6554 with restriction enzymes and Southern blot analysis with a MOL4070LTR-specific probe revealed clonal evolution of the resistant leukaemia (Fig. 3a). To identify candidate genes that might influence response to CI-1040, we exploited a shotgun cloning strategy¹² to characterize MOL4070LTR integrations. Sensitive parental AML 6554 and resistant leukaemias from CI-1040- and PD0325901-treated recipient mice shared some common integrations as well as unique insertions (Fig. 3a and Supplementary Table 1). Importantly, resistant leukaemias from independent recipients that were treated with CI-1040 or PD0325901 invariably showed the same integration patterns (Fig. 3a and Supplementary Table 1). These data and the rapid emergence of resistance imply that resistant subclones that are present within the initial AML are selected *in vivo* during MEK inhibitor treatment.

The patterns of MOL4070LTR integrations in sensitive and resistant AML 6554 suggested that *Rasgrp* genes might contribute to drug resistance (Supplementary Table 1). We developed quantitative real-time PCR (rtPCR) assays to correlate *Rasgrp1* insertion copy number and RNA expression in AML 6554 with the integration data shown in Supplementary Table 1. Whereas analysis of sensitive AML 6554 from eight independent recipients revealed only low levels of a unique integration junction fragment, four independent PD0325901-resistant leukaemias demonstrated 1,000-fold (range 500- to 1,500-fold) increases in DNA copy number. Similarly, *Rasgrp1* messenger RNA levels were increased an average of tenfold (range 6.5- to 19-fold) in resistant compared with sensitive leukaemias (Fig. 3b). RasGRP proteins stimulate guanine nucleotide exchange on Ras, which increases Ras-GTP levels (reviewed in ref. 13). We reasoned that increased *Rasgrp1* expression might result in elevated Ras-GTP levels in resistant AML 6554. Indeed, whereas basal Ras-GTP levels were low in the parental leukaemia and returned to baseline 60 min after exposure to GM-CSF, we observed constitutive Ras activation in the resistant AML (Fig. 3c). Resistant AML 6554 also formed cytokine-independent blast colonies in methylcellulose (Fig. 3d). This observation is consistent with biochemical and computational analyses in lymphocytes, which predict that Ras signalling becomes independent of receptor input when RasGRP levels are elevated¹⁴. To assess the functional importance of *Rasgrp1* overexpression in resistant AML 6554 further, we infected the sensitive and resistant leukaemias with a lentiviral vector encoding both a short hairpin RNA (shRNA) that efficiently reduces RasGRP1 protein (Supplementary Fig. 5) and a green fluorescent protein (GFP) marker. GFP-positive cells were isolated by sorting and plated in methylcellulose medium containing GM-CSF and a range of PD0325901 concentrations. Neither the *Rasgrp1* shRNA virus nor a control virus altered the sensitivity of parental AML blast colony-forming cells to the MEK inhibitor (Fig. 3e). By contrast, infecting resistant AML 6554 with the *Rasgrp1* shRNA lentivirus restored the sensitivity

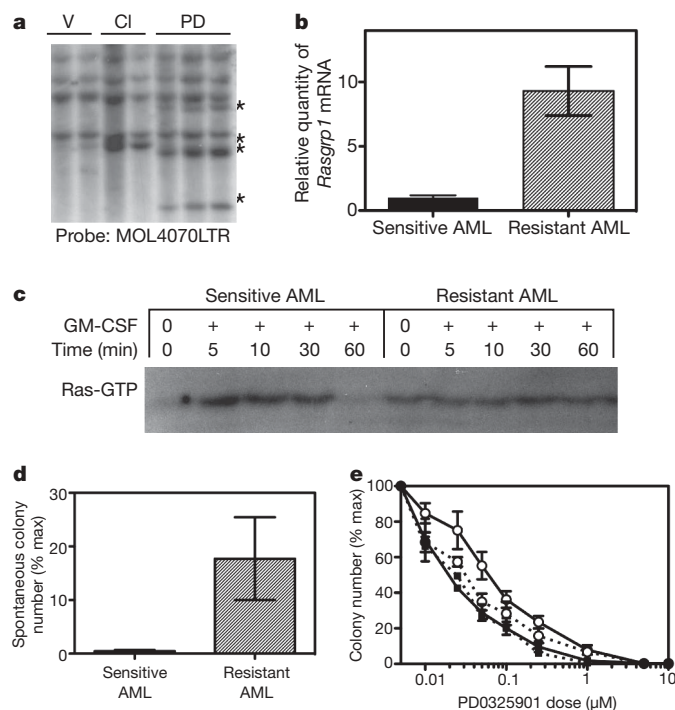


Figure 3 | Genetic and functional analysis implicates *Rasgrp1* overexpression as a resistance mechanism in AML 6554. **a**, Retroviral integrations in DNA samples from AML 6554 in independent mice after treatment with vehicle (V), CI-1040 (CI) or PD0325901 (PD). Stars denote restriction fragments that are present in resistant AMLs, but are not seen in the sensitive parental leukaemia. **b**, Quantitative PCR analysis of *Rasgrp1* expression in sensitive and resistant AML 6554 ($n = 3$ in each group, mean with s.d., $P < 0.002$ Student's t -test). **c**, Ras-GTP levels in AML 6554 show constitutive activation in the resistant leukaemia. **d**, Resistant AML 6554 demonstrates substantial cytokine-independent blast colony growth ($n = 5$), which is not seen in the sensitive leukaemia ($n = 6$) ($P = 0.0350$, t -test). **e**, Resistant AML 6554 that is infected with a *Rasgrp1* shRNA (open circles, dotted line, $n = 7$) demonstrates an $IC_{50} = 0.03 \mu$ M (95% CI 0.02–0.03), which is significantly lower than the IC_{50} of resistant cells infected with the control vector ($IC_{50} = 0.06 \mu$ M, 95% CI 0.05–0.07; open circles, solid line, $n = 7$). The IC_{50} of parental sensitive AML infected with shRNA vector to *Rasgrp1* ($IC_{50} = 0.02 \mu$ M, 95% CI 0.017–0.024; filled squares, dotted line, $n = 3$) or control vector ($IC_{50} = 0.02 \mu$ M, 95% CI 0.017–0.028; filled squares, solid line, $n = 3$) are not statistically significantly different than resistant AML 6554 infected with *Rasgrp1* shRNA. Error bars, s.e.m. in **d** and **e**.

of these cells to PD0325901, with a shift of the IC_{50} into the same range as in the sensitive parental AML (Fig. 3e).

Multiple recipients that were transplanted with AML 6537 relapsed with the same resistant clone after treatment with either CI-1040 or PD0325901 (Fig. 4a). This resistant leukaemia showed a distinct retroviral integration pattern, including one within *Mapk14*, which encodes p38 α (Supplementary Table 2). rtPCR of proviral/host DNA junctions confirmed that the inserted allele copy number is increased 1,000-fold (range 1,000- to 10,000-fold) in the resistant AML. The proviral insertion is in the anti-sense orientation, and Southern blot analysis supports inactivation of one *Mapk14* allele (Fig. 4a, b). Consistent with this prediction, basal p38 kinase activity is reduced in resistant AML 6537 (Fig. 4c). To investigate further whether decreased p38 α activity modulates resistance to MEK inhibitors in primary leukaemia cells, we enumerated blast colonies from AML 6537 in the presence of either CI-1040, SB202190 (a specific inhibitor of p38 α)^{15,16} or both drugs. SB202190 strongly antagonized the inhibitory effects of CI-1040 on the sensitive leukaemia, but had minimal effects on the resistant AML (Fig. 4d).

Cooperating mutations that induce progression of MPD to AML render these more aggressive leukaemias highly dependent upon

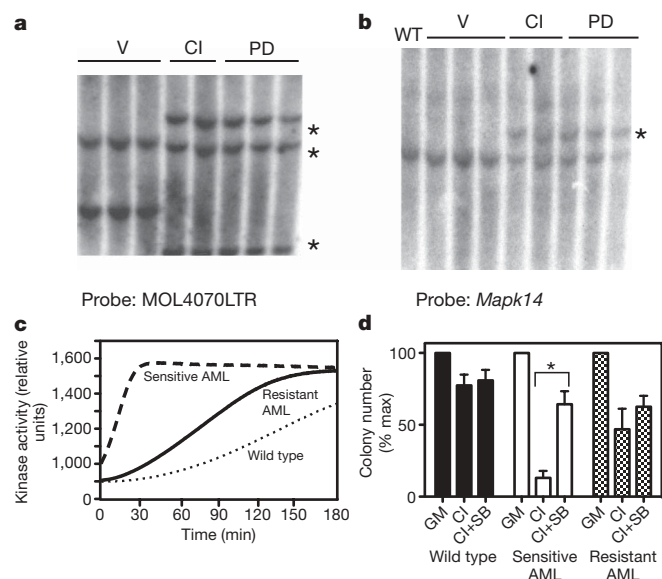


Figure 4 | Genetic and functional analysis of AML 6537 associates reduced p38 α kinase activity with resistance to MEK inhibition. **a**, Southern blot analysis of MOL4070LTR integrations of AML 6537 after treatment with vehicle (V), CI-1040 (CI) or PD0325901 (PD). Stars denote restriction fragments that are present in all the resistant AMLs, but are not seen in the sensitive leukaemia. **b**, Southern blot analysis of paired sensitive and resistant AML 6537 with a *Mapk14* probe. The resistant leukaemias shown in lanes CI and PD show a *Mapk14* hybridization fragment, which overlaps with one of the MOL4070LTR bands in the resistant leukaemias shown in **a**. **c**, Basal p38 kinase activity of resistant AML 6537 cells (solid line) is reduced compared with the parental leukaemia (dashed line), but remains elevated above wild-type bone marrow cells (dotted line). This is a representative example of three independent experiments. **d**, SB202190 (SB), a p38 α inhibitor, antagonizes the ability of CI-1040 (CI) to reduce blast colony inhibition in parental AML 6537 (white bars, $n = 7$) in the presence of GM-CSF (GM). Blast colony growth of sensitive AML 6537 is significantly increased by the addition of SB to CI-1040 ($*P = 0.0043$; unpaired t -test). By contrast, CI-1040 (2.5 μ M) has an inhibitory effect on wild-type CFU-GM colony (black bars, $n = 8$) and resistant AML 6537 (hatched bars, $n = 5$) blast colony growth, which is not affected by 2.5 μ M SB202190. Error bars, s.e.m.

MEK for proliferation and survival. The transient remissions induced by imatinib in advanced ('blast crisis') CML¹⁷ are remarkably similar to the responses of *Mx1-Cre*, *Nf1^{lox/lox}* AMLs to MEK inhibition. Relapse of blast crisis CML and of *Nf1*-mutant murine leukaemias is due to outgrowth of a minor population of drug-resistant cells that is present before treatment with targeted agents¹⁸. Similarly, 'back-tracking' experiments in acute lymphoblastic leukaemias showed that the dominant clone at relapse is frequently detectable before treatment¹⁹. Relapsed acute lymphoblastic leukaemia clones differ from the predominant clone at diagnosis by a few genetic changes²⁰. Diverse mutations of genes involved in lymphoid developmental programs, cell cycle control and DNA damage responses are enriched in drug-resistant clones, whereas alterations in drug import, export or metabolism are relatively uncommon²⁰. Understanding how pre-existing drug-resistant clones underlie cancer relapse has fundamental implications for developing better therapeutic strategies.

As MEK is one component of a complex network of Ras effectors, it is possible to envision multiple mechanisms of acquired resistance. Our data support this idea. A provocative implication of our studies of AML 6554 showing that *Rasgrp1* overexpression modulates the response to MEK inhibitors is that globally increasing Ras-GTP levels can overcome the effects of inhibiting a major Ras effector in some cancers. We implicated reduced p38 kinase activity as an alternative mechanism of MEK resistance in AML 6537. Interestingly, cancer cell lines that undergo apoptosis in response to oncoprotein inhibition show a rapid decrease in phosphorylated ERK followed by an increase

in phosphorylated p38 levels²¹. As *Nf1*-deficient AMLs have elevated basal p38 kinase activity, our studies suggest that inhibiting oncogenic Raf–MEK–ERK signalling results in unopposed p38 kinase activity, which contributes to cell death. This general idea is consistent with the observation that p38 inhibitors induce imatinib resistance in cultured CML cells^{21,22}.

The AMLs that we have characterized so far showed diverse retroviral integrations (Supplementary Tables 1–3), and comprehensive genetic and preclinical analyses are required to uncover the full spectrum of mutations associated with drug resistance. Despite this limitation, a broad implication of our data is that cell lineage, the nature of cooperating mutations and the order in which they are acquired in specific cancers will modulate the efficacy of targeted inhibitors of Ras effector pathways. Insertional mutagenesis in genetically accurate mouse cancer models is a powerful tool for dissecting the molecular basis of cellular responses to oncogenic stress and for uncovering genes that contribute to drug sensitivity and resistance.

METHODS SUMMARY

Inhibitors. CI-1040 and PD0325901 (Pfizer) were administered as described in Supplementary Methods. SB202190 (Calbiochem) was diluted in 100% dimethylsulphoxide.

Mouse strains and retroviral insertional mutagenesis: mice. All procedures involving mice were approved by the UCSF Committee on Animal Research. MOL4070LTR stocks were prepared as described⁶. Mice received a single intraperitoneal injection containing 10⁵ viral particles in 100 µl admixed with 500 µg of pI-pC (to activate *Mx1-Cre* expression) between days 3 and 5 of life. Mice with leukaemia were killed and bone marrow was cryopreserved. Leukaemias were classified based on established morphological and flow cytometric criteria²³.

Adoptive transfer and treatment. Cryopreserved AMLs were injected intravenously (10⁶ cells per mouse) into 6- to 8-week-old recipient mice that received a single radiation dose of 450 cGy. Recipients with leukaemic cells in the peripheral blood were randomly assigned to receive either CI-1040/PD0325901 or control vehicle. Mice were weighed weekly to adjust the drug dose, observed daily and killed when they became moribund or on the 28th day of treatment.

Myeloid progenitor growth and pharmacodynamics studies. CFU-GM and blast colonies were grown in methylcellulose medium M3231 (Stem Cell Technologies) and scored by indirect microscopy. MEK inhibition was assessed by stimulating bone marrow cells with GM-CSF and then measuring phosphorylated ERK levels by western blotting (see also Supplementary Methods).

Retroviral integrations and quantitative rtPCR. Junction fragments corresponding to retroviral integrations were identified as described²⁴. PCR primers were designed to detect integration junctions²⁵ (see also Supplementary Methods).

p38 kinase assay. Kinase activity of mice was quantified in 100-µg lysates with the Omnia Plate IP kit (BioSource), in which activation of a MAPKAPK2 evokes a change in fluorescent properties owing to chelation-enhanced fluorophore. A fluorescent plate reader in real-time kinetic mode quantified p38 kinase activities.

Full Methods and any associated references are available in the online version of the paper at www.nature.com/nature.

Received 22 May; accepted 7 July 2009.

Published online 2 September 2009.

- Downward, J. Targeting RAS signalling pathways in cancer therapy. *Nature Rev. Cancer* **3**, 11–22 (2003).
- Schubbert, S., Shannon, K. & Bollag, G. Hyperactive Ras in developmental disorders and cancer. *Nature Rev. Cancer* **7**, 295–308 (2007).
- Van Etten, R. A. & Shannon, K. M. Focus on myeloproliferative diseases and myelodysplastic syndromes. *Cancer Cell* **6**, 547–552 (2004).
- Lauchle, J. O., Braun, B. S., Loh, M. L. & Shannon, K. Inherited predispositions and hyperactive Ras in myeloid leukemogenesis. *Pediatr. Blood Cancer* **46**, 579–585 (2006).
- Shannon, K. M. *et al.* Loss of the normal NF1 allele from the bone marrow of children with type 1 neurofibromatosis and malignant myeloid disorders. *N. Engl. J. Med.* **330**, 597–601 (1994).
- Bollag, G. *et al.* Loss of *NF1* results in activation of the Ras signaling pathway and leads to aberrant growth in murine and human hematopoietic cells. *Nature Genet.* **12**, 144–148 (1996).

- Side, L. *et al.* Homozygous inactivation of the NF1 gene in bone marrow cells from children with neurofibromatosis type 1 and malignant myeloid disorders. *N. Engl. J. Med.* **336**, 1713–1720 (1997).
- Le, D. T. *et al.* Somatic inactivation of NF1 in hematopoietic cells results in a progressive myeloproliferative disorder. *Blood* **103**, 4243–4250 (2004).
- Wolff, L., Koller, R., Hu, X. & Anver, M. R. A Moloney murine leukemia virus-based retrovirus with 4070A long terminal repeat sequences induces a high incidence of myeloid as well as lymphoid neoplasms. *J. Virol.* **77**, 4965–4971 (2003).
- Sebolt-Leopold, J. S. *et al.* Blockade of the MAP kinase pathway suppresses growth of colon tumors *in vivo*. *Nature Med.* **5**, 810–816 (1999).
- Brown, A. P., Carlson, T. C., Loi, C. M. & Graziano, M. J. Pharmacodynamic and toxicokinetic evaluation of the novel MEK inhibitor, PD0325901, in the rat following oral and intravenous administration. *Cancer Chemother. Pharmacol.* **59**, 671–679 (2007).
- Dupuy, A. J. *et al.* Mammalian mutagenesis using a highly mobile somatic Sleeping Beauty transposon system. *Nature* **436**, 221–226 (2005).
- Stone, J. C. Regulation of Ras in lymphocytes: get a GRP. *Biochem. Soc. Trans.* **34**, 858–861 (2006).
- Das, J. *et al.* Digital signaling and hysteresis characterize ras activation in lymphoid cells. *Cell* **136**, 337–351 (2009).
- Bain, J. *et al.* The selectivity of protein kinase inhibitors: a further update. *Biochem. J.* **408**, 297–315 (2007).
- Fabian, M. A. *et al.* A small molecule-kinase interaction map for clinical kinase inhibitors. *Nature Biotechnol.* **23**, 329–336 (2005).
- Druker, B. J. *et al.* Activity of a specific inhibitor of the BCR-ABL tyrosine kinase in the blast crisis of chronic myeloid leukemia and acute lymphoblastic leukemia with the Philadelphia chromosome. *N. Engl. J. Med.* **344**, 1038–1042 (2001).
- Shah, N. P. *et al.* Multiple BCR-ABL kinase domain mutations confer polyclonal resistance to the tyrosine kinase inhibitor imatinib (ST1571) in chronic phase and blast crisis chronic myeloid leukemia. *Cancer Cell* **2**, 117–125 (2002).
- Choi, S. *et al.* Relapse in children with acute lymphoblastic leukemia involving selection of a preexisting drug-resistant subclone. *Blood* **110**, 632–639 (2007).
- Mullighan, C. G. *et al.* Genomic analysis of the clonal origins of relapsed acute lymphoblastic leukemia. *Science* **322**, 1377–1380 (2008).
- Sharma, S. V. *et al.* A common signaling cascade may underlie 'addiction' to the Src, BCR-ABL, and EGF receptor oncogenes. *Cancer Cell* **10**, 425–435 (2006).
- Parmar, S. *et al.* Role of the p38 mitogen-activated protein kinase pathway in the generation of the effects of imatinib mesylate (ST1571) in BCR-ABL-expressing cells. *J. Biol. Chem.* **279**, 25345–25352 (2004).
- Kogan, S. C. *et al.* Bethesda proposals for classification of nonlymphoid hematopoietic neoplasms in mice. *Blood* **100**, 238–245 (2002).
- Akagi, K. *et al.* RTCGD: retroviral tagged cancer gene database. *Nucleic Acids Res.* **32** (Database issue), D523–D527 (2004).
- Curtiss, N. P. *et al.* Isolation and analysis of candidate myeloid tumor suppressor genes from a commonly deleted segment of 7q22. *Genomics* **85**, 600–607 (2005).

Supplementary Information is linked to the online version of the paper at www.nature.com/nature.

Acknowledgements We are grateful to B. Braun, J. Downing, S. Lowe and C. Sawyers for discussion and advice throughout the project. We are thankful for C. Hartzell for studies on RasGRP protein expression. This work was supported by National Institutes of Health grants U01 CA84221, R37 CA72614, T32 CA09043, T32 HD044331 and K08 CA119105, by a Specialized Center of Research award from the Leukemia and Lymphoma Society (LLS 7019-04), by the US Army Neurofibromatosis Research Program (Project DAMD 17-02-1-0638), by the Ronald McDonald House Charities of Southern California/Couples Against Leukemia, by the Jeffrey and Karen Peterson Family Foundation and by the Frank A. Campini Foundation. S.C.K. is a Scholar of the Leukemia and Lymphoma Society of America. J.P.R. is a Kimmel Foundation Scholar. The Intramural Research Program of the National Cancer Institute's Center for Cancer Research supports research in the laboratory of L.W. at the National Institutes of Health.

Author Contributions J.O.L. and K.S. designed and performed experiments, analysed data and wrote the paper. D.K., D.T.L., M.C., K.K., K.W. and J.M.B. designed experiments, conducted studies, analysed data and provided input to the manuscript. K.A. performed bioinformatics analysis of retroviral insertion sequences. Q.L., K.M.C., E.D.-F., M.G. and M.T. designed and conducted experiments. J.P.R. provided critical reagents, assisted in experimental design and edited the manuscript. N.C., N.J. and L.W. provided retroviral reagents and training in experimental protocols. L.P. provided the mouse strain and input into the manuscript. J.S.-L. and S.P. developed protocols for suspending and administering the MEK inhibitor and provided the drug used in all studies.

Author Information Reprints and permissions information is available at www.nature.com/reprints. Correspondence and requests for materials should be addressed to K.S. (shannonk@peds.ucsf.edu).

METHODS

Preparation and administration of MEK inhibitors. CI-1040 and PD0325901 were dissolved in 100% DMSO for *in vitro* assays and suspended in 0.5% hydroxypropyl methylcellulose and 0.2% Tween 80 for administration to mice. For intraperitoneal injection of mice, 100 mg kg⁻¹ of CI-1040 was in a volume 100–150 µl and a concentration of 30 mg ml⁻¹. PD0325901 was administered in 150–200 µl volume by oral gavage (OG) to achieve doses of 2.5, 5.0, 7.5, 10.0 or 12.5 mg kg⁻¹.

Proliferation assay. Cells were plated in 6 ml of IMDM 20% FBS with a saturating dose of 2 ng µl⁻¹ of GM-CSF at a density no greater than 2 × 10⁶ cells per millilitre and incubated with 10 µM of CI-1040 or 0.2% DMSO for 22 h at 37 °C and 5% CO₂. Cells were pulsed with 5-bromo-2-deoxyuridine (BrdU) (BD Pharmingen FITC BrdU Flow Kit) and left to incorporate for 2 h. Cells were harvested from wells and washed with HBSS and 2% heat-inactivated FBS. Cells were treated with DNase to expose incorporated BrdU and stained with FITC conjugated anti-BrdU. Total intracellular DNA was stained with 7-AAD and samples were collected on a multicolour flow cytometer (LSR II) with a minimum of 10,000 total events.

GM-CSF stimulation and ERK phosphorylation. Femoral bone marrow cells were collected into 0.1% serum without growth factors. After 15 min, the cells were stimulated with 0 or 10 ng ml⁻¹ of GM-CSF and 0 or 10% fetal bovine serum for 10 min. The cells were washed once with PBS and lysed in 25 mM HEPES, pH 7.5, 150 mM NaCl, 1% NP-40, 0.25% Na deoxycholate, 10% glycerol, 10 mM MgCl₂, 25 mM NaF, 1 mM Na orthovanadate and Complete protease inhibitors (Amersham). Protein concentrations were quantitated and equalized for loading using the Bio-Rad protein assay (Bio-Rad). Samples were boiled for 5 min in 1 × Laemmli buffer, run on a 10% Tris-HCl Criterion Precast Gel (Bio-Rad) and transferred onto a nitrocellulose membrane. The membranes were blocked in TBS-Tween containing 5% milk for 1 h or in 5% BSA overnight before incubation at 4 °C with antiphospho-ERK 1/2 (1:1,000), anti-ERK (1:1,000) and anti-actin (1:500) (Cell Signaling Technologies). The blots were developed with a horseradish-peroxidase-conjugated secondary anti-rabbit antibody (Amersham). Proteins were visualized by enhanced chemiluminescence (Amersham).

Restriction digestion and Southern blotting. Bone marrow or spleen DNA from leukaemia mice was cut with HindIII, separated on an agarose gel, transferred onto a nylon membrane and hybridized overnight with a ³²P-labelled fragment of 4070LTR or *Mapk14*.

Cloning and bioinformatic analysis of viral insertions. Approximately 1 µg of genomic DNA was digested with NlaIII (IRDOR) or MseI and purified using a Qiagen column (QIAquick PCR purification). A 5-µl aliquot was added to a ligation reaction containing 150 µM of a double-stranded linker. Linkers were generated by annealing equimolar amounts of NlaIII linker+ (5'-GTAATAC GACTCACTATAGGGCTCCGCTTAAGGGACCATG-3') and NlaIII linker- (5'-/5Phos/GTCCCTTAAGCGGAG/3SpacerC3/-3') or MseI linker+ (5'-GTA ATACGACTCACTATAGGGCTCCGCTTAAGGGAC-3') and MseI linker- (5'-/5Phos/TAGTCCCTTAAGCGGAG/3SpacerC3/-3'). The 5' phosphate modification of the linker-oligonucleotide aids ligation of the linker, and the C3spacer modification at the 3' end of the linker-oligonucleotide prevents priming of *Taq* polymerase. Ligations were performed using high concentration T4 ligase (NEB) at room temperature for 2–3 h. After ligation digest with EcoRV to prevent amplification of the internal proviral fragment, primary PCR was performed using high-fidelity Platinum *Taq* (Invitrogen) and the linker primer 5'-GTAATACGACTCACTATAGGGCTCCG-3' and MuLV LTR3 5'-GCTAGC TTGCCAAACCTACAGGTGG-3'. Cycle conditions were as follows: 94 °C for 2 min, 94 °C for 15 s, 60 °C for 30 s and 72 °C for 1 min for 25 cycles followed by a final extension at 72 °C for 5 min. Primary PCR products were then diluted 1:50 in H₂O, and a 2-µl aliquot of the dilution was used for secondary PCR. Secondary PCR was performed using the nested linker primer 5'-AGGGCTCCGCTT

AAGGGAC-3' and MuLV LTR1 5'-CCAAACCTACAGGTGGGGTCTTTC-3'. Cycle conditions for secondary PCR were identical to the primary PCR. Secondary PCR products were purified using a Qiagen column (QIAquick PCR purification). A 3-µl aliquot of each sample was then ligated into the pCR-Blunt vector (Invitrogen) using high-concentration T4 ligase (NEB) and transformed into TOP10 cells (Invitrogen). Colonies were selected on kanamycin plates containing x-gal for blue-white screening. Ninety-six white colonies were picked from each sample, prepared for sequencing using the Qiagen DirectPrep 96 well kit and sequenced using the M13F(–20) primers. Using methods previously described, we compared retroviral integration sites against the public mouse genome database and identified annotated candidate genes located near each retroviral integration site. All sequences and tumour integration profiles will be deposited into the Retrovirus Tagged Cancer Gene Database (RTCGD).

Lentiviral shRNA RasGRP1 construct and infection. pSicoR-RasGRP1 shRNA-puro-t2a-EGFP was constructed by phosphorylating and annealing primers sh-sense-RasGRP1 5'-TGATCGCTGCAAGCTTTCCATTCAAGAGAT GGAAAGCTTGACGCGATCTTTTTC-3' and sh-antisense-RasGRP1 5'-TCG AGAAAAAAGATCGCTGCAAGCTTTCCATCTCTTGAATGGAAAGCTTGCA GCGATC-3' and ligating the mixture to HpaI/XhoI-digested pSicoR-puro-t2a-EGFP. This is designed to target base pair 1503 in mouse *Rasgrp1*. Control vector is pSicoR-puro-t2a-EGFP. 293T cells were plated to a density of 4 million 24 h before transfection. FuGENE 6 transfection reagent was used with 1.5 µg each of packaging plasmids pRSV-Rev, pMDLg-RRE, the envelope pVSV-G and 6 µg of pSicoR-RasGRP1 shRNA-puro-t2a-EGFP or pSicoR-puro-t2a-EGFP. After 72 h, supernatant was collected and concentrated at 25,000 r.p.m. in an ultracentrifuge for 1.5 h and brought to a final volume of 100 µl. Concentrated lentivirus was allowed to re-suspend overnight at 4 °C.

Bone marrow cells were harvested and kept in cytokine-rich media from 2 to 10 days before transduction. Three hundred and fifty thousand cells were plated, treated with polybrene and transduced with 30 µl of concentrated virus. Plates were spin-infected for 2 h, moved to an incubator for 2 h, and virus-containing supernatant was removed and cells placed in fresh cytokine-enriched media for 48 h before FACS analysis for GFP. GFP-positive cells were collected on an Aria sorter and plated in methylcellulose containing MEK inhibitor and GM-CSF 10 ng ml⁻¹ at consistent cell numbers in each independent experiment (range 1,200–15,000 cells per condition). Colony number was quantified after 8 days in methylcellulose.

Quantitative rtPCR. Quantification of proviral insertions was performed on DNA isolated from leukaemia mice and normalized for DNA quality based on threshold cycle of amplification of a control DNA region. The samples were amplified in an ABI Prism 7700 sequence detection system. The ΔC_t was calculated for each sample and compared with sensitive leukaemias as using the $\Delta\Delta C_t$ method. Fold increase or decrease was calculated using the $2^{-\Delta\Delta C_t}$. RNA was extracted using Qiagen RNeasy kit and cDNA was synthesized using the Superscript First-Strand Synthesis system for rtPCR (Invitrogen). GAPDH expression was measured in each sample to standardize each reaction. Fold increase or decrease was calculated using the $2^{-\Delta\Delta C_t}$.

Statistical analysis. Statistical analysis and graphs were generated using Prism 4 (GraphPad software). Survival curves were created using the product limit method of Kaplan and Meier, and compared using the log rank test (Mantel-Haenszel test) with a two-tailed *P* value. Colony growth was evaluated as percentage maximum growth ((average colony number in two replicate plates)/(average colony number in plates 0.2% DMSO) × 100). Mean percentage maximum growth was analysed with error bars representing the s.e.m. for independent samples. The significance of experimental results was determined by the Student's *t*-test unless otherwise noted. IC₅₀ values and 95% CI were calculated using nonlinear fit – log inhibitor versus normalized response variable slope program in Prism 5 software.

KDM1B is a histone H3K4 demethylase required to establish maternal genomic imprints

David N. Ciccone^{1,2}, Hui Su^{1,2}, Sarah Hevi^{1,2}, Frédérique Gay^{1,2}, Hong Lei^{1,2}, Jeffrey Bajko^{1,2}, Guoliang Xu³, En Li¹ & Taiping Chen^{1,2}

Differential DNA methylation of the paternal and maternal alleles regulates the parental origin-specific expression of imprinted genes in mammals^{1,2}. The methylation imprints are established in male and female germ cells during gametogenesis, and the *de novo* DNA methyltransferase DNMT3A and its cofactor DNMT3L are required in this process^{3–5}. However, the mechanisms underlying locus- and parental-specific targeting of the *de novo* DNA methylation machinery in germline imprinting are poorly understood. Here we show that amine oxidase (flavin-containing) domain 1 (AOF1), a protein related to the lysine demethylase KDM1 (also known as LSD1)⁶, functions as a histone H3 lysine 4 (H3K4) demethylase and is required for *de novo* DNA methylation of some imprinted genes in oocytes. AOF1, now renamed lysine demethylase 1B (KDM1B) following a new nomenclature⁷, is highly expressed in growing oocytes where genomic imprints are established. Targeted disruption of the gene encoding KDM1B had no effect on mouse development and oogenesis. However, oocytes from KDM1B-deficient females showed a substantial increase in H3K4 methylation and failed to set up the DNA methylation marks at four out of seven imprinted genes examined. Embryos derived from these oocytes showed biallelic expression or biallelic suppression of the affected genes and died before mid-gestation. Our results suggest that demethylation of H3K4 is critical for establishing the DNA methylation imprints during oogenesis.

KDM1B is related to KDM1 in that it possesses a flavin adenine dinucleotide-dependent amine oxidase domain and a SWIRM domain⁶. In KDM1, the amine oxidase domain contains the demethylase catalytic centre and the SWIRM domain is implicated in chromatin binding^{6,8,9}. To determine whether KDM1B also has demethylase activity, Flag-tagged wild-type KDM1B and KDM1B(K667A), which contains a point mutation (lysine 667 to alanine) in the amine oxidase domain, were expressed in HEK 293T cells and purified to near homogeneity (Fig. 1a). *In vitro* demethylase assays, using bulk histones as substrates, showed that KDM1B, but not KDM1B(K667A), substantially reduced the levels of H3K4 mono- and di-methylation (H3K4me1 and H3K4me2, respectively) without affecting the levels of H3K4me3, H3K9me2, H3K27me2 and H3K36me2 (Fig. 1b). To demonstrate the activity of KDM1B in cells, we expressed Flag-KDM1B or Flag-KDM1B(K667A) in NIH 3T3 cells and examined histone methylation by immunofluorescence microscopy. Both KDM1B and KDM1B(K667A) localized in the nuclei of transfected cells (Fig. 1c). KDM1B expression resulted in a drastic reduction in H3K4me2, only a slight reduction in H3K4me1, and no obvious changes in H3K4me3 and methylation at H3K9, H3K27, H3K36 and H4K20 (Fig. 1c and Supplementary Fig. 1). In contrast, KDM1B(K667A) expression showed no effect on H3K4me2 (Fig. 1c).

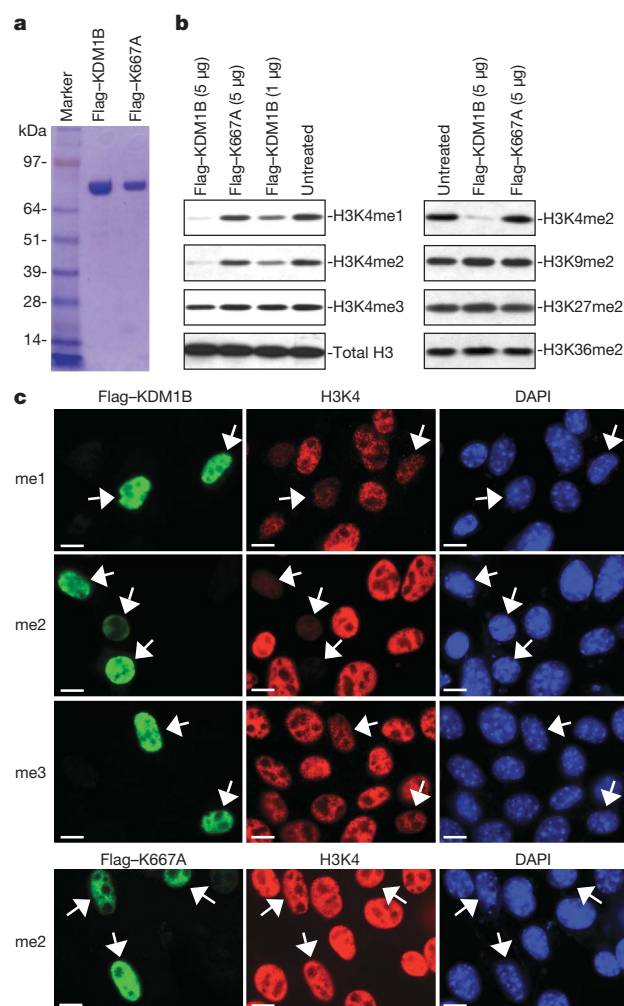


Figure 1 | KDM1B is an H3K4 demethylase. **a**, Coomassie blue staining of affinity-purified Flag-tagged KDM1B and KDM1B(K667A). **b**, *In vitro* demethylase assay. Bulk histones were incubated with Flag-tagged KDM1B or KDM1B(K667A) (1 or 5 µg) and analysed by western blotting. The H3K4me1, H3K4me2, H3K4me3 and total H3 blots on the left were from the same membrane. **c**, KDM1B activity in cells. NIH 3T3 cells transfected with Flag-tagged KDM1B or KDM1B(K667A) were co-immunostained with anti-Flag (green) and anti-H3K4me1, -H3K4me2 or -H3K4me3 (red), and their nuclei were stained with 4,6-diamidino-2-phenylindole (DAPI; blue). Transfected cells are indicated by arrows. Scale bars, 10 µm.

¹Epigenetics Program, ²Developmental and Molecular Pathways, Novartis Institutes for Biomedical Research, 250 Massachusetts Avenue, Cambridge, Massachusetts 02139, USA. ³The State Key Laboratory of Molecular Biology, Institute of Biochemistry and Cell Biology, Shanghai Institutes for Biological Sciences, Chinese Academy of Sciences, 320 Yueyang Road, Shanghai 200031, China.

These findings indicate that KDM1B is a bona fide histone demethylase specific for H3K4. The different efficiencies on H3K4me1 *in vitro* and in cells suggest that the action of KDM1B is modulated by cellular factors and/or the chromatin contexts of the histone substrates.

To study the biological function of KDM1B, we disrupted the *Aof1* gene in mice. Using the Cre/loxP recombination system, we generated a conditional *Aof1* allele, *Aof1*^{lox}, in which exons 14–16 were flanked by loxP sites. Cre recombinase-mediated deletion of the floxed region removed part of the amine oxidase domain and created a frameshift, thereby resulting in a functionally null allele, *Aof1*^{lox} (Supplementary Fig. 2).

We determined *Aof1* expression during development, taking advantage of the fact that cells containing the *Aof1*^{lox} allele express *lacZ* under the control of the endogenous *Aof1* promoter. X-gal (5-bromo-4-chloro-3-indoyl-β-D-galactoside) staining showed little expression of *Aof1* in embryos at 7.5 and 9.5 days post-coitum (d.p.c.) (data not shown). In adult mice, growing oocytes and intestinal gland showed high levels of *Aof1* expression, whereas all other organs examined showed little or no expression (Supplementary Fig. 3 and data not shown). Immunohistochemistry analysis confirmed the presence of KDM1B protein in growing oocytes of wild-type, but not of *Aof1*^{lox/lox} mice (Fig. 2a). To determine the timing of *Aof1* expression during oogenesis, we analysed ovaries at 5, 10, 15,

20 and 25 days post partum (d.p.p.) and adult stage (~60 d.p.p.). Irrespective of age, KDM1B was hardly detectable in oocytes of primordial and primary follicles, but showed a marked increase in oocytes of secondary follicles and the level persisted through later stages of oogenesis (Supplementary Fig. 3). Consistently, KDM1B deficiency resulted in a substantial increase in H3K4me2 in oocytes of secondary and antral follicles, but not in those of primordial and primary follicles (Fig. 2a and Supplementary Fig. 4). The levels of H3K4me1 and H3K9me2 showed no obvious alterations in *Aof1*^{lox/lox} oocytes (Supplementary Fig. 4). These results indicate that KDM1B demethylates mainly H3K4me2 in oocytes. Oogenesis seemed to proceed normally in the absence of KDM1B, despite the increase in H3K4me2.

Heterozygous *Aof1*^{lox/+} mice were normal and fertile. Intercrosses of *Aof1*^{lox/+} mice produced homozygous *Aof1*^{lox/lox} offspring at the Mendelian ratio, indicating that zygotic *Aof1* is not essential for mouse development. *Aof1*^{lox/lox} mice of both sexes were grossly normal and male mice were fertile. However, *Aof1*^{lox/lox} females showed a maternal-effect lethal phenotype; heterozygous progeny of *Aof1*^{lox/lox} mothers (we refer to such embryos as *Aof1*^{mat-/+}) showed severe placental defects and various embryonic abnormalities, including growth impairment, neural tube defects and pericardial oedema, and could not survive beyond 10.5 d.p.c. (Fig. 2b).

The phenotype was reminiscent of an imprinting defect, as observed in mice deficient for *Dnmt3a* or *Dnmt3l* (refs 3–5). We therefore analysed the DNA methylation status of the differentially methylated regions (DMRs) of imprinted genes in *Aof1*^{mat-/+} embryos. Heterozygous embryos that inherited the *Aof1* null allele from *Aof1*^{lox/lox} fathers (*Aof1*^{pat-/+}) were used as controls. Among the imprinted genes analysed, two (*Rasgrf1* and *H19*) are paternally methylated and seven (*Igf2r*, *Mest* (also known as *Peg1*), *Grb10* (also known as *Meg1*), *Snrpn*, *Zac1* (also known as *Plagl1*), *Lit1* (also known as *Kcnq1ot1*) and *Impact*) are maternally methylated. Bisulphite sequencing revealed that all DMRs analysed showed methylation in ~50% of the alleles in *Aof1*^{pat-/+} embryos, indicating normal allele-specific methylation. In contrast, four maternally methylated DMRs (*Mest*, *Grb10*, *Zac1* and *Impact*) were unmethylated in both alleles in *Aof1*^{mat-/+} embryos, whereas the two paternally methylated DMRs maintained normal allele-specific methylation (Fig. 3a). Similar results were obtained when placental DNA was analysed (data not shown). Southern blot analysis of embryonic DNA digested with methylation-sensitive restriction endonucleases confirmed the bisulphite sequencing results (Supplementary Fig. 5). All other sequences analysed, including repetitive sequences (the major satellite repeats and the intracisternal A-particle (IAP) retroviral elements) and a non-imprinted gene (β-globin), showed normal DNA methylation in *Aof1*^{mat-/+} embryos (Supplementary Fig. 5).

The methylation imprints inherited from the parental germline are maintained throughout development, and the maintenance DNA methyltransferase DNMT1 and the maternal factors PGC7 (also known as STELLA or DPPA3) and ZFP57 are required^{10–14}. To determine whether the absence of DNA methylation at the affected DMRs in *Aof1*^{mat-/+} embryos resulted from a failure in acquiring the methylation marks in *Aof1*^{lox/lox} oocytes or in maintaining the methylation marks during embryogenesis, we analysed the methylation status of the *Mest*, *Grb10*, *Zac1* and *Snrpn* DMRs in metaphase II oocytes. As shown in Fig. 3b, the *Mest*, *Grb10* and *Zac1* DMRs were fully methylated in wild-type oocytes, but unmethylated in *Aof1*^{lox/lox} oocytes, whereas the *Snrpn* DMR was fully methylated in both wild-type and *Aof1*^{lox/lox} oocytes. These results indicate that KDM1B is required for *de novo* DNA methylation of a subset of imprinted genes during oogenesis. The imprinting defect in *Aof1*^{lox/lox} oocytes did not seem to reflect a global DNA methylation defect during oogenesis, as methylation of repetitive sequences (IAP, Line1, and major and minor satellites), which accounts for the large majority of methylation in the genome, showed no obvious alterations (Supplementary Fig. 6). KDM1B deficiency also had no effect

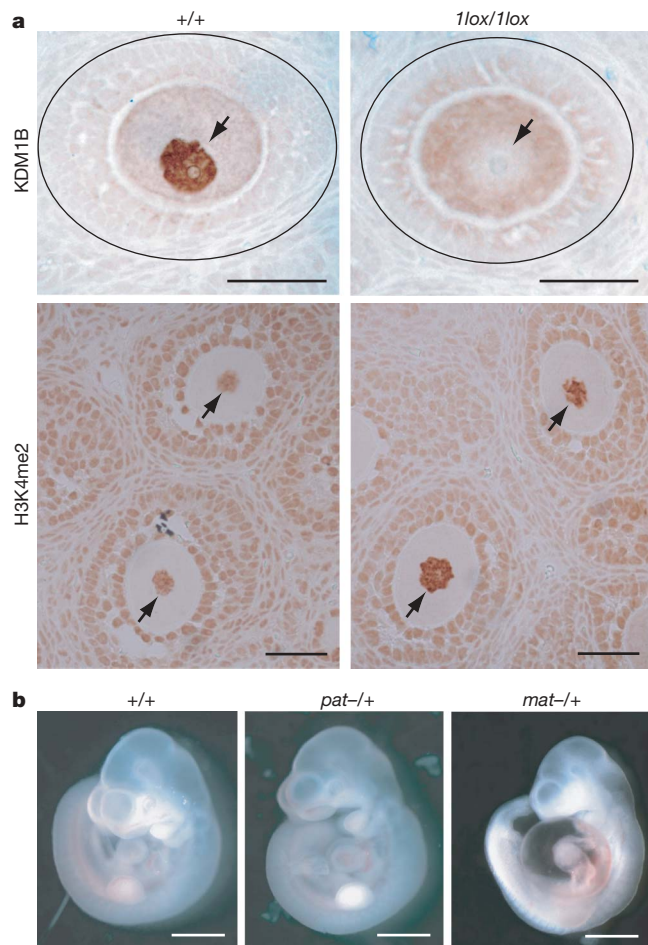


Figure 2 | KDM1B deficiency results in H3K4me2 elevation in oocytes and maternal-effect embryonic lethality. a, Immunohistochemistry analyses of KDM1B and H3K4me2 in developing oocytes in wild-type (+/+) and *Aof1*^{lox/lox} mice. Secondary follicles are shown (top: the follicle boundaries are defined by the ellipses). The nuclei of oocytes are indicated by arrows. Scale bars, 50 μm. **b**, Representative images of 10.5 d.p.c. wild-type (+/+) embryos and heterozygous embryos that inherited the *Aof1* null allele paternally (*Aof1*^{pat-/+}) or maternally (*Aof1*^{mat-/+}). Note the growth defects and pericardial oedema shown by the *Aof1*^{mat-/+} embryo. Scale bars, 1 mm.

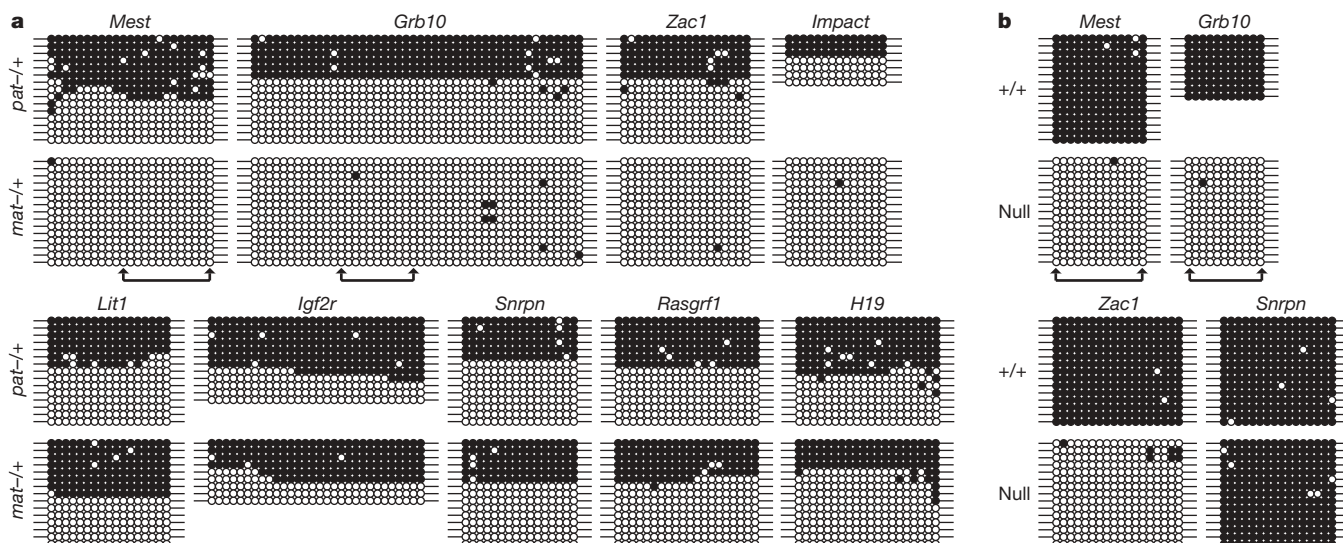


Figure 3 | KDM1B-deficient oocytes fail to establish DNA methylation imprints at multiple loci. **a, b,** Bisulphite sequencing analysis of DNA methylation at the DMRs of maternally and paternally imprinted genes in 9.5 d.p.c. *Aofl*^{pat-/-} and *Aofl*^{mat-/-} embryos (**a**) and in wild-type (+/+) and *Aofl*^{1lox/1lox} (null) oocytes (**b**). Open circles and filled circles represent

unmethylated and methylated CpG sites, respectively. Each oocyte DNA sample was from 80–100 metaphase II oocytes from 10 superovulated female mice of the same genotype. Smaller fragments of the *Mest* and *Grb10* DMRs (indicated by arrows in **a**) were amplified using oocyte DNA, because the limited amounts of DNA made PCR inefficient.

on the levels and localization of DNMT3A and DNMT3L in growing oocytes (Supplementary Fig. 7).

Disruption of imprinting in oocytes has been shown to cause biallelic expression of some imprinted genes (usually paternally expressed genes such as *Mest*, *Peg3* and *Snrpn*) and biallelic silencing of others (usually maternally expressed genes such as *Igf2r* and *p57^{kip2}* (also known as *Cdkn1c*))^{3–5}. To determine whether monoallelic expression of imprinted genes is affected in *Aofl*^{mat-/-} embryos, we analysed embryos derived from crosses between *Aofl*^{1lox/1lox} *Mus musculus* females and wild-type *Mus musculus castaneus* (CAST) males. Subspecies-specific polymorphisms allow discrimination of the parental origin of transcripts. As shown in Fig. 4, the paternally expressed genes *Mest*, *Zac1* and *Impact* were transcribed from both alleles, *Snrpn* was transcribed normally from the paternal allele only, and the maternally expressed gene *Grb10* was not transcribed from either allele in *Aofl*^{mat-/-} hybrid embryos, whereas these genes maintained monoallelic expression in the control embryos (derived from wild-type *M. musculus* × CAST crosses). Quantitative PCR with reverse transcription (RT-PCR) confirmed increased expression of *Mest* (~2.1-fold) and *Impact* (~2.6-fold) and no expression of *Grb10* in *Aofl*^{mat-/-} embryos (Supplementary Fig. 8). Thus, failure to establish germline imprinting in the

absence of KDM1B leads to loss of monoallelic expression of the affected genes in the offspring.

Histone methylation and DNA methylation are functionally linked in several systems^{15–19}. A role for histone modifications in regulating germline imprinting has long been suspected. We now provide genetic evidence for the involvement of an H3K4 demethylase in regulating the establishment of maternal genomic imprints at several loci. Our results indicate a protective function for H3K4 methylation against *de novo* DNA methylation at these loci during oogenesis. A recent study showed that DNMT3L interacts with histone H3 and that this interaction is strongly inhibited by methylation at H3K4 (ref. 20). Thus, the simplest explanation is that demethylation of H3K4 makes imprinted loci more accessible to the *de novo* DNA methylation machinery. Given the dramatic changes in bulk H3K4me2 observed in KDM1B-expressing NIH 3T3 cells and in KDM1B-deficient oocytes, KDM1B apparently acts on a large proportion of chromatin. Yet, KDM1B regulates DNA methylation at DMRs of imprinted loci, but not global DNA methylation, during oogenesis. Therefore, the specificity is probably conferred primarily by the *de novo* DNA methylation machinery. Structural studies suggest that the DNMT3A–DNMT3L complex methylates DNA sequences with a CpG spacing of 8–10 base pairs, which characterize maternally imprinted DMRs²¹. Why KDM1B deficiency affects some, but not all, maternally imprinted genes remains to be determined. On the basis of the timing of KDM1B expression, one possibility is that KDM1B only controls the genes that acquire the DNA methylation marks relatively late during oocyte growth. Indeed, KDM1B deficiency affects methylation at the *Mest* and *Impact* DMRs, which normally occurs at the secondary and antral follicle stages, respectively²², but does not affect methylation at the *Snrpn* and *Igf2r* DMRs, which normally occurs earlier²². It would be interesting to determine whether demethylation of H3K4 is required for *de novo* methylation of all imprinted loci and whether other histone demethylases or methyltransferases are involved.

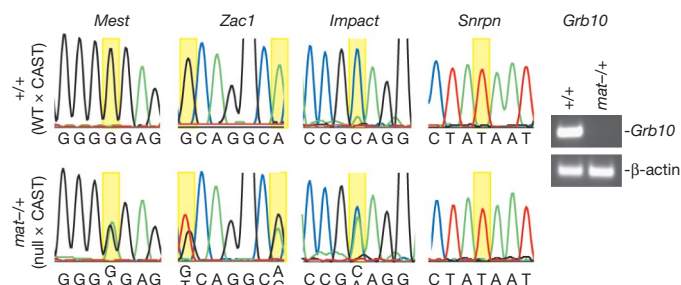


Figure 4 | *Aofl*^{mat-/-} embryos show loss of monoallelic expression of the affected imprinted genes. RNA was isolated from embryos derived from crosses between wild-type (WT) or *Aofl*^{1lox/1lox} (null) *M. musculus* females and CAST males. Regions containing polymorphisms (highlighted) were recovered by RT-PCR, and the products were analysed by direct sequencing or agarose gel electrophoresis.

METHODS SUMMARY

The demethylase activity of KDM1B was determined by *in vitro* biochemical assays⁶, using purified recombinant KDM1B proteins, and by indirect immunofluorescence microscopy, using NIH 3T3 cells with ectopic expression of KDM1B. *Aofl*-mutant mice were generated by gene targeting. *Aofl* expression was determined by whole-mount X-gal staining of *Aofl*^{3lox/+} embryos and adult tissues, using standard procedures. KDM1B and histone modifications in

oocytes were analysed by immunohistochemistry, using the VECTASTAIN ABC system (Vector Laboratories). DNA methylation was analysed by bisulphite sequencing and Southern hybridization²³. Parental allele-specific transcription of imprinted genes was determined by analysing hybrid embryos derived from *M. musculus* × CAST crosses, taking advantage of subspecies-specific polymorphisms. The relative levels of imprinted gene transcripts in embryos were determined by quantitative RT-PCR using TaqMan Gene Expression Assays (Applied Biosystems). All oligonucleotide primers and antibodies used in this study are listed in Supplementary Tables 1 and 2, respectively.

Full Methods and any associated references are available in the online version of the paper at www.nature.com/nature.

Received 9 April; accepted 23 July 2009.

Published online 2 September 2009.

- Reik, W. & Walter, J. Genomic imprinting: parental influence on the genome. *Nature Rev. Genet.* **2**, 21–32 (2001).
- Edwards, C. A. & Ferguson-Smith, A. C. Mechanisms regulating imprinted genes in clusters. *Curr. Opin. Cell Biol.* **19**, 281–289 (2007).
- Kaneda, M. *et al.* Essential role for *de novo* DNA methyltransferases Dnmt3a in paternal and maternal imprinting. *Nature* **429**, 900–903 (2004).
- Bourc'his, D., Xu, G. L., Lin, C. S., Bollman, B. & Bestor, T. H. Dnmt3L and the establishment of maternal genomic imprints. *Science* **294**, 2536–2539 (2001).
- Hata, K., Okano, M., Lei, H. & Li, E. Dnmt3L cooperates with the Dnmt3 family of *de novo* DNA methyltransferases to establish maternal imprints in mice. *Development* **129**, 1983–1993 (2002).
- Shi, Y. *et al.* Histone demethylation mediated by the nuclear amine oxidase homolog LSD1. *Cell* **119**, 941–953 (2004).
- Allis, C. D. *et al.* New nomenclature for chromatin-modifying enzymes. *Cell* **131**, 633–636 (2007).
- Stavropoulos, P., Blobel, G. & Hoelz, A. Crystal structure and mechanism of human lysine-specific demethylase-1. *Nature Struct. Mol. Biol.* **13**, 626–632 (2006).
- Chen, Y. *et al.* Crystal structure of human histone lysine-specific demethylase 1 (LSD1). *Proc. Natl Acad. Sci. USA* **103**, 13956–13961 (2006).
- Li, E., Beard, C. & Jaenisch, R. Role for DNA methylation in genomic imprinting. *Nature* **366**, 362–365 (1993).
- Howell, C. Y. *et al.* Genomic imprinting disrupted by a maternal effect mutation in the *Dnmt1* gene. *Cell* **104**, 829–838 (2001).
- Nakamura, T. *et al.* PGC7/Stella protects against DNA demethylation in early embryogenesis. *Nature Cell Biol.* **9**, 64–71 (2007).
- Hirasawa, R. *et al.* Maternal and zygotic Dnmt1 are necessary and sufficient for the maintenance of DNA methylation imprints during preimplantation development. *Genes Dev.* **22**, 1607–1616 (2008).
- Li, X. *et al.* A maternal-zygotic effect gene, *Zfp57*, maintains both maternal and paternal imprints. *Dev. Cell* **15**, 547–557 (2008).
- Tamaru, H. & Selker, E. U. A histone H3 methyltransferase controls DNA methylation in *Neurospora crassa*. *Nature* **414**, 277–283 (2001).
- Jackson, J. P., Lindroth, A. M., Cao, X. & Jacobsen, S. E. Control of CpNpG DNA methylation by the KRYPTONITE histone H3 methyltransferase. *Nature* **416**, 556–560 (2002).
- Lehnertz, B. *et al.* *Suv39h*-mediated histone H3 lysine 9 methylation directs DNA methylation to major satellite repeats at pericentric heterochromatin. *Curr. Biol.* **13**, 1192–1200 (2003).
- Vire, E. *et al.* The Polycomb group protein EZH2 directly controls DNA methylation. *Nature* **439**, 871–874 (2006).
- Wang, J. *et al.* The lysine demethylase LSD1 (KDM1) is required for maintenance of global DNA methylation. *Nature Genet.* **41**, 125–129 (2009).
- Ooi, S. K. *et al.* DNMT3L connects unmethylated lysine 4 of histone H3 to *de novo* methylation of DNA. *Nature* **448**, 714–717 (2007).
- Jia, D., Jurkowska, R. Z., Zhang, X., Jeltsch, A. & Cheng, X. Structure of Dnmt3a bound to Dnmt3L suggests a model for *de novo* DNA methylation. *Nature* **449**, 248–251 (2007).
- Obata, Y. & Kono, T. Maternal primary imprinting is established at a specific time for each gene throughout oocyte growth. *J. Biol. Chem.* **277**, 5285–5289 (2002).
- Chen, T., Ueda, Y., Dodge, J. E., Wang, Z. & Li, E. Establishment and maintenance of genomic methylation patterns in mouse embryonic stem cells by Dnmt3a and Dnmt3b. *Mol. Cell. Biol.* **23**, 5594–5605 (2003).

Supplementary Information is linked to the online version of the paper at www.nature.com/nature.

Acknowledgements We thank Y. Shi, J. Wang, G. A. Baltus, T. B. Nicholson, S. Kadam and H. M. Chan for discussions, and J. Wang, J. Kurash and G. A. Baltus for technical assistance.

Author Contributions T.C. planned and supervised the project. D.N.C. and T.C. designed the experiments and wrote the manuscript. D.N.C., E.L. and T.C. analysed the data. D.N.C., H.S., S.H., F.G., H.L., J.B. and T.C. carried out the experiments. G.X. generated the DNMT3A and DNMT3L antibodies.

Author Information Reprints and permissions information is available at www.nature.com/reprints. The authors declare competing financial interests: details accompany the full-text HTML version of the paper at www.nature.com/nature. Correspondence and requests for materials should be addressed to T.C. (taiping.chen@novartis.com).

METHODS

Vectors. The Flag–KDM1B expression plasmid was generated by subcloning the mouse *Kdm1b* cDNA into p3XFLAG-myc-CMV-26 vector (Sigma-Aldrich). Flag–KDM1B(K667A) was generated by site-directed mutagenesis. The *Aof1* gene-targeting vector, in which a 3.3-kb genomic region containing exons 14–16 is flanked by *loxP* sites, was generated by sequentially subcloning *Aof1* genomic fragments (the 5' arm, the 3' arm and the floxed region) and a floxed β -geo cassette into pBluescript II SK (Stratagene). The *Aof1* genomic fragments were generated by PCR (the primers are listed in Supplementary Table 1). All vectors were verified by DNA sequencing.

In vitro demethylase assay. The activity and specificity of KDM1B were tested using a biochemical assay⁶. Flag-tagged KDM1B and KDM1B(K667A) were expressed in HEK 293T cells and purified using anti-Flag M2 affinity gel (Sigma-Aldrich). Bulk histones purified from calf thymus (Sigma-Aldrich) were used as substrates. The reaction buffer contains 50 mM Tris, pH 8.5, 50 mM KCl, 5 mM MgCl, 0.5% BSA and 5% glycerol. For a typical reaction the volume is 50 μ l, which contains 5 μ g histones and 1–5 μ g Flag–KDM1B. The reaction

mixture was incubated for 1 h at 37 °C and then analysed by western blotting using methyl-specific antibodies (listed in Supplementary Table 2).

Indirect immunofluorescence analysis. NIH 3T3 cells cultured on coverslips were transfected with Flag-tagged KDM1B or KDM1B(K667A) using Lipofectamine 2000 (Invitrogen). Twenty hours after transfection, cells were fixed and co-stained with mouse monoclonal anti-Flag M2 antibodies (Sigma-Aldrich) and rabbit polyclonal antibodies recognizing specific histone modifications (listed in Supplementary Table 2).

Targeted disruption of *Aof1* in mice. Mouse embryonic stem (ES) cells were transfected with the *Aof1*-targeting vector and selected with G418. Correctly targeted ES clones (*Aof1*^{3lox/+}) were used to derive chimaeric mice and F₁ *Aof1*^{3lox/+} heterozygous mice. Deletion of the floxed exons and β -geo cassette, thereby generating the *Aof1*^{1lox} allele, was achieved by crossing *Aof1*^{3lox/+} mice with *Zp3*–Cre transgenic mice that express the Cre recombinase in the germ line. The mice were maintained on a C57BL/6 background. Genotypes were determined by PCR (the primers are listed in Supplementary Table 1).

Histone H2A.Z cooperates with RNAi and heterochromatin factors to suppress antisense RNAs

Martin Zofall^{1*}, Tamás Fischer^{1*}, Ke Zhang¹, Ming Zhou², Bowen Cui¹, Timothy D. Veenstra² & Shiv I. S. Grewal¹

Eukaryotic transcriptomes are characterized by widespread transcription of noncoding and antisense RNAs^{1–3}, which is linked to key chromosomal processes, such as chromatin remodelling, gene regulation and heterochromatin assembly^{4–7}. However, these transcripts can be deleterious, and their accumulation is suppressed by several mechanisms including degradation by the nuclear exosome^{8,9}. The mechanisms by which cells differentiate coding RNAs from transcripts targeted for degradation are not clear. Here we show that the variant histone H2A.Z, which is loaded preferentially at the 5' ends of genes by the Swr1 complex containing a JmjC domain protein, mediates suppression of antisense transcripts in the fission yeast *Schizosaccharomyces pombe* genome. H2A.Z is partially redundant in this regard with the Clr4 (known as SUV39H in mammals)-containing heterochromatin silencing complex that is also distributed at euchromatic loci, and with RNA interference component Argonaute (Ago1). Loss of Clr4 or Ago1 alone has little effect on antisense transcript levels, but cells lacking either of these factors and H2A.Z show markedly increased levels of antisense RNAs that are normally degraded by the exosome. These analyses suggest that as well as performing other functions, H2A.Z is a component of a genome indexing mechanism that cooperates with heterochromatin and RNAi factors to suppress read-through antisense transcripts.

Histones are a major structural component of chromatin, critical for packaging and regulation of eukaryotic genomes. Specialized chromatin can be differentiated by local incorporation of variant histones into a subset of nucleosomes¹⁰. A conserved variant histone, H2A.Z, has been linked to diverse chromosomal processes¹⁰, but its specific regulatory function(s) are unclear. Although H2A.Z is dispensable for viability in *Saccharomyces cerevisiae*, it is essential in *Drosophila* and mice, where it is linked to both transcriptional activation and repression^{10,11}. Evidence suggests that metazoan H2A.Z localizes to heterochromatic loci and its depletion causes defective chromosome segregation¹².

Here we used *S. pombe* to explore H2A.Z functions. The *S. pombe* genome contains large blocks of heterochromatin, the assembly of which requires histone H3 lysine 9 (H3K9)-specific methyltransferase Clr4, Swi6 (known as HP1 (also CBX5) in mammals) family proteins, and the RNAi machinery⁷. Deletion of *pht1*, the gene encoding H2A.Z, causes segregation defects¹³. However, it is not known whether this phenotype is linked to defective heterochromatin.

H2A.Z deposition is catalysed by the Swr1 complex in *S. cerevisiae*¹⁰. To establish whether a similar complex deposits H2A.Z in *S. pombe*, we purified factors associated with H2A.Z and Swr1 homologues. These analyses identified an analogous complex in *S. pombe*, which also contained a JmjC domain protein, Msc1 (Supplementary Fig. 1)¹⁴. Msc1, although dispensable for complex assembly (Supplementary Fig. 1), affected chromatin association of Swr1

(Fig. 1a). Both Swr1 and Msc1 were required for H2A.Z deposition at various sites, although $\Delta swr1$ was more defective (Fig. 1b and Supplementary Fig. 2a–d).

Chromatin-immunoprecipitation (ChIP) assay combined with microarray analysis (termed ChIP-chip) showed a non-random

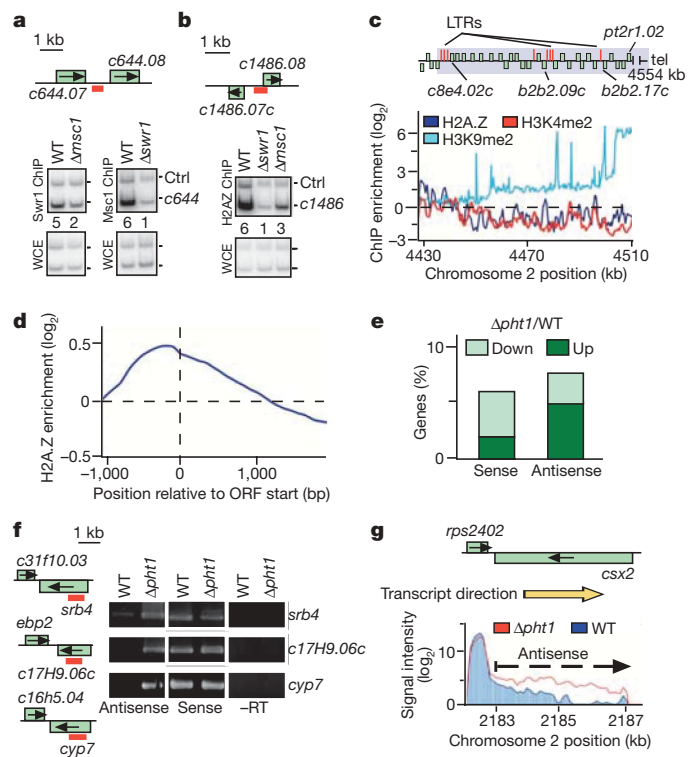


Figure 1 | *pht1* causes upregulated antisense transcripts. **a–d**, H2A.Z is targeted preferentially to the 5' ends of genes. **a**, ChIP analysis of Swr1 and Msc1. DNA isolated from ChIP and whole cell extract (WCE) was analysed by multiplex PCR. Control (ctrl) corresponds to gene-free region adjacent to SPAC5H10.03. Relative enrichment values are shown. WT, wild type. **b**, H2A.Z deposition requires Swr1 and Msc1. **c**, H2A.Z is slightly enriched at heterochromatin domains. H3K4me2 (ref. 15), H3K9me2 and H2A.Z distributions at a subtelomeric region. Note the long terminal repeat (LTR) cluster demarcating the border of the H2A.Z-depleted region. **d**, H2A.Z is enriched at 5' ends of genes. **e–g**, Upregulation of antisense transcripts at convergent genes in $\Delta pht1$ cells. **e**, The percentage of genes with >2-fold altered median transcript levels in $\Delta pht1$ cells. **f**, Strand-specific RT-PCR of RNAs isolated from wild-type and $\Delta pht1$ cells. **g**, Transcripts at the *rps2402* and *csx2* (also known as *cnt5*) locus were examined by expression analysis using tiling microarray.

¹Laboratory of Biochemistry and Molecular Biology, National Cancer Institute, National Institutes of Health Bethesda, Maryland 20892, USA. ²Laboratory of Proteomics and Analytical Technologies, Advanced Technology Program, SAIC-Frederick, Inc., NCI-Frederick, Frederick, Maryland 21702, USA.

*These authors contributed equally to this work.

distribution of H2A.Z across the genome (Supplementary Fig. 2c). H2A.Z is relatively depleted throughout heterochromatic domains enriched for methylated H3K9 (H3K9me) and lacking H3K4me (ref. 15; Supplementary Fig. 3a). At telomeres, H3K9me is distributed across a ~100 kilobase (kb) domain (Fig. 1c), beyond the heterochromatin domain previously defined using a less sensitive method¹⁵. H2A.Z is depleted in this entire H3K9me-coated domain (Fig. 1c). *Δpht1* causes a slight increase in silencing at the pericentromeric region, but H3K9me distribution at heterochromatic loci is not severely altered (Supplementary Fig. 4a). At euchromatic loci, H2A.Z localizes preferentially in intergenic regions (Supplementary Fig. 3b) with maximum enrichment occurring ~200 base pairs (bp) upstream of translation start sites (Fig. 1d). This pattern is similar in other organisms^{16–21}, suggesting that this is a general feature of H2A.Z deposition. Comparison of H2A.Z and RNA polymerase II (Pol II) distributions showed that *S. pombe* H2A.Z is preferentially enriched at repressed or weakly expressed genes (Supplementary Fig. 3c), as in *S. cerevisiae*^{16–18}.

To determine whether H2A.Z affects transcription, we monitored transcript levels from both strands using tiling arrays. Consistent with reports that most of the *S. pombe* euchromatin is transcribed^{1,2}, we detected widespread sense and antisense transcripts in wild-type cells. *Δpht1* caused only modest changes in sense transcription. The affected loci included subtelomeric genes, such as *tlh2* sharing homology to centromeric repeats (Supplementary Fig. 4b). Silencing of *tlh2*

and its paralogues requires heterochromatin machinery⁷ (Supplementary Fig. 4b), but H2A.Z, undetected in our assays, may also contribute to *tlh2* repression.

Δpht1 caused a disproportionate increase in antisense transcripts at many (~5–8%) euchromatic loci (Fig. 1e–g and Supplementary Fig. 5), as confirmed by PCR with strand-specific reverse transcription (RT-PCR; Fig. 1f). More than 90% of antisense RNAs mapped to convergent genes transcribed from opposite DNA strands. These antisense RNAs seem to result from read-through transcription (Fig. 1g and Supplementary Fig. 6; see later). Because heterochromatin factors have been implicated in the control of antisense transcripts²², including read-through transcripts at three convergent loci²³, we asked whether H2A.Z interacts genetically with heterochromatin machinery. When *Δpht1* was combined with mutant alleles of *clr4* or *rik1*—components of the ClrC-containing methyltransferase complex (ClrC)⁷—the resultant double mutants showed severe growth defects and a large, synergistic increase in antisense RNAs at >20% of genes (Fig. 2a and Supplementary Figs 5 and 7a, b). Consistent with ClrC directly participating in antisense suppression, Rik1 was found at the convergent loci (Supplementary Fig. 7c).

ClrC collaborates with RNAi factors including an Argonaute (Ago1)-containing RNA-induced initiation of transcriptional gene silencing (RITS) complex²⁴, to silence heterochromatic repeats⁷. We determined whether Ago1 contributes to antisense suppression. Combining *Δago1* with *Δpht1* resulted in synergistic upregulation of antisense transcripts, as in *Δclr4 Δpht1* (Fig. 2a). These data are consistent with RNAi-dependent heterochromatin assembly, especially Swi6 bound to H3K9me, recruiting cohesin to mediate transcription termination²³. However, antisense RNAs did not accumulate extensively in *Δswi6* cells and the synergistic increase in antisense RNAs observed in the *Δclr4 Δpht1* mutant was not observed in the *Δswi6 Δpht1* mutant (Fig. 2a). Thus, ClrC and Ago1 contribute to antisense suppression by a new mechanism(s).

To gain insight into the roles of H2A.Z and heterochromatin/RNAi in antisense suppression, we examined common features of antisense RNAs in different mutants. Similar to *Δpht1*, most loci affected in the *Δclr4 Δpht1* and *Δago1 Δpht1* double mutants were convergent genes, including loci affected in the single mutants. The average profile of relative changes between mutant and wild-type clearly demonstrates synergistic interactions of H2A.Z with Clr4 and Ago1 in suppressing antisense transcripts (Fig. 2c). The increase in antisense transcripts was not restricted to a specific region, but occurred uniformly throughout the gene body (Fig. 2c), consistent with read-through transcripts traversing adjacent loci (Supplementary Fig. 6). This is also illustrated in the average profile of antisense signal intensities (Fig. 2d). Examination of individual loci recapitulated the accumulation of open reading frame (ORF)-spanning read-through antisense transcripts in double mutants (Fig. 2b).

Northern analyses confirmed that antisense RNAs observed in *Δpht1*, *Δclr4* and *Δclr4 Δpht1* mutants correspond to read-through transcripts rather than new initiation events. Strand-specific probes for antisense transcripts at *cyp7* or *srb4* hybridized to long RNAs that accumulated in mutant backgrounds (Fig. 3a and Supplementary Fig. 8). The length and direction of antisense RNA, as determined by oligonucleotide-targeted RNase H cleavage, was consistent with read-through transcripts originating at the promoter of the adjacent convergent gene. Long read-through transcripts were also detected with probes used to detect sense transcripts at the *c16H5.04-cyp7* and *c29A3.19-c18e5.02c* gene pairs (Fig. 3a and Supplementary Fig. 9a). Notably, *Δpht1* and *Δpht1 Δclr4* mutants showed increased levels of antisense transcripts, but sense transcripts were not upregulated (Fig. 3a). Thus, H2A.Z and ClrC seem to specifically suppress read-through antisense transcripts.

The accumulation of antisense RNAs could result from defects in transcriptional termination and/or processing. Although termination failure cannot be completely excluded, levels of nascent antisense transcripts, as determined by a transcription run-on assay, were not

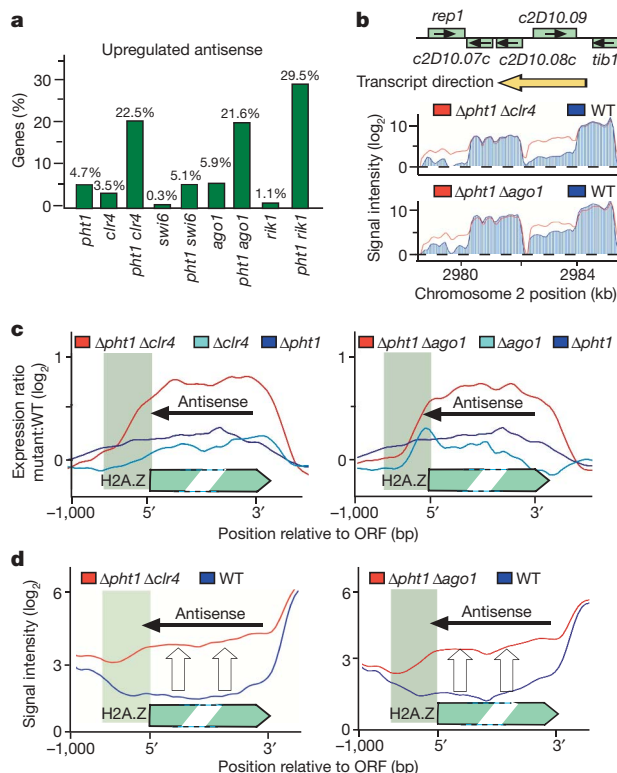


Figure 2 | H2A.Z acts in a synergistic manner with ClrC and Ago1 to suppress antisense transcripts. **a**, Cumulative derepression of antisense RNAs estimated as a percentage of genes with upregulated antisense. **b**, Representative examples with upregulated antisense in *Δpht1 Δclr4* and *Δpht1 Δago1* mutants. Signal intensity of transcripts from reverse/lower strand is plotted. **c**, Profile of average antisense signal ratios at convergent genes in single (*Δpht1*/WT, *Δago1*/WT and *Δclr4*/WT) and double mutants (*Δpht1 Δclr4*/WT and *Δpht1 Δago1*/WT). Double alignment at 5' and 3' ends of genes was applied and varied gene length compensated by compression of middle part of gene. H2A.Z localization is indicated in green. **d**, Cumulative profile of antisense transcripts in indicated strains. The average antisense signal profile was calculated for genes with increased levels of antisense in double mutants and compared with the profile in the wild type.

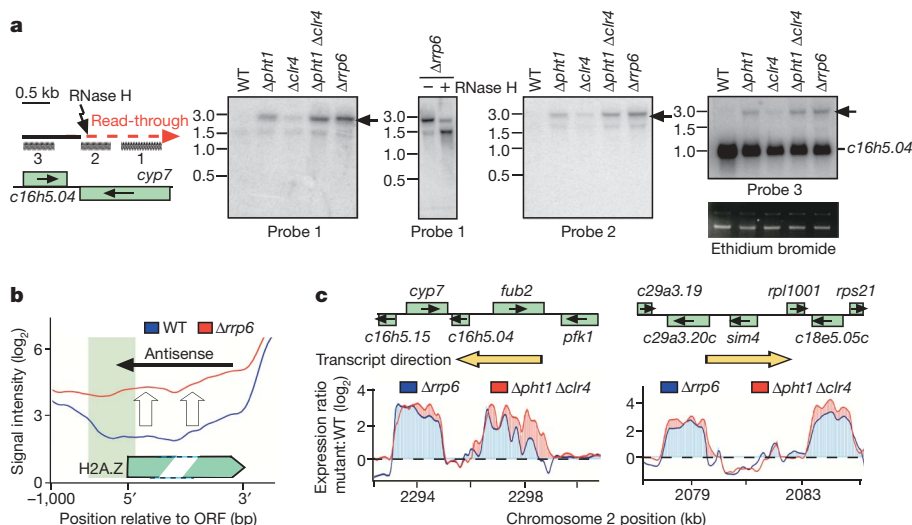


Figure 3 | Read-through antisense transcripts are suppressed by the exosome. **a**, Antisense transcripts upregulated in Δpht1 Δclr4 cells result from overlapping transcription at convergent genes. Northern analyses of RNAs at SPBC16h5.04-cyp7. Probes complementary to antisense (probes 1 and 2) and sense portion (probe 3) of SPBC16h5.04 transcript detected read-through RNAs. Oligonucleotide-targeted RNase H cleavage was used to determine the 3' end of transcripts. **b**, Cumulative profile of antisense transcripts in Δrrp6 and wild-type cells. The antisense profile was calculated for genes with upregulated antisense in Δrrp6 cells and compared with wild type. **c**, Expression profiling of antisense transcripts in Δpht1 Δclr4 and Δrrp6 cells.

considerably affected in the Δpht1 or Δpht1 Δclr4 mutants (Supplementary Fig. 9b). We proposed that H2A.Z and heterochromatin factors might selectively promote degradation of antisense RNAs. Indeed, aberrant transcripts including antisense RNAs are known to be degraded by the 3' to 5' exonuclease activity of nuclear exosome^{8,9,22}, which also processes heterochromatic repeat transcripts targeted by ClrC^{22,25}. Deletion of exosome subunit rrp6 led to an antisense profile closely resembling that of Δclr4 Δpht1, with read-through antisense RNA covering entire ORFs at convergent genes (Fig. 3b). Marked similarities in levels and patterns of antisense RNAs in Δclr4 Δpht1 and Δrrp6 mutants were observed at individual loci (Fig. 3c). Similar analyses revealed a notable correlation of antisense RNA upregulation between the rik1 pht1 or ago1 pht1 mutants and the rrp6 mutant (Fig. 4a). We conclude that read-through transcripts are produced in wild-type cells, but are processed by the exosome in a manner dependent on H2A.Z, ClrC and Ago1.

The histone deacetylase Clr6 complex suppresses antisense transcripts initiating from cryptic promoters by a mechanism involving the H3K36 methyltransferase Set2 (refs 22, 26). To compare distributions of antisense transcripts, we comprehensively profiled and correlated distributions of antisense RNAs in different mutants (Fig. 4b). The Δset1 Δpht1 mutant shows severe synthetic growth defects similar to the Δclr4 Δpht1 mutant²⁷, but did not exhibit cumulative upregulation of antisense RNAs. Correlation coefficients from pairwise comparisons of antisense profiles were used to perform hierarchical clustering (Fig. 4b), in which mutants were sorted according to similarities in their antisense profiles. Double mutants lacking Pht1 and Ago1 or ClrC subunits clearly belong to a distinct cluster that associated closely with Δrrp6. This cluster was separated from a second cluster that included the Δset2 and Clr6 complex mutants (Fig. 4b). Therefore, the effect of H2A.Z/ClrC on antisense RNAs is distinct from that of the histone deacetylase Clr6.

This study implicates H2A.Z and heterochromatin factors in the suppression of potentially deleterious antisense RNAs. H2A.Z nucleosomes might directly obstruct Pol II progression, or facilitate loading of factors involved in structural organization of chromosome, which in turn promotes RNA degradation by stalling Pol II. Alternatively, H2A.Z might signal to Pol-II-associated exosome²⁸ that transcription has escaped its natural termination and therefore produced an aberrant transcript (Fig. 4c). H2A.Z and ClrC (the Rik1 subunit of which resembles the cleavage and polyadenylation factor CPSF-A⁷) may be components of a RNA quality control mechanism, which stimulates exosome activity by exosome cofactors⁶. Indeed, the loss of the Cid14 subunit of TRAMP, implicated in exosome stimulation⁸, causes accumulation of antisense RNAs (Fig. 4b), and the *Drosophila* homologue of H2A.Z mediates targeting of messenger RNA processing factors²⁹. In addition to ClrC,

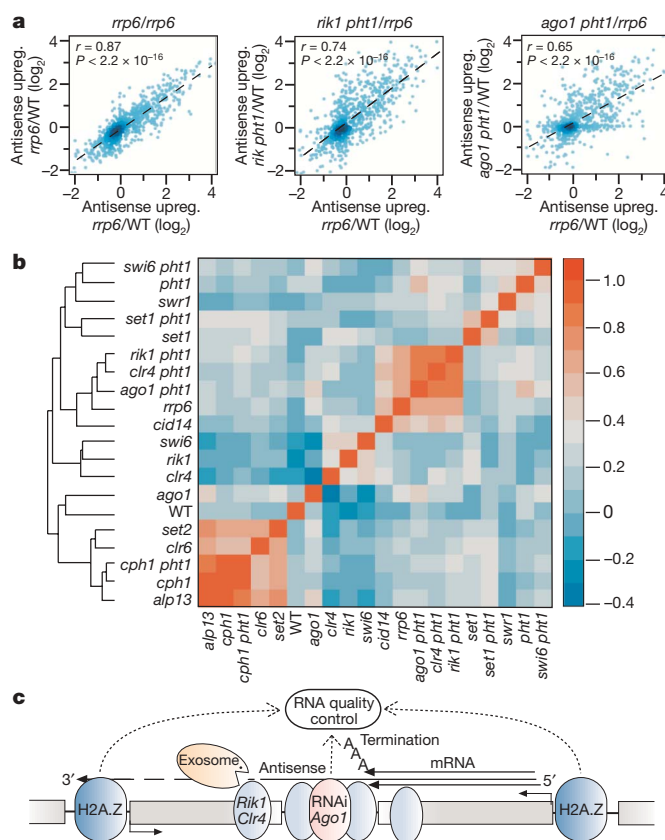


Figure 4 | H2A.Z and heterochromatin factors suppress antisense RNAs targeted by the exosome. **a**, Density plot comparing upregulation of antisense transcripts in indicated mutants. Median antisense upregulation (mutant/WT) was calculated for 842 genes. Pearson's correlation coefficient (*r*) and the *P* value of the linear regression are indicated. Panel comparing antisense profiles of two rrp6 mutants illustrates little variation between biological replicates. **b**, Hierarchical clustering of mutants on the basis of similarities of their antisense profiles. Pairwise comparisons of antisense profiles were performed as in **a**, and Pearson's correlation coefficients were converted into colour codes. **c**, Model for antisense suppression at convergent genes. H2A.Z at the 5' ends of genes contributes to suppression of read-through transcripts that are degraded by exosome. Antisense suppression also requires ClrC and Ago1, which along with H2A.Z may facilitate loading of other factors to block Pol II progression²³ and/or mediate the processing of RNAs by the exosome.

Ago1 also collaborates with H2A.Z to suppress antisense RNAs. Drawing from analyses at centromeric repeats⁷, Ago1 and ClrC might cooperate not only to process antisense RNAs but also to influence local chromatin to block antisense transcription²³. Exosome might contribute to the degradation of RNAs targeted by RNAi/ClrC in a manner similar to mRNAs targeted by RISC³⁰. Future studies will explore the interaction between chromatin and RNA processing factors in suppressing antisense RNAs.

Considering that H2A.Z localizes at the 5' end of genes in most eukaryotes^{16–21}, and that heterochromatin factors are found in euchromatic regions of different species⁷, the involvement of H2A.Z and heterochromatin machinery in antisense suppression might be conserved in other species. Defects in RNA processing could result in genome instability and might be partially responsible for chromosome segregation defects observed in H2A.Z and heterochromatin-defective mutants^{7,13}, similar to those seen in other mutants showing upregulation of antisense RNAs²².

METHODS SUMMARY

ChIP and ChIP-chip were performed as described previously¹⁵, except that hybridizations were performed as per manufacturer (Agilent) recommendation. Antibodies used were: Flag (M2; Sigma), H3K9me2 (Abcam), Pol II (8WG16; Covance) and Myc (Santa Cruz). For transcriptome analyses, total RNA was extracted with Master Pure Yeast RNA Purification kit (Epicentre) and 5 µg of RNA was reverse transcribed and labelled with Superscript Indirect cDNA labelling kit (Invitrogen). Data analysis was performed as described in the full Methods. Transcription run-on was performed as described previously²³. Standard methods were used to perform Northern analysis. RT-PCR experiments were performed with one-step RT-PCR kit (Qiagen).

Full Methods and any associated references are available in the online version of the paper at www.nature.com/nature.

Received 5 May; accepted 29 July 2009.

Published online 19 August 2009.

1. Wilhelm, B. T. *et al.* Dynamic repertoire of a eukaryotic transcriptome surveyed at single-nucleotide resolution. *Nature* **453**, 1239–1243 (2008).
2. Dutrow, N. *et al.* Dynamic transcriptome of *Schizosaccharomyces pombe* shown by RNA-DNA hybrid mapping. *Nature Genet.* **40**, 977–986 (2008).
3. Cawley, S. *et al.* Unbiased mapping of transcription factor binding sites along human chromosomes 21 and 22 points to widespread regulation of noncoding RNAs. *Cell* **116**, 499–509 (2004).
4. Martens, J. A., Laprade, L. & Winston, F. Intergenic transcription is required to repress the *Saccharomyces cerevisiae* *SER3* gene. *Nature* **429**, 571–574 (2004).
5. Hirota, K. *et al.* Stepwise chromatin remodelling by a cascade of transcription initiation of non-coding RNAs. *Nature* **456**, 130–134 (2008).
6. Camblong, J., Iglesias, N., Fickentscher, C., Dieppois, G. & Stutz, F. Antisense RNA stabilization induces transcriptional gene silencing via histone deacetylation in *S. cerevisiae*. *Cell* **131**, 706–717 (2007).
7. Grewal, S. I. & Jia, S. Heterochromatin revisited. *Nature Rev. Genet.* **8**, 35–46 (2007).
8. Houseley, J., LaCava, J. & Tollervey, D. RNA-quality control by the exosome. *Nature Rev. Mol. Cell Biol.* **7**, 529–539 (2006).
9. Wyers, F. *et al.* Cryptic pol II transcripts are degraded by a nuclear quality control pathway involving a new poly(A) polymerase. *Cell* **121**, 725–737 (2005).
10. Guillemette, B. & Gaudreau, L. Reuniting the contrasting functions of H2A.Z. *Biochem. Cell Biol.* **84**, 528–535 (2006).
11. Swaminathan, J., Baxter, E. M. & Corces, V. G. The role of histone H2Av variant replacement and histone H4 acetylation in the establishment of *Drosophila* heterochromatin. *Genes Dev.* **19**, 65–76 (2005).

12. Rangasamy, D., Greaves, I. & Tremethick, D. J. RNA interference demonstrates a novel role for H2A.Z in chromosome segregation. *Nature Struct. Mol. Biol.* **11**, 650–655 (2004).
13. Carr, A. M. *et al.* Analysis of a histone H2A variant from fission yeast: evidence for a role in chromosome stability. *Mol. Gen. Genet.* **245**, 628–635 (1994).
14. Shevchenko, A. *et al.* Chromatin Central: towards the comparative proteome by accurate mapping of the yeast proteomic environment. *Genome Biol.* **9**, R167 (2008).
15. Cam, H. P. *et al.* Comprehensive analysis of heterochromatin- and RNAi-mediated epigenetic control of the fission yeast genome. *Nature Genet.* **37**, 809–819 (2005).
16. Raisner, R. M. *et al.* Histone variant H2A.Z marks the 5' ends of both active and inactive genes in euchromatin. *Cell* **123**, 233–248 (2005).
17. Zhang, H., Roberts, D. N. & Cairns, B. R. Genome-wide dynamics of Htz1, a histone H2A variant that poises repressed/basal promoters for activation through histone loss. *Cell* **123**, 219–231 (2005).
18. Li, B. *et al.* Preferential occupancy of histone variant H2AZ at inactive promoters influences local histone modifications and chromatin remodeling. *Proc. Natl Acad. Sci. USA* **102**, 18385–18390 (2005).
19. Whittle, C. M. *et al.* The genomic distribution and function of histone variant HTZ-1 during *C. elegans* embryogenesis. *PLoS Genet.* **4**, e1000187 (2008).
20. Mavrich, T. N. *et al.* Nucleosome organization in the *Drosophila* genome. *Nature* **453**, 358–362 (2008).
21. Zilberman, D., Coleman-Derr, D., Ballinger, T. & Henikoff, S. Histone H2A.Z and DNA methylation are mutually antagonistic chromatin marks. *Nature* **456**, 125–129 (2008).
22. Nicolas, E. *et al.* Distinct roles of HDAC complexes in promoter silencing, antisense suppression and DNA damage protection. *Nature Struct. Mol. Biol.* **14**, 372–380 (2007).
23. Gullerova, M. & Proudfoot, N. J. Cohesin complex promotes transcriptional termination between convergent genes in *S. pombe*. *Cell* **132**, 983–995 (2008).
24. Zhang, K., Mosch, K., Fischle, W. & Grewal, S. I. Roles of the Clr4 methyltransferase complex in nucleation, spreading and maintenance of heterochromatin. *Nature Struct. Mol. Biol.* **15**, 381–388 (2008).
25. Murakami, H. *et al.* Ribonuclease activity of Dis3 is required for mitotic progression and provides a possible link between heterochromatin and kinetochore function. *PLoS One* **2**, e317 (2007).
26. Li, B., Carey, M. & Workman, J. L. The role of chromatin during transcription. *Cell* **128**, 707–719 (2007).
27. Roguev, A. *et al.* Conservation and rewiring of functional modules revealed by an epistasis map in fission yeast. *Science* **322**, 405–410 (2008).
28. Andrusis, E. D. *et al.* The RNA processing exosome is linked to elongating RNA polymerase II in *Drosophila*. *Nature* **420**, 837–841 (2002).
29. Wagner, E. J. *et al.* A genome-wide RNA interference screen reveals that variant histones are necessary for replication-dependent histone pre-mRNA processing. *Mol. Cell* **28**, 692–699 (2007).
30. Orban, T. I. & Izaurralde, E. Decay of mRNAs targeted by RISC requires XRN1, the Ski complex, and the exosome. *RNA* **11**, 459–469 (2005).

Supplementary Information is linked to the online version of the paper at www.nature.com/nature.

Acknowledgements We thank K. Noma for strain constructions, D. McPheeters for the run-on protocol, M. Lichten, F. Reyes-Turcu, E. Bartlett and H. Cam for comments on the manuscript, P. Fitzgerald for designing microarrays, and D. Venzon for advice with data analyses. This research was supported by the Intramural Research Program, and under Contract N01-CO-12400 of the National Institutes of Health, National Cancer Institute.

Author Contributions M.Zo., T.F. and S.I.S.G. designed research, M.Zo., T.F., K.Z. and M.Zh. performed experiments, B.C. contributed reagents, M.Zo., T.F., T.D.V. and S.I.S.G. analysed data, and S.I.S.G. wrote the paper.

Author Information Microarray data are available at the NCBI Gene Expression Omnibus (GEO) repository under the accession number GSE17271. Reprints and permissions information is available at www.nature.com/reprints. Correspondence and requests for materials should be addressed to S.I.S.G. (grewals@mail.nih.gov).

METHODS

Protein purification. Extracts were prepared from cells expressing H2A.Z–Flag, Swr1–3×Flag or Msc1–3×Flag. Specifically, exponentially growing cells were resuspended in 2× HC buffer (200 mM HEPES, pH 7.4, 250 mM KCl, 2 mM EDTA and 20% glycerol) supplemented with protease inhibitors, frozen and disrupted. Extracts were spun at 100,000g, pre-cleared with IgG and Flag-tagged proteins recovered by incubation with anti-Flag M2 slurry (Sigma) for 4 h, washed 12 times with 1× HC buffer, and eluted with Flag peptide.

Mass spectrometry. Purified proteins were separated by SDS–PAGE and stained using SimpleBlue (Invitrogen). Excised gel pieces were subjected to in-gel digestion using trypsin. Peptides extracted from the gel pieces were desalted using a C18 ZipTip (Millipore), lyophilized and resuspended in 16 µl of 0.1% trifluoroacetic acid (TFA) before analysis by microcapillary reversed-phase liquid chromatography–tandem mass spectrometry (LC–MS/MS). Each sample (6 µl) was loaded onto an Agilent 1100 nano-capillary HPLC system (Agilent Technologies) equipped with a 10-cm integrated nanoRPLC-electrospray ionization (ESI) emitter column (made in-house), coupled online with a linear ion-trap mass spectrometer (LTQ XP, ThermoElectron). After sample injection, a 20-min wash with 98% mobile phase A (0.1% formic acid) was applied, and peptides were eluted using a linear gradient of 2% mobile phase B (0.1% formic acid in acetonitrile) to 42% mobile phase B within 40 min at a constant flow rate of 200 µl min^{−1}. The seven most intense molecular ions in the MS scan were sequentially selected for collision-induced dissociation using normalized collision energy of 35%. The mass spectra were acquired over a mass-to-charge (*m/z*) range of 350–1,800. The ESI source capillary voltage and temperature were maintained at 1.5 kV and 200 °C, respectively. The MS data were searched against the UniProt *S. pombe* database downloaded from the European Bioinformatics Institute website (<http://www.ebi.ac.uk/integr8>) using SEQUEST (ThermoElectron) operating on a 10 node Beowulf parallel virtual machine computer cluster (Dell, Inc.). Up to two missed tryptic cleavage sites and oxidation of methionyl residues were allowed during the database search. Thresholds for legitimate peptide identifications were set as follows: minimum delta correlation (DC_n) ≥ 0.1 and charge state dependent cross correlation scores (X_{corr}) ≥ 2.0 for [M+H]¹⁺, ≥ 2.5 for [M+2H]²⁺, and ≥ 3.0 for [M+3H]³⁺.

Histone analysis. Cells expressing H2A.Z–Flag were resuspended in NIB buffer (0.25 M sucrose, 15 mM PIPES, pH 6.8, 60 mM KCl, 15 mM NaCl, 5 mM MgCl₂, 1 mM CaCl₂, 0.8% Triton X-100) supplemented with protease inhibitors, 2 mM ZnSO₄, 10 ng ml^{−1} trichostatin A, and homogenized with glass beads. Cell pellets were collected by centrifugation at 11,000g and histones were extracted with 0.4 M H₂SO₄ and precipitated with trichloroacetic acid. H2A.Z was detected by western analysis with Flag M2 antibody.

ChIP and ChIP-chip. ChIP was performed as described previously¹⁵. In brief, exponentially growing cells (5 × 10⁸) were fixed in 3% paraformaldehyde and chromatin was subsequently crosslinked by treatment of cells with 10 mM dimethyl adipimidate. Cells were washed with PBS, resuspended in lysis buffer (50 mM HEPES/KOH, pH 7.5, 140 mM NaCl, 1 mM EDTA, 1% Triton X-100, 0.1% DOC) and homogenized with glass beads. Chromatin was sheared by sonication to fragments of 500–1,000 bp, pre-cleared with protein A slurry and immunoprecipitated with 2–4 µg of antibody. Immunoprecipitated chromatin was recovered by incubation with protein A or protein G slurry, washed extensively and reverse crosslinked by incubation at 65 °C. Immunoprecipitated and DNA isolated from WCE were analysed by multiplex PCR or subjected to microarray-based ChIP-chip analysis.

For ChIP-chip, ChIP and WCE DNA samples were amplified using random-primed PCR and resulting samples were labelled with either Cy5 (ChIP) or Cy3 (WCE) dyes. Equal amounts of ChIP and WCE labelled DNA were hybridized to a custom Agilent 4×44K *S. pombe* oligonucleotide array containing 43,987 probes of 60-base oligonucleotides, which represent alternately the plus and minus strands, tiling a large part of chromosome II at 50-bp resolution. This array design also contains randomly spotted oligonucleotides that have no homology to the *S. pombe* genome but serve as controls for determining background signals. Hybridizations were performed according to Agilent recommended protocol. Microarrays were scanned using Agilent scanner (type-G2505B) with extended dynamic range, and data were extracted with Agilent feature extraction software (CHIP-v1_95_May07 protocol). Processed signals were normalized using combined rank consistency filtering with LOWES intensity normalization. PValueLogRatio that measures the significance of signal log ratio over systematic noise level of an individual spot were calculated by feature extraction program and were used for subsequent analysis. Enrichment values were calculated as a ratio of Cy5 processed signal/Cy3 processed signal. To

reduce random background noise inherent in microarray data, we subjected the data to a limited sliding-window average filter and smoothed the data with sliding weighted average of three neighbouring probes.

Expression profiling. Total RNA was isolated using Master Pure Yeast RNA purification kit (Epicentre). A RiboMinus Yeast kit (Invitrogen) was used to partly deplete ribosomal RNA from samples before the reverse transcription step. Reverse transcription was performed using random hexamer and anchored oligodT primer mix. Three micrograms of RNA was labelled with Superscript Indirect cDNA labelling kit (Invitrogen). Labelled complementary DNA samples from mutant (Cy5) and wild type (Cy3) were mixed and hybridized to a high-density microarray, as described above. Data were extracted with Agilent Feature Extraction Software (GE2-v5_95_Feb07 protocol) and processed using combined rank consistency filtering with LOWES intensity normalization. Expression ratios were calculated as Cy5 processed signal/Cy3 processed signal. Ratios with non-significant *P* values (PValueLogRatio ≥ 0.05) were set to 1. Background signal was estimated as a median processed signal of 152 oligonucleotides with no homology to *S. pombe* genome, randomly spotted on array. Owing to the column purification step in cDNA labelling method, very short transcripts (<100–150 nucleotides), such as those described around the promoter regions in the *rrp6* mutant strains in *S. cerevisiae* and other systems, might not be recovered. However, analysis of our data reveals a specific increase in short transcripts upstream of promoter regions in particular in *Δrrp6* cells, which is compatible with the recently reported results.

Average gene profiles. To calculate average gene profiles, 842 ORFs (region Chr2:1000000–Chr2:3049820) were aligned at the 5' end or double aligned at the 5' and 3' ends (see text). For double alignment, genes shorter than 1,650 bp were aligned without stretching. Genes longer than 1,650 bp were subjected to the following method: 14 probes from each end were included in data set without any change, whereas extra probes in the middle of gene body were linearly compressed into 5 points. Extremely short genes (<200 bp) were excluded from analysis. Intergenic regions upstream and downstream of ORFs were aligned according to translational start and stop sites, respectively. Probes represented in neighbour ORF were excluded. Intergenic probes within 1,000 bp region of both adjacent ORFs were included twice (once for each adjoined ORF), but weighted according to their distance from the ORFs. Repetitive probes (>80% homology with two or more chromosomal localization) were excluded from the averaging process. Expression profiles of genes (expression signal or expression ratio) were calculated similarly to the ChIP profiles with the exception that probes with multiple characteristics were weighted fully in the average.

Cross-correlation matrix and cluster analysis. Median antisense ratios (mutant/WT) for 842 genes (region Chr2:1000000–Chr2:3049820—excluded the heterochromatic regions and repetitive probes) were calculated for each expression data set. Linear regression analysis was carried out between data sets, and Pearson-correlation index was calculated. *r* values were converted into colour codes and plotted as a matrix. We repeated the analysis using the non-parametric Spearman's rank correlation coefficient, and observed very similar results (data not shown). Cluster analysis was carried out for Euclidean distance of the *r* values between mutant strains.

Transcriptional run-on assay. Transcriptional run-on was conducted essentially as described previously²³. Fifty millilitres of exponentially growing culture was cooled and collected at OD_{595nm} ~ 0.2, washed with ice-cold TMN buffer (10 mM Tris-HCl, pH 7.5, 5 mM MgCl₂, 100 mM NaCl), and resuspended in ice-cold water and supplemented with 10% *N*-lauryl sarcosine to a final concentration of 0.6%. Cells were incubated on ice for 25 min, pelleted and resuspended in 60 µl of 2.5× transcription buffer (50 mM Tris-HCl, pH 7.5, 80 mM MgCl₂, 500 mM KCl, 5 mM dithiothreitol (DTT)). Run was initiated by the addition of 0.5 mM rATP, rCTP, rGTP supplemented with 200 µCi of [α -³²P]UTP and incubated at 30 °C for 2 min. Reaction was stopped by addition of 1 ml of ice-cold TMN, and cells were pelleted. RNA was isolated as for northern blot analysis, precipitated and before hybridization treated with 0.15 M NaOH on ice for 5 min, neutralized, mixed with hybridization solution (10 mM Tris-HCl, pH 7.5, 82.5 µg ml^{−1} of yeast tRNA, 10× Denhardt's solution, 0.3 M NaCl, 10 mM EDTA, 1% SDS, 0.5% BSA), heat-denatured and hybridized to 10 µg of RNA probes slot-blotted to BrightStar-Plus membrane at 65 °C for 48 h. After hybridization, membranes were washed twice at 65 °C in 2× SSC supplemented with 1% SDS for 30 min.

Northern analysis. Total RNA was extracted from exponentially growing cells and northern blot analysis conducted using the NorthernMax kit (Ambion). Probes were synthesized by *in vitro* transcription with [α -³²P]UTP using the T7 MAXIscript kit (Ambion).

Bursts of retrotransposition reproduced in *Arabidopsis*

Sayuri Tsukahara^{1,2*}, Akie Kobayashi^{1*}, Akira Kawabe¹, Olivier Mathieu^{3,4}, Asuka Miura¹ & Tetsuji Kakutani^{1,2}

Retrotransposons, which proliferate by reverse transcription of RNA intermediates, comprise a major portion of plant genomes^{1,2}. Plants often change the genome size and organization during evolution by rapid proliferation and deletion of long terminal repeat (LTR) retrotransposons^{3,4}. Precise transposon sequences throughout the *Arabidopsis thaliana* genome and the *trans*-acting mutations affecting epigenetic states make it an ideal model organism with which to study transposon dynamics^{5–9}. Here we report the mobilization of various families of endogenous *A. thaliana* LTR retrotransposons identified through genetic and genomic approaches with high-resolution genomic tiling arrays and mutants in the chromatin-remodelling gene *DDM1* (*DECREASE IN DNA METHYLATION 1*)^{10,11}. Using multiple lines of self-pollinated *ddm1* mutant, we detected an increase in copy number, and verified this for various retrotransposons in a *gypsy* family (*ATGP3*) and *copia* families (*ATCOPIA13*, *ATCOPIA21*, *ATCOPIA93*), and also for a DNA transposon of a *Mutator* family, *VANDAL21*. A burst of retrotransposition occurred stochastically and independently for each element, suggesting an additional autocatalytic process. Furthermore, comparison of the identified LTR retrotransposons in related *Arabidopsis* species revealed that a lineage-specific burst of retrotransposition of these elements did indeed occur in natural *Arabidopsis* populations. The recent burst of retrotransposition in natural population is targeted to centromeric repeats, which is presumably less harmful than insertion into genes. The *ddm1*-induced retrotransposon proliferations and genome rearrangements mimic the transposon-mediated genome dynamics during evolution and provide experimental systems with which to investigate the controlling molecular factors directly.

In *A. thaliana*, precise sequence information is available for most heterochromatin regions, which are rich in repeats and transposons, making this organism an ideal material for the analysis of transposons at the genome sequence level^{5–7}. The most abundant families of transposons in the *A. thaliana* genome, and in plant genomes in general, are LTR-type retrotransposons^{3,7}. In *A. thaliana*, however, no transposition has been found for an endogenous LTR retrotransposon. Despite the significant impact of LTR retrotransposons on genome evolution, previous investigations of retrotransposition in *A. thaliana* have been limited to elements introduced from different species by transformation^{12,13}. If *A. thaliana* is to be used to understand LTR retrotransposon dynamics during evolution, the identification of mobile endogenous copies is essential.

Although most of the transposons and repeats are transcriptionally silent, they are often derepressed in mutants with decreased genomic DNA methylation. Methylation at CG sites and non-CG sites depends on the DNA methyltransferases MET1 and CMT3, respectively^{14–16}. In addition, a chromatin-remodelling ATPase, DDM1, is

involved in the maintenance of both CG and non-CG methylation^{10,11}. The loss of DNA methylation in these mutants is associated with transcriptional derepression in repeats and transposons^{8,9}. The *ddm1* mutation induces a variety of developmental abnormalities¹⁷. By means of a genetic analysis of one of the abnormalities, we previously identified a mobile DNA transposon *CACTA1* (ref. 18). Here we identify a mobile endogenous LTR retrotransposon through the characterization of another *ddm1*-induced phenotype, named *wavy-sepal* (*wvs*; Fig. 1a, b)¹⁹. *wvs* was inherited as a monogenic recessive trait (Supplementary Fig. 1). Fine genetic mapping and molecular characterization of the *WVS* locus revealed that the *wvs* trait is associated with the insertion of a 5,338-base-pair (bp) sequence into the *FASCIATA1* gene (Fig. 1c and Supplementary Fig. 2)²⁰. The sequence of the insertion was identical with that of a member (At3g11970) of the *gypsy* class retrotransposon family *ATGP3*. We named the identified copy *ATGP3-1*.

To determine whether *ATGP3-1* retrotransposes reproducibly in the *ddm1* background, we examined multiple self-pollinated *ddm1* lines by Southern blot analysis (Fig. 1d). In all 12 *ddm1* lines examined, new bands for *ATGP3* were found. In contrast, in all 12 sibling wild-type *DDM1* lines self-pollinated in parallel, the band pattern was identical with that of the parental wild-type plant. These results suggest that this element is immobile in the wild type but retrotransposed in the *ddm1* mutant. The retrotransposition was confirmed by determining the genomic regions flanking *ATGP3* in the self-pollinated *ddm1* lines (Fig. 1e). New insertions of *ATGP3* were identified in 16 loci. Sequencing of the transposed copy revealed that retrotransposition occurred for the original *ATGP3-1* (At3g11970) and for a related copy, which we named *ATGP3-2* (At1g36590). Transcript analysis also revealed that both *ATGP3-1* and *ATGP3-2* were derepressed in *ddm1* plants (Fig. 1f and Supplementary Fig. 3).

In wild-type plants, *ATGP3-1* and *ATGP3-2* were heavily methylated at both CG and non-CG sites (<http://neomorph.salk.edu/epigenome.html>; Supplementary Fig. 4), as is true for most transposons^{21,22}. The mobilization of *ATGP3* elements in *ddm1* lines is associated with a loss of methylation (Supplementary Fig. 4), suggesting that the silencing depends on DNA methylation. This was tested by using DNA methyltransferase mutants. In the double mutants of a CG methylase gene *MET1* and a non-CG methylase gene *CMT3*, transcriptional silencing of *ATGP3* elements was released (Fig. 1f) and retrotransposition was observed (Supplementary Fig. 5). The activation was not found in either *met1* or *cmt3* single mutants, suggesting that both CG and non-CG methylations contribute to the silencing (for further genetic analyses about the involvement of other epigenetic factors, see Supplementary Fig. 6 and Supplementary Discussion).

We then examined whether the loss of DNA methylation also mobilizes other families of retrotransposons. Because the retrotransposition

¹Department of Integrated Genetics, National Institute of Genetics, Yata 1111, Mishima, Shizuoka 411-8540, Japan. ²Department of Genetics, School of Life Science, The Graduate University for Advanced Studies, Yata 1111, Mishima, Shizuoka 411-8540, Japan. ³Department of Plant Biology, University of Geneva, Sciences III, 30 Quai Ernest-Ansermet, CH-1211 Geneva 4, Switzerland. ⁴Centre National de la Recherche Scientifique (CNRS), UMR 6247, GRD, INSERM U 931, Clermont Université, 24 avenue des landais, 63177 Aubière, France.

*These authors contributed equally to this work.

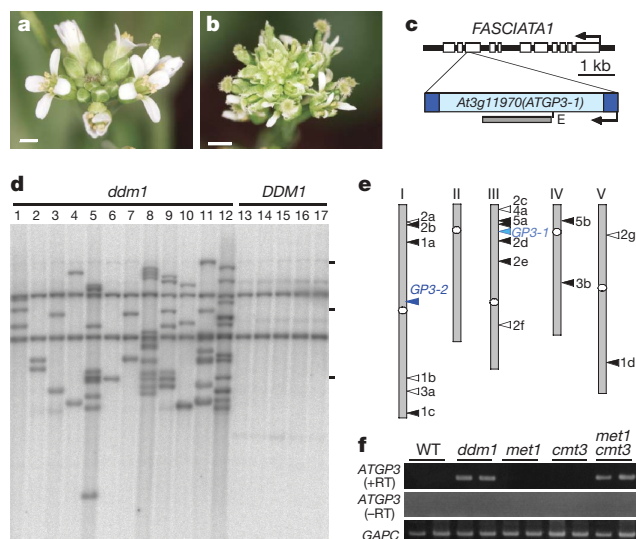


Figure 1 | Identification of a mobile gypsy element ATGP3 through characterization of a *ddm1*-induced developmental phenotype. **a, b**, Flowers without (**a**) and with (**b**) the *wvs* phenotype. The plants were siblings in the self-pollinated progeny of a heterozygous plant. Scale bars, 1 mm. **c**, Insertion of ATGP3-1 (At3g11970) found in the *FASCIATA1* locus. Exons and introns of *FASCIATA1* are shown by boxes and bars, respectively. In ATGP3-1, LTR regions are shown in dark blue. Details of the genetic analysis are given in Supplementary Figs 1 and 2. kb, kilobase. **d**, Southern blot analysis of genomic DNA digested with EcoRV. The probe position of ATGP3-1 is shown by the grey bar in **c**. The *ddm1* and *DDM1* lines used originated from self-pollinated progeny of a single *DDM1/ddm1* plant, and were additionally self-pollinated six or seven times in parallel. Shown are 5 out of 12 *DDM1* lines examined. The DNA length markers were 19.3, 7.74 and 4.26 kb long. **e**, Transposition of ATGP3 retrotransposons found in the self-pollinated *ddm1* plants. New integration sites of ATGP3-1 and ATGP3-2 are shown by white and black triangles, respectively. Original loci are also shown. The sequences flanking the insertions are given in Supplementary Information. **f**, Transcription of ATGP3 in DNA hypomethylation mutants. Total RNA from leaves were reverse transcribed and amplified by PCR with primers recognizing transcripts of both ATGP3-1 and ATGP3-2. Samples with (+ RT) and without (– RT) reverse transcriptase are shown. GAPC was used as a positive control.

normally results in an increase in copy number, we speculated that the retrotransposition might be detectable with the use of a genomic tiling array. For two independently self-pollinated *ddm1* lines, the amount of genomic DNA was assessed by the ratio of its hybridization signal to that of the parental wild-type strain Col. We used a high-density (about 100 bp resolution) tiling array, which covers the entire *A. thaliana* genome, including most of the transposon-rich heterochromatin regions. The tiling array detected an increased signal ratio for ATGP3-1 and ATGP3-2 in the *ddm1* line relative to that of the

wild-type control (Fig. 2a). This increase was not found for ATGP3-3 (At1g35370; Fig. 2b), the most similar member of the ATGP3 family, which has a nucleotide sequence similarity to ATGP3-1 of more than 77% in the integrase domain. This method can distinguish between transposons even within the same subfamily if the sequences are sufficiently different.

We then calculated the average relative hybridization signal for 15,988 cellular genes and 2,379 transposon-encoded genes and pseudogenes throughout the genome (Fig. 2c). At least seven families of

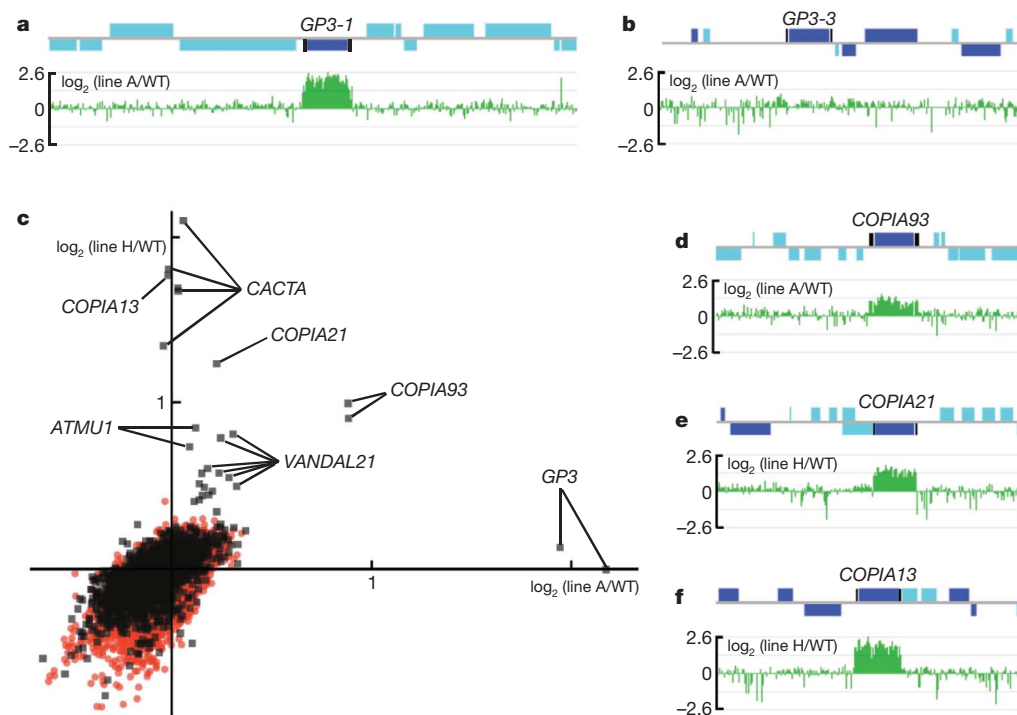


Figure 2 | Increases in copy number in transposons can be detected with a genomic tiling array. The \log_2 ratio of hybridization signals of the self-pollinated *ddm1* to those of wild-type Col was measured for probes over the entire genome. **a, b**, Signals for probes around the ATGP3-1 (At3g11970; **a**) and ATGP3-3 (At1g35370; **b**) loci. Dark and light blue boxes indicate transposon-encoded genes and cellular genes, respectively, oriented 5'→3' above the line and 3'→5' below. 5' and 3' LTRs are indicated by black bars. **c**, Average \log_2 signal ratio of the transcription unit in two self-pollinated *ddm1* lines, named A and H. The values are shown by a scatter plot for 15,988

cellular genes (red circles) and 2,379 transposon-encoded genes and pseudogenes (black squares). Transcription units covering less than 18 probes are not included. In addition, about 0.6% of the genome (bases 3,060,000–3,655,000 in chromosome 4 and 3,234,000–3,527,000 in chromosome 2) are not included, because these regions showed chromosome-level skews, possibly reflecting strain-specific rearrangements. WT, wild type. **d–f**, Newly identified retrotransposons showing the increased signal: COPIA93 (**d**), COPIA21 (**e**) and COPIA13 (**f**).

transposons showed an increased signal in the *ddm1* lines. In addition to *ATGP3* elements, three diverse families of *copia* type LTR retrotransposons (*ATCOPIA13* (At2g13940), *ATCOPIA21* (At5g44925) and *ATCOPIA93* (At5g17125)) showed stronger signals in the *ddm1* samples (Fig. 2c–f). Transpositions in the *ddm1* line have previously been reported for two DNA transposons, *CACTA1* (At2g12210) and *AtMu1* (At4g08680/At1g78095)^{18,23}, both of which showed an increased signal in the tiling array (Fig. 2c). In addition, a significant response was detected for *VANDAL21*, a *Mutator* element family without terminal inverted repeats²⁴ (Fig. 2c and Supplementary Fig. 7).

To examine whether the increased signals of these elements in the tiling array reflected transpositions, we examined them by Southern blot analysis. New bands were found in the self-pollinated *ddm1* line for the three families of *copia* retrotransposons and *VANDAL21* (Fig. 3a–c and Supplementary Fig. 7b). Each of the *ddm1* lines differed considerably in its degree of proliferation in each of the LTR retrotransposons. For example, extensive proliferation was observed in three of the five self-pollinated *ddm1* lines for *ATCOPIA93* (lanes

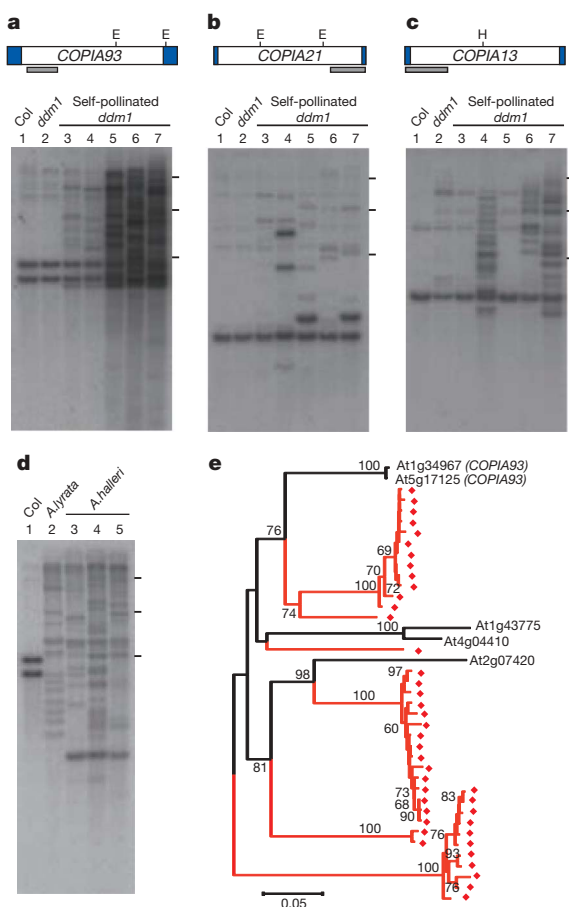


Figure 3 | Lineage-specific bursts of retrotransposition. **a–c**, Southern blot analysis of the self-pollinated *ddm1* plants. Lane 1, Col wild type; lane 2, *ddm1* plant self-pollinated once; lanes 3–7, *ddm1* mutant plants independently self-pollinated eight times. The same DNA samples were used for all blots. HindIII was used in **c**, and EcoRV in others. Probe positions are shown by grey bars in the diagrams above the blots. The DNA length markers were 19.3, 7.74 and 4.26 kb long. A summary of microarray results in all five *ddm1* lines is shown in Supplementary Table 3. **d**, Southern blot analysis of *ATCOPIA93* in *A. lyrata* and *A. halleri*. Plants in lanes 2–5 belonged to subspecies *lyrata*, *halleri*, *tatrica* and *ovirensis*, respectively. Conditions were as in **a**. **e**, Phylogenetic tree generated by the integrase domain sequences of *ATCOPIA93* and related copies in *A. thaliana* and *A. lyrata*. The *A. lyrata* copies are indicated by red diamonds. Trees were made by the Neighbour-Joining method (Supplementary Information). Bootstrap probabilities of more than 60% are shown beside the branches. A scale bar is below the tree.

5, 6 and 7 in Fig. 3a), and in two for *ATCOPIA13* (lanes 4 and 7 in Fig. 3c). The spectra of transpositions differed among the lines. *ATGP3* also showed different proliferation rates among the lines (Figs 1d and 2c).

The stochastic burst of proliferation of the activated element is consistent with extensive variation in the LTR retrotransposon abundance among related species^{3,4}. Indeed, although *ATCOPIA93* occurs at a low copy number in *Arabidopsis thaliana*, many copies were found in the related species *Arabidopsis lyrata* and *Arabidopsis halleri* (Fig. 3d, e). In the sequenced genome of *A. lyrata*, the *ATCOPIA93* copies form a cluster of subfamilies with very similar sequences (Fig. 3e), suggesting that the amplification was recent. The species-specific expansion of subfamilies of elements in *A. thaliana* and *A. lyrata* was also evident for other LTR retrotransposons that were found to be mobile in this study (Supplementary Fig. 8). In these LTR retrotransposons in *A. thaliana*, 5' and 3' LTR sequences were almost identical (Supplementary Table 1), suggesting that the integrations were recent.

Most of the *COPIA93* insertions in the *A. lyrata* genome were found in satellite repeats of centromeres (Fig. 4). Biased integration into centromeric heterochromatin would be less harmful than the

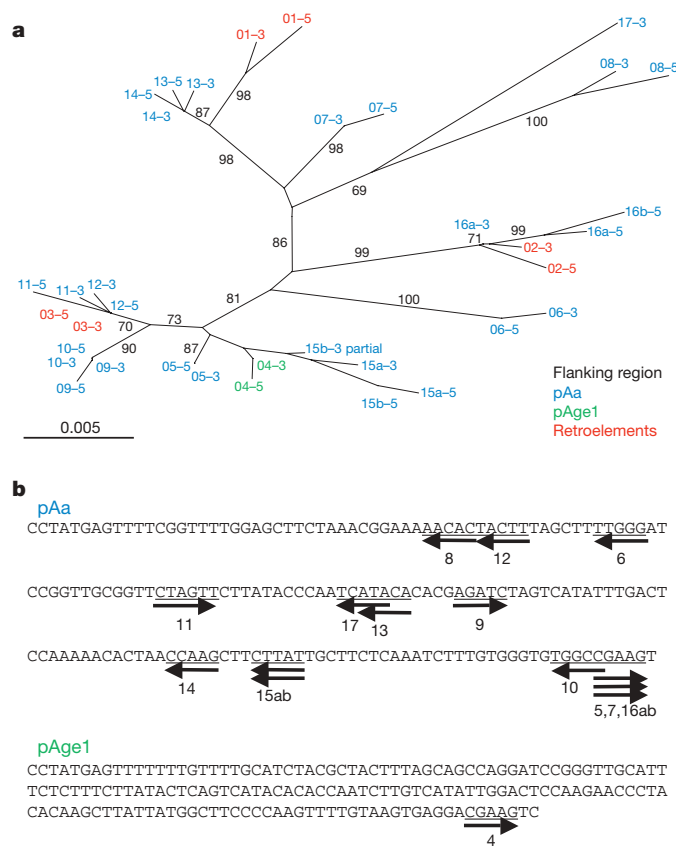


Figure 4 | Selective integration of *COPIA93* into centromeric satellite repeats of the *A. lyrata* genome. **a**, Phylogenetic relation between the LTR sequences. The cluster of *A. lyrata* sequences most similar to *COPIA93* (Fig. 3e) was analysed. Numbers correspond to those listed in Supplementary Table 2. Most of the *COPIA93* copies are inserted into centromeric satellites (pAa and pAge1, shown in blue and green, respectively), with three exceptions of integrations into other subfamilies of LTR retrotransposons (*COPIA20* and *GP5*; red). **b**, Target sites of the *COPIA93* integration within the centromeric satellite sequences. pAa (179 bp) and pAge1 (168 bp) are consensus sequences of the centromeric satellite repeats²⁶. Each integration was confirmed by the alignment of two flanking sequences 5' and 3' of the LTRs. Every integration site had 5 bp of target site duplications, which are shown by underlines and arrows. The arrow also shows the direction of *COPIA93* in each insertion. The number below the arrow indicates the element number.

disruption of a functional gene. This biased targeting to the gene-poor region is in sharp contrast with the integration of *EVD/ATCOPIA93* in the *A. thaliana* mutant, which is much less biased²⁵. These two systems provide interesting material with which to investigate target site specificity and the evolutionary dynamics of this family of LTR retrotransposons (further discussion appears in Supplementary Discussion). The results presented here and in the accompanying paper²⁵ also suggest diversity in the control of LTR retrotransposons. The identification of multiple mobile endogenous LTR retrotransposons of *Arabidopsis* has opened up ways of directly examining their impact in structuring the genome by molecular genetic approaches (specific approaches are discussed in Supplementary Discussion).

METHODS SUMMARY

The generation of independently self-pollinated *ddm1* and *DDM1* lines was described previously¹⁷. For the genome-wide analysis of transposon proliferation, we used a NimbleGen 3 × 385K array, which covers the entire sequenced *A. thaliana* genome with an interval of about 100 bp. The genomic DNA was sonicated to produce random fragments ranging in size from 200 to 1,000 bp, which were then amplified and hybridized to the array in accordance with NimbleGen's instructions, using a GenomePlex Complete Whole Genome Amplification Kit (WGA2; Sigma).

Full Methods and any associated references are available in the online version of the paper at www.nature.com/nature.

Received 1 June; accepted 27 July 2009.

Published online 6 September 2009.

- Kumar, A. & Bennetzen, J. L. Plant retrotransposons. *Annu. Rev. Genet.* **33**, 479–532 (1999).
- Havecker, E. R., Gao, X. & Voytas, D. F. The diversity of LTR retrotransposons. *Genome Biol.* **5**, 225 (2004).
- Vitte, C. & Bennetzen, J. L. Analysis of retrotransposon structural diversity uncovers properties and propensities in angiosperm genome evolution. *Proc. Natl Acad. Sci. USA* **103**, 17638–17643 (2006).
- Hawkins, J. S., Kim, H. & Nason, J. D. Differential lineage-specific amplification of transposable elements is responsible for genome size variation in *Gossypium*. *Genome Res.* **16**, 1252–1261 (2006).
- The Arabidopsis Genome Initiative. Analysis of the genome sequence of the flowering plant *Arabidopsis thaliana*. *Nature* **408**, 796–815 (2000).
- Le, Q. H., Wright, S., Yu, Z. & Bureau, T. Transposon diversity in *Arabidopsis thaliana*. *Proc. Natl Acad. Sci. USA* **97**, 7376–7381 (2000).
- Peterson-Burch, B. D., Nettleton, D. & Voytas, D. F. Genomic neighborhoods for *Arabidopsis* retrotransposons: a role for targeted integration in the distribution of the Metaviridae. *Genome Biol.* **5**, R78 (2004).
- Steimer, A. *et al.* Endogenous targets of transcriptional gene silencing in *Arabidopsis*. *Plant Cell* **12**, 1165–1178 (2000).
- Lippman, Z., May, B., Yordan, C., Singer, T. & Martienssen, R. Distinct mechanisms to determine transposon inheritance and methylation via small interfering RNA and histone modification. *PLoS Biol.* **1**, E67 (2003).

- Vongs, A., Kakutani, T., Martienssen, R. A. & Richards, E. J. *Arabidopsis thaliana* DNA methylation mutants. *Science* **260**, 1926–1928 (1993).
- Jeddeloh, J. A., Stokes, T. L. & Richards, E. J. Maintenance of genomic methylation requires a SWI2/SNF2-like protein. *Nature Genet.* **22**, 94–97 (1999).
- Lucas, H., Feuerbach, F., Kunert, K., Grandbastien, M.-A. & Caboche, M. RNA-mediated transposition of the tobacco retrotransposon Tnt1 in *Arabidopsis thaliana*. *EMBO J.* **14**, 2364–2373 (1995).
- Hirochika, H., Okamoto, H. & Kakutani, T. Silencing of retrotransposons in *Arabidopsis* and reactivation by the *ddm1* mutation. *Plant Cell* **12**, 357–369 (2000).
- Finnegan, E., Peacock, J. & Dennis, E. Reduced DNA methylation in *Arabidopsis thaliana* results in abnormal plant development. *Proc. Natl Acad. Sci. USA* **93**, 8449–8454 (1996).
- Bender, J. DNA methylation and epigenetics. *Annu. Rev. Plant Biol.* **55**, 41–68 (2004).
- Chan, S. W., Henderson, I. R. & Jacobsen, S. E. Gardening the genome: DNA methylation in *Arabidopsis thaliana*. *Nature Rev. Genet.* **6**, 351–360 (2005).
- Kakutani, T., Jeddeloh, J., Flowers, S., Munakata, K. & Richards, E. Developmental abnormalities and epimutations associated with DNA hypomethylation mutations. *Proc. Natl Acad. Sci. USA* **93**, 12406–12411 (1996).
- Miura, A. *et al.* Mobilization of transposons by a mutation abolishing full DNA methylation in *Arabidopsis*. *Nature* **411**, 212–214 (2001).
- Kakutani, T. Genetic characterization of late-flowering traits induced by DNA hypomethylation mutation in *Arabidopsis thaliana*. *Plant J.* **12**, 1447–1451 (1997).
- Kaya, H. *et al.* FASCIATA genes for chromatin assembly factor-1 in *Arabidopsis* maintain the cellular organization of apical meristems. *Cell* **104**, 131–142 (2001).
- Cokus, S. J. *et al.* Shotgun bisulfite sequencing of the *Arabidopsis* genome reveals DNA methylation patterning. *Nature* **452**, 215–219 (2008).
- Lister, R. *et al.* Highly integrated single-base resolution maps of epigenome in *Arabidopsis*. *Cell* **133**, 523–536 (2008).
- Singer, T., Yordan, C. & Martienssen, R. A. Robertson's *Mutator* transposons in *A. thaliana* are regulated by the chromatin-remodeling gene *Decrease in DNA Methylation (DDM1)*. *Genes Dev.* **15**, 591–602 (2001).
- Yu, Z., Wright, S. I. & Bureau, T. E. *Mutator*-like elements in *Arabidopsis thaliana*: structure, diversity and evolution. *Genetics* **156**, 2019–2031 (2000).
- Mirouze, M. *et al.* Selective epigenetic control of retrotransposition in *Arabidopsis*. *Nature* doi:10.1038/nature08328 (this issue).
- Kawabe, A. & Charlesworth, D. Patterns of DNA variation among three centromere satellite families in *Arabidopsis halleri* and *A. lyrata*. *J. Mol. Evol.* **64**, 237–247 (2007).

Supplementary Information is linked to the online version of the paper at www.nature.com/nature.

Acknowledgements We thank A. Terui for technical assistance, M. Nakamura for plant materials, M. Morita and M. Tasaka for genetic marker information, H. Tsukaya for advice on the wvs phenotypes, and E. Richards for critical comments on the manuscript. This study was supported by the Takeda Science Foundation and a Grant-in-Aid for Scientific Research.

Author Contributions S.T. identified and analysed *ATGP3*. A. Kobayashi collected and analysed tiling array data. A.M., S.T., A. Kobayashi and T.K. performed the Southern blot analysis. O.M. obtained the results shown in Supplementary Fig. 6, and A. Kawabe analysed the sequences. S.T. and T.K. wrote the manuscript. All authors discussed and commented on the manuscript.

Author Information Reprints and permissions information is available at www.nature.com/reprints. Correspondence and requests for materials should be addressed to T.K. (tkakutan@lab.nig.ac.jp).

METHODS

Plant materials. The isolation of *ddm1* mutants was described previously¹⁰. The mutant allele *ddm1-1* was used throughout. The procedure to establish the self-pollinated *ddm1* lines was described previously¹⁷. In brief, the original *ddm1-1* plant was backcrossed to the parental wild-type Col plant six times in the heterozygous state (*DDM1/ddm1-1*). A single *DDM1/ddm1-1* plant was self-pollinated, and multiple *ddm1-1/ddm1-1* plants and *DDM1/DDM1* plants were selected. These *ddm1-1/ddm1-1* and the control *DDM1/DDM1* plants were self-pollinated repeatedly in parallel¹⁷. The *DDM1* and *ddm1* plants in Fig. 1d were self-pollinated seven times after becoming homozygous, except the *ddm1* plant in lane 7, which was self-pollinated six times. The *met1-1* and *cmt3-i11* mutants were gifts from E. Richards and J. Bender^{27,28}, respectively. The original *cmt3-i11* is in the WS background and it was backcrossed six times to Columbia before use. The genetic mapping procedure of the WVS locus is shown in Supplementary Fig. 2. Origins of the *A. lyrata* and *A. halleri* plants in Fig. 3d are as follows: lane 2, *A. lyrata* ssp. *lyrata* strain MN47; lane 3, *A. halleri* ssp. *halleri* strain H-RB isolated in Bistrita, Romania; lane 4, *A. halleri* ssp. *tatrica* strain T-PLDH1 isolated in Vysoké Tatry, Poland; lane 5, *A. halleri* ssp. *ovirensis* strain O-AUO26 isolated in Karinthia, Austria.

Analysis of transposition and methylation of transposons. Southern analysis, suppression PCR and bisulphite sequencing were performed as described previously²⁹. The genomic DNA was digested by *DraI* and *HindIII* before bisulphite sequencing. The primer pairs used for bisulphite sequencing and suppression PCR are shown in Supplementary Table 4.

Expression of *ATGP3* retrotransposons. For RT-PCR, total RNA was extracted from leaf tissue with an SV Total RNA Isolation System (Promega) and treated with RQ1 RNase-Free DNase (Promega). From 2 µg of total RNA, complementary DNA was synthesized with a First-Strand cDNA Synthesis Kit (GE Healthcare) and a pd(N)₆ primer. A one-tenth aliquot of the RT reaction was

used as a template for PCR (total 10 µl). The PCR conditions were as follows: 94 °C for 3 min, then 25–33 cycles of 94 °C for 30 s, 55 °C for 30 s, and 72 °C for 60 s, and then 72 °C for 3 min. The PCR product was then separated by electrophoresis on 1.5% agarose. The primer pairs used for RT-PCR are shown in Supplementary Table 4.

Identification of related transposons and generation of phylogenetic trees.

A. lyrata sequences related to the transposons identified in this study were obtained from shotgun genome sequence data of this species (<http://genome.jgi-psf.org/Araly1/Araly1.info.html>) using the NCBI Trace archive BLAST website (<http://www.ncbi.nlm.nih.gov/Traces/trace.cgi?>) as conserved domain region sequences of *A. thaliana* copy as query. Sequences showing more than 60% identity with more than 70% coverage and having at least two shotgun reads in the *A. lyrata* genome sequence data were used for subsequent analyses. Because *A. lyrata* should have a heterozygous region in many chromosomal regions, there might be allelic sequences present. *A. thaliana* transposon loci were also identified by the same criteria. Phylogenetic trees were constructed by the Neighbour-Joining method with Jukes and Cantor distances using all type sites with MEGA4 (ref. 30). Bootstrap probabilities were obtained from 500 replicates.

27. Kankel, M. W. *et al.* *Arabidopsis* *MET1* cytosine methyltransferase mutants. *Genetics* **163**, 1109–1122 (2003).
28. Bartee, L., Malagnac, F. & Bender, J. *Arabidopsis* *cmt3* chromomethylase mutations block non-CG methylation and silencing of an endogenous gene. *Genes Dev.* **15**, 1753–1758 (2001).
29. Kato, M., Miura, A., Bender, J., Jacobsen, S. & Kakutani, T. Role of CG and non-CG methylation in immobilization of transposons in *Arabidopsis*. *Curr. Biol.* **13**, 421–426 (2003).
30. Tamura, K., Dudley, J., Nei, M. & Kumar, S. MEGA4: Molecular Evolutionary Genetics Analysis (MEGA) software version 4.0. *Mol. Biol. Evol.* **24**, 1596–1599 (2007).

Selective epigenetic control of retrotransposition in *Arabidopsis*

Marie Mirouze^{1*}, Jon Reinders^{1*}, Etienne Bucher¹, Taisuke Nishimura¹, Korbinian Schneeberger², Stephan Ossowski², Jun Cao², Detlef Weigel², Jerzy Paszkowski¹ & Olivier Mathieu^{1,3}

Retrotransposons are mobile genetic elements that populate chromosomes, where the host largely controls their activities^{1–3}. In plants and mammals, retrotransposons are transcriptionally silenced by DNA methylation^{1,4}, which in *Arabidopsis* is propagated at CG dinucleotides by METHYLTRANSFERASE 1 (MET1)⁵. In *met1* mutants, however, mobilization of retrotransposons is not observed, despite their transcriptional activation^{4–6}. A post-transcriptional mechanism therefore seems to be preventing retrotransposition. Here we show that a *copia*-type retrotransposon (*Évadé*, French for ‘fugitive’) evaded suppression of its movement during inbreeding of hybrid epigenomes consisting of *met1*- and wild-type-derived chromosomes. *Évadé* (*EVD*) reinsertions caused a series of developmental mutations that allowed its identification. Genetic testing of host control of the *EVD* life cycle showed that transcriptional suppression occurred by CG methylation supported by RNA-directed DNA methylation. On transcriptional reactivation, subsequent steps of the *EVD* cycle were inhibited by plant-specific RNA polymerase IV/V^{7,8} and the histone methyltransferase KRYPTONITE (KYP). Moreover, genome resequencing demonstrated retrotransposition of *EVD* but no other potentially active retroelements when this combination of epigenetic mechanisms was compromised. Our results demonstrate that epigenetic control of retrotransposons extends beyond transcriptional suppression and can be individualized for particular elements.

We established a population of epigenetic recombinant inbred lines (epiRILs) derived from a cross between a wild-type (WT) and a *met1* homozygous plant carrying a null mutation for *MET1* (*met1-3* mutant allele⁵). At the F₈ generation of inbreeding by single-seed descent in the presence of *MET1* (selected for in the F₂), these lines displayed mosaic epigenomes⁹. We found rare individuals with aberrant development among the epiRILs. For example, in F₈ line 12 (epi12), 4% of plants lacked male flower organs and petals (Fig. 1a), resembling mutations in the *LEAFY* (*LFY*) gene and subsequently confirmed by genetic mapping. A large insert at the *LFY* locus (Fig. 1b) was found to be a full-length *Ty1/copia* long terminal repeat (LTR) retrotransposon (5.3 kilobases (kb)) belonging to the *ATCOPIA93* family (Supplementary Fig. 1) and encoded by the *AT5G17125* locus (Fig. 1c), hereafter referred to as *EVD*. Two aberrant plants in epi49 (Fig. 1d, f) had an *EVD* insertion into the *BRASSINOSTEROID INSENSITIVE 1* (*BRI1*) (Fig. 1e) and *VARIEGATED 2* (*VAR2*) genes (Fig. 1g), respectively. Thus, *EVD* was independently activated in two different epiRILs and inserted into three unlinked loci (*LFY* on chromosome 5, *BRI1* on chromosome 4, and *VAR2* on chromosome 2). *EVD* was present as two nearly identical copies in WT plants and this was unaltered in the epiRIL parent *met1* (Fig. 1h). In contrast, *EVD* was amplified in epi12

and epi49, with hybridization signals at the size expected for *EVD* extrachromosomal DNA (Fig. 1h and Supplementary Fig. 2). Movement of *EVD* was detected in 29 of the epiRILs examined for *EVD* mobilization and extrachromosomal DNA (Supplementary Fig. 3). Previously we reported active transposition of the DNA transposon *CACTA* in 18 lines of the same epiRIL population⁹. Because the two transposons were simultaneously active in only six lines (Supplementary Fig. 3), it is unlikely that a common regulatory switch controls the activity of both elements.

To understand *EVD* mobilization in the epiRILs, its life cycle was examined in lines with active or immobile retrotransposons. Analysis of DNA methylation in the area of transcription initiation at the 5' LTR of *EVD* showed high CG methylation (³CG) levels in WT plants but ³CG was erased in *met1* and epi12 plants (Fig. 2a). However, ³CG was retained in epi07, where there was no sign of *EVD* activity (Fig. 1h and Supplementary Fig. 2). Thus, *met1* and WT parental epialleles of *EVD* were inherited in epi12 and epi07 plants, respectively. Remarkably, *EVD* 5' LTR methylation at CHH and CHG (H = A, T or C) sites was almost absent, even in WT plants (Fig. 2a).

We examined whether erasure of ³CG in *met1* and epi12 allowed the production of RNA spanning the entire retrotransposon. Transcripts about 5 kb long corresponding to full-length *EVD* were present in *met1* and epi12 plants but not in WT and epi07 plants (Fig. 2b). Two shorter non-polyadenylated transcripts were detected that may reflect aberrant or cleaved *EVD* RNAs (Fig. 2b), as observed previously for other retrotransposons¹⁰. Analyses of sequence polymorphism confirmed that all *EVD* transcripts originated from the *AT5G17125* locus (Supplementary Fig. 4). Thus, *EVD* transcription was silenced at *AT5G17125* by ³CG in WT and epi07 plants.

In the *EVD* life cycle, the long transcript should be translated and subjected to reverse transcription, leading to extrachromosomal DNA². Southern blot analysis with non-restricted DNA revealed the presence of *EVD* extrachromosomal DNA in epi12 plants but not in *met1* plants, although both the level and pattern of the *EVD* transcripts were very similar in the two lines (Fig. 2b, c). This suggested that translation and/or reverse transcription, which proceeded in epi12 plants, was blocked in *met1* plants.

Transposon silencing involves small RNAs (sRNAs) 24 and 21 nucleotides in length acting through RNA-directed DNA methylation (RdDM) or messenger RNA cleavage/translational inhibition, respectively^{11–13}. The absence of *EVD* extrachromosomal DNA in *met1* could result from translational inhibition, preventing accumulation of its reverse transcriptase. However, this is unlikely because 21-nucleotide sRNAs were present in both *met1* and epi12 plants (Fig. 2d). Although *EVD* RNAs could be guided for cleavage by the 21-nucleotide sRNAs, they nevertheless accumulated. Moreover,

¹Department of Plant Biology, University of Geneva, Sciences III, 30 Quai Ernest-Ansermet, CH-1211 Geneva 4, Switzerland. ²Max Planck Institute for Developmental Biology, 72076 Tübingen, Germany. ³Centre National de la Recherche Scientifique (CNRS), UMR 6247, GrED, INSERM U 931, 24 avenue des Landais, Clermont Université, 63177 Aubière, France. *These authors contributed equally to this work.

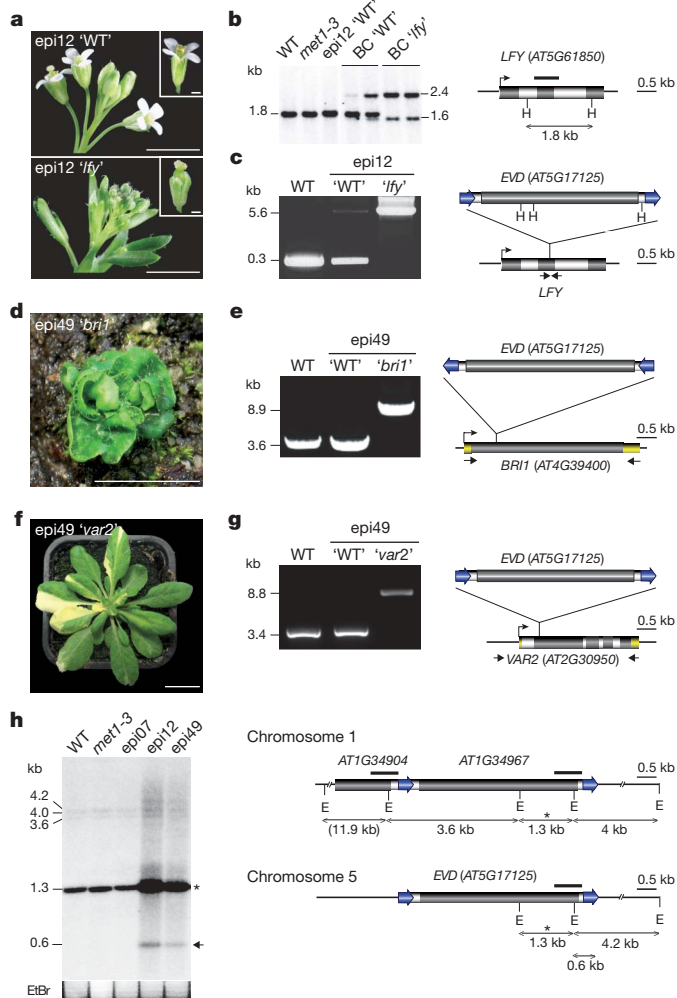


Figure 1 | Mobilization of EVD LTR retrotransposon in epiRILs. *LFY*, *BRI1*, *VAR2* and *EVD* loci structures are represented with the following components: grey, white and yellow boxes and blue arrows for exons, introns, untranslated regions and long terminal repeats, respectively. HindIII (H) and EcoRV (E) restriction sites, fragment sizes, primers (black arrows) and probe position (black bar) are indicated. White scale bars represent 1 cm (1 mm in insets). **a**, 'lfy' phenotype in epi12. WT (top) and lfy (bottom) epi12 inflorescences and magnified flowers are shown. **b**, Southern blot analysis using HindIII and *LFY* probe on F₂ progeny of the backcross between 'lfy' epi12 and WT plants with the WT or lfy phenotype (BC 'WT', and BC 'lfy', respectively). WT, met1-3 and epi12 'WT' are controls. **c**, PCR analysis and sequencing of the *LFY* locus. **d**, 'bri1' phenotype in epi49. **e**, PCR analysis and sequencing of the *BRI1* locus. **f**, 'var2' phenotype in epi49. **g**, PCR analysis and sequencing of the *VAR2* locus. **h**, Southern blot analysis with EcoRV and *EVD* probe A (black bar). epi07, epi12 and epi49 (F₈ generation) are compared with WT and met1-3 parents. The arrow and asterisk indicate extrachromosomal and internal *EVD* fragments, respectively. The ethidium bromide stained gel (EtBr) is shown as a loading control. Smears in epi12 and epi49 suggest somatic transposition. The restriction map shows *ATCOPIA93* loci on chromosomes 1 and 5.

although *EVD*-specific 24-nucleotide sRNAs were ubiquitous (Fig. 2d), the non-CG methylation hallmark of RdDM was absent from the 5' LTR (Fig. 2a). Thus, these sRNAs are not channelled to RdDM. The lack of a correlation between the *EVD*-specific sRNAs and any steps in retrotransposon mobilization raises questions about their regulatory function.

Because *EVD* seemed to be immobile in the strains parental to the epiRILs examined, the onset of its activity during inbreeding of epi12 was investigated. Beginning with the F₄ generation, extrachromosomal DNA was associated with an increased *EVD* copy number (Fig. 2e). New insertions were detected only in F₇ plants (Fig. 2e).

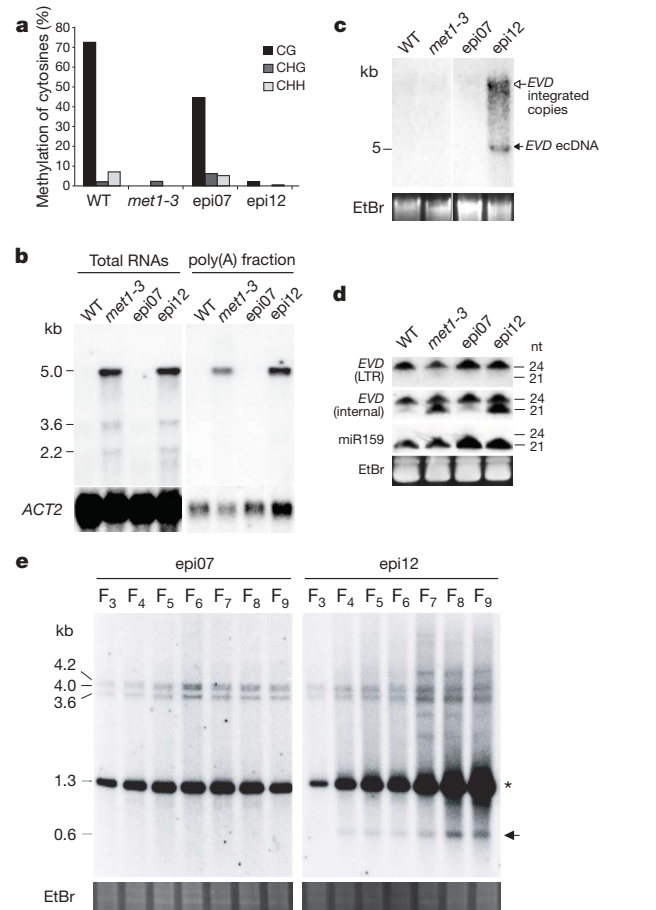


Figure 2 | EVD life cycle in epiRILs and the met1-3 parent. **a**, Bisulphite DNA methylation analysis at the *EVD* 5' LTR. Methylation levels are given at CG, CHG and CHH sites. **b**, Northern blot analysis with total and poly(A)⁺ RNAs probed with an *EVD* full-length probe. *ACTIN2* (*ACT2*) was used as loading control. **c**, Southern blot analysis with undigested DNA and *EVD* probe A (see Fig. 1h) revealed the presence of extrachromosomal *EVD* copies (*EVD* ecDNA) in epi12 plants but not in epi07 plants (both at F₈) or in the parents (WT and met1-3). The ethidium bromide stained gel (EtBr) is shown as a loading control. **d**, *EVD* small RNAs detection with an LTR probe and internal probe (*EVD* probe B, see Supplementary Fig. 8 for probe information). miR159 and EtBr are shown as loading controls. **e**, EcoRV-digested DNA from successive epi07 and epi12 generations was hybridized with *EVD* probe A (legend as for Fig. 1h). Smears in epi12 suggest increasing somatic transposition.

Mobilization of *EVD* therefore seemed to be progressive during epiRIL inbreeding.

We reported previously that self-propagation of *met1* mutants leads to stochastically formed and irregularly inherited novel DNA methylation patterns¹⁴. We therefore examined *EVD* transposition in *met1* mutants propagated by self-fertilization over four generations. Progressive *EVD* mobilization and accumulation of extrachromosomal DNA were detected from the second generation of homozygous *met1* plants (Fig. 3a and Supplementary Fig. 5). *EVD* transposition varied between *met1* lines (data not shown), probably as a consequence of stochastic changes in epigenetic marks characteristic of these strains¹⁴, which also occurred in the epiRILs⁹. Neither transposition nor extrachromosomal DNA accumulation was detected in the first generation of *met1*, suggesting that mechanisms other than ^mCG prevented *EVD* life-cycle progression.

To define these mechanisms, the function of RdDM was examined by depletion of either RNA polymerases IV and V (Pol IV and Pol V) or DOMAINS REARRANGED METHYLTRANSFERASE 2 (DRM2) by using mutations in *NRPD2/NRPE2* (ref. 8) (*nrpd2a-2*) encoding the common subunit of Pol IV and Pol V, or in *DRM2* (*drm2-2*)

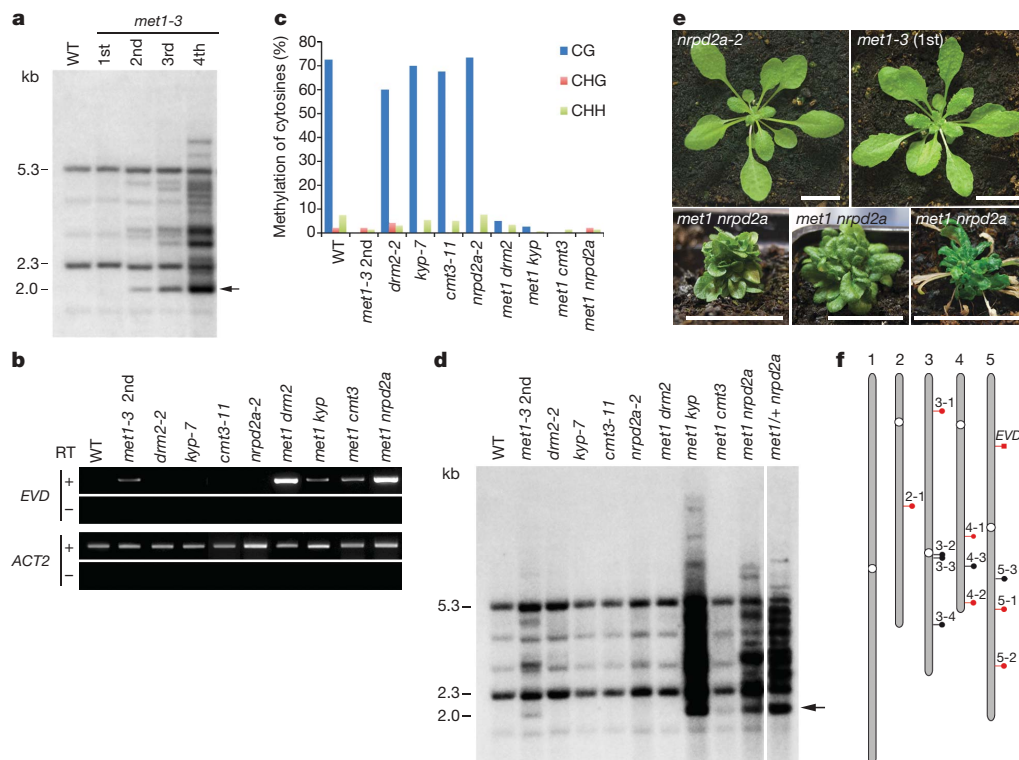


Figure 3 | Genetic analysis of *EVD* transposition control. **a**, Southern blot analysis of *EVD* transposition in successive *met1-3* generations. *SspI*-digested DNA was hybridized to an *EVD* fragment (probe C; see Supplementary Fig. 8). The arrow shows *EVD* extrachromosomal DNA. **b**, RT-PCR analysis of *EVD* transcripts. *ACTIN2* (*ACT2*) was used to normalize RNA template amounts; negative controls lacked reverse transcriptase (RT-). **c**, Bisulphite DNA methylation at the *EVD* 5' LTR, as described in Fig. 2a. **d**, Southern blot

analysis of the indicated genotypes performed as in **a**. **e**, Three independent *met1-3 nrpd2a-2* double-mutant plants show severe phenotypes compared with *nrpd2a-2* and *met1-3* single mutant siblings. Scale bar, 1 cm. **f**, Scheme of *Arabidopsis* chromosomes showing *EVD* retrotransposition events found in a *met1/+ nrpd2a* individual (filled circles). The original *EVD* locus is shown as a red square; red circles indicate *EVD* insertions verified by PCR assay (see Supplementary Fig. 7).

encoding the main *de novo* DNA methyltransferase in *Arabidopsis*. *EVD* transcription was not activated in *nrpd2a* or *drm2* single mutants (Fig. 3b), which is consistent with unaltered DNA methylation at the *EVD* 5' LTR (Fig. 3c). However, *met1 nrpd2a* and *met1 drm2* double mutants showed a synergistic increase in *EVD* transcript levels (Fig. 3b). Thus, in the absence of ^{me}CG, the RdDM pathway restrained the accumulation of *EVD* transcript, although this was not reflected by changes in DNA methylation (Fig. 3c). *EVD* extrachromosomal DNA accumulated and *EVD* transposed only in *met1 nrpd2a* plants but not in *met1 drm2* plants (Fig. 3d and Supplementary Fig. 6), revealing a functional separation of DRM2 and Pol IV/V in the control of *EVD* transposition. Moreover, this control was achieved beyond transcription, with NRDP2/NRPE2 having a central function independent of DRM2 and, thus, probably of RdDM.

Combinations of *met1-3* and *nrpd2a-2* alleles as double mutants were recovered only rarely. These plants displayed severe developmental abnormalities (Fig. 3e) reminiscent of *met1 kyp* mutants that we described previously¹⁴, which in addition to MET1 lacked the major histone H3 lysine 9 (H3K9) methyltransferase¹⁵. The *met1 kyp* double mutant also had high *EVD* activity (Fig. 3d) but, in contrast to *nrpd2a*, the *kyp* mutation combined with *met1* did not influence *EVD* transcript level (Fig. 3b). Thus, KYP restrained *EVD* mobilization exclusively at the post-transcriptional level. This control must differ from the previously reported transcriptional restriction of the rice *Tos17 copia*-like retrotransposon by H3K9 methyltransferase SDG714, which altered DNA methylation levels¹⁶. It is possible that KYP methylates a protein important for translation and/or reverse transcription of *EVD* transcripts. Indeed, recent studies have identified non-histone substrates for lysine methyltransferases^{17–19}.

It has been shown that KYP-mediated H3K9 methylation directs non-CG DNA methylation by the plant-specific CHROMO-

METHYLASE 3 (CMT3)²⁰. Mutations in *KYP* and *CMT3* genes could therefore have a similar outcome in terms of *EVD* transposition. As shown for *kyp*, mutation of *cmt3* did not influence the *EVD* 5' LTR methylation pattern or *EVD* transcript levels (Fig. 3b, c). However, in contrast with the *met1 kyp* double mutant, *EVD* extrachromosomal DNA accumulated to a low level in *met1 cmt3* first-generation double mutants, and no *EVD* insertions were detected (Fig. 3d and Supplementary Fig. 6). Thus, the function of KYP in post-transcriptional control of *EVD* seems to be independent of CMT3. However, possible functional redundancy between CMT3 and DRM1 and/or DRM2 (ref. 21) could be contributing to *EVD* control. To address this, *met1 drm1 drm2* and *met1/+ drm1 drm2 cmt3* individuals were also tested (*met1 drm1 drm2 cmt3* quadruple mutants are extremely rare and have severe developmental defects²²). Only marginal redundancy between DRM1 and DRM2 in controlling *EVD* activity was revealed (Supplementary Fig. 6). Our results therefore support the hypothesis that Pol IV/V and KYP control retrotransposition post-transcriptionally through a mechanism that is independent of DNA methylation.

We assumed that the epigenetic mechanisms involved in the control of *EVD* also protect the genome against mobilization of other transposons. We therefore sequenced the genome of a *met1/MET1 nrpd2a/nrpd2a* (*met1/+ nrpd2a*) mutant plant with high *EVD* activity (Fig. 3d and Supplementary Fig. 6). This could not be performed on a *met1 nrpd2a* double mutant because insufficient tissue was available (Fig. 3e). Sequencing identified new *EVD* insertion sites (Fig. 3f and Supplementary Fig. 7), but DNA transposons, including *CACTA*²³, non-LTR retrotransposons and other families of potentially active LTR-containing retrotransposons²⁴, remained immobile. These data suggest that *EVD* is the only transposon that moves in this genetic background.

Although DNA methylation has been associated with suppression of transposon-derived transcription, our results show that 'classical' epigenetic players also restrain subsequent steps of retrotransposition. Exemplified by *EVD*, we show that Pol IV/V and KYP are both required for post-transcriptional control after transcriptional reactivation. This regulation seems to apply only to *EVD*, suggesting that other retrotransposons remain immobilized by additional or alternative epigenetic mechanisms. In this respect, the SWI2/SNF2-like chromatin-remodelling protein DECREASE IN DNA METHYLATION 1 (DDM1) seems to have a pivotal function in controlling retrotransposition; however, inbreeding of *ddm1* mutants seems to be essential for the mobilization of retrotransposons, as shown in the accompanying paper²⁴. This resembles *met1* mutants¹⁴ and *epiRILs*⁹, in which inbreeding is associated with epigenetic instabilities and activation of transposition. In contrast, double-mutant combinations of *met1* *nrpd2a* or *met1* *kyp*, in which post-transcriptional control of *EVD* is compromised, activate transposition instantaneously and inbreeding is not required. It is now necessary to define how the host individualizes the control of different groups of transposons and how selectivity of this regulation has evolved.

METHODS SUMMARY

Genomic DNA analyses were performed by Southern blotting. DNA methylation levels at the *EVD* 5' LTR were assessed by bisulphite sequencing. Accumulation of *EVD* transcripts was determined by RT-PCR or northern blot analysis, and sRNA detection was performed by northern blotting. The genome of the *met1/+ nrpd2a* mutant line was analysed by Illumina sequencing-by-synthesis.

Full Methods and any associated references are available in the online version of the paper at www.nature.com/nature.

Received 1 June; accepted 27 July 2009.

Published online 6 September 2009.

- Slotkin, R. K. & Martienssen, R. A. Transposable elements and the epigenetic regulation of the genome. *Nature Rev. Genet.* **8**, 272–285 (2007).
- Beauregard, A., Curcio, M. J. & Belfort, M. The take and give between retrotransposable elements and their hosts. *Annu. Rev. Genet.* **42**, 587–617 (2008).
- Goodier, J. L. & Kazazian, H. H. Retrotransposons revisited: the restraint and rehabilitation of parasites. *Cell* **135**, 23–35 (2008).
- Zhang, X. *et al.* Genome-wide high-resolution mapping and functional analysis of DNA methylation in *Arabidopsis*. *Cell* **126**, 1189–1201 (2006).
- Saze, H., Mittelsten Scheid, O. & Paszkowski, J. Maintenance of CpG methylation is essential for epigenetic inheritance during plant gametogenesis. *Nature Genet.* **34**, 65–69 (2003).
- Lister, R. *et al.* Highly integrated single-base resolution maps of the epigenome in *Arabidopsis*. *Cell* **133**, 523–536 (2008).
- Pontier, D. *et al.* Reinforcement of silencing at transposons and highly repeated sequences requires the concerted action of two distinct RNA polymerases IV in *Arabidopsis*. *Genes Dev.* **19**, 2030–2040 (2005).
- Wierzbicki, A. T., Haag, J. R. & Pikaard, C. S. Noncoding transcription by RNA polymerase Pol IVb/Pol V mediates transcriptional silencing of overlapping and adjacent genes. *Cell* **135**, 635–648 (2008).
- Reinders, J. *et al.* Compromised stability of DNA methylation and transposon immobilization in mosaic *Arabidopsis* epigenomes. *Genes Dev.* **23**, 939–950 (2009).
- Hirochika, H., Okamoto, H. & Kakutani, T. Silencing of retrotransposons in *Arabidopsis* and reactivation by the *ddm1* mutation. *Plant Cell* **12**, 357–369 (2000).
- Matzke, M. A., Kanno, T., Huettel, B., Daxinger, L. & Matzke, A. J. Targets of RNA-directed DNA methylation. *Curr. Opin. Plant Biol.* **10**, 512–519 (2007).
- Brodersen, P. *et al.* Widespread translational inhibition by plant miRNAs and siRNAs. *Science* **320**, 1185–1190 (2008).
- Slotkin, R. K. *et al.* Epigenetic reprogramming and small RNA silencing of transposable elements in pollen. *Cell* **136**, 461–472 (2009).
- Mathieu, O., Reinders, J., Caikovski, M., Smathajitt, C. & Paszkowski, J. Transgenerational stability of the *Arabidopsis* epigenome is coordinated by CG methylation. *Cell* **130**, 851–862 (2007).
- Jackson, J. P. *et al.* Dimethylation of histone H3 lysine 9 is a critical mark for DNA methylation and gene silencing in *Arabidopsis thaliana*. *Chromosoma* **112**, 308–315 (2004).
- Ding, Y. *et al.* SDG714, a histone H3K9 methyltransferase, is involved in *Tos17* DNA methylation and transposition in rice. *Plant Cell* **19**, 9–22 (2007).
- Chuikov, S. *et al.* Regulation of p53 activity through lysine methylation. *Nature* **432**, 353–360 (2004).
- Kouskouti, A., Scheer, E., Staub, A., Tora, L. & Talianidis, I. Gene-specific modulation of TAF10 function by SET9-mediated methylation. *Mol. Cell* **14**, 175–182 (2004).
- Sampath, S. C. *et al.* Methylation of a histone mimic within the histone methyltransferase G9a regulates protein complex assembly. *Mol. Cell* **27**, 596–608 (2007).
- Jackson, J. P., Lindroth, A., Cao, X. & Jacobsen, S. E. Control of CpNpG DNA methylation by the KRYPTONITE histone H3 methyltransferase. *Nature* **416**, 556–560 (2002).
- Cao, X. *et al.* Role of the DRM and CMT3 methyltransferases in RNA-directed DNA methylation. *Curr. Biol.* **13**, 2212–2217 (2003).
- Zhang, X. & Jacobsen, S. E. Genetic analyses of DNA methyltransferases in *Arabidopsis thaliana*. *Cold Spring Harb. Symp. Quant. Biol.* **71**, 439–447 (2006).
- Miura, A. *et al.* Mobilization of transposons by a mutation abolishing full DNA methylation in *Arabidopsis*. *Nature* **411**, 212–214 (2001).
- Tsukahara, S. *et al.* Burst of retrotransposition reproduced in *Arabidopsis*. *Nature* doi:10.1038/nature08351 (this issue).

Supplementary Information is linked to the online version of the paper at www.nature.com/nature.

Acknowledgements We thank all members of the Paszkowski laboratory for discussion; L. Broger, M. Freyre, J. Nicolet, C. Mégies and J. Lafleur for technical assistance; M. Dapp and X. Zhang for *met1/+ ddm1/+ ddm2/+ cmt3/+* material; C. Lanz for help in preparing the Illumina libraries and running the instruments and P. King and E. Lacombe for critically reading the manuscript. This work was supported by grants from the Swiss National Science Foundation (3100A0-102107), the European Commission through The Epigenome (LSHG-CT-2004-503433) and Targeted Gene Integration in Plants (TAGIP; 018785) and the Max Planck Society.

Author Contributions M.M., J.R., J.P. and O.M. conceived the study. M.M., J.R., E.B., T.N. and O.M. performed the experiments. K.S., S.O., J.C. and D.W. contributed Illumina sequencing-by-synthesis data and analysis. M.M., J.R., J.P. and O.M. wrote the paper with contributions from all co-authors.

Author Information Reprints and permissions information is available at www.nature.com/reprints. Correspondence and requests for materials should be addressed to J.P. (jerzy.paszkowski@unige.ch) or O.M. (olivier.mathieu@univ-bpclermont.fr).

METHODS

Plant material. EpiRILs⁹, *met1-3* (ref. 5), *kyp-7* (ref. 25), *drm1-2* (ref. 21), *drm2-2* (ref. 26), *cmt3-11* (ref. 26) and *nprpd2a-2* (ref. 27) are all in the Col-0 background. Plants were grown in soil in long-day conditions (growth chamber, 16 h light, 8 h dark, 22 °C).

Genomic DNA analysis. DNA was extracted from leaf tissue with the MaxiPrep kit (Qiagen). Southern blotting was performed as described previously¹⁴ (see Supplementary Fig. 8 and Supplementary Table 1 for probe and primer details, respectively).

DNA methylation analysis. Bisulphite conversion was performed as described previously²⁸, using the Epitect kit (Qiagen). PCR products were cloned using the pGEMT vector (Promega). For each sample, 8–12 clones were sequenced. Sequencing data were analysed with CyMATE (<http://www.gmi.oew.ac.at/en/cymate-index/cymate-v2/>). Primers are listed in Supplementary Table 1.

Expression analysis. RNA was isolated from leaves by using TRI Reagent (Sigma), and RT-PCR was performed as described previously¹⁴. For northern blot and sRNA analysis, total RNA was isolated from flower tissue and enriched for sRNAs with the use of the mirVana miRNA isolation kit (Ambion). Northern blotting for large RNAs was performed with 10 µg of RNAs. Poly(A)⁺ RNAs were purified with the Oligotex kit (Qiagen), and 160-ng aliquots were used for northern blot analysis. sRNAs were detected as described previously^{29,30}.

EVD probes. The probe localizations are described in Supplementary Fig. 8. All EVD probes, except EVD probe C, were prepared as gel-purified PCR products (primers listed in Supplementary Table 1). For EVD probe C, the full-length EVD element was amplified from Col-0 genomic DNA using primers EVD_XhoI and EVD_XmaI (see Supplementary Table 1 for sequence information) and cloned into the pBSK(−) plasmid vector, and the probe was subsequently obtained by digesting pBSK:EVD with XhoI and SspI and gel-purifying the resulting ~2-kb fragment.

Illumina sequencing-by-synthesis (SBS). Genomic DNA libraries from the original Col-0 and the derived *met1/+ nprpd2a* mutant line were prepared as follows. Leaf tissue (0.5 g portions) was ground to a fine powder in liquid N₂ and transferred to a tube containing 10 ml of ice-cold nuclei extraction buffer (10 mM Tris-HCl pH 9.5, 10 mM EDTA pH 8.0, 100 mM KCl, 500 mM sucrose, 4 mM spermidine, 1 mM spermine, 0.1% 2-mercaptoethanol). The homogenized tissues were filtered through two layers of Miracloth (Calbiochem), and 2 ml of lysis buffer (10% Triton X-100 in nuclei extraction buffer) was added to the filtered homogenate and kept on ice for 2 min before centrifugation at 2,000g for 10 min at 4 °C. The nuclei pellet was resuspended in 500 µl of CTAB extraction buffer (100 mM Tris-HCl pH 7.5, 0.7 M NaCl, 10 mM EDTA pH 8.0, 1% CTAB, 1% 2-mercaptoethanol) and incubated for 30 min at 60 °C. After extraction with chloroform/isopentanol (24:1), DNA was precipitated with propan-2-ol and washed with 75% ethanol. Paired-end SBS library preparation, cluster generation and SBS sequencing were performed as described previously³¹, with the modification that a paired-end DNA sample kit (catalogue no. PE-102-1001; Illumina Inc.), a paired-end cluster generation kit (catalogue no. PE-103-1002; Illumina) and a sequencing kit (catalogue no. FC-204-2036; Illumina) were used on a Genome Analyser II (catalogue no. SY-301-1201; Illumina). DNA

fragments of ~300 bp were used for library production and a 42-imaging-cycle recipe was used in SBS sequencing. Image analysis of the output of ten lanes from two Genome Analyser II runs was performed with GAPipeline version 1.0, with default parameters, resulting in 6.81×10^7 and 7.72×10^7 read pairs for the mutant and background samples, respectively. Unfiltered reads were used as input for the SHORE pipeline, version 0.2.4beta (<http://1001genomes.org/downloads>)³¹. Reads were subjected to quality filtering, trimming and subsequent alignment against the unmasked *A. thaliana* reference sequence³² using GenomeMapper in accordance with the SHORE manual. Average genome read coverage was about 16× and 17× for mutant and background samples, respectively. To detect the locations of unknown retroelement insertions, we focused on read pairs derived from the edge of the new insertion sites, where one of the read pairs is sampled from the DNA near the insertion and the other from DNA within the insertion. The expectancy is that such read pairs feature one read with a unique alignment in the vicinity of the insertion site, and the other read aligns repetitively to the origin of the retroelement as well as to all its homologues in the genome sequence. We therefore analysed all read pairs in which one read mapped uniquely in the genome, whereas the read pair featured multiple alignments. We clustered all read pairs for which the unique alignments of the two reads were not farther apart than 500 bp. Additionally, at least 25% of the repetitive mappings of their read pairs did not exceed a pairwise distance of 300 bp. Any 500-bp window featuring a cluster with more than 14 members was considered to be near a potential insertion site, resulting in 547 such sites. From these we excluded clusters that were also discovered in the reads derived from the genomic background sequencing, that featured one of the repetitive alignments nearby, that had their insertion site in centromeric regions or that did not share similar repetitive alignments with other clusters and were thus probably false positives.

25. Mathieu, O., Probst, A. & Paszkowski, J. Distinct regulation of histone H3 methylation at lysines 27 and 9 by CpG methylation in *Arabidopsis*. *EMBO J.* **24**, 2783–2791 (2005).
26. Chan, S. W. *et al.* RNAi, DRD1, and histone methylation actively target developmentally important non-CG DNA methylation in *Arabidopsis*. *PLoS Genet.* **2**, e83 (2006).
27. Onodera, Y. *et al.* Plant nuclear RNA polymerase IV mediates siRNA and DNA methylation-dependent heterochromatin formation. *Cell* **120**, 613–622 (2005).
28. Reinders, J. *et al.* Genome-wide, high-resolution DNA methylation profiling using bisulfite-mediated cytosine conversion. *Genome Res.* **18**, 469–476 (2008).
29. Pall, G. S., Codony-Servat, C., Byrne, J., Ritchie, L. & Hamilton, A. Carbodiimide-mediated cross-linking of RNA to nylon membranes improves the detection of siRNA, miRNA and piRNA by northern blot. *Nucleic Acids Res.* **35**, e60 (2007).
30. Kanno, T. *et al.* A structural-maintenance-of-chromosomes hinge domain-containing protein is required for RNA-directed DNA methylation. *Nature Genet.* **40**, 670–675 (2008).
31. Ossowski, S. *et al.* Sequencing of natural strains of *Arabidopsis thaliana* with short reads. *Genome Res.* **18**, 2024–2033 (2008).
32. The Arabidopsis Genome Initiative. Analysis of the genome sequence of the flowering plant *Arabidopsis thaliana*. *Nature* **408**, 796–815 (2000).

Q&A

Rudi Balling is to be the first director of the planned Centre for Systems Biology, Luxembourg, at the University of Luxembourg.



How did you become a systems biologist?

Having managed large genomics programmes in Germany and seeing their complexity grow, I realized we needed a systems approach that could capture the scale and dynamics of the whole genome. But modern biology lacked engineering technology skills, so I tried to follow the connection between technology and the biological system.

What sparked this interest?

In 2005 I was reading a paper by David Baltimore about the identification of the molecular and cellular mechanisms of host–pathogen interaction when I stumbled across a formula crucial to understanding gene regulation. I had no clue what it meant, so I enrolled in a course in mathematics. I then became more and more aware of the similarities and interdependencies between mathematics and biology.

What are your current projects?

I've just spent seven months at the Massachusetts Institute

of Technology in Boston, working on large-scale mycobacteria sequencing and attending mathematics lectures.

Why are you going to the University of Luxembourg?

Small is beautiful. The university is young, dynamic and industry-friendly. Part of its strategy is to become a big player in biomedical research. Over the next five years it is laying out more than €140 million (US\$200 million) to develop programmes in human and mouse genetics and genomics, establish a biobank and create a Centre for Systems Biology, which I will direct. I couldn't resist this opportunity to build something from scratch.

What's your goal in comparative genomics of humans and mice?

Having tried for years to demonstrate how similar the mouse is to the human, I feel it might be time to explain why the mouse is not like the human, particularly when it comes to clinical symptoms. We need to understand these

differences if mice are to be more reliable models of human disease.

What has your proudest scientific moment been?

In 1986 I linked the mouse development gene *Pax* with Waardenburg syndrome, which is an inherited disease characterized by skull abnormalities and often accompanied in humans by deafness.

Was it challenging to build a large science programme in mainland Europe?

Research funding in Europe, including in Luxembourg, is very good. Europeans cooperate well with each other and have built large-scale biology programmes that could not be done by any single European country. The challenge is that many international research funding programmes require major efforts in coordination and organization. Filling out a European Union form to apply for a significant grant is an art in itself. ■

Interview by Flora Roenneberg

POSTDOC JOURNAL

Am I still a postdoc or not?



Our time in California is coming to an end. My husband has finished gathering deformed frogs by the bucket-load, and we are now off to Colorado for the remainder of his postdoc. California has been good to us, but living in a research house for the summer has presented some personal challenges.

One has been accepting my fate as housewife, mom and the only adult non-researcher in the house. While Brett and the PhD students went about their field and lab work, I sat on the sidelines, cooking

and cleaning. In my weaker moments I wanted to scream out: "I'm not just a housewife, I'm a postdoc too — and by the way, your analysis is wrong!"

But then I began to wonder: can I still call myself a postdoc? Or am I just clinging to that label to feel better about surrendering my career?

Feverishly trawling the web for definitions, I try to reassure myself. Surely a postdoctoral scientist includes all those who engaged in some sort of research after earning their doctoral degree in science? Alas, to my chagrin, all the

definitions point to the fact that, to be a 'postdoc', you actually do have to be employed, working in some type of research.

So I guess I'm not officially a postdoc anymore. But maybe that's OK. Through the peaks and troughs of this chaotic year, I am slowly realizing that my career does not define me. I define my career. ■

Joanne Isaac was a postdoc in climate-change effects on biodiversity at James Cook University, Townsville, Australia. She is now in the United States so that her husband can complete a postdoc.

IN BRIEF

How to talk to a politician

The Federation of American Societies for Experimental Biology (FASEB) has launched an online 'toolbox' to help scientists establish relationships with US congressional representatives.

The toolbox (<http://tinyurl.com/kt8mg8>) includes templates for meeting requests and follow-up letters; brochures and articles that promote research funding; and talking points on the importance of biomedical research.

FASEB argues that there is a critical need for science advocacy in the United States, especially with stimulus-funded biomedical research investments expiring next year. "The economic times right now are quite difficult and we are concerned about the need to sustain growth," says president Mark Lively.

No ethics, no grant

After this year, institutions that receive funds from the US National Science Foundation (NSF) must provide training and oversight in research ethics for their undergraduate and graduate students and postdocs. NSF grant applications must show that young scientists funded by the grants will receive formal training in what the NSF calls "responsible conduct of research (RCR)".

The NSF defines RCR as issues related to publication and authorship, the use of human subjects in research, conflicts of interest and intellectual-property rights. The US National Academies and the National Postdoctoral Association offer RCR training guidelines.

Lucrative industry links

Life-science researchers in US universities receive \$33,000 a year on average from the medical drug and device industry, according to a survey of 1,663 researchers published this month (D. E. Zinner and E. G. Campbell *J. Am. Med. Assoc.* 302, 969–976; 2009). The study found that some receive as much as \$110,000 from industry. More than half (51.9%) said they maintain a relationship with industry. The study found that such relationships provide significant benefits both to the researcher and to science. Among faculty members most involved with industry research, nearly half said it "contributed to their most important scientific work and led to research that would not otherwise have been possible".



Back to the beginning

Some think Osaka can once again be a centre for the biosciences industry. **David Cyranoski** calculates the odds.

Over the past few decades, Osaka University immunologist Tadamitsu Kishimoto has pulled off what most would consider an extraordinary success in translational science. Throughout the 1970s and 1980s, he pieced together the function of interleukin-6 (IL-6), a key molecule for stimulating the immune response. The result was the IL-6-inhibiting drug tocilizumab, approved by the science ministry for treatment of Castleman's disease in 2005. Later, rheumatoid and juvenile idiopathic arthritis were added to the list of indications. Other countries have approved or are considering indications as well. And clinical trials focused on pancreatic cancer are expected to start this month in Japan. Analysts say it could reap US\$2 billion per year in total profits as its indications expand. Already the drug has brought millions of dollars to Kishimoto, who owns most of the patents.

Unfortunately for Osaka and its research community, such success stories are rare. Despite the region's long-standing reputation as a locus for biomedical research, many of the companies that made Osaka famous in the late nineteenth century as a pharmaceutical base, such as Tanabe (now Mitsubishi Tanabe Pharma) and Takeda, have moved their main

research laboratories to the Tokyo area. There, they can plug into the growing bioscience prowess of many universities and research centres in the area and forge closer connections with federal drug regulators and other key government agencies. Even the research wing of the company that developed tocilizumab, Chugai Pharmaceutical, is based in the Tokyo area. And many Western drug companies have stopped doing research in Japan, including Pfizer, GlaxoSmithKline and Novartis.



"I want a postdoc at Osaka to be recognized around the world." — Tadamitsu Kishimoto

But Kishimoto, who is donating all his profits from tocilizumab to a Kishimoto Foundation that will support research at Osaka University, sees potential for the region and for new discoveries. "I want to support the immunological sciences in Osaka," he says, adding that the area's researchers could some day generate another discovery similar to his own.

Nor have other biomedical scientists and policy-makers lost faith in Osaka as a drug-manufacturing base. Programmes such as the government-led National Institute of Biomedical Innovation (NIBIO), set up in 2005, offer opportunities to bridge the gap between basic science and drug discovery. "The idea is that we will get some companies to move their research arms to Osaka, or at least get some biotechs

starting up," says Koichi Yamanishi, director of NIBIO, which is based near Osaka University's campus.

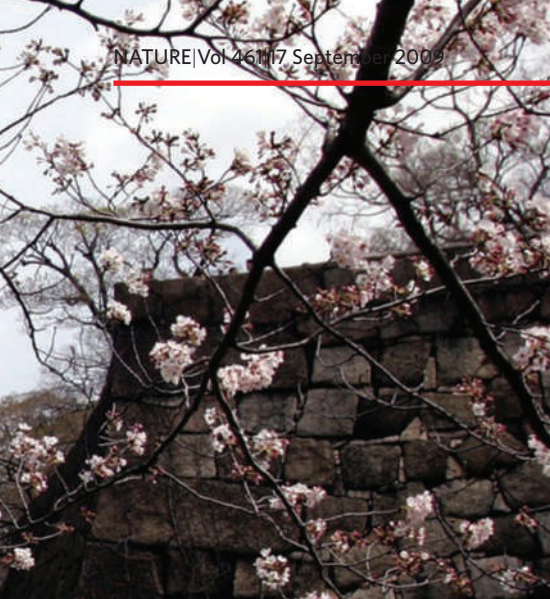
The health ministry is investing an annual ¥13 billion (US\$140 million) in NIBIO to carry out research in bioinformatics, proteomics and immunological regulatory mechanisms. Since 2008, it has been heading two 'super special consortia', large-scale collaborations among institutes throughout Japan. In one, the institute characterizes and standardizes dozens of induced pluripotent stem (iPS) cells that it hopes will become the foundation for national guidelines on the use of iPS cells for toxicological and clinical research. The other, headed by Yamanishi, aims to develop new adjuvants and novel vaccines against multiple infectious diseases.

The jobs no one wants

NIBIO is also charged with amassing, distributing and ensuring the quality of other resources for clinical studies including cultured cells from patients, cynomolgus monkeys and mice. "These are things that neither universities nor industry want to do, and that's been part of the problem," says Yamanishi.

NIBIO resources are shipped nationwide, so companies might not feel the need to rush to Osaka. But there are other reasons, according to the pharmaceutical company Shionogi, which was founded in Osaka in 1878. In 2007, the company set up a ¥5-million programme funding university researchers, starting with ten collaborations and adding five more in 2008. This March, it

E. K. BROWN/EPA/CORBIS



be used for tracers within the body without the need for a thick vault to block extraneous radiation. Osaka University's expertise in imaging will make drug discovery more efficient and boost the success rate of clinical trials, says molecular biologist Tsuneaki Sakata, a deputy general manager at Shionogi's strategic planning division. Shionogi is, however, one of a few drug companies keeping its research in Osaka. The city's biomedical hopes increasingly ride on biotechnology.

Biotech faces moment of truth

Japan's most prominent biotech, AnGes, is at a crossroads. Founded by Ryuichi Morishita, a professor in the department of clinical gene

therapy at Osaka University, AnGes has been developing a hepatocyte growth factor plasmid, Collatogene, since 2001. This is intended to treat peripheral arterial disease, a narrowing of the arteries that increases the risk of heart attack and stroke. Observers have long kept an eye on AnGes as a leader in Japanese biotech. The moment of truth is near. The company has been awaiting the

results of a regulatory review by the Japanese government of a drug application submitted for Collatogene in March 2008. AnGes is now revising its phase III clinical trial application in the United States to meet demands for additional information from the US Food and Drug Administration.

Local government support could nurture successful new biotechs, says Morishita. Two years ago, the governor of the prefecture of Osaka established a biotech strategy team to find ways to support businesses in the region. So far progress has been slow, but the team has set up a US\$10-million biotech venture fund.

Sosho, another biotech firm spun off from Osaka University, finds other advantages to operating in Osaka. It has succeeded in crystallizing some of the most difficult-to-crystallize proteins, and subcontracting this service is its core business. Recently its crystallization and analysis of a protein in HIV led to proposals of a possible catalytic mechanism for the virus and, potentially, new therapeutic targets (M. Adachi *et al. Proc. Natl Acad. Sci. USA* **106**, 4641–4646; 2009).

Sosho's president, Hiroaki Adachi, values proximity to Spring-8, among the world's most powerful synchrotron light sources, in nearby Hyogo prefecture, where the crystallized proteins can be analysed. The area's entrepreneurial atmosphere is also useful, he finds. Sosho, for example, has linked up with Osaka-based PharmAcess, which carries out analysis of proteins, to create a one-stop service.

A pharmaceutical renaissance may seem a distant hope, given the disappearance of some research arms of some Japanese firms from Osaka and the exodus of Western drug companies from Japan. Still, biotechs and the basic research that underpins them could flourish (see 'Building a better research institute in Japan'). If Kishimoto gets his way, resident researchers might replicate his success. Or it could at least be a stepping stone along the way. "I want people to be able to say 'I did a postdoc at Osaka,'" he says, "and have it be recognized around the world."

David Cyranoski is Nature's Asian correspondent.



OSAKA UNIVERSITY

IFREC (above) is the latest stage in Osaka's biomedical history.

invested ¥400 million in a molecular imaging centre on the Osaka University campus. A collaboration with the university's graduate school of medicine, the centre will include cutting-edge positron emission tomography equipment with a self-shielded cyclotron, which produces radioactive isotopes that can

BUILDING A BETTER RESEARCH INSTITUTE IN JAPAN

Traditionally, Japan has had difficulty establishing cutting-edge, scientifically nimble institutions that attract international talent. Osaka University's Immunology Frontier Research Center (IFREC), founded in October 2007, could turn out to be a notable exception.

One of five World Premier Institutes selected by Japan's science ministry, IFREC opened its first building this August. It will receive another US\$20 million from a stimulus package for a second building as well as US\$10 million every year for operating expenses and salary. Already IFREC has enviable expertise. Institute director Shizuo Akira had been the most cited scientist in the world for two consecutive years for helping

to unravel the complexities of the innate immune system (see *Nature* **450**, 475–477; 2007). Other famous Japanese scientists on the roster include Tadamitsu Kishimoto and Shimon Sakaguchi, who has pioneered efforts to understand how an immune system restrains itself to prevent autoimmune disease and allergies.

But plenty of foreigners have joined as well. So far, about 40% of IFREC's postdocs come from outside the country — a figure almost unheard of in Japan. Only two of its 21 principal investigators are foreign, though. That's a far cry from the 30% Akira hopes for. "It's hard especially for those with families, so it's probably more attractive for young singles," he

says, alluding to language and cultural adjustments. He notes that one married candidate had just dropped out at the last minute. Still, Akira refuses to lower the bar. "A lot of others, we can tell, just failed in the United States, so they thought they would try here. We reject them right away."

Akira has started a junior principal investigator programme to recruit young scholars who can take independent positions. The institute offers salaries in the ¥8-million (US\$87,000) range and guarantees three years of research funds, enough to cover a postdoc and a technician, so that researchers do not have to worry about grant applications. The centre also has the ability to adjust

salaries, a rarity in Japan. It took a large chunk of IFREC's budget to land Sakaguchi, who brought his whole team with him.

Those IFREC seeks are scientists with backgrounds in imaging, bioinformatics and systems biology. Akira says these skills could enable one to see the entire immune response rather than just the fragmentary pieces perceived in most studies to date. IFREC's Masaru Ishii, for example, is developing a two-photon microscopy system that can image living tissue up to depths of 2 millimetres, to look at bone homeostasis. "We want people who can discover things that have never been thought of before, not just confirm," Akira says. **D.C.**

Answers from the event horizon

The secrets of the Universe.

Mercurio D. Rivera

If our probe had the power to traverse this event horizon and enter the white hole, what would we find?

A universe very much like your own. Although there are an infinite number of realities beyond your cosmological horizon, each with its own unique physical properties, this conduit could only exist between superjacent dimensions in the transreality-froth. Passage is, in fact, possible if you could download an individual consciousness into a neutrino-flik and sail it across the event horizon at the correct angle.

What is the origin of life?

Biological life as you know it originated in your universe 13½ billion years ago in the heart of heated comets. Heat and cosmic radiation bombarded the carbon dioxide, methanol and ammonia they carried. As they neared their star during their elliptical orbits, the comets' frozen cores thawed, allowing those chemicals to interact in a semi-liquid medium and form rudimentary organic compounds — proteins and amino acids, the building blocks of life. Streaking past the six worlds of this solar system, they rained down those organic compounds in dust that settled in the planet's atmosphere and, eventually, onto its surface. On those planets with a heat source and a liquid medium, these compounds formed lipid membranes that facilitated the formation of self-replicating cells. These evolved into bacteria that over eons developed into simple bio-organisms, the first step in the slow, inexorable climb towards complexity. This process has repeated itself countless times throughout the cosmos over billions of years. This is why your universe teems with biological life.

Non-biological life incubates in the cool ether of dark matter shaped by processes beyond your current level of understanding. However, if our experience is any indication, in time you will come to know such life forms and recognize them as your brothers. In every universe we've explored, biological and non-biological life forms inevitably join together and lift each other to magnificent new heights.

With the data-file we provided detailing our biology, can you advise us how to cure the diseases we identified?

<File attached> This is not the most efficient use of our limited time together as you're already on the threshold of mastering

the genome, which will allow you to resolve these matters yourselves. Genetic engineering will also allow you to create life better suited to exploring your universe.

Does God exist?

Everything in existence has a creator, ad infinitum. Before the Big Bang there was neither time nor space nor matter, but consciousness. Formless. Eternal. Contemplating its creator. And contemplating others like itself that might exist across the infinite bubbles of reality. As time did not exist, we cannot say whether this omni-consciousness existed for a millisecond, a millennium or an eternity. But it jabbed with its thoughts at the weathered fabric between realities and poked an infinitesimal hole. And the entirety of a neighbouring universe — endless space and matter — flooded through that pinhole in a spectacular cosmic eruption. The omni-consciousness found that matter, gave it form, and it revelled in its multitudinous shapes. It discovered that matter — moulded by the flame of time and the winds of evolution — could eventually give rise to its own self-aware components, part of the omni-consciousness, yet separate from it. It delighted in each of the quadrillions of consciousnesses that flickered into and out of existence. It no longer knew loneliness. Time, space and matter continued to expand — prodded into acceleration by the omni-consciousness — hoping in vain to fill every crevice of infinity. This has happened in every bubble of the transreality-froth we've explored.

Can you describe a clean source of unlimited energy that we can utilize?

<File attached> You are already on the verge of discovering this for yourselves. We were very much like you at one time, distracted by the mundane. You're capable of accomplishing more than you can imagine.

What is the nature of reality and what part does quantum physics play in it?

You have a fundamental misunderstanding

of quantum phenomena: particles briefly effervescing into existence, waves of probability collapsing into a particular reality, the entanglement of photons without regard to distance. The reason you can't reconcile these quantum events with the

physical laws of your universe is because they are sparks of a superjacent reality in the froth, where the veil of your universe is worn thin. Eventually you too will be able to peer past that veil, if only for a limited amount of time, as we do now during this exchange.

How can we maintain our cultural and military superiority over those who would seek to undermine our way of life?

You've wasted much time in our prior two exchanges with questions like these. You're better than this. If this is to be our final communication before the fissure closes, you should endeavour to make it more productive.

What question should we have asked you that we didn't?

We wish you would have asked us about something important. About love. About compassion.

We weren't always sure we'd be able to overcome our own primitive aggressive impulses. Our species evolved from an ape-like mammal on a blue water-world circling a yellow sun, and, like you, we engaged in countless meaningless wars during our infancy. This is a familiar pattern, part of the growing pains all sentient species experience. So we take these final few seconds to urge you: imagine the inconceivable, strive for the impossible. The cosmic path is clear; you're on your way. And it's going to be an amazing journey, we promise. ■

Mercurio Rivera (www.mercuriorivera.com) is a New York attorney and science-fiction writer whose stories have appeared in *Interzone*, *Unplugged: The Web's Best Sci-Fi and Fantasy — 2008 Download* (Wyrms Publishing) and elsewhere. Join the discussion of *Futures in Nature* at <http://tinyurl.com/kkh3kt>



JACEY

VEGFR1-activity-independent metastasis formation

Arising from: R. N. Kaplan et al. *Nature* 438, 820–827 (2005)

Molecules such as vascular endothelial growth factor (VEGF) or placental growth factor—critical regulators of tumour angiogenesis—are also thought to mobilize into blood circulation bone marrow-derived cells (BMDCs)¹, which may subsequently be recruited to tumours and facilitate tumour growth and metastasis^{2,3}. A study⁴ has suggested that BMDCs form ‘metastatic niches’ in lungs before arrival of cancer cells, and showed that pharmacological inhibition of VEGF receptor 1 (VEGFR1, also known as Flt1)—cognate receptor for VEGF and placental growth factor—prevented BMDC infiltration in lungs and ‘metastatic niche’ formation. Here we report that blockade of VEGFR1 activity does not affect the rate of spontaneous metastasis formation in a clinically relevant and widely used preclinical model^{5–8}. Therefore, alternative pathways probably mediate the priming of tissues for metastasis.

We assessed the role of VEGFR1 activity in spontaneous formation of macroscopic metastasis after pharmacological inhibition of VEGFR1 (with MF1-blocking antibody). We generated chimaeric C57BL mice in which BMDCs express green fluorescent protein (GFP) after lethal irradiation and restorative bone marrow transplantation (BMT) with cells from Actb-GFP/C57BL mice (BMT-Actb-GFP/C57BL mice). After bone marrow reconstitution, we subcutaneously implanted Lewis lung carcinoma (LLC1/LL2, a BMDC-rich tumour) or B16 melanoma (a tumour with significantly fewer BMDCs). Continuous treatment with MF1 did not delay primary tumour growth compared to non-specific IgG. Moreover, MF1 treatment did not reduce BMDC infiltration in LLC1 or B16 tumours (Fig. 1). We resected these tumours when they had grown to 1 cm in diameter (after 15–17 days) and metastatic foci had already formed in the lungs^{5,6}. As no macroscopic metastases were detectable at the time of primary tumour removal, we measured the number of BMDCs in the lungs of BMT-Actb-GFP/C57BL mice before and after the formation of macroscopic metastases. BMDC infiltration at the time of resection (day 0) and at day 10 was relatively small but readily detectable and comparable with overall BMDC accumulation in tumour-free BMT-Actb-GFP/C57BL mice in both tumour models (Fig. 1).

This suggests a key role for activated pulmonary alveolar macrophages—BMDCs that reside in the normal lung in comparable numbers in tumour-free non-BMT C57BL mice—as opposed to *de novo* BMDC recruitment before spontaneous metastasis. When most mice spontaneously developed macroscopic metastases (day 14), we detected a significant increase in *de novo* BMDC accumulation inside

Table 1 | Quantification of spontaneous metastasis formation after blockade of VEGFR1 activity

Tumour / model		BMT-Actb-GFP/C57BL		C57BL	<i>flt1</i> ^{TK-/-} /C57BL
		MF1	IgG		
LLC1	No. of mice	9/9 (100%)	8/8 (100%)	6/8 (75%)	12/13 (92%)
LLC1	No. of nodules	13 ± 4	15 ± 6	10 ± 4	12 ± 4
P value		0.41		0.32	
B16	No. of mice	9/12 (75%)	9/13 (69%)	6/8 (75%)	7/14 (50%)
B16	No. of nodules	9 ± 4	6 ± 2	2 ± 1	3 ± 2
P value		0.21		0.32	

Data are shown as number of mice with spontaneous lung metastases on day 14 and as number of macroscopic lung tumour nodules per mouse (mean ± s.e.m.). P values were calculated with a Student's t-test and showed no significant difference. In addition, rank comparisons with the Mann-Whitney U-test showed no significant differences

the LLC1 metastatic nodules and in the peri-tumour lung tissue, but not in B16 metastases, akin to BMDC incorporation in the primary tumours in these models (Fig. 1). VEGFR1 blockade with MF1 significantly reduced BMDC accumulation in LLC1 metastases. Surprisingly, VEGFR1 blockade did not decrease the occurrence, number, size or overall burden of spontaneous lung metastases on day 14 after LLC1 or B16 resection compared to control-treated mice (Table 1).

Previous studies in mice genetically deficient in VEGFR1-tyrosine kinase domain (*flt1*^{TK-/-} mice) have shown that MMP-9 is induced by VEGFR1 signalling in lung stromal cells, which facilitates metastatic tumour growth in experimental metastasis models (that is, after intravenous infusion of cancer cells)⁹. When tested in *flt1*^{TK-/-}/C57BL mice, LLC1 growth was similar and B16 growth was slightly delayed compared to C57BL mice. However, when evaluated at day 14, the number of mice with spontaneous macroscopic lung metastases or the number of metastatic nodules was not significantly different (Table 1). CD11b (Mac1) immunostaining in normal and metastatic lungs of these mice showed comparable myeloid BMDC infiltration in *flt1*^{TK-/-}/C57BL and C57BL mice. Finally, since the extracellular domain of VEGFR1 is present on cells in *flt1*^{TK-/-}/C57BL mice, we measured by flow cytometry the number of VEGFR1⁺ cells in circulating blood and in the tumour tissue. We detected no significant difference in circulating VEGFR1⁺ cells in LLC1- or B16-burdened mice, or in tissue-resident VEGFR1⁺ cells in normal lung or LLC1 tumours, and only marginal differences in B16 tumours¹⁰.

In conclusion, VEGFR1 modulates BMDC infiltration and primary/metastatic tumour growth in some models, consistent with previous reports¹¹. However, pharmacological blockade or genetic deficiency in intracellular VEGFR1-TK domain neither eradicated nor significantly altered pre-metastatic BMDC infiltration or early spontaneous metastasis formation in lungs in these models.

METHODS

Flt1^{TK-/-}/C57BL (re-derived from *flt1*^{TK-/-} mice^{10,12}, kindly provided by M. Shibuya, Univ. Tokyo) and Actb-GFP/C57BL mice (Jackson Labs), C57BL mouse-syngeneic LLC1 lung carcinoma (CRL-1642) and B16 melanoma cell lines (CRL-6323)(both ATCC), the BMT and spontaneous metastasis formation models, and confocal microscopy and flow cytometric analyses have been previously described^{5,10,12}. We used Matlab software for quantification. Rat anti-VEGFR1 monoclonal antibody (MF1, a gift from ImClone Systems) or IgG (Jackson Labs) was administered intraperitoneally (20 or 40 mg kg⁻¹) to tumour-bearing mice three times per week¹³. We used Alexa-Fluor-647 (Molecular Probes)-labelled MF1 for flow cytometry. All other antibodies were purchased from BD-Pharmingen.

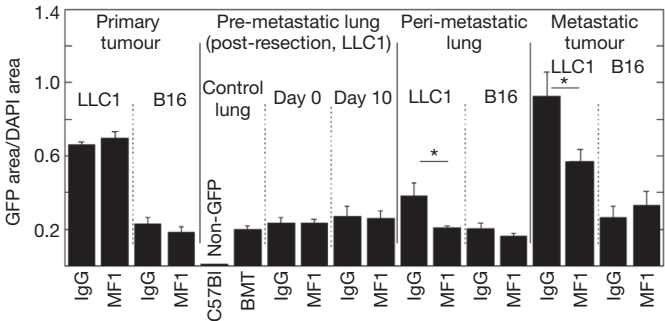


Figure 1 | Effect of blocking VEGFR1 activity on BMDC accumulation in tumours and metastatic lung tissues. The number of BMDCs was calculated as ratio of GFP-surface area to DAPI-surface area (±s.e.m.). DAPI was used to stain the nuclei of all cells (n = 6–8 mice per group). *P < 0.05.

Michelle R. Dawson¹, Dan G. Duda¹, Dai Fukumura¹ & Rakesh K. Jain¹
¹Steele Laboratory, Massachusetts General Hospital, Harvard Medical School, Boston, Massachusetts 02114, USA.
 e-mail: jain@steele.mgh.harvard.edu

Received 20 January; accepted 4 June 2009.

- Rafii, S., Lyden, D., Benezra, R., Hattori, K. & Heissig, B. Vascular and haematopoietic stem cells: novel targets for anti-angiogenesis therapy? *Nature Rev. Cancer* 2, 826–835 (2002).
- de Visser, K. E., Eichten, A. & Coussens, L. M. Paradoxical roles of the immune system during cancer development. *Nature Rev. Cancer* 6, 24–37 (2006).
- Pollard, J. W. *Nature Rev. Cancer* Tumour-educated macrophages promote tumour progression and metastasis. 4, 71–78 (2004).
- Kaplan, R. N. *et al.* VEGFR1-positive haematopoietic bone marrow progenitors initiate the pre-metastatic niche. *Nature* 438, 820–827 (2005).
- Duda, D. G. *et al.* Evidence for incorporation of bone marrow-derived endothelial cells into perfused blood vessels in tumors. *Blood* 107, 2774–2776 (2006).
- Gao, D. *et al.* Endothelial progenitor cells control the angiogenic switch in mouse lung metastasis. *Science* 319, 195–198 (2008).

- Ohtaki, T. *et al.* Metastasis suppressor gene KiSS-1 encodes peptide ligand of a G-protein-coupled receptor. *Nature* 411, 613–617 (2001).
- Padua, D. *et al.* TGFβ primes breast tumors for lung metastasis seeding through angiopoietin-like 4. *Cell* 133, 66–77 (2008).
- Hiratsuka, S. *et al.* MMP9 induction by vascular endothelial growth factor receptor-1 is involved in lung-specific metastasis. *Cancer Cell* 2, 289–300 (2002).
- Dawson, M. R., Duda, D. G., Chae, S.-S., Fukumura, D. & Jain, R. K. VEGFR1 activity modulates myeloid cell infiltration in growing lung metastases but is not required for spontaneous metastasis formation. *PLoS One* doi:10.1371/journal.pone.0006525 (2009).
- Fischer, C. *et al.* Anti-PIGF inhibits growth of VEGF(R)-inhibitor-resistant tumors without affecting healthy vessels. *Cell* 131, 463–475 (2007).
- Hiratsuka, S., Minowa, O., Kuno, J., Noda, T. & Shibuya, M. Flt-1 lacking the tyrosine kinase domain is sufficient for normal development and angiogenesis in mice. *Proc. Natl Acad. Sci. USA* 95, 9349–9354 (1998).
- Wu, Y. *et al.* Anti-vascular endothelial growth factor receptor-1 antagonist antibody as a therapeutic agent for cancer. *Clin. Cancer Res.* 12, 6573–6584 (2006).

Competing interests: R.K.J. is a consultant and receives research funding from AstraZeneca Pharmaceuticals and Dyax Corporation.

doi:10.1038/nature08254

Kaplan *et al.* reply

Replying to: M. R. Dawson *et al.* *Nature* 461, doi:10.1038/nature08254 (2009)

Commenting on ref. 1, Dawson *et al.*² claim that metastasis formation is independent of VEGFR1 activity, contradicting work by us and many others, including the original description of *flt1*^{TK-/-} (VEGFR1-TK^{-/-}) mice in the metastatic setting³. Contrasting the findings by Dawson *et al.*², here we show that VEGFR1 knockdown in myelomonocytic cells eradicates micro- and macrometastases in a non-amputation/resection tumour model.

Hiratsuka *et al.*³ originally reported that *flt1*^{TK-/-} mice have impaired metastatic progression due to a significant reduction in MMP9⁺CD11b⁺ (Mac1⁺) cell infiltration in pre-metastatic lungs following inoculation with LLC or B16 tumour cells. Moreover, several reports demonstrate that inhibition of VEGFR1 by anti-VEGFR1 peptide blocks micro- and macrometastasis, while overexpression of placental growth factor (PIGF), which signals exclusively through

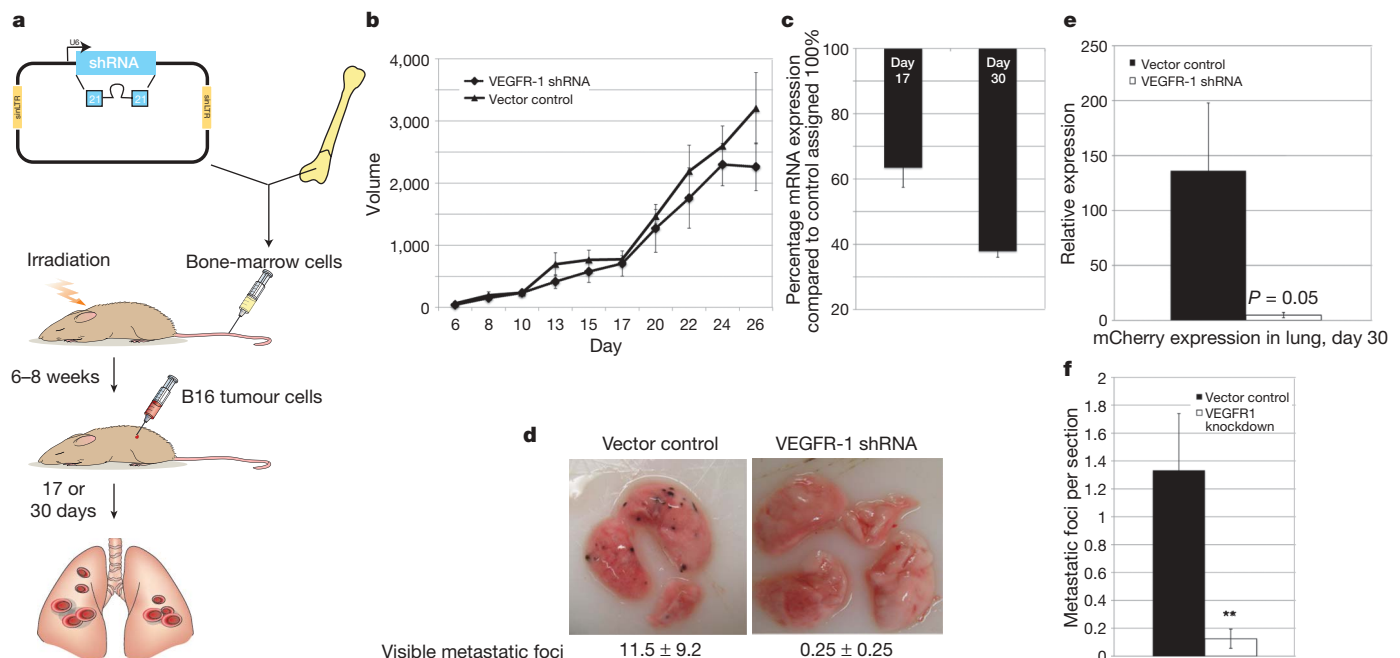


Figure 1 | Knockdown of VEGFR1 in the bone marrow inhibits metastatic progression. **a**, Schematic showing experimental design. Lineage-depleted bone marrow cells were transduced with a lentiviral vector driving ubiquitous expression of VEGFR1 shRNA. Transduced cells were used for bone marrow transplants. Six to eight weeks after transplantation, mice were given subcutaneous injections of mCherry-B16 tumour cells (day 0) and lungs were analysed at day 17 and day 30. **b**, Time course indicating primary tumour volume (v) throughout the experiment; v was calculated using $v = (lwh)/(2\pi/3)$, where l is length, w is width and h is height; $n = 7$ for days 0–17; $n = 4$ for days 18–26. **c**, Quantitative PCR analysis of VEGFR1

expression in peripheral blood of VEGFR1 shRNA mice at days 17 and 30. Data are represented as percentage of mRNA expression compared to average of vector control mice ($n = 4$). **d**, Images illustrating visible metastatic foci in lungs at day 30 after B16 melanoma tumour injection. Data are mean visible metastatic foci per lung \pm s.e.m. ($n = 4$). **e**, Quantitative PCR analysis of tumour-derived mCherry expression in lungs at day 30 ($n = 4$). **f**, Quantification of micrometastatic lesions (defined by >20 tumour cells) visible per lung section at day 30. Six sections per mouse ($n = 4$). Data are mean \pm s.e.m. $**P < 0.01$, Student's t -test.

VEGFR1, increases metastatic spread^{4,5}. Thus, caution is necessary when drawing conclusions from the findings of Dawson *et al.*² regarding the role of VEGFR1 in metastasis.

In deviation from metastasis models used by us and others to document the existence of the pre-metastatic niche^{1,3,6–9}, Dawson *et al.*² use a model whereby primary tumours were implanted in the hind limb and resected by amputation of the leg, thus producing a sizeable wound before examining metastatic progression in the lung. Resection of the primary tumour at this early time point eliminates several tumour-derived paracrine factors, including VEGF-A, TNF- α , TGF- β , S100A8-SAA3^{6,7}, lysyl oxidase⁸, IL6 and versican⁹, factors that have been shown to recruit myeloid cells to the pre-metastatic niche and promote metastatic progression. Thus, it is plausible that removal of the primary tumour and generation of a traumatic wound caused a significant modulation of systemic metastatic niche supportive factors, resulting in disabled recruitment and/or function of VEGFR1-expressing bone marrow-derived cells (BMDCs), at metastatic sites. Although their experimental design may provide a relevant model for the effects of primary surgical resection on metastasis, the findings by Dawson *et al.*² cannot exclude VEGFR1 function in metastasis in non-tumour resection/amputation models.

The methodology used to evaluate metastasis in the lung by Dawson *et al.*² was insufficient and further confounds interpretation of their findings. Metastasis was evaluated grossly by counting metastatic nodules (Fig. 1; ref. 2). More quantitative measures may yield differing results, given both the risk of underestimating tumour burden by gross examination and the role VEGFR1 may play in both micro- and macrometastatic disease.

Many studies have confirmed that infiltration of myeloid cells is essential for metastasis^{10,11}. Current data suggest that many pro-angiogenic myeloid cells express VEGFR1^{12,13}. Furthermore, these studies highlight inhibition of VEGFR1 to target metastasis and PlGF-dependent tumour models in which VEGFR1 signalling is specifically targeted^{10,14}. In these models, there is a profound defect in recruitment of pro-angiogenic and pre-metastatic VEGFR1+ myeloid cells, resulting in a reduction of metastasis.

An additional important consideration is that a complete absence of VEGFR1-mediated signalling in the *flt1*^{TK-/-} mouse model used in this study has not been proven. Given the promiscuity of tyrosine kinase receptors, it is likely that the extracellular domain of the kinase retains some signalling activity through cross-talk with other activated tyrosine kinases or integrins. This residual activity is also supported by the finding that *flt1*^{TK-/-} mice are viable, while mice lacking the full-length VEGFR1 die *in utero*¹⁵. In addition, VEGFR1 is expressed in many different cell types, including haematopoietic, endothelial and stromal cells, and non-cell-specific deletion of VEGFR1 in this model does not specifically address the role of its expression in BMDCs.

To address this question and expand on the brief functional analyses of VEGFR1 inhibition presented in ref. 1, we used lentiviral vectors to knockdown VEGFR1 activity specifically in BMDCs (Fig. 1a). Consistent with other reports^{1,3,7}, inhibition of VEGFR1 by short hairpin (sh)RNA did not significantly alter primary B16 melanoma tumour growth (Fig. 1b, c). However, analysis of the lungs 30 days post-implantation revealed a pronounced reduction in the number of metastatic lesions and total tumour burden in mice with

bone marrow transduced with VEGFR1 shRNA as compared to controls (Fig. 1d–f). This observation indicates that VEGFR1 expression by BMDCs is necessary for metastatic tumour progression. Thus, a genetic approach using a non-amputation/resection model can serve to resolve the controversy surrounding the function of VEGFR1 in mediating metastasis. We hope that the field of metastatic initiation continues to move forward, given its profound impact in the clinical setting. Moreover, anti-PlGF/VEGFR1 agents may provide novel means to block micrometastasis in an adjuvant setting and inhibit metastatic progression.

Rosandra N. Kaplan^{1,2,6}, **Rebecca D. Riba**^{1,2}, **Stergios Zacharoulis**^{1,2,6}, **Anna H. Bramley**^{1,2}, **Loïc Vincent**⁴, **Carla Costa**^{1,2}, **Daniel D. MacDonald**^{1,2}, **David K. Jin**⁴, **Koji Shido**⁴, **Scott A. Kerns**^{1,2}, **Zhenping Zhu**⁸, **Daniel Hicklin**⁸, **Yan Wu**⁸, **Jeffrey L. Port**⁵, **Nasser Altorki**⁵, **Elisa R. Port**⁷, **Daide Ruggero**⁹, **Sergey V. Shmelkov**^{1,2,4}, **Kristian K. Jensen**^{1,2}, **Shahin Rafii**^{3,4}, **David Lyden**^{1,2,6} & **J. Wels**^{1,2,§}

¹Department of Pediatrics and the Children's Blood Foundation Laboratories, ²Cell and Developmental Biology, ³Howard Hughes Medical Institute, ⁴Genetic Medicine and ⁵Surgery, Weill Cornell Medical College of Cornell University, 1300 York Avenue and

⁶Department of Pediatrics and ⁷Surgery, Memorial Sloan-Kettering Cancer Center, 1233 York Avenue, New York, New York 10021, USA. e-mail: dcl2001@med.cornell.edu

⁸Imclone Systems Incorporated, New York, New York 10014, USA.

⁹Fox Chase Cancer Center, Philadelphia, Pennsylvania 19111, USA.

§Extra author.

- Kaplan, R. N. *et al.* VEGFR1-positive haematopoietic bone marrow progenitors initiate the pre-metastatic niche. *Nature* **438**, 820–827 (2005).
- Dawson, M. R., Duda, D. G., Fukumura, D. & Jain, R. K. VEGFR1-activity-independent metastasis formation. *Nature* **461**, doi:10.1038/nature08254 (2009).
- Hiratsuka, S. *et al.* MMP9 induction by vascular endothelial growth factor receptor-1 is involved in lung-specific metastasis. *Cancer Cell* **2**, 289–300 (2002).
- Marcellini, M. *et al.* Increased melanoma growth and metastasis spreading in mice overexpressing placenta growth factor. *Am. J. Pathol.* **169**, 643–654 (2006).
- Taylor, A. P. & Goldenberg, D. M. Role of placenta growth factor in malignancy and evidence that an antagonistic PlGF/Flt-1 peptide inhibits the growth and metastasis of human breast cancer xenografts. *Mol. Cancer Ther.* **6**, 524–531 (2007).
- Hiratsuka, S. *et al.* The S100A8-serum amyloid A3-TLR4 paracrine cascade establishes a premetastatic phase. *Nature Cell Biol.* **10**, 1349–1355 (2008).
- Hiratsuka, S., Watanabe, A., Aburatani, H. & Maru, Y. Tumour-mediated upregulation of chemoattractants and recruitment of myeloid cells predetermines lung metastasis. *Nature Cell Biol.* **8**, 1369–1375 (2006).
- Erler, J. T. *et al.* Hypoxia-induced lysyl oxidase is a critical mediator of bone marrow cell recruitment to form the premetastatic niche. *Cancer Cell* **15**, 35–44 (2009).
- Kim, S. *et al.* Carcinoma-produced factors activate myeloid cells through TLR2 to stimulate metastasis. *Nature* **457**, 102–106 (2009).
- Fischer, C. *et al.* Anti-PlGF inhibits growth of VEGF(R)-inhibitor-resistant tumors without affecting healthy vessels. *Cell* **131**, 463–475 (2007).
- Shojaei, F. *et al.* Bv8 regulates myeloid-cell-dependent tumour angiogenesis. *Nature* **450**, 825–831 (2007).
- Du, R. *et al.* HIF1 α induces the recruitment of bone marrow-derived vascular modulatory cells to regulate tumor angiogenesis and invasion. *Cancer Cell* **13**, 206–220 (2008).
- Lin, E. Y. *et al.* VEGF restores delayed tumor progression in tumors depleted of macrophages. *Mol. Oncol.* **1**, 288–302 (2007).
- Luttun, A. *et al.* Revascularization of ischemic tissues by PlGF treatment, and inhibition of tumor angiogenesis, arthritis and atherosclerosis by anti-Flt-1. *Nature Med.* **8**, 831–840 (2002).
- Hiratsuka, S., Minowa, O., Kuno, J., Noda, T. & Shibuya, M. Flt-1 lacking the tyrosine kinase domain is sufficient for normal development and angiogenesis in mice. *Proc. Natl Acad. Sci. USA* **95**, 9349–9354 (1998).

doi:10.1038/nature08261